Radiance Trends and Magma Flux at Hot Volcanoes

Thesis

Radiance Trends and Magma Flux at Hot Volcanoes

A thesis presented for the degree of Doctor of Philosophy

By

Stephen James Donegan

B.Sc (Hons), Anglia Polytechnic University (1997); M.Sc, University of Leicester (1998)

Department of Earth Sciences

The Open University

April 2004

ProQuest LLC.
789 East Eisenhower Parkway
P.O. Box 1346
Ann Arbor, MI 48106 – 1346

Abstract

In this thesis I use a range of remote sensing data, ranging from simple ground-based radiometers, through thermal imaging cameras to the latest space-based high-resolution multispectral instruments for the observation of active volcanic phenomena. I consider small scale degassing events within the Pu`u`O`o crater of Kilauea volcano, and provide a critique of the often used "dual-band" method for obtaining sub-pixel thermal information. I go on to use improvements of this method to provide the basis of a comparison of the existing and well understood Landsat7 ETM+ with the new EO-1 ALI with respect to volcanic observations.

This thesis falls into two main sections. In the first section I use thermal data from an array of simple radiometers operated by the University of Hawaii and the USGS Hawaii Volcano Observatory, coupled with basic RSAM data to identify degassing events at a small vent within the Pu`u`O`o crater. I relate these events to the semi-diurnal and fortnightly lunisolar tides. I show that there is a very weak relationship between these events and the semi-diurnal tide, but conversely a stronger relationship exists between the degassing events and the fortnightly tide. I show that these observations are consistent with previous observations of the fluctuating levels of the 1919 Halema'uma'u lava lake on Kilauea, and may be used as part of a synergistic approach to aid understanding of the complex Pu`u`O`o plumbing system. I go on to use thermal diffusion modelling to determine the mass of ejecta associated with certain degassing events that appear to possess well defined cooling curves in the radiometer data. By using software modelling iteratively applied to thermal diffusion equations, I show that the time taken for the temperature record from a spattering event to return to the ambient temperature is a function of the mean size of spatter blebs associated with the event. I use both laboratory tests and actual data recorded from a two month study period in 2001. This section of the

thesis highlights that it is possible to obtain high-value information of active volcanic events without the cost of satellite data.

The second section of this thesis deals mainly with analysis of the dual-band method for extracting sub-pixel thermal information from multispectral satellite data. I use high-resolution ground based thermal imagery to generate simulated EO-1 ALI pixels, which can be adjusted to simulate a variety of likely volcanic scenarios. I apply the dual-band method to this simulated imagery and analyse the response in detail. I show that it is preferable to use relative estimates of sub-pixel thermal structure rather than the exact estimates provided of the resulting factors. I also show how the results returned by the dual-band method may change if the lava flow is angled with respect to the instrument, due to the combined effects of the slope angle down which the flow is moving and the instrument look angle.

I finally assess the response of the recent EO-1 Advanced Land Imager to the remote sensing of lava flows in comparison to the established Landsat7 ETM+. I use the dual-band technique as the basis of this comparison, despite the flaws previously discussed, because it provides a valid means of comparison that remains valid if used in a relative fashion. I show that the EO-1 ALI is of great use for the remote sensing of lava flows due to the provision of extra channels within the SWIR, not present on the ETM+. These extra channels provide better solutions to the dual-band method as they are less susceptible to saturation and better placed within the spectrum for detection of volcanic products, than those of the ETM+.

Acknowledgements

Well, the seemingly impossible has happened! I have managed to at least get this in a WHOLE 2 hours before the deadline... I have enjoyed immensely all the work as well as the people I have had the fortune to meet with during the course of my time here at the OU. There are plenty of people to thank here and I shall endeavour to try and remember most of them!

Firstly I want to thank Dave Rothery and Andy Harris for being my supervisors. They have done an excellent job here and have managed what must be an all time chapter review turnaround time. 4 Hours! I am especially indebted to them both for putting up with the last minute nature of most of my chapters, and doing a valiant effort to correct my dodgy grammar. This PhD was funded by a grant from the Open University.

In the same line I must also thank Luke Flynn of the University of Hawaii for giving me the opportunity to work at the University of Hawaii and also his help and encouragement in getting my first paper (based on chapter 6) sorted out. Thanks again to Andy Harris who, along with Luke, introduced me to the three little ducks and put up with my stumbling around and constant swigging on Gatarade trying to keep up with them on marathon treks across the flow field at Kilauea.

Harry Pinkerton (Lancaster University) also very kindly put me up for a month and made available much of his thermal camera data obtained from Mt Etna. Harry also provided a lot of advice, as did Mike James also at Lancaster. I must also thank Christina Heliker and others at the USGS Hawaii Volcano Observatory for giving me the opportunity of a lifetime and to spend 2 months perched on the rim of Kilauea Caldera looking out at what must be the best office window view ever. Thanks also to Hazel Rymer and Martin Wooster for spending the time examining this thesis and patiently suggesting how it could be improved.

There are many other people at the OU to thank. Firstly, John Murray who let me come along on one of his annual Etna trips and see my first ever volcanic eruption – awesome in the strictest sense! Dan Morgan, whose appreciation of both the fine art of home brew stout, curry and thermal diffusion has helped this thesis get where it is (big and thick!). Others include Dick Carlton for his help with my computer woes and Ashea Tambe for her help in various matters of working with the OU. Vic, Andy, Dawn, James, Yvonne, Siobhan, Aaron, Olwyn, the list goes on.. (I have probably forgotten someone...). All of them helped make life at the OU and Milton Keynes much easier and enjoyable with this old TGIF crew. I do miss those beers now I am in the world of work. In the ETB stub also, Anne, Luke, Kirti, Elske, Marie-Noelle etc for all making the boys room (5) a more pleasant working environment.

I must also thank Rob Wright for introducing me to the Makiki Inn and the infamous foot-long meatball sub – my life (and waist) will never be the same again! Dawn, for her very great help in aiding me in understanding all the forms etc that life in Hawaii required. Dawn, also showed me how to boogy-board, and with the aid of Lucia, Leon and John for helping me get sorted during my time in Hawaii. I still often dream of cocktails at the Surfrider Sheraton in Waikiki.

Back at home, of course there's Andy (Struan?), Stig, Matt, Anna who all provided excellent encouragement and always there in case I felt the need to splash out and buy anyone a pint. No after YOU Andy! (pub door manouverings –he who enters first, buys the first beer...).

A big thankyou must also go to Matt Pritchard, Stuart White, and Chris Mutlow at Rutherford Appleton Laboratory (NEODC), for firstly giving me a job and something useful to do, as well as very kindly let me finish the write-up and print this thesis.

And finally.. I want to thank my family: Mum, Dad, Michael, Catherine and Elizabeth (and Sam!) for being excellently supportive, bailing me out of motorcycle induced fiscal restrictions, always there when you need them and of course, being great. I am blessed to have a family such as mine. And of course, there's someone reading this probably wondering where she's got to…

Well the biggest and best thankyou (last, but most certainly not the least!), goes to my wife , Elly. She did me the favour of marrying me 2 years ago and no-one could ever be as supportive or thoughtful as she is. During the last hectic 6 months, she has looked after me so well, picked up the pieces when it all seemed too much and made me laugh when I needed cheering up (and just before I finished the corrected version of this thesis, gave me a beautiful baby son, Daniel Joseph). I could not have done this without her.

So Elly, this is for you.

Table of Contents

Table of Figures

1. Remote Sensing of Active Volcanoes

1.1.Introduction

In the past three decades satellite remote sensing has become invaluable for volcanology. Satellites with ever improving instruments have been and continue to be launched providing capabilities far exceeding the earliest instruments used to identify and record volcanic activity. There is now a wide variety of data available ranging from high-resolution hyperspectral imagery, to radar data providing topographic and interferometric maps. Improvements in spaceborne instruments have been accompanied by the steady development of ground based instruments, such as Fourier transform spectroscopy (FTIR) and thermal imaging cameras, able to provide a detailed temperature map of the surface of a lava flow at millimetre scale. The ever greater availability of technology at decreasing costs has provided the opportunity to obtain real-time thermal data from an active volcano using a network of simple radiometers telemetering the data to a ground-station. The creation of such a network on Kilauea volcano, Hawaii, has set the precedent for installation of similar networks on Mt Etna and Stromboli volcanoes. Such a wide range in types and capabilities of data at a variety of scales has enabled new insights into volcanic processes.

In this thesis I describe the observation of volcanic activity using various remote sensing instruments at a range of scales. I begin with the observation of small scale phenomena at Kilauea volcano using a system of simple radiometers, and I show how such relatively simple data can be used to extract meaningful information on volcanic activity. I then show how high quality data from a thermal imaging camera can be used to simulate the appearance of active lava flows and the like within data from an orbiting satellite instrument. This is an attempt to gain an intimate understanding of the response of the

"dual-band" model to realistic lava flows. This model has been fundamental in extracting estimates of the thermal composition within instrument pixels, and until recently it has been difficult to relate the results provided by this model to actual lava flows. I show the deficiency of this model, but also propose how the results may be optimised. In the final chapter I compare the performance of the established Landsat7 Enhanced Thematic Mapper plus (ETM+) and the recent EO-1 Advanced Land Imager for volcanological remote sensing. The ALI has been touted as a "technology try-out" for future Landsat instruments and uses extra channels situated at more useful wavelengths for the purposes of remote sensing of volcanoes. If any new Landsat instrument incorporates technology from the ALI, then this should considerably improve the quality of volcanic imagery.

Within this thesis I aim to show how simple ground based radiometers and thermal imaging cameras can be used synergistically with spaceborne instruments to enhance further understanding of volcanic processes. I also provide insights into the performance and future use of established instruments and methods.

1.2.The advantages of remote sensing of active volcanoes

Thermal anomalies have been identified at active volcanoes since the earliest satellites were launched with the intention of studying weather patterns (Francis & Rothery, 2000). Since the first generation of Earth observation satellites in the late 1960s and early 1970s, much work has been completed using such observations to analyse levels of activity and to track ongoing eruptions. It quickly became apparent that satellite-based instruments provide the useful ability to detect and track the progress of eruptions at remote volcanoes, reducing the need for costly field studies.

Satellite remote sensing offers many advantages to the study of volcanoes. A single satellite image may cover many thousands of square kilometres, depending on orbit and

instrument. Such a scene can provide coverage for an entire volcano so analysis of activity on the volcano in its entirety may be assessed. The Geostationary Environmental Operational Satellite (GOES) obtains imagery of almost an entire hemisphere. Two such GOES satellites (GOES 8 & 10) provide coverage of both seaboards of the USA. Data returned from such instruments can cover the entire Hawaiian island chain including all volcanoes on the Big Island (Harris et al, 2002). As the GOES instruments are geostationary, and are therefore positioned over a single point on the Earth's surface, they are at an ideal vantage point from which to continuously monitor volcanic activity. GOES 8 & 10 return images every 10-15 minutes, and thus it is possible to detect any new volcanic activity very quickly (Harris et al, 2002). A drawback of GOES data is that due to its high orbit, and therefore wide coverage it has a very large pixel size ranging from ~1 - 14 km. Pixels (or picture element) are the smallest elements from which an image is constructed, and in remote sensing terms will relate to a discrete area of the Earth's surface. Low resolution instruments such as GOES have large pixel sizes, whereas high resolution imagery such as IKONOS (a commercial imaging instrument) have much smaller pixel sizes. Because a single GOES scene images most of an entire hemisphere, pixels at the edge of a scene will be significantly larger than those pixels directly beneath the instrument (nadir) due to the curvature of the Earth. However, the size of a GOES scene allows detection of the spread of eruption clouds and their interaction with weather systems on a global scale.

Instruments placed on satellites that orbit at lower altitudes generally have smaller scene dimensions and correspondingly smaller pixel sizes. Optimal pixel size and scene dimensions are of course dependant on the intended use. Weather satellites require synoptic imagery covering large areas (i.e GOES), whereas instruments intended for observation of land surfaces such as the Landsat7 ETM+ may require higher resolutions (smaller pixels). The ETM+ has a pixel size of ~30m and a swath width of 183km. The ERS-2 ATSR2 orbits at a similar altitude to the ETM+ and has a pixel size of 1km, yet a

swath width of 512km. Due to the physical limitations of the instruments themselves, the space available for detectors at the focal plane of an instrument may be limited. Pixel size is therefore a function of the instrument optics, orbital altitude and the detector population on the focal plane (Cracknell, 1998). Instruments such as the ETM+ and EO-1 ALI with pixels sizes of 30m (or smaller, depending on channel) have scene dimensions large enough to observe an entire volcano in the majority of cases. Satellite imagery can therefore provide a unique vantage point from which to observe an eruption.

Most Earth observation satellites have been placed into an ingenious sun-synchronous polar orbit. This is so that as the platform moves along its orbit north to south (typically), the Earth rotates underneath. After a certain period, the platform will have passed over every point on the Earth's surface. The time taken for a particular instrument to image the entire Earth's surface is a function of the orbit and swath width of the instrument. The Landsat7 ETM+ has a 16 day repeat orbit, but any location on the Earth's surface is imaged roughly once every 3 days, even at the Earth's equator. This means that the ETM+ passes over exactly the same location every 16 days, but because of the instrument swath width, which extends either side of the satellite ground track, the same location will be covered at an oblique angle within the imagery every 3 days. Instruments with a wider swath will cover the Earth's surface in a shorter period.

This ability to repeat observations of any volcanic events (cloud cover permitting) is very useful for tracking the progress of eruptions. The July 2001 eruption of Mt Etna (Italy) was tracked on a daily basis by a number of NOAA Advanced Very High Resolution Radiometer (AVHRR) instruments (Pergola et al, 2003). Information obtained from this imagery was used in models to predict the likely extent of the resulting lava flows (Harris & Rowland, 2001). Therefore, near-real time imagery of an entire volcanic flow field can be used to constantly update eruption predictions, a feat very difficult to accomplish otherwise (Rothery et al, 2001). Furthermore, the nature of measurements from

spaceborne instruments allows a long time series of consistent observations to be constructed. This allows not only a record of activity at any particular volcano to be made, but the ability to readily spot new activity and to identify short and long period trends in thermal activity (Rothery et al, 2001).

One vital aspect provided by satellite instruments is the ability to obtain information on reflected and emitted radiation, not only at the visible wavelengths, but also within other regions of the electromagnetic spectrum. Channels situated at other wavelengths within the Short Wave Infra-Red (SWIR: 0.8→3μm) and Thermal Infra-Red (TIR: 3→15μm) in addition to the Visible and Near Infra-Red (VNIR: 0.5→0.8μm) can be used to infer properties of surface materials (i.e. minerals, vegetation) as well as the properties of the atmosphere itself (relative amount of water vapour) (Drury, 1987). The integration of information from a number of channels can aid in the identification not only of the differing geologic units upon a volcano but also the differing effusive volcanic products. For example channels located within the TIR of the MODIS (MODerate resolution Imaging Spectro-Radiometer) can detect the presence of volcanic ash within the atmosphere, as well as gases such as SO_2 associated with a volcanic eruption (Realmuto, 1995).

Observations of volcanoes using satellite instruments provide the ability to obtain data at a variety of scales and at differing wavelengths. Consistent observations may be accumulated over many years, providing an easily accessible archive that would otherwise be expensive to obtain in terms of time, material cost and personnel safety. To obtain such quality information using any other method would not be feasible. It is for these reasons that satellite remote sensing of volcanoes has become an invaluable tool for volcanology.

1.3.Problems associated with the remote sensing of active volcanoes

Despite the many advantages to conducting observations of volcanoes using remote sensing instruments, there are some drawbacks. One of the major problems encountered when conducting remote sensing of volcanology is that associated with sensor saturation. This occurs when the amount of detected electromagnetic radiation from a feature such as a lava flow or lava lake exceeds the instruments ability to meaningfully record the level of detected radiance. As a consequence, the Digital Number (DN) representing the scaled radiance will record a nonsensical value that is not representative of the actual emitted radiance from the feature. This problem is compounded by the initial design of remote sensing instruments, many of which are intended for weather observations or for high resolution remote sensing of the Earth's surface using reflected solar radiation rather than the emitted radiation from volcanic features. The placing of many of the spectral channels used by these instruments within the visible and infrared regions is such that they are designed to be used with reflected solar radiation and because of this they are more likely to saturate. This is a consequence of the Planck relationship which predicts the emitted radiation for any object at any temperature depending on wavelength, and is fully described in the following section.

The net result of this problem is that many spectral channels are placed in the visible and the near infrared (VNIR) and are not generally sensitive to volcanic activity. Another popular placement of spectral channels is within the thermal infrared to make use of atmospheric "windows" and features relating to water vapour within the atmosphere, and are therefore of meteorological use. However, these channels are highly sensitive to the emitted radiance from even moderate volcanic features (fumaroles, cooling lava flows) and therefore saturate easily. Indeed, until recently very few remote sensing instruments have been designed with the express intent of making useful remote sensing observations

of volcanoes and are intended for making meteorological use or for general purpose multi-spectral applications such as vegetation mapping. It has not been until recently that specific channels have been placed on remote sensing instruments (such as the Advanced Land Imager –ALI, described and discussed later within this thesis) to detect volcanic activity without easily saturating. However, due to the cost of development and use of remote sensing instruments and the relative user communities all instruments are at best, compromises, given the available resources.

A related problem is that weather satellites often have very large pixel sizes, required so as to provide a large scale synoptic vantage point. Pixels from such geostationary instruments (and therefore in a very high orbit) may be of the order of ~10 km, and therefore it is often difficult to detect the presence of even moderate volcanic activity in such large pixels. The reverse is true of relatively high resolution imaging satellites such as the Landsat7 ETM+. A pixel size of 30m x 30m may often be only slightly larger (if at all) of such features as lava flows, vastly increasing the likelihood that the emitted radiance from the flow will saturate many of the spectral channels.

Another major problem with remote sensing of volcanoes is the problems associated with scattering and absorption of the emitted radiation from such features as lava flows, eruptive activity and so on. The problem in many of these cases is that the heat generated by such features can distort the viewing conditions to an unknown degree that make it difficult to relate to atmospheric models as MODTRAN and LOWTRAN. This problem is further compounded by the gases and pyroclastic material associated with cooling lava flows and eruptive activity. Volcanoes in many cases tend to be in elevated positions, increasing the likelihood of cloud cover which will inhibit the creation of long term observations. All these factors make at best, any measurement of a thermal feature associated with active volcanoes an informed estimate and cannot be considered as absolute values.

The history of remote sensing of volcanoes has therefore been a catalogue of often ingenious methods combining data from several different instruments to provide the required spectral coverage to obtain meaningful information. The "dual-band" method that uses assumptions based on prior knowledge of eruption temperatures and two spectral channels of instrument data to return an estimate of the likely thermal structure within a pixel of satellite data is just such a method. This method is described and used later in this thesis. Others have used the way in which an instrument saturates to gain meaningful observations of eruptions (Dennis et al, 1998). The use of many different instruments together to study volcanoes introduces a margin or error, mainly due to the fact that the two (or more) instruments did not obtain their data at *exactly* the same time due to differing orbits. Volcanic activity can vary at very short timescales, and therefore it is difficult to relate a number of observations that may be separated in time by as much as a few days.

In section 1.6 I discuss these issues further when discussing the application of remote sensing techniques to the study of volcanoes.

In this thesis I tackle some of these issues, namely by using ground based thermal cameras that provide almost real time dedicated high resolution observations of such volcanic phenomena as degassing and molten spattering events from a single volcanic vent. Such systems can be considered a cheaper alternative to space-based remote sensing instruments, yet provide very high quality data and are tailored specifically to the observation of volcanic phenomena. I also look into the viability of some of the ingenious methods often used to deduce information from a *sub* pixel resolution. I will also conduct a comparison between established remote sensing instruments such as the Landsat7 ETM+ and the ALI, an instrument with spectral channels placed with the express intention of obtaining unsaturated high resolution data from active volcanic phenomena.

Although I have listed some of the drawbacks of remote sensing of volcanoes, they in no way exceed the advantages provided by the many forms of remote sensing. As

technology and financial resources improve with time, these current drawbacks can be overcome or worked around.

1.4.Obtaining surface temperature from IR instruments

All satellite instruments record a DN (Digital Number) value for each pixel. The DN is related to the total detected electromagnetic energy (radiance) within the footprint of the pixel. As the instrument platform travels forward along the orbital path a mechanism scans the area within the instrument optical field of view and translates the scene into an array of DN values which comprise a single image of the scene. There are many different methods by which this is accomplished, and an overview may be found in Lillesand & Keiffer (1994). The DN is stored an 8, 12 or 16 bit (depending on instrument), which can then be received and subsequently converted using empirically derived algorithms into a spectral radiance value representing the total emitted and reflected radiance within the pixel.

The emitted spectral radiance from a surface or material can be calculated at a given wavelength if the temperature of the surface or material is known. Planck's law governs this relationship between spectral radiance emitted from a black body source and its temperature.

$$L_{(\lambda,T)} = c_1 / \pi\lambda^5(\exp(c_2/\lambda T)-1) \qquad \text{(Equation 1.1)}$$

Where L is the emitted spectral radiance (measured in Wm^2 μm^{-1}), λ is the wavelength and T is the temperature (in K). The values $c_1=3.742x10^{-16}$ Wm^2 and $c_2=1.4388x10^{-2}mK$. Figure 1.1 depicts a set of curves for materials at different temperatures showing this relationship between emitted spectral radiance and wavelength.

As the temperature of the material increases, the emitted spectral radiance increases at all wavelengths. Importantly however, the wavelength at which the maximum emission of radiance occurs shifts towards shorter wavelengths. This function of Planck's law is known as Wien's Law. Note from figure 1.1 the non-linear rate at which the emitted spectral radiance increases with increasing temperature. As a result of this relationship, surfaces similar to the surface temperature of the Sun will emit radiance strongly within the visible region, hot volcanic surfaces in the region of 800-1100°C emit within the SWIR. Cooler surfaces such as solar heated ground will emit most strongly within the TIR.

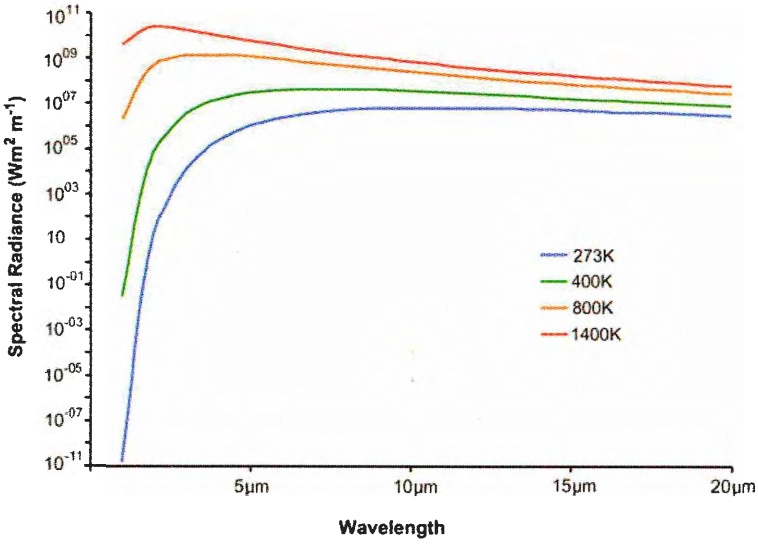

Figure 1.1: The relationship between emitted spectral radiance (log scale) and wavelength for materials at different temperatures.

Most imaging satellite instruments operating within the visible or infrared regions are designed to detect reflected solar radiation at the visible, VNIR and SWIR wavelengths. Solar irradiance at SWIR wavelengths warms the Earth's surface which then re-emits this energy at longer SWIR and TIR wavelengths due to the thermal properties of surface materials. Remote sensing of this re-emitted energy at TIR wavelengths is possible during the night as solar illumination is not required.

These relationships are simplified in figure 1.2, which shows that irradiance from the Sun is not only absorbed and re-emitted by the surface but also scattered, absorbed and re-emitted by the atmosphere. Any radiance emitted by such hot features as volcanic activity or vegetation fires will therefore be mixed with the solar radiative signal in daytime images. Therefore the at-satellite radiance may be described as:

$$L_{satellite} = \Sigma \left(L_{volcanic} + L_{atmosphere:Scattering} + L_{atmosphere:\ reflection} + L_{ground}\right)$$

(Equation 1.2)

The Earth's atmosphere is not transparent to electro-magnetic radiation at all wavelengths but possesses "windows" at various regions within the spectrum. In these atmospheric windows any signal is relatively unattenuated by preferential absorption by the various atmospheric gaseous species and aerosols. In order to observe the Earth's surface at wavelengths other than the visible, then instrument channels must be located within these atmospheric windows.

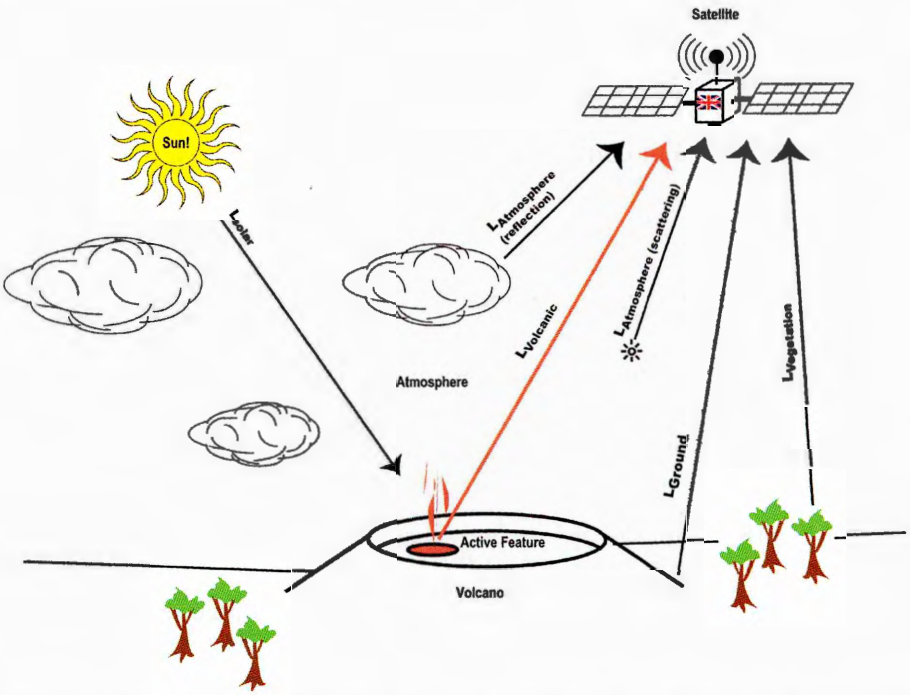

Figure 1.2: Diagram showing the relationship between emitted and reflected electromagnetic radiation and their interaction with the Earths atmosphere. The Earth's surface is illuminated not only by reflected solar irradiance, but also by the heat emitted from the surface warmed by the solar irradiance. Light is also scattered by the atmosphere (i.e. clouds and aerosols –dust). The reflected and re-emitted solar irradiance from the surface varies with wavelength, depending on the properties of the materials on the surface (i.e. bare rock, vegetation). A volcanic component, independent of the solar signal may be derived by radiance emitted from such features as fumaroles and heated ground which emit mainly within the TIR, through to lava flows and lakes which emit strongly within the SWIR. Many studies use night-time imagery to accurately detect the volcanic signal without contamination by the solar derived signal.

The at satellite radiance may be better represented for the detected radiance at a given wavelength by equation 1.3, which takes into account the radiance emitted and reflected by the atmosphere which varies with wavelength.

$$R_\lambda = \tau_\lambda \varepsilon_\lambda L_{(\lambda,T)} + \tau_\lambda \rho_\lambda R_{\lambda D} + R_{\lambda U} \qquad \text{(Equation 1.3)}$$

This is because the emissivity ε, which effectively describes the "efficiency" of the emitted radiance from a surface, varies with wavelength. τ describes the atmospheric transmissivity, which also varies with wavelength (hence the presence of atmospheric

windows). The spectral reflectivity of the surface, represented by ρ varies also with wavelength. These values may be obtained from published sources (i.e Buongiorno et al, 2002). $R_{(\lambda D)}$ is the reflected radiance from the surface and $R_{\lambda U}$ is the radiance emitted from the atmosphere itself. The radiance emitted from the ground surface is $L_{(\lambda,T)}$, and this value may be used to estimate the surface temperature. In the case of remote sensing of active volcanic surfaces, this value is a combination of the emitted radiance from both the hot volcanic surface as well as the re-emitted radiance due to solar heating.

Once the radiative component, $L_{(\lambda,T)}$ has been calculated from a pixel value at a particular wavelength then it is possible to calculate a surface temperature for the pixel by rearranging equation 1.1 (Equation 1.4). This single value is referred to as the Pixel Integrated Temperature (PIT).

$$T_\lambda = c_2 / \lambda([c_1 \lambda^{-5} / \pi R_\lambda] + 1) \qquad \text{(Equation 1.4)}$$

The temperature value T_λ representing the PIT returned by equation 1.4 must be considered unrealistic, especially in the case of such instruments as an ALI (Advanced Land Imager) or Landsat7 ETM+ pixel as it us unlikely that the entire $900m^2$ pixel is thermally homogenous. For a pixel with a IFOV comprising a volcanic situation, this scenario is especially unlikely as a certain fraction of the pixel may be at an elevated temperature due to the presence of a lava flow (or other feature such as a fumarole or lava lake). The remaining pixel fraction will be occupied by the ground surface at the ambient temperature. The calculated PIT will therefore represent the integrated temperature of all surfaces emitting within the pixel's Instantaneous Field Of View (IFOV). This value will be a weighted average as a consequence of Planck's law, as those areas within the IFOV emitting at higher volcanic temperatures will emit disproportionately more radiance than those surfaces at ambient temperature, as indicated by figure 1.1.

1.5. Loss of surface thermal information within a pixel

The inherent loss of information within the PIT is a big problem when considering application of the data to a volcanic context. For instance, the activity of a basaltic lava flow may be gauged by how fast it is moving, which is dependant on the rate of supply of fresh lava (effusion rate), the slope angle (if any), the viscosity of the lava and the rate of cooling. The velocity of the flow itself may be gauged by the relative proportion of cracks within the chilled upper crust exposing the hot inner regions of the flow. A flow moving relatively fast may display a great number of cracks, such as a'a flows that are associated with high effusion rates (Lipman & Banks, 1987). Temperatures ranging from the ambient (~20-30°C) to the near-magmatic temperatures of fresh lava > 1100°C may all be present within a single pixel (Pinkerton et al, 2002). This concept is represented in figure 1.3.

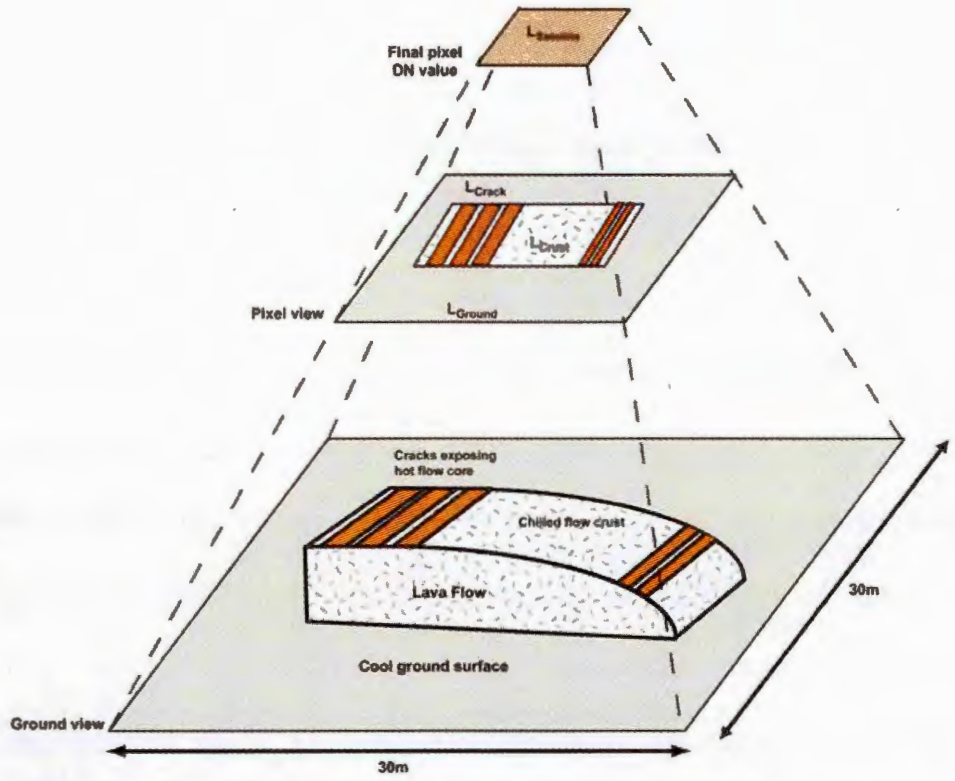

Figure 1.3: Schematic showing how a ground surface with a complex thermal composition is represented ultimately by a single pixel value, the Pixel Integrated Temperature (PIT) when imaged in a single spectral channel. In this scenario a simple model lava flow comprised of just two components, hot cracks exposing the flows inner core and the cooler flow crust (Crisp & Baloga, 1990). This simple flow is crossing a cool ground surface, therefore rendering this model as three main thermal components, L_{crack}, L_{crust} and L_{ground}. This model is described on page 41.

The inherent loss of information that occurs when using a single PIT to represent a thermally diverse surface such as that depicted in figure 1.3 can be represented graphically. A single PIT may be considered as the extent to which a thermal image of full resolution, where no thermal detail is lost, can be 'zoomed' out resulting in a single value. By considering the intermediate 'zoom out' levels between the original FLIR camera image and the final single PIT value it is possible to analyse the loss of thermal detail between the two extremes.

In figure 1.4 a thermal image of the central portion of an active channelised lava flow on Mt Etna shows the wide thermal variation present. In order to simulate zooming out, ultimately to a single PIT value, an integral radiance value was calculated for a number of the camera pixels. The temperature of the new single 'pixel' representing this

integral radiative value was calculated using equation 1.4. As the distance from the target flow was increased then the number of original camera pixels integrated to compose a new pixel also increases. This is shown in figure 1.4 as the increasingly pixellated images at the various zoom-out levels. A single temperature pixel will finally be calculated from the integral of all the original camera pixels, and this is identical in concept to a satellite PIT.

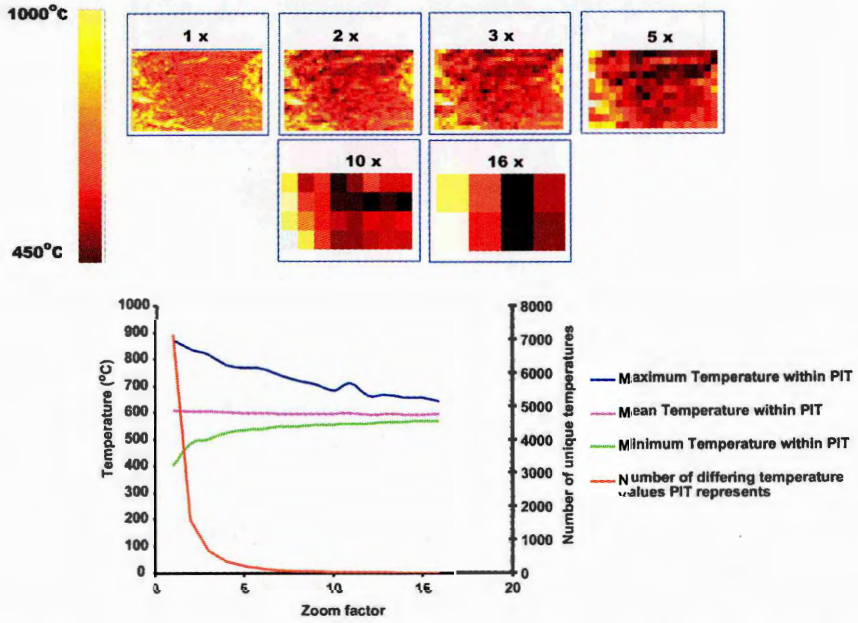

Figure 1.4: Graphical representation of the loss of thermal information from a simulated PIT calculated from thermal camera imagery of the central section of a lava flow on Mt Etna. Dark areas represent relatively cool regions, whilst light areas indicate higher temperatures. Images at the top display the effect of calculating the mean temperature, after conversion to radiance, for an increasing number of pixels. This is the equivalent to a 'zoom-out' function. The graph displays the statistical variation of temperature for each zoom-out step, and also the loss of thermal detail as the number of unique temperatures within each image. Each successive image has fewer component pixels, but the images have been rescaled to equivalent sizes to highlight the loss of information graphically.

As the number of pixels recalculated to create a single pixel within each successive zoom increases, the image becomes less sharp and any visible structure within the image loses definition.

The thermal structure of a lava flow with a well defined medial crust evident in the un-zoomed image at 1x, is still apparent at zoom-out 2x and even 3x. Some structure is apparent at zoom-out 5x, but by 10x and 16x the highly pixellated nature of the image precludes any basic visual identification of the image as that of an active lava flow. At

zoom-out 17x the image processing returns a single pixel. This loss of visual information with increasing zoom value is quantified within the graph represented in figure 1.4. The maximum temperature decreases and the minimum temperature increase, tending towards the mean temperature.

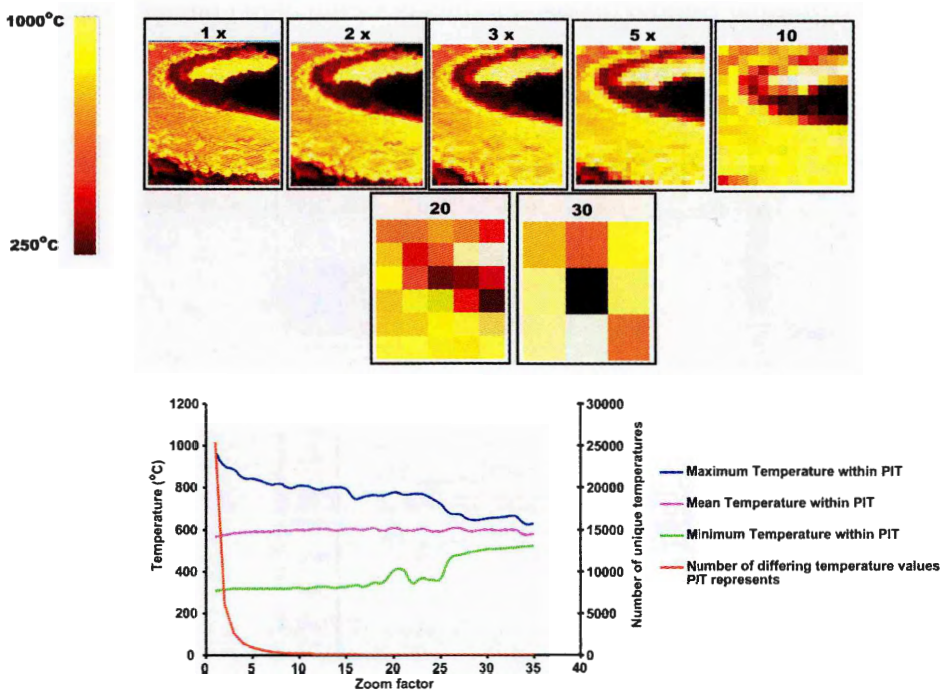

Figure 1.5: Similar representation of the loss of thermal information as in figure 1.4, but with the addition of cool surrounding ground.

Figure 1.5 displays a similar set of images and graph to that displayed within figure 1.4, but additional to the lava flow is an amount of material related to the channelised flow levees and cool background. This is a more realistic satellite pixel composition than that shown in figure 1.3. This makes for a distinct visible structure which is apparent in many of the zoomed out images until at least zoom-out 20x. As the images tend toward a single pixel value at 40x (not shown in figures 1.4 or 1.5), the visible thermal structure is still evident suggested by the presence of the dark centre pixel at 30x representing the medial flow levee.

Both figures 1.4 and 1.5 highlight the loss of thermal information present at the ground surface within the PIT calculated from a single pixel DN. They also show however, that it is possible to discriminate between the main thermal components of the scene (hot cracks, cool crust or background) at even high "zoom-out" factors. In section 1.7 I shall describe an ingenious method to extract the main thermal components from a single pixel, if multispectral information is available.

1.6.Application of remote sensing to volcanology

Until relatively recently with the introduction of such instruments as the Hyperion (Hyperspectral imager) and the Advanced Land Imager (ALI) onboard the EO-1, volcanologists with a taste for remote sensing had to be content with the provision of data from instruments primarily intended for weather or surface imaging (Francis & Rothery, 2000). None of these systems were designed specifically for monitoring active volcanism, and few had channels situated within the desirable mid-SWIR portion of the electromagnetic spectrum. The Planck relationship predicts that for active lava flows with initial surface temperatures in the region 900-1100°C, then an instrument channel placed in the region of ~1.2μm would be ideally situated for the remote sensing of high temperature volcanic features (Donegan & Flynn, 2004). Many of these instruments also had relatively poor spatial resolution, often in the range of 1-4km pixels sizes.

A further problem with the use of instruments originally designed to operate with reflected solar radiation in the SWIR, or from low emitted temperatures within the TIR is saturation of the instrument channel over hot volcanic surfaces e.g. Wooster & Rothery, 2002; Harris et al, 1999B; Rothery et al, 1988. Saturation of a channel occurs when the detected incoming radiance from the pixel exceeds the dynamic range of the sensor, and the DN records the maximum value within the bit range, or returns nonsensical values.

For example, the Landsat7 channel 6 (TIR) is designed to detect radiance values in accordance with a typical range of Earth surface temperatures of –28 to 50 °C. However, due to the Planck relationship any volcanic surface of any extent (i.e. a lava flow crossing the pixel) will emit more radiance at the channel 6 wavelength than the channel is designed to cope with, and will saturate the channel.

However, any volcanic surface filling even a significant fraction of a VNIR pixel will not emit sufficient radiance to register within the channel dynamic range. For example, Landsat7 channel 4 is situated at the longer wavelength region of the VNIR with the intention of studying spectral features in reflected solar irradiance from vegetation. An active lava flow filling a sizeable portion of a Landsat7 30m channel 4 pixel is likely to register only weakly (Wright et al, 2001).

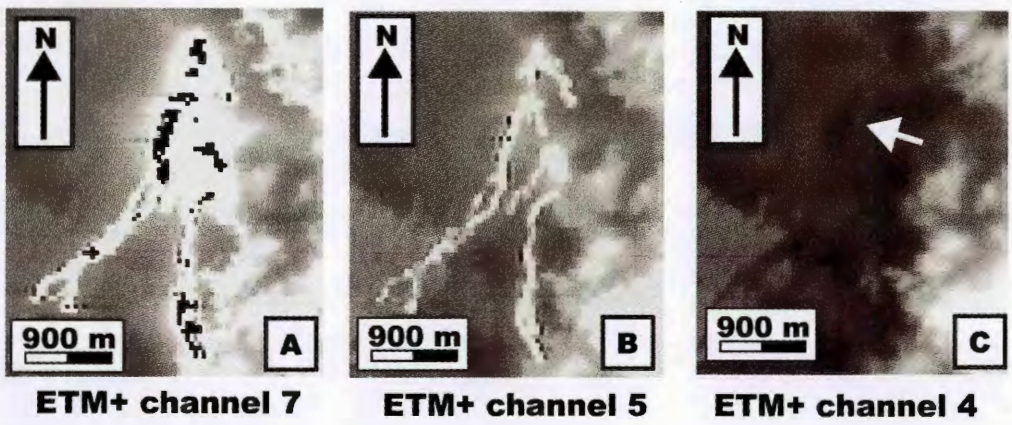

Figure 1.6: Example of active lava flows in channels 7, 5 and 4 of the Landsat7 ETM+. In these greyscale images the lighter tones indicate increasing detected radiance at the relative wavelengths. Note that the forked feature in panels A and B is the lava flow and is easily distinguishable in the SWIR channels 5 and 7, but is barely detectable in the VNIR channel 4. The dark pixels in the centre of the lava flows in A & B are where the instrument has saturated and recorded zero radiance.

Figure 1.6 clearly displays this effect, in which an active lava flow is clearly evident in the Landsat7 SWIR channels 5 and 7 (panels A and B) yet is barely detectable in the VNIR channel 4 (panel C). The lava flow considered here resulted from the July 2001

eruption of Mt Etna and was actively fed from a number of vents in the upper region of the image. This flow has actually easily saturated ETM+ channel 7, indicated by the presence large numbers of dark pixels in the centre of the flow which is the most active region with the largest amount of fresh exposed lava at > 1000°C due to the movement of the flow. In this case these DN's are represented by zero's therefore resulting in these dark pixels. The apparent blurring obscuring the clarity of the lava flow in A and B is due to the extreme saturation of the sensor and the local scattering of emitted radiance by the associated gas and ash present at such an effusive eruption. These effects render the data from these pixels useless. A similar problem has also affected channel 5, albeit to a lesser extent. However, figure 1.6C shows the same lava flow in the VNIR channel 4 and is barely detectable. Figure 1.6 highlights the problem of high resolution instruments such as the Landsat7 ETM+, as the SWIR channels are easily saturated, yet the VNIR channels (channel 4) barely register the anomalous thermal radiance of the very active lava flows associated with the July 29th 2001 eruption of Mt Etna.

These shortcomings however, have not stopped the development and use of techniques to extract information on active volcanic phenomena from a wide variety of instruments. The choice of systems used has fallen into two broad categories, those systems with frequent repeat times for a given location on the Earth's surface yet with lower resolution imaging capability. The second category consists of those instruments with relatively high resolution, yet infrequent overpasses of the same location. Both these approaches have their relative merits.

1.6.1. Remote sensing of volcanoes using low/medium resolution instruments

Instruments that tend to have lower image resolutions are often those that have the fastest repeat cycle for a given location, due to the large physical area within a single

scene. Instruments with frequent overpasses of the same location, such as a volcano, provide the benefit of rapid detection of the onset of new activity (Harris et al, 1997b). One of the many problems involving the remote sensing of volcanoes is local weather conditions, that often obscure the summit region and any activity present. This effect is exacerbated by the tendency of volcanoes to be high, increasing the chance of cloud cover. Frequent overpasses will increase the likelihood of making successful observations of the volcano, free or only partially obscured by cloud.

The first instrument to be used in this way was the NOAA AVHRR (Advanced Very High Resolution Radiometer) series of instruments, with a nominal pixel size of 3-4km (Harris et al, 1997b). This instrument provided repeat capability over the span of just a few days, and methodologies developed with this series of AVHRR instruments from the mid-1970s to the late 1980s set the trend for introduction of instruments with a similar repeat capability. Instruments such as the Along Track Scanning Radiometers (ATSR) on the ERS series of satellites complimented the later series of AVHRR instruments (Wooster & Rothery, 1997A). These instruments benefit from the addition of higher pixel resolutions and a greater number of spectral channels. These instruments have been successfully used to record radiance trends at many volcanoes, including Mt Etna and Mt Erebus in Antarctica (Harris et al, 1997b) since the mid 1990s. Such an archive can be used to help spot new phases of activity at currently active volcanoes as well as to spot new activity. More recently the MODIS instrument on the Terra satellite has been used to provide a near-real time volcanic alert system available online. The improvisation of an algorithm using a ratio of two of the MODIS TIR bands enables an alert to be generated if a threshold value has been exceeded, indicating the onset of new activity (Wright et al, 2004). This system has proved extremely affective at spotting new activity, and logging known activity. For example new activity had been found at the remote South Sandwich islands in the Southern Ocean. This activity has only recently been confirmed by survey

expeditions, and the MODIS data helped the interpretation of the ongoing eruption (Patrick et al, 2004).

The detection of thermal anomalies preceding an actual volcanic eruption by such instruments is well documented (Francis & Rothery, 2000), (Harris et al, 1998). Thermal anomalies within instrument channels reflect DN values elevated above the immediate surrounding DN values. The elevated DN value may be related to the presence within the pixel ground footprint of a high temperature source, such as a lava flow or lava lake. This source may not fill the pixel area sufficiently to saturate the instrument channel, but must be extensive enough to raise the overall PIT. In certain cases a thermal anomaly may be indicated by the saturation of a channel (Oppenheimer, 1993). Such anomalies may be related to the opening of a new vent within a summit crater, effusion of lava flows or as subtle as an increase in fumarolic activity. All such phenomena may indicate the imminent onset of eruptive activity. The magnitude of the thermal anomaly, and which instrument channels the anomaly registers in, indicates the likely cause of the anomaly. Anomalous pixels in SWIR channels may be related to high-temperature products such as the effusion of a new lava flow. Thermally anomalous pixels within TIR channels may relate to the heating of the ground surface on a volcano by the close proximity to the surface of a new magma body within the volcanic edifice. This may be accompanied by an increase in fumarolic activity with heating of the surrounding ground (Oppenheimer & Francis, 1997). Such an increase may be only a few degrees above the ambient temperature, and therefore visible only within TIR channels.

The recent addition of a second MODIS instrument aboard a second polar orbiting satellite, Aqua, doubles the likely frequency of observations. Although these observations are not available every 10-15 minutes as in the case of the geostationary GOES instruments, polar orbiting medium resolution instruments such as the ATSR2 and MODIS provide good coverage and the ability to detect activity with a broad range of spectral

channels. The increasing number of such medium resolution instruments in orbit increases the likelihood of the detection of the onset of new eruptive activity, which can then be incorporated into global alert schemes such as those that warn air traffic of volcanic ash hazards.

1.6.2. Remote sensing of volcanoes using high resolution instruments

The second major category of instruments used in the application of remote sensing to volcanology, is those with low repeat frequencies but relatively high image resolutions. Typical of such instruments is the Landsat series of Thematic Mapper instruments. These instruments have proved the workhorse of high resolution remote sensing volcanology, with much research completed involving these instruments.

In the early 1970s the first dedicated Earth observing satellite was launched, and was subsequently dubbed Landsat1. This platform was host to just 2 instruments, a visible imager and the Multi-Spectral Scanner (MSS). Both these instruments had pixel sizes of 80m. Over the following 10 years two similar Landsat satellites were launched with similar imaging capabilities. Landsat4 was launched in 1984 with the first Thematic Mapper (TM) instrument, which possessed additional spectral channels in the SWIR and TIR. Landsat5 was a duplicate of Landsat4 and launched in 1984 and currently operational[1]. The most recent Landsat7 incorporated the Enhanced Thematic Mapper, with additional channels. The TM/ETM+ series of instruments provide a range of spectral channels within the visible/VNIR/SWIR and TIR regions. This series of instruments has been subject to an evolution towards ever increasing pixel resolutions and numbers of spectral channels that has been accompanied by the range of applications for which these instruments may be used.

[1] At the time of writing (April 2004), according to http://landsat7.usgs.gov/history/Land4-5.html

This wide spectral coverage, coupled with high pixel resolutions of 30m has proved most useful to the remote sensing of volcanoes, despite the non-ideal location of the various channels for the purposes of detecting hot volcanic products without saturation (Flynn et al, 2001). Despite this, channels 5 and 7 are still very sensitive to the emitted radiance from such features as active lava flows or lava lakes, but saturate relatively easily due to the dynamic ranges of these channels (Flynn et al, 2001).

Application of Landsat imagery to the study of volcanoes has ranged from the use of the TIR channel 6 in identifying the extent of fumarolic activity and the location of sub-surface lava tubes at Kilauea volcano, to mapping the extent of active lava flows and lava lakes and predicting the associated mass flux from an eruption (Harris et al, 1998). The smaller pixel size of the TM/ETM+ allows easier constraint on the dimensions of features such as lava flows or lakes as it is likely that many pixels (at $30m^2$) will be required to cover the entire feature. Thermal anomalies such as these, may only register within a single $1km^2$ pixel from such instruments as MODIS, ATSR2 and AVHRR (Harris et al, 1999). Imagery from the TM/ETM+ instruments has been used extensively in the development of techniques to extract information on the sub-pixel thermal resolution, which I briefly describe later (Flynn et al, 2001).

Although the Landsat series of instruments have provided the majority of high-resolution data since the 1970s, recently new systems have been launched that build upon Landsat's capabilities. In 2000 the Terra satellite was launched carrying several instruments (including MODIS), one of which is the Advanced Spaceborne Thermal Emission and Reflection radiometer (ASTER). ASTER was intended to compliment the MODIS instrument by providing high resolution imagery in 14 separate spectral bands with pixel sizes ranging from 15m (VNIR) through 30m (SWIR) to 90m (TIR). Certain of these channels approximately correspond to TM/ETM+ channels but the provision of extra channels results with an instrument of improved capabilities for remote sensing of

volcanoes (Harris et al, 1999B). The Terra platform has a repeat cycle of 16 days. However, the ASTER instrument has a limited ability to aim at points of interest either side of the Terra platform's ground track, reducing the repeat time to ~5 days (Ramsey & Dehn, 2004). ASTER is a very versatile instrument and is also capable of producing Digital Elevation Models (DEM) based on the differing look angles between two channels. The greater thermal sensitivity of ASTER has been used to help predict eruptions from Aleutian and Kamchatkan volcanoes (Ramsey & Dehn, 2002), and also to provide high resolution data to the KVERT warning system for air traffic developed by the Alaskan Volcano Observatory (AVO).

The Earth Observer 1 (EO-1) satellite was also launched in 2000 and carried onboard a hyperspectral imaging instrument (Hyperion) and the Advanced Land Imager (ALI), an instrument considered as a technology "try-out" for a future replacement Landsat instrument (Donegan & Flynn, 2004). Both these instruments apply new solid state and 16 bit technologies not previously attempted in space based instruments. Hyperion is the first orbital hyperspectral imaging instrument with 236 continuous channels within the VNIR and SWIR, in addition to a high resolution pixel size of 30m. Hyperion provides the ability to map the continuous spectral response of surface materials within this wavelength range, and is invaluable to the study of volcanoes as in certain of these channels remain unsaturated over active volcanic surfaces (Flynn & Donegan, 2002).

The ALI possesses the same spectral channels as the ETM+ (apart from the TIR channel6), so that these new technologies may be directly compared with the ETM+ (EO-1 follows Landsat7 by 1 minute at the same orbital altitude). Vitally however, the ALI possesses extra channels within the SWIR. These channels are in the region where active volcanic features emit the most radiance according to the Planck relationship (Donegan & Flynn, 2004). This extra channel is of paramount importance to the future success and development of remote sensing of volcanoes. In chapter 6 of this thesis I conduct an

investigation into the relative performance of the Landsat7 ETM+ and EO-1 ALI with respect to remote sensing of volcanoes, and a detailed discussion of these instruments is given therein.

The availability of data from these and any future instruments derived from them, ensures that it will be possible to further develop current methods for extracting sub-pixel information. Even with instruments such as ASTER or ALI providing data at pixel resolutions from 15-30m, there is still a large amount of vital thermal information obscured by the single PIT value. This information is highly useful for the assessment of parameters relevant to aspects of the eruption, such as effusion rate. In the next section I show how multiple channels from high resolution instruments such as the TM/ETM+, ASTER or ALI can be used to extract information on the likely thermal composition *within* a pixel.

1.7.A method for obtaining sub-pixel information

The ability to transcend the PIT information barrier allows an estimate of the overall thermal composition of the ground surface to be made. This method is important for the analysis of any pixel with a footprint incorporating material at an anomalously elevated temperature due to volcanic activity. Products of volcanic activity may only rarely fill the pixel IFOV of even high resolution instruments such as the ETM+ or ASTER. It is therefore imperative to obtain information on not only the relative portion of the pixel occupied by the products of volcanism, but also if possible, information of the thermal make-up of the volcanic signal within this pixel fraction.

For example, the total emitted radiance from a lava flow may indicate whether the supply of new lava driving the flow has changed, or whether the physical dimensions of the flow have changed in response to the local topography. Lava flows that advance relatively rapidly, such as a'a flows on Kilauea, possess cracks within the chilled crust

exposing the hot inner core. The rate at which the flow crust material is entrained into the flow interior, opening new cracks is a function of the velocity of the flow advance (Lipman & Banks, 1987). Rapid forward movement will quickly rupture the cooler flow crust, and therefore active flows will display larger numbers of cracks exposing high temperature material and therefore increasing the overall radiative output of the flow. The speed at which a flow advances is related to the rate of supply of new lava to the flow, the width and depth of the channel, the gradient down which the flow is moving as well as the viscosity and crystallinity of the lava itself (Harris & Rowland, 2001). The supply of material feeding the flow is related to the effusion rate of the eruption. Of course, there are many other factors affecting the movement of the flow, such as the cooling of the flow due to local conditions as well as the topography (i.e. is the flow filling a depression?).

Therefore the ability to distinguish the relative amount of fresh exposed lava may ultimately allow an estimate of the effusion rate and mass flux of an ongoing eruption.

Dozier (1981) outlined a method (subsequently dubbed the 'dual band' method) that used the non-linear nature of the Planck function to estimate the temperatures and component fractional areas of a thermally diverse pixel. This was originally developed to identify sub-pixel sized industrial hotspots and gas flares (Matson & Dozier, 1981). The model was later used by Rothery et al (1988) to investigate high temperature volcanism.

In the case of a pixel with an IFOV incorporating an active lava flow moving over a much cooler ground surface (or a lava lake surrounded by cooler material), the Planck function predicts different radiant temperatures for the same pixel in 2 distinct instrument channels of separate wavelength. This method models the pixel radiance value in the 2 selected channels in terms of two fractional areas possessing differing surface temperatures, using two non-linear simultaneous equations (equations 1.5 & 1.6).

$$R(\lambda_1,T) = \tau \varepsilon (P_C L_1(\lambda_1,T_C) + (1-P_C) L_1(\lambda_1,T_H)) \qquad \text{(Equation 1.5)}$$

$$R(\lambda_2,T) = \tau \varepsilon (P_C L_2(\lambda_2,T_C) + (1-P_C) L_2(\lambda_2,T_H)) \qquad \text{(Equation 1.6)}$$

$R(\lambda_1,T)$ and $R(\lambda_2,T)$ are the in-channel measured radiances obtained from the instrument data in the two respective channels. T_C and T_H are the temperatures of the cool thermal component, at fraction P_C and hot component P_H (equivalent to $1-P_C$) respectively. $L_N(\lambda_N,T_H)$ and $L_N(\lambda_N,T_C)$ are the resulting modelled radiances derived from the Planck function, emitted by the relevant thermal component in either channel calculated at the appropriate wavelength. τ is a factor of atmospheric transmission and thus attenuation of the signal from the surface to the instrument, whilst ε defines the emissivity of the radiating surface. By the assumption of any 1 of the 3 unknowns (fractional area, T_H or T_C) then the simultaneous equations can be solved (Rothery et al, 1988).

1.7.1. Use of the dual-band procedure for analysis of volcanic surfaces

In order to apply this method to any pixel incorporating hot volcanic material, it is necessary to idealise the wide thermal composition present on any such surface. Crisp & Baloga (1990) proposed that a simple two component lava flow model would more accurately represent the surface of a lava flow than the thermally homogenous models or 'non-radiant crust models' used previously. These earlier models assumed erroneously that the cooler crust at 100-400°C could be ignored as only the hot component at 700-1000°C+ radiated sufficiently enough to be used (Harris et al, 1999). The Crisp & Baloga model represents an active lava flow surface comprising two thermal components: a cooler component representing the lava flow's chilled crust, and a hot component representing a fraction of exposed flow core due to processes within the active flow (Crisp & Baloga, 1990). This model can be most accurately applied when the lava flow in question fills the

entire IFOV of the pixel. This model is the one represented in figure 1.3 (p28). For the application of this model to the dual band method, T_H relates to the temperature of the cracks exposing the hot flow core within the relatively cool crust at temperature T_C. We can relate this model to the flow imaged within figure 1.4 (p29), which consists of two endmember temperatures-the hot cracks and cooler crust.

This model has been widely applied to a range of scenarios involving hot volcanic material located within an instrument pixel. Early application of the dual band method to volcanoes included the estimate of surface temperatures of a lava dome within Lascar volcano, Chile (Francis & Rothery, 1987). Work by Oppenheimer (1991) found that it is easier to assume the hot component T_H within the model as this value is easier to constrain than the cool component T_C which can vary widely depending on a large number of factors. Assumption of T_H became the accepted form for the application of the dual-band method to volcanic products.

However, in the likely situation where a lava flow or other volcanic feature does not fill the pixel IFOV, then a third component must be used to denote the temperature of the surrounding ground surface (Oppenheimer, 1993). This problem is highlighted within figure 1.5 (p30), which shows the presence of the three main thermal components, hot cracks, cool crust and cooler surrounding materials. One of the problems with the addition of this extra component is that when using Landsat TM/ETM+ data, only channels 5 and 7 are useful. Channel 6 within the TIR (and therefore sensitive to emitted radiance from cool surrounding ground) has a different pixel size of 60m. This is because it is difficult to obtain high resolution imagery at TIR wavelengths due to the extra sensor integration time required (effectively, the sensor needs a longer "exposure" time to gather the required TIR sample) and the orbital speed of the platform. Therefore, the TIR channels have a larger IFOV as a trade-off. Any surface sufficient to register or saturate channels 7 & 5, is unlikely to register within channel 4. This problem led to the use of low resolution

instruments such as the AVHRR or ATSR2 for estimating the temperature of the cool third component (Harris et al, 1999C). Any feature such as a lava flow or lake which may fill a significant fraction of a $30m^2$ TM/ETM+ pixel will only fill a small fraction of the $1km^2$ pixel size of instruments such as the ATSR2. Thus, the TIR channels of these instruments may not saturate over active volcanic features such as these, as the contribution of emitted radiance from these sources is only a fraction of the entire pixel area. This approach was used by Harris et al (1999C) to help identify mass fluxes from lava lakes such as those at Mt Erebus, Antarctica.

The dual-band method is at best an approximation of the representation of active volcanic features using spectral radiance measured in different channels. The biggest problem with this approach is that it fails to represent the wide thermal variations present on the surface of lava flows. However Wright & Flynn (2004) found that it is possible to use 5 to 7 differing thermal components that better represent the thermal variation on a lava flow surface. These thermal components may be resolved using a number of the 66 possible SWIR channels available using the Hyperion hyperspectral instrument. It is clear that the future use of such imagery may provide more accurate estimates of sub-pixel thermal resolution for volcanic features, but at present data from Hyperion is limited by the high transmission and storage requirements and hampered by its narrow 7.5km swath (Flynn & Donegan, 2002). In the interim period until similar instruments with greater data procurement and availability are ready, I discuss in chapters 4 and 5 improved interpretation of dual and triple band results using the ALI.

1.8.Aims and structure of this thesis

In this thesis I aim to show how a variety of remote sensing applications, ranging from the use of simple radiometers and thermal imaging cameras can provide counterpoint

to the use of satellite based systems such as the Landsat7 ETM+ and EO-1 ALI. I hope to show that even a simple radiometer can be used to extract meaningful information, and with the correct interpretation provide insights into ongoing physical processes at an active volcano.

This thesis falls into two main sections. The first (chapters 2 & 3) deals with the interpretation and analysis of thermal data returned by a network of radiometers installed on the Pu`u`O`o cone of Kilauea volcano, Hawaii (Harris et al, 2003). My aim in these two chapters is to show that satellite-based data is not necessary to obtain real-time data from an active volcanic situation. In chapter 2 I identify thermal anomalies within the radiometer data by synergistic use with simple RSAM data, and tie these events to large scale Earth system processes such as the tidal variation. In chapter 3 I show how it is possible to estimate the mass of molten ejecta associated with these events within the Pu`u`O`o crater described in chapter 2 by using thermal diffusion modelling. This information may then subsequently be used to monitor the dynamics and plumbing of vents at Pu`u`O`o. The net result of these two chapters is the ability to extract meaningful information on physical processes within a volcanic crater by the simple use of radiometer data.

The second section of this thesis centres on the use of the dual-band technique, and how it is applied to high resolution satellite data from such instruments as the Landsat7 ETM+ and the EO-1 ALI. Although this is a subject considered at length elsewhere, I use thermal camera imagery obtained from active lava flows at Mt Etna to form the basis of accurate models of the thermal composition of lava flows within a single pixel. As these models can be adjusted at will to simulate various scenarios any satellite pixel is likely to encounter, I use this to accurately assess the response of the dual-band procedure to these models. This has not been possible before, as previous studies have all considered the likely response of the procedure to a simple two or three component simulated pixel and

then extrapolate these findings to actual situations. I also show how three-component modelling is much more effective at extracting the likely thermal composition within a pixel.

In chapter 6 I use the dual-band model as the basis of a comparison between the established and well understood Landsat7 ETM+ instrument and the recently launched EO-1 ALI instrument. The ALI incorporates many new technologies intended as a trial run for a future ETM+ replacement instrument. The ETM+ has been regarded as a workhorse for volcanological remote sensing, so it is important to assess the next generation of instruments, especially when equipped with extra spectral channels within the SWIR designed specifically for the use of remote sensing of volcanoes.

In the final concluding chapter 7, I suggest some direction for future research arising from work completed in this thesis.

Therefore the overall theme of this thesis is the use of various remote sensing methods, ranging from simple ground based radiometer to the latest state of the art satellite instruments. All these methods can provide vital insights into processes associated with active volcanism.

1.9.Contributions from others to this thesis

The work represented within this thesis is my own, including analysis and interpretation. This PhD research was funded by a grant from the Open University graduate research fund. Dave Rothery (OU) and Andy Harris (University of Hawaii) as supervisors have reviewed this work and contributed suggestions. Chapters 2 and 3 made use of data returned by the HIGP/HVO radiometer setup on Kilauea volcano, whilst help and advice (not to mention accommodation and supervision as part of the USGS HVO volunteer program) was provided by Christina Heliker and others at HVO. Jo Gottsman

provided me with QuickTide software for the calculation of the tides within chapter 2. Dan Morgan (OU/University of Durham) helped me with the choice and understanding of the correct thermal diffusion equations as well as the laboratory testing of the model. Dan also helped review Chapter 3. The thermal camera imagery used within Chapters 4 and 5 was kindly provided by Harry Pinkerton of Lancaster University. Harry also provided information and advice on how and where the thermal camera imagery was obtained. Chapter 6 is based on a paper submitted to the Journal of Volcanology and Geothermal Research and is expected to be published in the summer of 2004. This paper was co-authored by Luke Flynn of the University of Hawaii, who also provided financial support for my stay in Hawaii as well as the satellite imagery used within chapter 6 (Landsat7 & EO-1). Luke also helped review this chapter.

2. Investigating a possible link between thermal anomalies detected within the Pu'u'O'o crater of Kilauea volcano and the Lunisolar tide.

2.1.Introduction

An easy assumption to make when considering the remote sensing of active volcanoes is that satellite data can provide all the solutions to most of the problems associated with obtaining a complete record of volcanic activity. In time with enough funding and technology this assertion may well hold true. At present however, many problems encountered with remote sensing of active volcanoes such as heavy cloud and fume cover associated with altitude and activity plus often inadequate pixel spatial resolutions prevent accurate and constant observations using satellite instruments. There is a paradox in volcanic remote sensing in which satellite instruments that can provide constant near real-time observations have very poor spatial resolution (i.e. GOES), whereas those instruments with high spatial resolution (i.e. ETM+, ALI, ASTER) may only pass over the same location on the Earth's surface once every few days. In this chapter I shall show data from a simple, relatively cheap system of radiometers providing real-time high spatial resolution data from within an active volcanic crater can be used to relate and infer ongoing processes that would be extremely difficult to attempt otherwise with satellite data.

A system of ground based instrument radiometers installed on the rim of the Pu`u`O`o crater of Kilauea volcano, Hawai'i (Harris et al, 2004) satisfies this criteria. This system consists of three individual radiometers (referred to as "Ducks") that continuously record the temperature fluctuations within three separate thermally anomalous "targets" within the crater. This system is relatively cheap, resilient, adaptable and provides thermal information at a level not currently available with satellite data. This system may be

cheap, but is superior to satellite systems in that it provides a continuous record of thermal activity at a high spatial resolution. Satellite instruments in the main only provide single snapshots of the thermal activity once per overpass. This is important as a thermal signature can be attributed to different types of volcanic activity, and we can use this to identify and understand processes within the greater volcanic system.

There has been frequent speculation about the relationship between the gravitational tides due to the motion of the Moon and the Sun relative to the Earth, and volcanic phenomena. Many previous researchers have commented on the possible relationship between effusive volcanic phenomena such as degassing and fire-fountaining events with this "Lunisolar" tide. Shimozuru (1987) recalls observations by H.Jaggar of the 1919 Halema`uma`u lava lake. The level of the lava lake appeared to fluctuate in response to the changing tidal forces. Williams-Jones et al (2001) observed that tremor events at Arenal in Costa Rica also seemed to coincide with minima of the Lunisolar tidal potential. Other studies of Mt Etna in Sicily also suggest a relationship between Lunisolar Earth tides and effusive activity (Patané et al, 1994).

The system of radiometers at Pu`u`O`o began to record thermal anomalies from within the crater at the start of September 2001, and in this chapter I consider those anomalies recorded during both September and October 2001. These anomalous thermal signals are manifested as an initial rapid rise in temperature, that in some cases quickly decays, whilst in other cases the decay of the anomaly took longer with a shape suggestive of a cooling curve. On certain days many anomalies were recorded within the space of 2 to 3 hours. At other times, few or no anomalies were recorded over the course of 1 to 2 days. The peak temperatures achieved by these signals often varied greatly between 10 - 15°C above the ambient temperatures and up to 150-200°C above the ambient temperature. Such apparently ephemeral events within the Pu`u`O`o crater invite an attempt to detect a link with the ever changing Lunisolar tide.

In this chapter I investigate these anomalous thermal signals obtained with the radiometer system from the Pu`u`O`o crater during the study period of September & October 2001. I explore their relationship with low level seismic tremors recorded simultaneously and attempt to relate these signals with the Lunisolar tide.

2.2.Background to activity at Pu`u`O`o crater

Kilauea volcano is the youngest of the five major coalescing volcanoes that comprise the Big Island of Hawai'i, USA. Kilauea is also one of the world's most active volcanoes and has erupted 2 km^3 of lava into 105 km^2 of lava flows, emitted from the East rift zone since 1983 (Heliker & Mattox, 2003).

Kilauea has been erupting continuously since 1983 and this eruption has progressed in 3 main episodes. The first of these involved fire fountaining and a'a lava flows issuing from vents that had opened on Kilauea's East rift zone in late 1983. These gradually created a cinder and spatter cone that was ultimately named Pu`u`O`o (Heliker & Mattox, 2003). After 3 ½ years, activity transferred to the creation of a lava shield, 2½km further down the rift zone. The Kupaianaha vent as it became known, supplied many tube fed pahoehoe lava flows that often reached the Pacific coast ~13km away. This activity continued for 5 ½ years after which the main focus of activity switched back to Pu`u`O`o, where effusion from vents on the flank of the cone further supplied a network of tube-fed pahoehoe flows onto the coastal flats and into lava deltas at ocean entry points (Heliker & Mattox, 2003).

The Pu`u`O`o cone has itself gone through a varied and well documented evolution, and is well documented elsewhere (i.e Heliker & Mattox, 2003). However, prior to the study period the crater had been subject to low levels of activity since February 1998. Any activity present was limited to a small number of vents, such as the July pit and

Beehive vents within the crater floor (Heliker & Mattox, 2003). Other vents were also present on the crater floor at the time of the study period, such as the South Wall Hornito that was often associated with night-glow identified within the video telemetry. This activity was often limited to glowing vents and brief gas jetting episodes. The thermal data from the Pu`u`O`o crater discussed in this chapter were obtained during September and October 2001, whilst the crater floor was in this configuration. Shortly after this study period, the Pu`u`O`o crater floor was resurfaced in early 2002 by fresh lava issuing from some of these vents that eventually filled the crater floor to a level within 15m of the crater rim (Heliker & Mattox, 2003).

At the time of the study period the Pu`u`O`o crater had recently been subject to a further slight floor collapse on the 25th August 2001 (Heliker.C pers.com), revealed within telemetered video footage obtained from the rim of the crater (Thornber, 1997), (Harris & Thornber, 1999). This created a large collapsed area within the centre of the crater surrounded by terraces.

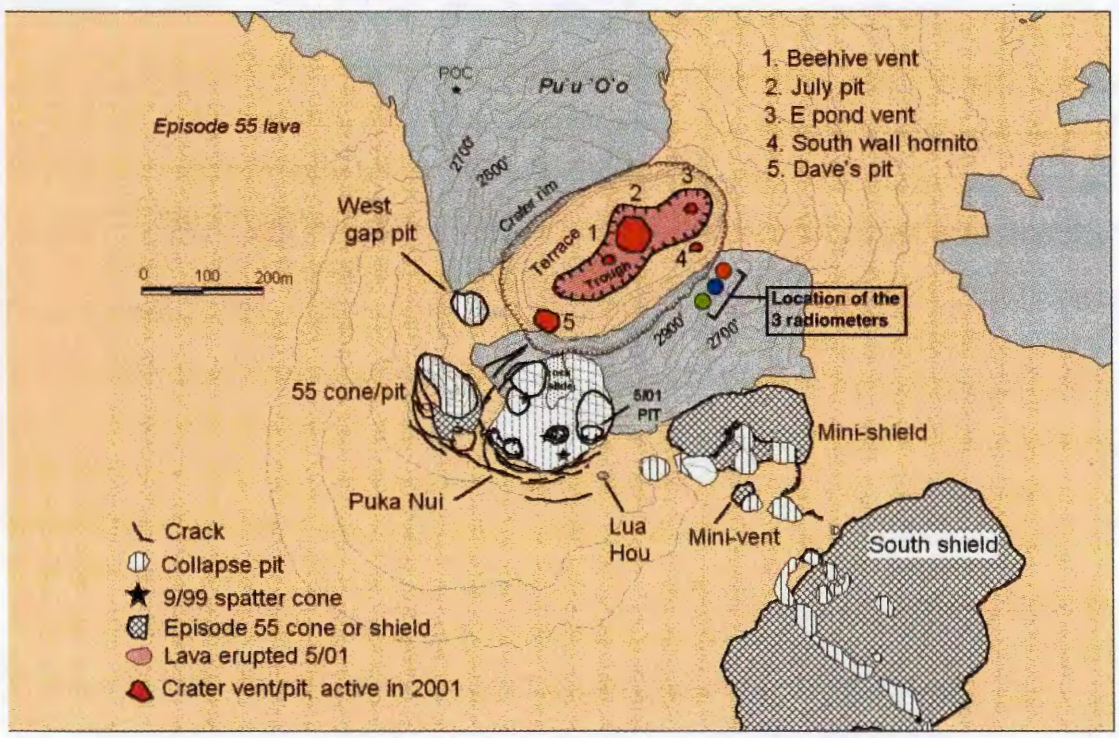

Figure 2.1: Map of the crater floor, cone and immediate vicinity of Pu`u`O`o as it was during the study period of September and October 2001. The approximate location of the Ducks is also marked upon this map. The Ducks were targeted at the Beehive Vent and July pit during the study period of September and October 2001. Map courtesy of U.S. Geological Survey, Hawaiian Volcano Observatory.

Figure 2.1 shows the relationship of the various vents upon the crater floor and the morphology of the interior of the crater as it appeared in late 2001 before the crater was repaved by fresh flows issuing from within the crater in early 2002. The crater floor was in this configuration during the September-October 2001 study period. The collapsed area of the crater floor associated with the 25th August 2001 collapse is visible as the trough, in which the Beehive Vent, July Pit and East Pond Vent are located. Dave's Pit and the South Wall Hornito are located on the terrace surrounding the trough.

Night-time video imagery obtained from the rim of the crater showed that various vents on the crater floor were glowing sporadically. Due to the dark conditions it was not possible to determine whether this was due to changing conditions within the vents themselves, or due to intermittent clearing of cloud and fume that often obscures the crater floor within the video imagery.

2.3.Installation of 3 radiometers on rim of Pu`u`O`o crater

Three autonomous radiometers were placed on the rim of the Pu'u'O'o crater in late 2000 with the intent of providing a continuous and accurate record of thermal activity within the crater. These radiometers (affectionately referred to as the "Ducks") telemeter thermal information back to a base station situated within the Hawaii Volcano Observatory (HVO). A dedicated computer there compiles and records the resulting data. The three Ducks work in conjunction with a remote video camera that provides real-time imagery from the Pu`u`O`o crater back to HVO (Thornber, 1997). The Ducks make use of the existing infrastructure provided by HVO for the operation of the video camera. This system uses a repeater station situated on the flanks of the adjacent Mauna Loa volcano to

relay the data from Pu`u`O`o to HVO, as there is no line-of-sight from Pu`u`O`o to HVO on Kilauea's summit (Thornber, 1997).

The radiometer used within each "Duck" is sensitive to Thermal Infrared Radiation (TIR) in the wavelength range of 8 to 14μm. Due to the effects of the Planck relationship (refer to figure 1.1) this makes the Ducks very sensitive to temperatures at the average ambient temperature of 15 to 30°C, likely to be encountered at Pu`u`O`o, as well as the elevated temperatures associated with volcanic thermal anomalies exceeding 300°C (Harris et al, 2003). Therefore this system is ideally suited to detecting temperature changes associated with the changing conditions and activity of vents situated within the Pu`u`O`o crater.

The three Ducks (christened Huey, Dewey and Louie) were targeted individually at discrete areas within the Pu`u`O`o crater. These areas were chosen due to anomalously high temperatures compared with those of the surrounding surfaces within the crater. These targets had been identified first with a hand held radiometer (Minolta Land). Each duck was then aimed at this feature, the final position being where the highest temperature is recorded from the target on an internal read-out. The map of the Pu`u`O`o crater in figure2.1 shows the approximate location of the three Ducks with respect to the crater floor. Figure 2.2 displays a simple overview of the position and the target vents of the three Ducks.

Duck	Bearing	Field of View (FOV)	Target
Huey	155° 16°±1° below Horiz	1°	Beehive Vent
Dewey	159-161° 15° below Horiz	60°	July Pit & Beehive Vent
Louie	135° 20° below Horiz	1°	July Pit

Table 2.1: Bearings of the Ducks at the time of the study and their targets. After the 25th August collapse the areas of the July pit and Beehive vent were still visible, and nightglow was often identified in video camera imagery of the collapsed floor.

In mid-July 2001 the Ducks were re-targeted to acquire new high temperature targets on the crater floor, and the Ducks were in this configuration during the period of this study. Table 2.1 summarises the orientation of the Ducks in this configuration.

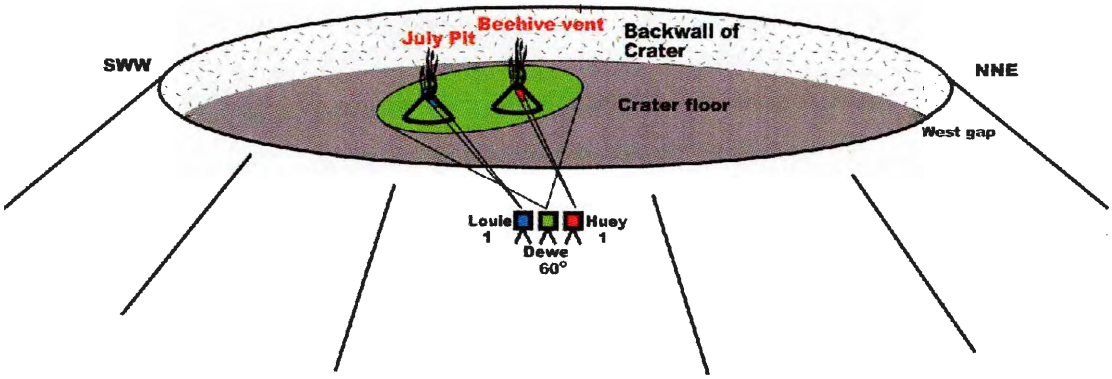

Figure 2.2: Schematic of the layout and targeting of the three radiometer "Ducks" on the rim of Pu`u`O`o crater during September and October 2001.

It was intended that the field of view (FOV) of the wide angle Duck (Dewey) should cover the combined FOVs of the two narrow angle Ducks (Huey & Louie) so that confirmation of any thermal activity at the target areas within the two narrow angle FOV Ducks could be provided by the wide FOV Duck. The wide FOV Duck monitors activity within a large swathe of the crater floor, and so provides the capability to monitor large scale phenomena in addition to the information obtained from two small target areas within the narrow angle Duck FOVs.

The thermal data obtained by the three Ducks from the Pu`u`O`o crater is automatically displayed in near-real time on a display within the foyer of HVO, and also on a Hawaii Institute Geophysics Planetology (HIGP) hosted website: http://hotspot.higp.hawaii.edu/puuoo/. The temperature records for each of the Ducks is compiled into a single file complete with a correction factor to counter the loss of signal associated with the Selenium Arsenide glass window through which the radiometer

observes the target feature (Harris et al, 2003). Each of these files records the temperatures sampled at two second intervals for each day.

A complete temperature record is therefore available for each of the target areas, in which the diurnal temperature variation is present, as well fluctuations due to the changing levels of cloud and fume obscuring the target areas. The thermal spikes discussed within this chapter are superimposed upon this constantly fluctuating pattern of temperatures. A full description of the installation, subsequent use and interpretation of events during the initial period of Duck operations can be found in Harris et al (2003). Information on the installation and use of the remote video camera can be found in Harris & Thornber (1999).

2.3.1. Thermal data returned by the Ducks

Since their installation on the rim of Pu'u'O'o, the Ducks have returned reliable information about events on the floor of the crater. This includes the diurnal thermal fluctuations within the crater as well as periods of increased activity within the crater, as typified by lava ponds within the July pit (Harris et al, 2003). In the period prior to this study the Ducks had been centred on various interesting thermal features on the floor of the crater with the purpose of recording the thermal flux over a long time span.

Since the re-targeting of the Ducks to aim at the July Pit and Beehive Vent in July 2001 the Pu`u`O`o crater floor suffered a partial collapse on 25th August 2001. This has been confirmed by seismic data for that day and was also indicated later in pictures obtained from one of the routine helicopter over-flights (C.Heliker pers. com). The area affected included the location of the July Pit and Beehive vents, and immediately after the event no thermal readings above the background temperature within the crater were received. However within a week, Huey had begun to report small thermal spikes in the

data and the occurrence of these spikes increased in frequency and magnitude into early September at the start of the study period. Figure 2.1 shows that despite the 25th August collapse the July Pit and Beehive vents were still present within the central crater trough. Therefore it appears that the Ducks had reacquired thermal signals from these vents once debris associated with the floor collapse had cleared or new vents in these locations had formed in the new floor within the central trough.

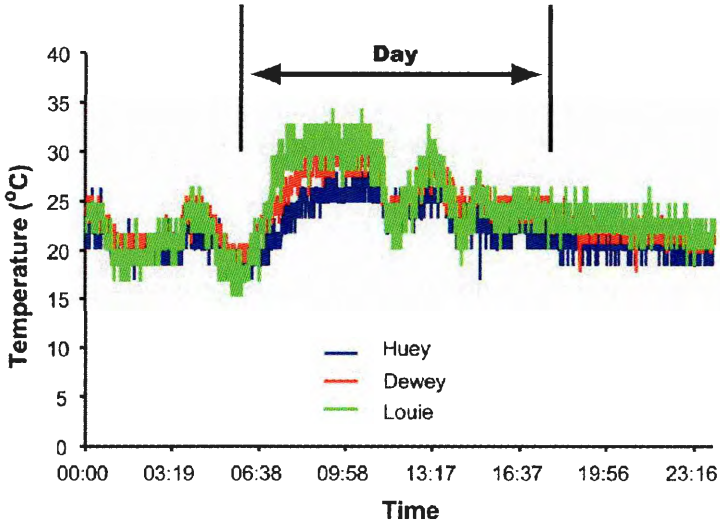

Figure 2.3: Record of temperatures from all 3 Ducks for 1st September 2001. Note the consistently higher temperatures during daylight hours than during the dark hours.

Figure 2.3 displays a typical thermal record for a whole day returned by the three Ducks from the crater floor from 1 September 2001 at the start of the study period. This particular record does not display any of the spurious thermal spikes that are the focus later in this chapter, but what is apparent is the ambient diurnal temperature variation. Temperatures recorded during daylight hours are on average higher than those recorded during the hours of darkness. This is of course due to the effects of solar heating of the ground and the local atmosphere. The temperature difference indicated by all 3 Ducks is of the order 8-10°C. There are also changes in temperature due to the amount of cloud and fume obscuring the target vents on the crater floor from the Ducks on the crater rim. This obscuration attenuates part of the incoming infrared signal detected by the Ducks, and is thus recorded as a period of lower temperatures. There is also a small fluctuation in the

temperatures recorded by the Ducks of the order of 1-3°C that varies over the course of 1 to 3 seconds. These fluctuations are due to the small scale changes in viewing conditions as well as variations in the emitted radiance from the target vents due to changes in emitted hot gases etc.

What is apparent from the study of such a record is that the thermal anomaly associated with the target vents is not consistently elevated over the ambient background temperatures, and that fluctuations can occur over the course of just a few seconds. It is unreasonable to assume that the radiative output from a small volcanic vent situated on the floor of a crater will produce a thermal anomaly of consistent temperature. These fluctuations are due to the combined effects of changing viewing conditions and small scale changes in the output of the target vent. A daily "eruption-update" is maintained on the HVO website that often details conditions at Pu`u`O`o, (http://hvo.wr.usgs.gov/kilauea/update/main.html). Pu`u`O`o crater is often described as "socked in" by cloud, fume and even rain as indicated by field excursions and video telemetry. This indicates that clear viewing conditions are the exception rather than the norm. However, analysis of the video telemetry in conjunction with the Duck data during the study period showed that conditions often cleared momentarily throughout most of the study period. Sometimes the crater floor and all the features present were clearly identifiable, whilst at other times only brief hazy glimpses of certain features were possible. This shows the high degree of variability of the conditions present at Pu`u`O`o.

2.4.Thermal anomalies recorded within the Duck data

During September & October 2001 anomalous spikes were recorded within the thermal data from one narrow-angle FOV duck (Huey) and one wide-angle FOV Duck (Dewey). These signals took the form of a sharp rise in temperature over the space of 1 to

5 seconds, that would in some cases quickly drop off, yet in other cases the signal would decrease at a slower rate down to the background ambient temperature. For those thermal spikes that achieved temperatures 60°C or more, a response was also often evident in data from the wide angle Duck, Dewey. The thermal spikes continued to occur in Huey and Dewey data until late October. No thermal anomalies were recorded at all within Louie data and it is assumed that whatever feature on the crater floor which was responsible for the anomalies in the Huey and Dewey data was not present within the FOV of Louie. Figure 4 shows a typical record of the temperatures recorded within the Duck data over the course of the afternoon of 18th September 2001.

Figure 2.4 shows a number of thermal spikes ranging from those that possess a quick return to the ambient background temperature with little or no response within the data from Dewey (60° FOV), to spikes that tend to take a little longer to return to the ambient temperatures. Many of these also display a response within Dewey data.

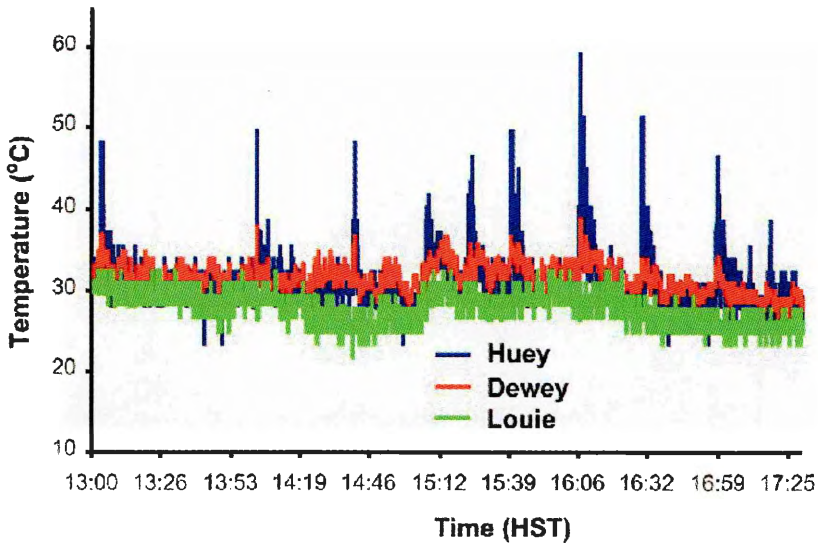

Figure 2.4: Thermal record for the afternoon of 14th September 2001 showing thermal spikes. Note the apparent regularity of some of the spikes and how certain spikes appear to possess a slower rate of drop-off towards the background ambient temperature

The most apparent feature of these thermal records is that the spikes occur only within Huey (1° FOV) and Dewey data. No spikes were ever evident within data from the other 1° FOV Duck, Louie. Hence, it therefore appears that these thermal

anomalies are associated with the Beehive vent, at which Huey was aimed, and which was also present within the FOV of Dewey.

The spikes displayed within figure 2.4 reach a peak temperature of ~59°C. Other spikes frequently achieved peak temperatures in excess of 100°C.

Figure 2.5 shows two large thermal anomalies recorded from the afternoon of September 18th 2001. The peak temperatures here are well in excess of 100°C and a strong response is also recorded within data from Dewey. A third smaller spike is also recorded at ~ 16:20, but this spike does show a sustained and gradual drop-off to the ambient temperature. A lesser response from the wide angle Dewey (with a FOV encompassing that of Huey's) is expected as the FOV of Dewey is greater than that of Huey's. Therefore, any temperature record of the same area of material at an elevated temperature above the background temperature will appear higher within the smaller FOV than the equivalent record from the wider FOV record.

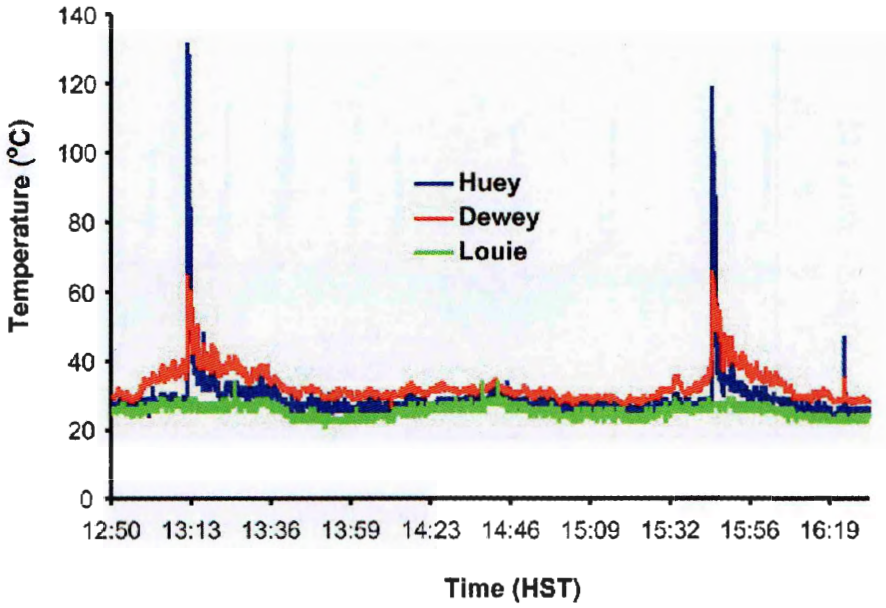

Figure 2.5: Thermal record from the afternoon of 18th September 2001 showing two distinct large thermal anomalies. Note the strong response in records from Huey and Dewey and no response from Louie.

2.4.1. Recording all thermal anomalies in September & October 2001

In order to analyse all thermal anomalies recorded from the three Ducks within the two month study period, I wrote software in Research Systems IDL. This software read the complete thermal record for each Duck on each day of the study period. The software compensated for attenuation of the incoming signal by the Selenium Arsenide window using empirically derived formula (Harris et al, 2003), but the resulting derived temperatures cannot be considered to be absolute due to a combination of factors including the complexity of the materials within the FOV (fresh lava, older material, gas & fumes as well as the differing emissivity values for this range of materials). As Harris et al (2003) point out, what is of most use and interest is the relative values present within the duck data. This and other factors relating to the interpretation and use of thermal data returned by the Ducks can be found in Harris et al (2003). The thermal anomalies were identified automatically within the IDL software by setting a threshold temperature. Any time this threshold temperature was exceeded within Huey data, the time and the temperatures at the remaining Ducks were recorded. The threshold temperature was set by using a "moving window" technique within the software. As the program looped through all the temperatures, recorded at intervals of 2 seconds, a running mean temperature was calculated for the preceding 30 minutes. If this mean temperature was exceeded by 5°C within the space of 1-2 minutes then this would be considered a thermal anomaly, or "spike". The software would also calculate the duration of the spike using a similar technique. Once the temperature within the duck record had returned consistently to within +/- 1-2°C of the mean temperature for the current hour (30 minutes ahead and behind of the current point considered) for 1 minute, then event was considered over.

This "moving window" method allowed an amount of automation and consistency in the process of anomaly detection, the alternative being to manually set a threshold

temperature for the whole day. This threshold temperature should be high enough so that the constantly fluctuating temperatures (usually in the range 25-35°C) detected by the Ducks do not register as anomalies. Due to the diurnal temperature range displayed within the duck data, the extent of which depended on the current viewing conditions within the Pu`u`O`o crater (i.e. amount of fume), the manual selection of an arbitrary threshold temperature proved less satisfactory than the adoption of the "moving window" technique described above. This method also allowed a much more quantitative method of identifying the likely duration of an anomaly. The provision of information on the anomaly duration is used in conjunction with the maximum temperature achieved in the next chapter. These parameters will be used to infer the presence and amount of solid ejecta within the duck's FOV at the time of the anomaly.

2.4.2. Variation in the number of recorded thermal anomalies during the study period

Figure 2.6 shows the number of thermal anomalies recorded for each day within the 2 month study period. Over 500 thermal anomalies were detected during the study period, and as figure 2.6 shows, they are not distributed evenly during the study period but appear to fall into a cyclic pattern. It appears that the number of anomalies broadly increase to a maximum number, after which the number of anomalies subsequently falls. This pattern repeats itself a number of times during the study period. This pattern may be due to a variety of causes, ranging first from the possibility that changing crater conditions are modulating the detection of the anomalies to the possibility that the root cause of the anomalies themselves is fluctuating with time.

I have also plotted on figure 2.6 what I term the "Tide Fluctuation Index" (or TFI). I discuss the creation and calculation of this later within this chapter (p81). The TFI is simply a measure of the relative amplitudes in the semi-diurnal fluctuation of the tides due

to the combined gravitational forces of the Sun and the Moon on the Earth. The TFI ranges between 0 and 1. As the TFI tends towards 0 from 1, the ratio between the amplitudes experienced within the semi-diurnal tidal range increases. This relates to an increase in tidal force, such as that experienced at new and full Moons. The opposite is true as the TFI tends towards 0 from 1.

Figure 2.6 suggests the possibility of a link between the thermal anomalies recorded within the duck data and the magnitude of the changing tides due to the gravitational forces of the Sun and Moon. It appears that the number of anomalies recorded within a day within the duck data are at their lowest when the TFI is at a minimum. Although those days which see the greatest number of thermal anomalies do not appear to particularly coincide with the points when TFI is at a maximum, the number of anomalies per day over the span of 3-5 days seems to increase in conjunction with the TFI as it waxes from a minimum towards a maximum. This translates as when the actual Lunisolar tide is increasing to a maximum, the number of thermal anomalies recorded is also increasing.

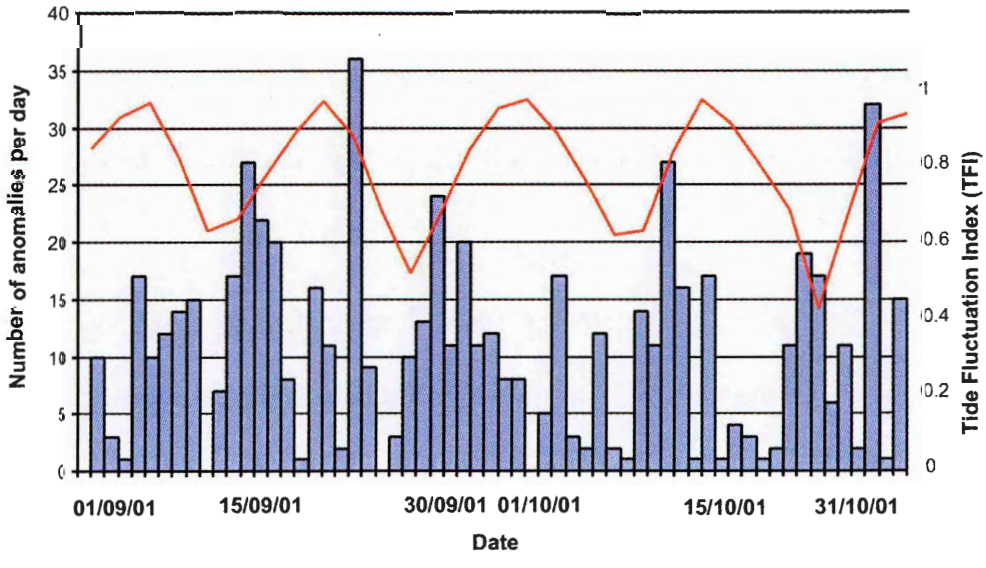

Figure 2.6: The number of thermal anomalies recorded during the two month study period (columns). On those days where no anomalies were recorded, the number of anomalies is represented by a zero. The red line indicates the Tide Fluctuation Index (TFI) that is described on p81. The TFI is simply a measure of the range in tide potential relating to the changing gravitational force due to the motion of the Sun and the Moon. This is based on the Lunisolar tide at the coordinates and altitude of the Pu`u`O`o crater on Kilauea.

In order to fully explore the possible relationship between the thermal anomalies recorded from the floor of Pu`u`O`o with the tides we first need to identify the physical processes responsible for these anomalies.

During the 2 month study period, I was present at HVO and had the task of recording any events visible within the Pu`u`O`o crater in the video telemetry system discussed previously. For the majority of the time the default viewing condition was that the crater was full of fumes that obscured any view of the crater floor. Very occasionally, brief clearings exposed the crater floor but these clearings most often did not last. An early assumption was that the thermal anomalies were related to clearing viewing conditions exposing a vent on the crater floor within the Duck FOV. It was soon apparent that clearing conditions were not responsible for the anomalies as it was easy to cross check the viewing conditions at the time of any anomaly using the archive of images from the video telemetry system (Thornber et al, 1999). Therefore another process must be responsible for the thermal anomalies.

Fortunately at the same time anomalies were first spotted within the data returned by the Ducks from the Pu`u`O`o crater floor, anomalous episodes were also recorded by the HVO RSAM network and interpreted as originating on the Pu`u`O`o floor. Any correlation between these events may allow us to identify the cause of the signals recorded by the Ducks.

In the next section I relate the thermal anomalies to these signals recorded simultaneously within the HVO RSAM network, and then in the subsequent section, I will try to identify the presence of a link between these events and the tides.

2.5. Anomalous seismic signals detected within the Pu`u`O`o crater

2.5.1. The RSAM system

Real time Seismic Amplitude Monitoring (or RSAM) is a system for recording the seismic amplitude without focussing on extracting the location or magnitudes of any earthquakes (Endo & Murray, 1991). RSAM was developed by the USGS as it is desirable to access any seismic data in a volcanic crisis quickly without disturbing the 'traditional' analogue recording drums used. The RSAM system calculates and digitally records the average seismic amplitude over a period of 10 minutes. A bonus of this method is that it provides real–time monitoring (Ewert et al, 1993). The resulting data are used to analyse any changes in tremor that may indicate any change in seismicity associated with a forthcoming volcanic crisis (Ewert et al, 1993). This system was first used operationally by USGS CVO (Cascades Volcano Observatory) with considerable success. RSAM is used by HVO to constantly monitor the current state of volcanic tremor on Kilauea and has been successfully used to detect a range of phenomena pertaining to the ongoing Pu`u`O`o eruption.

2.5.2. Anomalous RSAM signals in September and October 2001

HVO maintain an RSAM network at a number of stations on Kilauea, including the "Steam Cracks" detector (STC), which is closest to the Pu`u`O`o cone at a distance of 1km. At the start of September 2001 low amplitude "cigar-shaped" tremor had been noticed within RSAM data returned from STC. The next nearest station at Kalula cone (KLC) showed no evidence of these signals. The cigar shaped signals were therefore interpreted by HVO scientists as events originating at Pu`u`O`o, probably degassing from a vent on the crater floor. A crater floor collapse on 25th August 2001 had been inferred from

large tremors and reports from helicopter overflights. Information from clear periods observed within the video telemetry of the crater floor confirmed a limited collapse. The anomalous RSAM signals were interpreted by HVO scientists at the time as resulting from degassing episodes from a vent created or reactivated by this crater floor collapse event.

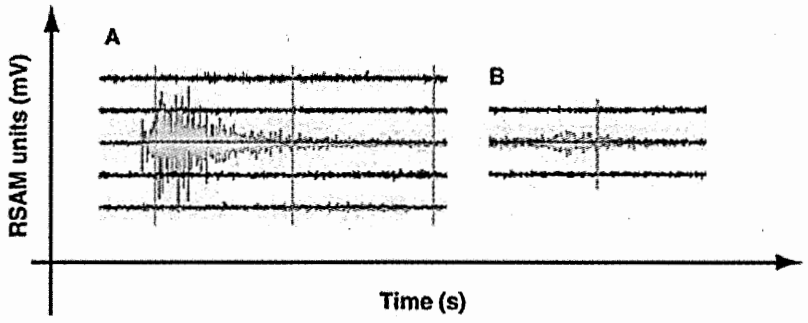

Figure 2.7: Example RSAM records. **A:** RSAM record for a typical rockfall event within the Pu`u`O`o crater during the study period. These are characterized by a rapid increase in amplitude followed by a quick drop off to background noise levels. **B:** A typical 'cigar shaped' RSAM record attributed to a degassing event within the Pu`u`O`o crater. This type of record is typified by a relatively slow increase in amplitude then followed by a slow drop off in amplitude. More persistent records display sustained periods of increased amplitude. The duration of the cigar shaped RSAM anomaly is taken to be equivalent to the duration of the degassing event from the vent within the crater.

As these anomalous RSAM signals began at a similar time to the thermal anomalies within the duck data it was natural to investigate whether both these sets of anomalous data were linked. If they were indeed linked then we might be able to infer that the Ducks were detecting hot gas and/or ejecta associated with a degassing vent on the Pu`u`O`o crater floor. In order to check for a possible correlation it was necessary to identify and record all instances of the RSAM anomalies. This was accomplished by recording the times of the onset of any anomaly where the RSAM amplitude exceeded a set threshold. The RSAM data I used to accomplish this were in the form of hardcopy on paper sheets recorded on a cylindrical drum recorder located in the HVO foyer. In this format, tick marks indicate individual minutes with 15 minutes of data recorded in one complete revolution of the drum. The lines were spaced so that 24 hours of data was recorded on a single sheet, with the start and end times recorded so that accurate extraction of the time of any event could

be accomplished. The amplitude recorded in this method takes the form of 1mm = 1mV (RSAM units are recorded in mV). In a similar fashion to the duck thermal data recorded, there was consistent fluctuation in amplitude due to background noise (ranging from strong winds and rockfalls to low flying helicopters!). This fluctuation never exceeded 1-1.5mm, and 1.5mm was therefore used as a threshold value. Whenever the amplitude exceeded this threshold for longer than 10s, then the start time, duration and maximum amplitude was recorded, as well as the time taken for the maximum amplitude recorded to be achieved.

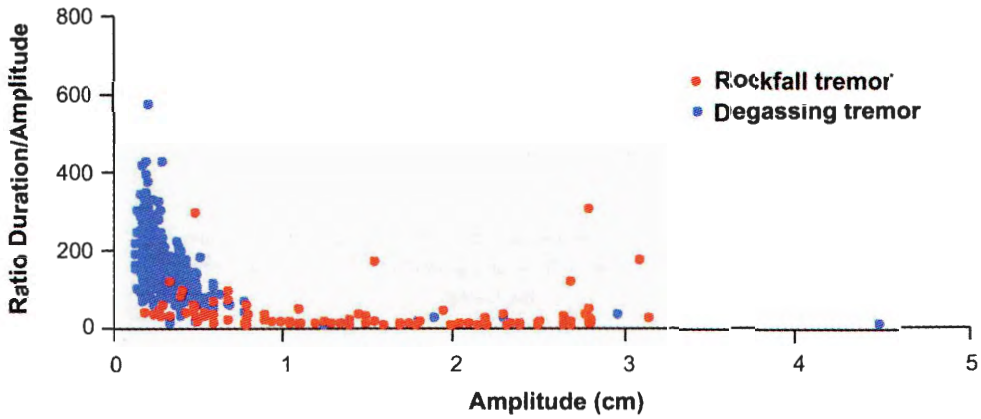

Figure 2.8: Ratio of the duration to the amplitude plotted against the amplitude for each measured September-October 2001 for STC station. Blue points indicate those events identified within the HVO eruption update as 'cigar' shaped low amplitude events, whereas the red points indicate local area earthquakes or rock-falls. They are easy to distinguish as degassing harmonics are characterised by long records with low maximum amplitudes, whereas those associated with local area earthquakes or rock-falls often have very high initial maximum amplitudes that tail off quickly.

Figure 2.7 is an example of the two main types of anomalous RSAM signal encountered. The first (A) is typical of a rockfall event which is easily characterized as a sharp and sudden increase in amplitude followed by a decrease to the ambient amplitude level. Frequent rockfalls were recorded and are to be expected in an active volcanic crater with areas of loose and friable material. Such events had been continuously recorded prior to the August 25 collapse. Figure 2.7 (B) is typical of the anomalous RSAM records that occurred during September and October 2001. These are characterized by low maximum

amplitude that occurs some time into the event, which then drops off –slowly returning to the background ambient levels. Over 750 anomalous RSAM events were recorded during the study period.

Although the method of data collection from hardcopy is non-ideal, it must be stressed that major items of interest to be extracted were the times of the anomalous signals, and if possible some idea of their duration. These could be obtained accurately from the paper hardcopy and it is worthwhile considering that the RSAM system was designed with the intent to warn of impending volcanic events based on an increase in the total amount of tremor detected, rather than to quantitatively identify any of the signature parameters of that tremor (which are obtained using different instruments). In a similar manner to the consideration of the duck thermal data, it is the relative changes in signal that are of interest rather than the absolute figures.

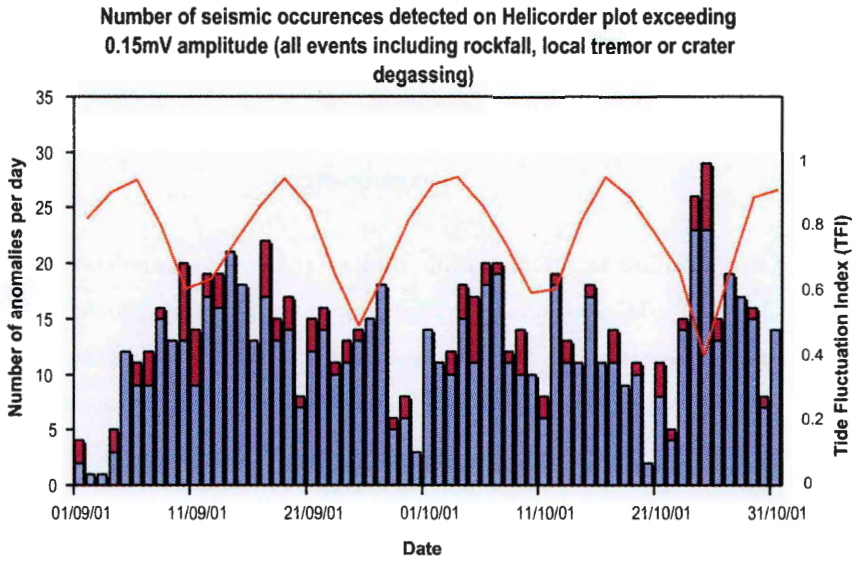

Figure 2.9: All the seismic data recorded from the STC helicorder data over the study period. This shows the low amplitude cigar shaped degassing episodes (purple) and those records associated with local area earthquake or rock-falls (maroon). The red line is the TFI, the same as that shown in figure 2.6

Figure 2.9 is a summary of all the RSAM anomalies recorded within the study period. This chart is explicitly the same as that shown in figure 2.6 for the number of thermal anomalies, but with the added feature of the distinction between the types of RSAM record. Rockfall (or non-"cigar-shaped" tremors) are indicated in maroon and

identified using the aforementioned method. Also shown is the Tide Fluctuation Index (TFI), as used within figure 2.6 (p61). If we consider merely the non-rockfall type tremors then a similar (although not as explicit) pattern between these signals and the state of the Lunisolar tides appears to be present. Again, this apparent relationship invites further investigation. The number of rockfalls per day remains fairly constant throughout the study period, whilst the remaining "cigar" shaped tremor fluctuates in a very similar manner to that of the thermal anomalies in figure 2.6. In the next section I attempt to relate these RSAM anomalies with the Thermal anomalies, after which I discuss the possible mechanisms that may account for this.

2.6.Correlation between the Duck thermal anomalies and the RSAM signals?

In order to ascertain whether the anomalous thermal signals within the duck data correspond with the anomalous RSAM signals, further IDL software was created to analyze the timings of the two sets of events. This software simply searches for the occurrence of both the thermal and RSAM anomalies within a certain time span. I used a time threshold of +/- 5 minutes when correlating the duck times with that recorded on the STC helicorder drum in the HVO foyer. This accounted for any deviation in the hand recording of the RSAM anomalies from the hardcopy. In order to simplify this process I converted the date (Julian) and time for each thermal and RSAM anomaly into total elapsed seconds from the start of the study period i.e. 01:00hrs on September 1st 2001 is 3600 total elapsed seconds.

A total of 628 thermal anomalies were recorded during the study period and 178 of these were found to have occurred close to the occurrence of an RSAM anomaly within the set threshold period. I have also included 3 sets of randomly generated thermal anomalies in order to provide control data for basing a statistical comparison for any relationship

between the thermal anomalies and RSAM events. These artificial anomalies were created using the "random" feature in Microsoft Excel using the maximum and minimum recorded temperatures and times (total elapsed seconds) as the limits for this function. I created 628 artificial anomalies to match the 628 recorded anomalies. These control anomalies were subsequently sorted into an ascending time series so as to provide random anomalies throughout the 2 month study period. The same IDL software was applied to these artificial anomalies, by searching for any RSAM event within the same threshold period.

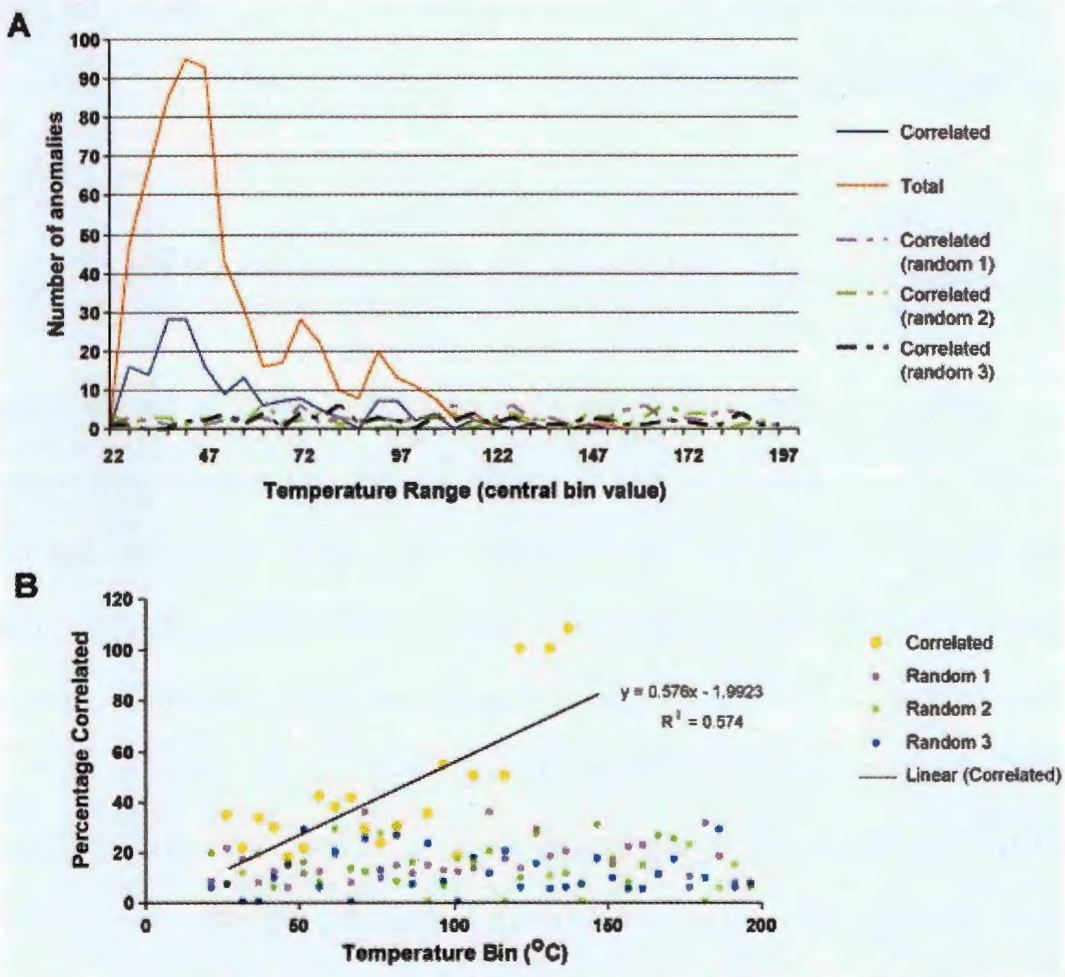

Figure 2.10: Graphs showing the relationship between the detected thermal anomalies and the RSAM anomalies. A shows that the most common thermal anomaly temperatures lie within the range 30 to 50°C, as indicated by the red 'Total' line showing all the recorded anomalies. The number of thermal anomalies decrease with increasing peak temperature. This distribution of anomalies about the peak achieved temperature is not replicated by the randomly generated anomalies. **B** shows the relationship between the relative proportion of correlated anomalies within a temperature range and the total number of anomalies within the same range expressed as a percentage. The trend line and r^2 value of 0.574 suggest a relationship where more correlated thermal anomalies are detected at higher temperatures than at lower temperatures. Such a trend is not observed in the randomly generated datasets.

Figure 2.10 displays the total number of detected thermal anomalies, the number of RSAM correlated thermal anomalies and the distribution of maximum detected temperatures. In order to represent this information graphically the numbers of thermal anomalies shown in figure2.10 A and B are the numbers of anomalies within individual temperature bins of 5°C, spanning the whole range of temperatures achieved by the thermal anomalies. The artificial random anomalies are represented by the dashed lines

Figure 2.10A shows that the most common thermal anomaly temperatures lie within the range 30 to 50°C, as indicated by the red 'Total' line representing all recorded anomalies. The number of thermal anomalies per temperature bin drop as the maximum achieved temperature increases. This pattern is replicated in the number of correlated thermal anomalies (those thermal anomalies that coincided with an RSAM event within the threshold period), shown by the blue line. However, this distribution of anomalies about the peak achieved temperature is not replicated by the randomly generated anomalies. This suggests a relationship between the thermal anomalies and the RSAM events, as the distribution of correlated events echoes the overall distribution of thermal anomalies. This might be expected if a relationship did indeed exist as the correlated anomalies must be a subset of the total recorded anomalies. As the greatest number of anomalies recorded lie within this duration range then it must be expected that a larger number of correlated anomalies will also lie within this duration range.

In order to further explore this possible relationship, figure 2.10B plots the percentage of correlated anomalies in each individual 5°C temperature bin against the temperature of that particular bin. This value is calculated using the total number of anomalies present within the given temperature bin. A trend line is highlighted on this graph and is accompanied by an r^2 value of 0.574. This suggests a moderate relationship where more correlated thermal anomalies are detected at higher temperatures than at lower temperatures. No such relationship is observed in the 3 randomly generated datasets. If

these events are degassing episodes from the Beehive vent, as initially suggested by HVO, then the radiometers will be more likely to detect higher magnitude thermal events as the signal is initially stronger so there will be less chance that the anomaly will be masked by signal attenuation by cloud and fume within the crater. This is assuming that for similar given levels of fume, a larger thermal signal (due to more emitted gas/ molten material/combination of both) within the radiometer FOV will be attenuated less by scattering and absorption than a lesser thermal signal (less emitted gas/molten material). However, the constantly fluctuating levels of fume and viewing conditions within the crater will also attenuate the signal to varying extents making direct comparison between any two thermal events impossible to compare accurately.

Other effects present in the crater may also contribute to mask the relationship hinted at in figure 2.10B. The morphology of the vent itself may change during the two month study period (especially if we consider that a crater floor collapse took place on August 25th so some continuing movement may well be expected), the supply of degassing magma providing the impetus for the degassing events may well change, as may the level of the free magmatic surface within the vent from which (if any) molten material may be ejected from. If molten material is indeed being ejected from vent, then some of this material may be emplaced on the rim of the vent, building it up in the style of a Hornito or spatter rampart. Similarly, not all material ejected or degassed may be within the FOV of the radiometer. For instance, any ejecta might land behind the vent and be obscured from the radiometer.

All or some of these processes may have been in operation during the study period and would serve to detract from the relationship shown in figure 2.10B. Therefore if the trend-line in figure 2.10B suggested no relationship, then this would not be categorical proof that the thermal events detected were not related to the RSAM events because of the above environmental conditions.

Hence the existence of the weak/moderate relationship suggested by this trend line, the fact that 178 of the 668 anomalies detected occurred close to an RSAM event (a much higher figure than the random anomalies), suggests that the thermal events are related to the RSAM events. As the 'Huey' radiometer was aimed at the Beehive vent, then in all probability the radiometer was detecting degassing events from this vent, possibly associated by molten material..

2.7.Degassing activity at the Beehive vent

The wide variation in duration and maximum temperatures achieved by these degassing events suggest a spectrum of activity levels. The presence of what appear to be a classic cooling curves in many of the spikes (such as those in figure 2.5) suggests that an amount of molten ejecta has accompanied the degassing event, perhaps similar to that displayed in figure 2.11. The cooling curves present within some of the duck thermal anomalies are reminiscent of those published by Hon et al (1995).

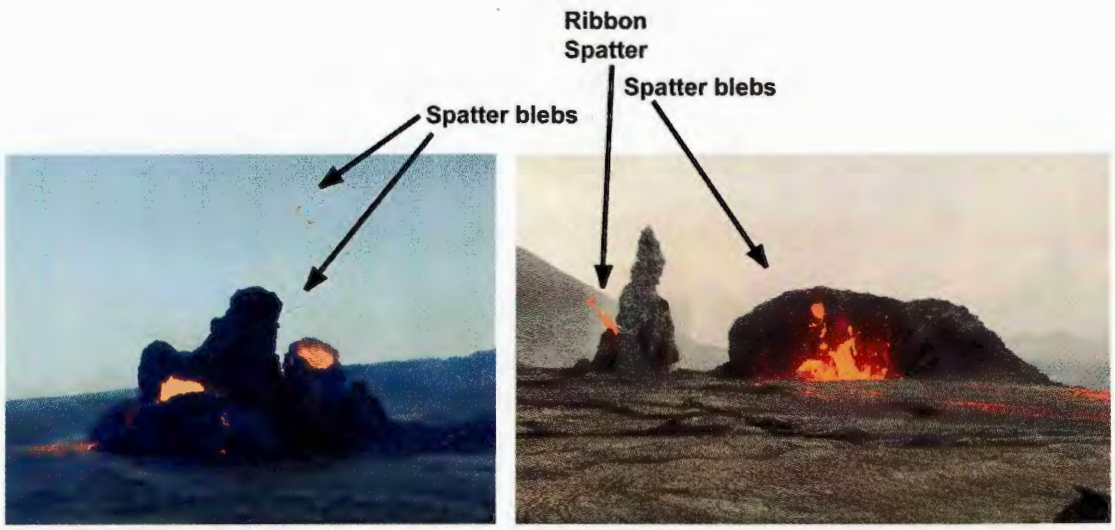

Spattering from Hornitoes in Pu`u`O`o crater (west gap pit) 2003 -2004
(Photographs courtesy of USGS Hawaii Volcano Observatory)

Figure 2.11: Examples of gas driven spattering from hornitoes and vents within the Pu`u`O`o crater in late 2003 and early 2004. Note the differing sizes and shapes of the spatter, as well as the just visible fumes associated with these features.

Other anomalies possessed a very quick return to the ambient background temperature, and it is possible that with these anomalies Huey has detected the passage of hot gas through its FOV. This gas will rapidly rise due to a combination of its motion on exiting the vent and its buoyancy within the atmosphere of the Pu`u`O`o crater. Gases have a very low emissivity, emitting much lower levels of radiance than a solid material such as basalt at the same temperature. Therefore the temperature detected by the duck will be lower. Due to a combination of dispersal and mixing within the atmosphere, the hot gas emitted from the vent will appear to cool very quickly within the duck thermal data. Any molten ejecta associated with a degassing event will cool much slower, depending on its initial temperature, volume and density.

Harris et al (2003) have created a catalogue of thermal forms recorded by various expeditions using radiometers very similar to those discussed here. These waveforms were recorded not only at Pu`u`O`o, but also Stromboli (Italy), Masaya (Nicaragua) and Soufriere Hills (Montserrat) among others. This catalogue was compiled by visually identifying degassing and spattering episodes at differing levels of activity from active vents at these sites, and then relating them to the record of thermal anomalies recorded within the radiometer data. In this way the catalogue of known thermal traces and actual events relating to differing types of activity was built up with each radiometer deployment. This activity ranged from persistent degassing at a single vent, regular "puffing" of hot gasses to small lava flows within the FOV of the radiometer.

Using this range of identifiable behaviour it is possible to identify the anomalous thermal waveforms observed during the study period at Pu`u`O`o as most closely approximating Strombolian type behaviour (those anomalies with possible cooling curves) and gas pistoning events (those anomalies with a rapid drop off from peak temperature). This comparison with Harris et al's (2003) catalogue strongly suggests the likelihood that

the thermal anomalies present within the duck data from Pu`u`O`o are associated with a mixture of degassing events often including ejecta.

This issue is considered in the next chapter where I use the information on initial temperature and cooling rate from the duck data to infer the volume and mass of material ejected during one of these thermal anomalies.

Now that we have a mechanism to account for the thermal and RSAM anomalies, namely degassing from a vent on the Pu`u`O`o crater floor, we can consider using the information on the timing of these events to investigate whether they are in fact linked to the state of the Lunisolar tides, as hinted at within figure 2.6. In the next section I shall investigate whether this is the case, and what it can tell us about the system at Pu`u`O`o, and the Beehive vent in particular.

2.8.A possible link between degassing events at Pu`u`O`o and the tides?

It is not unreasonable to believe that there is a link between the tides resulting from the gravitational force of the Moon and the Sun and degassing from a fluid magma reservoir within an active volcano. After all, these same tides have an effect on the oceans and also the solid Earth (Kasahara, 2002). Tidal fluctuations have also been observed in the water level within deep boreholes (Shimozuru, 1987) as well as having been linked to seismic activity and degassing at volcanoes such as Arenal in Costa Rica (William-Jones et al, 2001) and Mt. Etna in Italy (Patané et al, 1994). A link between the level of lava within the 1924 Halema`uma`u lava lake, within Kilauea caldera itself, and the semi-diurnal tide was made by H.Jaggar in 1919 (Shimozuru, 1987). Therefore, to look at the timings of the anomalous signals returned from the thermal and seismic data with an eye to seek a link to the Lunisolar tides, is not unreasonable. In order to do this though, there are a number of considerations that must be made, especially considering the case of Pu`u`O`o.

It is ironic that one of the greatest certainties about the 'plumbing' of the Pu`u`O`o conduit system is its great complexity (Barker et al, 2003). Little else is known for sure. It is possible that the crater floor collapse of 25th August 2001 rearranged the local plumbing of vents, such as the Beehive vent at which Huey was pointing. This change may have made it possible for magma to make its way to the surface via new pathways, or at least provide new paths for gas exsolved from the source reservoir to escape to the surface. It may be that the collapse event itself blocked off existing paths and created new ones in the process.

Pu`u`O`o is situated on the east rift zone of Kilauea, and is at the 'head' of an active system which supplies lava through a system of lava tubes (Heliker & Mattox, 2003). These transport lava down the flanks of Kilauea to surface flows and onto the ocean flats. These tubes also supplied lava to an ocean entry in the West Highcastle area at the time of the study. The amount of 'free' magma at Pu`u`O`o may well be dependant on the overall supply of fresh magma into the system, and where and how in this system it is transported into this network of lava tubes feeding the ocean entries. For instance, a temporary blockage upstream of the lava tube network may cause lava to back up to Pu`u`O`o itself, and it is surmised that this process was the cause behind the late 2001-early 2002 flows within Pu`u`O`o (Heliker & Mattox, 2003).

Therefore, it is possible that any link between degassing events at Pu`u`O`o and the Lunisolar tide may be obscured by ongoing physical processes affecting the supply of fresh magma elsewhere within the Pu`u`O`o system. However, the possible link between these two processes hinted at within figure 2.6 (p61) suggests that further analysis of the link between the degassing events at the Beehive vent, and fortunately recorded within the radiometer data, and the Lunisolar tides should be made.

2.9.The Lunisolar tide

Every point on the Earth's surface is affected by the gravitational attraction of the Sun and the Moon. These tides vary as the Earth rotates on its axis, as the Moon orbits the Earth and also as the Earth progresses in its orbit about the Sun. The tides are present as both short term semi-diurnal oscillations as well as medium term oscillations with a fortnightly period (Melchoir, 1978). Figure 2.12 displays the Lunisolar tide calculated for the location of the Pu`u`O`o cone.

The basic semi-diurnal tidal oscillation is a result of the apparent motion of the Moon due to the daily rotation of the Earth. The fluid ocean responds to this tide in the form of a "high" tide as the ocean nearest to the Moon is attracted the greatest. This lobe has a counterpart on the opposite hemisphere of the Earth as the ocean here is attracted the least (Melchior, 1978). Low tide is recorded in the oceans perpendicular to the hemisphere that is currently experiencing high tide. This semi-diurnal variation within the tides is readily apparent within figure 2.12. However this semi-diurnal oscillation is not constant in magnitude, and the overall pattern observes periods where the maximum tidal potential is increasing, and others where the potential is decreasing. This variation is the fortnightly tide, and is attributable to the varying gravitational force due to the motion of the Moon in its twice fortnightly orbit about the Earth. This is further complicated by the fact that that the Sun also has a similar effect due to the same processes (Shimozuru, 1987).

This constantly fluctuating tidal potential acts in three dimensions due to the nature of the Earth-Moon-Sun system, and because of this, the tidal potential encountered varies not only at differing longitudes but also at differing latitudes and elevations (Melchior, 1978). It is therefore important to ensure that the tidal potential is calculated at the correct location for the point of interest.

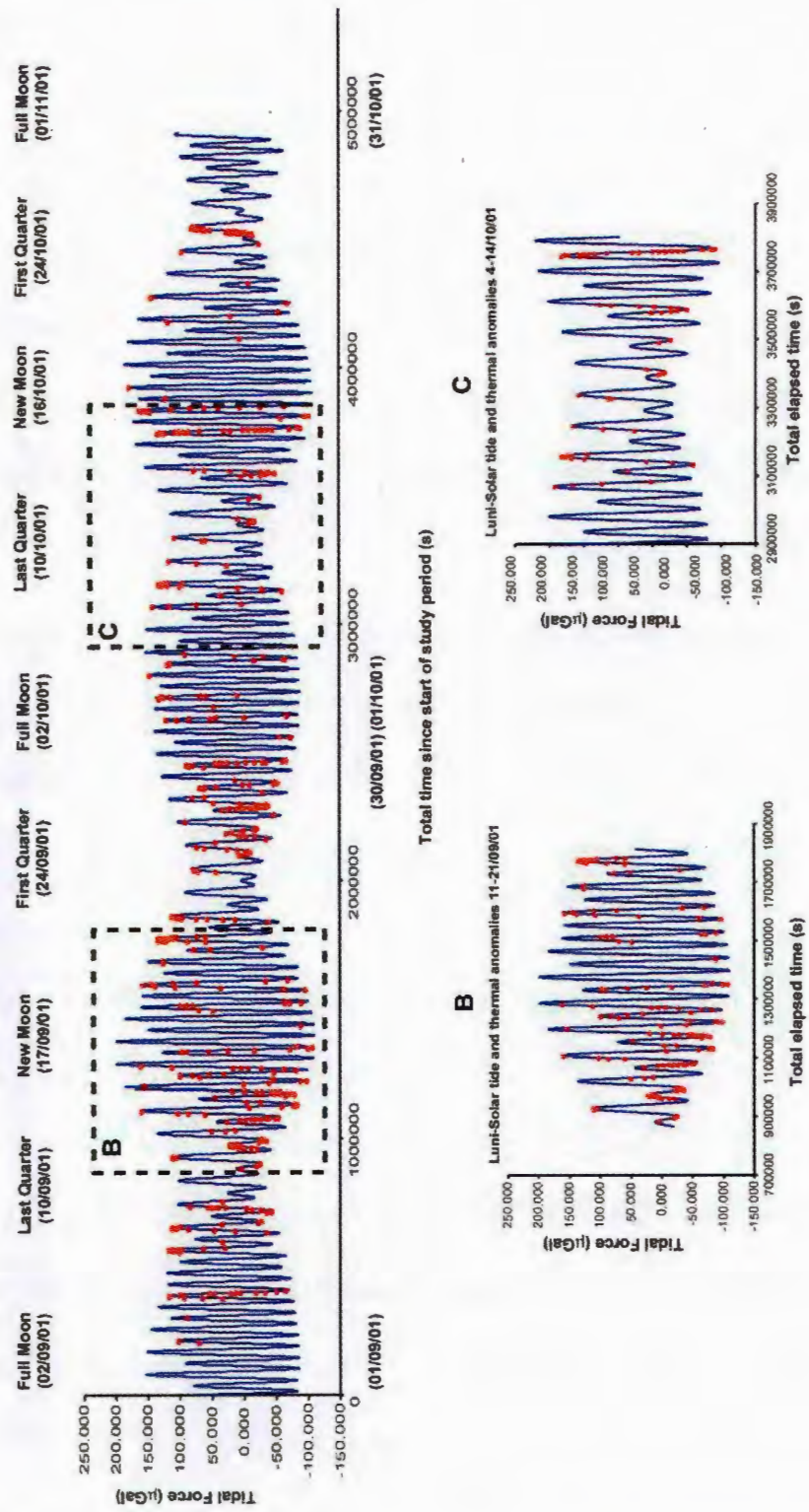

Figure 2.12: A: The variation in Lunisolar tide during the entire study period calculated using QuickTide software, for the coordinates of the Pu'u'O'o crater. The red dots indicate the occurrence of a thermal anomaly detected within Huey data. B: Focus on tide and thermal anomalies during the period 11-21st September 2001. C: Focus on tide and thermal anomalies during the period 4th -14th October 2001. These are highlighted in dashed squares indicating there location within the study period.

Tides within the solid Earth are also present, and this phenomenon is well documented (Kasahara, 2002; Patané et al, 1994 among others). Earthquake activity on the sea floor has been linked to the changing mass of the overlying ocean (Tolstoy et al, 2002). Solid Earth tides have been linked to seismicity within the Earth's crust (Kashara, 2002) as well as seismic activity at Arenal volcano (Williams-Jones et al, 2001). It is noted that for locations closest to the ocean, the changes in crustal stress are the greatest (Kasahara, 2002). Shimozuru (1987) relates the changing level of lava in the 1919 Halema`uma`u lake to the Earth tide, by relating the effect to an enclosed magma chamber with a single small conduit leading to the surface. As the Earth tide affects the dimensions of the magma chamber, this will affect the level of the fluid magma within the conduit system (Shimozuru, 1987). Shimozuru (1987) also notes that changes in the level of water within wells have also been related to the lunisolar tide, and such a scenario may be analogous to the magma chamber and conduits leading to vents within the Pu`u`O`o crater. As water is less viscous than the basaltic magma at Kilauea, the effect of the lunisolar tide will be more pronounced in water wells. It is therefore clear that the tides can affect volcanic processes.

Figure 2.12 displays a plot of the variation in tidal force calculated for Pu`u`O`o, with both the semi-semi-diurnal and fortnightly fluctuations clearly visible. I use here QuickTide software to calculate the changing tidal forces for the location of Pu`u`O`o. It is clear that at the times of the new and full Moon the semi-semi-diurnal tide displays the greatest variation in amplitude. Conversely when the Moon is in its first or last quarter phase the semi-diurnal variation tends to the lowest range in amplitude. Also plotted within figure 2.12 are the times of the thermal anomalies. These are represented as roundels superimposed upon the tidal force plot. The timings of the anomalies with respect to the local phases of the semi-diurnal and fortnightly tides appear random on first impressions. On closer inspection it appears that greater numbers of thermal anomalies are related to the waxing of the fortnightly tide to a maximum (panel B), than with the waning and minimum within the fortnightly tide (panel C). At many points the thermal anomalies

appear to be related to the tidal minimum, or at least more thermal anomalies seem to be superimposed upon the timing of the tidal minimum than the tidal maximum.

In the next section I show whether the semi-diurnal tide can be linked to events at the Beehive vent. I go onto to establish whether any relationship exists between these events and the fortnightly tide.

2.10. Relating the thermal anomalies with the semi-diurnal tide

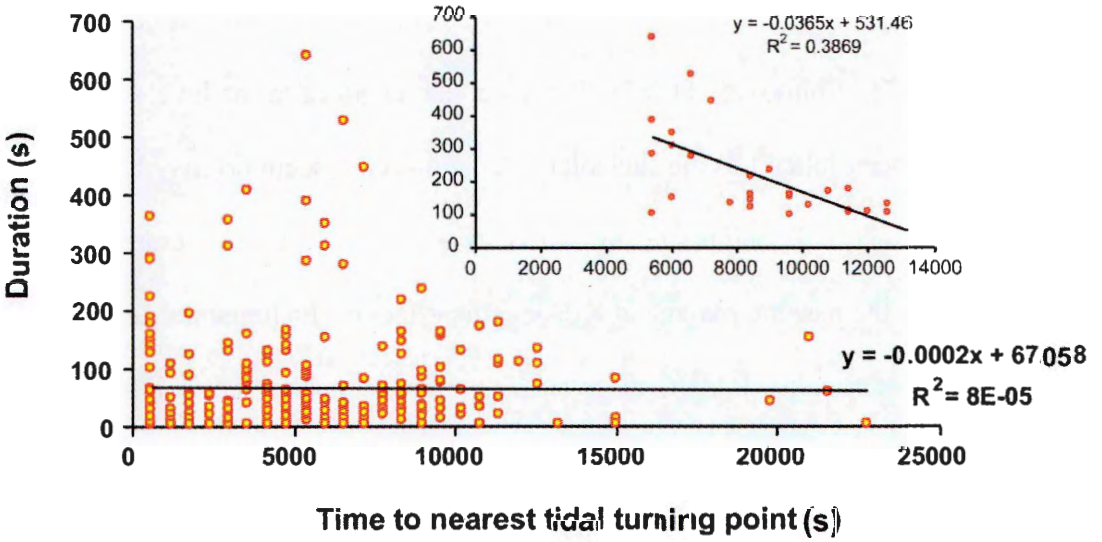

Figure 2.13: Chart showing the time period (s) between the occurrence of a degassing episode at the Beehive vent and the nearest semi-diurnal tidal turning point plotted against the measured duration of the thermal anomaly. Inset shows derived relationship when times to nearest tidal turning point has been restricted to the range 5000 to 15000 s and only those anomalies with durations greater than 100s used.

In this section I investigate the possibility of a link between the semi-diurnal tides and the occurrence of the thermal anomalies. In order to accomplish this I wrote IDL software that takes as its input the time of each thermal anomaly and the tidal force calculated for Pu`u`O`o during the two month study period, and outputs the time interval separating the tidal turning points and the thermal anomalies. The tidal force information was obtained from QuickTide software that calculates the tidal potential at 10 minute

intervals. For easy comparison with the Duck data, time was calculated for both datasets as total elapsed seconds from 00:00:00 hours on September 1st 2001.

Figure 2.13 shows the interval in seconds between each correlated thermal anomaly and the nearest tidal turning point (i.e. as it changes from waxing to waning and vice versa). If any relationship exists between the minima and maxima within the semi-diurnal tide and the thermal anomalies then it should show within figure 2.13 as a clustering of anomalies close to the origin, as this represents the occurrence of the tidal turning point. However, the trend line shown in figure 2.13 does not show this, but there does appear to be a clustering of anomalies with the longest durations a short period (4000 – 6000s : ~ 1 to 2 hours) after the tidal turning point. This may be indicative of a lag between these turning points, and therefore the time of the most stress induced by the changing lunisolar tide (Shimozuru, 1987). Such a lag may be because of the delayed effect of variation of the magma degassing rate due to a change in the rate of gaseous exsolution from the magma because of the changing forces imparted on the magma column by the lunisolar tide. A lag in the system must be involved due to the certain amount of time (dependant on the plumbing of the Pu`u`O`o conduit system) for this exsolved gas to reach vents, such as the Beehive vent, and to drive phenomena such as those I am studying here. This is discussed at greater length in section 2.14.

The graph inset within figure 2.13 shows a trend line calculated for only those anomalies that occurred between 5000s and 15000s and with durations greater than 100s in an attempt to highlight this clustering. The derived relationship shown by the trend line in the inset graph suggests a stronger possible relationship if we compensate for these lag effects within the Pu`u`O`o system. This particular finding indicates that those thermal anomalies detected at the Beehive vent with the longest duration and with compensation for the system lag time *may* occur preferentially near the semi-diurnal tidal turning points. However, due to the lower overall number of longer duration anomalies in comparison

with the more common shorter duration anomalies within the study period, it is difficult to identify this relationship. In the next chapter I suggest that those anomalies with the longest duration (cooling interval) are associated with the greatest ejected mass at the Beehive vent.

It may also be possible to relate the amount of change within the semi-diurnal tide within a discrete period, such as a single day, to the rate of degassing at the Beehive vent: i.e. do periods in the semi-diurnal tide with the greatest fluctuation in tidal force have any greater effect on the number of degassing events than other periods when the semi-diurnal tidal fluctuation is less? In order to better assess any such possible relationship I have created what I call the Tidal Fluctuation Index or "TFI".

2.11. The Tidal Fluctuation Index ("TFI")

I define the TFI as a ratio between the range in tidal force experienced between one set of semi-diurnal tidal turning points (i.e. a minimum → maximum) and the range experienced in the subsequent set of turning points (i.e. a maximum → minimum). This concept is displayed in figure 2.14. The smaller range is always divided by the larger range, irrespective of which came first. This methodology restricts the TFI to a positive range from 0 to 1.

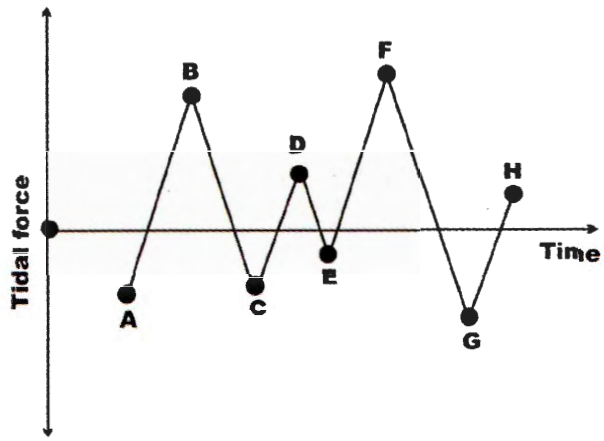

Figure 2.14: How the Tidal Fluctuation Index (TFI) is calculated. The TFI effectively calculates the relative ratio of the inter-turning point values between a set of three points (i.e. A→B: B→C). The largest value is always divided by the small value and is calculated irrespective of sign. This restricts the value of the TFI to the range 0 to 1.

Where these relative amplitudes are of a similar range (in figure 2.14 A→B:B→C), such as at times of new and full Moon then the TFI will tend towards 1. This indicates a higher variation between the maximum → minimum → maximum (or vice versa) during one cycle, *and therefore a higher variation in absolute tidal force encountered*. For example, at time of new and full Moon the highest tides are encountered, but the intervening low tide is of a similarly low magnitude relative to the mean level.

Where the difference in relative amplitudes is largest (in figure 2.14 D→E:E→F), such as at the times of the first and last quarter Moon then the TFI will tend towards 0. This indicates a lower variation between the maximum → minimum → maximum (or vice versa) during one cycle, *and therefore a lower variation in absolute tidal force encountered*. For example, at times of first and third quarter Moons, the least variation between high and low tides are encountered relative to the mean level.

Figure 2.15 displays the calculated variation in tidal force calculated for the longitude and latitude of Pu`u`O`o, and the derived TFI. The TFI calculated over a single cycle of point1→point2→point3, shows a waxing and waning between 0 and 1 in sequence with the fortnightly tide. However, this "single" cycle TFI shows considerable variation

due to the complex interplay of the Lunisolar tidal forces. It is still possible to identify that where the variation in tidal force is least, then the TFI tends towards 0. In order to clarify this, the third line shown within figure 2.15 represents the TFI integrated over 8 tidal cycles.

It must be remembered that the TFI is a relative measure rather than an absolute measure, so at those times in the Lunisolar cycle where there is very little variation between low and high tides, but the actual range between the maximum and the minimum is still relatively low the TFI will still tend to 1. This anomalous effect can be compensated for by integrating the TFI over several cycles. I use the integrated TFI in the next section to relate the variation of the fortnightly tide with degassing events at the Beehive vent.

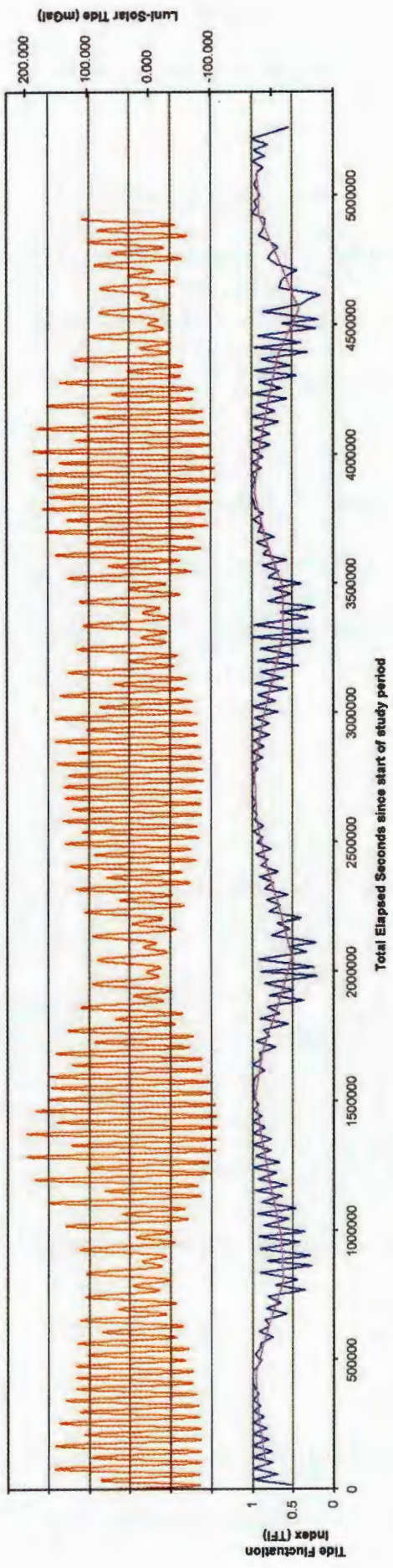

Figure 2.15: Graph showing the Lunisolar tide during the study period. The Tide Fluctuation Index (TFI) is also plotted as well as a curve showing an integrated TFI over 8 cycles. The TFI is an index based on the ratio between the range in tide values between any given tidal extreme and the preceding and succeeding tidal extreme. Therefore on days where the tidal range is similar a TFI of ~1 is calculated. The TFI tends towards 0 with increasing disparity between the two ranges

In figure 2.16 I have plotted the number of degassing events recorded over discrete intervals within the single cycle TFI. This is an attempt to relate the number of degassing events to the Lunisolar tide, as suggested by the apparent preference of degassing events for tidal minima observed in figure 2.12. In figure 2.16 there appears to be a weak relationship indicated by the positive gradient of the trendline, suggesting that as the TFI tends towards 1, then the number of recorded degassing events also increases. The TFI tends to 1 at times of the greatest tidal variation, such as the new and full Moons. However, due to the nature of the TFI it is difficult to relate the particular phase of the Lunisolar cycle to the process responsible for increasing the rate of degassing events- i.e. we cannot tell from this whether it is the relatively higher maxima or the relatively lower minima at these times triggering the events. In section 2.14 (p91), I discuss this further and relate this observation to those of degassing events and tidal processes on other volcanoes.

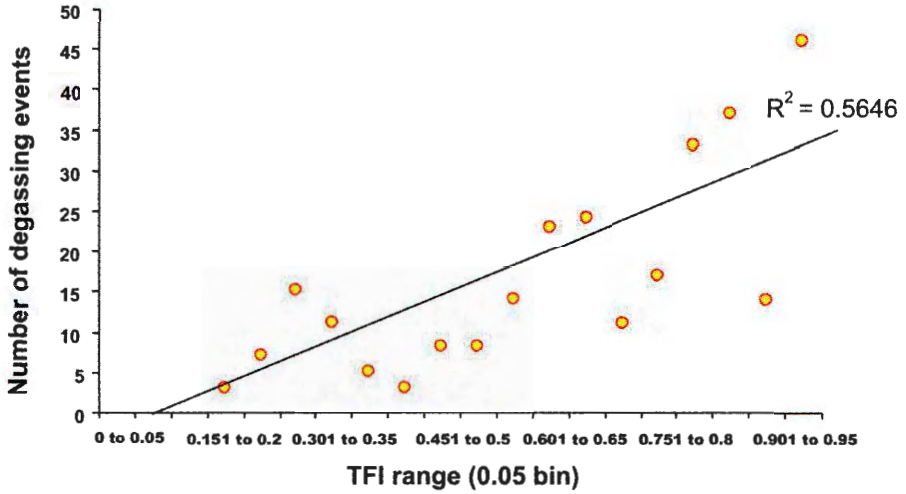

Figure 2.16: The number of correlated degassing events plotted as occurring within discrete 0.05 ranges of the TFI. This graph shows as the value of the TFI increases, so does the number of degassing events occurring. This suggests that more degassing episodes occur when the semi-diurnal tidal variation is least.

The lack of any clear relationship within figure 2.13 between the actual turning points within the semi-diurnal tide and the occurrence of degassing events does not

categorically rule out the actual presence of a stronger relationship. Any relationship may be obscured by such factors as crater fume conditions, the temporal resolution of the data and even the system of analysing the data. These clouding effects are not aided by the restrictive two month study period. However, a relationship is suggested in figure.2.16 between the TFI and the occurrence of degassing events. This relationship intimates that the majority of degassing events occur when the TFI tends towards 1, and therefore the greatest difference in tidal range, although it is impossible to definitively state here whether it is the relatively large maxima or minima at such times which may be triggering the degassing events.

In the next section I investigate the relationship between degassing at the Beehive vent and the longer period fortnightly tide, as it is possible that the Pu`u`O`o system may respond more obviously to tidal forces that change over a longer period, and hence overcome effects that may obscure the relationship over shorter timescales.

2.12. Relating the Beehive degassing events to the fortnightly tide

In the previous section I investigated the possibility of a link between the semi-diurnal tide and the degassing events at Pu`u`O`o with limited success. It is important to also try to link these events with the fortnightly tide, as the Pu`u`O`o system may be responsive to changes in tidal forces over longer time periods. Dzurisin (1980) found that eruptions at Kilauea occurred in a cycle of 14.7 days, based on records since 1832 (Dzurisin, 1980). Of Mauna Loa's most recent historical eruptions, 37 appear to occur randomly and appear to possess no obvious relationship with the fortnightly tide. Eruptions at Stromboli appear to be linked to the minimum within the fortnightly tide (Shimozuru, 1987). It is therefore of interest to investigate whether smaller scale events such as

degassing from the Beehive vent are also related to the maximum within the fortnightly tide.

As shown within figure 2.12, the waxing and waning of the fortnightly tide is present as the variation in the maxima and minima of the semi-diurnal tidal force over the course of the two weeks. The integrated TFI represents this fortnightly variation in the semi-diurnal tide.

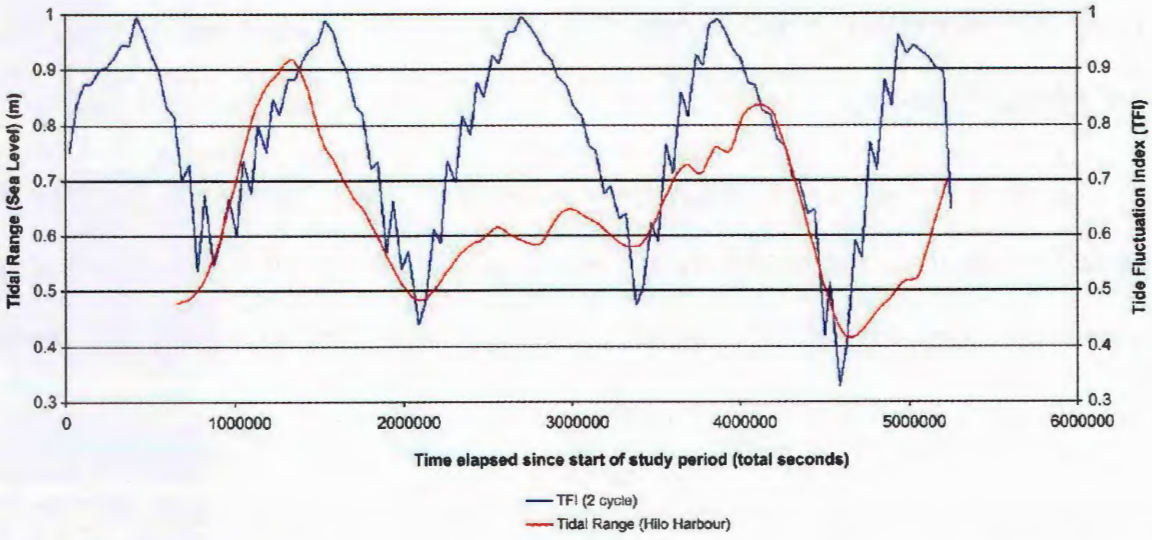

Figure 2.17: The TFI integrated over 2 cycles (blue) and the tidal sea level change in Hilo Harbour (red) during the study period.

Figure 2.17 shows the relationship for the calculated TFI (integrated over 2 cycles) and the tidal range in sea level (m) during the study period recorded at Hilo seafront east of Pu`u`O`o. The oceans rise and fall on a daily basis in response to the semi-diurnal tide, but the range in sea level between the high and low ocean tides also changes in response to the fortnightly tides. I have included this to show that the TFI can be related to known phenomena that are affected by the fortnightly variation in tidal forces. Although the match is not identical between the tidal range at Hilo harbour and the TFI, it can be seen that when the TFI is increasing to 1 after a minima, then the tidal range is also increasing after a short lag, although the magnitude and rate of this increase does not always match that of the TFI (i.e. in early October).

The tidal range of sea level is greatest at times where the TFI is closest to 1, and the fortnightly tide is at a maximum. The variation in sea level does not match the TFI exactly, but increases in range when the TFI is increasing towards a maximum and similarly decreases in range when the TFI is decreasing. The range in sea level recorded at Hilo possesses a small lag compared to the TFI calculated for Pu`u`O`o, and also the range in variation differs. The lag may be due to the fact that Hilo is some 30 miles east of Pu`u`O`o and possesses a slightly different tidal vector at slightly different timings (Melchior, 1978). The differing range in variation is because the change in sea level in response to the changing tidal force is highly dependant on the local bathymetry and ocean currents as well as the inertia of the sea mass itself (Melchior, 1978).

2.13. Is there a link between degassing and the fortnightly tide?

The timing of past events at Kilauea have been clearly linked to the fortnightly tidal maximum (Dzurisin, 1980), such as the fluctuations in the level of the Halema`uma`u lava lake measured in 1924 by H.Jaggar (Shimozuru, 1987). Here I am trying to relate a lower level of effusive activity at Kilauea with the fortnightly tide. Figure 2.18 relates the degassing events that occurred at the Beehive vent to the TFI calculated and integrated over 2, 4 and 8 cycles (A, B & C respectively). Clearly evident within A & B are the smaller peaks and troughs resulting from the integration of the TFI over too few cycles, whilst C displays a smooth response to the changing phase of the fortnightly tide.

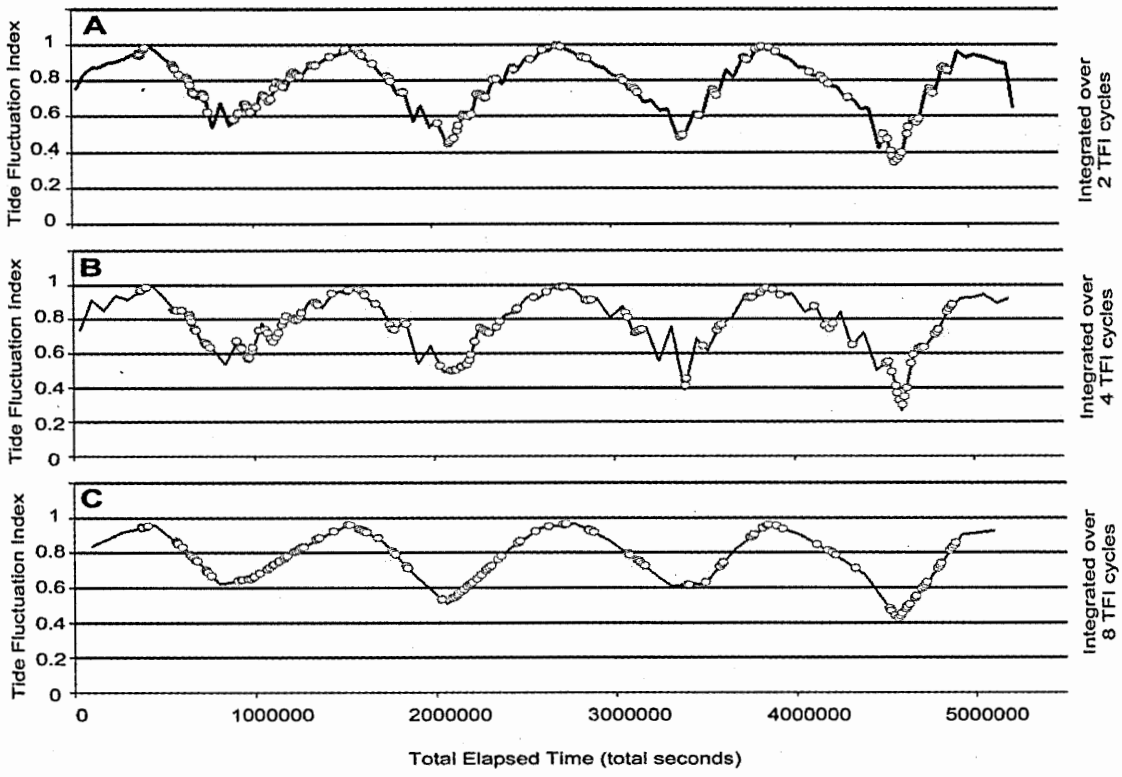

Figure 2.18: Plots of the Tide Fluctuation Index (TFI) relating to the relative ratios in tidal range integrated over 2 (A), 4 (B) and 8 (C) TFI cycles. The TFI integrals chart the variation in tidal force over a number of days and aids in relating Lunisolar tidal force to events that may possess a lag due to physical processes (i.e. rate of degassing from magma within the Pu`u`O`o system). Note that the smoothest TFI integral (C) accurately reflects the change in amplitudes of the diurnal Lunisolar tide displayed in Figure 2.15. Also plotted on these curves are the times of the thermal anomalies coinciding with RSAM signals. Note that in C it appears that more anomalies appear to be located on the waxing slope of the TFI curve as it trends from ~0 to ~1 than on the waning slope.

I found that by integrating over 8 cycles a smooth curve would result, clear of any intermediate peaks and troughs within integral TFI's calculated over 2-7 cycles. The times at which the degassing events occurred at the Beehive vent are represented as dots plotted upon the line representing the TFI in figure 2.18. It is perhaps evident within figure 2.18 (C) that these instances of degassing appear to occur preferentially as the TFI is increasing, rather than periods when the TFI is decreasing. This shows that as the fortnightly tidal force is increasing towards the time of a new or full Moon, then the number of degassing events recorded is higher than at those times the new or full Moon is waning towards the first or last quarter moons.

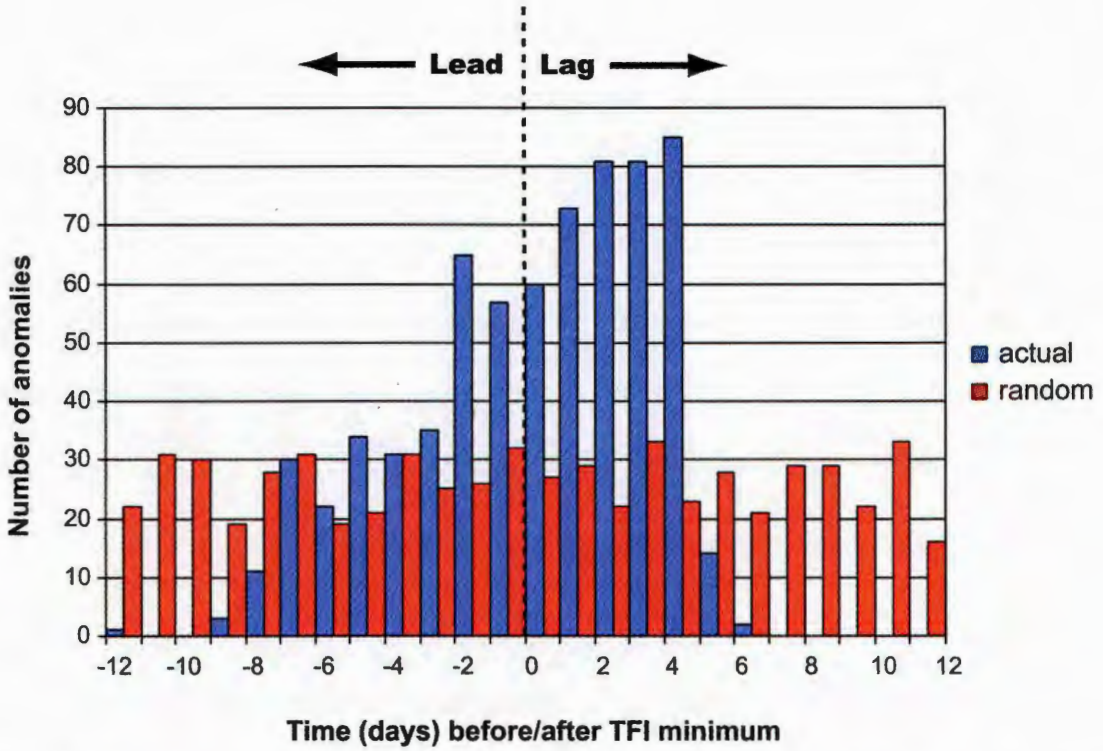

Figure 2.19: Two histograms showing the frequency distribution of both correlated thermal anomalies and a set of randomly generated anomalies. There is a distinct relationship in which the thermal anomalies cluster around t=0, indicating the TFI minimum in the fortnightly tide. This relationship is not evident in the randomly generated dataset.

Figure 2.19 attempts to clearly highlights this relationship by plotting all the actual degassing anomalies that occur both after (lag) and before (lead) a minimum turning point within the TFI integrated over 8 cycles. As figure 2.19 clearly shows, there is a definite clustering of these actual thermal anomalies about the TFI minimum (t=0) that is certainly not replicated in the set of randomly generated anomalies plotted in red. I found that for the actual thermal anomalies shown in figure 2.19, 64% occur after the TFI minimum, and 36% before. If there was no relationship between the phase of the fortnightly tide, as summarised by the TFI curve, and the occurrence of degassing events then we might expect a roughly 50% lead and 50% lag figure. Applying the same method to the randomly generated set of anomalies in figure 2.19, 51% occur as a lag and 49 % as a lead.

The pattern of actual thermal anomalies about t=0 in figure 2.19 shows a distribution with the number of anomalies increasing 7 to 8 days before the minima in the

fortnightly tide and decreasing to background levels 6 days after the minimum point. There is an important distribution shown by the pattern of thermal anomalies in figure 2.19: the peak number of recorded thermal anomalies occurs 4 days after the minimum turning point and tails off over the next 2 days at a much quicker rate than the build-up before the turning point. This pattern of anomalies about t=0 shows a skewed distribution, and may be important in identifying the processes and mechanisms responsible for these degassing events. In the next section I attempt to relate this pattern shown in figure 2.19 to the possible mechanisms responsible.

The skewness of this distribution (obtained using the MS Excel Statistical Analysis Toolpack) has been calculated as 0.68 for the actual thermal anomalies (if the number of anomalies exhibited a normal distribution about t=0 then the skewness would tend to 0). The standard error of skewness (SES), can be calculated from $\sqrt{(6/n)}$, where n is the number of samples. In this case, I calculate SES as 0.09. Using the "twice the standard error of skewness" rule (Tabachnik & Fidell,1996), the skewness of 0.68 is greater than 0.18 suggesting that this skewed distribution is significant. Therefore, this pattern of the number of recorded thermal anomalies cannot be regarded as insignificant and must be related to ongoing processes relating the fortnightly tide to the occurrence of the thermal anomalies. This implies that more degassing episodes occur as the fortnightly tide is increasing towards the time of maximum fortnightly tide.

However, it is difficult to conclusively prove this relationship as this dataset spans just two months, which is insufficient to prove the association of events with a fortnightly cycle. It is not possible to extend the thermal anomaly dataset significantly as the Huey radiometer lost track of the thermal anomalies 2-3 weeks after the 2 month study period in September and October 2001. The low number of fortnightly tidal cycles within such a short study period precludes a more extant statistical analysis due to the small spread and lack of range within the data. Hence, I interpret the apparent preferential occurrence of

degassing episodes on the waxing fortnightly tide as suggestive of a relationship that warrants further and longer study to definitively prove the existence of this relationship. In the next section I investigate the possible causes behind such a relationship.

2.14. Mechanisms to account for preferential tidal degassing at the Beehive vent.

In this section I investigate the various mechanisms by which the changing tidal force may affect the rate of degassing at the Beehive vent and detection of the thermal anomalies within data from the Huey Duck.

Observations made by H.Jaggar of the Halema`uma`u lava lake in 1919 suggested a possible semi-diurnal oscillation of the level of the lake (Shimozuru, 1987). When the tidal force was at a minimum, the level of lava was at its highest (Shimozuru, 1987). If a similar process is effecting the magma within the Pu`u`O`o conduit, then at times of tidal minima, the level of the magma will be relatively high. This might modulate the degassing events at the Beehive vent in quite a simple manner. If the magma level is highest at these times it might be possible that the free-magmatic surface within the Beehive vent is closer to the actual vent opening within Huey's FOV. Any degassing from this surface will be more likely to be detected by the Duck when the level is highest, as any gas and/or ejecta will be emplaced onto the crater floor and within the Duck FOV. This is especially true for molten ejecta. When the free-magmatic surface is lower, any material released from this surface as ejecta by the passage of the gas will be more likely to remain hidden from the Duck's view by the walls of the Beehive vent.

Shimozuru (1987) calculates that it is possible when considering a volcanic system as a simple chamber with a single open conduit through which the fluid magma can rise and fall in response to the tides, for the level of magma to change by several tens of centimetres. This is in response to the dilation of the Earth's crust which is affected by the

tidal force. In effect, the magma as a fluid is 'squeezed' upwards. This can have a marked effect on even smaller bodies of fluid such as water within a borehole, changing the level by a number of centimetres (Kasahara, 2001). Shimozuru (1987) analysed the recorded fluctuations of the lava lake in response to the tides present in 1919, and deduced that the Halema`uma`u lava lake was supplied not by a single magma reservoir, but by a larger reservoir surrounded by a number of smaller interconnected reservoirs. Due to the known complexity of the conduit system at Pu`u`O`o coupled with the complex plumbing of the Beehive vent, likely due to the August 25th crater floor collapse event (the degassing events were only noticed at the Beehive vent after this collapse), it is likely that the response of the level of the free magmatic surface within the Beehive vent will also be complicated. This will affect the relationship between degassing events and the tides.

If changing levels of the free-magmatic surface within the Beehive vent are responding in this manner to the semi-diurnal or fortnightly tides, then we might expect that those degassing events possessing a thermal signature with a prolonged cooling duration occur predominantly at times when the semi-diurnal tide is at a minimum. Such thermal anomalies may be indicative of the presence of molten ejecta due to the nature of the cooling curve, and may be related to stronger degassing events required to eject such a mass as well as a higher level of the free magmatic surface. This may be the case is if we assume a parallel with the semi-diurnal oscillations recorded at the Halema`uma`u lava lake in 1919, where the highest lake levels were associated with tidal minima (Shimozuru, 1987). In figure 2.13 (p78), the anomalies with the greatest duration appear to occur closest to both the semi-diurnal tidal turning points.

This situation may be clarified if we consider figure 2.16 (p84) and also if we consider another mechanism that may be contributing to the detection of thermal anomalies at the Beehive vent. If the level of magma is at its highest at the minimum tide value, then there may be a change in the rate of vesiculation within the magma at depth. This will

occur due to the changing column mass of overlying magma (Shimozuru, 1987). This in turn will affect the 'budget' of exsolved gases available to drive degassing events at the Beehive vent. If the level of the magma column is at its highest at times of the tidal minimum then it might be expected that this will decrease the rate of vesiculation due to the greater mass of magma in the column, and hence restrict the volume of exsolved gases and ultimately, therefore, the rate of degassing. This type of scenario has been suggested for Arenal volcano (Williams-Jones et al, 2001) and Masaya volcano (Stoiber et al, 1986). Increased levels of exsolution of gas will drive more vigorous degassing from a vent, and more likely the accompaniment of ejecta as the gas escapes from the free-magmatic surface within the vent. Therefore degassing is more likely to occur when the magma column is lowest, and therefore the pressure created by the overlying magma within the system is lowest. The level of magma, if we remain consistent with the comparison with the Halema`uma`u lava lake, will be lowest at times of maxima within the semi-diurnal tide.

Figure 2.16 suggested a relationship between the greatest range in the semi-diurnal tide as indicated by increasing TFI and the number of degassing events recorded at these times. If we consider the exsolution scenario above, which may modulate the rate of degassing, and apply this to the interpretation of figure 2.16 then it may be the maximum in the tide at times of the greatest variation in the tides that will trigger increased numbers of degassing events. Therefore, the weak relationship displayed in figure 2.16 may be positive proof of this hypothesis. This observation is also valid if we consider the apparent relationship between the fortnightly tide and the preference of degassing events to occur as the tide is waxing towards maximum.

The relationship between the number of thermal anomalies and the minimum turning points in the TFI in figure 2.19 (p89) describes a definite pattern that may assist in identifying the above process. The number of thermal anomalies gradually increase from 8

days before a minimum turning point, continue to increase in number as the minimum turning point (or t=0) passes until a peak is reached 4 days after the turning point, after which the number of events drops sharply. This pattern is very consistent if we consider that as the TFI is approaching a minimum turning point, then the related effects on the magma column will become apparent before the actual turning point has been reached. According to the TFI, similar variation in the magnitude of the variation in tidal force is apparent at 2 days before and after the turning point. Hence, it is difficult and perhaps inadvisable, to try and relate only those degassing events that occur after a minimum turning point in the TFI as the fortnightly tide is having an increasing effect towards the time of the TFI minima. The increasing number of events before the minima at t=0 in figure 2.19 are indicative of this process. **<??? Adjust???>**

Such a relationship will be confused, however, by a supply of fresh magma into the system which will also increase the levels of exsolved gasses with which to drive degassing events at the Beehive vent (Williams-Jones et al, 2001). Hence, all these factors may only serve to obscure any relationship between degassing events detected by the radiometers and the changing tidal force.

It is quite clear that the Pu`u`O`o system is complex, with other vents within the crater tapping an ephemeral supply that often also varies the supply to lava flows elsewhere on the east rift zone (Heliker & Mattox, 2003). The sudden manner in which thermal anomalies where recorded from the Beehive vent after the 25th August crater floor collapse also suggests a level of uncertainty in the plumbing of that vent. It is unclear whether this configuration changed during the course of the study period, and it is certainly possible that the vent itself might change during the course of the study period. Prior to the study period, lava had last ponded within the Pu`u`O`o crater in 1997 (Heliker & Mattox, 2003). Two months after the study period considered here in January 2002 lava issued from various vents on the Pu`u`O`o crater floor, eventually filling the crater to within 50m

of the rim (Heliker & Mattox, 2003). One of the vents involved was possibly the Beehive vent. It is possible that activity further down the flow field caused the lava in the system to "back-up", causing renewed activity at Pu`u`O`o. This shows that the supply of magma at Pu`u`O`o is subject to fluctuations due to activity elsewhere on Kilauea.

If molten ejecta often accompanied degassing events from this vent, then it is possible that an amount of this may form a small spatter rampart or similar structure around the vent. If this was the case, then we might very well expect the amount of molten ejecta events observed by the radiometer to decrease during the study period, or at the very least to confuse the relationship between the magma level within the vent and the changing tides. Visual observations were not possible during the viewing period from either the video camera, or personally due to the viewing conditions. The presence of 'tube' like Hornitoes created by just this method within the west gap of Pu`u`O`o in January 2004 as shown in figure 2.11 (p71), certainly suggests that this must be considered the case for any spattering events at the Beehive vent within the study period.

All these processes greatly complicate the identification of a true relationship between degassing from the Beehive vent and the tides by simply detecting hot emitted material with the aid of a simple radiometer system such as the Ducks. The constantly fluctuating viewing conditions experienced by the Ducks also compound this problem, and make it difficult to definitively relate any single process as all processes are linked in this highly complex system.

The relatively short two month study period and the unavailability of Duck data after the study period, due to the loss of signal (A.Harris pers.comm), also compound this problem. It is difficult to relate such a two month study period to the fortnightly tide and expect to find obvious and meaningful relationships. The possible link found between the increasing fortnightly tide and the occurrence of degassing events may just be an artefact, and would not be apparent if a longer duration study period was used.

In order to reduce these errors and shortcomings leading to the uncertainties of the data discussed here, a future study must be undertaken that will relate not only activity at a single vent within the Pu`u`O`o crater, but overall effusive activity on the scale of Kilauea itself. Such a study may take into account the total lava supplied to the active flow-field on the south flanks of the volcano as well as the rate of degassing from Pu`u`O`o and the entire south east rift zone, even that from the Kilauea caldera itself.

Such a locally expansive study would be able to relate the overall rate of degassing and total volume of lava erupted, and this may counter the local problems of viewing conditions of a single radiometer at a single vent as well as the complexity of the supply conduit to that vent. These shortcomings and suggested remedies are further discussed in the final chapter of this thesis.

Conclusions

Thermal anomalies detected within radiometer data returned from the Pu`u`O`o crater have been linked to degassing events from the Beehive vent. This was accomplished by showing that the times of the thermal anomalies matched the times of increased seismic amplitude recorded within RSAM data at HVO. The RSAM anomalies had been independently interpreted as degassing events within the Pu`u`O`o crater, due to the sustained low amplitudes of these anomalies caused by the passage of gas through the vent walls. There were two main types of thermal record associated with these correlated anomalies. The first type is typified by a sharp onset in recorded temperatures followed by a similarly prompt return to the previous background temperatures. These have been interpreted as the detection of the hot gas escaping from the Beehive vent. The sharp drop-off in temperature is attributable to a combination of the rapid dispersal and mixing of the hot gas within the relatively cool atmosphere of the crater and the movement of the gas

upwards and out of the FOV of the radiometer. The second form of thermal anomaly recorded with the radiometer data displays a similarly rapid onset in temperature but a much more pronounced degradation in temperature back to the previous ambient temperatures. The decrease in temperature is reminiscent of the cooling curve described by cooling lava flows (Hon et al, 1995). These events at the Beehive vent are interpreted as degassing accompanied by an amount of molten ejecta. This scenario is considered in more depth in the next chapter.

The thermal anomalies relating to degassing events at the Beehive vent are not evenly spread throughout the study period, suggesting a non random origin. As figure 2.6 (p61) shows, the number of degassing events fluctuates with an apparent pattern. This pattern appears to be related to the fluctuation within the fortnightly tide, as related by the TFI, also plotted on figure 2.6. Further investigation revealed that the number of degassing events may occur preferentially on the fortnightly tide as it waxes towards tidal maximum. On a shorter time scale, analysis of the number of degassing events recorded appears to increase at times of maximum semi-diurnal tide. This suggests a link between the exsolution of gases and the changing height of the magma column in response to the tide.

These findings are in accordance with observations of the Halema`uma`u lava lake in 1919 (Shimozuru, 1987; Dzurisin, 1980), which displayed high lake levels at times of tidal minima. Using this logic, low levels of magma within a column will occur at times of tidal maximum. These findings agree with previous research on Kilauea (Shimozuru, 1987) which link eruptions of Kilauea to the maximum fortnightly tide.

It is most likely that the degassing events at the Beehive vent respond to the changing tides in a number ways. It is possible that the tides affect the level of magma within the Beehive vent, from which exsolved gases escape, often accompanied by an amount of molten ejecta. At times this level is higher, making it more likely that ejecta can land on the crater floor. There does not appear to be a strong correlation linking thermal

records associated with degassing events accompanied by molten ejecta (i.e. an increase in number of thermal records with a distinct cooling curve) at times of low tidal force, when the level of the magma is highest (Shimozuru, 1987). There are a number of issues with this mechanism, not least the likelihood that repeated molten spatter within the vent walls will only serve to increase the height of the vent opening, leading to a decreasing number of such thermal records with the passage of time. Also likely, is the possibility that the changing tidal potential is affecting the rate of vesiculation within the magma at depth. However, as the Pu`u`O`o system is not closed, there will be at some stage the supply of new fresh magma that will degass at an increased rate. This supply of new material into the system, the unknown relationship between the plumbing of the Beehive vent and the rest of the Pu`u`O`o plumbing and lava supply will only serve to cloud the identification of a true relationship between the Lunisolar tides and events related to degassing from the Beehive vent.

All this highlights the difficulty in proving a relationship between degassing events at the Beehive vent and the tides. In order to definitively answer this question a wider ranging study must be undertaken which investigates the rate of degassing from a vent and the amount of spattering experienced, and also obtain definitive information on the rate of supply of fresh gaseous magma to that vent. Physical measurements of the level of magma within the vent must also be taken, perhaps by using the VLF instrument (Kauhikauau et al, 1996). Visual observations of the vent itself must be made so that any change in vent geometry may be accounted for. Such a wide ranging study may definitively be able to relate degassing and spatter events from a single vent to the changing tides.

Despite this, there does appear to be a tantalising relationship between the changing tides and the events detected by the radiometer and RSAM instruments at the Beehive vent, but more detailed and wider ranging work needs to be accomplished to conclusively prove this.

I would like to gratefully acknowledge the help of the USGS Hawaii Volcano Observatory in providing me with the opportunity to spend September and October 2001 as a volunteer. The work completed during this time at HVO forms the basis of this chapter. I would also like to thank and acknowledge Luke Flynn of HIGP, University of Hawaii, Manoa for providing financial and logistic support during July 2001- June 2002, without which this work would not have been possible.

3. A technique for estimating the mass of molten ejecta from degassing events from a single 'Duck' radiometer

3.1.Introduction

In the previous chapter I investigated the possibility that thermal anomalies associated with degassing events at a vent in the Pu`u`O`o crater of Kilauea volcano are linked with the changing Lunisolar tide. The anomalies were detected in radiometer data returned from the edge of the crater and can be placed into two main categories. The first category consists of those anomalies characterised by a rapid onset in temperature followed by an equally rapid decline back to the ambient temperature. These were inferred to be the detection of hot gases ejected from the Beehive vent passing through the radiometer field of view (FOV) and dissipating in the crater. The second category consists of anomalies that were characterised by an equally rapid rise in temperature but with a much slower decline in temperature. This decline in temperature is reminiscent in form of the cooling curves measured from lava flows elsewhere on Kilauea volcano (Kesthelyi, 1995; Hon et al, 1995), suggesting the presence of molten material in the radiometer FOV. These anomalies were interpreted as being due to degassing events with associated molten ejecta emplaced in the radiometer FOV and are further studied within this chapter.

I shall show how a simple temperature record representing a single discrete area of the Pu`u`O`o crater floor can be used to estimate the mass of molten material ejected from a single vent. I shall base this on the premise that large spatter blebs will take longer to cool to a certain temperature than smaller spatter blebs. I shall use the two dominant features of the thermal anomalies, the maximum temperature and the duration, as input into a model based on thermal diffusion in a single spatter bleb to estimate the mass of molten ejecta associated with each event.

By gaining an understanding of the size and mass of any spatter ejected during a degassing event it is possible to infer the strength of the event expelling the gas escaping from the free magmatic surface in the Beehive vent. This adds extra utility to the relatively cheap, yet highly capable system of radiometers used at Pu`u`O`o

3.2.Temperatures detected from in Pu`u`O`o crater

In the previous chapter I investigated the causes of thermal anomalies in radiometer data from the Pu`u`O`o crater during September and October 2001. I found that it was likely that at least some of the events may be interpreted as degassing events accompanied by molten material ejected from the free magmatic surface in the Beehive vent. In this chapter I use the same derived parameters of anomaly magnitude (maximum temperature achieved) and duration from the same temperature dataset as used and described in the previous chapter. This description and discussion can be found in section 2.3.

3.3.Modelling the cooling of a molten spatter bleb

In the initial development stages of the simulation of the cooling of molten spatter, I investigated the use of equations for the cooling of molten lava derived empirically by Hon et al (1995). These were derived from radiometer measurements of the cooling surface of a Hawaiian lava lake. I found these cooling rates of lava not to be consistent with the cooling trends apparent in the degassing thermal anomalies, as might be expected. A lava lake as measured by Hon et al (1995) is a much greater "thermal reservoir" than a single bleb cooling from molten, and hence the time taken for the surface to cool was much longer than that observed in the "duck" radiometers. Therefore by using the premise that

larger molten blebs will take longer to cool than smaller blebs due to the difference in volume and surface area and the actions of the various cooling mechanisms, I investigated the use of alternative methods to simulate the cooling of various bleb sizes.

Hot molten ejecta separated from the original magmatic material in the Beehive vent and emplaced into the relatively cool surroundings of the open Pu`u`O`o crater will cool until the material is in thermal equilibrium with its surroundings. Once any fresh basaltic molten material is exposed to the atmosphere it will rapidly chill and form a thin glassy layer (Hon et al, 1995). This is often visible on fresh lava flows as the very thin layer that spalls off as the flow is emplaced (Keszthelyi et al, 1998). Any molten ejecta is subject to the same rapid process of chilling, especially considering the passage of the ejecta through the atmosphere. The rate at which such a spatter 'bleb' will cool is dependant on a number of factors, including the thermal properties of the material itself, and the rate of conduction of heat into the surrounding atmosphere (convective cooling) and also into the ground after impact.

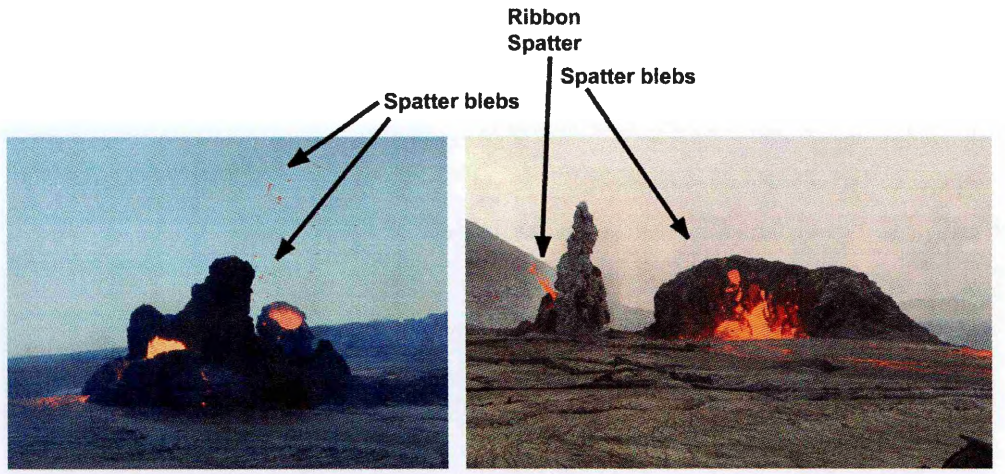

Spattering from Hornitoes in Pu`u`O`o crater (west gap pit) 2003 -2004
(Photographs courtesy of USGS Hawaii Volcano Observatory)

Figure 3.1: Spatter blebs and ribbons resulting from degassing through a free-magmatic surface at vents on the Pu`u`O`o crater floor in later 2003 and early 2004.

Any analysis of spattering from vents or hornitoes upon the Pu`u`O`o crater floor shows that spatter blebs are emplaced in a variety of shapes and sizes. Figure 3.1 shows a

pair of spattering episodes in the Pu`u`O`o crater during 2003 and 2004. There is a wide variety in shapes and sizes resulting from even a single degassing event. Larger ejected fragments such as ribbon spatter or even bombs may also break apart on impact, often akin to fluidal splashing (Sumner et al, 2004).

It is a complex problem to predict the cooling of a number of spatter blebs ejected onto the crater floor. Some factors are unknown for each degassing event, such as the vesiculation present in the bleb, the heat loss while the bleb was in free-fall, whether the bleb was originally part of a larger bleb before emplacement in the radiometer FOV and so on. Furthermore, estimates of heat loss due to convective cooling also vary considerably due to the effects of wind velocity (Keszthelyi & Denlinger, 1996).

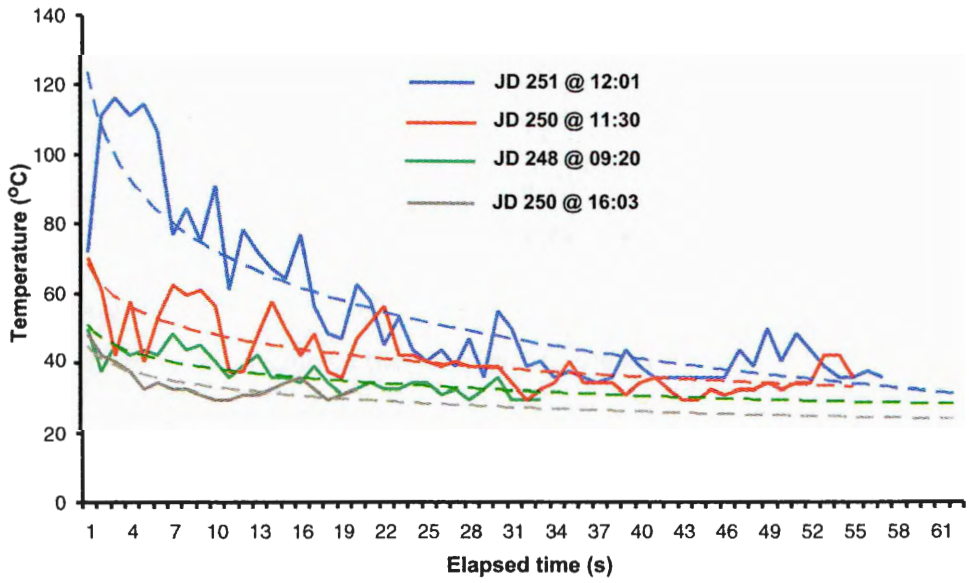

Figure 3.2: Different rates of cooling with differing initial temperatures for various anomalies detected in the radiometer FOV suggest different sizes of molten ejecta. The dashed lines are exponential best-fit lines approximating the cooling of each event.

This is understood to be an important heat loss mechanism for the lava flows with a large surface area (Keszthelyi & Denlinger, 1996), but it is poorly understood for small amounts of spatter.

In essence, at Pu`u`O`o all we have is a record of the relative cooling of hot material in the radiometer FOV (Harris et al, 2003) so we must therefore create an idealized scenario of spattering from the Beehive vent on which to base a model to match this single thermal record.

Such a set of thermal records is shown in figure 3.2, for a number of distinct anomalies obtained for different days. What is apparent in even this small subset of over 500 individual anomalies (refer to chapter 2) is the variation in initial peak temperature and the interval that the anomalies take to return to the ambient temperatures in Pu`u`O`o. The rate at which the anomalies cooled also varies. As figure 3.2 shows, the largest anomaly for Julian Day (JD) 251 decays at a lower rate than the anomaly at 16:03 on JD 250. It is this variation in cooling rates that I intend to use to estimate the difference in size of molten ejecta.

3.4.An idealised shape for a spatter bleb

Any liquid material in a state of free-fall will assume a spherical form due to the surface tension of the liquid (Chapman, 1995). In an atmosphere such as the Earth's, aerodynamic forces will shape the sphere if it is moving, into a tear-drop form with the axis of elongation parallel to the direction of motion. The rate at which this will occur is a function of the liquid viscosity and surface tension. Molten lava of a mafic composition is no exception due its lower viscosity resulting from the geochemistry of such magmas and the relatively high eruption temperatures (Flynn et al, 1994). Vesiculation of the lava also decreases the effective viscosity of the material (Harris & Rowland, 2001).

Larger pyroclasts such as spindle bombs are so named because of this aerodynamic sculpting. Smaller pyroclastics such as ash particles or lapilli with a mafic composition are subject to the same forces resulting in similarly sculpted forms but on a smaller scale,

such as 'Pele's tears' (HVO), commonly found on Kilauea. These result from the solidification of small molten droplets that have fallen out of a fire-fountain plume (Sumner et al, 2004).

Size is an important controlling factor on the rate of cooling of a spatter bleb. Small blebs, or lapilli, may cool sufficiently to solidify before impact on the ground (Vergniolle & Mangan, 2000). Wolff & Sumner (2000) record that larger spatter clasts (10cm +) resulting from Strombolian fire-fountaining will still develop a chilled crust that often ruptures on impact. The still molten material in the interior then spills onto the ground surface, often forming an agluttinated spatter rampart or contributing to a clastogenic lava flow (Wolff & Sumner, 2000). Other such larger clasts, if still fluid at the time of impact may 'splash', resulting in a number of smaller blebs. However, the scale of a fire-fountaining episode is much larger, in terms of both the volume of material and magnitude than the degassing events with associated molten spatter I consider here. Larger irregular sized spatter is apparent in figure 3.1, and it is unlikely that such large spatter clasts resulting from any similar activity at the Beehive would cool sufficiently to develop a chilled rind strong enough to resist deformation on impact.

Smaller lapilli or blebs are more likely to retain a spherical shape, such as Pele's tears, due to the cooling of the surface by their passage through the atmosphere. Wolff & Sumner (2000) observe that smaller lapilli on the periphery of fire-fountaining events and in low density spattering events are more likely to develop a chilled rind on passage through the atmosphere. Such clasts or blebs are less likely to deform on impact, or even shatter (Sumner et al, 2004). If the bleb retains a spherical shape, then the rate at which heat will be lost from the bleb by conduction to the ground surface will be much lower than if the bleb had deformed. This is because a much smaller surface area is present at the interface between the bleb and the ground surface, as the spherical surface of the bleb will be tangential to the ground surface (Figure 3.7B on page 119). Conversely however, a

spherical form will increase the rate of heat loss due to convective cooling to the atmosphere as the spherical bleb has a greater surface area than an approximated hemispherical bleb deformed due to impact with the ground.

It is therefore clear that due to the large number of factors, many of which cannot be easily assumed, it is difficult to decide the form that initially molten blebs will take subsequent to impact on the ground surface. It is within the bounds of probability that due to the low magnitude of the recorded events at the Beehive vent, the degassing was not of a strongly vigorous nature, and therefore resulting molten ejecta may be of a small size. If this is the case, then it may be likely that the ejecta may take a roughly spherical form akin to Pele's tears during the airborne phase and retain this shape on impact with the ground. Therefore for the purposes of an idealised "Ejecta-Mass" model for spattering from the Beehive vent, I will consider the blebs to be spherical.

3.5.An Idealised model for detection of molten ejecta at the Beehive vent

In the previous section I proposed that for the purposes of the model to estimate the mass of molten material ejected at the Beehive vent, then it is adequate to assume a spherical bleb. In this section I show how the setup of the radiometers at Pu`u`O`o can be used to calculate the areal extent of the FOV, and how the occupying fraction of any molten material in the FOV may be calculated. This is vital for inclusion into the Ejecta-Mass model, as without any information on the likely areal extent of any ejecta then it will be impossible to derive the volume of material ejected.

3.6.Calculation of the radiometer FOV

In order to estimate the area of the Pu`u`O`o crater floor covered by the radiometer FOV we must know the optical properties of the radiometer and the distance of the

radiometer to its target, the Beehive vent. I use here an idealised setup of the radiometer on the crater rim with respect to the crater floor, based on simple field measurements. One of the conclusions of the previous chapter was that the Beehive vent would in all likelihood increase in height due to the accumulation of spatter on its rim. I use here an idealised scenario in which the Beehive vent is a simple opening on a horizontal crater floor. The exact form and dimensions of the Beehive vent during September and October 2001 is difficult to determine, and this idealised scenario is in keeping with the assumptions on the consistent spherical form of the spatter blebs from the Beehive vent.

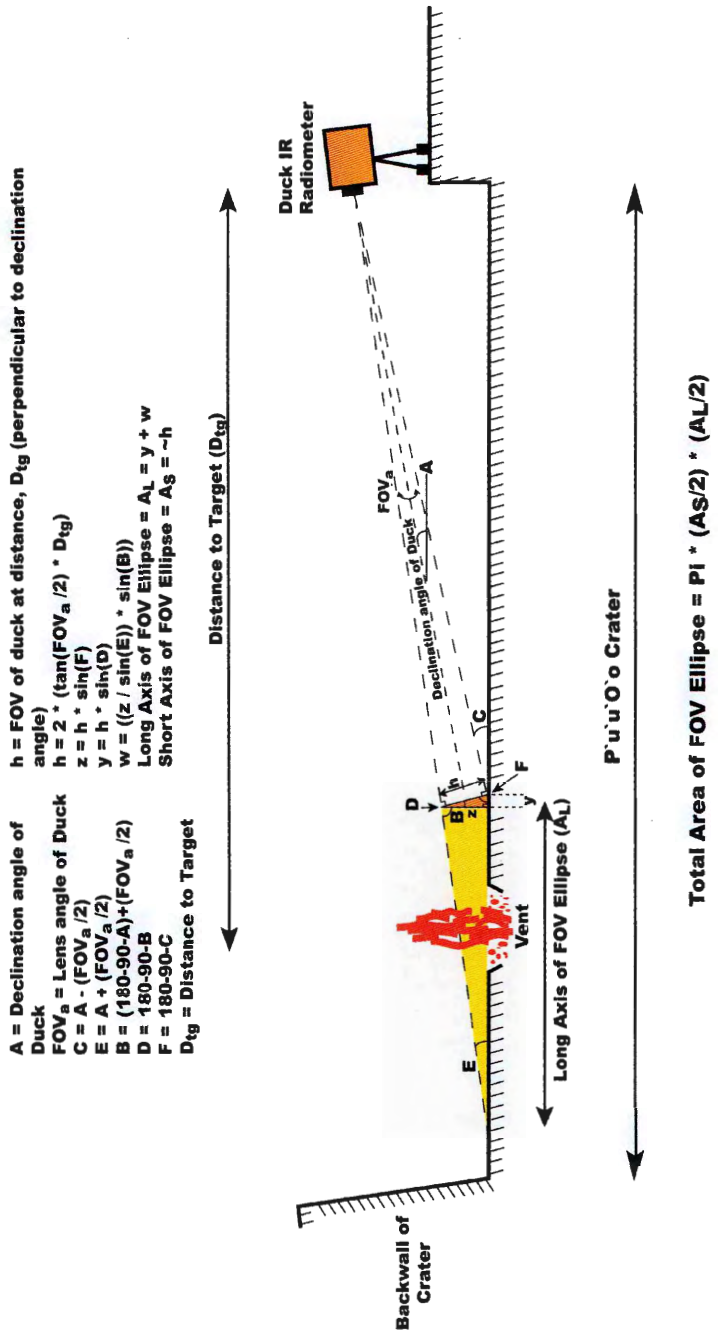

Figure 3.3: Simple schematic cross section of the installation of the radiometers on the rim of Pu`u`O`o. The method in which the long axis of the elliptical FOV is calculated (see figure 3.4) is also shown, based on the low inclination angle of the conical radiometer FOV and its intersection with the assumed horizontal crater floor.

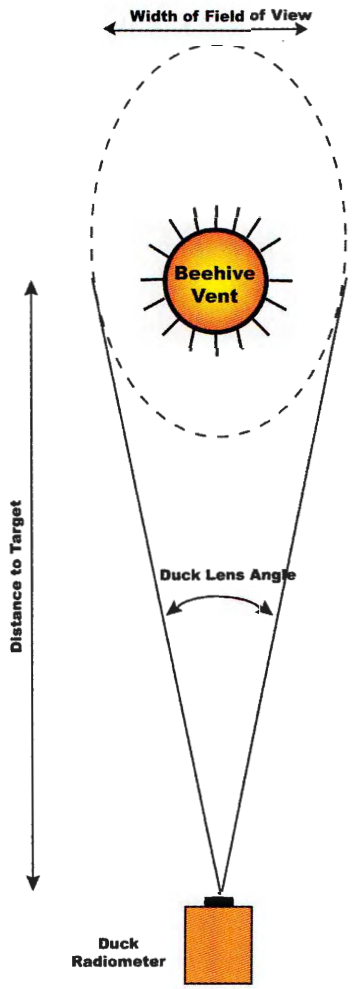

Figure 3.4: Simple schematic plan section of the radiometer installation at Pu`u`O`o. The FOV of the radiometer will assume an elliptical form due to the intersection of the conical field of view with the horizontal crater floor. In this idealized scenario the semi-minor axis of the ellipse is equivalent to the diameter of the conical FOV at the target distance

The linear FOV of the radiometer will expand with distance in a conical fashion, at a rate governed by the lens angle and focal length. In this case, the Huey radiometer has a 1° lens attached, compared to the 60° lens angle of the wide angle radiometer, Dewey. As the radiometer is inclined downwards towards the crater floor, the 'footprint' of the FOV will take the form of an ellipse as the conical FOV intersects the supposedly horizontal crater floor. In this configuration the semi-minor axis of the ellipse will be equivalent to the diameter of the conical FOV at the target distance. This is represented

graphically in figure 3.4 as a plan view of the radiometer with respect to the vent. The semi-minor axis A_{Sm} of the resulting FOV ellipse will therefore be:

$$A_{Sm} = 2 \text{ Tan } (\theta/2)\, d \qquad \text{(Equation 3.1)}$$

Where θ is the lens angle and d is the distance from the radiometer lens to the centre line of the target vent.

The calculation of the semi-major axis (A_{Lm}) of the elliptical FOV is more complicated. This is because the semi-major axis is a function of not only the angle of inclination of the radiometer with the level surface, but also the conical expansion of the FOV with distance due to the lens angle. This problem is represented as a schematic with vertical section in figure 3.3. A simplified mathematical overview of the problem is also represented in figure 3.3. The semi-major axis of the elliptical FOV is equivalent to the combined values of the 'adjacent' of the yellow right angle triangle in figure 3.3 (w), and the 'opposite' of the smaller orange right angle triangle (y). Therefore:

$$A_{Lm} = y + w \qquad \text{(Equation 3.2)}$$

The FOV of the radiometer, considered as an ellipse is therefore equivalent to:

$$\text{Elliptical FOV } (m^2) = \pi(A_{Sm}/2)(A_{Lm}/2) \qquad \text{(Equation 3.3)}$$

If the radiometer was positioned vertically above the vent, then the FOV would be circular. As the angle of the radiometer moves away from the vertical, then the FOV becomes increasingly elliptical. An angle of 15° from the horizontal was measured for the radiometer on 15th July 2001, and the radiometer was in this configuration during the study period.

The straight-line distance from Huey on the eastern edge of the Pu`u`O`o crater, to the Beehive vent on the crater floor has been estimated as roughly 115m by the use of a laser ranger over several attempts (A.Harris, pers.comm). This may be regarded as a rough estimate as it is not known how the constantly variable levels of fume emitted in the crater will attenuate the range finder signal. However, consultation of the HVO map in figure 2.1 suggests that this figure of 115m is reasonable. By using the above equations, a FOV of approximately area $12m^2$ was calculated for Huey. I use this figure in all subsequent calculations.

3.7.Extracting the thermal composition in the radiometer FOV

For the purposes of the idealized model I assume that the radiometer FOV encompasses the entire Beehive vent. Any ejected spatter will therefore occupy a certain fractional area of the radiometer FOV. The remaining fraction of the FOV will be occupied by ground at ambient temperature. By assigning estimated temperature values for these two fractional areas, it is possible to estimate the relative occupying fractions. This concept is adapted from a model proposed by Rothery et al (1988) for a simplified radiant model of fresh lava flows and is shown in equation 3.4. L_{total} is the total emitted

radiance from a discrete area, in this case the radiometer FOV. L_{total} is the combined radiative flux from the hot ejected spatter (L_H) of fractional area *f*, and that from the cool background (L_C) of fractional area 1-*f*.

$$L_{total} = \varepsilon\tau ((f L_H) + ((1-f) L_C)) \qquad \text{(Equation 3.4)}$$

For the purposes of the Ejecta-Mass model I use an idealised situation in which all molten spatter is emplaced in the radiometer FOV, as depicted in figure 3.5. As a simplification for this model, I assume that once emplaced, the only hot material within the radiometer FOV is the molten ejecta. This is because it is very difficult to ascertian the temperature of the open vent, as well as the size of the vent itself.

Equation 3.4 shows this relationship applied to the case of molten spatter from the Beehive vent. L is the total emitted radiance ($Wm^2\ \mu m^{-1}\ sr^{-1}$) emitted from in the FOV of area A (m^2), and which may be calculated according to equation 1.1. ε is the emissivity of the material in the radiometer's FOV. I use a value of 0.92 for ε for basalt, based on Harris et al (1998). τ represents the attenuation of the signal by scattering and absorption by the atmosphere in the crater.

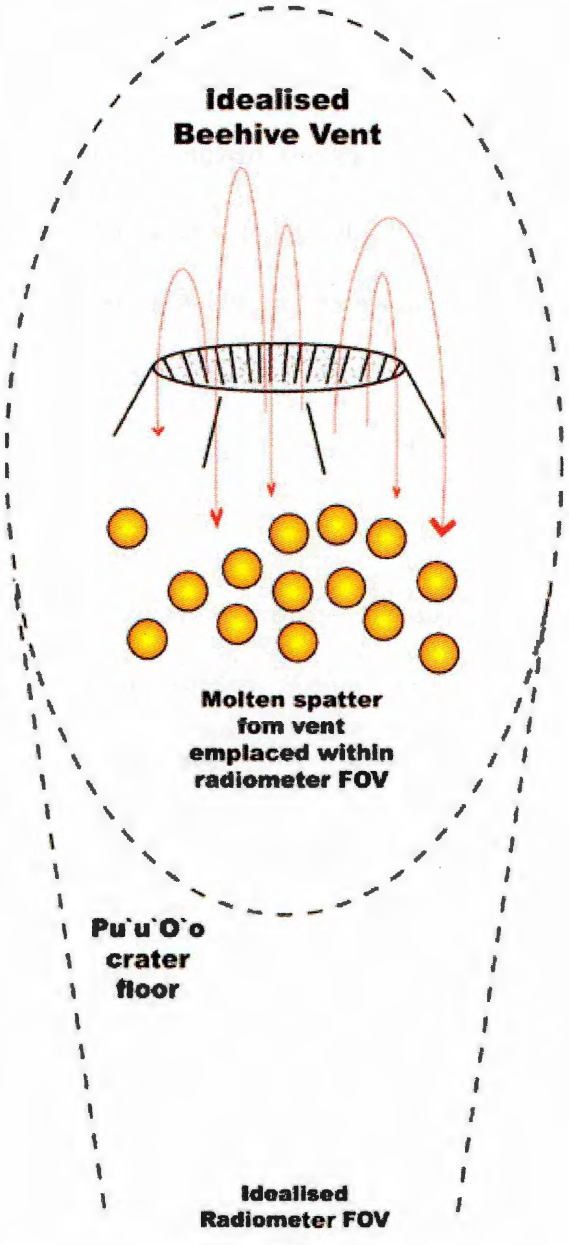

Figure 3.5: Idealised mechanism of emplacement of spatter blebs in the radiometer FOV. We assume that all spatter is emplaced in the FOV of the radiometer, without occlusion by any surrounding blebs. Note also the spherical blebs, with exaggerated size for clarity.

Previous studies using equation 3.4 applied to mafic volcanism such as that at Pu`u`O`o, use the initial magmatic temperature of ~1373°K to represent cracks in a chilled flow crust. In the case the Ejecta-Mass model we may consider a temperature for T_H less than this value due to the cooling of any ejecta by passage through the atmosphere. In a later discussion on the application of the Ejecta-Mass model I use a variety of values of T_H in order to match the observed cooling periods from the radiometer thermal anomalies with the model results. Values for T_C may be easier to constrain, if we consider the ambient temperature to be in the region of ~300°K, which is the approximate value for temperatures recorded in the radiometer FOV not associated with any thermal anomalies at the Beehive vent.

A final point to consider when estimating and using temperatures from the radiometers, is that the signal will be degraded by absorption and scattering by the atmosphere in the crater (τ in equation 3.5). Such factors may be very small over similar distances in a clear atmosphere, far removed from the effects of the mix of volcanic gases and aerosols present in the crater. However, the presence of such factors at Pu`u`O`o ensures that the temperatures detected by the radiometers will be an underestimate of the true values.

In order to calculate the fractional area *f* in equation 3.4, and as we know the total FOV, then we may calculate the total emitting area of ejected spatter blebs as follows. As we are assuming a spherical form for an idealized spatter bleb then the cross-sectional area of such a sphere is given in equation 3.5, where r is the sphere radius.

$$\text{Spherical cross sectional area } A_S = \pi r^2 \qquad \text{(Equation 3.5)}$$

If all ejected spatter blebs are of equal size then the total emitting area A_T, will be equivalent to the number of blebs multiplied by the cross sectional area A_S. If there are a range of different sized blebs present, then A_T will be equivalent to:

$$A_T = \pi (r_a^2 + r_b^2 + r_c^2 + r_d^2 \ldots\ldots r_{nn}^2) \qquad \text{(Equation 3.6)}$$

The calculation of emitted radiance using equation 1.1 takes into account the effect of the conical propagation of radiance by the inclusion of π to counter for the solid angle. We may therefore consider the total emitting area of hot material associated with the ejecta to be equivalent to A_T. The choice of a sphere as the idealized form of spatter in the Ejecta-Mass model ensures that whatever the orientation of the radiometer FOV with respect to the cross sectional area of the sphere, the cross sectional area remains constant. This principle is shown in figure 3.6.

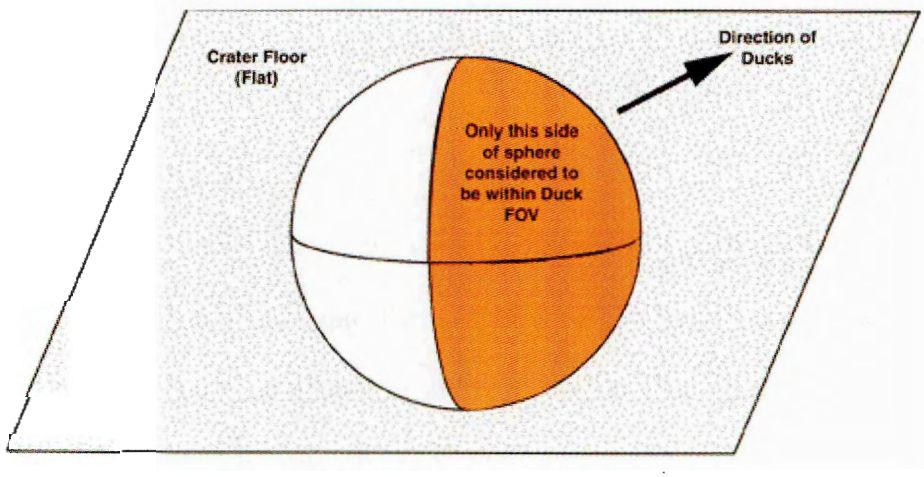

Figure 3.6: Idealised representation of a single spatter bleb on the crater floor. For the sake of simplicity within the model the emitting surface is represented as a disk of the same diameter as the spherical bleb. From this we can calculate the occupying area of all spatter blebs in the radiometer FOV using the concepts shown in figures 3.3 and 3.4.

Therefore the fractional area *f* representing the calculated total emitting area A_T is equivalent to:

$$f = (1 / \text{Radiometer FOV}) * A_T \qquad \text{(Equation 3.7)}$$

By using equations 3.4 to 3.7 it is possible to calculate the total emitting area of the ejected spatter at the assumed temperature T_H and relate it to the total detected radiance calculated for the radiometer FOV.

We now have an idealized scenario for the emplacement of spatter in the radiometer FOV, and the ability to calculate the cross-sectional areal extent of the hot spatter. In the next section I consider the various cooling mechanisms that any ejecta will undergo, and propose a method that allows an estimation of the size of a bleb based on the observed rate of cooling. By combining such an estimate of the size of a spatter bleb with the above methods on extracting the total area of hot material from the radiometer FOV I estimate the total number of ejected spatter blebs, and therefore the total ejected mass.

3.8.Cooling mechanisms of hot spatter

If we consider a single spatter bleb, emplaced and cooling from the original magmatic temperature then the outer surface will have been cooled due to the passage of the molten bleb through the atmosphere. Once the bleb has landed, it will cool further by conduction into the ground if the ground surface is cooler than the bleb itself. In addition to this the bleb will also cool due to convective heat transfer into the atmosphere. The rate at which the bleb will lose thermal energy or cool is summarized in equations 3.8 and 3.9.

Equation 3.8 predicts the amount of heat that will be conducted through a material of known thermal conductivity. The thermal conductivity is defined as the rate at which heat is transferred in the material, and is considered as ratio of heat flux to the temperature

gradient. Materials with a high thermal conductivity will warm or cool relatively rapidly. Rocks generally have low thermal conductivities, and are good insulators (Chapman, 1995). We can consider Q as the quantity of heat ($M\ L^2\ T^{-2}$) (Chapman, 1995), that may flow through an area A of thickness l in time t. Thermal conductivity is represented by k and entropy is represented by the minus sign before k (Chapman, 1995). $\Delta\theta$ is the difference in temperature across the distance l.

$$Q = - k\ t\ (A/l)\Delta\theta \qquad \text{(Equation 3.8)}$$

This modification simply shows that entropy decreases with time, i.e. the material will cool rather than heat with time! Equation 3.8 can be modified so that we can express the transfer of heat as per unit time or area:

$$q = -Q/A\ t = k\ \Delta\theta/l \qquad \text{(Equation 3.9)}$$

Equation 3.9 results with q conventionally expressed in units of mWm^{-2} (Chapman, 1995). The thermal conductivity of a material is inherently related to the physical properties of the material in question. Equation 3.10 displays these relationships and how the thermal conductivity k ($Wm^{-1}K^{-1}$) can be calculated (Crank, 1975).

$$k = \rho C_p K \qquad \text{(Equation 3.10)}$$

Where ρ is the density of the considered material ($kg\ m^{-3}$), $C_p$is the specific heat capacity ($j\ kg^{-1}\ K^{-1}$) and K is the thermal diffusivity of the material ($m^2\ s^{-1}$). The thermal diffusivity can be considered as the ratio of thermal conductivity to heat capacity, and in

effect represents the efficiency of the material as a conductor. Equation 3.11 shows how thermal diffusivity may be calculated (Crank, 1975).

$$K = k/\rho C_p \qquad \text{(Equation 3.11)}$$

Materials with a low thermal diffusivity conduct heat poorly, whereas materials with a high thermal diffusivity are good conductors of heat. Equations 3.8 to 3.11 all predict the manner in which a material, such as the basalt at Pu`u`O`o will cool over time given a certain considered volume. In one way the scenario of molten ejecta emplaced onto the crater floor proves a bonus, as all the materials are of a similar basaltic composition, and therefore adds an in-built degree of simplification to the problem. However, the difference in these parameters for basalts of different ages and vesiculation is not well known, although the differences between basalt and other rock types are better known (Vosteen & Schnellschmidt, 2003).

The vesiculation of any molten ejecta at Pu`u`O`o complicates the calculation of the above parameters, due to the effect on the overall bleb density. It is expected that increasing rates of vesiculation will increase the effectiveness of basalt as an insulator. As the number of vesicles increases the overall density of the material will decrease, and therefore the number of conductive 'pathways' of non-vesiculated material seperating the vesicles will also decrease. Therefore, it is probable that highly vesiculated basaltic spatter blebs will possess low thermal diffusivities and conductivities.

Heat lost due to convective cooling is summarized by equation 3.12, in which Q is the heat lost (W), A is the surface area in question (m^2), T_S and T_C are the surface temperature and air temperature respectively. The factor h_c may be obtained from published sources and effectively quantifies the relationship between the surface roughness of the considered object and the wind velocity.

$$Q = A\, h_c\, (T_S - T_C) \qquad \text{(Equation 3.12)}$$

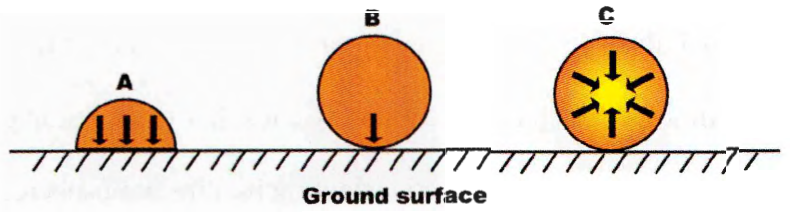

Figure 3.7: Cooling of spatter blebs. A). A greater rate of conduction of heat energy away from the interior of the bleb is possible if the bleb deforms on impact. B). If the spatter bleb retains a spherical shape, then conduction of the internal heat energy to the cooler ground surface is impeded by the small surface contact area. C). Consideration of the cooling bleb as an isothermal front moving inwards with time. This thermal diffusion considers the temperature gradient between the entire bleb and the cooler material it is immersed in.

Equations 3.8 and 3.9 consider the rate at which thermal energy is transferred across a gradient separating the warmer material from the cooler material. If the bleb deforms on impact, increasing its surface area as it flattens whilst still semi-molten, then the rate at which the bleb will lose thermal energy due to conduction will be much higher than if the bleb does not deform and remains spherical. Figure 3.7A displays a simple rendition of this principle. The chilled rind of such a spatter bleb may well be relatively strong, resulting from the visco-elastic nature of the chilled molten material (Vergniolle & Mangan, 2000). The low mass of smaller spatter blebs, resulting from their small size and low density due to the relatively high levels of vesiculation diminishes the possibility that the bleb may shatter on impact.

In the idealised model for spattering in the confines of the Pu`u`O`o crater, I consider each bleb (at least post-groundfall) as a smooth sphere. In this respect, heat loss due to convective cooling is minimized, and at least in the idealised model at this stage may be discounted due to the poor understanding of the effects of convective cooling on smaller objects. If we assume a stable still atmosphere in the crater, which is not unrealistic due to the relatively sheltered conditions provided by the Pu`u`O`o crater, then

we may be justified in neglecting convective cooling at this stage in the model development.

By using this idealised scenario, I show in the next section how by considering heat loss solely by thermal diffusion in the idealised spherical spatter bleb we can better simulate the cooling of a spatter bleb than by simply considering the cooling by conductive cooling with the ground surface and convective cooling into the atmosphere.

3.9.Thermal diffusion in a sphere

In the previous section I proposed an idealised model in which any molten ejecta is considered spherical after groundfall. Equations 3.8 to 3.11 depict the cooling across a thermal gradient due to conduction, but if we use a spherical bleb then the bleb-ground interface will be small, impeding cooling by conduction into the ground.

However, we can use thermal diffusion modeling to predict the cooling in the spherical bleb as an isotherm of decreasing temperature that encroaches inwards with elapsed time, as depicted in figure 3.2 C. This assumes the spherical bleb is initially at a hot temperature T_h, and is subsequently surrounded by material at a cooler temperature T_c. Thermal diffusion modelling allows the prediction of the temperature for any point in the sphere at any time, and takes into account the cooling in the entire sphere based on the thermal characteristics of the materials involved. This thermal diffusion modelling is in essence an adaptation of the conduction equations 3.8 to 3.11 to consider heat loss in the sphere, and of course takes into account the volume and surface area of the sphere. As the size of the sphere is considered in such equations, then this allow us to adjust the idealised bleb parameters in an attempt to match the cooling curves in the radiometer data on the premise that larger blebs will take longer to cool than smaller blebs.

Figure 3.8 depicts a simple model of thermal diffusion in a bar composed of material with known thermal properties. If we assume that one end of the bar is exposed to a hot thermal source T_h and the opposing end is exposed to a cooler thermal source T_c, then a temperature gradient will develop along the length of the bar. There will be a continuum of temperatures separating the two endmember temperatures. The temperature at any point along the length of the hypothetical bar can then be calculated for any particular time.

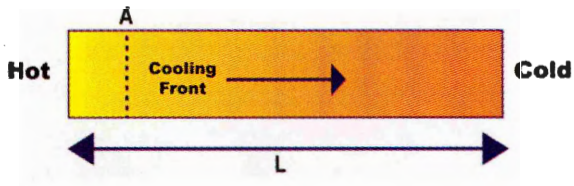

Figure 3.8: Simple thermal diffusion model of a single bar of length L, with one end exposed to a high temperature and the opposite end to a cooler temperature. Using thermal diffusion modelling it is possible to calculate the temperature at point A after an elapsed time period if the thermal properties and volume of the material is known.

The left-hand section of equation 3.13 on page 123 (after Carslaw & Jaeger, 1954) depicts such a scenario, and allows the calculation of the temperature (C) at a point A of known distance along the length (L) of the bar. The temperature difference, C_o, is defined as T_h - T_c, time (t), thermal diffusivity (K) are all known (Crank, 1975). This equation allows the calculation of the position of isotherms that depict the rate of cooling over time in the bar, once the heat sources are removed.

The same principle of thermal diffusion may be applied to a spherical object. Figure 3.9 depicts an idealised model of a spherical bleb cooling by thermal diffusion, if the sphere itself, initially at a hot temperature is surrounded by material at a cooler temperature.

Figure 3.9 is a schematic representation of equation 3.13. The spherical thermal diffusion equation 3.13 models the temperature at a set point, A at a defined time, t if the temperature difference C_o is known. The point A can lie at any point along the diametric

axis through the centre of the sphere, and the equation effectively models the balance in heat flux between the point A and both ends of the diametric line. These widths are represented as 'a – r' and 'a + r', and this is how the equation counters for the thermal differences between A and the cooler exterior. If the point A lies at some point along the diametric axis other than at the centre, then the 'cooling influence' of the closer surface will influence the temperature at A sooner than the cooling influence on the opposite, further cooling surface.

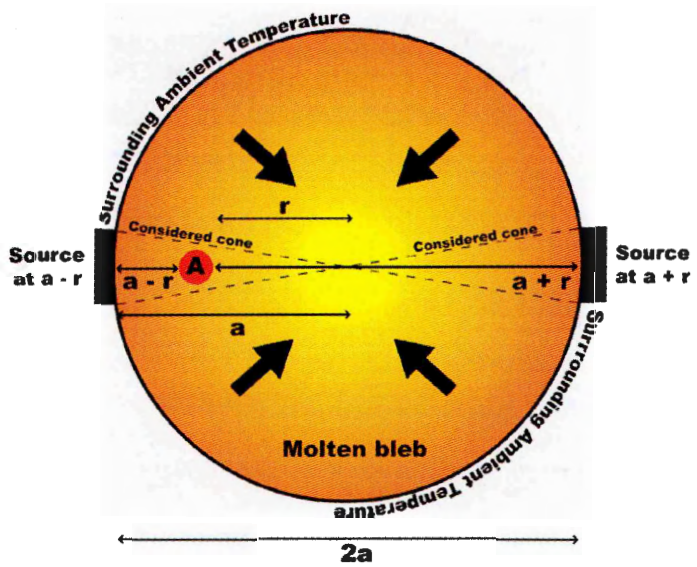

Figure 3.9: Simple schematic of thermal diffusion in a spherical bleb, of radius a. The spherical thermal diffusion equation considers diffusion in a bar (as in figure 3.7), but corrected for the 'wedging' effects and thermal influence of the surrounding mass of the sphere. Cooling of the sphere is represented as an isotherm parallel to the cooling surface, in this case the isotherm will therefore also be spherical if the initially hot sphere is surrounded by cooler material. The isotherm will progress inwards over time, as represented by the inward pointing arrows. The thermal diffusion equation allows the calculation of temperature at point A at time t.

This concept is represented in figure 3.9, as the point A is off-centre. An inwardly encroaching isotherm from the source at 'a – r' will affect point A sooner than the source at 'a + r'. The section left of the subtraction sign in equation 3.13 considers the thermal diffusion in a simple bar, but it is the section to the right of the subtraction that provides such a correction for the thermal influence in the remaining spherical portion of the bleb. A radial correction is applied to counter the wedging effects due to the pie slice geometry

of the two "considered cones". This is because the model takes into account the three dimensions of the sphere, rather than just the two-dimensional rectangle considered by the left hand section of the equation and visualised in figure 3.8 (Crank, 1975) and pers.comm. D.Morgan.

Conductive cooling between two sources/sinks

Correction for spherical modelling-consists of two opposed cones

$$C=\frac{1}{2}C_0\left\{erf\left(\frac{a-r}{2\sqrt{Kt}}\right)+erf\left(\frac{a+r}{2\sqrt{Kt}}\right)\right\}-\left(\frac{C_0}{r}\sqrt{\frac{Dt}{\pi}}\left[\exp\left\{-\frac{(a-r)^2}{4Kt}\right\}-\exp\left\{-\frac{(a+r)^2}{4Kt}\right\}\right]\right)$$

(Equation 3.13)

A drawback of this equation is that it assumes that the hypothetical sphere is surrounded by material of the same composition and thermal dynamics. In the case of a basaltic spatter bleb emplaced onto the ground surface (in the case of the Pu`u`O`o crater we assume the ground surface is also of a similar basaltic nature), then it will be surrounded by the atmosphere. However, in our idealized scenario I assume that the bleb is spherical and at least semi rigid so it does not deform on impact. This is due to the formation of a chilled rind due to the passage of the initially molten bleb through the atmosphere. Observations of Pele's tears in the field at Kilauea, which are tear drop shaped lapili that were obviously originally molten but solidify after ejection whilst still airborne, retain their teardrop shape after landfall. If this is the case, then we may consider that the bleb is indeed surrounded by cooler material of the same composition – the chilled rind.

This concept is further supported by the fact that equation 3.13 cannot predict the temperature on the surface of the sphere as the model would not be able to track the balance in heat flux at A if a-r = 0. In this instance the temperature at A will always be

equivalent to the cooler surrounding material, as the thermal diffusion over such an infinitesimally small distance would be almost instantaneous, especially considering the time taken for thermal diffusion from the opposite surface at a + r. Equation 3.13 is still viable if A is set only a small width from the outer surface, and in my model I regard this width as equivalent to the thickness of the chilled rind.

However, this does not bypass the problem of the detection of the cooling bleb as a hot thermal anomaly. The radiometer can detects only the radiance emitted by the surface material, as predicted by the Planck relationship (equation 1.1) for a bleb of temperature, T at wavelength λ (not withstanding the remaining material at different temperatures in the radiometer's FOV). In effect, the radiometer only detects the 'skin' temperature of the hot bleb.

In the next section I describe how this problem may be overcome and the adaption of the thermal diffusion equation into an "Ejecta-Mass " model for estimating the mass of molten spatter ejected at the Beehive vent during a single event.

3.10. Creation of a model using thermal diffusion to estimate Ejecta-Mass

3.10.1. Testing the thermal diffusion equation

In order to resolve this problem I undertook an experiment in which a known quantity of Hawaiian basalt was heated using a laboratory furnace, and the subsequent cooling was observed with a radiometer. I then attempted to use the model outlined above using equation 3.13 to predict the observed cooling. By contrasting the observed with the predicted then it will be possible to verify the use of the above model. If the above model using thermal diffusion to accurately predict the cooling of a spatter bleb is possible, then we can attribute the different rates of cooling observed for different thermal anomalies

(figure 3.2) to different sizes of spatter blebs. This would have been otherwise very difficult to achieve if we considered the simple cooling by conduction with the ground surface.

The cooling of this artificial 'bleb' was monitored using a small radiometer mounted on a tripod, until the temperature of the fake bleb dropped below the sensitivity of the radiometer. This simple set-up is analogous to the basic setup of the radiometers at Pu`u`O`o. These laboratory conditions however did not present similar conditions in terms of cloud and fume as usually prevalent at Pu`u`O`o, but small corrections can be made for the estimated attenuation of the signal by these factors.

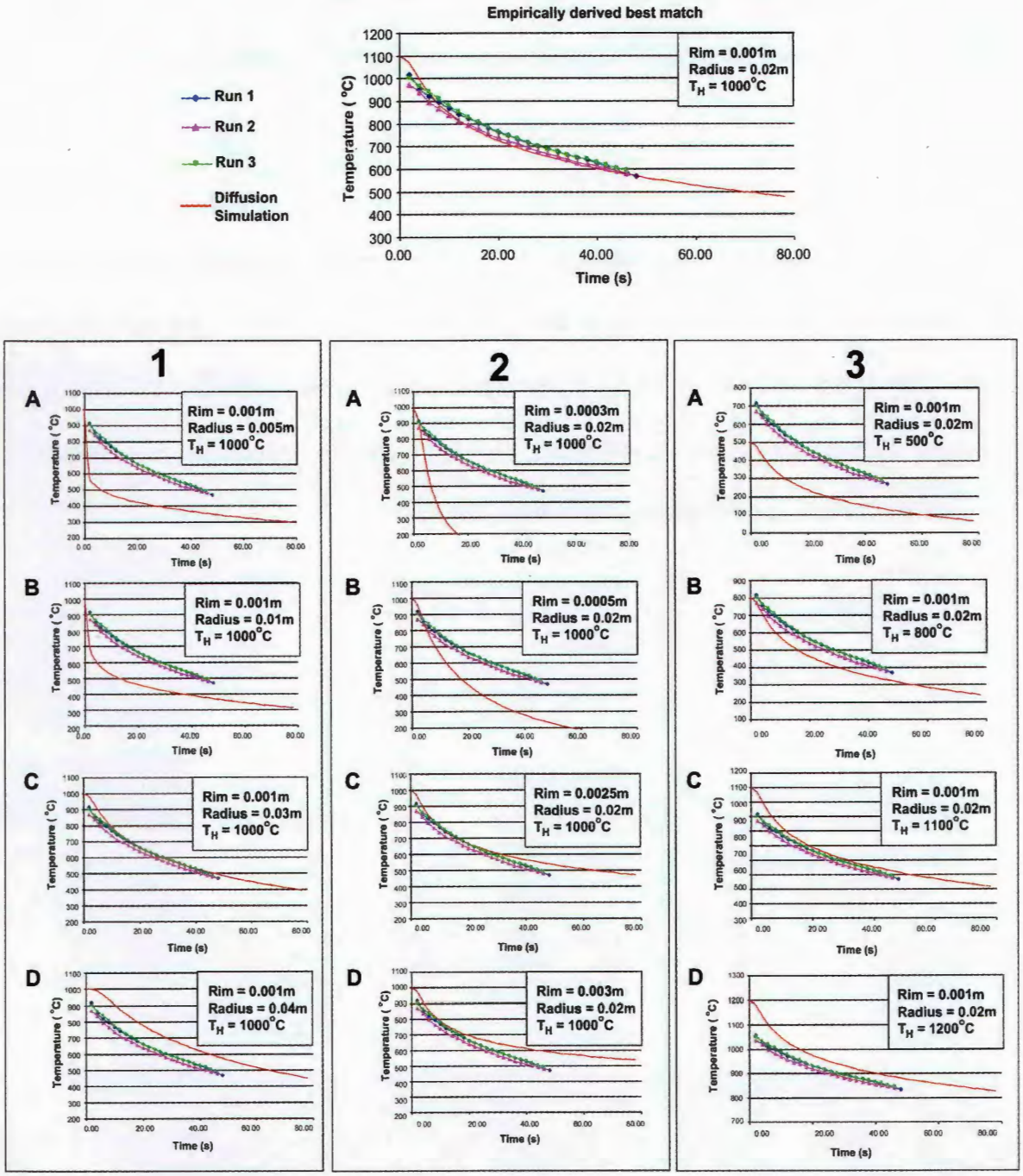

Figure 3.10: Cooling of an artificial spatter bleb. Although the fake-bleb was not spherical but assumed a semi-viscous hemisphere (as they would in reality) the predicted cooling compares well with the measured cooling.

The material used was a powdered lapilli field sample collected from the vicinity of a defunct vent on the flanks of Mauna Loa (courtesy K.Sharma), and was originally well vesiculated. This material is close to a Kilauean basalt in terms of bulk composition as might be found in the vicinity of Pu`u`O`o, and was all that was available at the time of study. This powdered material was mixed with a flux powder in a small crucible and

placed in a laboratory furnace and heated until the flux and pulverized basalt had become molten once ~1373K had been exceeded.

Once the mixture was verified as molten it was extracted from the furnace and poured onto a "warm-plate" (a cool surface at room temperature will have caused the fake molten bleb to shatter due to thermal shock). Once the artificial bleb had cooled it had formed a disk approximately 40mm in diameter. The cooling of this fake bleb was then recorded using a small radiometer, and the temperature sampled every 2s. It was verified that at the small distances involved in the lab, the molten bleb filled the radiometer FOV. This process was repeated three times and the results are shown in figure 3.10 as lines 1, 2 and 3.

In order to simulate the measured surface temperature of this artificial bleb, I applied equation 3.13 using a system of Microsoft Excel Spreadsheets and Visual Basic used as part of the "Ejecta-mass" model. These are described later in section 3.13 on p131, with example software code shown in Appendix II. Figure 3.10 shows a series of estimated cooling trends each with the actual observed cooling trends. These show the sensitivity of the thermal diffusion model to variation in the parameters of bleb size and external temperature for C_O. In these models a value for thermal diffusion (K) of 9.47×10^{-7} was calculated using equation 3.11 (p118), by using a value for the density of basalt (Dense Rock Equivalent- DRE). $\rho = 2280 kg\ m^{-3}$ (courtesy A.Harris), thermal conductivity $k = 3\ Wm^{-1}\ s^{-1}$ (courtesy A.Harris) and a specific heat capacity for basalt of $C_p = 1225\ J\ kg^{-1}\ K^{1}$.

Figure 3.10 shows the sensitivity of the thermal diffusion model to variation in the input parameters. This is important to know, as for the application of this modelling to the observed cooling curves derived from the radiometer data at Pu`u`O`o (described in Chapter 2) we need to use a value for the rim dimension which is vital to the application of the model. However, this value is difficult to isolate from the artificial anomaly test run

shown in the top panel of figure 3.10 as it is impossible to ascertain this dimension whilst the artifical bleb was initially molten. As the bleb cools, the rim dimension, or chilled rind, will change as the 'cooling front' moves inwards in accordance with the diffusion modelling. Therefore in order to derive this initial value, I adjusted the various parameters until the modelled curve from the application of equation 3.13 matched that of the observed cooling trends of the artificial bleb. The rim value a at which this occurs may therefore be considered a good approximation of the actual value and could therefore be used in the modelling described later in this chapter.

Using this empirical method, I found that a 'rim' value of 1mm resulted in the closest match between the thermal diffusion modelling (represented as a solid red curve in figure 3.10) and the true cooling shown in figure 3.10. This successful application suggests that it is possible to relate the cooling of a small spatter bleb with the thermal diffusion approach of equation 3.13.

Figure 3.10 also shows the sensitivity of the thermal diffusion model to the actual variation in input parameters. Panels 1A to 1D show the response of the diffusion model to simulated blebs of varying diameters. These values are considered either side of the empirically derived values in the top panel. Figure 3.10 1A shows the most rapid cooling with the smallest bleb, whilst the slowest rate of cooling is associated with the largest simulated bleb in figure 3.10 1D. In later sections I show that the size of the blebs associated with molten spatter is the dominant factor that controls the cooling durations recorded within the radiometer data from the Beehive vent. Panels 2A to D show a similar set of cooling curves for variation in the applied rim value. Those models with the thinnest rim cool very much quicker than those models with thicker rims. Variation in the initial assumed temperature does not show such a marked variation in cooling times. The main effect of this variation shown in panels 3A to 3D is in the initial rate of cooling. After 20 seconds, each of these 4 models possess very similar cooling times.

This thermal sensitivity modelling therefore suggests that the model is very much more sensitive to the bleb size and considered rim (chilled rind) values than the initial assumed temperature. This is important as the initial temperature value used later in this chapter is derived from the radiometer data obtained from events at the Beehive vent. As I show later, the thermal diffusion model is applied iteratively until the simulated model cooling matches the observed cooling trend, with the intent of deriving the size of the molten spatter. The lack of sensitivity to initial temperature in terms of the total cooling duration lessens the likely error from radiometer measurements when deriving the bleb size.

3.11. Points to consider for the application in thermal diffusion modelling

There are some problems in relating the observed cooling of the spatter bleb in the laboratory conditions outlined above with the thermal diffusion model. Firstly, the molten bleb deformed into a simple flattened hemisphere, once it had been poured from the crucible. This is directly analogous to the likely processes resulting from the impact of the molten spatter. However, the fake bleb eventually formed a disk ~40mm in diameter once cooled. This shape would increase the rate of conduction through the base of the bleb with the ground surface.

Secondly, the temperature of the bleb in the radiometer FOV is calculated from the radiance emitted from the surface only. This model predicts the temperature at the boundary between the chilled exterior rind, and the hot inner region of the bleb as a consequence of using the thermal diffusion equation 3.13. The close comparison of the modeled curve with the observed curves in figure 3.10 suggests that despite this paradox the thermal diffusion model is able to predict the likely cooling of a spherical spatter bleb with time. In reality there must be cooling effects due to forced convection into the

overlying atmosphere and conductive cooling into the medium that the bleb has been emplaced. These processes may be combining to produce this counter effect which is compensated by the empirical adjustments to match model with reality. However, in this model I propose an initial development using thermal diffusional modelling for simplicity but further study must be undertaken to understand the interplay between these various cooling processes. The empirical rim width of 1mm might not be a true approximation of the actual rim width in the fake bleb itself, but the adoption of this value may counter for the effect of the emitted radiance on the surface representing the temperature of a layer beneath the actual surface, (in which case, by using such a rim value of 1mm we are countering for this discrepancy).

The idealised ejecta model is a method for deducing the approximate amount of molten ejecta in the radiometer data, and due to the idealised nature of this model errors will be introduced. I acknowledge the above apparent discrepancy, but this method does appear to work in terms of predicting the temperature observed in a radiometer. I therefore suggest that the model can be used but may only predict the relative strength of a degassing event in terms of the ejected mass rather than providing a rigorous value for that ejected mass. As the temperatures returned from the radiometers can only be regarded as accurate relative to each other (Harris et al, 2003) then any features interpreted from this data can therefore only be regarded as relative rather than absolutely quantitative anyway.

3.12. Effects of the thermal diffusion modelling when applied to volcanic spatter

Figure 3.11 displays the relationship between the size of a bleb and the calculated time taken to cool to a set threshold, according to the thermal diffusion model. It is clear from figure 3.11 that there is a difference of an order of magnitude between the cooling duration of a bleb with diameter 0.01m and a bleb with a diameter of 0.1m. A bleb of this

size might be better classified as a small bomb, or perhaps an example of ribbon spatter as shown in figure 3.2 (p103). It is therefore clear that there is a large difference between the cooling duration between blebs with differences in diameters of even a few millimetres.

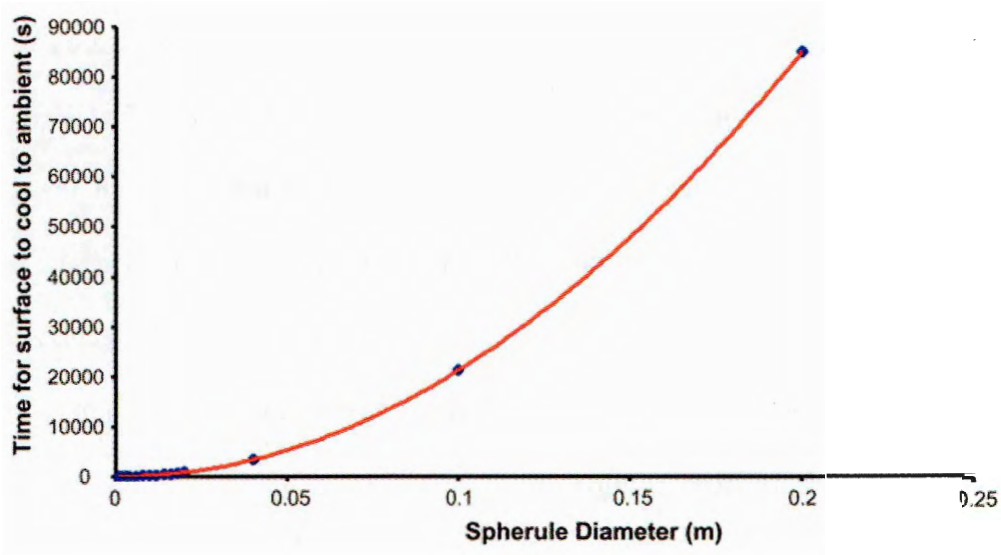

Figure 3.11: Variation in time taken to for various sizes of bleb/spherule to cool to the ambient temperature (within 1°C). As the bleb increases in diameter then the longer it takes to cool to the same ambient temperature as a smaller bleb.

3.13. Synthesis of idealised Beehive vent scenario and thermal diffusion modelling into the "Ejecta-Mass " model

In order to combine the thermal diffusion equation 3.13 with the idealized scenario for spattering from the Beehive vent, it was necessary to combine the use of Microsoft Excel and Visual Basic to create an iterative feedback model. In this section I give a brief overview of this process that takes as input the maximum temperature and cooling duration of any particular thermal anomaly (such as those in figure 3.4 p103). The end result of this software modeling is an estimate on the number and size of spatter blebs in the radiometer FOV. A full description and screenshots of this combined software approach is given in Appendix II. Figure 3.12 shows the algorithm applied by this combined MS Excel-VB approach.

I decided that the best method to apply the thermal diffusion equation was to use an iterative feedback approach in which the thermal diffusion model of a single bleb is used to create an artificial radiometer anomaly comprised of a number of identical sized blebs. By comparing the resulting cooling duration and initial temperature with the observed values extracted from the actual Duck radiometer data, a feedback loop in the software can adjust the values in the model until the simulated matches reality in a specified error. The feedback loop adjusts the size of the single bleb in the model to match the cooling duration, and the number of blebs until the estimated radiometer fractional area f is matched. These concepts are based on the observations in the previous sections in that cooling duration is controlled by bleb size, whereas f is controlled by the number of blebs if we assume an initial 'hot' temperature T_H.

The various formulae in the model are calculated in separate worksheets in a single MS Excel file. MS Visual Basic is used to adapt the various macros enabled in the MS Excel file and to control the operation of the feedback loop in which comparison between the simulated and actual anomalies are actioned. This method allows simple operation of the model, with the only required input being the initial temperature and cooling duration of observed anomalies in the radiometer data described in the previous chapter.

In the Ejecta-Mass model I use the values for the thermal properties of basalt described in section 3.7.1 (p**Error! Bookmark not defined.**). In order to estimate the occupying fraction of hot ejecta a range of values for T_H were used, from 600K to 1373K, as described in section 3.4.2. A value for T_C of 303K was used, calculated from the mean daily temperatures returned from the radiometers. A discussion on the resulting effect of differing T_H values on the final Ejecta-Mass estimate is given later. I use a worst case value of 5K to represent the degradation in radiometer signal at Pu`u`O`o, therefore I estimate that any temperature values returned by the radiometers are at least an underestimate of 5K. A fuller description of the setup and development of the Duck

radiometer system at Pu`u`O`o is given in Harris & Thornber (1999) and Harris et al (2003), as well as in the previous chapter.

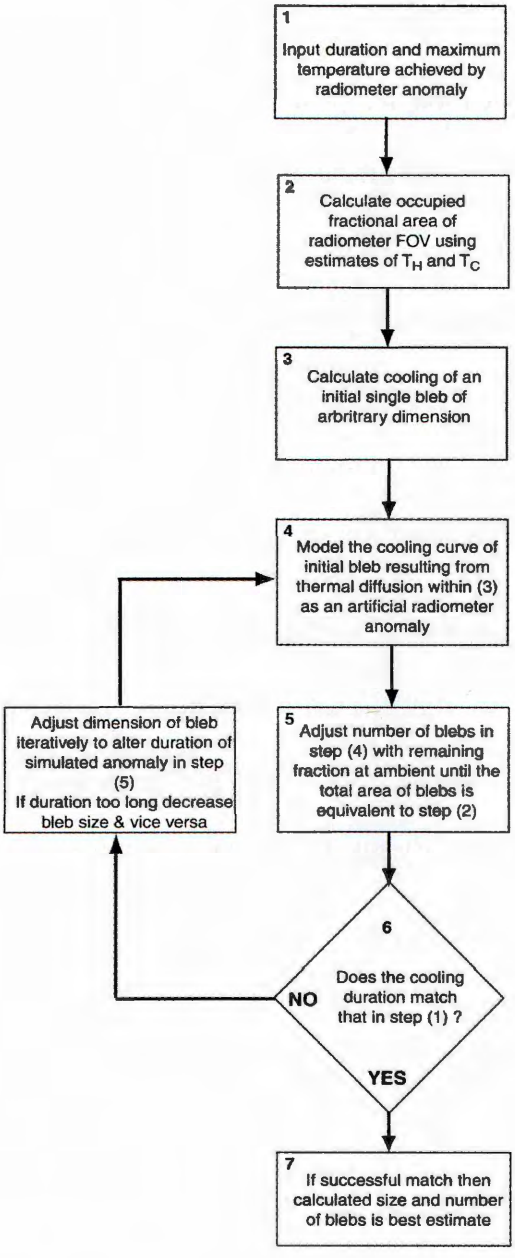

Figure 3.12: Flow chart depicting the basic algorithm applied to the thermal diffusion modeling. Model takes as input the maximum temperature and event duration (time taken to cool to within 5°C of ambient), then by adjusting the number of blebs and their radius in the thermal diffusion equation the model matches a simulated anomaly with the actual anomaly.

In the previous chapter I described how the thermal anomalies associated with degassing events at the Pu`u`O`o crater were recorded and identified. The cooling duration of an anomaly at the Beehive vent was defined as the time taken for the anomalous

temperatures to descend below a threshold temperature calculated from "moving window" average, to counter for diurnal and crater clearing effects on the thermal signal. In the Ejecta-Mass model, in which simulated thermal anomalies are matched to actual anomalies, a threshold temperature value equivalent to the daily mean temperature (303K) plus the estimated signal attenuation temperature (5K) was used. This is because a threshold temperature is required in the Ejecta-Mass model due to the logarithmic shape of the cooling curves. Once the modeled cooling curve is within 5K of the ambient temperature at which the thermal diffusion model attempts to reconcile the bleb cooling with, then the time taken for the cooling curve to reduce by even 1K becomes disproportionately longer than when the temperature difference is greatest. This effect is shown in both figure 3.2 (p103) and figure 3.10 (p126).

The output of this Ejecta-Mass model is an estimate of the size and number of ejected blebs associated with the original thermal anomaly. It is possible to estimate the ejected mass from this information, using the DRE density values obtained from example Pu`u`O`o spatter (A.Harris, pers.com) applied to the known volume of the spherical blebs.

$$\text{Bleb Volume } V_B = 4/3\pi r^3 \qquad \text{(Equation 3.14)}$$

Spherical bleb volume (V_B) can be calculated using equation 3.14, where r is equivalent to the bleb radius. The total mass of ejecta E_M can there be calculated as:

$$\text{Ejecta-Mass } E_M = nV_B \rho \qquad \text{(Equation 3.15)}$$

Where n is the total number of blebs and ρ is the density of the basalt. I use here a value of 2280kg m^3 for ρ. In reality due to the vesiculated nature of ejecta at Pu`u`O`o, estimated at 13 – 17% (A.Harris, pers.com) the volume of the ejected material will be

greater as the blebs are considered un-vesiculated and the DRE density used in the Ejecta-Mass model.

Using the process described here it is possible to apply the idealized scenario for mass ejection at the Beehive vent to the results obtained for the various thermal anomalies detected in the radiometer data, and return an estimate on the mass of material associated with each event. In the next section I shall investigate the relevance of this model using simulated thermal anomalies and discuss the issues raised. I shall conclude this chapter by analysing the results of this Ejecta-Mass model applied to the actual thermal anomalies at the Beehive vent with consideration of the issues raised by the idealised nature of this model.

3.14. Application of Ejecta-Mass model to simulated thermal anomalies

Any event at the Beehive vent resulting with molten spatter will more than likely result in the emplacement of more than just a single bleb considered in the basic thermal diffusion model. Figure 3.2 displays a typical set of such spattering episodes. In the Ejecta-Mass model for spattering at the Beehive vent, the radiometer FOV will detect a thermal signal comprised of the cumulative cross-sectional areas of all the blebs. Figure 3.13 displays a set of curves depicting the cooling durations for a simulated set of thermal anomalies comprised of a varying number of identical sized blebs. These were created using a set of idealised thermal anomalies input into the Ejecta-Mass model described in the previous section.

It is indeed apparent that the dominant factor governing the cooling duration of such anomalies is governed by the size of the blebs. A large number of smaller blebs will take a much shorter time to cool to a set threshold temperature than a lesser number of

larger spatter blebs. Therefore the duration of any thermal anomaly recorded from the Beehive vent is modulated by the size of the spatter blebs ejected.

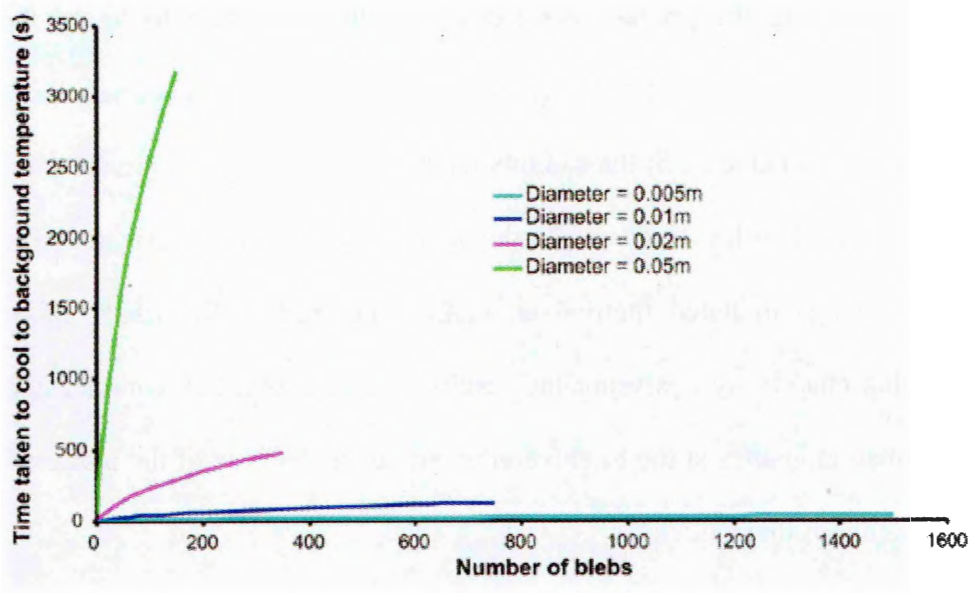

Figure 3.13: Relationship between the number of cooling blebs in the radiometer FOV and the time taken to cool to within 5K of the background temperature. Simulated anomalies shown here consist of varying numbers of blebs with 4 different diameters. Bleb diameter is the dominant factor in the cooling rate (figure 3.10), irrespective of the number of blebs of a similar size in the FOV. Here I show that even a relatively large number of smaller blebs will cool much quicker than a lower number of larger blebs. We can relate this behaviour to the cooling rates of thermal anomalies in figure 3.2 (p103).

If we consider a highly idealised model of spattering events from the Beehive vent then we might assume that all ejected blebs are of identical size. This is the assumption used to create the artificial anomalies depicted in figure 3.13, and is an unlikely scenario. There will of course be a range of bleb sizes present from any spattering event such as those in figure 3.1 (p102). It is therefore necessary to ascertain the relationship between the inferred number and size of spatter blebs present in any Duck radiometer anomaly and the estimated size and number of blebs returned by the thermal diffusion model.

In order to assess this relationship, a set of simulated spattering events was created involving varying amounts and sizes of ejecta. These models include a range of spattering combinations (i.e. large amounts of smaller ejecta, fewer but larger spatter blebs or a combination of these instances). In the absence of quantitative estimates of spatter bleb

numbers and sizes from actual events at the Beehive vent, this method should provide an opportunity to assess the results returned from the Ejecta-Mass model and to compare with the statistics of the 'original' events.

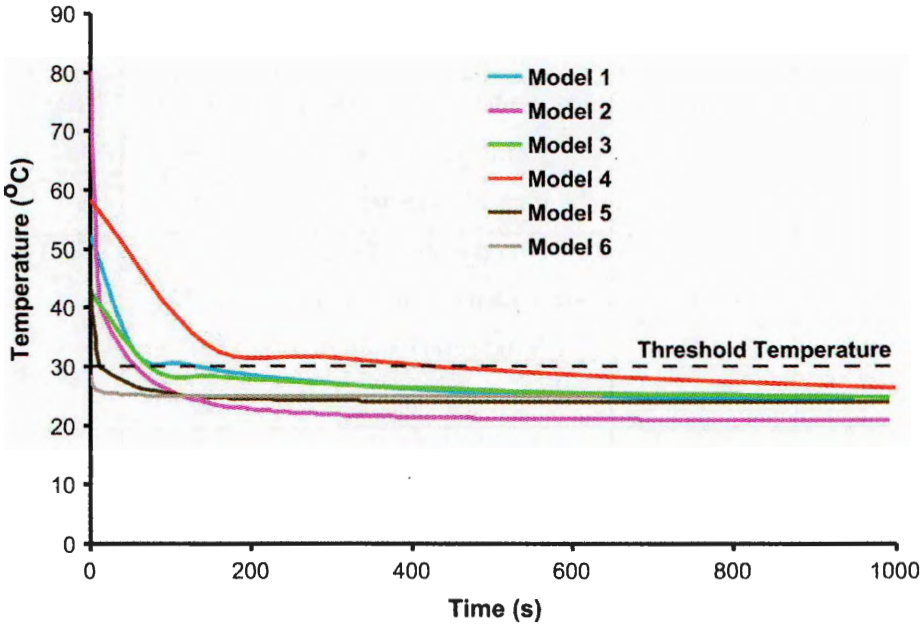

Figure 3.14: This chart represents a number of simulated anomalies comprised of differing numbers and sizes of blebs. This was undertaken to compare the response of the modeling algorithm that returns an estimate of the number of blebs and their diameter (assumes all the same size), to different populations of ejecta. This provides a more realistic scenario than the assumption that all blebs of molten ejecta are of the same dimensions.

Figure 3.14 displays a set of artificial thermal anomalies for 6 spattering models, in which varying sizes and number of blebs were used to calculate the likely radiometer signal. This was accomplished by 'reverse engineering' those portions of the Ejecta-Mass model (steps 4 & 5 in figure 3.12 on p133) and calculating the likely radiant exitance in the radiometer FOV. The modelled radiance in the radiometer FOV can then be converted back to a temperature value using equation 1.5. By calculating the mean temperature over time for the differing cooling rates of the different sized blebs in the model, a single cooling curve is created. Table 3.1 indicates the range of bleb sizes and numbers used to create each model.

The initial temperature and cooling duration of this artificial anomaly is recorded, and these values may then be input to the standard Ejecta-Mass model.

Model	Number	Diameter (m)		Simulated	Thermal Diffusion Results (T_h 300 to 1100 °C)
1	100	0.01	**Number of blebs**	280	58 - 315
	100	0.02	**Mean bleb dia (weighted)**	0.033 m	0.047 - 0.053 m
	30	0.1	**Total actual mass**	57.36 kg	7 - 55 kg
	50	0.07	**Total mass (weighted dia.)**	13.06 kg	
2	700	0.01	**Number of blebs**	2300	673 - 4165
	800	0.02	**Mean bleb dia (weighted)**	0.022 m	0.02 - 0.022 m
	500	0.03	**Total actual mass**	47.51 kg	6 - 49 kg
	300	0.04	**Total mass (weighted dia.)**	28.21 kg	
3	40	0.05	**Number of blebs**	90	47 - 241
	20	0.06	**Mean bleb dia (weighted)**	0.062 m	0.04 - 0.047 m
	20	0.07	**Total actual mass**	31.25 kg	3 - 29 kg
	10	0.1	**Total mass (weighted dia.)**	25.89 kg	
4	300	0.02	**Number of blebs**	360	243 - 1645
	30	0.08	**Mean bleb dia (weighted)**	0.033 m	0.025 - 0.026 m
	20	0.1	**Total actual mass**	85.37 kg	4 - 32 kg
	10	0.15	**Total mass (weighted dia.)**	15.52 kg	
5	200	0.01	**Number of blebs**	850	209 - 985
	500	0.02	**Mean bleb dia (weighted)**	0.02 m	0.02 - 0.023 m
	100	0.03	**Total actual mass**	12.06 kg	1 - 15 kg
	50	0.04	**Total mass (weighted dia.)**	8.12 kg	
6	50	0.01	**Number of blebs**	200	50 - 334
	50	0.015	**Mean bleb dia (weighted)**	0.017 m	0.016 m
	50	0.02	**Total actual mass**	1.67 kg	0.22 - 1.51 kg
	50	0.025	**Total mass (weighted dia.)**	1.28 kg	

Table 3.1: Comparison between different populations of bleb sizes in each model representing a simulated thermal anomaly. Also shown is the calculated weighted mean from the simulation, calculated based on the relative numbers of size of bleb present within the model. The right-hand column displays the results from the model algorithm. The estimated ejected mass returned is the mass range resulting from the range of temperatures used for T_h. We can compare this to the two estimates for mass in the "simulated" column.

As figure 3.14 shows, the difference in the returned cooling rates for the various models is distinct and reminiscent of the actual cooling rates depicted in figure 3.2 (p103). The total mass of ejecta for each model was calculated using equations 3.14 and 3.15 (p134). The total actual mass for the ejected material for each model indicated in table 3.1 corresponds well with the rate of cooling for the anomalies shown in figure 3.14. Those models involving the largest mass (i.e. models 4 & 3) cool slowest, whereas those models with the least mass (i.e. models 5 & 6) cool the quickest. With these models I have attempted to replicate a variety of sizes and numbers of blebs associated with differing spattering events. For example, model 2 has greater numbers of smaller blebs (0.01 – 0.02m diameter) and a lesser number of slightly larger blebs in the 0.03 – 0.04m range. This results in a relatively quick cooling time as indicated in figure 3.14. Model 6 has low numbers of smaller blebs (0.01 – 0.025m diameter) and displays a very quick cooling time. Model 4 has relatively high numbers of larger blebs relative to the other models, and displays a slower cooling time. I use observations from the HVO website on such spattering events at various vents in the Pu`u`O`o crater and elsewhere, as well as from various footage of spattering events ("Kilauea Eruption Update: 2002") as the basis of these basic spattering models.

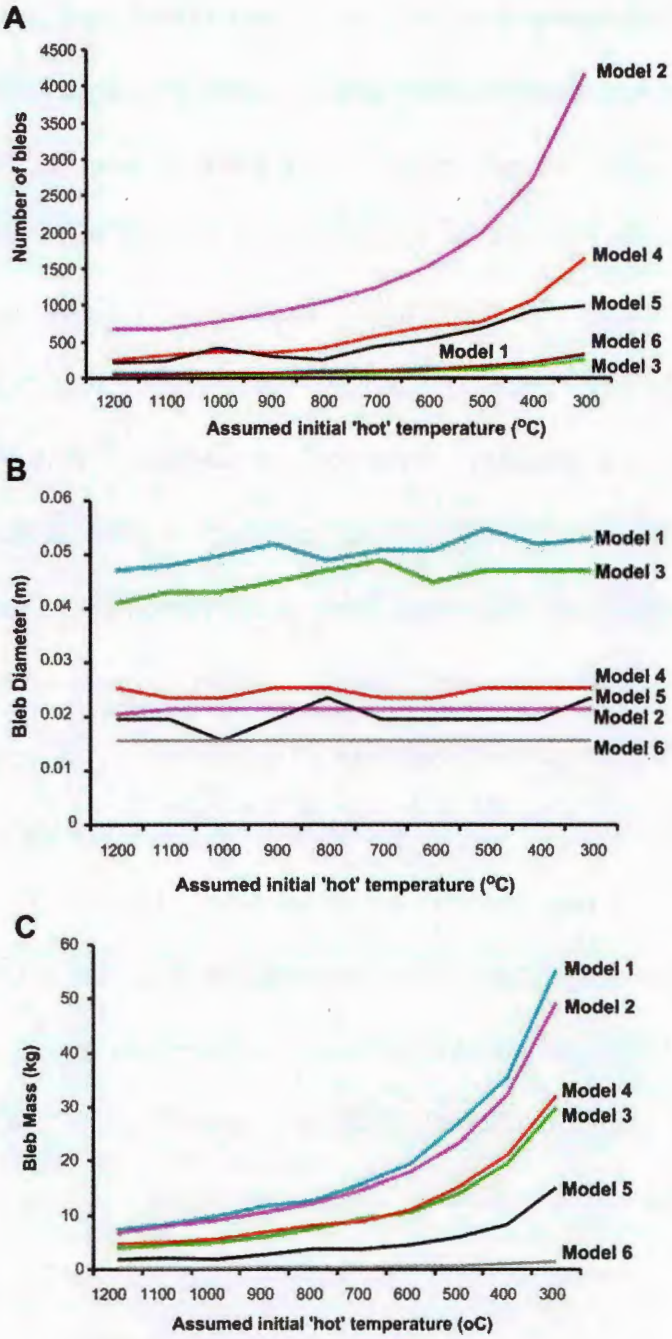

Figure 3.15: These charts show the variation in response for different assumed emplacement temperatures to the six different models shown in figure 3.14. A: The variation in estimated number of blebs with differing T_H. Note that Models 1 & 6 describe very similar curves. B: Variation in estimated bleb diameter with differing T_H. C: Variation in estimated total Ejecta-Mass with differing T_H.

The ability to combine different sizes of blebs in such models allows the creation of compound cooling curves that are far better representations of actual cooling records obtained from the Beehive vent by the Duck radiometers than simulations using various numbers of identical sized spatter blebs. Model 1 displays such a compound cooling

curve, in which the initial rapid drop in temperature over time is associated with the majority number of smaller blebs. This is followed by a sharp decrease in cooling rate as the lesser number of larger blebs provide the majority of heat detected by the radiometers. Model 2, in which there are similar numbers of blebs of relatively low diameter do not describe such an obvious compound cooling curve, as the cooling curve does not have such a pronounced 'elbow' as shown in the curve for model 1. We can be more confident using such realistic thermal anomalies in relating the results of the Ejecta-Mass model to actual thermal anomalies.

3.15. Response of Ejecta-Mass model to simulated anomalies

Figure 3.15 shows a set of curves describing the response of the Ejecta-Mass model to the 6 models described above. These results are also shown in comparison with the original model specifications in the "simulated" column in table 3.1.

In the application of the Ejecta-Mass model I have used various values for T_H, which are used to calculate the initial fraction of the radiometer FOV occupied by the molten ejecta. The highest values of T_H used here are close to the original magmatic temperatures recorded for various Hawaiian basalts (Keszthelyi et al, 1998) and also by myself in the field using a handheld radiometer. Due to the problems in estimating the decline in temperature of the molten spatter due to the cooling of the bleb from its flight through the atmosphere until landfall, I have used a range of values for T_H. This is to assess how different values of T_H affect the results of the Ejecta-Mass model. A range of 300 to 1200°C covers all likely values of T_H. However, the most likely values of T_H obtained suggested from field data obtained by myself and others (Pinkerton et al, 2002; Flynn et al, 1994) suggest a narrower range of 700 to 1000°C.

Figure 3.15A shows the variation in estimates for the number of blebs returned by the Ejecta-Mass model using the various estimates of T_H. All models show an increase in the estimated number of blebs as the value of T_H drops. The greatest difference between the numbers of blebs is for models 2, 4 and 5. These models originally possess the greatest number blebs, and this is consistent with the returned estimates as shown in table 3.1. Conversely, the lowest variation in bleb numbers with T_H is with those models that have originally the least number of blebs. However, the greatest disparity between the estimated number of blebs for each model lies in the lower range of T_H estimates (< 600°C). If we restrict estimates of T_H to the likely range of 700 to 1100°C, then the returned estimates of bleb numbers from the Ejecta-Mass model encompass the actual numbers in the original 6 models. This is the case for each model.

Figure 3.15B shows the variation in the estimate of the bleb diameters with varying T_H. The estimate for bleb size does not change in the same fashion as the estimate for numbers of blebs, and these estimates compare well with the true values shown in table 3.1. In table 3.1 I give both the actual diameters used for the simulated spattering events as well as a weighted mean diameter, calculated using the relative numbers of bleb sizes comprising each model. The returned estimates for bleb diameter all fall in the range of the actual values used in each model, and overall tend to be a slight underestimate of the calculated weighted mean diameter, by on average 2 – 5mm. Therefore the estimates on the size of spatter blebs returned by the Ejecta-Mass model respond to the changes to the changes in bleb size in the artificial anomalies, and may be regarded as an estimate of the mean size of the blebs involved with actual anomalies.

The Ejecta-Mass model returns more consistent estimates on the mean bleb size than the estimates for the number of blebs present. It is apparent that the Ejecta-Mass model is sensitive to the size of the blebs involved in a spatter episode, but a meaningful estimate of the value of T_H is required to obtain an accurate estimate on the number of

blebs involved. Therefore the calculation of the total mass ejected during a spattering event will also be sensitive to the value of T_H used as this requires the number of blebs, as shown in equations 3.14 and 3.15 (p134). This is shown in figure 3.15C, and the same pattern of variation with the estimated values of T_H is returned. If a likely range of 700-1100°C for T_H is again used, then the variation in the estimate of ejecta mass is minimised. This is especially true for those models in which the total original model ejecta mass is the lowest. Table 3.1 shows that the range of masses returned by the Ejecta-Mass model encompasses those values based on the weighted mean diameter of the ejecta in each model, and apart from model 4, also provides a good indication of the total actual mass from the original model.

From this analysis of the application of the Ejecta-Mass model to the artificial spattering events, I have shown that the model can provide good estimates for the mass of material ejected based on the cooling curves from each of the simulated spattering events. The model is sensitive to the values of T_H used to calculate the original area of ejected 'hot' material in the radiometer FOV, but returns good estimates of the mean bleb sizes involved with an event if values of T_H in the range of 700-1000°C are used. In the next section I use the Ejecta-Mass model to extract estimates on the masses of ejecta associated with actual thermal anomalies detected at the Beehive vent.

3.16. Response of Ejecta-Mass model to actual anomalies detected at the Beehive vent

In the previous chapter I investigated the timings of thermal anomalies with the Lunisolar tides. In this section I apply the Ejecta-Mass model to these same thermal anomalies in which the cooling duration and initial temperatures have been identified. This process was described in section 2.5 <***???update this link???***>.

I first investigate the sensitivity of the ejecta mass model to a selection of anomalies at various recorded durations in order to provide an estimate of error intrinsic to this model. I will then apply these derived errors in the subsequent section where I analyse the relationship between the recorded anomaly duration and the amount of ejecta associated with each anomaly.

3.16.1. Calculation of the thermal sensitivity and errors in the Ejecta-Mass model

I have shown in the preceding sections how the Ejecta-Mass model can be used to derive an estimate of the mean mass of ejecta associated with a simulated cooling trend using only the parameters of maximum achieved temperature and event duration. In this section I shall attempt to derive the thermal sensitivity of the model by using the known errors in the detection of these two defining parameters for each thermal anomaly. In chapter 2 I discussed the sources of error present in the Duck radiometers at Pu`u`O`o, namely the constantly varying levels of fume within the crater which attenuate (by scattering and absorption) the signal received by the ducks. Such effects may not only mask the true maximum temperature detected of a degassing event with resulting molten ejecta, but also make it difficult to identify the true duration of a thermal anomaly due to the cooling ejecta. In Chapter 2 I described how the IDL software used a "moving window" technique to identify anomaly duration. This technique used a calculated mean over a 10 second window and compared it to a mean calculated for a much longer period of 30 minutes. Once the elevated temperatures associated with a thermal anomaly had fallen to the longer duration mean, then the event was deemed over. This technique allows both a relatively accurate detection of thermal anomalies despite the constant fluctuation of temperatures over 2-4 second intervals imparted by changing fume conditions attenuating

the signal as well as compensation for the diurnal change in temperatures due to solar heating during the day.

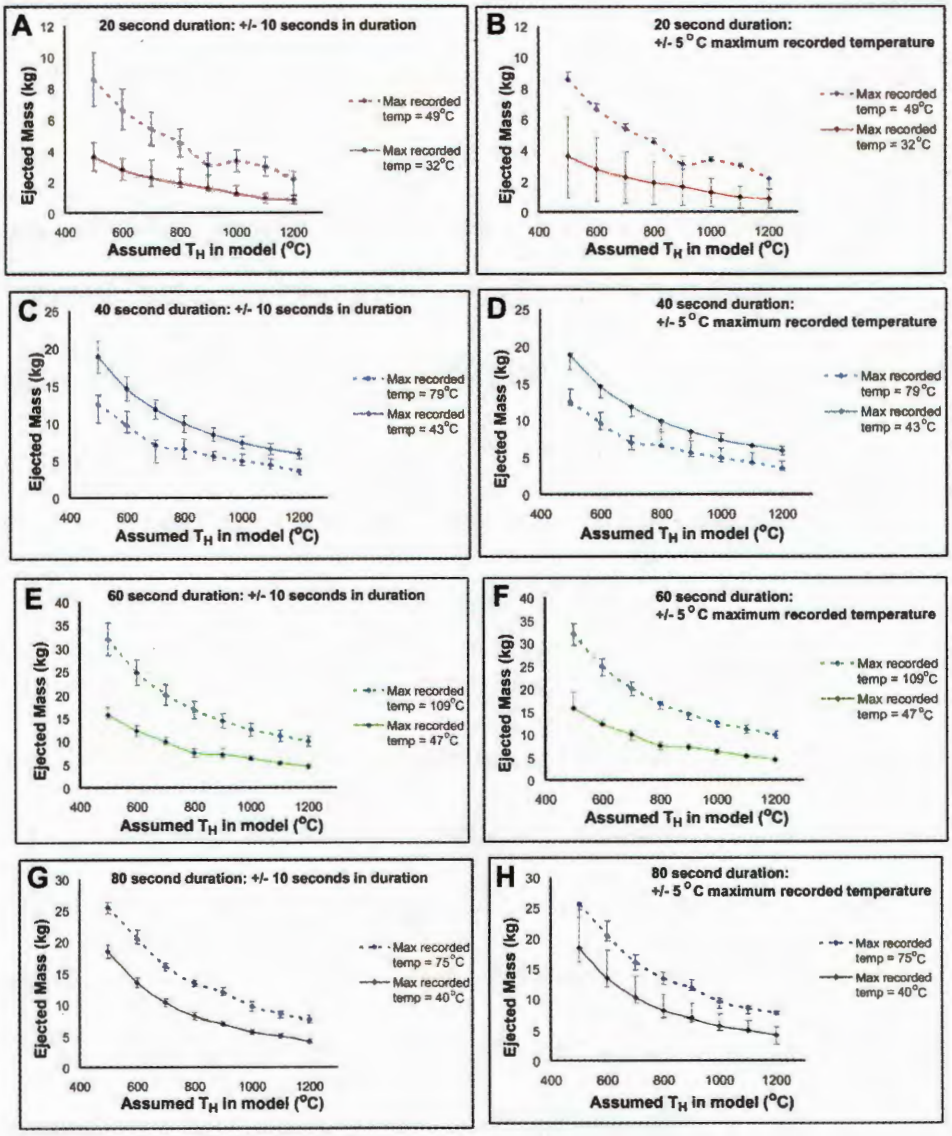

Figure 3.16: Sensitivity of the Ejecta Mass model to variation in detector error. The Ejecta Mass model takes as its input the recorded duration and maximum achieved temperature of the thermal anomaly. Due to the variable viewing conditions within the crater, which constantly vary, the maximum recorded temperature may vary as much as +/- 5°C. Panels B, D, F and H show the error in the mass estimate for the maximum detected temperature +/- 5°C plotted against increasing assumed values of T_H for sample anomalies of 20, 40, 60 and 80 seconds duration respectively. The constant fluctuation in temperature also introduces error in detecting the true duration of an anomaly. Panels A, C, E and G show the error due to +/- 10 seconds of the detected anomaly duration for the same set of anomalies as panels B, D, F and H.

In order to calculate the sensitivity of the Ejecta-Mass model to these incipient errors I extracted two sets of representative thermal anomalies with durations of 20, 40, 60 and 80 seconds with relatively high and low maximum achieved temperatures. This was to

identify any variation in calculated error with event duration and/or maximum recorded temperature (magnitude). Figure 3.16 shows the estimated ejecta mass for these anomalies calculated for various assumed values of T_H with error bars showing the variation in estimated ejected mass for maximum recorded temperature +/- 5°C (panels B,D,F & H) and recorded anomaly duration +/- 10 seconds (panels A, C, E & F). These error bars show the error in actual mass, rather than a percentage. This method not only allows us to identify the variation in estimates of ejecta mass due to the errors within the Duck radiometer data, it also allows us to closely analyse the sensitivity of the model to small changes within the input parameters and therefore understand the performance of the model when applied to actual thermal data. The values used to generate the error bars were derived from separate model runs with the input parameters changed accordingly.

Figure 3.16 shows that those sample anomalies with the largest errors bars tend to be those of shorter duration and/or low maximum recorded temperatures. This might be expected as it is more difficult to isolate the true extent of such anomalies from the background noise than for those anomalies with higher temperatures which are more easily distinguished from the background ambient. Furthermore, as I have already shown, the main factor controlling the duration of a thermal anomaly will be the actual size of the ejected blebs. Therefore for those anomalies of lower maximum recorded temperature the Ejecta-Mass model may find it more difficult to arrive at solutions which match the observed parameters due to the size of the iterative steps employed by the model. As the +/- 5°C error margin used is a relatively larger proportion of the lower temperature anomalies, the resulting errors for such anomalies will be disproportionately larger than those for higher temperature errors.

All panels within figure 3.16 show that estimates of total ejecta mass decrease inversely proportionately to the increasing values of T_H used to calculate the area within the Duck radiometer FOV. This is because as T_H increases, it takes a disproportionately

smaller area of the FOV at higher temperatures to produce the same total detected radiance than for larger areas within the FOV at lower values of T_H (assuming a constant T_C representing the ambient temperature). This is a consequence of the non-linear nature of Planck's law, and is discussed in greater detail in the next chapter. If a smaller area is calculated at T_H then there must be a lower amount of molten material within the FOV, and therefore a lower mass ejected. For anomalies of longer duration implying larger blebs ejected, there must therefore be fewer blebs. In such cases with relatively fewer blebs, even a small variation in number of blebs due to errors in the input parameters such as those discussed here will have a larger impact on the estimate of total ejected mass.

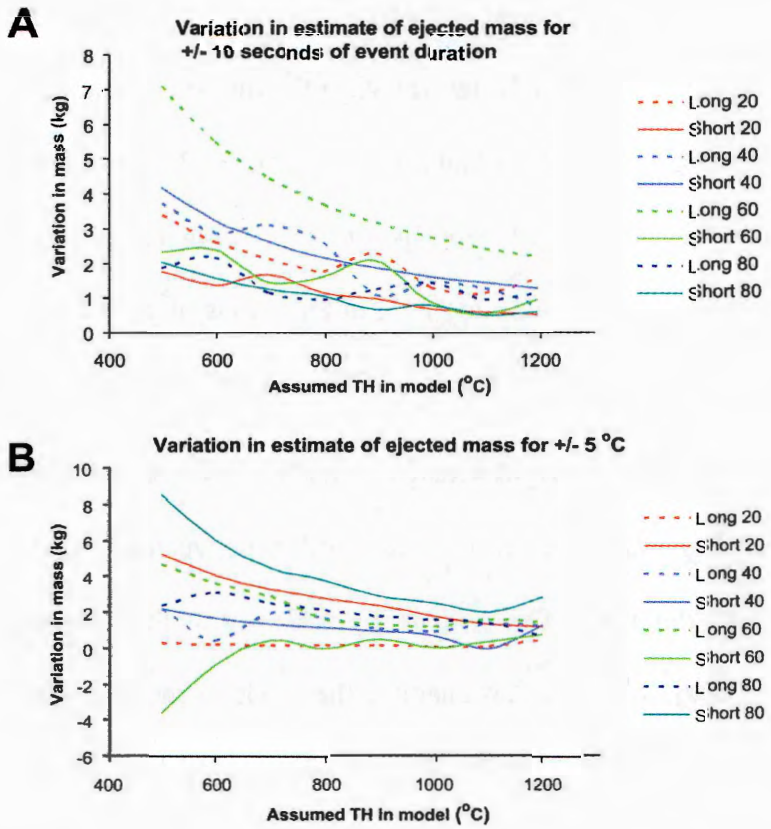

Figure 3.17: Variation of maximum range in errors for recorded event duration (A) and maximum recorded temperature (B). The errors shown here are those collated from figure 3.16.

It is apparent that the margin of error calculated for the various sampled thermal anomalies in figure 3.16 decreases with increased anomaly duration. The Ejecta-Mass model appears to be most sensitive to changes in input parameters for shorter duration

anomalies, especially those with lower maximum recorded temperatures. This sensitivity is less pronounced for anomalies with higher maximum temperatures and longer durations. In order to better quantify this sensitivity, figure 3.17 displays the maximum variation in ejecta mass for each of the thermal anomalies recorded in figure 3.16.

Figure 3.17A shows that the Eject-Mass model is less sensitive to errors in recorded anomaly duration than errors associated with the magnitude of the maximum temperature achieved in figure 3.17B. However, these differences are more pronounced at lower assumed values of T_H. In previous sections I discussed the problems associated with choosing an accurate value of T_H (and is a subject addressed in the following two chapters), and surmised that most accurate values of T_H will fall in the region 700°C to 1000°C. In figure 3.17A and B, the margin of errors for estimated ejecta mass narrows from T_H = 800°C onwards, and is more marked in figure 3.17B. This shows that the model is less sensitive to variations in input parameters at higher values of T_H. These higher values for T_H are consistent with my own observations using a hand held radiometer and other field observations by Pinkerton et al (2002) and Flynn et al (1994).

Analysis of the pattern of sensitivity for the sampled thermal anomalies in figures 3.16 and 3.17 suggests that there is a relationship between the model sensitivity and the thermal anomaly duration. The error margins narrow with increasing anomaly duration. By using this relationship we can quantify the model error for a given anomaly duration and apply this to the model estimates to provide a confidence envelope for estimates of total ejecta mass associated with a degassing event. I have combined these calculated errors from all these runs to produce a combined error which can be related to the anomaly duration.

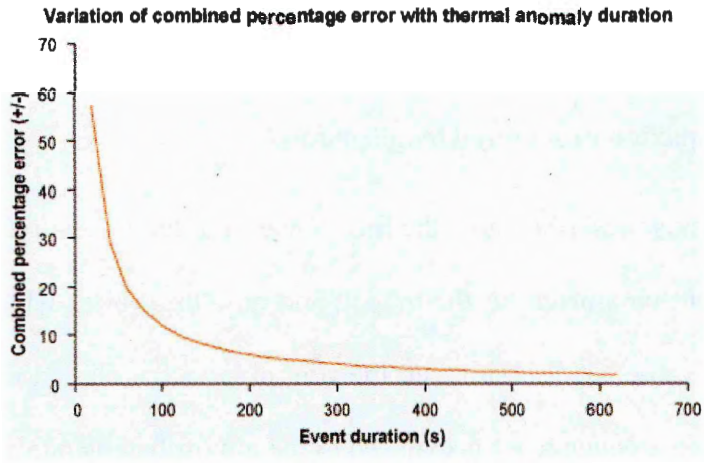

Figure 3.18: The combined percentage error calculated from errors introduced by the maximum recorded anomaly temperature and anomaly duration used as input for the Ejecta Mass model.

This was achieved by calculating the mean error from the relative high and low maximum achieved temperatures for each of the sampled anomalies for both errors due to anomaly duration and maximum temperature. These values were summed for each of the 4 samples to create a maximum error envelope, and then expressed as a percentage portion of the total estimated ejected mass. The resulting values were then plotted against the sample anomaly duration and a trend line applied. I found that the resulting relationship could be defined by equation 3.16:

$$\text{Percentage Error } y = 1076.9x^{-0.9786} \qquad \text{Equation 3.16}$$

Where y is the percentage error of the total estimated ejecta mass in kg, and x is the anomaly duration in seconds. Equation 3.16 was found by best fit applied to the measured values with an R^2 of 0.8. Application of equation 3.16 allows the +/- error envelope to be applied to any estimate of ejecta mass using the model. Figure 3.18 shows this calculated combined error as a percentage figure of the estimated total ejecta mass using equation 3.16. As figure 3.18 shows, the model is most sensitive to small changes in input errors for shorter duration anomalies than longer duration anomalies and therefore the ejecta mass

model is more accurate when used to make estimates for the longer recorded anomaly durations. This is especially the case where the shorter duration anomalies coincide with low recorded maximum achieved temperatures.

I have now described how the Ejecta-mass model is sensitive to variation and errors in the two input parameters to the model, and how this varies with the value of T_H used. However, the value used to simulate the rim, akin to the chilled rind which immediately forms on molten ejecta once it is exposed to the atmosphere is one other parameter that has a bearing on the sensitivity and accuracy of this model. I have previously discussed the use and reasoning behind the rim values used within the thermal diffusion calculations which are core to the Ejecta-mass model.

I will show here how variation in the rim size value selected for use within the model affects the resulting estimates of ejected mass. In order to accomplish this, I ran the model twice for all recorded thermal anomalies with a T_H of 1000°C, in the first run using a rim size of 0.001m and in the second run a rim size of 0.003m. By comparing the resulting estimates for ejecta mass for each anomaly using these two rim sizes for each of the thermal anomalies it was possible to calculate the difference in ejected mass, and therefore the variation. Figure 3.19 shows this variation calculated as a percentage of the estimated total ejecta mass plotted against duration. This representation allows direct comparison to the sensitivity analysis shown in figure 3.18.

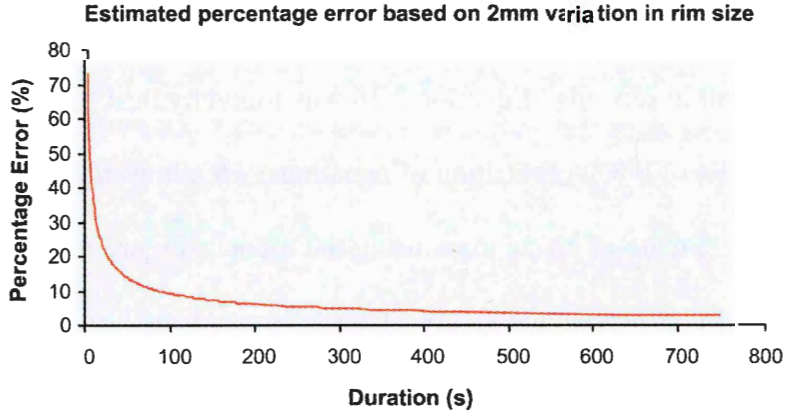

Figure 3.19: Calculated error based on variation of 2mm rim size used within the Ejecta Mass model

The model is much more sensitive to the rim size values used for anomalies of shorter duration than for anomalies of longer duration. This distribution may be explained if shorter duration anomalies are associated with smaller blebs sizes rather than larger bleb sizes. This is because larger values used for the rim size will generate much larger variations in estimates as the rim size used will approach a significant fraction of the actual diameter of the bleb itself, producing inaccurate results from the thermal diffusional modelling. For larger blebs, the variation in rim size will be a much smaller fraction of the bleb size. In section 3.10.1 on page 124 I discuss the best rim value to be used, empirically derived from laboratory testing of an artificial bleb. I found that a value of 0.001 provided the best match between the model and the measured cooling of the bleb in laboratory conditions. However, in reality such factors as the vesicularity and small changes in the mineral content etc may affect the thermal resistance and conductivity of the material resulting in inaccurate estimates by the model. These effects may be countered by varying the rim size used within the thermal diffusion calculation which takes into account the values of thermal resistivity and conductivity of the sample material (Crank, 1975). Although only one rim size can be currently used within the Ejecta-mass model it is still important to understand the relationship between the value used in the model and the resulting effect on the models estimate of ejecta mass.

It is apparent from this analysis that the Ejecta-mass model is more sensitive to variations in the input parameters for smaller blebs than for larger blebs and is also more accurate for assumed values of T_H greater than 800°C. The model is therefore more accurate for larger blebs where high values of T_H are used. I have shown that this sensitivity can be represented as a function of anomaly duration and can therefore be used to provide an error envelope for actual predictions of ejecta mass. In the next section I

investigate whether there is indeed a relationship between the anomaly duration and the size of the molten ejecta, as well as the total ejected mass.

3.16.2. Response of Ejecta-Mass model to actual anomalies detected at the Beehive vent

Figure 3.20 displays the results from the application of the Ejecta-Mass model to the majority of Beehive vent thermal anomalies from the September and October 2001 study period. In this application I use only those anomalies that had a duration exceeding 8-10s, as only anomalies with cooling durations longer than this appear to be associated with varying quantities of ejecta. Nearly 500 anomalies satisfying this criteria were identified. This was a requirement to remove those anomalies associated purely with ejection of gas and which provided no evidence for molten material cooling in the radiometer FOV. This type of anomaly is characterised by a rapid rise in temperatures with a subsequently fall in temperature. This is due to the rise of the hot and buoyant gas emitted from vent upwards and out of the FOV of the radiometer. This effect has been used at Stromboli volcano (Italy) in which a series of 'stacked' radiometers were used to estimate the vertical velocity of emitted volcanic gases (Harris et al, 2003). The low inclination angle of the radiometer (figure 3.3 on p108) ensures that any gas rising upwards exits the radiometer FOV very quickly. The rapid fall in detected temperature is also attributable to the rapid cooling and diffusion of the gases in the atmosphere at Pu`u`O`o crater.

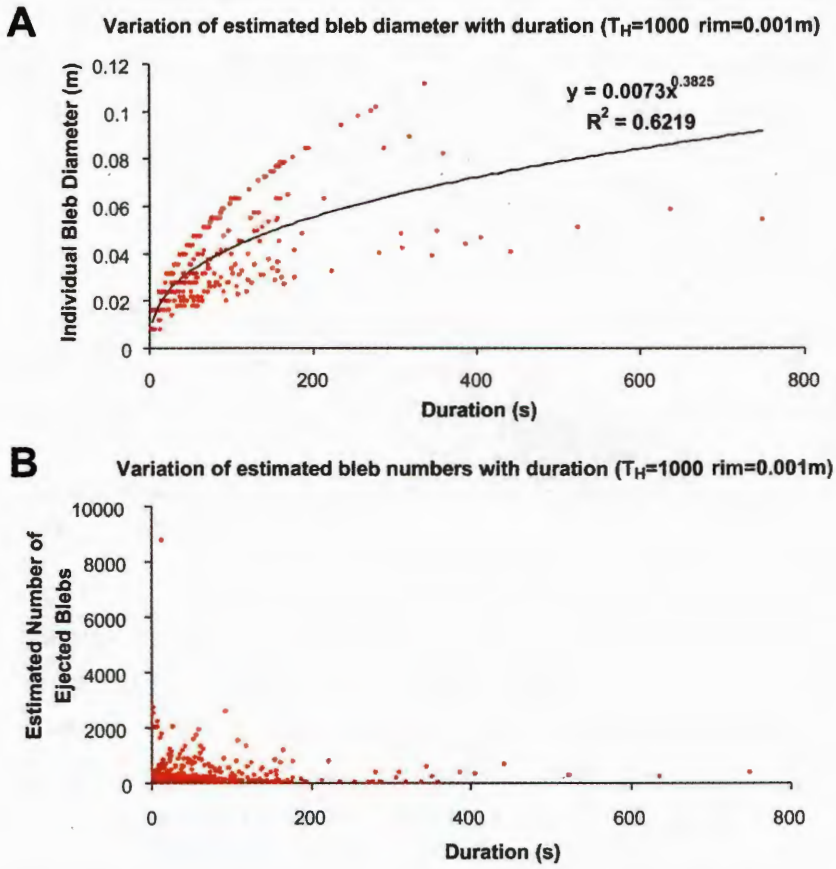

Figure 3.20: Estimates of individual bleb diameter (A) and number of blebs (B) versus the recorded anomaly duration for thermal anomalies within the September and October 2001 study period.

Figure 3.20A displays the estimated bleb diameter as output by the Ejecta-mass model plotted against the duration of each anomaly. There is an apparent relationship between the bleb diameter, or size, and anomaly duration implying that larger blebs are associated with longer duration anomalies. This relationship is indicated by a trend line. However, figure 3.20B shows the returned number of blebs for each anomaly as output by the model plotted again against the duration, yet no relationship is readily apparent. However, it is clear that only lower numbers of blebs per episode are present for the longer duration anomalies. Figure 3.21 shows these results combined to produce the actual estimated mass of ejecta for each anomaly, using equations 3.14 and 3.15 and a value of 2280 kg m^3 for ρ. Figure 3.21 also incorporates the combined error estimates described in

the previous section. Clearly evident is a relationship between the ejecta mass and the anomaly duration.

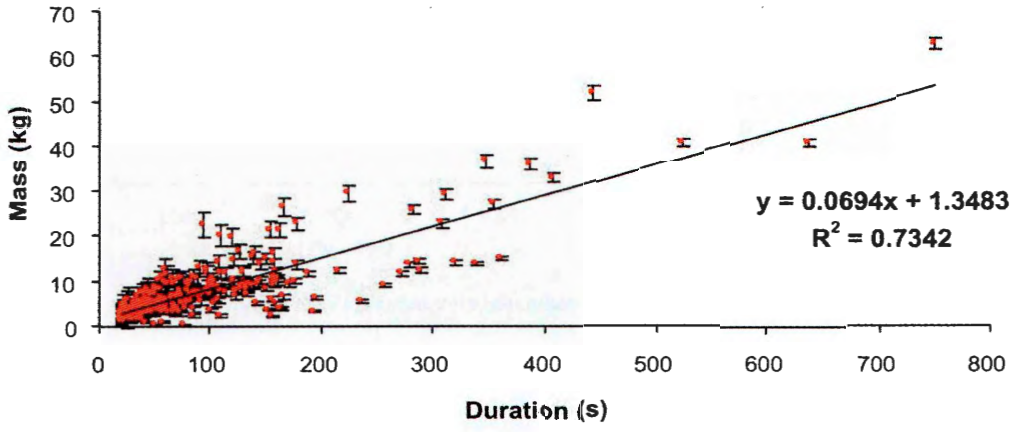

Figure 3.21: Scattergraph displaying the total estimated ejected mass calculated for each degassing event during the study period plotted with the thermal record duration. The trend lines indicate a linear regression line calculated from the relevant points. The error bars show the sensitivity of the model to errors introduced by the Duck radiometer setup and are calculated from the combined percentage error discussed in section 3.16.1. This shows the general trend that thermal anomalies of greater duration tend to be associated with the greatest ejected mass.

It is clearly the size of the spatter blebs from the relationship in figure 3.20A that is the dominant factor in the relationship shown in figure 3.21. As I have shown in previous sections it is the size of the spatter bleb that governs the rate of cooling as they have the greatest thermal inertia and will take longer to cool. Due to the relationship between the combined error and the anomaly duration the uncertainty in the estimate of ejecta mass for those events with the greatest ejected mass is less than for lower estimates of mass.

A possible explanation of this observation is that those degassing events which expel molten spatter from the Beehive vent with the largest estimated ejected mass and longest anomaly duration are related to the most forceful expulsion of gas from the vent. We might expect this as more force is required to expel a larger amount of material from the surface, than a lesser amount of material. This may only be true if the blebs themselves are fewer in number, but of a larger size as greater force is required to eject larger single blebs. This effect is evidenced by the very low number of blebs associated with longer

duration anomalies shown in figure 3.20A. A large number of smaller blebs may not require such forceful expulsion of gas from the vent.

The dominant factor upon the style and size of spatter is not only the expulsive force of the gas release from the free-magmatic surface, but also the viscosity of the material (Wolff & Sumner, 2000). Lower viscosity will allow easy fragmentation and the ejection of smaller blebs, whereas a higher viscosity will prevent the easy dissemination of the material into smaller blebs by gas expulsion of a given strength. The viscosity of the magma is a function of the eruption temperature, gaseous content and crystallinity (Cashman et al, 1999). These controls upon the viscosity will also affect the surface tension of the liquid free-magmatic surface, and this may also in turn affect the shape, size and range of ejected spatter. If we assume a consistent viscosity and conditions at the beehive vent for ejecta, then we can certainly infer that degassing events must be stronger where a greater mass of ejecta is calculated than in those instances where there are lower estimates of Ejecta-Mass.

Figure 3.22 displays a histogram showing the size distribution of spatter blebs associated with those degassing events shown in figure 3.20A. Analysis of the frequency distribution of bleb size may allow for further interpretation and identification of the eruptive mechanisms present at the Beehive vent. The basic distribution appears to be a normal distribution with most blebs in a size range of 0.02 – 0.04m in diameter. However, there are certain episodes where larger blebs ranging upto 0.11m in size are recorded. In addition to this there is a large number of degassing events with blebs of sizes ~ 0.01m. This may be indicative of a modal process ongoing at the Beehive vent which preferentially results in spatter blebs of this size.

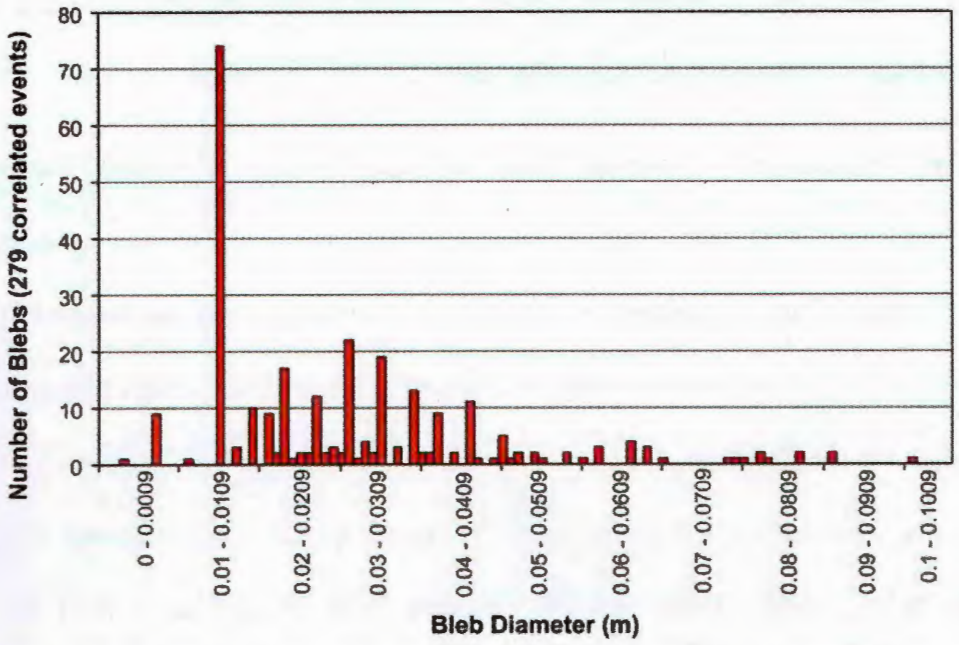

Figure 3.22: Histogram showing the size distribution of correlated spatter blebs during the September and October 2001 study period. I use here correlated events rather than all events so as not obfuscate any possible relationship. The model was run assuming T_H =1000°C and rim = 0.001m.

One of the conclusions of the previous chapter was that the level of the free-magmatic surface in the Beehive vent may change in response to the gravitational tidal forces from the Sun and Moon, as well as variations in the supply of magma to the vent and elsewhere in Pu`u`O`o. If the level of the surface in the Beehive vent is low enough, then any degassing activity driving spattering may not be of sufficient vigour to drive the ejecta over the vent ramparts and into the radiometer FOV. Smaller blebs will be more likely to exit the vent ramparts in this way due to their lower mass, whilst larger spatter will be more likely to fall back or to adhere to the vent's agglutinated ramparts (Sumner et al, 2004). In the Ejecta-Mass model the idealised scenario considers the Beehive vent as a simple level opening in the Pu`u`O`o crater floor, yet figure 3.1 (p102) reveals vents and hornitos upon the crater floor consisting of tube structures created by successive spattering. Such a process may well skew a frequency distribution of ejecta size such as that in figure 3.22, with lower mass ejecta being preferentially recorded in the radiometer data due to the greater likelihood that it will clear the confines of the vent. In a similar fashion, larger blebs such as the ribbon spatter etc will clear the vent walls due only to infrequently large

degassing events that may coincide with higher levels of the magmatic surface in the vent. The consistent low numbers of such larger blebs in figure 3.22 may be representative of this effect.

Figure 3.22 may show just this type of distribution, with the distortion of the distribution due to the modulation of the actual mass of ejecta displaced from the magmatic surface in the vent, by the morphology of the vent itself. Therefore, by analysis of the returned distribution of ejecta size it is perhaps possible to infer greater detail on the morphology of the vent itself and therefore gleaning yet more information about the beehive vent from a simple radiometer record. In effect, we can infer the expulsive force, relative viscosity, style and amount of molten ejecta from a volcanic vent using this model. However, there are several drawbacks to this which I discuss in the final section. This is still a very useful ability, as highlighted by the difficulty in the last chapter of ascertaining the level of the magma surface in the Beehive vent.

3.17. Discussion & Conclusions

I have shown here that simple thermal diffusion modelling applied to simple radiometer data can be used to estimate the mass of ejecta associated with spattering from the Beehive vent in the Pu`u`O`o crater. This is possible due to the presence of two key characteristics in the radiometer record of degassing events: the initial temperature achieved by an anomaly and its cooling duration. These parameters were used in the "Ejecta-Mass" model which applied the thermal diffusion model based on equations from Carslaw & Jaeger (1954) and Crank (1975) to an idealised spattering scenario. This idealisation considered both the morphology of the Beehive vent itself and the form of all ejecta. This idealisation is necessary due to the uncertainties and ever changing nature of vents in Pu`u`O`o crater. The idealised spherical form for all ejecta in the model is an

extension of observed behaviour (i.e. Pele's tears). Because of the wide variety of forms taken by any actual ejected material (which in itself is due to viscosity, levels of vesiculation, initial ejection force and so on), there was a requirement that the form be easy to model and to relate to actual events. A spherical form for ejecta also lends itself most easily to the consideration of the thermal diffusion equations which form the basis of the premise that smaller spatter blebs will cool quicker than larger blebs. The Ejecta-Mass model was created in a manner so that the only input required was the initial temperature and the cooling duration, and the output result is an estimate of the mean size of the ejected spatter blebs and their number. The total ejected mass can therefore be calculated, as the density of the basaltic magmas at Pu`u`O`o is known.

There are many apparent drawbacks to this model which on immediate inspection suggest that it may not meet the rigorous considerations required by the actual events at the Beehive vent. Interpretation of the returned thermal data from the Duck radiometers may be considered trustworthy only for relative comparison (Harris et al, 2003), hence the results of the Ejecta-Mass model may only be used as a tool to interpret the relative strengths of spattering events at the Beehive vent. For simplicities sake, I have not in any detail considered in this model the small amounts of heat loss due to conduction into the ground surface as well as heat loss due to convective cooling. I have also not considered here the vesiculated nature of the ejected material. I have only used DRE values for the density of basalts at Pu`u`O`o. The decrease in density wrought by the vesiculation of the majority of effusive material at Pu`u`O`o will serve to increase the estimate of cooling times in the model. The vesiculated material is 10-17% less dense than the DRE values I consider in the model (A.Harris, pers.com) and this counters the effect on cooling time when considering the estimate of total ejecta mass. I have instead concentrated upon the consideration of the spherical bleb as a cooling sphere of molten material encased in a chilled rind. Despite the emitted radiance paradox from such a surface (the radiometer can only detect emitted radiance from the surface of the bleb, yet the Ejecta-Mass model

calculates the temperature at the rim depth), laboratory studies suggested that this thermal diffusion model could predict the cooling of hot molten basaltic material once that material was exposed to a cooler environment.

Further problems derive from the idealised scenario for spattering from the Beehive vent. I assume that all material is emplaced in a single episode of degassing, yet it is common in degassing from vents such as the Beehive vent that molten ejecta is emplaced in a series of pulses. Although the number of spatter blebs is calculated from the initial temperature T_H, any subsequent material emplaced in the FOV will affect the cooling duration of the anomaly. It is the rate of cooling that is the key to the Ejecta-Mass model. Any such "multi-stage" spattering events extend the total cooling duration by the addition of new material. This results in an over-compensated estimate for the total ejected mass, as the anomaly has been prolonged by the addition of new material since the initial emplacement. I also assume that all ejecta from a spattering event falls entirely in the radiometer FOV. Due to the lack of visual observations of spattering at the Beehive vent it is impossible to ascertain whether this is a realistic assumption based on the likely strength of spattering and the sizes of the vent and the radiometer FOV.

Therefore, although this model is far from absolute it *does* allow a simple assessment of the relative strength of degassing from a vent using purely thermal data, and adds to the many capabilities of the cheap portable radiometer system deployed by HIGP and HVO. Further observations of spattering from a vent coupled with simultaneous radiometer measurements with the application of this Ejecta-Mass model may enable this model to be further refined.

Even so, this model allows an extended capability that belies a simple radiometer setup. Despite the often cloudy and fume filled conditions within the Pu`u`O`o crater, this model applied to the Duck radiometers to estimate the presence and amount of molten ejecta on the crater floor from the safe vantage point of the crater rim. The video camera

telemetry system set in place by HVO cannot provide such visual estimates because of these viewing conditions. Extended use of this model and comparison with visual data would enable the accuracy to be improved and set the basis for the model to be used extensively to help refine estimates of total effusive flux from the entire Pu`u`O`o system. The rate and force of degassing detected using this model may be related to the overall degassing detected using COSPEC analysis (Mangan et al, 1995) to provide a fuller picture on such events. Even in its most simple form, the model applied to the Duck data allows an easy distinction between the presence of the degassing events with and without molten ejecta, and an estimate of the ejected mass.

In order to for this model to fully realise its capabilities it must be related to simultaneous visual observations of such events in order to be refined and improved, as well as further analysis of the effects of viscosity and initial cooling of spatter once it has made landfall. However in the current absence of such observations, I present this model as a method for making a relative estimate on the mass of molten material ejected from a vent using a simple thermal record from a single radiometer.

4. Analysis of the accuracy of the dual-band method for extracting estimates of sub-pixel thermal resolution

4.1.Introduction

The dual-band method is a procedure that has been widely used to extract estimates of the thermal structure found within satellite instrument imagery obtained over lava flows. I investigate here the accuracy of the dual-band method when applied to simulated satellite imagery based on ground based infrared imaging camera, in light of recent observations on the application of this procedure to satellite imagery of lava flows.

The dual-band method uses two simultaneous equations applied to two channels of satellite instrument data to estimate the two fractional areas of a simplified surface of a lava flow based on the Crisp & Baloga model (1990). This information can be used to infer the levels of activity present within the pixel instantaneous field of view (IFOV). This method has been applied to a variety of volcanic phenomena, some of which has been outlined within chapter 1. Few studies have sought to exactly quantify the accuracy of the method with regards to ground based data. I choose to restrict this chapter to the study of the application of the dual-band model, despite the development of an updated model, the "triple-band" model (Oppenheimer, 1993; Harris et al, 1998) as the dual-band model continues to form the basis of many studies (Donegan & Flynn, 2004).

Certain studies, most notably those of Flynn et al (1994) and Harris et al (1998) investigate the use and application of the assumed temperature within the two simultaneous equations, and what this actually relates to on the surface of the lava flow. Wright & Flynn (2003) go on to highlight the problems encountered with the dual-band method by showing that the temperatures and areas returned by this method do not relate in any practical reality to actual values extracted from active pahoehoe lava flows (Wright & Flynn, 2003).

They show that methods using 3 or more channels provide much greater accuracy in quantifying the thermal structure of a lava flow surface. Satellite instruments that currently provide this ability are limited. An analysis of the EO-1 Advanced Land Imager (ALI) and the Landsat 7 Enhanced Thematic Mapper Plus (ETM+) within chapter 6 of this thesis, uses the dual-band method as a basic means of comparing the response of the newer ALI with the older ETM+ over active lava flows. The patterns of solutions and interpretations obtained from the ALI were consistent with ground observations of the behaviour of the flow-field at Mt Etna at the time. These results showed that the dual-band procedure can be used to distinguish various features within the flow-field based on a synergistic analysis of the resulting estimates for P_H and T_C (Donegan & Flynn, 2004).

I investigate here in detail the response of the dual-band method by using ground based thermal imagery and simulated imagery based upon it, to analyse the performance and accuracy of the dual-band method. I accomplish this by reproducing the synthetic thermal distribution as it would appear within various SWIR channels of the Advanced Land Imager (ALI). I choose to replicate the ALI due to the number of channels within SWIR that are ideally placed within the infrared spectrum for the remote sensing of lava flows, and the high spatial resolution of its SWIR channels. This is discussed in detail within chapter 6.

By using such data it is possible to change the thermal distribution within a single pixel, which in turn will affect the single radiance value representing the integral of all radiances within the area subtended by the pixel. By contrasting the changing nature of the synthetic data supplied to the procedure and noting the variation of the returned estimates it will be possible assess the accuracy of the procedure. In this way we can relate the observations made by Wright & Flynn (2003) and those from Donegan & Flynn (2004). I also describe a method in which the dual-band method can be used as an indicator of the

likely thermal distribution within a pixel in the absence of accurate estimates of sub-pixel thermal resolution.

4.2.The Dual band Procedure

The dual band procedure has been previously described within chapter 1 as a method of extracting an estimate of the sub-pixel thermal structure using just 2 bands of satellite instrument SWIR channel data. This model works by assuming one variable, within two simultaneous equations (Equations 1.5 & 1.6) applied to the radiance values returned for the same pixel in two separate instrument bands. It is then possible to identify the remaining 3 variables (Rothery et al, 1988). These components are the fractional areas of the "hot" (P_H) and "cool" (P_C=1-P_H) components and their respective temperatures (T_H and T_C). When used for identifying sub pixel thermal structure over lava flows the hot temperature, T_H is assumed as this is the easiest to constrain (Harris et al, 1997c). T_H is easier to constrain as fresh lava will be close to the original magmatic temperature. For Mt. Etna this is usually in the range of 900-1070°C (Harris et al 1998). Fresh lava with no crust present will consistently be within this temperature range. Studies by such workers as Flynn et al (1994) highlight the importance of the use of a reasonable value used for T_H, and investigate the effects of differing values of T_H on results obtained from the dual-band procedure for pahoehoe lava flows on Kilauea volcano, Hawaii. If the cool temperature, T_C was to be assumed there is a much wider range of possible temperatures within the pixel that might be present. This would range from ambient ground temperature, 0-30°C, depending on season. I have recorded ground temperatures of ~70°C for solar heated ash and scoria covered ground on a trip to Mt Etna in June 2000. Temperatures will be even higher for ground heated by the emitted radiance from a nearby lava flow. In addition to this, the wide range of temperatures found throughout a lava flow, from flow levees to a well developed crust compound the problem of consistently assuming a single temperature

for input into the dual-band procedure. Hence it is easier to assume T_H and have returned T_C representing the remaining pixel thermal component.

This model therefore allows the user to estimate the sub-pixel thermal structure, and from that, an overall assessment of the lava flow itself. The greater the area of the "hot" temperature exposed, coupled with a higher "cold" temperature then the more vigorous a lava flow is likely to be. Likewise, a lower value of P_H with a lower value of T_C, then the less active the flow, as there is less "hot" material exposed. This method, based on the two component lava flow model proposed by Crisp & Baloga (1990) has been used extensively (Donegan & Flynn, 2004, Wright et al, 2001b) to analyse various lava flows at Basaltic volcanoes such as Mt. Etna, Sicily and Kilauea, Hawaii.

4.3.The EO-1 Advanced Land Imager (ALI)

Channel	Wavelength (μm)	Saturation Radiance (W/(m² sr μm))	Dynamic Range (T°C)	Pixel size (m)
1p	0.433 - 0.453	~1000	738 - ~1139	30
1	0.45 - 0.515	~1050	821 - ~1246	30
2	0.525 - 0.605	~690	605 - ~958	30
3	0.63 - 0.69	~450	491 - ~802	30
4	0.775 - 0.805	~280	375 - ~644	30
4p	0.845 - 0.89	~240	324 - ~577	30
5p	1.2 - 1.3	~210	170 - ~374	30
5	1.55 - 1.75	~85	69 - ~231	30
7	2.08 - 2.35	~21	-18 - ~101	30
Pan	0.48 - 0.69	~88	~420 - ~808	10

Table 4.1: Basic instrument characteristics of the ALI. The shaded cells indicate the channels within the SWIR wavelength region most conducive to remote sensing of active lava flows, and for import into the dual-band method.

The ALI is one of several instruments aboard the NASA Earth Observing 1 satellite launched in late 2000. The ALI is considered to be an operational technology try out mission for the next generation of the well established Landsat Thematic Mapper series of instruments (Bicknell et al, 1999). A summary of the spectral channels provided by the ALI can be found in Table.4.1. Many of the channels possessed by ALI are duplicated within the same wavelength regions as channels from the ETM+. Within the SWIR, pixel sizes are identical for both instruments. ALI has the benefit of 2 extra channels within the SWIR and 1 extra channel within the VNIR.

The additional ALI SWIR channels assist in the application of the dual-band procedure to active lava flows as they expand the coverage provided by the ETM+ (Donegan & Flynn, 2004). The ALI is less susceptible to saturation within channels 7 and 5 than the equivalent channels of the ETM+, whilst the addition of the two extra channels 5p & 4p provide enhanced coverage within the SWIR of thermally anomalous pixels associated with active lava flows (Mendenhall et al, 2002). These extra channels when used within the dual-band procedure enable successful solutions from active lava flows that would otherwise saturate channels 7 and 5 (Donegan & Flynn, 2004). A full description of this can be found in chapter 5 in which the dual-band procedure is used as a basis to compare the performance of the ALI with the existing ETM+.

4.4.Ground Based Thermal Imagery

Ground based thermal imagery provides an excellent resource to assess the validity of satellite instrument derived estimates of the thermal structure of a lava flow within a single pixel (Pinkerton et al, 2002). Many previous studies have based assessments of this thermal structure on readings from point measurements obtained from radiometers at

various points across the surface of an active lava flow (Oppenheimer et al, 1993). Thermal camera imagery has the advantage that it can instantaneously map the thermal distribution across a lava flow at a single point in time. A lava flow has a dynamic thermal structure, with changes in the cooling rate, growth of a crust and the exposure of the incandescent interior coupled to such factors as local topography, effusion rate, weather conditions and lava rheology (Harris & Rowland, 2001). All these factors act on timescales ranging from seconds to hours with the net result of changing the character of the flow. These factors contribute to a highly changeable thermal structure which varies from the millimetre scale upwards to scales of tens of metres to kilometres for an entire flow. Single point measurements made with a radiometer will only offer a small insight into this thermal structure, whilst within the time needed to obtain similar measurements the dynamics of the lava flow may change.

Although undoubtedly useful, radiometer measurements of a lava flow's thermal structure fail to capture a "snapshot" of the whole flow at any one time. When modelling any space-based instrument's response to an active lava flow, we need to be able to identify as much of the thermal structure as possible and as quickly as possible, so as to mimic the satellite instrument's data acquisition rate.

In this section I will discuss the data obtained from the FLIR imagery and how and why synthetic FLIR data is used to assess the estimates returned from the dual-band method. I will also show how the thermal distribution found within a scene obtained from the FLIR camera can be summarised and used to define the properties of any surface within the IFOV of a single pixel value representing the surface.

4.5.Infrared Camera description and use on lava flows

The ground based thermal imagery used in this study was obtained using a FLIR Systems PM390 portable thermal imaging camera. This camera operates within the SWIR 3.4-5μm wavelength range. This range enables the camera to be sensitive to scenes with low temperatures from -10 to 450°C. For high temperature scenes it is possible to attach a 3.9μm 'flame' filter so as to extend the camera's range for such high temperature scenes as industrial blast furnaces. This additional filter is placed over the main lens and acts as a band-pass filter, and hence restricts the incoming radiative energy to a ~single wavelength. This extends the temperature range to ~1500°C. The thermal camera manages the entire temperature range of -60 to 1500°C by splitting into 4-5 separate ranges. These must be pre-selected for the temperatures likely to be encountered. Any temperatures recorded below the selected range will be assigned false and uncalibrated temperatures. For instance, recording imagery from an active lava channel on Mt Etna the highest temperature range of 750-1500°C would have to be selected to cope with the 1050-1070°C magmatic temperatures that may be encountered (Wright et al, 2001b). The 3.9μm flame-filter would be required to achieve this range. The camera provides an accuracy of +/- 2°C for each pixel temperature recorded.

The thermal imagery described here was kindly provided by Prof. Harry Pinkerton of Lancaster University, UK. This thermal imagery was obtained over 6 field excursions to Mt. Etna, Sicily: March 1999, May 1999, August 1999, October 1999, July 2000 and July 2001. There was a variety of volcanic activity present on all trips, including fire fountaining, crater overflows, a range of lava flows at differing levels of vigour, cooling stagnant lava flows and low temperature fumarole fields. Much of the imagery was obtained with the intent of studying various rheomorphic and physical characteristics of lava flows, and not initially with the intent of modelling and comparison with satellite data. Much of the imagery is therefore lacking definite scale. Also there are few distance

measurements from the flow targets and records of camera elevation angle, as would be preferred if this imagery was originally intended to be used for this style of study.

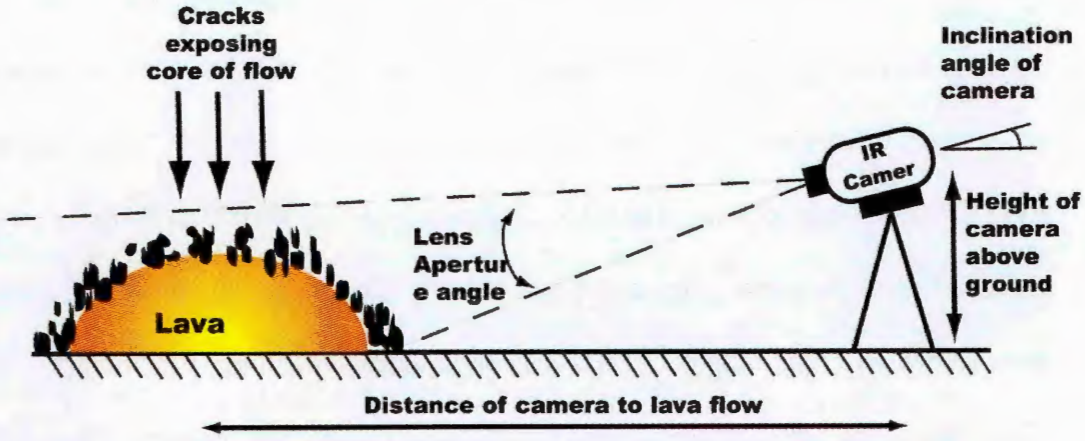

Figure 4.1: Schematic of typical camera orientation towards lava flow. Camera is often placed with the viewing plane aligned along the flow direction for channelised flows, so that the camera records a 'side' view. Typical other scenes may involve the camera looking up or down flow from the same vantage point, depending on local topography, which often tends to be extremely uneven.

The FLIR camera required that distinct temperature ranges be used depending on the temperatures likely to be encountered. Low temperature fumaroles, ambient ground studies and distant imagery of the summit crater complex from the lower slopes of Mt Etna required the selection of the -10 to 65°C range. Most of the imagery used in this study made use of the 750-1500°C temperature range. For active lava flows observed from 1km+, sometimes from the vantage point of a helicopter, the 250-450°C or 450-750°C temperature range is required to be selected. It is important to note that temperatures below the set temperature range are still recorded within the image data. Any temperatures below the prescribed range are deemed to be out of calibration, and hence unusable. This is especially the case when studying data of a lava flow using the 750-1500°C range. Temperatures as low as 230°C are recorded over the ambient ground, which is clearly inaccurate. This effect is recorded in the FLIR software which lists the minimum

temperature as <230°C. In such an image, only lava flow data within the range can be used.

Figure 4.1 shows a simple depiction of the typical camera orientation towards a lava flow under study.

4.6.Using FLIR imagery to analyse thermal distribution

It is possible to summarise the range of temperatures present upon a lava flow surface within the FLIR imagery by performing a simple statistical analysis on the number of temperature values present within a specific temperature range or "bin". This method of summarising the data is referred to as a probability density function (PDF) and is represented as a histogram (Drury, 1987).

The shape of a PDF histogram is highly informative of the contents of an image or region of interest (ROI) within the image. For histograms depicting pixels from an image covering a lava flow, such features as the amount of cool crust, areas at or near eruption temperature, ambient background temperature can all be identified. The relationship between these features within the histogram is also informative about the type of activity present. A peak of histogram columns within the temperature bin range of 800-1000°C indicates a large amount of molten material present within the image, and this can be identified as an active lava flow. If this peak dominates the entire histogram with no lower temperatures present in the 0-100°C bin range, then no ground surfaces at or near ambient temperature are present.

A clustering of columns forming a histogram peak within the bin range of 300-600°C decreasing towards the magmatic temperature bin range of 800-900°C suggests the presence of a significant amount of crusted lava present on the surface of the flow. Levees present on the boundary of a channelised flow may cause a similar cluster of temperature bins occupying a similar temperature range to that of the crust. The flow crust itself may

have a number of cracks revealing the molten core of the flow. These are indicated by a number of columns within the higher temperature range.

By analysing the relationships within the histogram it is possible to determine the extent of lava flow activity within an image. The histogram thus provides an excellent method of determining the thermal detail present within a FLIR image prior to the simulation of the ROI as a single PIT. I use the histogram in later sections to demonstrate the thermal distribution within simulated pixels supplied to the dual-band procedure.

An example of the use of histograms to indicate the thermal distribution within the FLIR image can be found within figure 4.4 on page 178.

4.6.1. Problems encountered when using ground based FLIR Imagery

Because of the near vertical (nadir) orientation of a satellite instrument with respect to the ground surface, any simulation using a ground based FLIR data of a satellite instrument would ideally also be obtained with a vertical orientation. This is especially the case when simulating an ALI pixel as the ALI has a narrow ground data swath of 75km (Bicknell et al, 1999). This means that even features at the extreme edge of this swath will be effectively almost directly under the instrument, due to the ALI orbital altitude of 702km (Bicknell et al, 1999).

Many FLIR scenes were obtained of active flows from vantage points that enabled viewing angles looking down onto the flows by as much as 30°. No scenes involving thermal imagery at or near nadir (90°) were available. This lack of scenes taken at nadir compounds a problem of viewing lava flows at low declination angles (0-45°). A'a flows often exhibit a relatively cool, highly rubbly surface possessing many cracks exposing the incandescent core (Lipman & Banks, 1987). A'a flows are common on Mt Etna. Many of the cracks in such an a'a flow often penetrate many tens of centimetres into the flow and

tend to be narrow and irregular. Viewing from even a relatively high angle, the base of the crack will be occluded by the foreground permitting only the crack wall to be observed. Thermal camera scenes taken at low declination angles provide an oblique side view of the flow, and so will not detect the true amount of flow core exposed through cracks in the rubbly crust. Channelised flows resulting from eruptions with high effusion rates often demonstrate a less rubbley surface, but one that is still broken by many cracks exposing the flow core (Cashman et al, 1999) The FLIR camera will therefore record only a disproportionately low level of radiative output from material at the base of the crack, and a disproportionately high amount of radiative output from material in the crack wall, cooler crust and even the background and atmosphere depending on the camera angle.

Because of the non-linear nature of the Planck relationship (Francis & Rothery, 2000), areas within the flow at higher temperatures will radiate more strongly than cooler areas. Therefore the thermal distribution within the FLIR imagery will be skewed towards high temperature areas within the foreground of an image, resulting in an inaccurate thermal distribution and hence introducing error into the analysis of the solutions returned from the dual-band procedure for modelled data based on such an image or ROI.

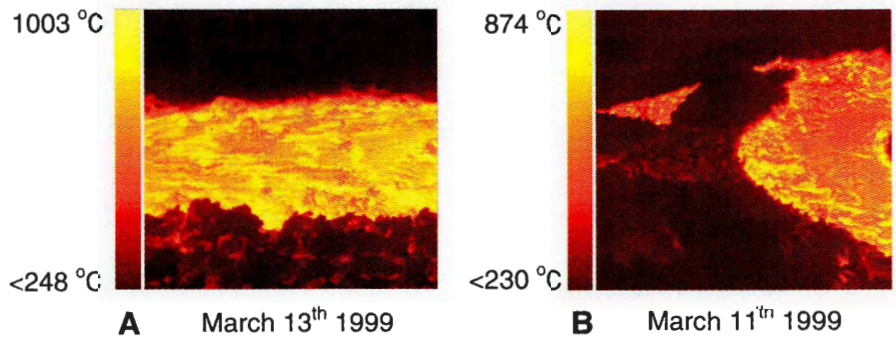

Figure 4.2: Example FLIR imagery. A: In this type of imagery the camera elevation angle is lower than that in B, and hence cannot view as effectively into the cracks within the lava flow crust. Image A records a higher maximum temperature than that in B as the flow in A is near the vent and a well developed crust has not yet developed. The flow in B is of a similar flow further from the vent, and a crust has had chance to form. Another factor on temperature is the distance of the camera to the flow. The camera is closer to the flow in A than in B. The further the camera is away, then the greater surface area covered by a single pixel will be, and as the pixel records the mean radiative temperature, the lower this value will be.

Figure 4.2 highlights these problems. The low elevation angle of the instrument with regards to the flow surface ensures that fractures within the flow crust are not fully exposed to the camera, and hence do not provide a full picture of the actual thermal distribution.

A second major problem encountered when using the raw FLIR data to simulate an instrument pixel is the range of temperatures found within each FLIR scene. In order to image such high temperature scenes such as lava flows on Mt Etna, the FLIR camera range has to be set to 700 to 1500°C with the use of the 3.9μm flame filter. Any values below the indicated minimum temperature of the range (<230°C), will be recorded as being at 230°C rather than the actual temperature. This effect results in cool ambient solar heated ground in the range of 0 to 100°C, depending on surface type and composition (sky, ice, scoria etc), being recorded as having significantly higher temperatures. In some cases FLIR imagery was obtained of the same scene of a lava flow, but within the lower temperature range of -10 to 65°C resulting with areas corresponding to the lava flow recorded as saturated. However these scenes do not correspond with useable scenes suitable for simulation as an ALI pixel. This scenario is commonly encountered during analysis of satellite imagery of lava flows. An ALI pixel is 30m x 30m and is likely to contain a fraction of cooler material associated with the flow levees or cool ground at the background ambient temperature even when imaging the most active flow fields. Lava flows are rarely >30m wide even on Mt Etna!! (Harris et al, 1998) Therefore it is likely that the IFOV of an ALI pixel will contain a range of temperatures associated with the surrounding ground as well as the diverse range of temperatures associated with cooling lava flows (Rothery et al, 1988).

A method must therefore be found that enables the full range of temperatures likely to be found within an ALI instrument pixel located over an active lava flow-field. In the

next section I shall describe the creation of synthetic FLIR data based on the histograms of temperatures present within a range of differing scenes of FLIR data.

4.7.Creation and use of synthetic thermal distributions based on FLIR imagery

In order to obtain the most accurate representation of such surfaces in order to test the response of the dual-band procedure I choose to use synthetic FLIR data. This will be based on the thermal distributions present within actual FLIR data of a variety of surfaces associated with active lava flows. By using synthetic data based on the FLIR data it will be possible to adjust such parameters as the temperature and activity associated with the histograms governing the lava flows, and to then assess how the dual-band procedure responds to these various models. In this section I describe how this is accomplished and "presented" as ALI data to the dual-band procedure.

4.8.Creation of synthetic image data based on FLIR imagery

I have described how the shape of a histogram describing the thermal distribution within an image can be related to a range of thermally diverse features found upon the surface of active lava flows. In this section I shall describe the creation and use of synthetic histogram curves based on the output from the FLIR imagery. The features and response of the synthetic histogram curve are then applied to an image of defined size. This method will be able to provide the entire range of scenarios with which to analyse the performance of the dual-band procedure in depth, and also to adjust such parameters as the relative activity of the flow and amount of flow core exposed. This synthetic FLIR imagery enables us to bypass many of the problems discussed in the previous section. This will enable the production of a synthetic image obtained at 'nadir', where we can discount

the effects of foreshortening and other optical and perspective problems incumbent with the use of low angle ground based imagery to simulate satellite imagery obtained at or near nadir.

4.9.Simple models for creation of synthetic FLIR data

In this section I shall describe the construction of synthetic images based upon modelled Histograms. These are themselves based on observations from FLIR imagery of various flows and image thermal compositions in the manner described within the previous section.

Relatively simple models of the thermal structure represented by a lava flow are easy to produce if one considers a lava flow as merely two thermal components in the manner of Crisp & Baloga (1990). In such a model the lava flow is represented with a cool component represented by temperature T_C occupying a fractional area P_C and a hot component T_H occupying area P_H. This cooler component representing the flows crust is interspersed by cracks exposing the inner core at T_H and fractional area P_H $(1\text{-}P_C)$ (Crisp & Baloga, 1990). This is the basic theory behind the dual-band procedure. A simple pixel representing this structure might contain a temperature, T_C of ~300°C occupying a fractional area of 0.9 (90%) and a T_H of 1000°C comprising the remaining 0.1 (10%) of the pixel. This approach completely ignores the wide thermal variation present upon the surface of a lava flow in the interests of producing a simplified model of the flow surface (Wright & Flynn, 2003), (Pinkerton et al, 2002). Such a model surface is represented as an 'image' and associated histogram within figure 4.3a. Such a two component model may also be used to describe a pixel whose contents contain a lava flow crossing cool ground. In this case the flow itself will be described wholly by P_H, and the cool background area by P_C. Unfortunately this also implies that a single temperature, T_H must represent the entire

lava flow thermal structure. The cool background (i.e. the ground surface) which is likely to be of a less thermally diverse nature is described by T_C. The histogram and P_H curve displayed for such a modelled pixel within figure 4.3a will of course not resemble in any manner the histograms representing an actual lava surface, such as those exhibited within figure 4.4 (p178).

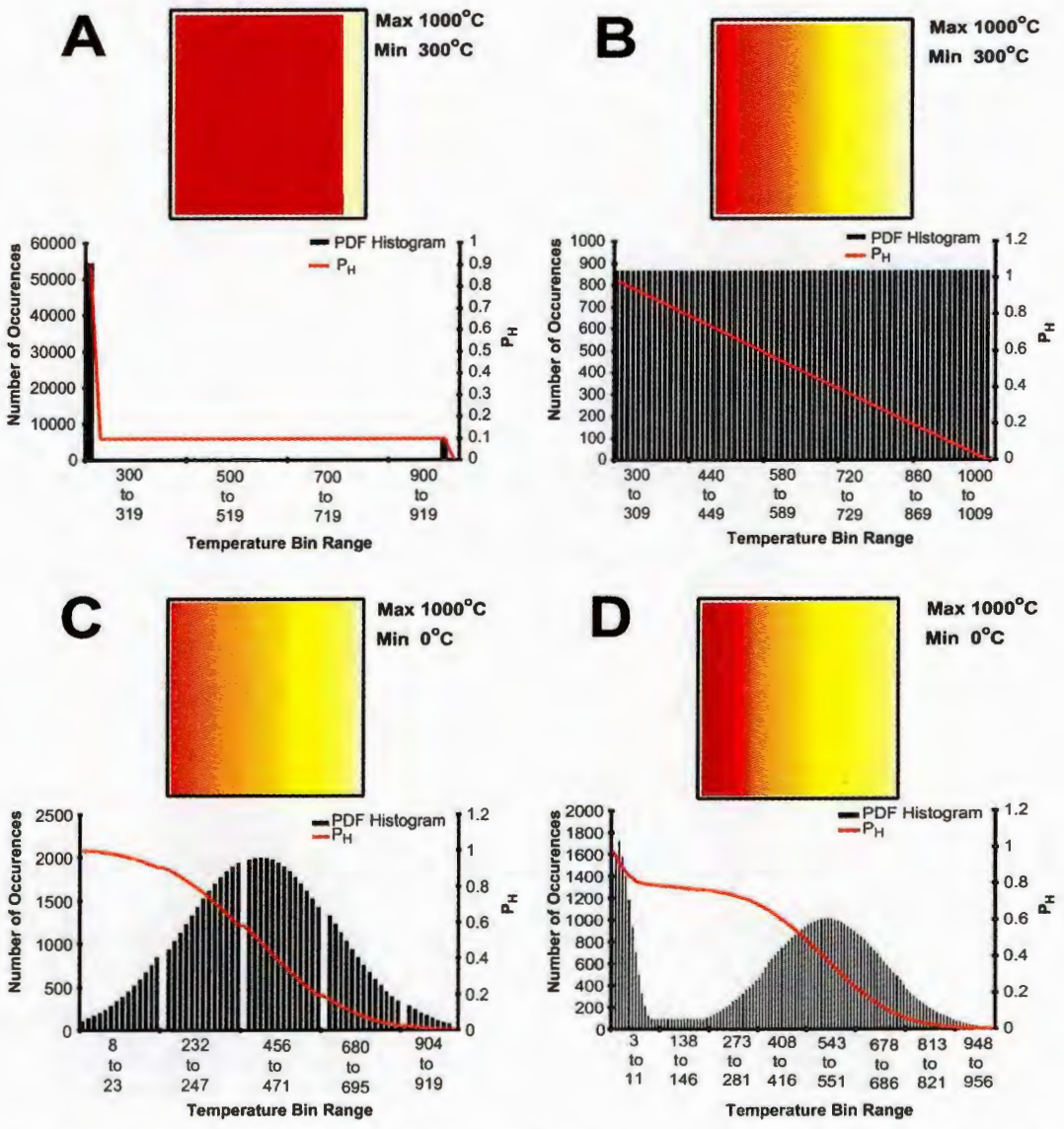

Figure 4.3: Development of synthetic data based on histograms from FLIR data of active lava flows. A: simple 2 component pixel model with 90% at TC and 10% at TH. B: Pixel model with continuum of temperatures from TC to TH with all intermediate values occupying equal area. C: Pixel model based on bell shaped curve thermal distribution of pixels from FLIR imagery obtained solely from a lava flow. D: Addition of 2 bell shaped curves simulates bimodal thermal distribution observed within FLIR data of lava flows crossing cooler ground or incorporating cooler material.

An alternative procedure to obtain a more realistic thermal distribution is to model an image whose thermal structure mirrors the wide continuum of temperatures encountered upon the surface of a lava flow. This may be done by producing a series of equal fractional areas each occupied by a single temperature. Rather than being restricted to just 2 components, P_H and P_C at their respective temperatures T_H and T_C, we may use P_1, P_2....P_n, with the sum of these fractional areas equal to 1. Each of these fractional areas will be at their respective temperatures of T_1, T_2....T_N. For example, if a simulated pixel requires a minimum temperature of ~300°C representing cooler flow crust or levee material and a maximum temperature of ~1000°C representing the core material temperature, then a finite series of fractional areas, i.e. 1000 may be used to calculate the intermediate temperatures. If we use an image array of equal size to the original FLIR imagery of 255 x 239 pixels, giving a total of 60945 pixels, then each of the fractional areas describing in part the thermal variation will occupy ~60 pixels, or a fractional area of 0.001, each separated by a temperature increment of (1000°C-300°C)/1000 = 0.7°C. This is equivalent to fractional areas P_1, P_2 .....P_{1000}. Each of these individual fractional areas will be occupied by a unique temperature T_1 = 300°C, T_2 = 300.7°C, T_3 = 301.4°C .....T_{999} = 999.3°C and finally T_{1000} = 1000°C. Figure 4.3b visualises such a synthetic image comprised of equal areas representing a wide thermal continuum.

Although such a synthetic image mirrors the wide thermal distribution encountered upon the surface of an actual flow, the nature of this distribution is far too ordered as indicated by the histogram within figure 4.3b. This absolutely level histogram with each temperature bin displaying consistent values bears no relationship to those histograms returned from an actual lava flow in the FLIR imagery such as those within figure 4.4 (p178). Pixel models such these are a simple, but flawed method of testing the dual-band method. Therefore a more accurate method of replicating the thermal distribution described within the FLIR imagery is required for full and accurate application to the dual-band procedure.

4.10. Construction of accurate synthetic imagery based on FLIR imagery

In this section I shall show how the shape of a histogram defining the thermal distribution can be used to infer the type of flow activity within a scene. I shall then show how this can be utilised to create accurate synthetic data. Figure 4.4 shows a selection of FLIR images of lava flows on Mt Etna and the associated histograms extracted from the surface of the flows.

Figure 4.4a depicts a flow with a well developed clinkery crust. There is a wide thermal distribution here spanning the crust as well as the incandescent interior, and this distribution is reflected within the histogram which is very similar to that of the flow with well developed crust in figure 4.6 discussed briefly above. Extracts from subsequent scenes in figure 4.4b to figure 4.4d describe increasingly active flows in terms of amounts of crust possessed by the flow, but also the range of temperatures present.

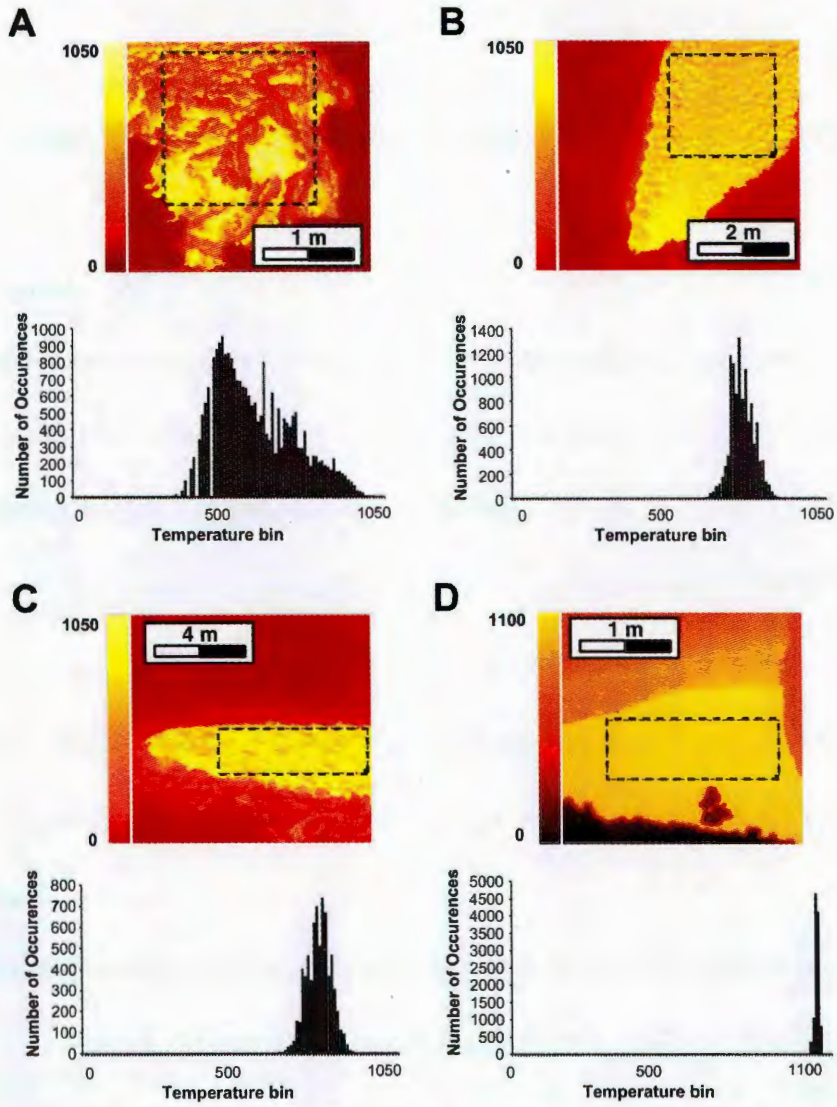

Figure 4.4: Comparison of Histogram for various types of lava flow in differing circumstances. Dashed rectangle describes the area selected for each extract (ROI) and highlighted within each histogram. Note that the ROIs are of differing dimensions, and hence the number of pixels possessed by the ROI will be reflected within the numbers available for each bin. Also note that the scale of each feature within each image varies. Hence a direct comparison of numbers of pixels within each histogram for the various flows here is not adviseable. A: Lava flow with well developed clinkery crust. B: Lava flow within several metres of vent. C: Lava flow issuing from vent at left. D: View of flow through skylight. Please note that the bin size in D is different to the preceding 3 examples due to the large number of high temperature pixels.

Figure 4.4b depicts a flow downstream by several metres from the vent, figure 4.4c a flow immediately proximal to the vent and figure 4.4d a flow imaged through a skylight. The imagery shown here varies in scale from the close-up view of the clinkery flow front within figure 4.4a to the proximal vent flow within figure 4.4c. This series of images aims

to highlight the variation in thermal structure associated with several types of lava flow type irrespective of scale. In each of these histograms describing the thermal distribution, the peak of the histogram shifts towards increasingly higher temperatures. In addition to this, the shape of the curve forming the histogram also changes.

With the procession towards ever lower amounts of cooler crust and increasing amounts of exposed core with resulting high temperatures the curves become narrower and higher. This is due to a restriction of the thermal range within each flow imaged, as the thermal continuum encountered trends towards the homogenous magmatic temperature. The curve becomes higher in terms of the number of pixels within each bin because the restriction within the thermal range concentrates the available number of pixels within progressively fewer temperature bins within the histogram, resulting in a higher histogram curve.

This change in form of the curve represented within the histograms is not restricted to extracts containing thermal information solely for lava flows. Extracts with boundaries that encompass cooler material such as levees or cool background in the manner of that displayed within figure 4.6 (p189) will also exhibit the above tendencies for the lava flow in addition to a histogram curve describing the distribution of the cool material. This results in a histogram possessing a bimodal temperature distribution such as that shown in figure 4.6 (p189). The shape of the histogram curve describing the temperature distribution of the cooler material will also be governed by the same principles defining the shape of the curve restricted to purely lava flow temperatures. Increasingly narrower and taller curves describe an increasing restriction of the temperature distribution, irrespective of the temperatures involved. The location of the curve respective to the x-axis and the temperature bins for the histogram, simply identifies the actual temperature range involved and hence the likely lava flow surface type (i.e. crust or cracks) of the flow. A bimodal thermal distribution such as that highlighted within figure 4.6 (p189) that describes a

channelised lava flow combined with cooler bounding levees, may be considered as two separate curves, one for each main thermal component.

This progression in the form of the histogram curve with changing surface type is what may be used when creating synthetic FLIR imagery from modelled histograms to create a range of synthetic flow types. Adjustment of the parameters comprising an equation that mathematically describes a curve of this nature will effectively adjust the properties within the synthetic FLIR image.

The thermal distributions that we shown from the FLIR imagery describing lava flows are similar to the bell-shaped curves describing a Gaussian probability distribution. A Gaussian distribution, also known as the normal distribution (Waltham, 1995), describes the relationship between the mean value, the standard deviation within a data series and the probability of a value occurring within a specified range. If this distribution of values within a data series is normally distributed about the mean value, then the curve described by the probability function will be a bell shaped curve, or a Gaussian distribution (Waltham, 1995). I shall show in the next section how by creating and manipulating a bell shaped curve it is possible to "create" a temperature distribution, which can then be applied to a simulated thermal scene of greater accuracy than the simple models shown within section 4.9.

4.11. Construction of an artificial scene based on a synthetic histogram curve

The equation that defines a bell shaped curve is given as:

$$f(x) = (1/(\sigma\sqrt{2\pi})) * e^{-(x-\mu)^2 2\sigma^2} \qquad \text{(Equation 4.1)}$$

Where σ is the standard deviation of the dataset, μ is the mean value within the dataset and x designates the position along the x axis. By adjusting the values representing the standard deviation or the spread of the curve and the mean value of the data we can adjust a synthetic histogram curve to simulate a typical thermal distribution found within the FLIR data. In this way we use the standard deviation to control the spread or thickness and height of the returned curve and the mean value to control the position of the curve with respect to the x-axis. By controlling the thickness of the curve we are simulating the spread of the curve and hence the range of temperatures involved within the synthetic thermal distribution. By adjusting the height of the curve we control the number of values associated with the mean temperature.

The modelled image must be of a known dimension. Here I choose to use to the 255 x 239 pixel array the same as that used by the FLIR imagery, and therefore the number of pixels within the synthetic image will be 60945. By controlling the height of the bin representing the mean value within the artificial histogram we are controlling the mean temperature present within the synthetic image. This will be related to the thermal distribution and hence the width of the curve, and hence adjustment of the standard deviation within equation 4.1.

The mean temperature of the curve can be chosen positioning the synthetic curve within a specified range. For example if a mean temperature within the region of 500 to 600°C is selected then we are simulating a lava flow with a relatively well developed crust. By adjusting the overall height of the curve and the rate of drop off either side of the mean value we are controlling the amount of pixels in the higher temperature range. Adjustment of the spread of the curve in conjunction with the position of the mean value allows the number of pixels representing cracks exposing the simulated flows core through the crust indicated by the peak value. In this way it is possible to simulate flows of differing levels of activity, such as those within figure 4.4 (p178).

A single bell shaped curve can be used to describe the range of values solely related with the surface of a lava flow. As indicated within the FLIR data and discussed previously, many thermal distributions accurately describing a volcanic surface display a bimodal distribution. This may also be accomplished by modelling 2 curves and then joining them within the relative temperature bin region. The spread and number of pixels allocated within each synthetic bin will control the relative proportions of the artificial scene. For a synthetic scene in which a lava flow crosses cool ground, the spread of the curve describing the flow will be greater due to the wider range of temperatures involved, whereas the curve describing the cool background will be narrower due to the restricted range of temperatures (0 to 50°C) encountered here. The relative heights of the curves will depend on the required fraction of the artificial scene allocated to each surface type. Where two curves are used to describe the thermal distribution within a scene these curves may be joined by the overlap between the two curves, or by a set value describing the number of pixels within the saddle region between the two curves.

In the case where the 2 curves of the bimodal distribution are widely separated thermally, such as in the case of a lava flow crossing cool ground, the provision of the ability to define the number of pixels within this saddle region is important. Observations of FLIR imagery depicting such instances identify the existence of low numbers of pixels connecting the two curves. This may be due to a combination of radiant and conductive heating of the ground in the immediate vicinity of the flow as well as low amounts of chilled crust that have come in contact with the cool ground, and therefore approaching the temperatures associated with cool ground.

These considerations are all taken into account when simulating a FLIR scene. The ability to fully define the temperature range within a single image is not possible with the actual FLIR data due to the nature of the camera and the requirement to select distinct temperature ranges dependant on the nature of the scene under study. Figure 4.3c & d

(p175) highlight the output of a single modelled histogram representing an active lava flow and an active flow crossing a cool ground surface respectively.

The synthetic image is created by importing the finalised curve from the original Microsoft Excel ® file used to create the synthetic curve into a program written and compiled in the Research Systems IDL ® language. This IDL program interprets the imported curve and calculates the series of temperature bins based on the temperature range present within the imported curve. The total of 60945 pixels resulting from the 255 x 239 pixel array used are then used to calculate the number of pixels assigned within each temperature bin, depending on the value of the curve within that bin value. The program then writes the required number of pixels to a file which is then output as a separate image file.

This file is in the form of an ASCII tab delimited text file comprised of an array of temperature values, identical in nature to the processed FLIR temperature output files. As the output of this IDL program is identical in nature to that of the FLIR data, this synthetic output imagery can then be processed within the dual-band programs also written in IDL and applied to the FLIR data described previously. The actual creation of the synthetic histogram curves within MS Excel and the subsequent creation of an image based upon this curve in the IDL programming language are fully detailed within Appendix 3.

Simulated FLIR scenes are compared against actual FLIR scenes within section 4.6.

4.12. Converting synthetic pixel to simulate ALI imagery

In this section I shall describe how once a simulated scene has been finalised as a temperature map of similar dimensions to the original FLIR scene, it can be modelled as a single pixel of ALI data.

Any pixel of actual ALI data is represented by a single DN number which is scaled to the amount of radiance detected within the respective ground area subtended by the pixel (Mendenhall et al, 1999). Within this area, temperatures can vary widely, especially if such a feature as a lava flow is present. A single pixel DN represents the integral of all radiances emitted within the area occupied by a single pixel (Wright et al 2001b). This single radiance value can be back calculated to temperature, dependant on wavelength using equation 1.4 (Rothery et al, 1988). This value is referred to as the Pixel Integrated Temperature (PIT). Due to the Planck relationship that links emitted radiance, temperature and spectral wavelength, the integral radiance representing a single pixel at the various SWIR wavelengths occupied by ALI channels will vary with wavelength. Hence the actual PIT will also vary with wavelength.

This effect is highlighted within figure 4.5 which displays the relationship between the emitted radiance present at the wavelengths occupied by the ALI SWIR channels and the portion of a simple pixel model occupied by molten material at ~ 800°C (T_H). In all channels, as the occupying fraction of hot material, P_H increases towards 1, the radiance increases. Table 4.1 (p164) summarises the various channels and surface temperature range to which both instruments are sensitive to. Those channels situated at longer wavelengths, such as channels 5 & 7 are more sensitive to even small areas of the hot component and soon saturate. Shorter wavelength channels such as channel 4 in both instruments are less sensitive to increasing P_H and barely register. Figure 4.5 does not show the minimum radiance level to which each channel is sensitive. Channels placed at shorter wavelengths within the SWIR such as channel 4 (both instruments) will be barely sensitive to a surface such as that described in Figure 4.5 due to the nature of the Planck relationship, and hence the lack of response compared to channels situated at longer wavelengths within the SWIR.

Once a simulated image array has been finalised it is possible to convert it into a PIT value at each of the ALI channel wavelengths by calculating the radiance for each temperature within the array, and then calculating the integral radiance from the total number of values present. This can then be converted into temperature using equation 1.4, resulting in a basic PIT value for each of the channel radiances. We used the central wavelength value for each channel for those channels we chose to model when simulating an instrument PIT. The single integral radiance values resulting from this process can then be compensated for the simulated effects of atmospheric transmissivity and emissivity of the lava.

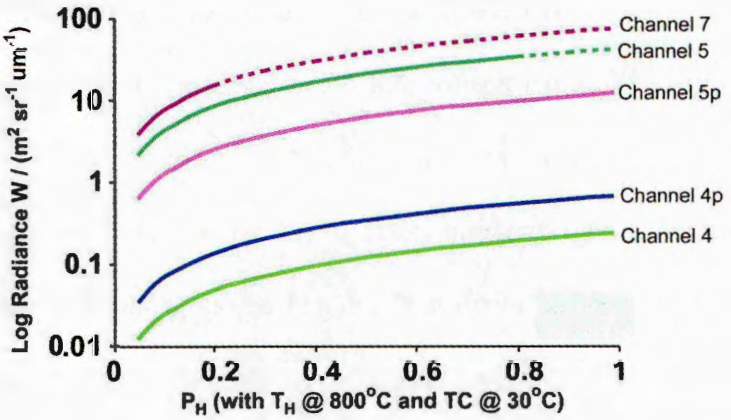

Figure 4.5: Response of a ALI pixel to a surface with a varying proportion of material at 800°C exposed. The remaining fraction of the pixel is set at 30°C. The lines for each SWIR instrument channel show the increase in radiance emitted as the portion of the hot pixel component increases. Dotted lines indicate where the channel in question has saturated.

The Planck equation assumes that the emitter is a perfect blackbody, and that all radiance is emitted into an infinite cone. However, due to the non-blackbody nature of the surface of a lava, we use a value for the emissivity, ε . The emissivity is effectively the efficiency at which the lava surface is radiating. A blackbody has an emissivity of 1. In this study we use an ε value of 0.95 to represent the emissivity of an Etnaean basalt (Harris & Rowland, 2001), and correct for the solid angle by using π within equation 1.1. This solid angle correction corrects for the actual amount of detected radiance along a single

radiance from the total radiance emitted from all surfaces within the simulated pixel IFOV propagating outwards in all directions. In this manner we can relate any lava surface within the FLIR imagery to the incoming radiance detected by any satellite instrument.

The final integral radiance values can then be supplied to the IDL algorithm that calculates dual-band solutions between various channel combinations.

4.12.1. Effect of ALI instrument characteristics on use and interpretation of simulated ALI data

There is a range of ALI SWIR channel combinations available for input into the dual-band procedure. We must ensure that the calculated integral radiances representing the scene at each ALI channel wavelength must fall within the published dynamic ranges of the ALI instrument. The dynamic range of a channel can be defined as the radiance range to which the channel is sensitive (Donegan & Flynn, 2004). This is comprised of both a minimum radiance level below which the channel will not register information and a maximum radiance, over which the channel will be saturated and no meaningful information is recorded. The integrated radiance value calculated for a simulated scene at a certain ALI channel wavelength must fall within that channels dynamic range. If it fails to fall within these ranges (table.4.1 page 164), despite any returned solutions, then any solution using these radiance values must be discounted as inaccurate. As we are attempting to assess the performance of the dual-band procedure using simulated scenes and how they appear within ALI instrument data, then we must comply with the limitations of actual ALI data.

4.13. Correction for solar component of temperature within FLIR and satellite imagery used

Another factor to consider when using the FLIR imagery to simulate the response of any satellite instrument is the contribution of reflected and scattered radiation due to sunlight (Wooster & Kaneko, 2002). Lava flows will emit strongly within the SWIR due to their own heat derived from the original magmatic source (Rothery et al, 1988). However, for those FLIR scenes obtained during daylight hours we must take into account the contribution of solar radiance scattered or reflected into the FLIR image. Although the peak radiative output from the Sun is situated within the visible region of the spectrum, a certain amount of radiance is still emitted within the SWIR as predicted by the Planck function (Francis & Rothery, 2000). This radiance can be corrected for in a similar manner to the corrections performed on satellite data for extracting daytime thermal data on lava flows (Wooster & Kaneko, 2001).

One method to perform this correction is to simply subtract the known radiance in each channel associated with a surface not associated with the lava flow, and at ambient temperature (Oppenheimer, 1993). In this study I use a mean value obtained from FLIR imagery of various features such as the immediate foreground, or areas obviously unrelated to any flow activity to provide an indication of the ambient background temperature. The FLIR camera -10 to 65°C temperature range was used to accomplish this. This temperature is then converted to a radiance value at the various channel wavelengths to be modelled, and then subtracted from the final modelled PIT at the respective wavelength. The satellite imagery was corrected using the "per-pixel" method described by Wooster & Kaneko (2001) and covered in more detail in chapter 6.

4.13.1. Correction for atmospheric absorption of modelled PIT when compared to actual satellite data.

A final factor to consider when creating a simulated satellite pixel PIT in ground based FLIR data is to compensate for the signal attenuation due to atmospheric absorption and scattering of the incoming signal at the satellite instrument (Oppenheimer, 1993). If we are to arrive at comparable PIT values derived from the FLIR data with satellite values a correction must be made for atmospheric attenuation (τ). The wavelengths at which channels from such instruments as ETM+ and ALI are placed for observation of surface based phenomena, are situated within atmospheric 'windows' (Mendenhall et al,1999). These windows are regions within the spectrum in which absorption by the various atmospheric constituents is at a relative minimum (Lillesand & Kiefer, 1994). MODTRAN atmospheric modelling software enables an estimate of the overall signal attenuation at various wavelengths, conditions and global position. A simple model run was performed to establish a figure that we could attenuate the simulated PIT by. A value of $\tau = 0.95$ was used within the simulations.

4.14. Comparison of simulated FLIR data with actual FLIR data

Before applying the dual band procedure to various types of synthetic FLIR imagery it is necessary to compare the two types of data to verify the accuracy of the synthetic FLIR imagery. I shall do this by producing simulated scenes based on an original FLIR scene, and comparing the results obtained from the dual-band procedure for both scenes. This shall be accomplished for both a basic "unimodal" scene and a "bimodal" scene.

4.14.1. A note on the visual representation of synthetic FLIR imagery

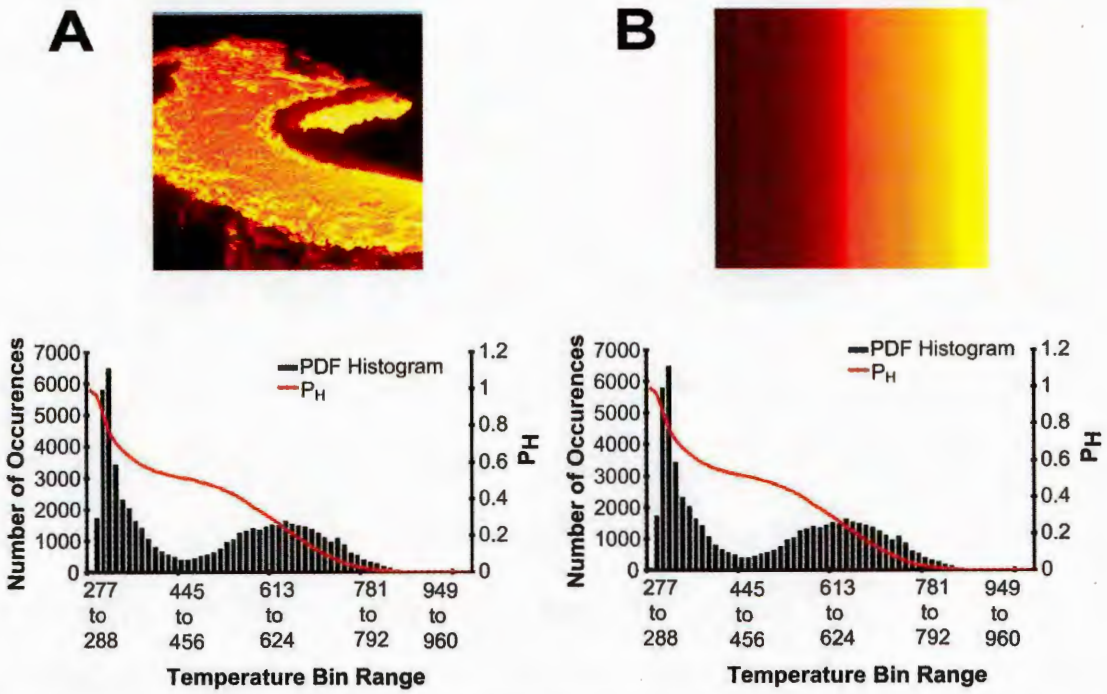

Figure 4.6 Original FLIR data from March 10th 1999 (A) and resorted image (B). Both display the same histogram, and therefore same thermal distribution.

Figure 4.6a displays a typical FLIR scene of an active lava flow. Figure.4.6b displays exactly the same thermal image data as the FLIR scene as that in fig4.6a, but the pixels have been sorted into ascending numerical order and reinserted into a pixel array of the same dimensions as the original image. This graded image is visually very similar to the output of the synthetic FLIR scenes constructed from modelled histograms based on those from original FLIR scenes. The imagery used within this chapter to visually depict the synthetic thermal distribution bears in no way any visual resemblance to the visible structure within the actual original FLIR scene. The thermal distribution is represented by the histogram, rather than the visual structure of the original FLIR scene, such as the lava flow crossing cooler ground within figure 4.6a.

The two scenes may not at all be visually comparable, but the thermal distribution and therefore the final single PIT representing them is identical. The histograms for each

image within figure 4.6a & b are identical, as the thermal distribution is identical despite neither image bearing any visual resemblance to each other. Hence although the simulated FLIR scenes described within this chapter may bear no visual structural resemblance to the original FLIR scene, the thermal distribution closely resembles reality.

4.15. Comparison of a simple asymmetric unimodal scene

Figure 4.7a displays an extract of a FLIR scene from the centre of an active channelised lava flow. The histogram describing the thermal distribution within this extract displays a single asymmetric curve. The synthetic histogram within figure 4.7b was created by the amalgamation of two separate bell-shaped curves to create a similar histogram curve as that displayed in figure 4.7a. An approximation of the curve is the main requirement in the creation of the simulated FLIR imagery in order to capture the overall thermal distribution. It would be hard (and unnecessary) to reproduce exactly the 'noisy' curve describing the thermal distribution from the original FLIR extract within fig4.7a. It is likely that these spikes within the histogram are due to a combination of factors associated with the cooling of the flow crust such as fluctuations within the effusion rate, the rate at which the crust is entrained back into the core as the flow advances and even the rate of cooling due to wind flowing across the active lava flow (Harris & Rowland, 2001).

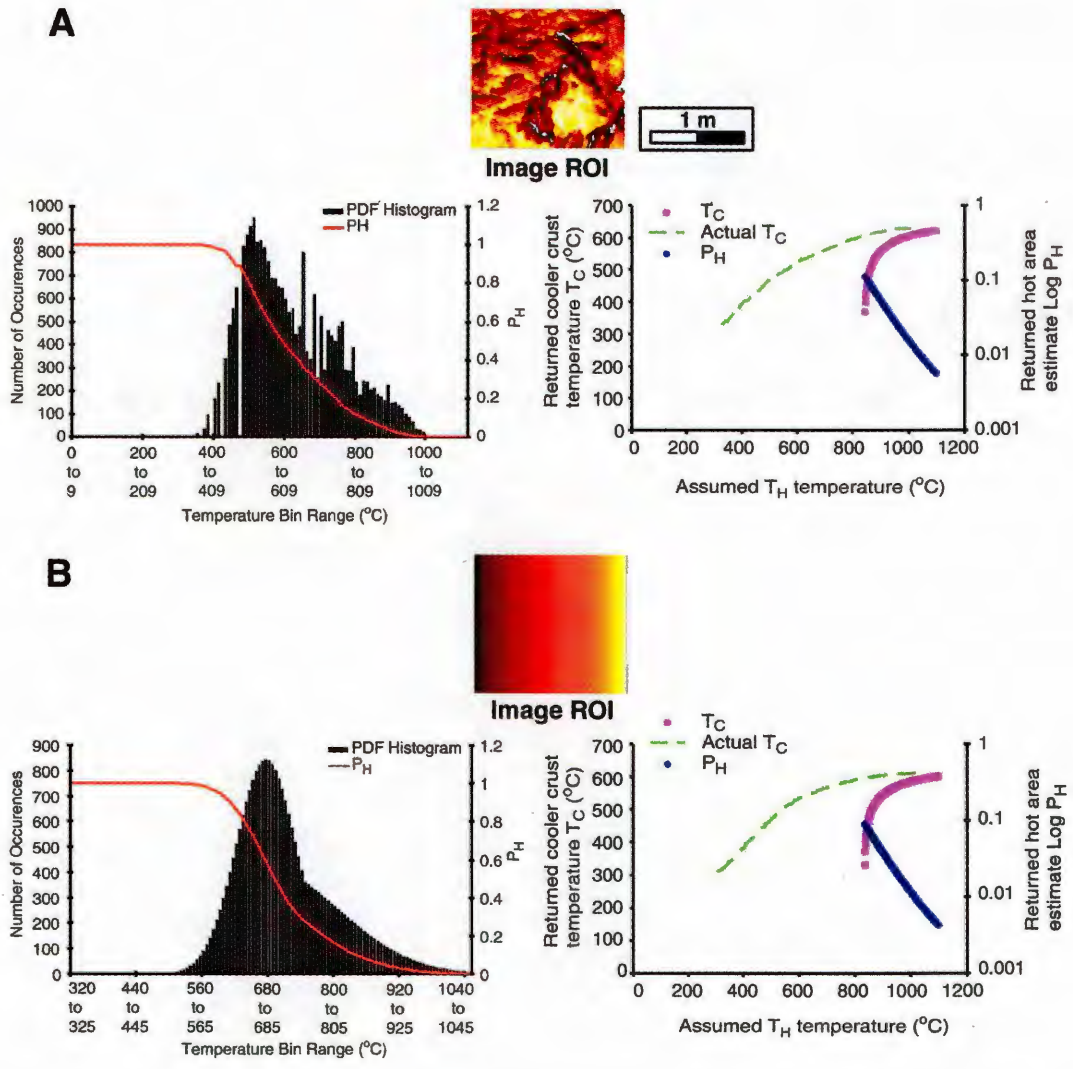

Figure 4.7: Comparison of FLIR data (A) with synthetic FLIR data based on modelled histogram (B). Note that temperature bins chosen within the histograms are indicative of temperature range

In imagery of small scale features such as this, these effects will be concentrated and therefore more noticeable within the histogram. If the selected ROI was of a greater area then subsequently a smoother distribution within the histogram curve will be returned due to the larger area and greater number of pixels. This image is used here merely to highlight the effect of asymmetric thermal distribution within a single ROI.

The attendant dual-band solutions obtained from the imagery shown within figure 4.7 are obtained by using various values of T_H (x-axis) to determine the pattern of solutions in terms of P_H and T_C. The actual value for T_C has also been extracted at each value of T_H used within each solution. This allows a comparison to be made between the actual

temperature of the entire area represented by the cooler component of the model and the estimated temperature returned by the procedure. These graphs also show how the returned estimates of P_H and T_C change with each value of T_H supplied to the procedure. How these estimates relate to the actual values from the various models is discussed within section 4.8.

The close agreement between the two graphs within figure 4.7a & b suggests that this method of producing an artificial FLIR scene from a simulated histogram curve is viable. These dual-band solutions are available at the outset from the same values of T_H used, return very similar (+/- 5 to 10°C) values for T_C and also return very close estimates for P_H. The actual values calculated for T_C from the initial imagery used also compare extremely favourably. This shows that by simply merging two bell-shaped curves, the thermal structure within a simulated FLIR image of a lava flow comprised of a cooler crust interspersed with cracks exposing warmer core material can be modelled successfully and accurately.

4.16. Comparison of a simple bimodal scene

Results of a similar comparison can be found in figure 4.8a & b, in which a surface with greater thermal diversity has been modelled. Figure 4.8a displays a ROI extracted from the FLIR imagery from the same active lava flow within figure 4.4c. In this instance the ROI includes hot material from the flow proximal to the vent and additional cooler material associated with the bounding levees of this flow. This thermal structure produces a bimodal histogram. The FLIR histogram within figure 4.8a has been reproduced as a synthetic histogram in figure 4.8b also by the amalgamation of two separate bell-shaped curves. In this case the two curves are separated by a saddle region representing pixels

produced by the cooling of material from the flow accreting to the levees and producing a chilled crust.

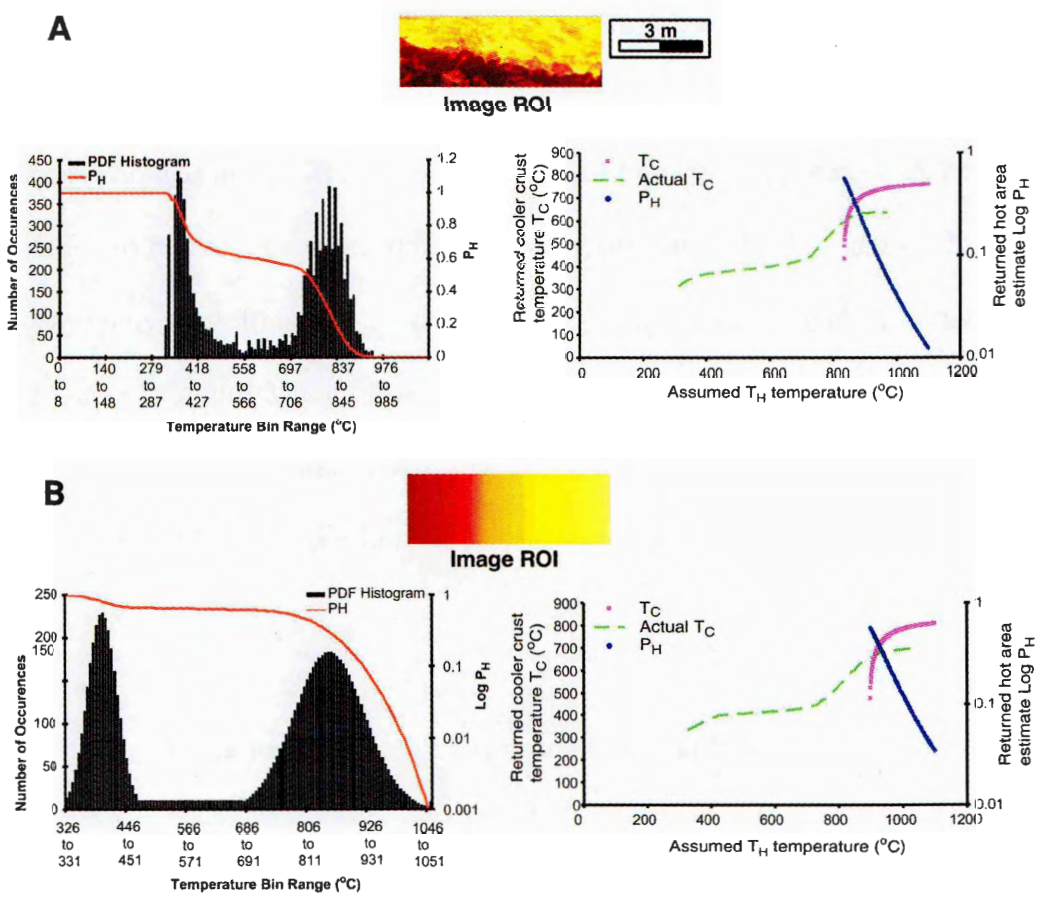

Figure 4.8: Comparison of FLIR data for a bimodal surface temperature distribution (A) with synthetic FLIR data based on modelled histogram (B). Note that temperature bins chosen within the histograms are indicative of temperature range.

Dual-band solutions become available from the same T_H value in both datasets. Almost identical values for P_H and T_C are returned for each value of T_H used. The returned estimates of P_H and T_C from the simulated imagery match those estimates returned from the selected region within the actual FLIR imagery. The pattern of results with changing T_H value is also closely reproduced. The kinked curve depicting the actual values of T_C obtained from the imagery itself is present within both diagrams. This appearance is due to the bimodal thermal distribution. It is clear that the accurate simulation of an actual FLIR

scene possessing a bimodal thermal distribution is possible with the use the two bell-shaped curves representing the individual thermal components.

The close similarities between actual FLIR data of both types of thermal distribution and the simulated scenes indicate it is therefore possible to expand the use of the production of accurate synthetic FLIR scenes over lava flows. In section 4.8 I shall use a variety of synthetic FLIR scenes incorporating temperature ranges and distributions not possible within a single FLIR scene to investigate the response of dual-band procedure. I will compare the resulting estimates of P_H and T_C with actual values obtained from the imagery itself. However, in order to do this I will first describe which bands of ALI data I choose to model, as this is important to the accurate interpretation of dual-band results.

4.17. Choosing a suitable dual-band channel combination for analysis of synthetic FLIR scenes

A series of dual-band solutions using various ALI channel combinations are shown in figure 4.9. These solutions involve a single integrated radiance value calculated for a histogram lava flow model displayed within figure 4.10j (p205). This particular model simulates the largest area of exposed core material of the 10 model runs within figure 4.10. A full description of the reasoning behind the creation of this particular model is given within section 4.8.1 (p204). The single values for each ALI channel were obtained in the manner described within section 4.5.5 by calculating the integrated radiances of all pixels within the synthetic images at the ALI channel wavelengths.

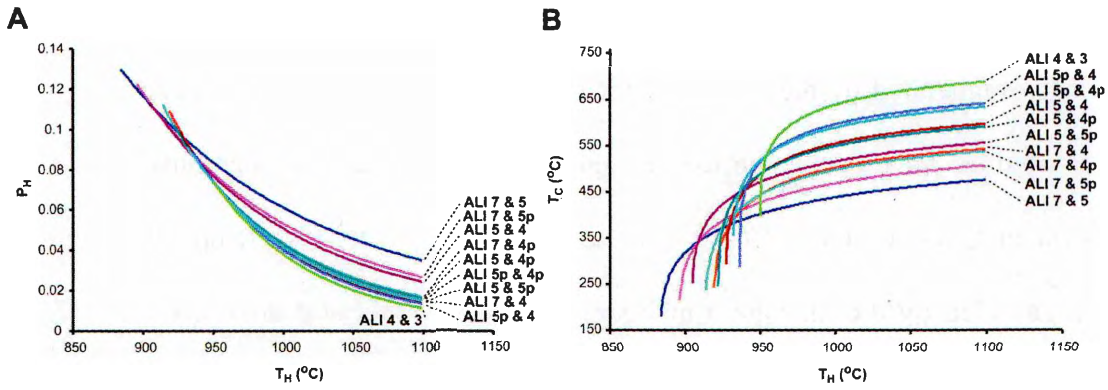

Figure 4.9: Dual-band solutions for a synthetic FLIR image (refer to figure 4.10J). All available channels combinations are used here to demonstrate variation in returned PH and TC values at progressive values of TH supplied to the procedure.

It is necessary to determine which ALI channel combinations provide the most accurate estimates of P_H and T_C for consistent use within the following discussion. Figure 4.9 depicts the dual-band solutions for a range of T_H values supplied to the procedure. These range from ~200°C to 1100°C. Figure 4.9 and subsequent figures highlighting the returned solutions for P_H and T_C are plotted in a similar fashion in order to analyse the variation in solutions for any reasonable assumed T_H value. As highlighted within section 4.2 (p163) the selection of T_H is important, and by plotting the dual-band solutions in this manner we can chart the variation in returned solutions for a range of assumed temperatures for a variety of modelled surfaces.

4.17.1. Analysis of returned values for P_H in the various ALI channel combinations

It might be expected that all channel combinations supplied to the dual-band procedure will return similar results for the same input scene. But because the calculated radiance for each channel based on the temperatures within each simulated scene will be different as a consequence of the Planck relationship, then disparities between differing

channel combinations supplied to the dual-band procedure will become apparent. This effect is exaggerated by the differing dynamic ranges of the various ALI channels. Dual-band solutions have been returned in which certain channel combinations where one or both channels are at or very near to saturation. The relatively high temperature simulated scene provided by the histogram in figure 4.10j easily saturates channels 5 and 7. It is apparent from figure 4.9a that channel combinations with at least one of these channels provide solutions for P_H that are consistently higher than those combinations involving unsaturated channels such as 4, 4p and 5p. Those combinations which involve both channels that remain unsaturated and fall within the dynamic range of the particular channel provide consistently close values for P_H over the range of T_H values supplied to the procedure.

A channel combination involving channels 7 & 4 appears to provide solutions consistent with the unsaturated channel combinations. However, the calculated integrated radiance at the channel 4 wavelength is only barely sufficient to register within the actual channel 4 dynamic range. Any scene that is of high enough temperature to register within the channel 4 dynamic range will in reality saturate channel 7 (Wright et al, 2001b). It is due to a quirk of the dual-band processing method that a solution is registered within this channel combination, primarily due to the 'excess' radiance within channel 7, countered by the barely sufficient radiance calculated for channel 4. There is also a series of solutions provided by the channel 4 & 3 combination. As the integrated radiance at the channel 4 wavelength is barely sufficient to register within the channel 4 dynamic range, then the integrated radiance at the channel 3 wavelength will be unlikely to register within the channel 3 dynamic range. Solutions using this channel combination are consistently lower than those solutions using combinations of unsaturated channels.

Solutions using combinations of channels 7 & 4 and 4 & 3, as well as those involving channel 5 must therefore be discounted because of these problems where the

input radiances fall outside of the dynamic range of the channel. Situations such as this must be taken into account when using results from the dual-band method. Solutions for P_H involving unsaturated channels are consistently close to each other throughout the range of assumed T_H values supplied to the procedure. It is from these channels that a suitable channel combination must be sought.

4.17.2. Analysis of returned values for T_C in the various ALI channel combinations

Figure 4.9b displays the dual-band solutions for T_C obtained in conjunction with those solutions for P_H within figure 4.9a. There is a much greater variation between T_C temperatures returned for each T_H input value than between the associated solutions for P_H. Those channels involving longer wavelengths provide solutions for T_C over a wider range of supplied T_H values and result in a lower overall range of resulting T_C temperatures for a given input of T_H. This might be expected as channel combinations involving channels at longer wavelengths (7 & 5) will be more sensitive to lower temperatures, than those channels situated at shorter wavelengths (3,4,4p, & 5p).

There is no indication within this set of returned T_C values of which particular channel combinations involve radiance values outside of the dynamic ranges of the channels involved, in the manner of the solutions involving P_H. Each returned T_C value may be considered as the mean temperature of all the thermal components comprising the fractional area P_C, or $1-P_H$. It is clear from consultation of the histogram within figure 4.10j that solutions providing estimates of T_C in the range of 180°C to 500°C using channels 7 & 5, are substantially underestimating the true value of T_C. These channels provide a P_C solution of 0.88 to 0.96 (792 to 864m^2 of a 900m^2 pixel), and these solutions imply that the greater area within the synthetic FLIR scene must therefore be within the temperature range of 180°C to 500°C.

This is nonsense, as the minimum temperature within the synthetic scene is in the region of 450°C, and the vast majority of the temperature distribution is greater than 650°C according to the asymmetric histogram curve. It is therefore apparent that channel combinations involving channels whose radiance value is outside of the actual channels dynamic range can not be used as the resulting solutions for T_C are far too low. Channel combinations involving the shorter wavelength channels provide solutions for T_C in the region of 600°C + are far more realistic when the original histogram curve is taken into account.

4.17.3. Suggested channel combinations to use for dual-band procedure applied to synthetic FLIR imagery

A channel combination for successful extraction of dual-band results must involve channels which do not saturate and remain within the dynamic range over the most active flow surfaces, such as that within figure 4.10j. The chosen channel combination must provide ample coverage throughout the SWIR where the peak variation in radiances associated with active lava flows is found. Channels 5 and 7 saturate far too easily considering the nature of a simulated pixel within figure 4.10j whilst channels 3 and 4 barely register the resulting radiance values. Channels 5p and 4p situated within the SWIR provide such coverage. Figure 4.9a indicates that P_H solutions involving this channel combination are very close to the other SWIR channel combination estimates. Figure 4.9b confirms that the estimates of T_C are not unrealistically low considering the nature of the simulated scene.

Due to the changing nature of many of the simulated FLIR scenes of lava flows, in various stages of activity and occupying areas, it is also necessary to consider channel 5 as a SWIR channel combination component. The basic simulated scene within figure 4.10a

with very low numbers of pixels representing the exposed hot core of a flow, does not provide an integrated channel radiance sufficient to register within the channel 4p dynamic range. In such instances a viable channel combination is channels 5 & 5p. This channel combination also provides realistic estimates of P_H and T_C when compared to the original simulated FLIR scene.

By excluding channel combinations whose integrated channel radiances do not fall within the required dynamic ranges of the actual instrument, we are ensuring a greater likelihood of gaining accurate estimates of P_H and T_C when testing these values against the actual values from the synthetic imagery. In the following discussion dual-band solutions are therefore obtained using channel combinations of 5p & 5 and 5p and 4p.

4.18. Using Heat flux as a measure to analyse the response of the dual-band method to simulated pixels.

In the previous sections I have described the values of P_H and T_C returned by the dual-band method and used these to select the optimum ALI spectral channels to produce solutions that we can relate to the simulated pixels. This process highlights the problem in relating simple estimates of the fractional areas at an assumed temperature, to the actual thermal structure within a simulated pixel. The simulated pixels described in the previous sections are comprised of a thermal continuum, the same type of thermal structure found on the surface of actual lava flows and defined by histograms such as that in figure 4.7. It is meaningless to try and quantify such a thermal structure in terms of a pair of simple fractional areas, P_H and P_C at their respective temperatures T_H and T_C, as it is impossible to accurately relate these to an equivalent discrete area of the original thermal structure.

For the sake of comparison it is therefore easiest to use the calculated radiated heat flux, Q_{rad}, emitted from the simulated thermal structures described in the following

sections. Q_{rad} can also be calculated from the results returned by the dual-band method. This approach is consistent with the use of software models such as FLOWGO, described in Harris & Rowland (2001), who use the detected heat flux to predict the extent and activity of lava flows. The use of such a parameter allows a quantifiable and direct comparison of the results returned by the dual-band method.

The heat flux, Q_{rad}, can be defined as the energy radiated per unit area and time over all wavelengths and is described by the Stefan-Boltzmann equation:

$$Q_{rad} = A\varepsilon\sigma T^4 \qquad \text{(Equation 4.2)}$$

In which A is the considered area (m^2), ε is the measured emissivity integrated across all wavelengths and σ is the Stefan-Boltzann constant, 5.67 x 10^{-8} Wm^{-2} K^{-4}. Equation 4.2 may be adapted for application to the values returned by the dual-band method:

$$Q_{rad} = A\varepsilon\sigma(P_H T_H^4 + P_C T_C^4) \qquad \text{(Equation 4.3)}$$

And for application to the simulated thermal structure as represented by a histogram, where each bin is represented by temperature T_{BinN} and with area P_{BinN} where N is the number of bins used in the simulation, can be obtained by:

$$Q_{rad} = \Sigma\,(A\varepsilon\sigma(P_{Bin1} T_{Bin1}^4 + P_{BinN} T_{BinN}^4)) \qquad \text{(Equation 4.4)}$$

By calculating the heat flux radiated from the simulated models it will be possible to ascertain whether the equivalent heat flux calculated from the dual-band results returned for the same model pixel approaches, exceeds or under-estimates this value.

In the next section I describe the 5 simulated models and show how the calculated heat flux responds as the models change in order to simulate changing levels of activity and changing thermal structure. I will then show how the heat flux calculated from the dual-band method compares to these models.

4.19. Results of dual band modelling on a variety of modelled synthetic volcanic surfaces

In order to study the response of the dual-band procedure over a range of lava flow types and scene compositions, a series of artificial FLIR scenes were constructed in accordance with the discussion in section 4.7 (p173). Here we investigate first the response of the procedure for a pair of simulated scenes solely filled by the temperatures associated with a lava flow.

The first of these (model 1) is a simple lava flow, but over the course of 10 model runs the fraction of material within the ~700°C to 1050°C range is progressively increased. This effectively simulates a series of flows in increasing stages of activity, as the fractional area of hot core material is increasingly exposed. The second such model (model 2) considers a pixel IFOV filled solely with a lava flow, but with a thermal distribution which progressively shifts the histogram to increasingly higher temperatures, whilst progressively narrowing the curve over the course of the 10 model runs. This simulates a series of flows of increasing juvenility in the manner of the series of flows described within the FLIR imagery within figure 4.4 (A to D).

I shall then investigate the response of the procedure to three sets of bimodal scenes possessing a combination of lava flows and cool ground or a chilled crust with levees, in the manner of that shown within figure 4.7. The first of these scenes (model 3) considers the scenario where a lava flow is crossing cool ground and occupying a single pixel area. Over the course of the 10 model runs, the fraction of pixels occupied by the flow increases whilst the fraction occupied by the cool ground decreases. The second bimodal (model 4) scenario considers a similar pixel layout to the first, only that the pixel area is comprised of the lava flow and a certain amount of warm material representing the levees of the channelised flow or a stagnating flow possessing an extensive crust. The 10 model runs progressively increases the relative pixel area occupied by the active flow simulated by the second curve. The final bimodal scenario (model 5) is again similar to the first in which the pixel area is comprised of lava crossing cool ground. In this particular model the character of the flow itself is altered within each model run in the same manner as that the second of the simple pixel models, in which the flow displays a progressively higher mean temperature and restriction of the thermal range.

The actual results of the dual-band method applied to the simulated models discussed in the following sections are presented within Appendix IV, with relevant diagrams and discussion detailing the comparison of the returned values for P_H and T_C with the estimated values from the actual simulations. The heat flux discussed in the following sections was calculated from these dual-band estimates using equation 4.3.

Figure 4.10 shows the calculated heat flux for each of these 5 model scenarios calculated using equation 4.4. In each case the trend is of increasing heat flux as each model run progresses from A through J. Different models progress at different rates, depending on the content and style of the modelled thermal structure. Model 1 shows relatively little variation over the course of the 10 runs as this model describes the increasing asymmetry of a histogram representing the increase in the number of cracks

exposing hot material in the flow core. There is still a large fractional area of this model occupied by relatively cool material. Model 2 however displays a much greater variation between the first and last model runs as this simulation increases the area occupied by higher temperature core material at the expense of those areas occupied by cooler material. Model 5 with a bimodal thermal distribution displays a similar trend as this model has a similar situation to model 2, but with a fixed area of cooler material representing cooler ground. The other bimodal distributions represented in models 3 and 4 show a lesser rate of variation between start and end model runs, predominantly as these models simulate a much larger fractional area occupied by cooler material.

The T^4 relationship employed by the Stefan-Boltzmann law in equations 4.2, 4.3 and 4.4 ensures that a relatively small change in the area representing hot material in the simulation will have a greater effect on the emitted heat flux, than a larger change in the area occupied by cooler material.

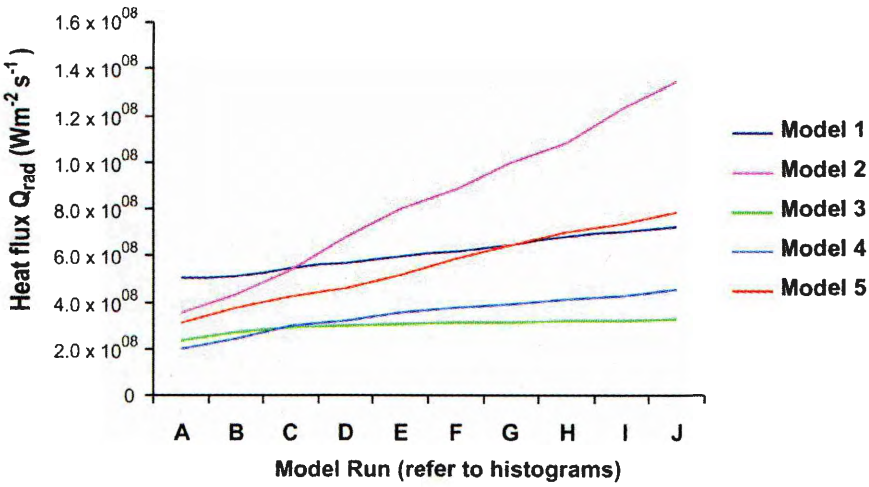

Figure 4.10: The total heat flux calculated for each of the 5 simulated pixel models for each of the 10 (A to J) runs simulating changing thermal structure.

These 5 model scenarios will provide a platform to progressively assess the dual-band procedure and assess its sensitivity to changing flow types as well as the accuracy of its extraction of quantitative data from known thermal distributions.

4.20. Response of the dual-band method to simple synthetic lava flow with increasing numbers of cracks within crust (model 1)

The series of synthetic histograms displayed within figure.4.11 A to J depict 10 model runs in which a simple lava flow, with a thermal distribution similar to that displayed within the FLIR imagery of figure 4.6, is altered to include increasing amounts of exposed core material. This is a unimodal histogram curve, and as such depicts a modelled ALI instrument pixel solely filled by the modelled lava flow.

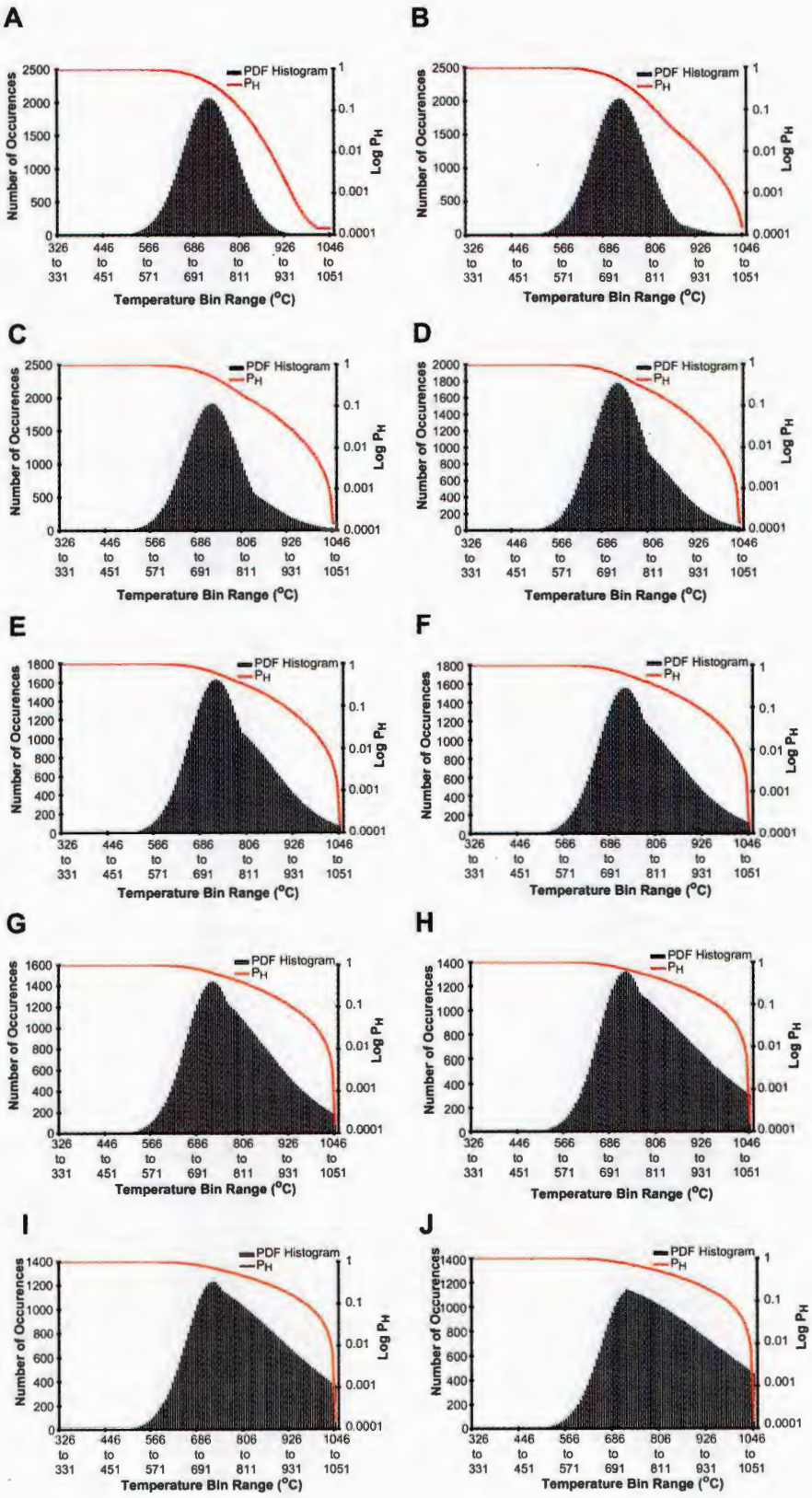

Figure 4.11: Series of Histograms depicting a pixel solely filled by a lava flow. Increasing asymmetry of the bell shaped curve indicates increasing amounts of core material exposed through the crust.

By progressively increasing the asymmetry of the histogram curve in this manner and then charting the resulting dual-band solutions for the processed synthetic imagery, we will be able to assess the ability of the dual-band to respond to flows with increasing numbers of cracks exposing the hot flow core.

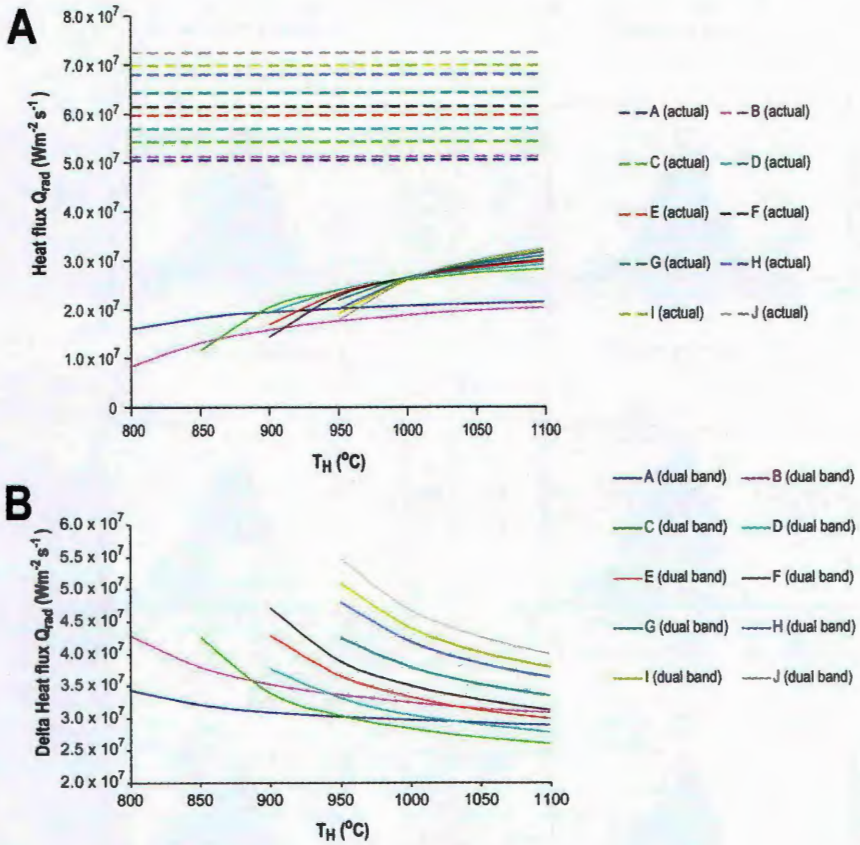

Figure 4.12: Response of the dual band method converted to heat flux for model 1 for each of the 10 model runs for a 900m2 ALI pixel. A: The actual emitted heat flux calculated for both the actual simulation (dashed lines) and the heat flux calculated from the dual-band results (solid lines) at varying assumed values of TH used in the dual-band model. B: The calculated difference in heat flux between the actual and estimated values for assumed TH. Please note the line colours are consistent between panels A & B and I have represented the heat flux for each of the 10 model simulations as constant as varying TH only applies to the dual-band results.

Figure 4.12A shows the calculated heat flux, Q_{rad}, from the dual-band results applied to the simulated ALI pixel, and in each case the returned result is a severe underestimate of the actual value calculated from the simulated thermal structure of model 1. The dashed lines indicating Q_{rad} for the simulated scene, show increasing Q_{rad} as the model progresses from A through model J. However, the results from the dual-band

method are calculated for various assumed values of T_H used in the dual-band method and therefore the resulting estimates of P_H, P_C and T_C used to calculate Q_{rad} will change accordingly. As T_H increases, so does Q_{rad}. Even at the highest values of T_H used, the difference between the actual and estimated values is still large, but as figure 4.12B shows this difference does diminish with increasing T_H.

However, figure 4.12A shows that the estimates for Q_{rad} returned from the dual-band method for each of the model runs A to J reflect the relative order of Q_{rad} for the actual simulated scenes, despite the underestimate in absolute values. This effect is only valid for values of $T_H > 1000°C$. This suggests that the dual-band method is responding to the changing thermal structure within the simulated scene, and is correctly showing that this structure is becoming increasingly active in terms of Q_{rad}. The estimates of Q_{rad} from the dual-band method do not show the absolute separation in actual values as shown for Q_{rad} calculated from the actual simulated scene. This effect is especially noticeable for the later model runs with the largest relative amount of hot material incorporated into the simulated pixel, where the distinction between values for Q_{rad} is more pronounced than those returned by the dual-band method.

4.21. Response of the dual-band method to simple synthetic models of an increasingly active lava flow (model 2)

In the previous section I have shown that the dual-band method is capable of detecting the change within a pixel with an area occupied solely by a single lava flow with increasing amounts of exposed flow core. I will now investigate in this section a similar scenario in which the pixel area is still occupied by a single flow, but with increasing levels of activity. Figure 4.13 displays a set of 10 histograms demonstrating the thermal distribution with a set of 10 synthetic images. Figure 4.13a presents an image with a lava

flow with a typical bell-shaped curve describing the thermal distribution on the surface of an active flow. The successive 9 images (b to j) display increasingly active flows.

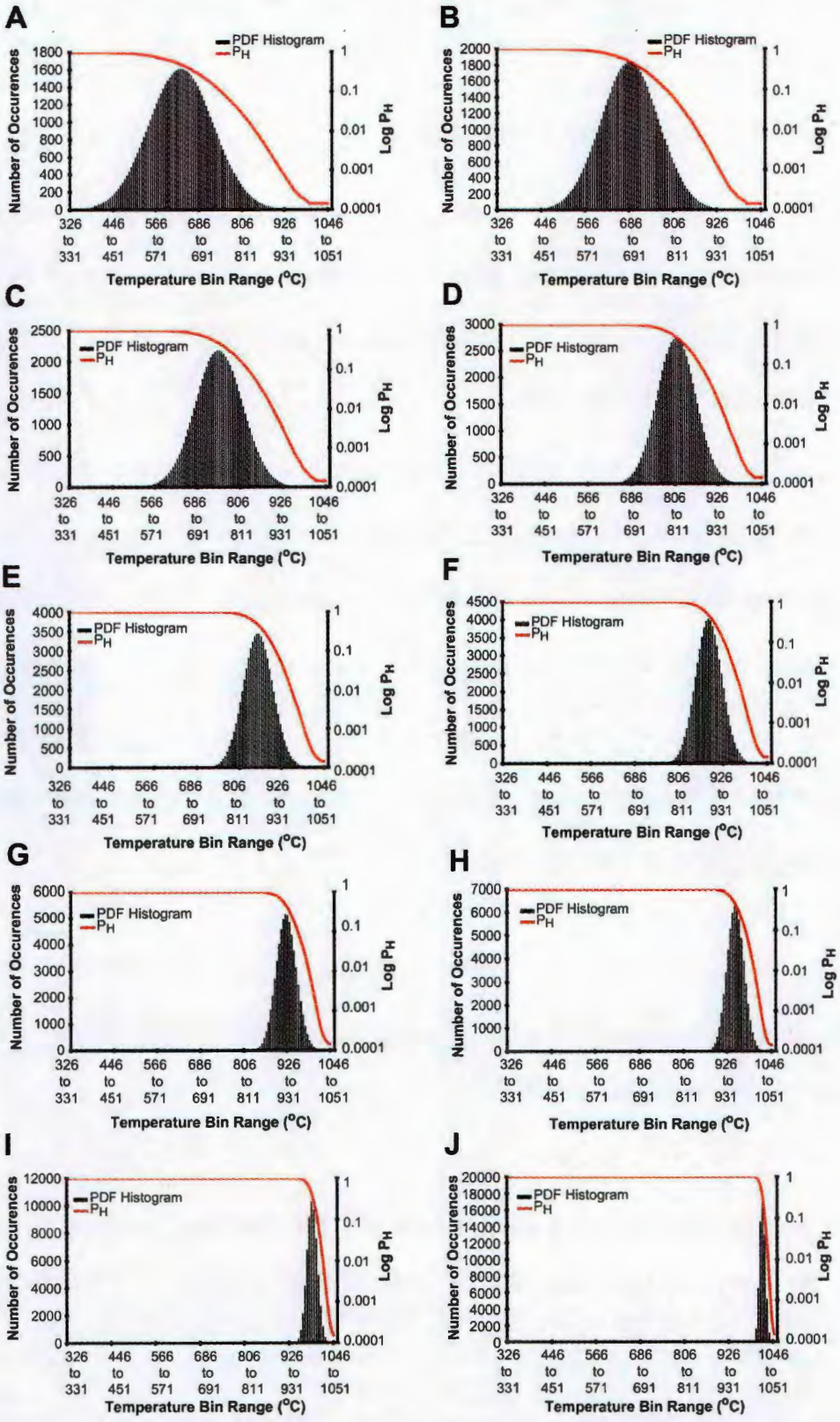

Figure 4.13: Series of histograms depicting a pixel solely filled by a lava flow. The mean temperature of the flow is increasing with each model run (A to J) and the curve is narrowing indicating a restriction if thermal variety. This simulates a series of flows of increasing overall vigour/ youthfulness.

The increase in the mean temperature indicated by the peak of the histogram curve is coupled with a restriction in the width of the curve, so that figure 4.13j describes a flow in which the temperature range spans only ~150°C from 950-1100°C. This type of flow is unrealistic, so it is easier to consider this synthetic imagery as describing a section from the surface of a flow at various stages of development. The increase in activity displayed within figure 4.13 is an attempt to simulate the histograms depicting the various flows imaged by the FLIR camera within figure 4.11 (A to D).

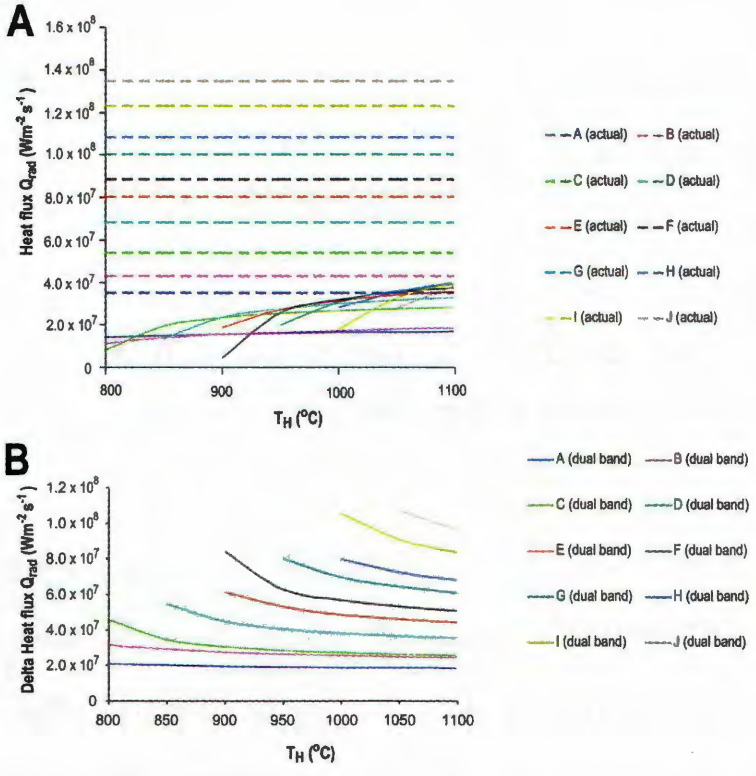

Figure 4.14: Response of the dual band method converted to heat flux for model 2 for each of the 10 model runs for a 900m2 ALI pixel. A: The actual emitted heat flux calculated for both the actual simulation (dashed lines) and the heat flux calculated from the dual-band results (solid lines) at varying assumed values of TH used in the dual-band model. B: The calculated difference in heat flux between the actual and estimated values for assumed TH. Please note the line colours are consistent between panels A & B and I have represented the heat flux for each of the 10 model simulations as constant as varying TH only applies to the dual-band results.

Figure 4.14 displays the estimates for Q_{rad} calculated from the results from the dual-band method applied to the 10 runs from the simulated pixel described by model 2. It

is clear from figure 4.14A that the values for Q_{rad} calculated from the dual-band estimates are again an underestimate of the true values for Q_{rad} calculated from the actual pixel simulation, as shown in figure 4.14B.

The actual values for Q_{rad} are spread across a greater range (~ 4 x 10^7 to ~ 1.4 x 10^8 Wm^{-2} s^{-1}) than the equivalent values for model 1 (~ 5 x 10^7 to ~ 7 x 10^7 Wm^{-2} s^{-1}). This reflects the intended nature of this simulation (the relative values for Q_{rad} for the simulated scenes are shown in figure 4.10). This wider spread in actual Q_{rad} is reflected in a wider separation between dual-band values for Q_{rad} than that shown for Q_{rad} from the dual-band estimates in model 1. The ordering of the estimates for Q_{rad} calculated from the results from the dual-band method again reflect the increasingly active simulations indicated by the dashed lines showing actual Q_{rad}.

4.22. Response of the dual-band method to a simple bimodal synthetic image containing cool ground and a lava flow of increasing area (model 3)

I have shown that the dual-band method is capable of detecting change within a pixel possessing a unimodal thermal distribution. In order to assess the response of the procedure to a variety of different types of surface likely to be encountered then we must consider surfaces possessing a bimodal thermal distribution. In this section we consider a pixel with an amount of cool ground at ambient temperature being crossed by a simple lava flow. Over the course of the 10 model runs the fractional area occupied by the lava flow increases whilst the area occupied by the cool ground correspondingly decreases.

Figure 4.15 displays the histograms describing each of the 10 simulated images A to J. Figure 4.15a displays the histogram of the modelled pixel with the least area occupied by the lava flow and the largest fractional area occupied by cool ground.

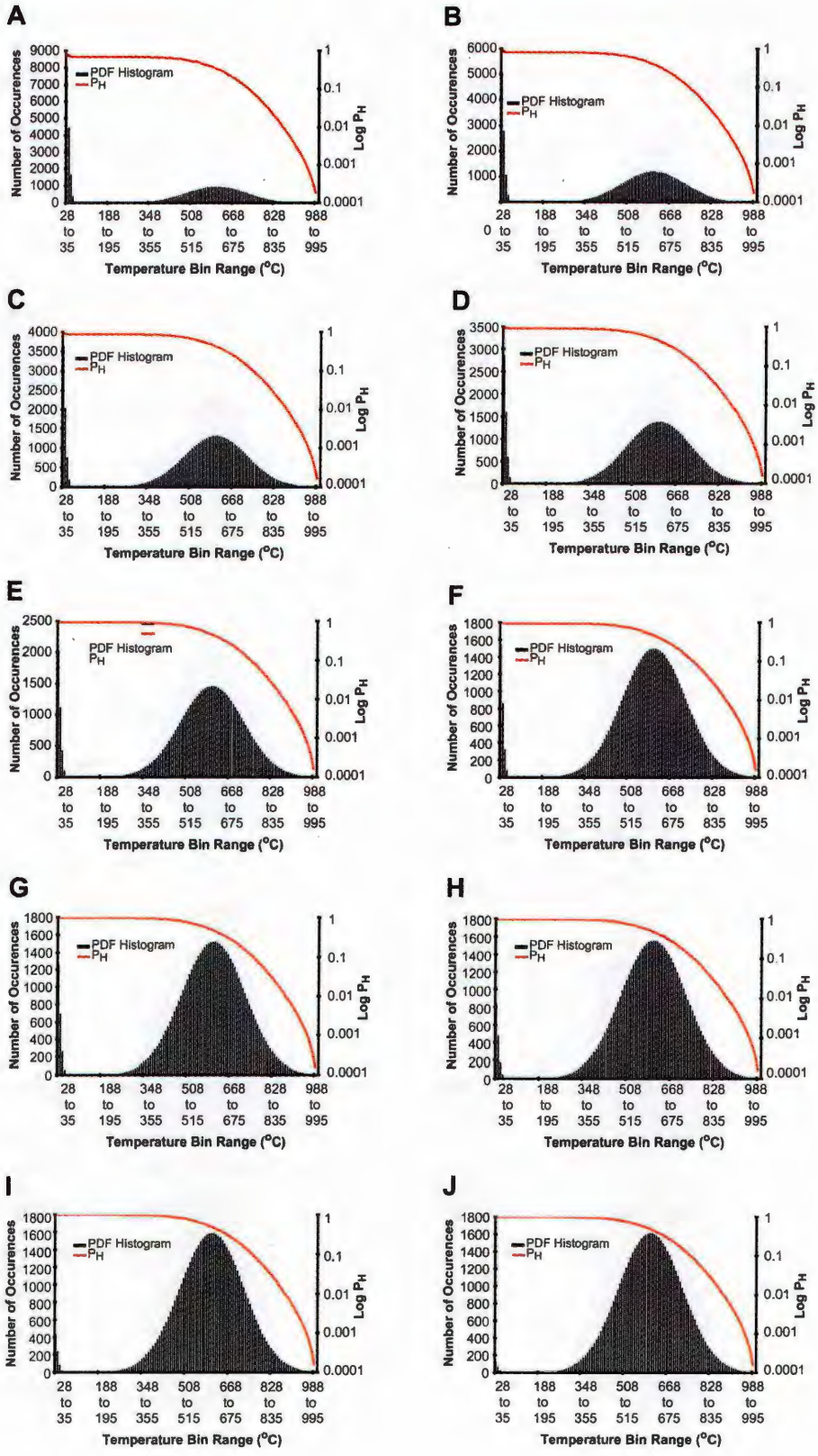

Figure.4.15: Series of histograms depicting a pixel occupied by ground at ambient temperature and a lava flow. The increasing height of the curve describing the thermal distribution of the lava flow with each model run (A to J) indicates that the area within the pixel occupied by the flow increases with each run.

Figure 4.15j shows the pixel with the greatest area occupied by the flow. The cool ground is depicted as a narrow range of temperatures in the region of 0 to 40°C, consistent

with solar heated ground measured by myself during field studies on Mt. Etna. The lava flow itself is represented as a channelised flow with a similar thermal span as the flow depicted within the FLIR imagery of a flow such as the one depicted within figure 4.6 (p189).

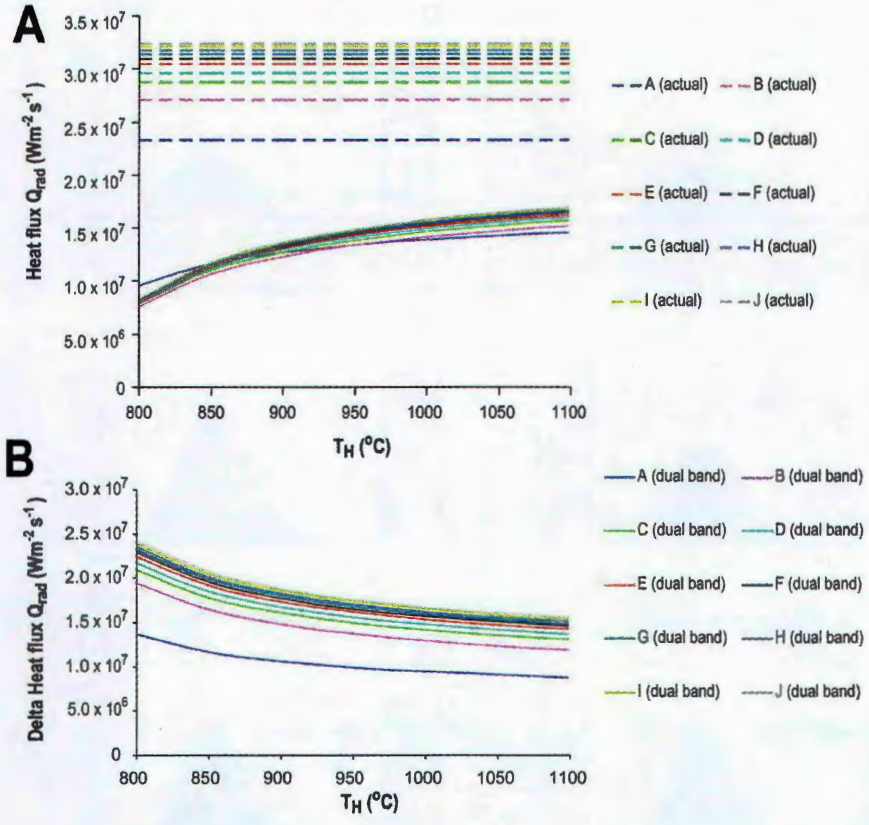

Figure 4.16: Response of the dual band method converted to heat flux for model 3 for each of the 10 model runs for a 900m2 ALI pixel. A: The actual emitted heat flux calculated for both the actual simulation (dashed lines) and the heat flux calculated from the dual-band results (solid lines) at varying assumed values of TH used in the dual-band model. B: The calculated difference in heat flux between the actual and estimated values for assumed TH. Please note the line colours are consistent between panels A & B and I have represented the heat flux for each of the 10 model simulations as constant as varying TH only applies to the dual-band results.

The bell-shaped curve simulating this flow increases in height with each successive model. This maintains the ratio between the number of pixels between each temperature bin. This in effect simulates a pixel partly occupied by a flow of the same type and activity, but at increasing fractional areas.

Figure 4.16 displays the comparison between the actual values of Q_{rad} calculated for the simulated scenes shown in figure 4.15, and those values of Q_{rad} derived from results from the dual-band method. In this bimodal scene, there is a lesser spread of actual values of Q_{rad} between 2.3×10^7 and 3.3×10^7 Wm^{-2} s^{-1}. This is due to the inclusion of a relatively large amount of cooler material representing the cool ground surrounding a lava flow. The second curve used in the model to simulate the lava flow is not dissimilar to that used in the initial runs of model 1, and hence has relatively few cracks through which the hot flow core is exposed. This combination is responsible for this limited range in Q_{rad}.

Estimates for Q_{rad} from the dual-band method are again severe underestimates of the actual values discussed above, but are also much more restricted in variation echoing the restriction in Q_{rad} variation calculated from the simulated imagery in the model runs. These values for estimated Q_{rad} from the dual-band method also show less variation for the various values of T_H used, and are again ordered in the correct sequence of magnitude as the values for Q_{rad} derived from the various runs for this model.

4.23. Response of the dual-band method to a bimodal synthetic image containing cool ground and a lava flow of increasing area (model 4)

I have shown in the previous section the the response of the dual-band method to a simple bimodal synthetic image composed of cool ground at ambient temperature and a simple lava flow of increasing fractional area. Here we again use similar synthetic imagery, but use a bimodal distribution comprising a simple lava flow similar to that discussed within the previous section and an amount of material relating to an extensive chilled crust or bounding levees. This scenario depicts a thermal distribution similar to that shown within figure 4.15a. Figure 4.17 displays the histograms of the 10 simulated flows simulating a similar scene.

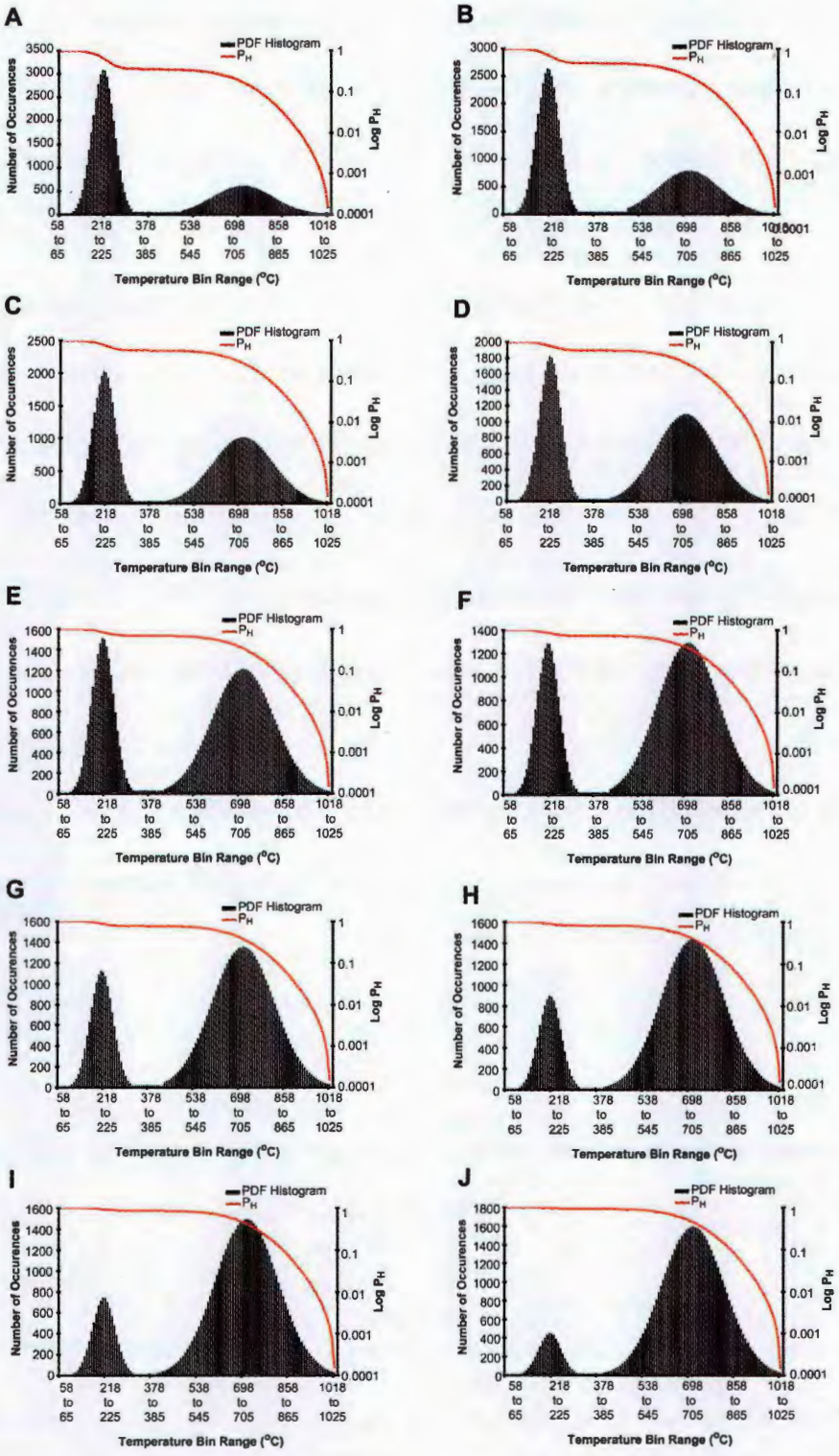

Figure.4.17: Series of histograms depicting a pixel occupied by both a lava flow and cooler material representing varying amounts of levees and stagnating flow material. The increasing height of the curve describing the thermal distribution of the lava flow portion with each model run (A to J) indicates that the area within the pixel occupied by the actual flow increases with each run, whilst the area occupied by the levee material etc, decreases.

Figure 4.17a depicts a pixel with a bimodal thermal distribution with a relatively large fractional area occupied by material within the temperature range of 60°C to 350°C.

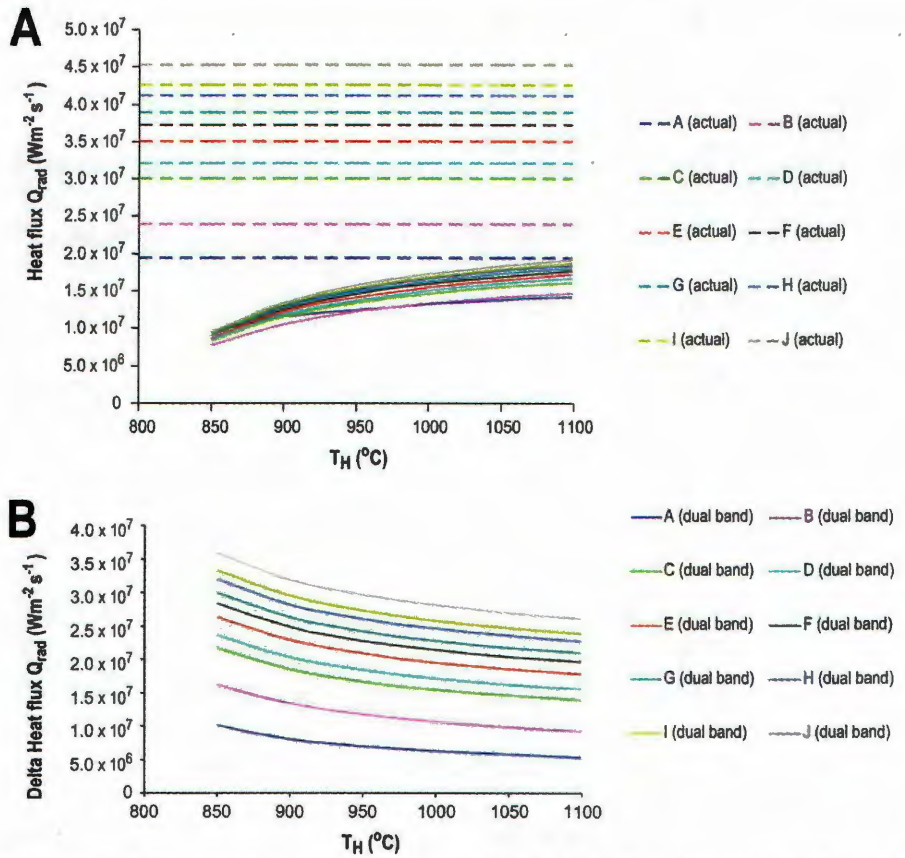

Figure 4.18: Response of the dual band method converted to heat flux for model 4 for each of the 10 model runs for a 900m2 ALI pixel. A: The actual emitted heat flux calculated for both the actual simulation (dashed lines) and the heat flux calculated from the dual-band results (solid lines) at varying assumed values of TH used in the dual-band model. B: The calculated difference in heat flux between the actual and estimated values for assumed TH. Please note the line colours are consistent between panels A & B and I have represented the heat flux for each of the 10 model simulations as constant as varying TH only applies to the dual-band results.

This first curve represents temperatures simulating the levees of the flow, an extensive chilled crust and also cool ground in close proximity to the flow that has been heated by conduction and thermal radiation emitted by the flow. The second curve spanning a temperature range of ~440°C to 1025°C represents the lava flow. This second curve increases in height in the same manner as that discussed in the previous section, whilst the first curve decreases in height. Both curves remain within the same temperature ranges over the course of the 10 model runs. This scenario effectively simulates a pixel

with an increasing fractional area attributable to the active flow, whilst the fractional area occupied by chilled lava correspondingly decreases.

The early model scenarios are akin to a situation where a number of ALI pixels are located over the periphery of an active flow field with bounding levees as well as those areas which may have slow or stagnating flows, possessing an extensive chilled crust. The later models are akin to pixels with an IFOV containing an active channelised flow that fills the majority of the IFOV. These later model runs have a decreasing portion of the IFOV containing the flow bounding levees and a small fraction of heated surrounding surface. Such situations are likely to be encountered within satellite imagery of an active flow field in a number of different pixels.

Figure 4.18 displays the resulting values of Q_{rad} for both the actual simulated scenes and the estimates returned by application of the dual-band method. Despite the similarity of this series of simulations to the previous model (figure 4.16) there is a greater range of actual values for Q_{rad} of between 2×10^7 and 4.5×10^7 Wm^{-2} s^{-1} that reflects the proportional increase of actual flow area at the expense of the area of cooler surrounding ground within the simulated pixel FOV. This difference is also highlighted in figure 4.10. The values for Q_{rad} calculated from the dual-band estimates again reflect this wider spread of actual Q_{rad} but are still underestimates of the actual values. Again, the dual-band estimates return Q_{rad} values in the same order as the original model runs in terms of consistent magnitude suggest that the dual-band method is able to identify the changing the heat flux over the course of the 10 simulations for this model.

4.24. Response of the dual-band method to a bimodal synthetic image containing cool ground and a lava flow of increasing activity (model 5)

Previous sections have considered simulated pixels with a bimodal thermal distribution composed either of cool ground and a lava flow, or a mixture of a cooling lava flow/flow levees/heated ground and a flow similar to the first scenario. Here we shall investigate a bimodal distribution comprised of an amount of cool ground similar to that shown within figure 4.17 and a flow of increasing activity, similar to that shown within figure 4.15.

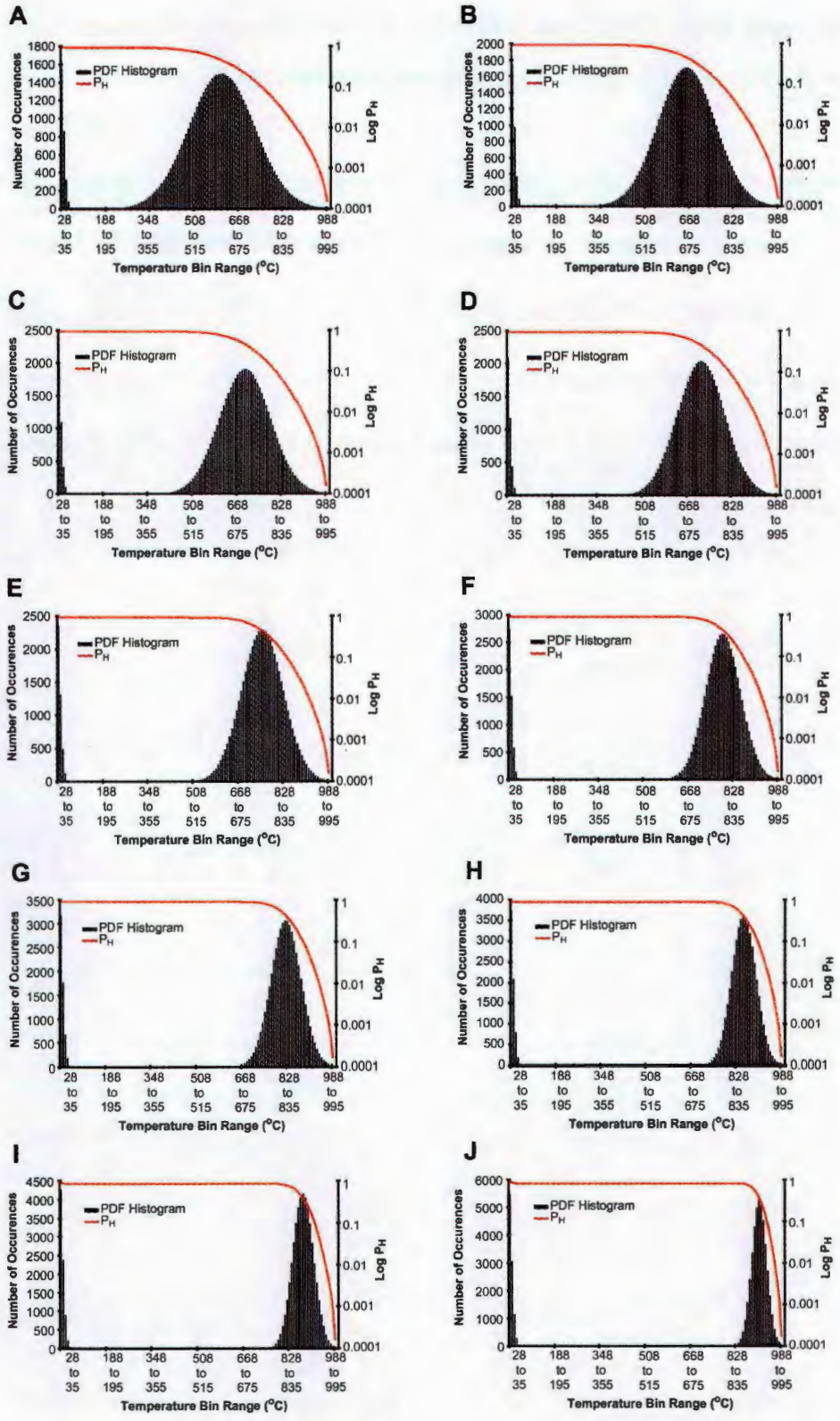

Figure.4.19: Series of histograms depicting a pixel occupied by cool ground and a lava flow. The lava flow in each model run maintains a similar occupying portion of a single pixel area, but increases in mean and in flow vigour indicated by the increasing restriction and profile of the flows curve in each successive model run A to J.

The previous bimodal models have allowed us to assess the response of the dual-band procedure to differing bimodal combinations where a flow has increased in fractional area within the pixel. Here we shall see how the procedure responds to a flow of increasing activity but of consistent fractional area within the pixel.

Figure 4.19 displays ten simulations of a bimodal pixel temperature distribution. The first model figure 4.19a displays a scenario similar to those depicted within figure 4.17 involving a similar amount of cool ground, but with the fractional area occupied by the flow increasing.

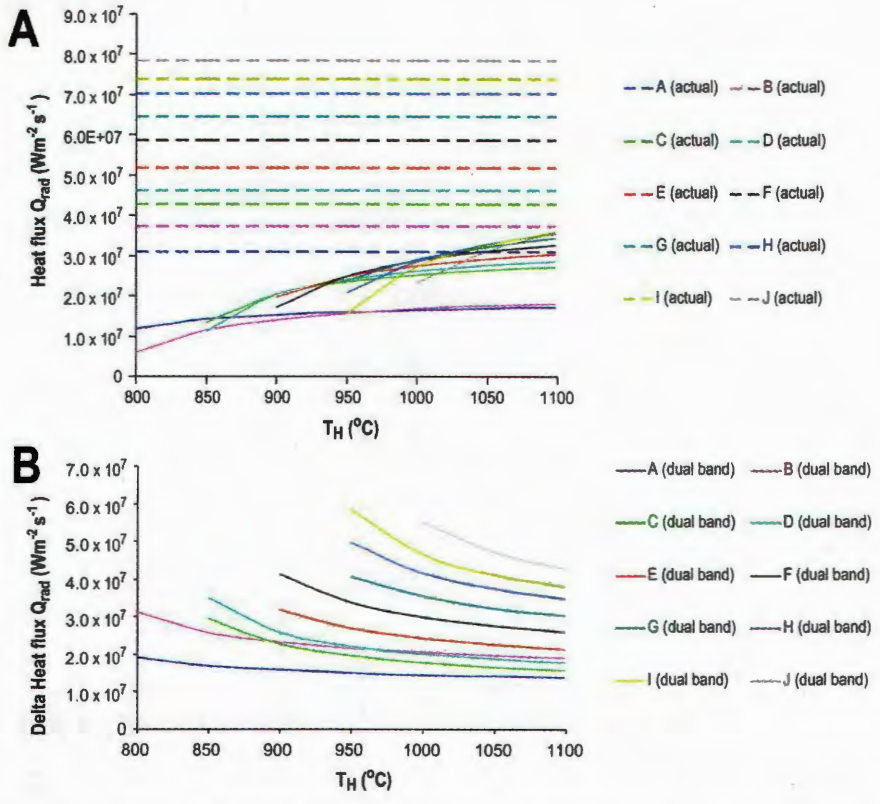

Figure 4.20: Response of the dual band method converted to heat flux for model 5 for each of the 10 model runs for a 900m2 ALI pixel. A: The actual emitted heat flux calculated for both the actual simulation (dashed lines) and the heat flux calculated from the dual-band results (solid lines) at varying assumed values of TH used in the dual-band model. B: The calculated difference in heat flux between the actual and estimated values for assumed TH. Please note the line colours are consistent between panels A & B and I have represented the heat flux for each of the 10 model simulations as constant as varying TH only applies to the dual-band results.

In figure 4.19 the flow maintains a consistent pixel fraction but increasing in activity. This is indicated by the mean temperature of the second curve within the

histogram, indicated by the peak of the second bell-shaped curve, shifting towards higher temperatures within each successive model. As the peak shifts towards increasingly higher temperatures the curve of the histogram itself restricts. This is in the same manner as that discussed about figure 4.20 and based on the series of actual flows observed within the FLIR data in figure 4.4 (p178).

Figure 4.20 displays the actual values of Q_{rad} and also those returned from the dual-band method for this final model 5. This model is similar to model 2 in that it possesses a large variation in calculated Q_{rad} between runs A and J (between 3×10^7 and 8×10^7 Wm^{-2} s^{-1}). This is due to the similar nature of the lava flow considered in the second curve within this models bimodal thermal distribution, and the static fraction of cool ground surrounding the increasingly active lava flow in this simulation. The results for Q_{rad} returned by the dual-band method are again a severe underestimate of the actual values calculated for Q_{rad}, yet display an accordingly wider range for the Q_{rad} values that are returned. This pattern is very similar to those results returned for model 2 and shown in figure 4.14. The results for Q_{rad} are again ordered to reflect the increasing activity simulated in runs A to J.

4.25. Validity of the response of the dual-band procedure to known pixel parameters

The simulation of likely thermal distributions encountered within ALI pixels located over an active lava flow-field has enabled us to replicate the likely response of the dual-band procedure to such pixels. The reproduction and manipulation of such simulated pixels based on the thermal distribution observed within ground-based FLIR data from lava flows on Mt Etna has shown that there are distinctive trends within the dual-band solutions, and therefore also the derived heat flux, Q_{rad}, obtained from these synthetic pixels.

The values for Q_{rad} obtained from the P_H and T_C estimates returned by the dual-band method have consistently been shown to be serious underestimates of the actual values obtained from the original synthetic pixels. These values from which Q_{rad} was calculated can be found in Appendix IV with accompanying discussion. This underestimate of the actual values obtained from lava flows agrees with the findings of Wright & Flynn (2003).

However, the different trends identified within the dual-band solutions from the various synthetic pixels supplied to the procedure, replicate the trends in Q_{rad} observed in the actual simulated data, albeit replicated at much lower values of Q_{rad}. This finding suggests that the method is able to distinguish between the differing models based on the *relative* values of P_H and T_C returned from the procedure, so long as the actual values of Q_{rad} are understood to be underestimates of the true value. This suggests that the dual-band method may still provide the ability to identify the thermal structure within a pixel of an instrument such as ALI. In the next section I propose a method for applying this finding.

The consistent difference in response between the results obtained from the different synthetic model pixels used here may explain the apparent relationships between the dual-band solutions obtained from ALI imagery of lava flows associated with the 2001 Mt Etna flank eruption discussed within Donegan & Flynn (2004) and covered in chapter 6 of this thesis. Those findings suggest that the dual-band method can be used to identify areas of varying lava flow activity, in apparent contradiction of Wright & Flynn (2003).

In the next section I shall show how the pattern of dual-band solutions in terms of the returned values of P_H and T_C obtained from the synthetic imagery can be used to identify these trends and the thermal distribution present within the pixel. I shall then finally show how this method can be applied to actual ALI data obtained from lava flows on Mt Etna to identify the nature of the thermal distribution within a pixel.

4.26. Use of trends identified within dual-band solutions to identify nature of sub-pixel thermal distribution

In this section I describe a method using the actual values of P_H and T_C returned as "raw" values from the dual-band method rather than heat flux Q_{rad}, to identify the possible contents of a pixel IFOV. The actual values for the 5 models described in section 4.19 in terms of P_H and T_C and used in this section are listed, described and discussed in Appendix IV.

The apparent trends visible within the values of Q_{rad} calculated from the dual-band solutions obtained from synthetic imagery are clearly highlighted within figure 4.21. Each of the five main synthetic pixel types described within section 4.19 occupy different areas of X-Y space within the two charts of figure 4.21. This suggests that it is possible to identify differing types of thermal distribution within a pixel based on the relationships between the returned solutions and the PIT of the pixel corresponding pixel. Figure 4.21 displays the dual-band solutions obtained for each model run of the five different types of synthetic pixel described using simulated PIT's within ALI channels 5 & 5p. Each value for P_H or T_C displayed has been obtained at a T_H temperature of 1000°C. This is partly due to increase the clarity of figure 4.21 as representing all solutions for each value of T_H (200°C to 1100°C) used within the dual-band solutions discussed within Appendix IV would muddy the relationships between the different trends depicted by each synthetic pixel type. A T_H of 1000°C is also widely used in dual-band solutions for lava flows from Mt Etna as this temperature is close to the magmatic temperature at Mt Etna. A fuller description on the assumption of T_H for use in obtaining dual-band solutions can be found within chapter 5.

It is important to note that in the solutions obtained from all the synthetic pixels a T_H of 1000°C lies well within the "stabilised" region of solutions after the rapid initial onset of solutions described within Appendix IV. By using the dual-band solutions

obtained from a single T_H value it is easier to chart the solutions from the different synthetic pixels with respect to each other.

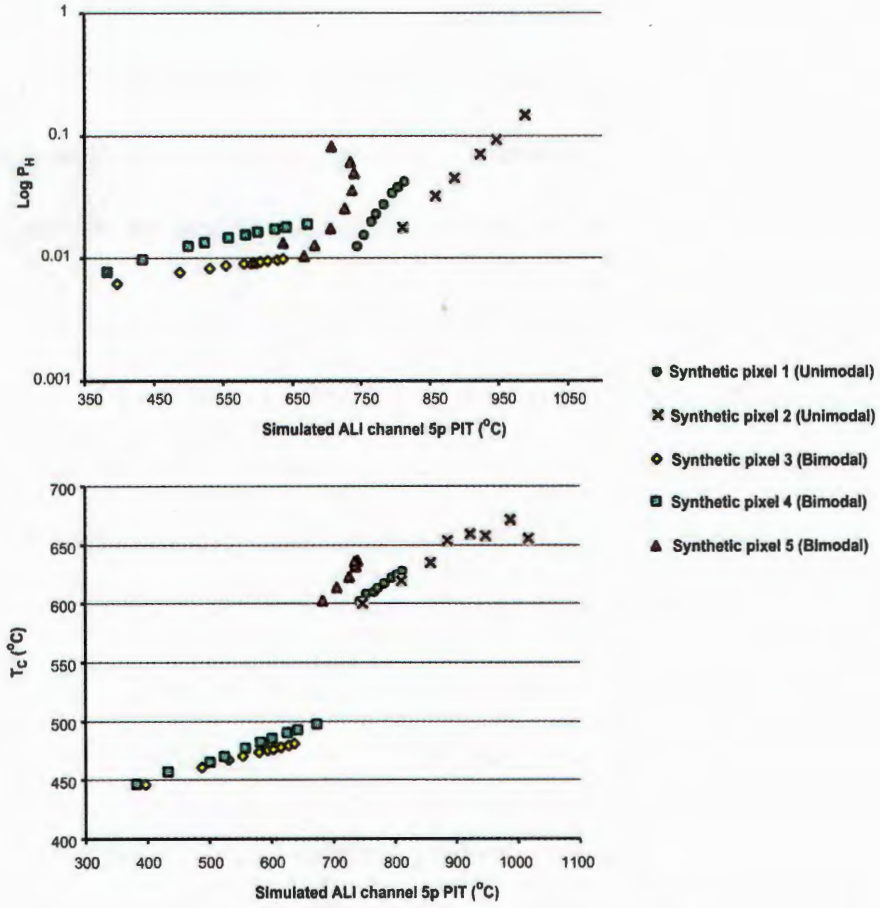

Figure 4.21: Plot of PH values returned from the dual-band solution obtained at TH 1000°C returned from all model runs for each type of simulated pixel type Vs the corresponding simulated ALI channel 5p PIT (top). Lower graphic relates to the equivalent solutions for T_C. Synthetic pixel 1: relates to a simple unimodal pixel with an increasingly asymmetric histogram due to increasing fractional area occupied by hot material >850°C (figure 4.11 p204). Synthetic Pixel 2: Simple unimodal thermal distribution simulating lava flows of increasing activity indicated by increasing mean temperature and narrowing histogram curve (figure 4.13 p208). Synthetic pixel 3: Bimodal thermal distribution, initially with relatively large area occupied by cool ground and a small fractional area occupied by a lava flow. Fractional area occupied by lava flow subsequently increases (figure 4.15 p211). Synthetic pixel 4: Bimodal thermal distribution comprising initially large fractional area occupied by extensive crust/channel levees/stagnating flow material with remaining fractional area occupied by an active lava flow, increasing with each model whilst cooler material decreases (figure 4.17 p214). Synthetic pixel 5: Bimodal thermal distribution comprised of cool ground (fixed fractional area with each model run) and an active lava flow of increasing activity, similar in nature to synthetic pixel 2 (fixed fractional area with each model run) (figure 4.19 p218).

In figure 4.21 I plot P_H and T_C (Y-axis) against the simulated PIT at the ALI channel 5p wavelength, as channel 5p was used within these dual-band solutions. The

temperature of the surface of the lava flows and the channel 5p wavelength equips the resulting PIT's with sufficient variation in values to provide a suitable basis to easily differentiate between values in the X-axis domain.

The PIT at the channel 5p wavelength is a very good indicator of the likely activity within a flow as channel 5p is very sensitive to changes in emitted SWIR radiance. Active flows with areas of flow core extensively exposed and/or possessing little or no crust will emit strongly within the SWIR.

Likewise, flows with extensive crusts that are stagnating or slowing due to the effects of the local topography, reduction in effusion rate or the formation of a lava tube will not radiate as strongly within the SWIR. Dual-band solutions that return relatively high estimates for P_H indicate that the pixel in question contains a relatively higher fractional area occupied by high temperature material. Similarly, low returned estimates for P_H imply that there is little or no material actually at the particular T_H temperature used.

The dual-band procedure works on the principal that the combination of the emitted radiance from the two fractional areas results in a single radiance value. Once the two calculated radiances from the two simultaneous equations (equation 1.5 and 1.6) match each other and the observed radiance value, then a valid solution has been obtained. As the modelled radiance is a combination of two emitted radiances, it is possible that a very small fractional area occupied by material at $T_{H\ (1000°C)}$ combined with the majority fractional area at T_C will possess the same combined radiance as that emitted from two fractional areas emitting at lower temperatures. Therefore lower values of P_H may indicate that there is little or no material within the pixel IFOV actually emitting at the temperature of T_H, especially if the temperature used for T_H is of a high order and close to the eruption temperature of the lava. If this scenario is correct and there is little or no material at or near temperature T_H, then the remaining fractional area P_C at temperature T_C, will correspondingly record relatively lower temperatures for T_C than that from a pixel IFOV

incorporating material at higher temperatures for T_C and a higher associated fractional area P_H.

We can therefore combine this with the corresponding PIT information. Solutions with lower estimates for P_H and T_C that plot with a lower PIT will indicate a pixel possessing a thermal distribution with a lower overall temperature range. This is the lower-left region of the two charts within figure 4.21. Conversely, solutions from pixels with higher values of P_H and T_C that correspond with a higher PIT value indicate a pixel possessing a thermal distribution incorporating higher temperatures within the pixel IFOV. This area corresponds with the upper-right region within both charts of figure 4.21.

The solutions from the various model runs of the five separate synthetic pixels all lie in such a lower-left to upper-right envelope within both charts of figure 4.21. Solutions plotting in the lower-left relate to the synthetic pixels incorporating bimodal distributions of cool ground and a lava flow of increasing area (section 4.8.3), and levee/cool crust material and a lava flow of increasing area (section 4.8.4). The bimodal synthetic pixel models incorporating cool ground and a lava flow of increasing area (section 4.8.5) is positioned midway between the former two bimodal synthetic pixels and the two unimodal synthetic pixels which are positioned within the upper-right region of both graphs. These two unimodal model pixels both possess a IFOV wholly occupied by a lava flow. The highest estimates for P_H and T_C are returned by the pixel model run describing a series of flows of increasing activity (model 2). This is clearly identified within figure 4.21 (top chart) where each model is clearly distinguished.

The pixel model that incorporates a series of runs in which the initially symmetric bell-shaped curve describing the thermal distribution becomes increasingly asymmetric, (model 1) also demonstrates a clear separation of points in P_H Vs PIT_{5p} space within figure 4.21. This model simulates a flow with increasing exposed flow core whilst the overall activity of the flow does not change. This is similar to what might be expected if the flow

had suddenly traversed a change in gradient which has caused the flow to accelerate and increase frictional forces with confining levees, causing an established crust to rupture increasing exposure of the flow core.

Within the previous section I surmised that the dual-band procedure and calculated Q_{rad} was more sensitive to changes in the fractional area occupied by hot flow material than changes concerned with cooler material, whether in the form of cool surrounding ground or levees/extensive crust/stagnating flows. This is due to the non linear nature of Planck's law which describes the T^4 relationship between temperature and emitted radiance. This is supported by figure 4.21 which shows that those synthetic flows that demonstrate the greatest increase in fractional area occupied by material >800°C possess the greatest variation between the end-member model runs. This is especially the case for those models which simulate increasingly active flows (models 2 & 5). Those models which simulate a lava flow of constant activity (i.e. the Histogram curve depicting the flow does not shift position or constrict with each model run) that increase in fractional area whilst the fractional area occupied by the cooler component declines, do not demonstrate such a great variation between end-member model runs (models 3 and 4).

It is clear from figure 4.21 that those pixels possessing a bimodal thermal distribution have lower PIT values due to the incorporation of cooler material in addition to the lava flows. This effect is noticeable even for those bimodal pixels with high levels of lava flow activity (series 5) in addition to the cooler component.

Figure 4.21 only depicts dual-band solutions for a single T_H temperature of 1000°C, whereas within section 4.19 I used a range of T_H temperatures from 600 to 1100°C. The overall pattern of solutions resulting from the procedure was that lower values of T_H supplied to the procedure will consistently result with higher solutions for P_H and lower values of T_C. As T_H increases in value, P_H decreases whilst T_C increases.

The adoption of T_H temperatures lower than the common value of 1000°C used for figure 4.21 will affect the points representing the various models within figure 4.21 by increasing the values of P_H and decreasing the values for T_C. Most importantly the relationships between the individual points will be maintained so that the different pixel models may still be identified by the relative location in terms of P_H/T_C Vs PIT. In the following chapter I discuss the effect that varying the effective elevation angle of the instrument with respect to a lava flow surface has upon solutions obtained from the dual-band procedure.

It was apparent that increased angles of instrument elevation with respect to the local surface (i.e. the flow might be travelling down a steep gradient) coupled with the deep, narrow cracks results with the dual-band solutions underestimating the values of P_H and T_C obtained for the same flow at nadir. This is because the viewing geometry prevents the observation of the base of cracks where the hottest material is found. As the estimates for P_H and T_C are already serious underestimates of the true values, the effect of view angle serves to compound this error by decreasing these estimates further. This will affect the results within figure 4.21 in a similar manner to the effects resulting from the use of lower values of T_H within the dual-band procedure. As the PIT is reduced due to the decrease in effective fractional area within the pixel IFOV because of declining instrument elevation angles, the resulting solutions for P_H and T_C will also decrease.

It is clear from figure 4.21 that it is possible to identify different types of thermal distribution within a pixel IFOV based on the position of the dual-band solutions when plotted against the corresponding PIT. By obtaining a selection of dual-band solutions for a number of pixels at different locations within an active flow-field, it should be possible to identify from the relationships between the individual solutions the nature of the thermal distribution within each pixel's IFOV. In the next section I used actual data from ALI to test this.

4.27. Analysis of sub-pixel thermal resolution identified within actual ALI data from lava flows on Mt Etna

ALI Imagery of lava flows resulting from the July-August 2001 flank eruption of Mt Etna provides an excellent opportunity to test the suppositions of the previous section. A full description of this eruption and the processing of the available ALI imagery obtained on 29th July 2001, can be found within chapter 6. Figure 4.22 highlights a series of flows resulting from this eruption travelling downhill in the area of the Monti del Lago vents on the southern flank of Mt Etna. A number of pixels were selected at various locations within this imagery and supplied to the dual-band procedure in a similar manner to that described for the synthetic imagery described within section 4.5 and within the following chapter.

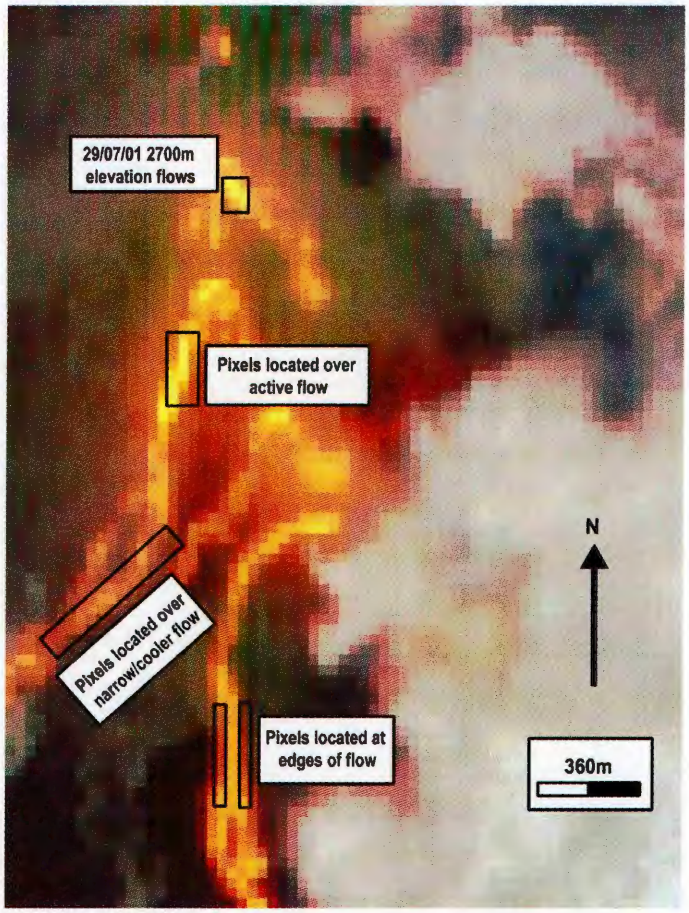

Figure 4.22: R-G-B image comprised of ALI channels 5p-5-4p from Mt Etna flank eruption on 29th July 2001. These flows are located close to the Monti del Lago vents and the indicated 2700m vents. Areas with pixels used for dual-band analysis in figure 4.23 are indicated. Image courtesy of Luke Flynn, HIGP.

Figure 4.23 displays the resulting solutions in a similar manner to those displayed for the synthetic imagery within figure 4.21. It is immediately apparent that the resulting dual-band solutions plot in discrete areas within a similar envelope of solutions to those found within figure 4.21.

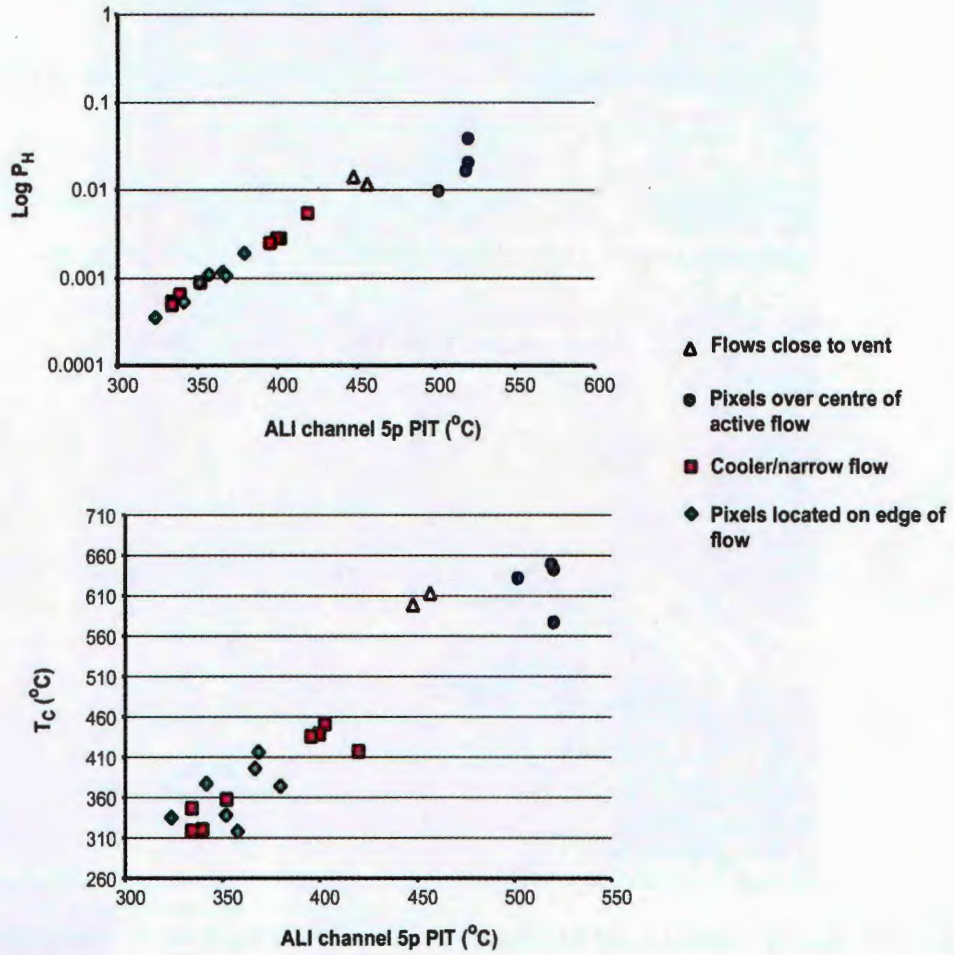

Figure: 4.23: Dual band solutions obtained using ALI channels 5 & 5p from the pixels indicated within figure 4.22. Solutions for PH (at TH 1000°C) and TC are plotted in the same manner as those within figure 4.21 against the corresponding PIT within ALI channel 5p.

Figure 4.22 highlights that the pixels used have been chosen on the basis of location and the apparent level of flow activity. A number of pixels have been selected that are located over active flows, both close to the erupting 2700m elevation vent, as well as other flows further downstream. A number of these pixels were selected as they appeared to be within the centre of a large flow.

These pixels are characterised by lighter tones within the R-G-B ALI channel 5-5p-4p image. Other pixels have been chosen because of their location over apparently cooler regions of the flow, indicated by darker pixel tones. A final set of pixels were chosen because of their location on the edges of an active flow. All these areas have been indicated within figure 4.22.

These different groups of pixels plot within different regions of the solution envelope within figure 4.23. The set of pixels located at the edge of the active flow are indicated as thermally anomalous due to the elevated channel radiances above the surrounding cool ground. The radiance values for these pixels are considerably lower than the radiance values for those pixels with very light tones located over or near the centre of the active flow. These pixels with darker tones situated on the edge of the flow may be expected to possess a combination of cool background material as well as a certain areal fraction occupied by the lava flow itself. These flow-edge pixels plot in the lower-left of the two charts within figure 4.23. This is consistent with the location of the bimodal synthetic pixels within figure 4.21, comprised of a combination of cool ground and an active lava flow. This confirms that these pixels within the ALI data possess a bimodal thermal distribution.

Also plotting within the lower-left portion of the two charts within figure 4.23 are pixels indicated as being located over a relatively cooler or narrower flow than those pixels located near the 2700m vent. These pixels demonstrate a wider range of P_H and T_C values within figure 4.23 than the pixels known to be located on the edge of the flows discussed above. This suggests that at least a number of these pixels plotting within the bimodal region might be located over regions of the flow where the flow is not wide enough to fill the 30m width of the ALI pixel. Lava flows 30m wide are rare on Mt Etna (Harris et al, 1998), so it is likely that the IFOV of most of the selected pixels within figure 4.22 will possess any combination of cool ground, ground heated by the flow, flow levee as well as the flow itself.

This thermal distribution is highlighted within the FLIR imagery displayed within section 4.4, and will be effectively a bimodal distribution comprised of the cooler ground material and any surface associated with the flow itself. Pixels with a IFOV including a

narrow flow will still plot further in the lower left of fig4.23 than pixels with a larger portion of the IFOV filled by active flows, due to the resulting lower PIT values.

The pixels identified within figure 4.22 situated over the active lava flows or close to the 2700m vent, plot within the upper-right region of the solution envelope within figure 4.23. This is consistent with a thermal distribution comprised of higher temperatures within the IFOV of these pixels. Those pixels situated over the bright active flows within figure 4.22 are indicated as possessing higher temperatures within their IFOV than those flows close to the actual vent, due to their placement in the extreme upper-right of the solution envelope. A number of the pixels located close to the active 2700m vent were recorded as saturated (the emitted radiance has exceeded the upper detection limit of the detector) within channel 5. No dual-band solutions were therefore available.

The remaining unsaturated pixels displaying bright tones within figure 4.23 close to this vent are located over lava flows proximal to the vents. We would still expect these solutions to plot within the upper-right region of figure 4.23 exceeding the results obtained from the pixels located over the active flows. Flows proximal to the vent would display very little developed crust on the surface of the flow, whilst the surface of the flow will be closest to the eruption temperature than at any other point downstream. This apparent incongruity may simply be attributable to the fact that the proximal vent flows may be narrower than those active flows imaged downstream resulting with a lower PIT. Another reason may be that those flows close to the vent might well be traversing the steep incline of the cone associated with the 2700m vent, and therefore the viewing geometry between the flows and the ALI instrument will not be conducive to obtain a PIT value truly indicative of the surface temperature. In a similar fashion, flows issuing from a vent and down the steeply inclined slopes of a pyroclastic cone are often narrow due to the high flow regime. This is a result of the eruption rate and flow velocity due to the combined

effects of the effusion rate and slope gradient, making wide flows unlikely on a steep incline.

Another possibility is that eruption products such as ash, gas and steam associated with the active vent and proximal lava flows are attenuating the radiance signal emitted from these proximal flows by a greater margin than the $\tau 0.95$ value allowed for within the IDL processing algorithm. This will result in an underestimate of the PIT value. This might well be a contributing factor as the dual-band solutions obtained for these proximal vent pixels display similar values of P_H and T_C to those obtained for the active flows downstream, but plot with lower channel 5p PIT's.

The pixels associated with the active flows downstream of the 2700m vent display a range of solutions for P_H from f 0.01 to 0.005, whilst T_C spans 570°C to 655°C. These bright pixels interpreted as located over the centre of an active flow are preceded by darker pixels, similar to those pixels chosen for the narrow/cool flow. Successive pixels down-flow from the bright pixels also display darker tones indicating lower PIT values. No active vent is located at the position of these bright pixels. A sudden increase in PIT values traversing down-slope in this manner might be attributable to possible scenarios. An increase in the width of the flow or the bifurcation of a single channel into two flow arms (such as that imaged within figure 4.2 on p171), will increase the fractional area occupied by flow material within the pixel IFOV increasing the PIT value.

Alternatively, an increase in slope gradient may cause the flow to accelerate, rupturing the crust, and exposing hot flow core material with a resultant increase in PIT value. In the former scenario, a widening of the flow may be accompanied by a reduction in slope gradient which may ultimately result in a relative increase in the growth of a surface crust, reducing the area of exposed flow core. This will result in a lower ultimate PIT than that of a PIT comprised of a relatively narrow flow with an increased area of

exposed flow core. As we have shown in section 4.8 the dual-band solution is most sensitive to an increase in fractional area occupied by exposed flow core.

The ALI SWIR channels used within figure 4.22 will also be most sensitive to changes in the area of exposed high temperatures (Donegan & Flynn, 2004). Therefore, in the instance of these pixels we might conclude that the large P_H values coupled with high channel 5p PIT's suggest that the flow has accelerated due to an increased slope gradient. This has ruptured the existing crust exposing larger exposed areas of flow core than that exhibited within the previous or successive pixels located over this flow.

4.28. How do the dual-band solutions using ALI data compare with those from the synthetic imagery?

The solutions for P_H and T_C extracted from the ALI imagery within section 4.9.2 display values that are lower overall than the values obtained from similar synthetic imagery within section 4.9.1. This may be due to a combination of factors. The largest such factor is that most of the flows present within figure 4.22 will only rarely equal the 30m width of an ALI pixel (Harris et al, 1998). As we have discussed, this will result in most of these pixels possessing a bimodal thermal distribution resulting in a lower PIT value than if the pixel concerned was completely filled by the lava flow. This in turn will result with lower estimates for P_H and T_C obtained from the dual-band solution.

There will be a large variation in the amount of volcanic haze and ash within the atmosphere local to a flank eruption. Some of this is clearly visible in the lower-right of the R-G-B ALI imagery within figure 4.22. This will attenuate the signal received by ALI and ultimately result in a lower PIT value, resulting in low dual-band estimates for P_H and T_C.

Another factor to consider is the overall orientation of the flows with respect to the ALI instrument. I will discuss the effect of how the slope angle down which a flow is travelling can affect the detection of the hot material at the base of the cracks in the following chapter. High angles between the flow surface and the instrument will increasingly obscure the hot base of any cracks. This is especially the case if the cracks concerned are narrow and relatively deep. In this instance the PIT recorded will be an underestimate of the true value recorded as if the instrument was located at nadir. This will again reduce the resulting estimates of P_H and T_C obtained from the dual-band procedure.

All the above effects will lower the actual results obtained for P_H and T_C from the dual-band procedure from the equivalent results obtained from a synthetic pixel PIT assuming a level surface and providing an overestimate of the thermal distribution within the pixel. An underestimate of the actual atmospheric transmissivity τ will exaggerate the underestimates of P_H and T_C. The net cumulative result will be to shift the results plotted within $P_H - PIT_{5p}$ or $T_C - PIT_{5p}$ space towards the lower-left of the diagram. This is precisely what is observed when comparing the results from the actual ALI data within figure 4.23 with those of the synthetic imagery within figure 4.21.

It is clear that it is possible to obtain an understanding of the various types of thermal distributions present within a range of pixels obtained from satellite imagery of an active lava flow-field by obtaining dual-band results for the range of thermally anomalous pixels present. By plotting the resulting estimates of P_H and T_C against the PIT obtained from one of the channels used within the dual-band procedure, it is possible to discriminate between the different types of thermal-distribution present. The different thermal distributions present will plot within discrete regions of the solution 'envelope'. Pixels with an actual large fractional area consisting of highly active flows with large exposed areas of flow core will plot within the upper-right region of the resulting graphs. This is because pixels with such a thermal distribution will exhibit relatively high PIT values.

Pixels that do not possess such a high fractional area occupied by active flows, or with flows with diminishing levels of activity, will increasingly plot along a trend towards the lower-left of the graph. It is possible to identify pixels that have a low PIT value, but relatively high values of P_H and T_C as belonging to active flows that do not fill the entire pixel IFOV. This scenario was encountered with the flows close to the vent within the 29th July ALI imagery. Relatively low PIT values were recorded, but estimates of P_H and T_C were of a similar order to those of pixels with a high fractional area occupied by flows. This is because the dual-band procedure is most sensitive to changes within areas occupied by high temperature material. Analysis of the results from the synthetic imagery goes on to show that for such pixels (series 5) the recorded PIT may not change much, but the large range of estimates of P_H indicate the increasing levels of flow activity.

By using such an approach it is possible to identify, if not actually obtain accurate quantitative estimates of P_H and T_C, an accurate estimate of the likely thermal distribution within each pixel based on the relative position that each pixel occupies within $P_H/T_C - PIT_{channel}$ space.

4.29. Conclusions

I have shown here how the findings of Wright & Flynn (2003) on the poor performance of the dual-band procedure can be reconciled with the observations extracted from dual-band procedure on the relative observations upon the changing conditions within a lava flow-field made by Donegan & Flynn (2004). By using synthetic thermal distributions typical of an active lava flow-field within a single pixel based on actual ground based FLIR data, I have shown that the dual-band procedure consistently returns serious underestimates of the fractional area and heat flux Q_{rad} occupied within a pixel of material at an assumed temperature. These errors were less for pixel thermal distributions

where the pixel IFOV was filled by the flow itself (unimodal), although the results themselves were still considerable underestimates. Those pixels with a thermal distribution incorporating an amount of cooler material as well as a certain fractional area occupied by the lava flow itself (bimodal) produced results worse than those obtained from the unimodal models.

The use of synthetic thermal distributions allows the control of the parameters controlling the thermal distribution within a single pixel. With this method the fractional area occupied by cracks within the flow crust exposing the hot flow core could be altered, as well as the fractional area occupied by material at a lower temperature. The overall character of the flow itself can also be altered by changing the shape and position of the histogram with respect to the temperature bins describing the thermal distribution within the lava flow surface. By progressively varying these parameters it is possible to simulate within a series of model pixels an increasingly active lava flow. It was then possible to investigate how the dual-band procedure responds to the changing thermal distribution within the model pixels by comparing the values for heat flux, Q_{rad}, calculated from these returned parameters from the dual-band method with Q_{rad} calculated from the synthetic pixel.

The dual-band procedure is most responsive to changes in fractional area occupied by the hottest regions within the pixel IFOV, due to the exaggerated response of the Planck function to high temperatures at these wavelengths. The procedure also correctly identified pixels with the greatest changes in thermal distribution. I found however, that as the fractional area occupied by the hottest material increases, then so does the scale of the underestimate of the returned dual-band parameters. The dual-band procedure proved to be sensitive to increasing flow activity, with clear increases in both returned values for P_H and T_C and therefore Q_{rad}, that would be expected to correspond with an increase in flow activity. The dual-band procedure is also sensitive to changes within the area and activity

of lava flows within synthetic pixels that also have a fractional area occupied by cool background material at ambient temperatures. The estimates for P_H and T_C and resulting Q_{rad} are lower because of the lower PIT values resulting from the inclusion of an amount of cooler material within the pixel IFOV. Certain synthetic models tested the response of the procedure to changes in the fractional area occupied by the cooler component within bimodal thermal distribution models. The procedure was only able to respond to changes within the "hot component", even when the cooler component was comprised of relatively warm material such as stagnating flows or flow levees.

The lack of sensitivity of the procedure to cooler surfaces is mainly due to the Planck relationship between the emitted radiance and temperature of a surface and the wavelength. At the SWIR wavelengths in which the ALI channel used and simulated here, 5, 5p & 4p, sensitivity is much greater to hot material at the temperatures of active lava flows, rather than cooler ground at ambient temperatures. A shortcoming of the dual-band procedure is that any channel sensitive to radiances from cooler material will likely be swamped by emitted radiance from even a relatively small area at lava flow temperatures.

Another difficulty is the likely thermal distribution found within an actual ALI instrument pixel obtained from a lava flow-field. Very few pixels will possess an IFOV entirely filled by a lava flow. Therefore the vast majority of pixels will display a bimodal thermal distribution, broadly comprised of the cool ground at ambient temperature and the lava flow. This goes some way to invalidate the simple two component model for the surface of an actual lava flow comprised of cool crust interspersed by cracks exposing the flow interior proposed by Crisp & Baloga (1990), and used as a basis for the application of the dual-band method in terms of T_H and T_C. In the more likely bimodal scenario, the dual-band method would ideally return P_H as the fractional area occupied by the entire flow. T_H would then represent the mean temperature of the flow itself. Due to the problems outlined above regarding the relationship between emitted radiance and

temperature at lava flow temperatures within the SWIR, this does not happen. T_H ultimately represents an area P_H unrelated to the actual area occupied by the flow itself, but to some fractional area occupied by material within an uncertain temperature range. This error is compounded by the difficulty in actually defining an area upon the surface of a lava flow at a single temperature (T_H), due to the wide continuum of temperatures encountered on such a thermally diverse and dynamic surface.

The dual-band procedure therefore cannot provide quantifiably accurate estimates of the actual area inhabited by material at temperature T_H because of a combination of these problems. However, by plotting the resulting P_H and T_C estimates against the corresponding PIT value from one of the channels used within the procedure, it is possible to ascertain the likely thermal distribution found within the pixel in question. This method is able to distinguish between pixels with a large proportion of the IFOV occupied by active lava flows and pixels that possess a large fractional area occupied by cooler material. This method also serves as a good indicator of the levels of flow activity within a pixel. Flows that expose a large amount of flow core will return relatively high estimates of P_H. Such a pixel thermal distribution will also result in a high PIT value. Within a diagram such as figure 4.21 and figure 4.23, pixels such as this will plot within the upper-right region. Pixels with an IFOV encompassing an area of cool ground material in addition to a lava flow will have a lower PIT value and return relatively lower values of P_H and T_C. These pixels will plot within the lower-left region of such diagrams as figure 4.21 and figure 4.23. Thus, a solution envelope spanning the lower-left to upper-right within P_H or T_C Vs $PIT_{channel}$ space is produced, and it is possible to gain from this the relative levels of activity present within a number of pixels plotted upon such a diagram.

The solution envelope will trend towards the upper-right in accordance with increasing levels of activity and the pixel IFOV completely filled by the flow. Because of the greater sensitivity of the dual-band procedure to changes within the area of the hottest

flow material, it is also possible to identify pixels with a bimodal thermal distribution that have the most active flows. In such pixels the relative estimates for P_H correspond with lower PIT values, resulting from the inclusion of an amount of cooler material. Because of the relatively large amount of radiance emitted at shorter wavelengths by the active flow, the procedure returns relatively high estimates of P_H. These points will lie off the lower-left to upper-right trend, with P_H values similar to the highest P_H values recorded for the most active flows. Such a scenario is interpreted for the ALI pixels indicated as close to the 2700m vent within figure 4.23.

By using such a method it is possible to identify the types of lava-flow activity present and also to classify the thermal distribution within pixels present by plotting all solutions for available pixels within the same chart. The Dual-band method is perhaps best used in this context as an indicator of the extent and character or flow activity within a pixel, rather than a measure to obtain exact fractional areas of exposed flow core. More advanced procedures for extracting quantitative estimates on the areal extent and thermal nature are now possible using instruments such as the Hyperspectral Hyperion instrument and discussed within Wright & Flynn (2003).

5. Effect of instrument elevation angle on estimates of sub-pixel resolution obtained by the dual-band solution

5.1.Introduction

In chapter 4 I described how modelled ALI pixels using synthetic data based on actual FLIR camera imagery of active lava flows can be used to analyse estimates of thermal detail within a pixel returned by the dual-band procedure. The resulting solutions were compared with the actual estimates of these values obtained from the original synthetic images. The synthetic images were used to vary parameters such as the amount of flow core exposed through fractures within the flow crust. The observation and detection of such features upon and within the surface of an actual lava flow will depend on the elevation angle of the instrument and its orientation with respect to the flow surface. Sections 4.7 to 4.9 all consider and simulate level lava surfaces within ALI data, and assume that the instrument is directly overhead. This control over the parameters used to create the original synthetic pixels can be extended to varying the look angle of the instrument. We may then analyse any difference in response from the dual-band procedure caused by varying instrument elevation angle.

This modelling ability is important when considering that lava flows tend to travel down-slope and are thus rarely actually imaged by satellite instruments in plan view. A similar effect is apparent when any lava flow is located on the edge of the ground data swath of space-based instruments. This can lead to perspective effects hiding sunken features within the flow crust. However the ALI possesses a relatively narrow swath width of ~75km (Lencioni et al, 1999). This results in an effective instrument elevation angle of 89.24° at the extreme edge of the instrument swath width, which is very close to the nadir view.

Instruments with a much greater swath width than the ALI, such as MODIS or AVHRR, will be affected to a greater extent by the angle subtended between the Earth's surface and the instrument when considering locations at the extreme edge of the data swath.

The effect of instrument view angle for pixels containing a lava flow within its FOV can be particularly important for flows that possess a well developed crust interspersed by many fractures exposing the flow core. If the viewing instrument is positioned at any angle other than at nadir (or vertical with respect to the flow surface), then a certain amount of exposed core will be occluded by the foreground of the surface of the flow. A greater area of the walls of the crack will also be exposed, which would not otherwise be detected if the instrument was at nadir. The walls of the crack will be at an intermediate temperature between the flow core and that of the crust (Lipman & Banks, 1987). The instrument will therefore detect an amount of exposed flow core inconsistent with the actual area exposed. The extent of this error will be compounded by the number and size of the cracks present exposing the flow core, the viewing angle of the instrument and the depths of the cracks themselves.

Many of the flows on Mt Etna when the original FLIR imagery was acquired were channelised flows with a well developed crust. Such flows on Mt Etna often possess a crust in the form of a rubbly and clinkery surface interspersed by many small cracks (Cashman et al, 1999). The type of crust possessed by a lava flow is a function of the viscosity, chemistry, temperature and the angle of the slope down which the flow is moving (Harris & Rowland, 2001). The more mature a flow then generally the thicker the crust will be (Calvari & Pinkerton, 1998). Any exposed core material will quickly chill towards temperatures associated with the flow crust. As a flow matures and slows the crust will grow in thickness and any cracks within this flow crust exposing the hottest temperatures associated with the flow core must be deep and narrow because of the nature of this crust.

Active flows may expose a larger fractional area of the exposed high temperatures associated with the core of the flow due to the constant entrainment of any developed crust and tearing apart due to frictional forces between the flow itself and any confining levées present (Lipman & Banks, 1987). Such fractures may be shallower as the more active flow has not developed a thick crust, and wider as the less developed crust is likely to be warmer and more ductile facilitating wider cracks. If the flow is moving then any cracks exposing the hot flow core will be deeper and narrow as a consequence of this type of crust (Lipman & Banks, 1987). Slopes with a high gradient often have the effect of accelerating the flow which leads to an increased rate of crust break-up and entrainment exposing the flow core (Harris & Rowland, 2001).

Any instrument observing such flows at nadir will be able to obtain a plan-view of the flow and detect these narrow cracks. If the flow is imaged by an instrument at an angle slightly off nadir, then the cracks may become indistinguishable in the resulting data. If the flow lies at the edge of the imaging swath or is moving down a slope angle away from the instrument nadir angle, then this will act to increasingly occlude any cracks present within the flow surface. We can replicate these effects within simulated imagery such as that used in chapter 3, and investigate the extent to which the dual-band procedure is sensitive to changing view angle.

5.2.Simulating varying instrument view angle within a simulated pixel

I have used here the same procedure as described in section 4.5 to create a simulated pixel at varying instrument angles. In order to model the presence of a number of cracks within the crust of the simulated flow it is necessary to discuss the requirements needed by the model in order to create a thermal distribution as close to that observed

within the FLIR data as possible. Figure 5.1 highlights the main problem associated with the detection of hot flow core material at the base of cracks in a flow crust. For simplicity the cracks within the model flow surface are modelled as linear furrows of constant depth and width orientated 90° to the look direction. As the elevation angle of the instrument decreases from 90° (nadir) to the horizontal then the apparent exposure of base of the cracks within the crust will decrease as the foreground of the image increases in apparent fractional area within the pixel FOV. Due to the instrument orientation an area occupied by the vertical crack walls will also increase in apparent fractional area as the angle of elevation decreases. This effect also applies if the flow is located on a slope, even if the instrument is at nadir.

This former effect will cease once the camera elevation angle is so low that the base of the crack becomes completely occluded by the foreground. At ever decreasing elevation angles below this angle, the apparent fractional area of the foreground crust will gradually occlude the apparent fractional area of the crack wall. At very low instrument elevation angles any cracks within the flow crust will be only indicated by a very small area of crack wall. This effect is apparent within the actual ground-based FLIR imagery (discussed in Chapter 4) obtained from lava flows on Mt Etna which have the added complexity of the inclusion of areas of background and sky within the FLIR image of lava flows. This is due to the low elevation angle of the FLIR camera mounted on a tripod with respect to the flow surface, and adds to the problems of simulating near-nadir satellite imagery.

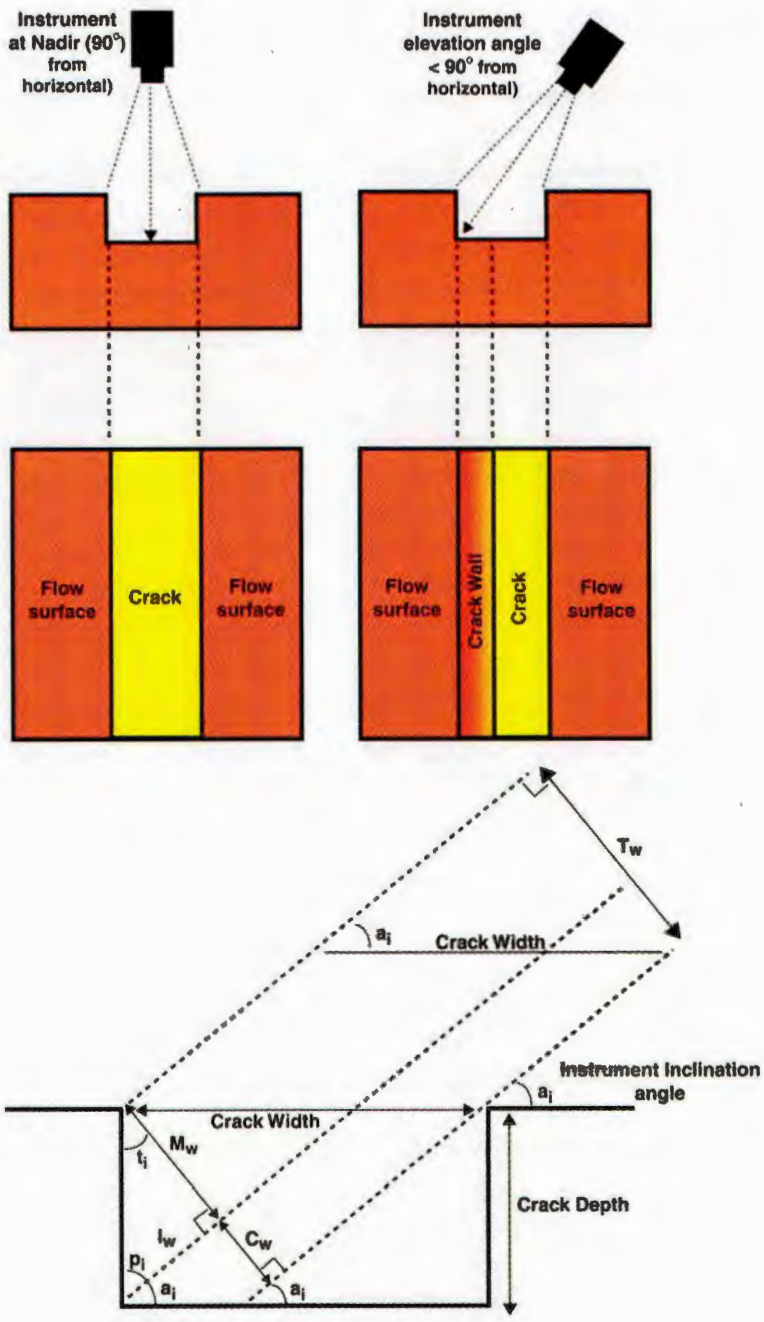

Figure 5.1: Diagram showing how the relative portions of crack floor and crack wall change as the instrument elevation angle changes.

Figure 5.1 displays these effects upon a simple case of a lava flow possessing a single 'crack' in the crust. As instrument elevation angle a_i decreases from nadir at 90° then the apparent area of crack wall will increase from nil when the instrument is at nadir. The following equations allow an estimate of the fractional area of the base of the crack, crack wall and the encroaching foreground to be made with varying elevation angle if the crack width and depth are known.

Using the notation in figure 5.1, T_w is the apparent width of the entire crack at angle a_i. M_w is the apparent dimension occupied by the crack wall within T_w, and C_w is the apparent dimension of the visible crack floor. If the elevation angle a_i=90° (nadir) then C_w=crack width. Hence,

$$T_w = \text{crack width} \cdot \sin(a_i) \qquad \text{(equation 5.1)}$$

$$M_w = (\text{crack depth} \cdot \cos(a_i)) \qquad \text{(equation 5.2)}$$

$$C_w = Tw - M_w \qquad \text{(equation 5.3)}$$

The minimum angle at which any crack floor material can be detected by the instrument may be given as:

$$\text{Minimum Angle} = 90 - \tan^{-1}(\text{crack width/crack depth}) \qquad \text{(equation 5.4)}$$

The relative areas of visible crack floor and walls are obtained by multiplying the dimensions returned from equations 5.1 to 5.4 by the chosen length for the cracks. The total fractional area occupied by the cracks in the simulated image is governed by the number of cracks required in the simulated image.

For the purposes of modelling, once the total required areas of the visible crack floor and the crack walls are known, these values are supplied to the IDL procedure used to create the simulated FLIR imagery based on artificial bell-shaped curves (section 4.6). A listing of this procedure is located in appendix IV. Temperature thresholds were used to identify the material found at the base of the cracks representative of the flow core (>850°C). As the area of the simulated pixel of ALI data is known (~900m^2), which is comprised of the initial 255 x 239 temperature pixel array (as we are simulating the original thermal camera, and assuming that its coverage is equivalent to an ALI pixel), then

it is possible to calculate the number of pixels associated with the material at the base of the cracks. Any pixels within this crack base-range of >850°C to the maximum temperature (~1043°C) that are in excess of the required number of pixels within this range, are reassigned temperatures consistent within the flow crust temperature range, defined as spanning from the minimum temperature (~300°C) to ~600°C. The number of pixels to be changed is based on the number of pixels occupying the fractional area to be adjusted. In addition to this the required number of pixels calculated within the crack wall temperature range (~601°C to 849°C) are checked, and if necessary reassigned to the crustal temperature range. The reassignment of pixels from one defined range to another is completed on a statistical basis within the model PDF histogram. Temperature bins within the range of temperatures for pixels to be reassigned with the greatest number of pixels, are assigned a correspondingly larger number of pixels from the original temperature range having pixels extracted than those temperature bins with fewer pixels. The temperature range associated with the crack walls are defined is spanning from the minimum temperature associated with the flow core range to the maximum temperature of the surface crust.

By adjusting the number of cracks and the viewing angle of the instrument and superimposing this changing thermal structure upon the original PDF histogram, an analysis of the sensitivity of the dual-band method to these changes within a simulated pixel can be attempted. This method allows only a simple replication of the complex dynamics governing the formation and changing nature of the crust of an active lava flow. This model considers only cracks of a uniform depth and size orientated in a single direction that possess vertical walls perpendicular to base of the crack. Therefore this model can only provide the simplest approximation of the true nature of a flow with a crust interspersed by a large number of fractures orientated in many different directions and at different depths. This method however, provides the ability to hint at the response of the dual-band procedure to changes associated with the elevation angle of the instrument.

5.3.Simulated pixel models with varying fractional crack areas exposed at different instrument elevation angles

Figure 5.2 displays a set of PDF histograms based on a simple unimodal pixel thermal structure with an increasing number of cracks of 0.1m depth, 0.1m wide and 1m long. Figure 5.2a depicts the simulated pixel as it appears within the image at nadir or plan view, the same as that used in the sections 4.5 to 4.9.

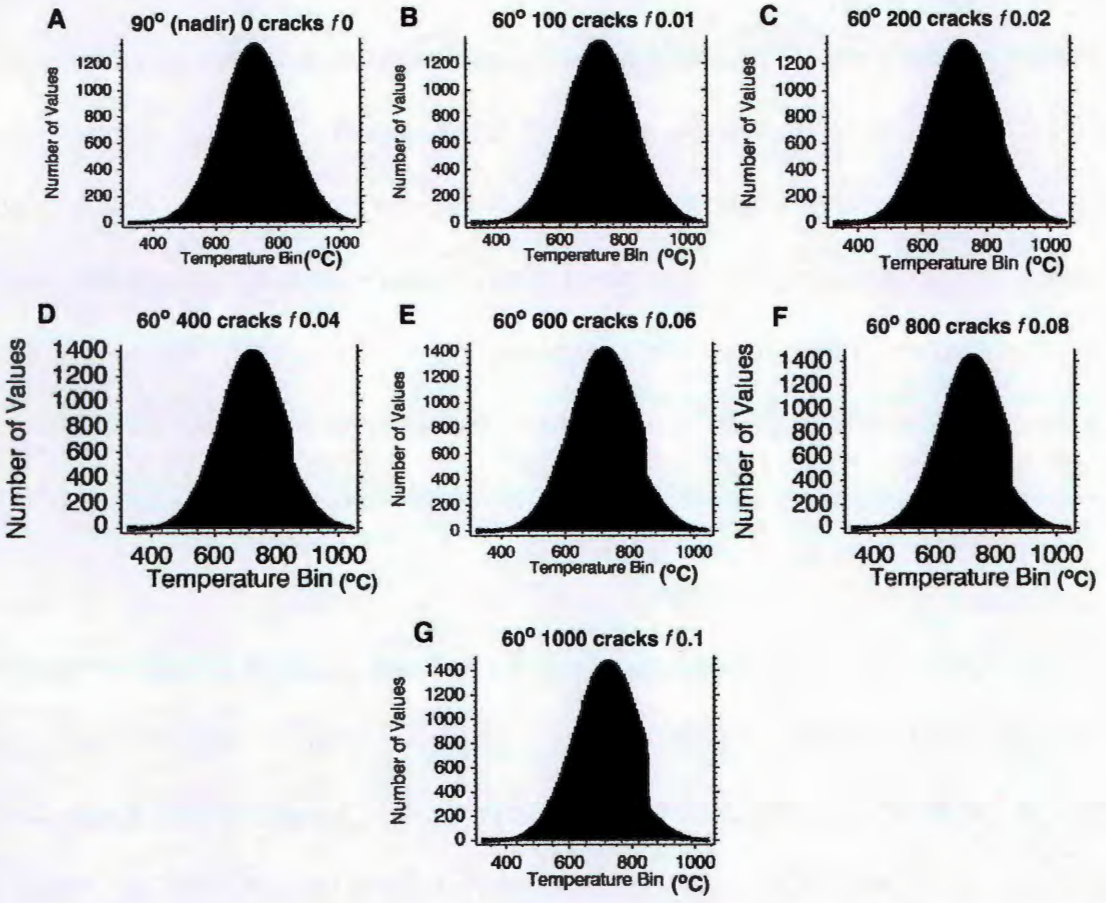

Figure 5.2: Simulation of increasing number of cracks within flow crust of a simple lava flow within a simulated pixel, and the effect upon the PDF histogram. In this instance each crack is simplified as 0.1m deep and 0.1m wide and as numbers increase within the simulations A to G the fractional area occupied by the cracks if viewed from directly above, increases. The view angle of the instrument is set at 60° from the horizontal.

The other 6 histograms in figure.5.2 show the change in shape of the PDF histogram due to the increasing number of cracks at a simulated image elevation angle of 60° from the horizontal.

This instrument elevation angle is equivalent to a surface slope angle of 30°. This is also a similar angle to that which might be expected if a lava flow was situated close to the edge of the imaging swath of an instrument such as ALI. As the fractional area occupied by the cracks within the simulated pixel FOV increases, the shape of the bell-shaped curve becomes increasingly skewed. This is due to the small amount of high temperature flow core material visible at the base of each crack because of the relatively low instrument elevation angle and the square profile of the crack (0.1m depth x 0.1m width).

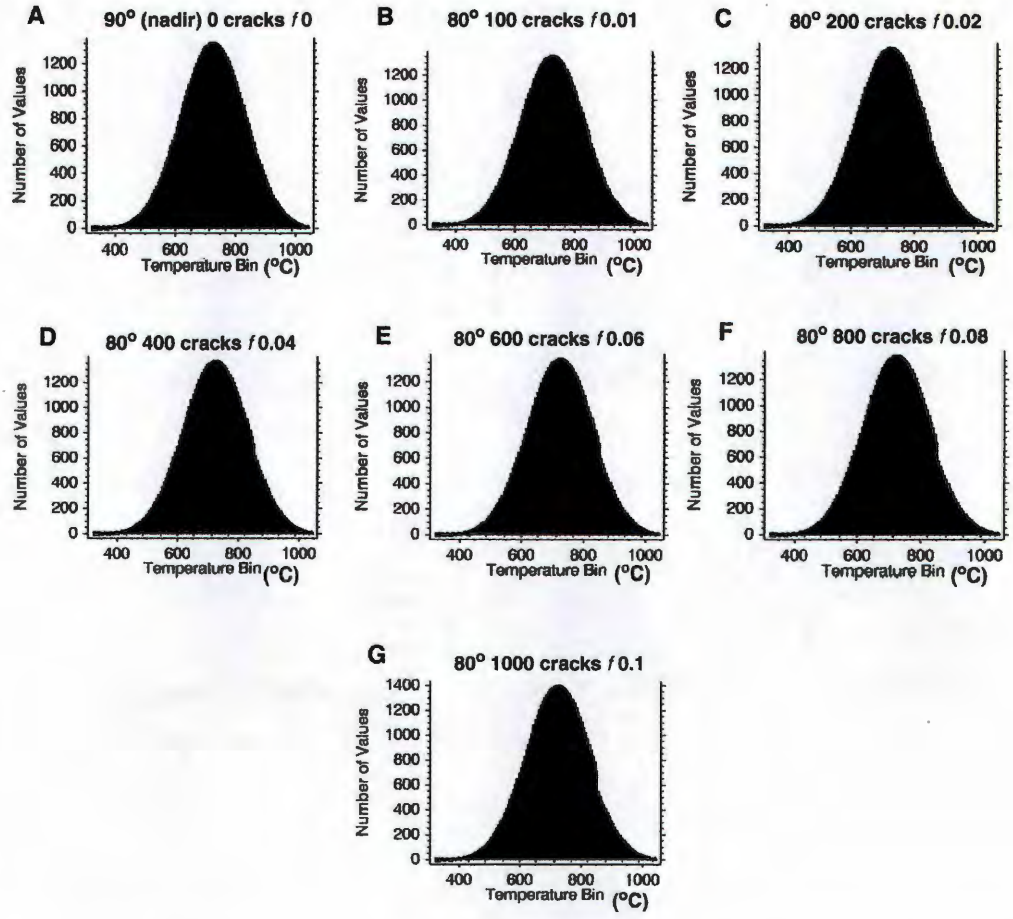

Figure 5.3: Simulation of increasing number of cracks within flow crust of a simple lava flow within a simulated pixel, and the effect upon the PDF histogram. In this instance each crack is simplified as 0.1m deep and 0.1m wide and as numbers increase within the simulations A to G the fractional area occupied by the cracks if viewed from directly above, increases. The view angle of the instrument is set at 80° from the horizontal but is otherwise identical to figure5.2.

This is why the number of pixels within the temperature range associated with the crack becomes increasingly low, whilst the height of the curve increases as pixels are reassigned to the crack wall temperature range. At this elevation angle there are more pixels associated with crack walls than with the crack base.

Figure 5.3 displays a set of 7 PDF histograms similar to those within figure5.2. These PDF histograms use the same crack dimensions and increasing fractional area within each model, but consider an instrument elevation angle of 80°. This is equivalent to a surface slope angle of 10° if viewed from nadir. This lower effective angle clearly relates to a set of less-skewed PDF histograms as there is a consistently less obscured area of material at the base of cracks within this set of models.

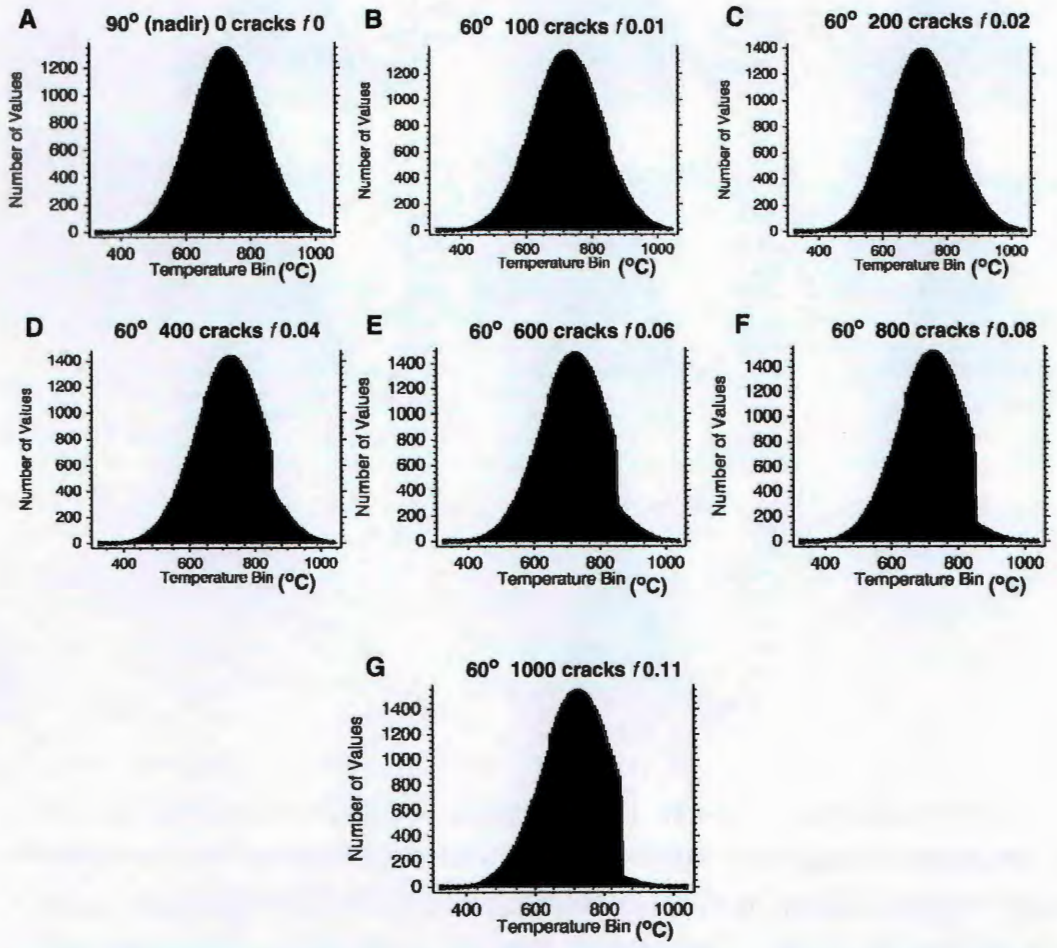

Figure 5.4: Simulation of increasing number of cracks within flow crust of a simple lava flow within a simulated pixel, and the effect upon the PDF histogram. In this instance each crack is simplified as 0.2m deep and 0.05m wide and as numbers increase within the simulations A to G the fractional area occupied by the cracks if viewed from directly above, increases. The view angle of the instrument is set at 60° from the horizontal.

Consequently there will be less pixels available to reassign to the temperature range consistent with the crack walls. This leads to the less skewed appearance of this set of PDF histograms than those within the previous figures.

In figure 5.4 I consider a set of simulated pixels in a similar manner to those displayed within figure5.2, except that the cracks modelled are narrower and deeper than those in the two earlier models with a depth of 0.2m and a width of 0.05m.

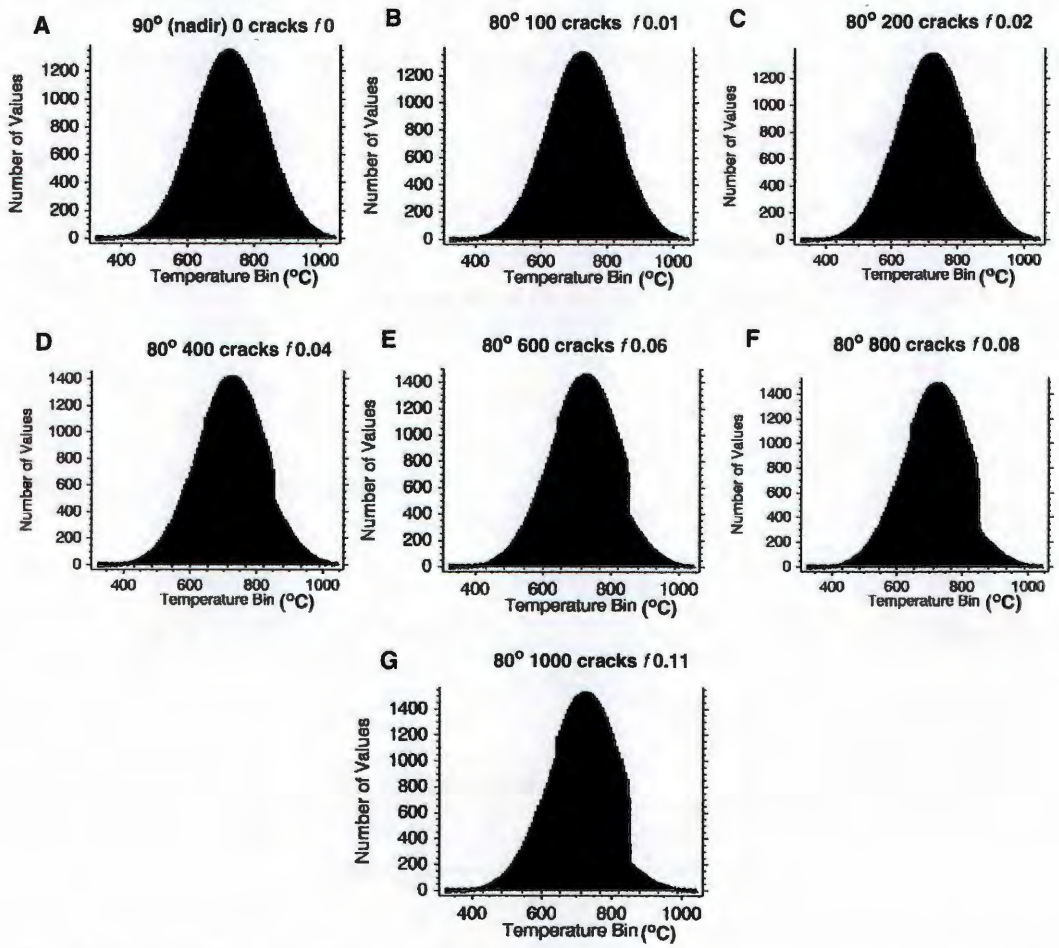

Figure 5.5: Simulation of increasing number of cracks within flow crust of a simple lava flow within a simulated pixel, and the effect upon the PDF histogram. In this instance each crack is simplified as 0.2m deep and 0.05m wide and as numbers increase within the simulations A to G the fractional area occupied by the cracks if viewed from directly above, increases. The view angle of the instrument is set at 80° from the horizontal but is otherwise identical to figure 5.4.

With this slope angle and narrower but deeper cracks the base of the crack floor is obscured as the slope angle is less than the maximum angle of 75° obtained by using

equation 5.4. This has resulted in a set of PDF histograms with a more skewed appearance and with very few pixels with temperatures greater than 850°C, than those model pixels at the same angle but different crack geometry within figure5.2.

In figure 5.5 I consider a set of model pixels with the same crack geometry increasing in numbers at the same rate as those in figure 5.4 but viewed at an effective instrument elevation angle of 80°. This is the same angle as used in figure 5.3 and is equivalent to an effective slope angle of 10°. The resulting PDF histograms display a less skewed nature than those within figure 5.4, but due to the narrower and deeper cracks a significant number of pixels above the 850°C crack base threshold temperature have been reassigned with increasing crack numbers.

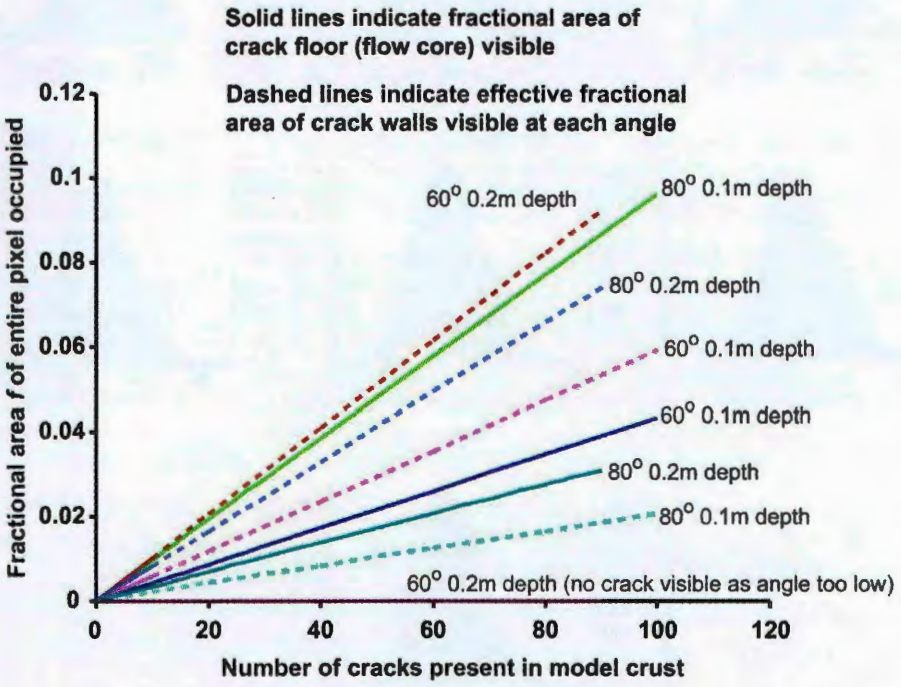

Figure 5.6: Variation of actual exposed flow core at base of crack within flow crust and view angle (solid lines). Dashed lines indicate the apparent fractional area within the simulated pixel FOV occupied by the crack walls. Note that for simulation involving cracks at 0.2m depth at an instrument angle of 60°, no crack floor is visible as crack floor is occluded by the flow crust in the foreground of the pixel FOV.

This set of simple simulated pixel models allows an assessment of how the dual-band procedure responds to the more realistic scenario of pixels containing lava flows situated on slopes or at the extreme edges of the image swath. Figure 5.6 summarises the

PDF histogram models within figures 5.2 to 5.5 in terms of the total pixel fractional areas occupied by the crack and walls, and how these values vary with changing view angle.

Figure 5.6 shows that the visible fractional area associated with the walls of the cracks (dashed lines) is greater for models with deeper and narrower cracks at both 60°and 80°. The shallower 01.m deep by 0.1m wide cracks possess fractional areas *f* 0.01 to *f* 0.02, lower than the deeper crack model for the final model run with the maximum number of cracks. The deeper crack models consistently record greater areas of exposed crack wall than the shallower crack models. Conversely the deeper crack models record consistently lower fractional areas for the exposed crack floors, than those areas for the shallow crack models. Figure 5.6 highlights that for any effective instrument elevation angle, narrow deep cracks will expose lower fractional areas from the base of the cracks than shallower wider cracks. Deep and narrow cracks will contribute a greater range of temperatures associated with temperatures ranging from the near-magmatic core temperature to the chilled crust temperature.

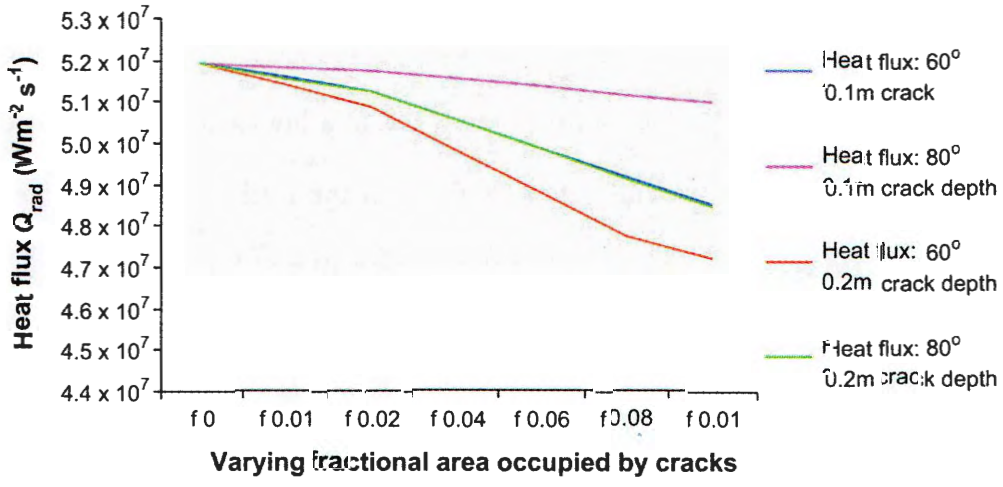

Figure 5.7: Variation in emitted heat flux, Q_{rad}, calculated for the 4 synthetic pixels described over the varying numbers and depths of cracks.

In the previous chapter I used the heat flux, Q_{rad}, calculated using the Stefan-Boltzmann equation to provide a basis for the comparison between the results obtained from the dual-band method and the thermal structure within a simulated pixel. I will use the same analysis process here in order to analyse the variation in Q_{rad} due to changing view angle and simulated surface morphology.

The actual values of Q_{rad} were calculated from the 4 models outlined in figures 5.2, 5.3, 5.4 and 5.5 using equation 4.4 for each of the 7 levels of variation in crack area exposing the flows hot inner core. Figure 5.7 displays the variation in Q_{rad} for each of the 4 models over these 7 levels of fractional area occupied by cracks. The general trend of a decrease in Q_{rad} is because as the number of cracks within the modelled flow surface increase then the area of material radiating at higher temperatures representing the crack floors will decrease due to the greater area of the cooler crack walls exposed as a consequence of the off-nadir viewing geometry. This effect will be most noticeable for those models with the lowest viewing inclination angle and the deepest cracks, and this is exactly what is shown by figure 5.7. The red line indicating the greatest decrease in Q_{rad} over the 7 variation levels is the model with deeper cracks and an inclination angle of 60°. The green line also displays a significant decrease in Q_{rad} and this line indicates the response of the model with deep, narrow cracks but at a higher inclination angle of 80°. The deeper cracks are of the same width as those in the earlier model and this relative narrowness increases the likelihood that cooler crack wall material will be detected rather than the hot crack floor material, and therefore a decrease in Q_{rad}. Conversely, the model with the shallower cracks and with the highest inclination angle close to nadir of 80° shows the least decrease in Q_{rad}. Therefore, it is possible to relate the variation in detected heat flux, Q_{rad} to the surface morphology of a lava flow and the viewing angle used. In the next sections I will investigate whether this can be replicated using the dual-band method.

5.4.Response of the dual-band procedure to synthetic pixels of a simple lava flow imaged at various angles

Single integrated radiance values were calculated for each of the simulated pixels in figures 5.2 to 5.5 and were supplied to the IDL procedure that calculates dual-band solutions for each model over a range of assumed T_H temperatures (described in section 4.8). The subsequent dual-band solutions were then converted to heat flux Q_{rad} using equation 4.3 in order to provide a consistent comparison. The results are shown in figures 5.8, 5.9, 5.10 and 5.11. Each model within the original PDF histograms with increasing numbers of cracks is identified by the total occupying fraction of cracks superimposed upon the basic histogram. The model "f 0" is the control pixel of the basic model PDF histogram obtained at nadir. No crack walls are visible at all within this pixel model, and the original PDF histogram therefore remains unaltered. With an increasing number of cracks the fractional area f increases and the original PDF histogram is adjusted accordingly. Therefore when the model pixel is considered at nadir the full amount of material associated with the temperatures found at the base of cracks is present. With increasing numbers of cracks the area occupied by material at these temperatures is correspondingly reduced. Those areas in the simulated model at temperatures within the range of the crack walls are then increased accordingly.

The values for Q_{rad} shown in figure 5.8 (60° inclination angle) spans a greater range than the equivalent values for Q_{rad} plotted in figure 5.9 (80° inclination angle). The cracks in both these sets of models possess the same geometry, only the instrument inclination angle changes. Solutions in these two figures become available from increasingly higher T_H values, therefore Q_{rad} may only be calculated for these higher values.

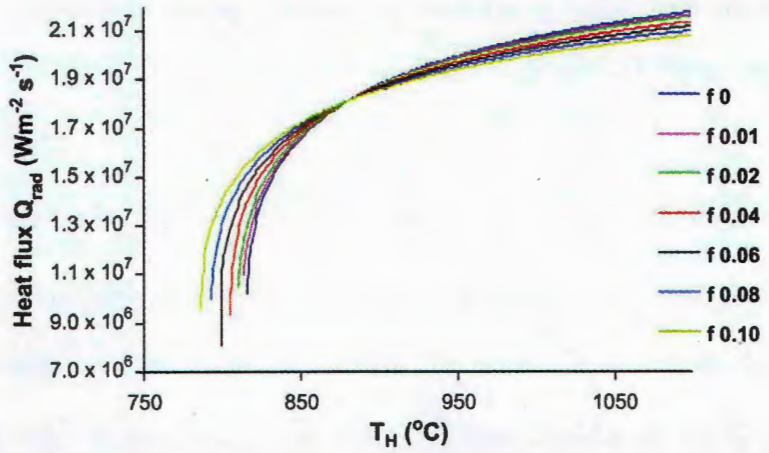

Figure 5.8: Results from dual-band procedure converted to heat flux for the simulated pixels in figure 5.2 with shallow (0.1m) cracks and at an inclination angle of 60°.

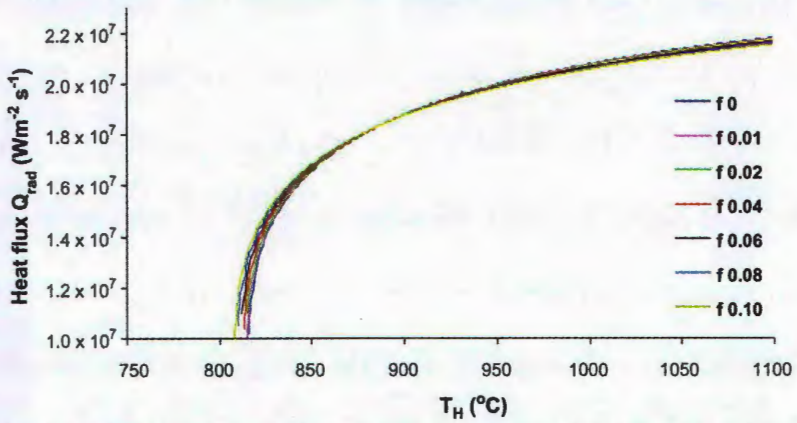

Figure 5.9: Results from dual-band procedure converted to heat flux for the simulated pixels in figure 5.3 with shallow (0.1m) cracks and at an inclination angle of 80°.

The greatest range in calculated Q_{rad} at higher values of T_H is given in figure 5.8, which reflects the trend shown for this series of model runs in figure 5.7, in which those simulations with the lowest simulated instrument inclination angles displayed the greatest variation in Q_{rad} than those models at higher instrument inclination angles. The spread of the values for Q_{rad} in figure 5.9 at the same higher T_H values as in figure 5.8, is much more restricted, and is difficult to distinguish between the individual model runs. The fractional area occupied by hot material associated with the crack floor changes less in the latter set of both models, and this is reflected in these values for Q_{rad}. Where the amount of exposed crack floor material is at its lowest in model f 0.1 when viewed at 60°, then this is identified by the procedure as returning the lowest estimates for Q_{rad} at f 0.1 in figure 5.8. We would expect to record lower values for Q_{rad} with decreasing instrument elevation

angle as the FOV is increasingly filled by cooler crust as the hottest material at the base of the cracks is occluded by material within the foreground. This effect will be more noticeable for the second model with an 80° as more crack floor material will be consistently visible than for the model at 60°.

Therefore it is clear from figures 5.8 and 5.9 that they reflect the trends shown in figure 5.7. However, by comparison with figure 5.7 it is immediately apparent that estimates for Q_{rad} obtained using the dual-band method are severe estimates of the actual values. This is consistent with the findings of Chapter 4, as is the observation that the dual-band method can detect the relative variation in the actual values of Q_{rad}. It is apparent that the dual-band procedure displays a greater response to the change in fractional area associated with hot material exposed at the base of cracks and crack walls apparent within the set of models viewed at lower effective instrument elevation angles than those models viewed at higher angles.

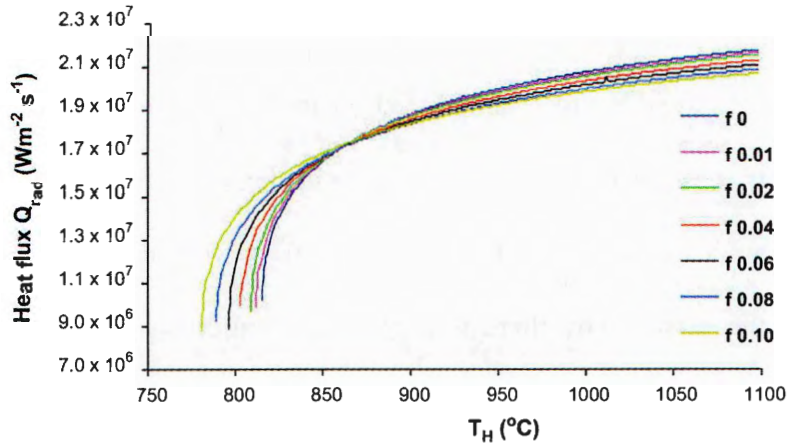

Figure 5.10: Results from dual-band procedure converted to heat flux for the simulated pixel in figure5.4.

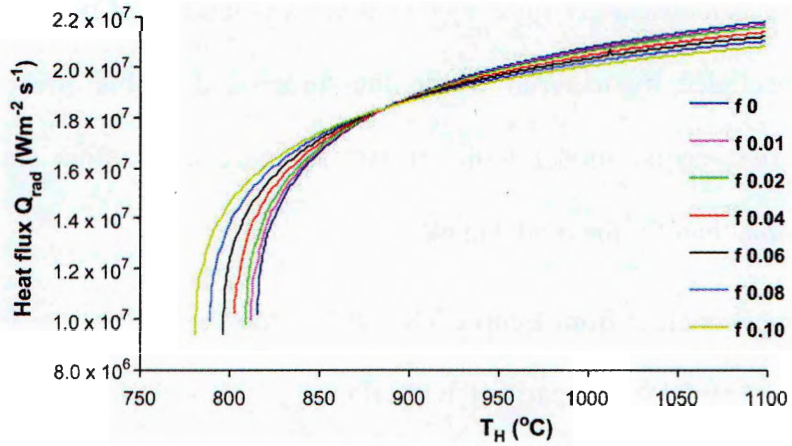

Figure 5.11: Results from dual-band procedure converted to heat flux for the simulated pixel in figure5.5.

Figure 5.10 displays the corresponding set of values for Q_{rad} calculated from solutions obtained for the two sets of models in figure 5.4 and 5.5 using a deeper modelled crack depth of 0.2m. The pattern of values of Q_{rad} returned for these two model runs is very similar to those in figure 5.8. However, there is much less variation between the values of Q_{rad} for each temperature T_H supplied to the two models in figures 5.10 and 5.11 at the two different instrument inclination angles, than those within figures 5.8 and 5.9. In figure 5.7 I showed how the actual values of Q_{rad} can change at high instrument inclination angles in a more pronounced manner if the considered cracks were deeper. In this simulation the cooler crack walls will fill a greater fraction of the FOV due to the deeper crack. This is the reason why there is a greater variation in Q_{rad} in figure 5.11 at an inclination angle of 80°. This reflects the similar trends shown in figure 5.7 for decrease in Q_{rad} with modelled crack fractional area.

The values for Q_{rad} calculated from the set of dual-band solutions shown in figures 5.10 and 5.11 highlight again that the procedure is sensitive to high temperature material associated with exposed fresh lava, more so than even moderately hot exposed surfaces such as flow crust in the region 650 to 850°C. The greatest variations between dual-band estimates for Q_{rad} are associated with model pixels possessing the greatest variation in the amount of hot material exposed at the base of the modelled number of cracks.

Further consultation of figure 5.7 shows that the values for Q_{rad} obtained from the results of the dual-band methods are again a severe underestimate. But yet again, it is apparent that the dual-band method applied to heat flux, is still able to detect the variation in Q_{rad} due to effects related to relatively small changes in the surface morphology of lava flows and viewing instrument inclination angle with respect to the flow.

5.5. Conclusions & discussion: To what extent does the elevation angle of the instrument affect the dual-band procedure?

It is apparent from the study of the previous figures that the dual-band procedure is sensitive to changes in the amount of hot core exposed in fractures and observed at different angles. The models described and used are an extensive simplification of the true nature of such a surface found in reality. Cracks in the crust of real lava flows are almost always extensive and orientated at many angles. The cracks themselves are of varying sizes and dimensions and the walls of the cracks will be at differing angles so that the simple rectangular "trench" considered as cracks within my model are a gross-simplification.

However, the results obtained here by simulation of the thermal structure within an ALI pixel serve as an indication of the processes affecting the number and type of dual-band solutions obtained with actual ALI data. The variation in emitted radiance from the simulated pixels resulting from the adjustment of the effective instrument elevation angle with respect to the flow surface and the fractional area occupied by cracks exposing the flow core, has been shown here to produce the greatest variation in results at low angles. Cracks possessing narrow and deep geometries where the greatest amount of flow core is hidden, even at relatively high effective instrument elevation angles, also result in a larger variation in emitted Q_{rad} from the simulated pixel. This scenario relates mainly to lava

flows situated on the extreme edge of any viewing instruments data swath, or flows that are travelling down-slope.

In these cases the dual-band procedure provides estimates of Q_{rad} for all assumed values of T_H that are below those estimates obtained as if the flow was level (i.e. the control value give at $f0$ in each of figures 5.7 to 5.11). As I found in the previous chapter, values of T_H> ~950°should be used to provide consistent results. This is due to the decrease in apparent emitted Q_{rad} due to the viewing geometry. Figures 5.8, 5.9, 5.10 and 5.11 indicate that the greater the actual number of cracks exposed, then the greater the underestimate for Q_{rad} provided by the procedure at the lowest inclination angles. This effect is greatest at lower inclination angles where the majority of cracks are deep and narrow.

When this summary is considered in addition to the conclusions from chapter 4 it is clear that the dual-band procedure will return estimates further removed from reality for surfaces inclined away from the instrument. However, it is clear that despite this the dual-band method can be used to provide estimates of Q_{rad} that can distinguish between the greatest variation between flow surfaces that possess the greatest areas of exposed hot temperatures.

The findings of this chapter show the importance of an integrated approach that must be used when applying such models as the dual-band method to Earth Observation data, such as that from ALI, Landsat ETM+, ASTER among others. Although I have shown that estimates of heat flux calculated using the dual-band method are severe underestimates, yet still provide important thermal structure information, this study highlights the need for consideration of the ground situation. It is not enough to derive estimates for heat flux from a simple EO scene and expect this to be a realistic representation of the actual values. This study shows that the inclination angle of an instrument is important when considering the total heat flux from a lava flow. The

inclination angle of the lava flow with respect to the satellite instrument will be a combination of the position of the satellite with respect to the ground location (i.e. nadir, edge of swath etc) as well as the local topography (i.e. a lava flow located on the steep flanks of a cinder cone). Such models as FLOWGO described in Harris & Rowland (2001) require a satellite estimate of Q_{rad} as part of this model, yet also use topographical data (whether derived from radar derived DEM {Digital Elevation Models} or from maps) to provide a basis for estimating the rate of advance due to slope angle. The findings of this chapter strongly suggest that the ground situation must be considered, and therefore possibly such data as used here from the EO-1 ALI must be used in conjunction with DEM's to provide an estimate of the orientation of the lava flow with respect to the instrument.

However, in order to accomplish this, further work needs to be undertaken to specifically relate the variation in Q_{rad} with viewing orientation as well as the surface morphology of the flow. The FLIR thermal camera imagery which provided the basis for the simulation lava flows used in this and the previous chapter was obtained at low elevation angles by necessity of the field conditions at the time. A specific campaign needs to be undertaken to fully understand these relationships and with different types of lava flows. For instance, the flows used in the FLIR camera imagery were A'a flows on the flanks of Mt Etna in Sicily. These rough surfaces will not translate to the smoother Pahoehoe lava flows commonly erupted at Kilauea in Hawai'I for example. Channelised flows, as well as spatter fed rootless lava flows resulting from fire fountaining events all need to be measured in such a way as to provide an analysis of the variation of Q_{rad} with respect to instrument inclination angle and/or underlying topography. This study is no mean feat, and will be costly and complicated to implement, especially in safety. Therefore, software modelling of the surface thermal structure such as that undertaken here, albeit further developed, must be used to provide valuable input for estimates of Q_{rad} for lava flows from space-based instruments.

This study further highlights the trends shown within chapter 4: the more accurate a simulated surface (or pixel area) is, then the greater the underestimates of f provided by the dual-band method. Better methods of modelling the thermal structure in a pixel, as described here and in chapter 4, clearly show the shortcomings of the dual-band method, yet if used synergistically as suggested in Chapter 4, can still provide a valuable reference as to the likely thermal structure within a pixel.

6. Comparison of the response of the Landsat 7 Enhanced Thematic Mapper + and the Earth Observing-1 Advanced Land Imager over active lava flows

A paper based on this chapter was submitted 05/2002 to the Journal of Volcanology and Geothermal Research as the following paper: "Comparison of the Landsat 7 ETM+ and EO-1 Advanced Land Imager over Active Lava Flows,; Stephen J. Donegan and Luke P. Flynn, Journal of Volcanology and Geothermal Research, 2004, V 135, N 1-2

6.1.Introduction

High spatial resolution remote sensing instruments such as the Landsat 7 Enhanced Thematic Mapper Plus (ETM+) have been successfully used to identify and interpret a wide variety of volcanic features since the 1970's. Since then an archive of data has been gradually constructed from the 6 previously successful Landsat missions enabling consistent monitoring of volcanic systems for periods spanning years to decades. In the near future there is a requirement for a Landsat 8 mission equipped with an instrument similar to the ETM+. Any future replacement instrument must satisfy data continuity requirements so that the current archive can be maintained. That is, data resulting from newer instruments must be directly comparable to the preceding Landsat data. The Advanced Land Imager (ALI) is one of three instruments operational on the Earth Observing 1 (EO-1) satellite launched in November 2000, and is intended to test new technologies for such a future Landsat mission.

With regards to volcanological observations we aim in this paper to assess the performance of the ALI with respect to ETM+ by analysing their relative responses to active lava flows using the well established 'dual-band' technique for extracting sub pixel thermal information. This technique was first described by Matson & Dozier (1981) and

has been further adapted by Rothery et al (1987) and used by many workers such as Pieri et al (1990), Oppenheimer (1991) and Oppenheimer et al (1993). The dual-band procedure has proved a highly useful method of extracting information on sub-pixel thermal resolution, and is a familiar method to use to assess various properties of active volcanic features. This method has been described with in chapter 1 and discussed within chapters 4 and 5.

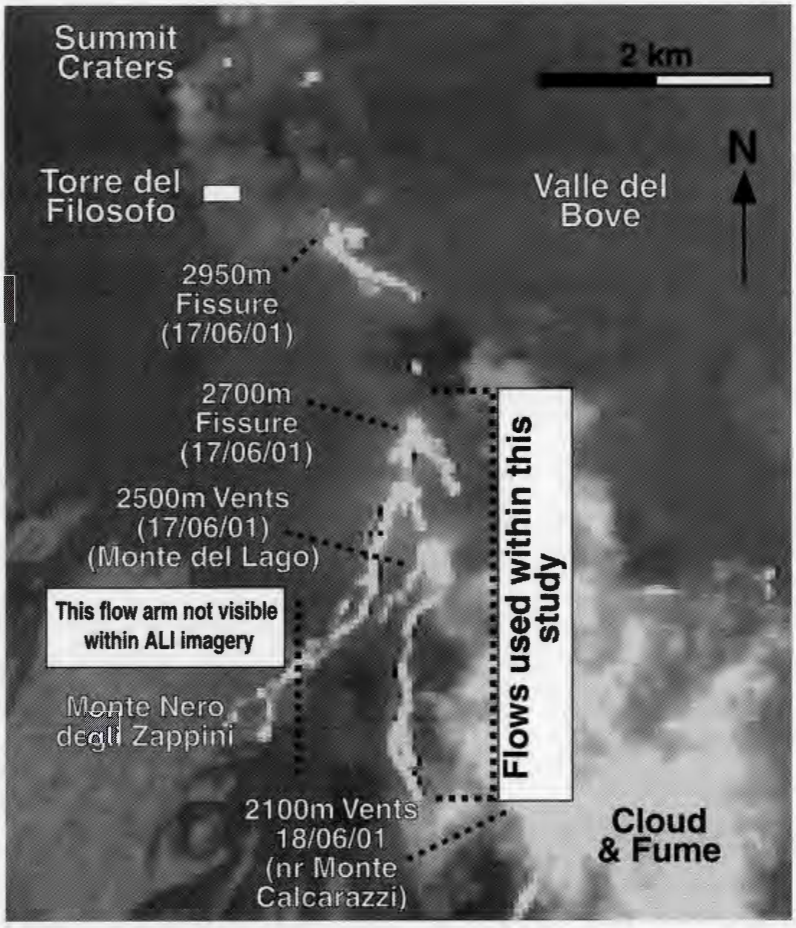

Figure 6.1: Image of the main Mt Etna flow-field extracted from ETM+ imagery from July 29 2001. Flows not included here are in the Valle del Leone to the north of the Valle del Bove and the continuation of the south flank flows from the vents at 2100m fissure in the area of Monti Calcarazzi towards the town of Nicolosi. The flows discussed in the main section of the paper are highlighted. Information summarised from Behnke & Neri (2003).

The response of the ETM+ and many of its predecessor instruments to active lava flows as well as other volcanic phenomena is well documented as are the resulting problems with sensor saturation and malfunction encountered over such flows (e.g. Flynn

& Mouginis-Mark, (1994), Harris et al, (1998),Flynn et al, (2001)). By using near-simultaneously acquired ETM+ and ALI data from the July 2001 Mt. Etna eruption we investigate the equivalent response of the ALI to active lava flows. I show how the new SWIR channels present on the ALI aid in obtaining successful dual-band solutions.

6.2.The 17th July-9th August 2001 flank eruption of Mt. Etna

Mt Etna is a large complex stratovolcano situated north of the city of Catania on the Mediterranean island of Sicily. Activity at Etna has been often documented since continuous records began at least 4 centuries ago (Romano & Sturiale, 1982). Activity since 1993 has often been confined to paroxysmal Strombolian eruptions from the summit craters feeding rootless lava flows. These eruptive phases have been interspersed by almost continuous degassing from the summit crater complex. In 1991 a flank eruption began which saw eruptive fissures open on the flanks of the volcano, feeding flows into the Valle del Bove which continued for 2 years (Wright et al, 2000).

6.3.Use of ALI & ETM+ data for remote sensing of volcanoes

(a) Landsat 7 Enhanced Thematic Mapper plus

Channel	Wavelength (μm)	Saturation Radiance (Low gain) W/(m^2 sr μm)	Saturation Radiance (High gain) W/(m^2 sr μm)	Dynamic Range (T°C) (Low gain)	Dynamic Range (T°C) (High gain)	Pixel size (m)
1	0.45 - 0.52	285.7	190.0	1181 - 1547	1071 - 1502	30
2	0.53 - 0.61	291.3	193.7	995 - 1525	893 - 1292	30
3	0.63 - 0.69	225.0	149.6	849 - 1159	755 - 1120	30
4	0.78 - 0.90	225.0	149.6	669 - 952	588 - 915	30
5	1.55 - 1.75	47.3	31.5	258 - 440	209 - 416	30
6	10.4 - 12.5	17.21	12.78	-91 - 76	-28 - 50	60
7	2.09 - 2.35	16.7	11.10	132 - 276	93 - 256	30
8 (Pan)	0.52 - 0.90	235.0	15.63	799 - 1094	728 - 1056	15

(b) EO-1 Advanced Land Imager

Channel	Wavelength (μm)	Saturation Radiance W/(m^2 sr μm)	Saturation Temperature (T°C)	Pixel size (m)
1p	0.433 - 0.453	~1000	~1775	30
1	0.45 - 0.515	~1050	~1666	30
2	0.525 - 0.605	~690	~1424	30
3	0.63 - 0.69	~450	~1215	30
4	0.775 - 0.805	~280	~1007	30
4p	0.845 - 0.89	~240	~919	30
5p	1.2 - 1.3	~210	~670	30
5	1.55 - 1.75	~85	~471	30
7	2.08 - 2.35	~21	~285	30
Pan	0.48 - 0.69	~88	~1182	10

(c) ALI Vs. ETM+ instrument characteristics

	ALI	ETM
Data rate (Mbps)	300	150
Signal to Noise Ratio Estimated at 5% Earth surface reflectance (Bicknell et al, 1999)	ALI: 5-6 x ETM+ equivalent band	
Quantisation	12 bit	8bit

Table 6.1: Basic characteristics of the two instruments. (a) ETM+ (Channel gain settings used in "Volcano mode" indicated in bold and shaded), (b) ALI (Original instrument units quoted in $mW/(cm^2\ sr\ \mu m)$ but converted here to $W/(m^2\ sr\ \mu m)$ for straight comparison with ETM+) and (c) Instrument statistics. Information for ALI summarised from (Mendenhall et al, 1999). ETM+ information summarised from the Landsat 7 Science Data Users Handbook

The next flank eruption to take place on Mt. Etna began on 17th July 2001 and continued until 9th August 2001 (Behncke & Neri, 2003). Figure 6.1 displays a scene taken from ETM+ channel 5 and highlights the main features of the resulting flow-field, as well as the flows used in the main section of this study as a basis for the comparison. This eruption began with various fissures opening at different levels between 2100m and 2950m elevation on the north and south flanks of Mt. Etna. Over the following 2 days, lava flows descended eastwards into the Valle del Bove and southwards towards the town of Nicolosi. On the night of 19th/20th July a fissure opened up on the north flank of Etna within the Valle del Leone, which fed a flow that travelled towards Monte Simone in the northern part of the Valle del Bove. By 29th the activity at the Valle del Leone vent had declined and the flow had begun to stagnate. The main fissures still actively erupting by 29th July were the 2900m, 2700m and 2100m fissures, which continued to actively feed large flows down the south flank past the Riffugio Sapienza and Monte Silvestri towards Monte Concillio (Behncke & Neri, 2003).

This eruption provided an excellent opportunity to use the resulting lava flows to compare the recently launched ALI against ETM+ in terms of solutions to the dual-band model.

A major factor in deciding the effectiveness of an instrument for the remote sensing of high temperature surfaces such as lava flows is the dynamic range of each of the instrument channels. The dynamic range is the span of radiances to which each channel is sensitive. Radiance exceeding the detector limit for a channel will result in that channel becoming saturated. Each channel also has a minimum radiance threshold. Any surface

emitting radiance below the channel threshold will remain undetected by that channel. The dynamic range of both the ETM+ and ALI instruments is highlighted within table 6.1.

Planck's law describes the relationship between the surface temperature of a blackbody and the emitted radiance with wavelength.

$$L_{(\lambda T)} = c_1 / \pi\lambda^5(\exp(c_2/\lambda T)-1) \qquad \text{(Equation 6.1)}$$

Where $c_1 = 3.742 \times 10^{-16} W/m^2$, $c_2 = 1.4388 \times 10^{-2}$ m K, $L_\lambda(T)$ is the spectral radiance calculated from the pixel DN, λ is the centre wavelength of the ETM+ or ALI channel in use and T is the temperature in kelvins (Rothery et al, 1988). Planck's law predicts that hot surfaces will radiate more than a cooler surface at all wavelengths, but increasingly so at shorter wavelengths. This has implications for remote sensing of volcanoes with instruments such as ETM+ and ALI with a number of channels placed at discrete wavelengths. Lava flows emit strongly in the SWIR spectral region (Rothery et al, 1988), in which both ETM+ and ALI have several channels. A lava flow with a surface temperature in the region of 900°C will radiate strongly at 1.5 – 3.5µm whereas the cool ground surrounding a lava flow with a surface temperature of ~10-20°C will radiate most strongly in the wavelength region of 10-12µm. Therefore increasingly active lava flows (i.e. those with greater areas of high temperature material exposed) will emit more strongly within channels placed at shorter wavelengths within the SWIR (ETM+ channel 5, ALI channels 5, 5p and 4p) than those channels at longer wavelengths within the SWIR (ETM+ and ALI channels 7).

6.4.ALI & ETM+: Instrument description

ETM+ is the result of 27 years of constant development from the first multispectral imaging instruments placed aboard Landsat 1 in 1972. The Landsat program has provided over 25 years worth of high spatial resolution calibrated data. It is therefore possible to accurately compare recently acquired ETM+ imagery with data acquired by the earlier Landsat Thematic Mapper (TM) instruments. It is vital to verify that any future replacement instruments can maintain this historical data continuity. The development and improvement of each successive TM instrument has resulted in the ETM+, an instrument with 7 channels placed at various wavelengths conducive to various scientific investigations. These 7 multispectral channels span the visible and near infrared (VNIR) and short-wave infrared (SWIR) spectral regions with a ground resolution pixel size of 30m, and the thermal infrared (TIR) spectral region with a ground resolution pixel size of 60m. ETM+ also incorporates a panchromatic channel with an improved spatial resolution of 15m pixel size. Table 6.1a summarises the spectral placement and radiometric parameters of ETM+.

The ALI is one of three instruments aboard the EO-1, the first satellite of NASA's New Millennium Program (Lencioni et al, 1999). ALI was designed with the intent to provide images that are directly comparable to Landsat 7 ETM+, but with the addition of three extra channels (Lencioni et al, 1999). This had to be achieved for significantly less cost within a physically smaller instrument package with the view that the technology would be incorporated into a future replacement ETM+ instrument. The ALI incorporates 9 multispectral channels, 6 of which are equivalent to ETM+ channels. Of the three additional channels, ALI 4p lies within the ETM channel 4 bandpass; ALI 5p is situated between ETM+ channels 5 & 4, and ALI 1p is placed within the visible region. These additional channels were included to avoid water vapour absorption lines (splitting of ETM+4 into ALI4 & ALI4p) (Bicknell et al, 1999) and to increase coverage within the

SWIR. ALI also includes a panchromatic channel similar to that on ETM+. The pixel size of the ALI panchromatic channel is 10m with a narrower bandpass centred at a slightly shorter wavelength than the panchromatic band of ETM+. ALI does not have a channel within the TIR equivalent to ETM+ channel 6. Table 6.1b summarises the main features of ALI.

The ETM+ orbits at an altitude of 705km with a 10am equator crossing time, which when combined with the 185km ground image swath width results in a 16 day repeat cycle to cover the entire globe. ALI orbits 1 minute behind ETM+ and at the same altitude (Mendenhall et al, 1999), with a ground image swath width of 37km resulting in a longer repeat cycle. This close formation enables EO-1 to image scenes very shortly after Landsat 7, and hence maximise the validity of comparison of data.

The sensitivity of each of the multispectral bands of the ETM+ can be changed by adjusting the gain state for each channel in question. Output in a low gain setting enables surfaces of higher radiance or solar reflection to be imaged without saturation of the channel. Conversely a high gain setting may be applied which narrows the dynamic range with the advantage of increasing the radiometric sensitivity to cooler surfaces. ETM+ has preset settings for the application of differing gain states for each of the bands depending on ground location (Landsat7 Science Data Users Handbook,). Over likely active volcanoes there is a certain pattern of gain states applied to the various channels. Channels 1 to 4 and Panchromatic are set to high gain, whilst channels 5 to 7 are set to low gain to minimize possible saturation by any active volcanic features present.

The ALI employs a different system based on 12 varying gain settings. By changing the integration time over which a particular sensor is exposed to the incoming signal at the focal plane, the gain setting can be changed which delays sensor saturation by extending the dynamic range (L.Ong, pers.comm). ALI achieves an improved instrument performance level over ETM+ by employing solid state sensor electronics using passive

and thermoelectric cooling of the sensor array (Mendenhall et al, 1999) without the complication of cryogenic cooling of the sensor array as used by ETM+ (Landsat7 Science Data users Guide). This results in better signal to noise ratios than ETM+ whilst the 12 bit quantization of the ALI data results in an instrument with increased radiometric sensitivity relative to that provided by ETM+ (Table 6.1c).

6.5.A Method for deducing sub-pixel resolution detail

Each pixel within an ETM+ or ALI image represented by a DN value can be converted into a radiance value. The radiance represented by a single pixel at a certain wavelength is in fact the integral of all emitted radiances from all surfaces at differing temperatures within the ground surface area represented by the field of view (FOV) of that pixel (Oppenheimer, 1993). If all surfaces within the pixel FOV are radiating at similar or identical levels then that radiance value will represent a reasonable estimate of the true radiative flux within the pixel FOV (Oppenheimer, 1991). If the ground surface within the pixel FOV is thermally heterogeneous, with any area radiating at a different temperature than the surrounding area then the pixel radiance value will represent only a poor approximation of the ground surfaces true radiative value (Rothery et al, (1988); Oppenheimer, (1993); Harris et al, (1999)) . Matson & Dozier (1981) outlined a method which utilised the non-linear nature of the Planck function to estimate the temperatures and the component fractional areas of a pixel possessing such a thermally heterogeneous structure, using two separate channels of multispectral instrument data. This method has subsequently become known as the "dual-band" procedure.

In the case of a pixel with a FOV incorporating an active lava flow moving over a much cooler ground surface, the Planck function predicts different radiant temperatures for the same pixel in 2 distinct instrument channels of separate wavelength. The dual-band procedure models the pixel radiance value in the 2 selected channels in terms of two

fractional areas possessing differing surface temperatures, using two non-linear simultaneous equations (equations 6.2 & 6.3).

$$R(\lambda_1,T) = \tau \varepsilon (P_C L_1(\lambda_1,T_C) + (1-P_C) L_1(\lambda_1,T_H)) \qquad \text{(Equation 6.2)}$$

$$R(\lambda_2,T) = \tau \varepsilon (P_C L_2(\lambda_2,T_C) + (1-P_C) L_2(\lambda_2,T_H)) \qquad \text{(Equation 6.3)}$$

$R(\lambda_1,T)$ and $R(\lambda_2,T)$ are the in-channel measured spectral radiances obtained from the instrument data in the two respective channels. T_C and T_H are the temperatures of the cool thermal component, at fraction P_C and hot component P_H (equivalent to $1-P_C$) respectively. $L_N(\lambda_N,T_H)$ and $L_N(\lambda_N,T_C)$ are the resulting modelled radiances derived from the Planck function (equation 1), emitted by the relevant thermal component in either channel calculated at the appropriate wavelength. τ is a correction to account for atmospheric attenuation of the signal from the radiating surface to the instrument, whilst ε defines the emissivity of the radiating surface (Oppenheimer, 1991).

Oppenheimer (1991) states the importance of using suitable values for τ and ε. Incorrect choices for these values will cause an underestimate of the modelled channel radiances within the dual-band procedure, which will lead to erroneous results extracted from the procedure. Such an error may result in an overestimate of the fractional area occupied by the "hot" component, P_H. By the assumption of any one of the unknown parameters within equations 2 and 3 (fractional area, T_H or T_C) then these simultaneous equations may be solved (Rothery et al, 1988). By applying an iterative software approach to these equations we can deduce estimates of the area of each of the individual radiative components once the modelled radiance, as represented by the main body of either equations 2 or 3, matches the measured radiances within the respective instrument channels.

Crisp & Baloga (1990) proposed that a simple two component lava flow model would more accurately represent a hot lava flow surface than the thermally homogenous models or 'non-radiant crust models' proposed by Rothery et al (1988). This 'non-radiant crust' model assumed erroneously that the cooler crust at 100-400°C could be ignored as only the hot component at 700-1000°C+ radiated sufficiently enough to be used (Harris et al, 1999). This model represents an active lava flow surface comprising two thermal components: a cooler component representing the lava flow's chilled crust, and a hot component representing a fraction of exposed flow core due to processes within the active flow (Crisp & Baloga, 1990).

This model can be most accurately applied when the lava flow in question fills the entire FOV of the pixel. In this study we use P_C to denote the chilled crust that develops on the surface of a lava flow and P_H to describe the fractures which develop within the chilled crust of a lava flow, exposing the hot flow core. For the application of the dual-band method here, we assume a value for T_H of 1000° representing P_H. This value for T_H is assumed as it is easier to constrain the higher near-magmatic temperature for a lava flow than the cooler crust temperature which can vary widely depending on a large number of factors such as age of the flow, proximity to vent, effusion rate etc (Oppenheimer, 1993). This value is consistent with temperatures recorded from the core of a'a flows on Mt. Etna (Harris & Rowland, 2001), (Calvari & Pinkerton, 1999).

Some studies suggest the adoption of lower values for T_H (~750 to 800 °C) in order to gain more accurate estimates for the actual area within the flow occupied by T_H (Harris & Rowland, 2001), (Flynn et al, 1994). However, our aim here is to establish the relative capabilities of the two instruments in obtaining successful dual-band solutions, rather than to gain quantifiably highly accurate estimates of the thermal structure of the flow itself. There is great difficulty in actually defining the exact area represented by T_H and to what it relates. We refer the reader to the cited references to provide an indication of the extent of

this difficulty. We therefore use the dual-band procedure here as a simple analysis of the relative activity displayed by and within various lava flows. Higher values for P_H and T_C relate to ever increasing levels of flow activity. For instance, fresh lava flows close to the erupting vent or fissure will have little or no crust, and the surface temperature of the flow will be close to the original magmatic temperature. This will result in a higher value of T_C and P_H. Lava flows resulting from a vent or fissure with a high effusion rate will tend to repetitively entrain any developed crust back into the core as well as tear the crust open as a consequence of the flow's movement and friction with confining levees (Lipman & Banks, 1987) ,(Harris & Rowland, 2001). Again, this scenario will produce high estimates for P_H and T_C relative to those for a stagnating flow with a thick well developed crust that is moving slowly or has even stopped.

We therefore adopt a value for T_H of 1000°C as a reasonable estimate of the temperatures associated with the core of active lava flows on Mt. Etna in order to simply obtain successful solutions.

6.6.Preparation and manipulation of ETM+ and ALI data

We use here imagery from the morning of 29th July 2001 of the lava flows in the region of the Monti del Lago vents. These flows here were moving southwards towards the Riffugio Sapienza and included a flow arm branching south-westwards towards Monte Nero degli Zappini. This area is highlighted within Figure 6.1. The narrow swath width of ALI has caused the western extremity of the image over the western flow arm towards the Monti Nero degli Zappini Figure 6.1d to h to become truncated. The terminus of this western flow arm is therefore not visible within this ALI imagery. In both sets of ETM+ and ALI imagery the eastern flow arm close to the Monte del Lago vents has been obscured by cloud cover. These flows form part of the main sequence of flows from the July flank eruption and at the time of 29th July ETM+ & EO-1 overpass, flows downslope

of these images were in the process of threatening the cable car stations and the Riffugio Sapienza (Behncke & Neri, 2003). Table 6.2 documents the data scenes used for this study.

ALI

Date	Time	Scene ID	Path	Row	Level	Format
29th July	09.25	EO1188034200121011 1P0_SGS_01	188	33	1R	HDF-EOS

ETM+

Date	Time	Scene ID	Path	Row	Level	Format
29th July 2001	09.24	LE72188034_03420010729	188	34	1R	GeoTIFF

Table 6.2: Data scenes used for this study. Study area is a subset from these scenes.

Both the ETM+ and ALI data used for this study are subsets from a full scene, and were converted to radiance units as described in the Landsat 7 Science data users handbook for ETM+, and as outlined within (Mendenhall et al, 1999) for ALI. A solar correction was applied to isolate the thermally anomalous volcanic data from reflected solar radiation. We used the per-pixel method described by Oppenheimer et al (1993) and discussed in Wooster & Kaneko (2001), and applied it to both data sets. This method involves obtaining the average ratio of any particular pixel DN within a single SWIR channel, to the equivalent pixel DN within a channel at a shorter wavelength.

It is important that these pixels are a selection of non-thermally anomalous pixels adjacent to the areas of interest (Oppenheimer, 1993). Once this average ratio has been established, which is effectively a measure of reflected solar radiance, it can then be applied to all thermally anomalous pixels in the assumption that the same ratio applies to these pixels (Wooster & Kaneko, 2001). Wooster and Kaneko (2001) use a ratio between ETM+ channels 7 & 4 and channels 5 & 4 to demonstrate this method. All DN values for each pixel within a non-thermally anomalous area were plotted between these channel combinations to provide a scattergraph, with a least-squares regression line demonstrating

the correlation between each pair of channels. Any thermally-anomalous pixels deviate from this regression line as they will emit thermal radiation within the SWIR channels (7 & 5), but not at the shorter wavelength channel. Wooster & Kaneko (2001) use ETM+ channel 4 as the shorter wavelength channel within the solar correction ratio. I used the same method to estimate the contribution of reflected solar irradiance.

For both ETM+ and ALI the temperature of the fractional 'hot' area was assumed to be 1000°C. Atmospheric transmissivity τ, was set to a value of 0.95 as indicated by using MODTRAN software to model the likely atmospheric attenuation in the required wavelength regions at the altitude and geographic location of Mt. Etna. Emissivity ε, for the basaltic lavas erupted by Mt. Etna surface was set to 0.92 (Harris et al, 1998). The resulting dual-band solutions are output as the fractional hot area P_H at the assumed T_H and the lava flow crustal temperature, T_C. P_C is equivalent to 1- P_H.

Once the solar correction had been completed, it was possible to attempt dual-band solutions on the resulting corrected radiances. An area was selected from the respective ETM+ and ALI imagery of 29th July 2001 including the lava flows in the vicinity of Monti del Lago. This selected area contained all pixels covering the main area of the chosen flow itself, as well as those values within the immediate vicinity of the flow. All pixel radiance values for each instrument channel within this selected area were then supplied to the dual-band procedure, which was then performed using various channel combinations (i.e. ETM+ 7 & 5, ETM+ 5 & 4, ALI 7 & 5, ALI 7 & 5p and so on).

Certain channel combinations input to the dual-band procedure will however not provide any meaningful results. For example, any surface hot enough to register within channel 4 of either sensor will easily saturate channel 7 (Wright et al, 2001). Therefore any solutions from a combination of channels 7 & 4 must be discounted. By supplying all pixel radiances within the selected area to the procedure in this way can assess the relative success in extracting all dual-band solutions over the entire flow area used as the basis for

this comparison. The dual-band solutions can therefore be represented within a format that bears a direct resemblance to the original flow imagery.

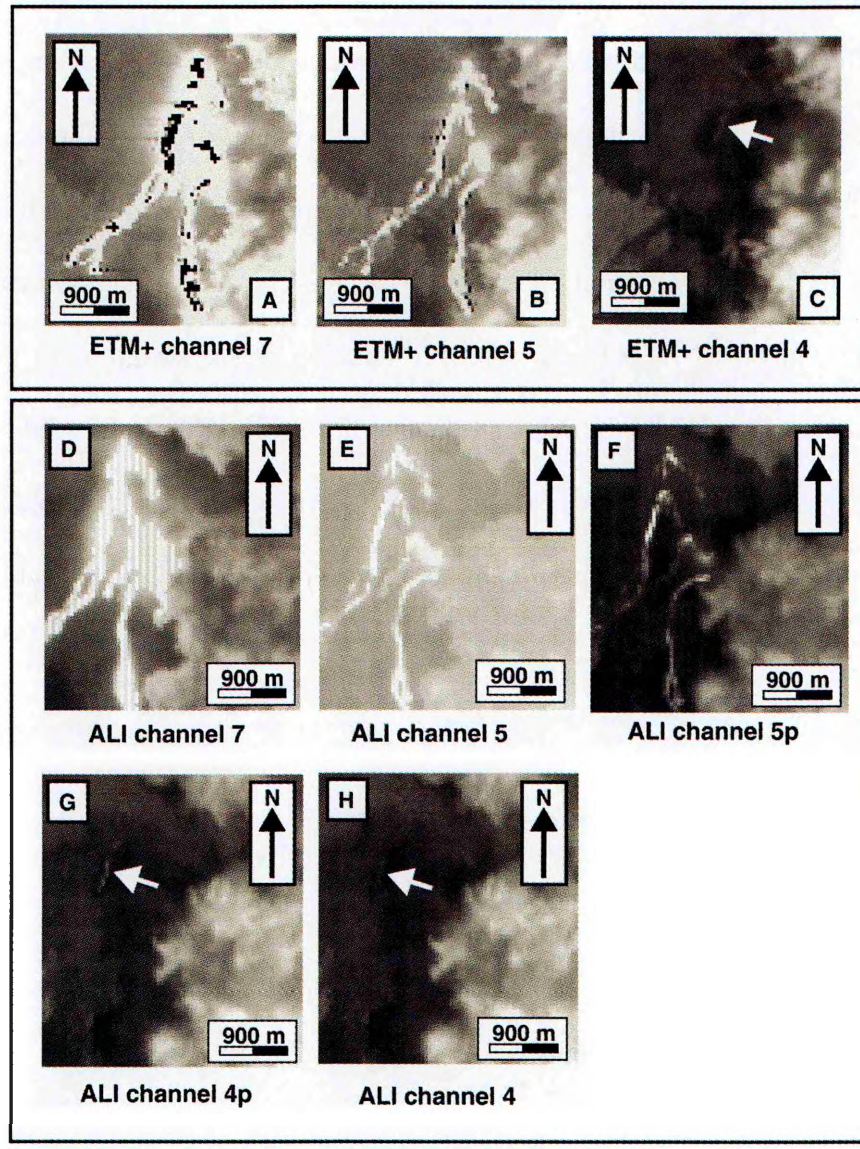

Figure 6.2: Lava flows in the vicinity of Monti del Lago imaged at certain instrument channels. ETM+ channels 7, 5 & 4 are represented within a,b and c respectively. ALI channels 7,5,5p,4p & 4 are represented by d,e,f, & h respectively. Arrows indicate the location of lava flows in VNIR and SWIR channels.

I use roundels superimposed upon a thermal map of the original flow (Figures 6.3 and 6.4) to represent the dual-band solutions. The size of the roundel within figures 6.3 and 6.4 is directly proportional to the calculated area of P_H whilst the tone of the dot is related to the crustal temperature of the lava flow, T_C. These dots are plotted on a

background based on the radiative flux within the SWIR channels so as to indicate the relative activity of the flow.

In order to identify invalid solutions due to saturation of one or both of the channels used within the various dual-band channel combinations, despite any seemingly successful solutions, we provide similar imagery which maps the extent of this saturation within the various ETM+ and ALI channels. This method also enables a comparison to be made of the relative susceptibility to saturation over a given area of a flow of the ALI channels with respect to the equivalent ETM+ channel. Presentation of the solutions in this synoptic manner enables the returned solutions and the extent of saturation to be readily compared with the original flow imagery in figure 6.1. This method also enables the easy identification of relationships between solutions from different channel combinations and instruments to be made.

6.7.Comparison of the extent of sensor saturation

Sensor saturation occurs when incoming radiance detected within an instrument channel exceeds the channels dynamic range and no corresponding increase in sensor DNs are recorded. Saturation within ETM+ data is easily identified where pixel DN values of 255 have been recorded. In instances where the amount of incoming radiance has far exceeded the dynamic range of channel 7, the sensor malfunctions and records a DN within the range of 0 to 3 (Wright et al, 2001). It is possible to verify that channel 7 is malfunctioning over these flows as thermally anomalous SWIR radiance is still detected by channel 5. Any radiance sufficient to register within channel 5 must be sufficient to register in or saturate channel 7 (Wright et al, 2001).

This effect is evident within figure 6.2a that highlights the response of ETM+ channel 7. Extensive saturation of ETM+ channel 7 is indicated by the white pixels within

this greyscale and these are accompanied by black pixels at the centre of the feature. These black pixels represent the malfunction in which the incoming radiance far exceeds the dynamic range of channel 7. Thermally anomalous channel 5 pixels in the same locations (figure 6.2b), which are often saturated too, coincide with these channel 7 malfunctioning pixels.

Pixels within ALI imagery can be identified as saturated once the original DN values have been converted to radiances and confirmed as exceeding the channel's published dynamic range (Mendenhall et al 1999). Because of the greater difficulty in identifying saturated ALI pixels we provide a map indicating which channels of ETM+ and ALI are saturating and malfunctioning (ETM+) over the study area (figures 6.3 & 6.4 respectively).

Consultation of the channel saturation maps within figures 6.3 and 6.4 in conjunction with the imagery displayed within figure 6.1 clearly shows the extensive saturation of channel 7 (boxes with half-triangle) in both ETM+ and ALI data. Saturated channel 7 pixels occur in both instruments, not only over the active lava flows, but also over the immediate area surrounding the lava flows. The channelised lava flows present within this imagery (Behncke & Neri, 2003) are more accurately delineated by elevated channel 5 pixels in data from both instruments. Much of the extensive saturation within ETM+ channel 7 is attributable to a feature of the ETM+ instrument itself. Over highly thermally radiant surfaces the sensor response time may not be sufficient to reset to zero in time for the next pixel 'in-line' to be imaged (Flynn et al, 1994). This is due to the method of image acquisition by cross-track scanning instruments such as ETM+. Such instruments employ a rotating scan mirror to transfer the signal from the optics into the sensors at the focal plane. Data for each pixel is acquired sequentially in an east-west direction (Flynn et al, 1994). If any surface within a pixel area is highly thermally radiant resulting in saturation and possible malfunction then subsequent pixels after this pixel may falsely

record thermally anomalous DNs. The result of this is the leakage of signal from one pixel to adjacent pixels causing contamination of the signal (Rothery et al, 1988). This effect can clearly be seen in Figure 6.1a. in which ETM+ channel 7 saturation is indicated by white pixels (where DN = 255) and black pixels where the sensor has malfunctioned (DN >> 255) and recorded DN's of 0 to 3. There is also a streaking effect which occurs in the same pixel row as those pixels covering the most extreme surfaces.

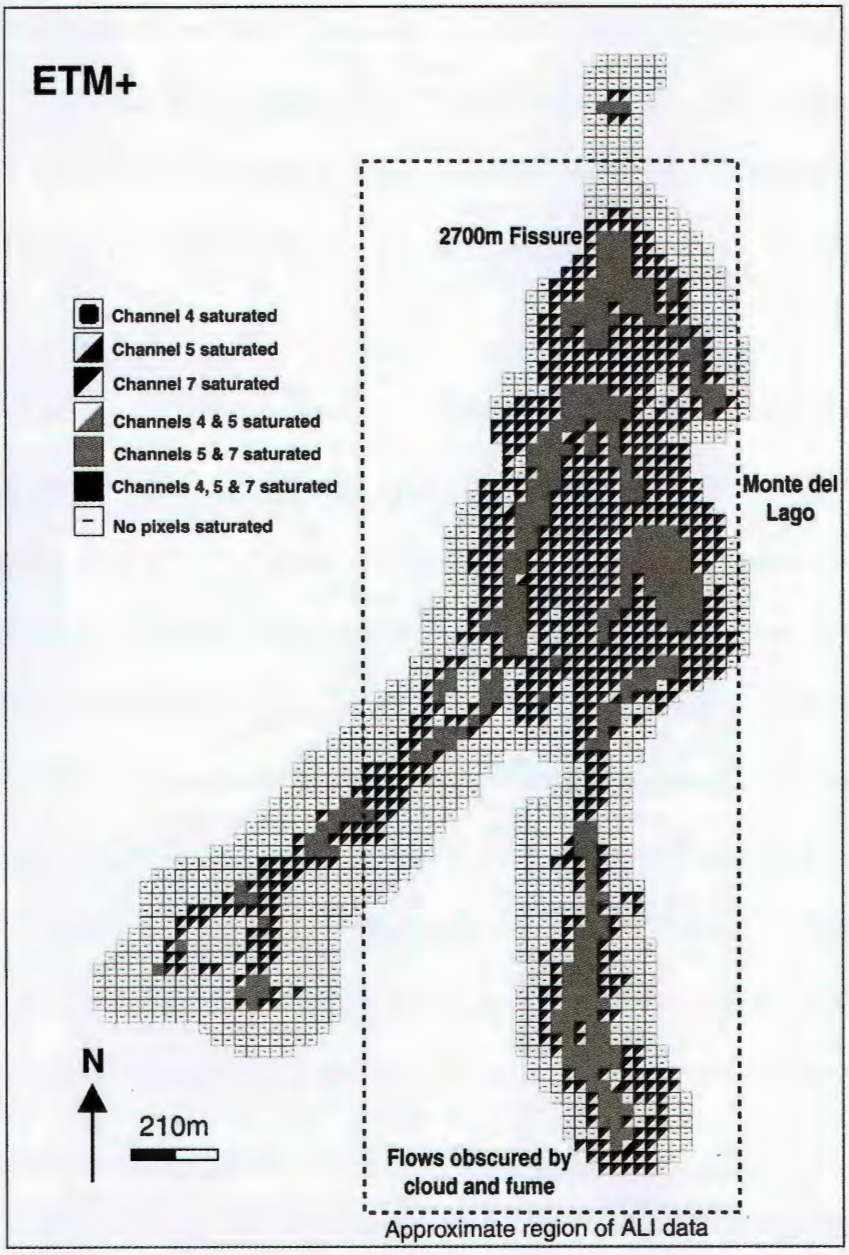

Figure 6.3: Saturation response map showing the various saturated ETM+ channels on a pixel by pixel basis. These are represented so as to bear familiarity with the original imagery within figure 6.2

Extensive saturation of ALI channel 7 is also evident. ALI uses a solid state focal plane and optics with no moving parts. ALI does not therefore exhibit the east-west streaks evident within the ETM+ channel 7 data due to the motion of the scan mirror. Saturation may therefore be attributable to another effect. It is possible that the large amounts of volcanic haze associated with gases emitted from the vents as well as the flow itself, coupled with the heat haze associated with heating of the atmosphere by the flow will scatter the radiance from within one pixel FOV into the FOV of surrounding pixels. Such blurring would be most evident at longer wavelengths within the SWIR as it is in this wavelength region that most radiance is being emitted. There is no evidence of blurring of the few thermally anomalous pixels within figure 6.2c, g & h, which display imagery from the shorter SWIR channels. The effect will of course contribute to the blurring and saturation of ETM+ channel 7 too.

Another effect is also apparent within the ALI channel 7 imagery. The image thresholding applied to figure 6.2d in order to obtain the best contrast within this image has highlighted the slight difference in recorded radiances between individual detectors within the ALI 'pushbroom' scanning sensor array (Mendenhall et al, 1999). In this type of scanning array a single pixel subtends a continuous path in the along-track direction. These stripes are probably due to the difference within the response coefficient values recorded within the ALI Level0 data within these saturated pixels. This stripe effect is not apparent within pixels not recorded as saturated.

The saturation map displayed within figures 6.3 and 6.4 clearly highlights the relevant extent of saturation within channel 5 of the two instruments. The ETM+ imagery shows far greater susceptibility to saturation of both channels 7 and 5 than ALI. This scenario is indicated by a filled grey box. There are isolated instances where ETM+ channel 5 is recorded as saturated whilst channel 7 remains unsaturated. This is an unlikely situation and is due to a processing error involving a low channel 7 DN due to sensor overload and

malfunction. Channel 5 in both ETM+ and ALI is less prone to saturation than channel 7 because of its higher dynamic range (table 6.1), and placement at a shorter SWIR wavelength.

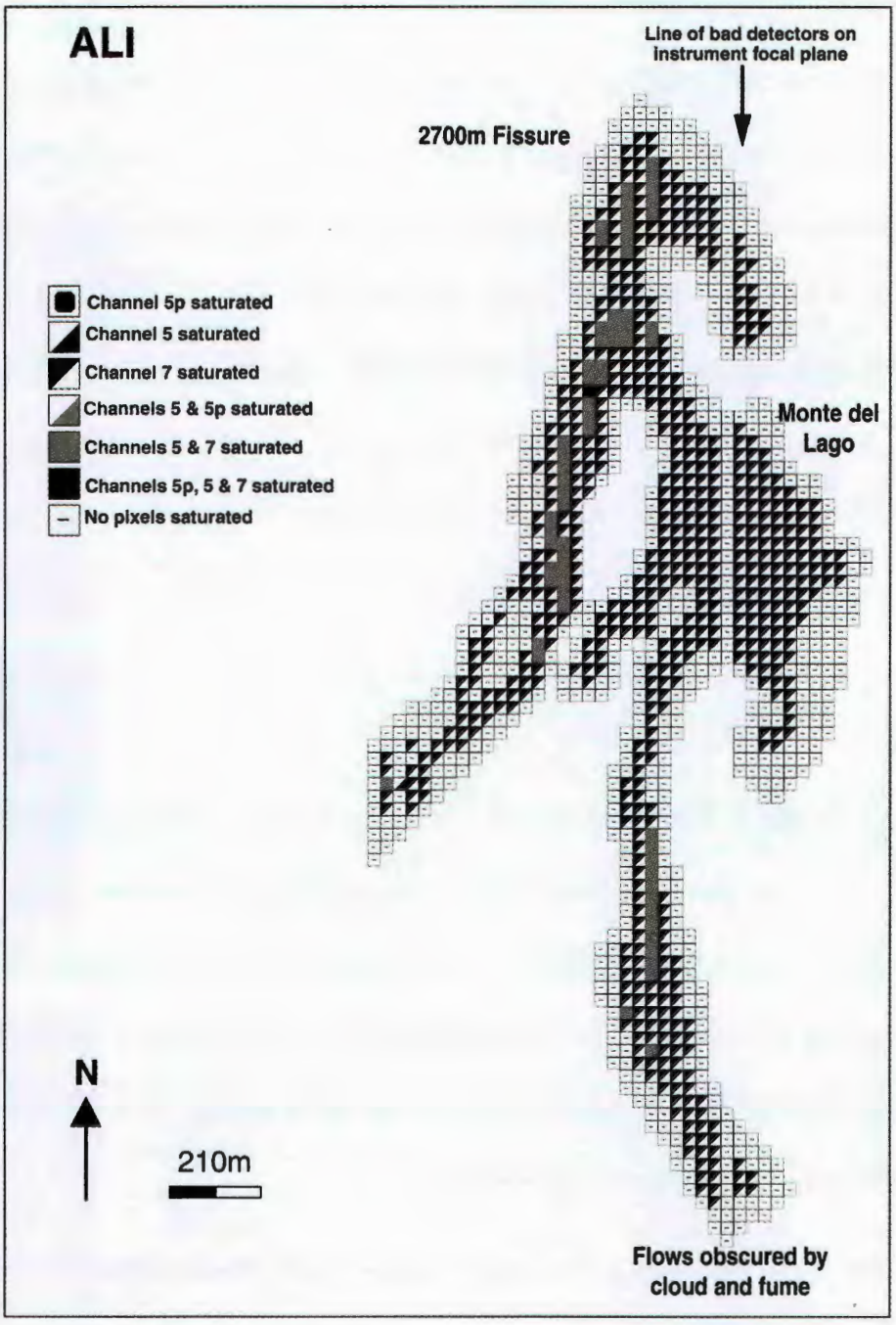

Figure 6.4: Saturation response map showing the various saturated ALI+ channels on a pixel by pixel basis. These are represented so as to bear familiarity with the original imagery within figure 6.2. Note the truncation of the western flow arm in the area of Monti Nero degli Zappini and the line of unsaturated pixels associated with a bad detector on the ALI focal plane.

Channel 5 therefore has a lower sensitivity than channel 7 to active lava flows, which results in the location and course of the active lava channels to be identified by highly thermally anomalous and saturated channel 5 pixels. This effect is also evident within figure 6.2b as the lava channels are clearly picked out, albeit with some blurring similar to that occurring in channel 7.

The extent and vigour of flow activity in this area close to the Monti del Lago vents has resulted in near continuous saturation of ETM+ channel 5 over the active lava flows. The corresponding pixels within ALI channel 5 display overall lower levels of saturation. Figure 6.4 indicates that ALI channel 5 is less prone to saturation than ETM+ channel 5. The flows imaged here, causing a large number of ETM+ pixels to saturate relative to ALI pixels would not have cooled sufficiently within the 1 minute interval separating the ETM+ and ALI overpasses to account for this difference. Changes in signal attenuation by the local effects of scattering by volcanic aerosols and haze and also cloud cover, may account for some decrease in saturation between the two overpasses. However the relative lack of saturation in ALI channel 5 occurs over the entire flow region in question.

Table 6.1 shows that ALI channel 5 will saturate at a Pixel Integrated Temperature (PIT) of 471°C, whilst a lower saturation PIT value of 416°C is stated for ETM+ channel 5. This predicts this relative lack of saturation found in ALI channel 5 shown in Figure 6.2. Table 6.1 indicates similar saturation PIT's for both ETM+ and ALI channel 7. This accounts for the similar extent of saturation within channel 7 of both instruments.

Many of the pixels recorded as saturated within channels 7 & 5 of both instruments record thermally anomalous radiances slightly elevated above the background solar signal within channel 4. Such a pattern of sensor saturation and malfunction is indicative of increasing levels of emitted radiance within the SWIR-VNIR and is consistent with increasing areas of the active flow at or near magmatic temperatures (Rothery et al, 1988). These pixels are highlighted by arrows within figure 6.2c & h. Channel 4 in either

instrument does not demonstrate any saturation, and the overall magnitude of the thermally anomalous pixels over even the most active areas of the flows recorded within channel 4 is low. Flynn et al (2001) discussed a similar situation observed from lava flows associated with the October 1999 Mt. Etna Bocca Nuova overflow. They suggested that a spectral band placed in the gap between ETM+ channels 5 and 4 would go someway to alleviating the problem of saturation of the longer wavelength ETM+ channels 5 and 7 (Flynn et al, 2001). Such a channel could also provide accurate estimates of radiant flux from very active flows without extensive saturation and the subsequent loss of information.

The ALI incorporates such a channel at 1.2-1.3μm (5p) and the relevance of this to deducing quantifiable estimates of sub-pixel structure is apparent when discussing the sensitivity of certain channels to differing levels of lava flow activity. Figure 6.2f displays the imagery obtained over these flows and it is immediately apparent that there is an overall lack of saturation and of the blurring evident in both channels 7 and 5. The course of the lava channels within this sector of the flow-field is accurately delineated and more distinct than that shown by channel 5 (figure 6.2e). Thermally anomalous pixels occur over the entire flow and are much more readily identified than the anomalous pixels identified within channel 4 of both instruments. Figure 6.4 highlights one instance where ALI channel 5p is saturating in addition to channels 5 and 7 (filled black box). This location coincides with a break in slope where tensional forces on the crust of the flow may be causing fractures to open (Pieri et al, 1990) exposing the flow core to a greater extent than observed elsewhere on the flow. The related increase in emitted SWIR radiance is enough to saturate ALI channel 5p, but insufficient to saturate or register strongly within ETM+ channel 4.

ALI possesses one extra channel that indicates thermally anomalous pixels over this flow-field. The imagery within figure 6.2g indicates that ALI channel 4p is able to identify such pixels more readily than ETM+ channel 4. However as table 6.1 indicates,

ALI channels 4p and 4 are both situated within the bandpass of ETM+ channel 4. ALI channel 4p is at a slightly longer wavelength (0.87μm) than ALI channel 4 (0.79 μm), and will therefore be slightly more sensitive to hot surfaces. Despite this there is no indicated saturation of ALI channel 4p within figure 6.4. ALI channel 4p is therefore sensitive only to the most active areas of flow activity, in a similar manner to the channel4 possessed by both instruments.

The depiction within figures 6.3 and 6.4, of precisely which pixels are saturating in both ETM+ and ALI data, aid in identifying the valid dual-band solutions as saturated pixels will lead to inaccurate solutions. This is especially useful for ALI where no obvious indication of saturation is given in the Level1R data used for the dual-band solutions, as the data has been manipulated radiometrically for this level of data. It is therefore difficult to easily identify which pixels are saturating from the DN's in the data provided (i.e. for a 16 bit instrument a "saturated" DN would be identified as 65536 in a similar manner 255 indicates saturation in the 8 bit ETM+).

6.8.Dual-band solutions using ETM+ data

Two sets of dual-band solutions using two separate channel combinations were obtained for all pixel values within the selected area of lava flows in the region of the Monte del Lago vents. Many of the pixels within this area were saturated in one or both channels as previously discussed. We used the information within figures 6.3 & 6.4 to identify and flag these particular pixels as unsuitable for successful dual-band solutions. Figures 6.5 and 6.6 display ETM+ dual-band solutions obtained using valid pixel radiance values.

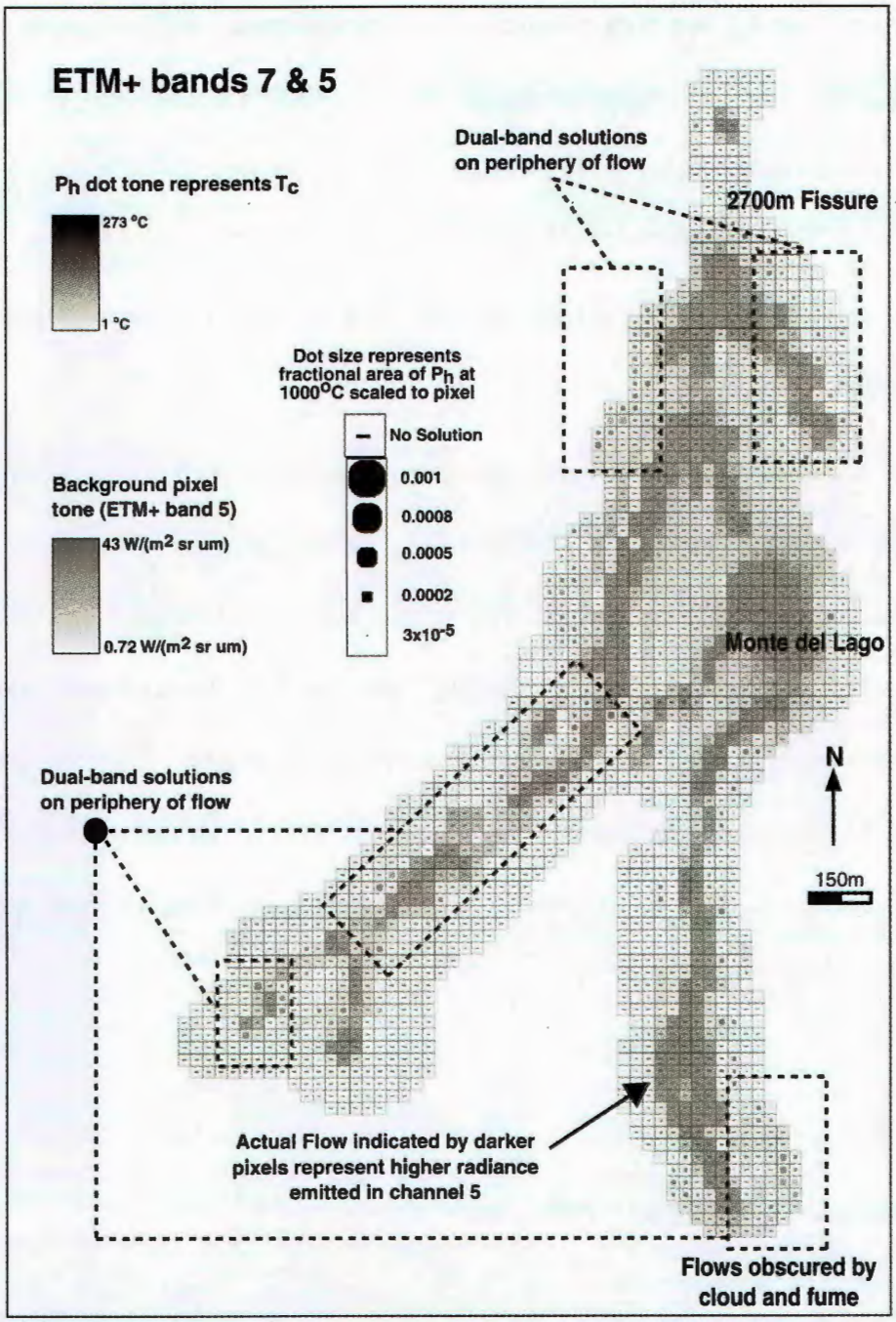

Figure 6.5: Map showing valid dual band solutions for a combination of ETM+ channels 7 & 5. The dots here represent the size of the fractional area P_h of incandescent cracks at 1000°C in the chilled crust of the lava flow at temperature T_c indicated by the shade of the dot. This is in accordance with the two component lava flow model suggested by Crisp & Baloga (1990). The tone of the box surrounding the dot is related here to the radiant flux for the pixel in question in ETM+ channel 5. Darker tones indicate the presence of the actual flow channel.

There is a limited number of solutions using a combination of channels 7 & 5. Very few of these solutions occur over the actual flows themselves, instead they tend to be in pixels peripheral to the flows. The position of the flows within the selected area

supplied to the dual-band procedure is indicated by the background shading within each box representing each pixel supplied to the procedure.

Darker shades indicate a higher level of emitted radiance detected by ETM+ channel 5, and effectively represent the flows as depicted within figure 6.2b. No valid solutions were available using this channel combination for pixels centred over these flows. The extensive saturation of channels 5 and 7 over these flows is due to a combination of instrument error and blurring due to scattering within the SWIR that has prevented any solutions using this particular channel combination.

The solutions depicted on the edge of the flows can be attributed to pixels with a FOV which encompasses the physical boundary between the lava flow and the ground over which it is moving. Such a scenario comprises at least three thermal components which will not be well represented by the dual-band procedure (Oppenheimer, 1993; Harris et al, 1999). This effect is to be expected when obtaining dual-band solutions in such a synoptic manner over the study area, as pixel boundaries will only rarely coincide with the boundaries of the flow itself. This scenario produces a lower integrated radiance value representing the entire pixel FOV which enables solutions within this particular channel combination to be recorded.

Other solutions obtained using this combination of channels 7 & 5 are recorded from pixels further removed from the flows indicated by the lighter tones of the background pixels in figure 6.5 representing emitted radiance within channel 5. Such solutions are attributable to a combination of the scattering of SWIR radiance by the high levels of cloud and fume associated with the flows themselves and the nearby vents as well as problems with the detector response and recovery. Such pixels may not be centred over the flows themselves but are recording false thermally anomalous values as 'spill-over' from previous pixels scanned which have saturated and malfunctioned (Wright et al, 2001; Rothery et al, 1988). These pixels will therefore record false solutions.

The only other possible channel combination for possible input into the dual-band solution with ETM+ data, are channels 5 & 4. Figure 6.6 attempts to displays these solutions. No valid solutions were obtainable with this channel combination, even for those pixels indicated as displaying a low-level thermal anomaly in figure 6.2c. However, 2 dubious solutions were originally recorded.

The location of these solutions did not coincide with the channel 4 thermally anomalous pixels indicated within figure 6.2c. This area of channel 4 anomalous pixels coincides with saturated channel 5 pixels, indicating the extent of flow activity in this area. Further study of the figure 6.2a,b & c imagery suggests the possible presence of thin cloud or fume within these pixels

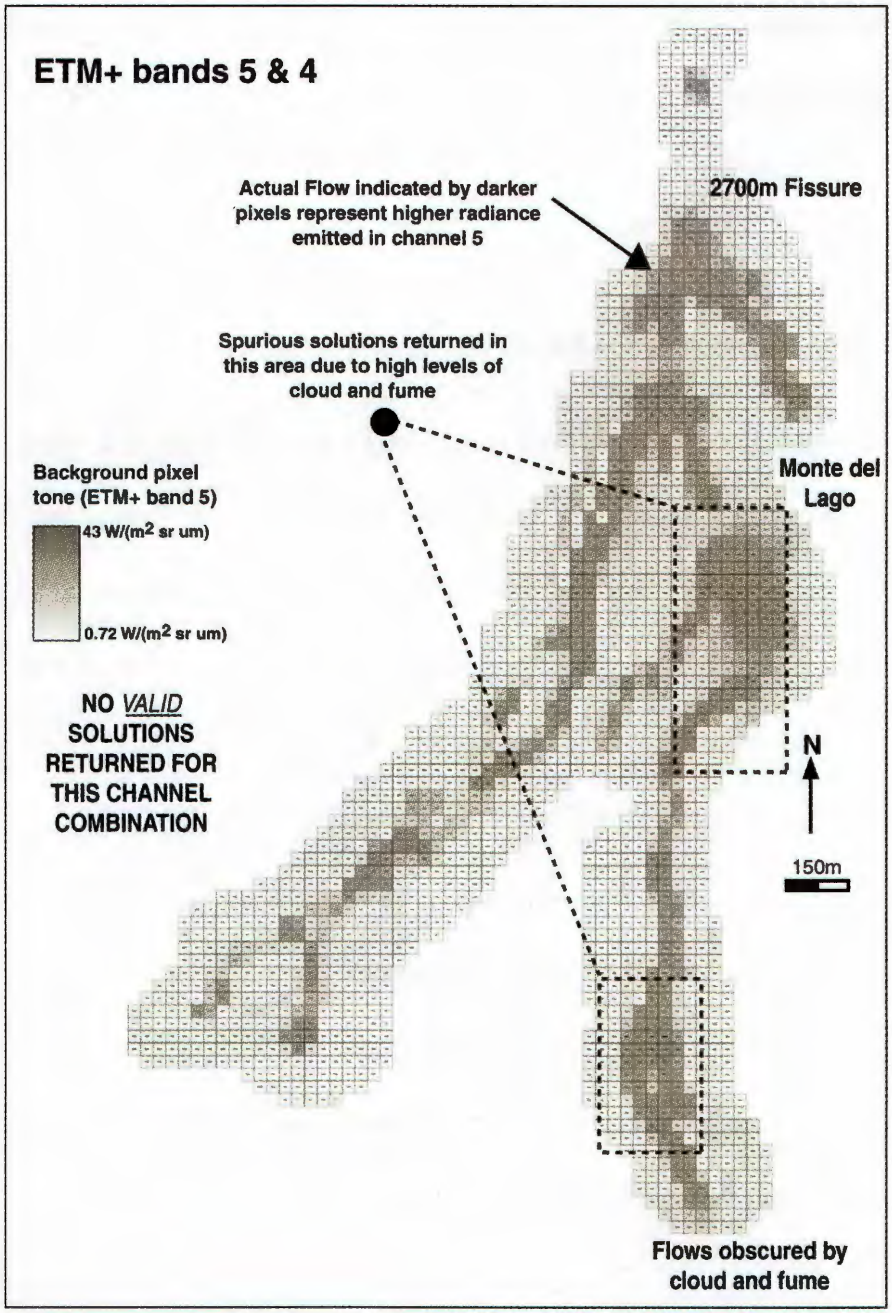

Figure 6.6: Map showing valid dual band solutions for a combination of ETM+ channels 5 & 4. No solutions are recorded here, however we indicate the area where dubious solutions were obtained from scattered SWIR radiance by cloud and fume.

. Large amounts of cloud present within the eastern side of the available imagery are recorded as light-grey to white in all 3 channels visualised within figure 6.1a, b & c. This is because the cloud is scattering large amounts of solar reflected radiation which is recorded as high DN values within these channels. A lower amount of cloud within the pixels that have recorded dual-band solutions using the ETM+ channels 5 & 4 combination, may only scatter enough solar radiance within channel 4 to register the pair

of 'successful' solutions obtained with the channel 5 pixels. This confirms that no solutions are possible when using ETM+ channels 5 and 4 (Wright et al, 2001).

6.9.Dual-band solutions using ALI data

Valid dual-band solutions using pixel radiances from ALI for the study area were checked and plotted in the same manner as those from ETM+ data. Due to the extent of saturation over the active flows within ALI channel 7 we do not include any solution maps using this channel. Therefore figures 6.7 and 6.8 are maps of valid solutions provided by using combinations of channels 5 & 5p and 5p & 4p respectively. No solutions were obtained using ALI channel 4 in any channel combination.

There are many valid solutions provided by a combination of ALI channels 5 & 5p, and displayed within figure 6.7. These solutions appear in places to accurately trace the course of the main channels within the flow field. This is indicated by a line of continuous solutions of similar magnitude (P_H ~0.004) recorded for pixels with the darkest background shading representing high levels of emitted radiance within ALI channel 5.

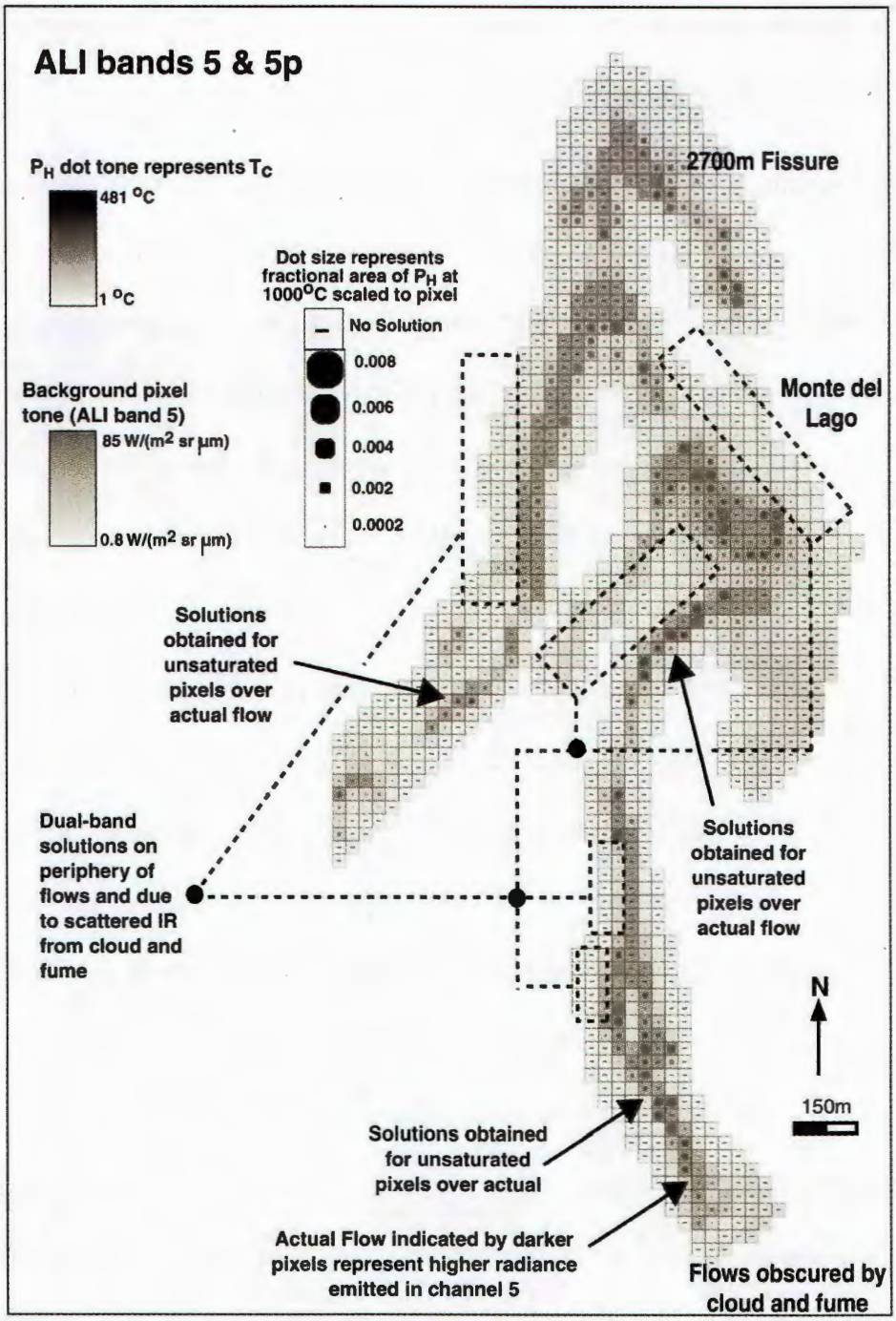

Figure 6.7: Map showing valid dual band solutions for a combination of ALI channels 5 & 5p. The dots here represent the size of the fractional area P_h of incandescent cracks at 1000°C in the chilled crust of the lava flow at temperature T_c indicated by the shade of the dot. This is in accordance with the two component lava flow model suggested by Crisp & Baloga (1990). The tone of the box surrounding the dot is related here to the radiant flux for the pixel in question in ALI channel 5. Darker tones indicate the presence of the actual flow channel.

The pattern of thermally anomalous pixels highlighted over the flow-field within figure 6.2f is often reproduced within the dual-band solutions using this channel. This

channel combination provides realistic estimates of P_H and T_C from these pixels of 0.001-0.0043 (1.8-7.4m^2) and 350-480°C respectively.

These compare well with P_H estimates gained from FLIR thermal camera imagery obtained on the ground from nearby flows (<1km at Monte Calcarazzi) on this date, of P_H ~0.001- ~0.008 (H.Pinkerton, pers.com). In those areas of the flows possessing high levels of fresh exposed lava flow core, indicated by highly thermally anomalous pixels within channels 5p and 4p, channel 5 is saturating. This particular channel combination cannot provide successful solutions over the most active flows with large areas of exposed flow core.

Also evident are a number of solutions recorded on the edges of the flows, in a similar manner to that observed when using a combination of ETM+ channels 7 & 5. These areas are highlighted within figure 6.7. These solutions provide distinctly lower estimates of P_H and T_C than those recorded for valid solutions obtained for pixels with a FOV entirely filled by the lava flows. This indicates that in these peripheral pixels the pixel is not wholly occupied by the lava flow, and the pixel FOV consists of both lava flow and cool ground. A number of solutions further removed from the flows by 2-3 pixels, are also available. As with those similar solutions obtained with ETM+ channels 7 & 5, these solutions are attributable to SWIR radiance scattered into the FOV of these pixels by the high amount of volcanic haze and fume, and must therefore be ignored.

The second available ALI channel combination to provide valid dual-band estimates uses channels 5p & 4p (figure 6.8). The solutions resulting from this channel combination occur over regions of the flow that have saturated both ALI channels 7 & 5. The single saturated channel 5p pixel identified within figure 6.4 has been removed to prevent any dubious solutions.

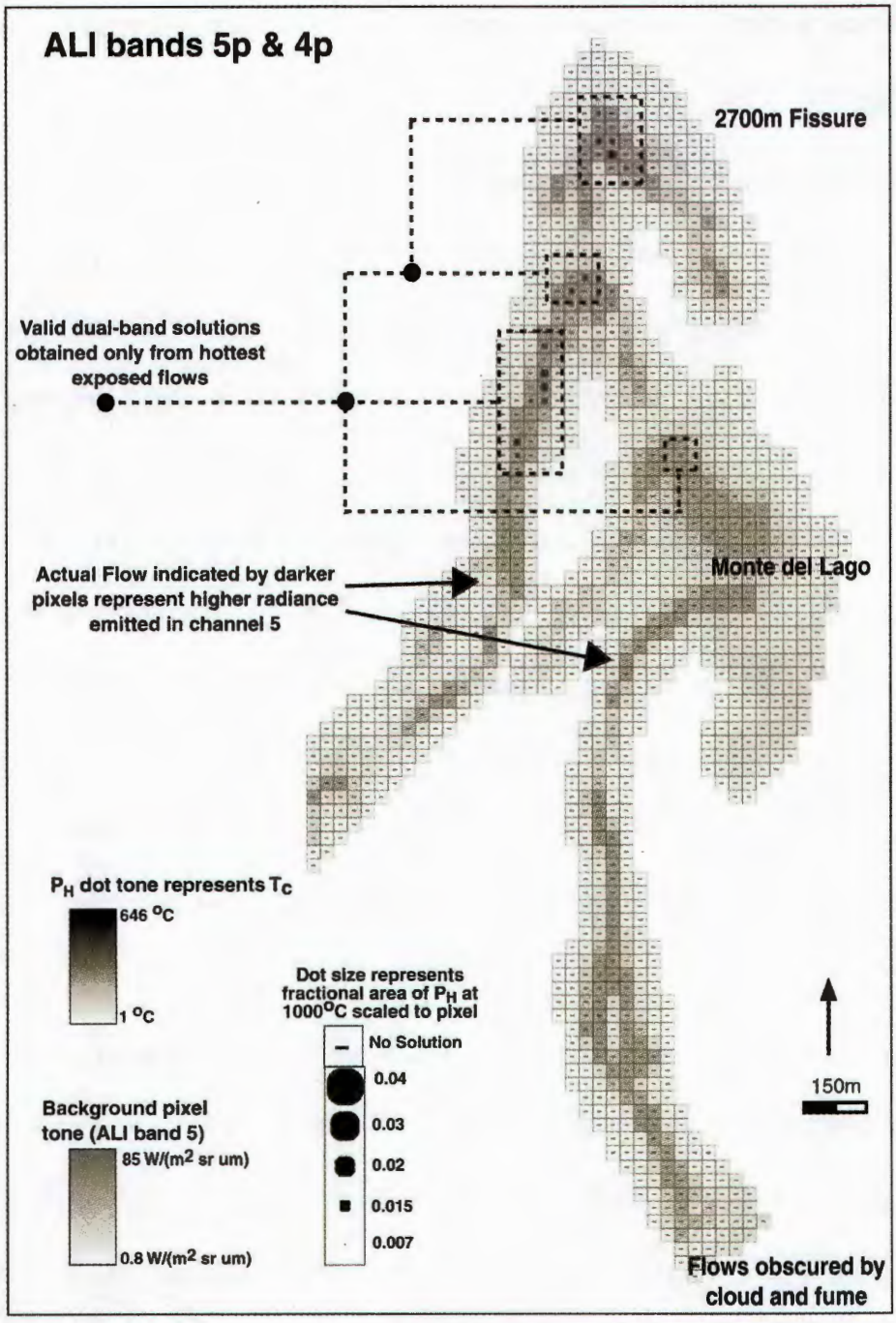

Figure 6.8: Map showing valid dual band solutions for a combination of ALI channels 5p & 4p. The dots here represent the size of the fractional area P_h of incandescent cracks at 1000°C in the chilled crust of the lava flow at temperature T_c indicated by the shade of the dot. This is in accordance with the two component lava flow model suggested by Crisp & Baloga (1990). The tone of the box surrounding the dot is related here to the radiant flux for the pixel in question in ALI channel 5. Darker tones indicate the presence of the actual flow channel.

The solutions obtained from this combination of channels 5p & 4p are clustered in those areas with the highest channel 5 radiance indicated by the background pixel shading. This includes the locality of the single saturated channel 5p pixel. This suggests that these

areas are located over the most active flow activity with the greatest areas of exposed flow core and juvenile crust.

The northernmost solutions obtained coincide with the probable location of the 2700m fissure (general location marked within figure 6.8). The actual vent itself is obscured by saturating pixels within ALI channels 7 & 5. The remaining solutions returned from this channel combination may alternatively be due to a change in slope gradient over which the lava flow is moving. This may cause the crust upon the surface of the flow to rupture and expose the flow core (Lipman & Banks, 1987). This particular scenario should result in higher flow crust temperatures (T_C) obtained from the dual-band procedure and relatively larger estimates for the exposed core indicated by P_H. This is because larger areas of exposed core will result in a higher mean flow crust temperature due to the relatively large area of new crust forming from the freshly exposed core. This will increase the overall integrated radiance temperature for that particular pixel, resulting in a higher T_C value.

Higher estimates for the value of P_H will occur because of the increased area of the flow emitting radiance at shorter wavelengths within the SWIR, to which the shorter wavelength of the two channels used will be more sensitive. The 5p & 4p channel combination in figure 6.8 describes just this pattern with P_H estimates of $P_H \sim 0.01$-0.02 (9-18m^2) and T_C's of 600-646°C returned. These compare favourably with previously obtained field data based on such flows as well as ground-based thermal camera imagery obtained for these flows at the time of the overpass (H.Pinkerton, pers.comm).

This set of solutions for this channel combination indicates the sensitivity of this channel combination to extract solutions from active flows that easily saturate other channels placed at longer wavelengths within the SWIR.

6.10. Dual-band coverage over a range of flow types

ETM+

Date	Flow feature	Number of solutions	
		7 & 5	5 & 4
29/07/01	Fissure flow in Valle Del Leone	0	0
29/07/01	17/07/01 2900m flow into Valle Del Bove	0	0
29/07/01	17/07/01 2700m, fissure flows in the region of Monti del Lago	5	0
29/07/01	Continuation of above flow downhill, passing Monte Nero & interspersed by cloud cover	17	0
29/07/01	27/07/01 lava flow from vent on Monti Del Lago heading into Valle Del Bove	0	0
Percentage of successful dual-band solutions obtained by ETM+ for these band combinations		18%	2%

ALI

Date	Flow feature	Number of solutions			
		7 & 5	7 & 5p	5 & 5p	5p & 4p
29/07/01	Fissure flow in Valle Del Leone	3	1	1	0
29/07/01	17/07/01 2700m, fissure flows in the region of Monti del Lago	0	1	184	18
29/07/01	17/07/01 2950m fissure flows	0	0	30	3
29/07/01	Flows nr Monti Calcarazzi flowing downhill towards Nicolosi	0	0	23	3
29/07/01	17/07/01 2700m eruptive fissure	0	0	2	0
Percentage of successful dual-band solutions obtained by ALI for these band combinations		22%	19%	66%	18%

Table 6.3: Number of dual band solutions available for all areas of flows using ETM+ and ALI from the 29th July 2001 scenes. Entries marked in bold indicate the series of flows discussed in detail. Only valid dual-band solutions obtained from pixels displaying unsaturated values and no contamination from scattered SWIR radiance by volcanic gas and fume are listed here. The final row in each table gives an estimate of the number of successful solutions obtained from the dual-band procedure relative to the total number of solutions sought from the total number of pixels supplied to the procedure.

Table 6.3 displays the total number of valid dual-band solutions determined using the ALI and ETM+ data for all flows visible within the whole ETM+ and ALI scenes obtained on 29th July 2001.

Those figures relating to the flows in the vicinity of Monti del Lago previously discussed are listed in bold type. This table allows a bulk assessment between the relative numbers of solutions recorded between ETM+ and ALI, and the coverage provided between differing channel combinations for varying levels of flow activity. We only list dual-band solutions involving unsaturated pixels as well as solutions obtained from directly over the flows so as to minimise the inclusion of dubious solutions due to scattered SWIR radiation.

Table 6.3 dramatically highlights the difference in numbers of successful dual-band solutions obtained over the range of flows present on Mt. Etna on July 29th 2001. Very few valid dual-band solutions are returned using a combination of ETM+ channels 7 & 5 from the flow field, the majority of which is displayed within figure 6.1. This is predominantly due to the extensive saturation within channel 7, and to a lesser extent channel 5. A small number of solutions have been obtained over the flows moving down slope in the vicinity of Monti Calcarazzi and the Riffugio Sapienza. These flows are a continuation of the flows discussed in the main body of this paper and can been seen in the lower half of figure 6.1. These flows are some distance down slope from the main vents and will therefore have had time to develop a mature crust. This may explain the small number of solutions obtained using ETM+ channels 7 & 5. No corresponding solutions are available using the ALI channels 7 & 5 combination as these ETM+ solutions were obtained for flows that were not included in the ALI's narrower swath (indicated in figure 6.1).

However, there are a small number of solutions recorded using this channel combination from a stagnating flow in the Valle del Leone on the northern flank of Mt. Etna. No solutions are recorded using ETM+ channels 7 & 5 over this flow. This flow

originated from a fissure that opened on July 20th, and was reported to have slowed in the days prior to the 29th July imagery used here (Behncke & Neri, 2003). On such a flow displaying a markedly lower level of activity, when compared to those flows previously discussed in the vicinity of Monti del Lago, we might expect to obtain more successful solutions from a combination of channels 7 & 5 in both instruments. Single solutions gained using ALI channel combinations 7 & 5p and 5 & 5p over this Valle del Leone flow hint at the fact that the flow may still have been displaying some residual activity at the time of the ETM+ and ALI overpass, which has prevented any solutions using the readily saturated ETM+ channels 7 & 5.

Table 6.3 highlights the complete lack of successful solutions gained usingETM+ channels 5 & 4, despite the presence of a number of thermally anomalous channel 4 pixels highlighted in figure 6.2c. This dearth of solutions is not matched by the combination of ALI channels 5 & 5p and 5p & 4p. The former channel combination provides solutions over each flow within the entire flow-field. The greatest number of solutions using this channel combination, are for the flows in the vicinity of Monti del Lago previously discussed. Solutions are also widely available for the flows in the area of Monti Calcarazzi and the Riffugio Sapienza as well as the flows emanating from the 17th July 2950m fissure. Solutions using the ALI channel combination of 5p & 4p have also identified the areas of greatest flow activity close to the 17th July 2950m fissure, as well as those areas saturating the greatest number of channel 7 & 5 pixels on the flows near Monti Calcarazzi. No ALI channels 5p & 4p solutions were obtained from the less active Valle del Leone flow.

The success of the ALI in obtaining dual-band solutions relative to the ETM+ is highlighted in the final row of the relevant tables in table 6.3. Many more solutions are obtained using the ALI data than from the equivalent bands of ETM+ data. ALI returns a solution for 66% of the pixels supplied to the procedure using bands 5 and 5p. This figure is unprecedented in the ETM+ data and is indicative of the success of using the extra

channel 5p in the SWIR. The extra channels within the SWIR provided by ALI have clearly aided in providing suitable channel combinations for dual-band modelling over a range of lava flows. The channel combinations using the shorter SWIR channels: 5 & 5p and 5p & 4p have proved the ability to extract meaningful solutions over active flows that would otherwise saturate longer wavelength SWIR channels such as 7 & 5 present on both the ETM+ and ALI. ETM+ is handicapped in this respect as the placement of channel 4 and its dynamic range is too high in combination with channel 5 to extract successful dual-band solutions over active lava flows.

Wright et al (2001) cited this problem and suggested that the ETM+ panchromatic channel (8) can be used to identify thermally anomalous pixels associated with hot active lava flows. This is because ETM+ channel 8 possesses a wide wavelength bandpass encompassing the ETM+ channel 4 bandpass, and is thus more sensitive to emitted radiance from an active lava flow. ALI channels 4 & 4p is in effect the equivalent of ETM+ channel 4 split into two separate channels. ALI channel 4 situated in the shorter wavelength region whilst ALI channel 4p is placed at a slightly longer wavelength within the ETM+ channel 4 bandpass (Mendenhall et al, 1999). This split results in ALI channel 4p possessing greater sensitivity to active lava flows than ETM+ channel 4.

This provides the benefit of more successful dual-band solutions for lava flows when used in conjunction with ALI channel 5p. The placement of ALI channel 5p between ETM+ channels 4 and 5 has greatly increased the likelihood of obtaining dual-band solutions for lava flows due to its sensitivity within the SWIR to such features

6.11. Consideration of the observations made in Chapter 4 on the application of the dual-band procedure

In this chapter I have considered a straightforward application of the dual-band method: by simple assumption of a temperature T_H representing the "hot" portion within a pixel then the resulting fractional area occupied by T_H, the temperature T_C representing the "cool" portion of the pixel and their respective fractional areas may be deduced. The dual-band method, as I stated earlier in this chapter, is a well understood method and has been used by many workers (Francis & Rothery, 2001; Oppenheimer et al, 1993; Harris et al, 1999 to name but a few). I have used the dual-band method in this work as it provides a suitable vehicle for comparing the data obtained by the Landsat7 ETM+ over lava flows with data from the new ALI instrument. The ALI possesses extra channels within the SWIR making the ALI ideal for such volcanological remote sensing with a decreased likelihood of sensor saturation. As I have shown in the previous sections, the provision of extra channels within the SWIR does indeed make the ALI a more capable instrument for remote sensing of active lava flows.

In Chapters 4 and 5 I discussed the theory and application of the dual-band method and the drawbacks associated with using the resulting estimates of the sub-pixel thermal structure. I used these estimates to estimate the heat flux Q_{rad} and then compared this with the "actual" value calculated from advanced simulations of volcanic surfaces. I found that Q_{rad} derived from the dual-band results were severe underestimates of the actual values of Q_{rad}. These findings were in agreement with those made by Wright & Flynn (2004) who were in no doubt of the poor performance of the dual-band method and suggested that to simulate the thermal structure present on the surface of an active lava then at least 7 components must be used if a representative structure is to be retrieved. This is undeniably true, but in order to apply this recommendation to the remote sensing of lava flows such as those discussed in this chapter using space-based instruments, then hyperspectral data must be used. Currently, there is only one such instrument: Hyperion, based on the EO-1 platform alongside the ALI. The narrow 7.5km swath and 236 spectral channels located within in the VNIR and SWIR can provide a detailed model of the thermal structure

present on the surface of active lava flows. However, the drawback is the scarcity of Hyperion data, the narrow swath and high rates of data transmission, and thus storage, make Hyperion unsuitable for the timely and cost effective study of new and ongoing volcanic eruptions.

The dual-band method as described here, therefore still provides a "work-horse" ability- it is easy to apply in terms of computational effort and can be used with a range of different instruments. In chapters 4 and 5, I concluded that the dual-band method does indeed provide severe underestimates of the thermal distribution at a sub-pixel resolution, and thus inaccurate estimates for Q_{rad}. It is difficult to try and relate the thermal continuum that is the surface of a lava flow in only two components. However, I found that the dual-band method could still distinguish between the different thermal structures supplied via the synthetic pixel simulations. I could establish this as it was possible to tune these simulations to provide a passable (when compared with FLIR camera imagery obtained of active lava flows) simulation of any likely lava flow activity present within a pixel possessing a unimodal or bimodal pixel frequency distribution. It was possible to analyse the response of the dual-band method to these simulations, and in each case it was possible to relate the P_H and T_C estimates to the intended simulation.

In chapter 4 I used the same ALI imagery of lava flows from the July 29th 2001 eruption of Mt Etna and applied the dual-band method in the same way as that discussed within this chapter. In chapter 4 I advised that in order to relate the various thermal distributions present, all returned estimates for thermally anomalous pixels from the lava flow for PH and TC must be plotted against the PIT from an unsaturated channel. All the thermally anomalous pixels within the selected scene are plotted in PH – PITN space including those that are only part filled by the lava flow, those with cool surrounding ground or levee material as well as those pixels with a large fractional area occupied by the active lava itself. It is then possible to identify the likely sub-pixel thermal structure by the

relative position in PH – PITN space. For example, pixels incorporating a large amount of fresh lava at > 900°C will return a high value of PH and the pixel will have a high PIT, and therefore plots in the upper-right of PH – PITN space.

By using this approach we are taking into account the known problems with the dual-band method. In this chapter, however, I have chosen to represent the solutions for P_H and T_C in a graphical map representing solutions for each of the pixels within the image sub-selection. In figure 6.7 for example, I have plotted all solutions for the dual-band method applied to ALI bands 5 and 5p. This combination provides the greatest sensitivity to active lava with relative lack of saturation due to the provision of channel 5p, and therefore returns many more successful solutions. The large number of successful solutions, obtained over even the most active areas of the flow, allow certain important observations to be made. The highest values for P_H and T_C were obtained for the pixels located over the central portions of the flow. In this case the flow was channelised and therefore moving relatively quickly with subsequent entrainment of the crust and constant exposure of fresh material at near-magmatic temperatures in the flow core. The dual-band method applied to the ALI data has successfully identified these areas, and by applying the relative approach discussed in Chapter 4 we can be sure that these pixels (prior knowledge notwithstanding) are more active than the surrounding pixels. Although this is obvious by simple measure of the PIT returned for such pixels, the dual-band method can still roughly identify the likely sub-pixel structure present with some confidence, be it a cooling lava with relatively high values for T_C, a pixel with substantial flow levee's or a pixel entirely filled by an active flow. The extra provision of channels in the SWIR on the ALI that make these retrievals possible, allows the continued use of the dual-band procedure so long as the results are considered to be relative rather than absolute.

6.12. Conclusions

We have demonstrated the extensive application of the dual-band method of extracting information on sub-pixel resolution hot spots in ETM+ and ALI data over active lava flows. The ability to obtain a successful solution requires the use of unsaturated instrument data within the SWIR. The extent of saturation observed within ETM+ channels 7 and 5 has prevented the successful use of this method for even moderate levels of lava flow activity observed within the study area. Similar levels of saturation have been found in ALI channel 7 that have prevented the use of this channel in the dual-band calculations. ALI channel 5 also displays saturation over the most active flows and vents imaged within the study area.

However, due to its wider dynamic range and higher saturation radiance, ALI channel 5 is less susceptible to saturation than the equivalent ETM+ channel 5. ALI channel 5p placed within the SWIR between ETM+ channels 4 and 5 saturated only once over even the most active regions within the study area. ALI channel 4p showed no saturation, but was sensitive to even the most active lava flows. ALI channel 4p also displayed a greater sensitivity to thermally anomalous areas than either ETM+ or ALI channel 4. This is due to its placement at a shorter wavelength within the ETM+ channel 4 bandpass. This greater sensitivity enables its use within the dual-band procedure applied to ALI channels.

The ALI instrument has demonstrated that it is possible to gain successful dual-band estimates of sub-pixel thermal detail over hot active lava flows that are not available or reliable when using ETM+ data. This is due to the addition of the two extra SWIR channels, 5p and 4p. Different band combinations available using unsaturated ALI data are sensitive to differing P_H & T_C combinations providing coverage for a range of lava flows from cooling stagnating flows to active flows proximal to the vent using channel combinations at progressively shorter wavelengths. This is not possible with ETM+

because the relevant channels do not exist. Considering this we have established that for vigorous active lava channels ALI bands 5p & 4p may be used, whilst for moderately active lava flows ALI bands 5 & 5p may be used for obtaining dual-band solutions. ALI channels 7 & 5 and 7 & 5p can be used for less active or stagnating flows.

The increased signal to noise ratio of the ALI and better radiometric sensitivity coupled with the extra SWIR channels has produced an instrument that is highly capable in terms of remote sensing of active lava flows. If ALI technology were to be incorporated into a replacement Landsat instrument then the resulting data would prove highly useful in the analysis of active lava flows to an extent not previously possible. We look forward to the application of ALI data to a wider variety of volcanic phenomena and the possibility of an ALI based ETM+ replacement.

7. Summary and further work required

7.1. Outline of thesis

In this thesis I have approached the subject of remote sensing of active volcanoes at a range of scales using a range of instruments. This approach has seen the use of radiometers recording spot-temperatures, through very high spatial resolution thermal camera imagery to one of the latest space-borne instruments, the EO-1 Advanced Land Imager (ALI). This has shown that relatively simple systems, such as a radiometer mounted on a tripod can return information on active volcanic processes of a high quality and use comparable to the data returned from the vantage point of high resolution (spectral and spatial) space-based systems.

This thesis can be divided into two main sections, chapters 2 and 3 describe and use data from a set of radiometers located at the Pu`u`O`o crater on Kilauea volcano, Hawaii. In the final three chapters, I deal with data returned from high resolution satellite instruments such as the Landsat7 Enhanced Thematic Mapper plus (ETM+) and the ALI. In chapters 4 and 5 the two extremes of ground-based data and that returned from satellite systems meet, as I use imagery returned from a ground based thermal imaging camera to simulate data returned from the ALI. The work undertaken in this thesis has raised a number of issues and here I discuss how best to proceed and why.

7.2. Remote sensing of volcanoes using ground-based instruments

In chapter 2 I used three radiometers located on the rim of the Pu`u`O`o crater of Kilauea volcano to record a thermal time series from various locations on the crater floor over the course of two months. One such target was the small Beehive vent. The thermal

record from this vent often displayed a series of anomalies, with a sharp rise in temperature interspersed at various intervals. These anomalies fell into two categories: 1. a sharp rise in temperature with a rapid fall in temperatures over 5-20 seconds after which the thermal record indicated ambient temperatures. 2. A sharp rise in temperature with a much less rapid return to the ambient background temperature.

During the September and October 2001 study period anomalous seismic events had been recorded from the Pu`u`O`o crater using the Hawaii Volcano Observatories RSAM network. These anomalies were attributed to degassing events occurring from a vent within the crater.

I undertook a study to infer whether the two sets of anomalies were related, and if so to identify any pattern in the occurrence of these anomalies. I wrote software that automatically identified the defining characteristics of the thermal anomalies, maximum achieved temperature and duration from the record and compensated for the constant fluctuation in temperature due to the changing crater viewing conditions. I recorded by hand the RSAM data from the HVO helicorder drums. I found that the two sets of anomalies were indeed coincident and that in fact, the RSAM anomalies were the seismic record of degassing events of which the thermal signal was being recorded by the "Huey" radiometer. Therefore we had a record of degassing from a single vent over the course of two months.

There degassing events when considered over the study period did not appear to occur at evenly spaced intervals – it may not be unreasonable to assume that if the degassing rate at Pu`u`O`o is constant then we might expect to see regular degassing events in much the same way that the Old Faithful geyser in the Yellowstone National Park operates (despite the obviously different eruption medium and mechanisms!). I therefore undertook a study to analyse the occurrence pattern of the anomalies and whether the two types of anomaly recorded could be used to infer the various mechanisms.

Studies of previous eruptions at Kilauea and the observation of the variation in such features as lava lakes, most noticeably by H.Jaggar in 1919, have often attempted to relate the variation to the changing Lunisolar tide. Therefore I was interested to see if such a link was present within the thermal record from Pu`u`O`o. I found that such a link was suggested and could be found in the pattern in the number of anomalies occurring in response to the fortnightly tide. It appeared that more anomalies occur at the time when the fortnightly tide is at a minimum and is waxing towards a maximum. However, it is very difficult to relate just two months worth of anomaly data to a fortnightly cycle. Hence it is imperative that to definitively prove this relationship a longer study period must be undertaken. Furthermore, the study in Chapter 2 only considered degassing detected from a single vent, yet in order to relate large scale effects such as the Lunisolar tide to the Pu`u`O`o or Kilauea system such a future study must consider the degassing from the entire system and all vents. . As the Pu`u`O`o system is known to be complicated and there were at least 4-5 other vents on the crater floor, an ideal situation would be to have monitoring camera's for each of these vents. In this way, the total degassing from the various vents could be linked to each other and therefore an analysis of the plumbing system could be made.

This may be unfeasible to accomplish with just a set of radiometers so any future work must be obtained in conjunction with other measures of effusive activity. The overall rate of degassing, in terms of SO_2, from Kilauea is currently monitored by HVO using the COSPEC instrument on a regular basis. Such a study may also encompass analysis of the rate of magma flux through the entire tube system that supplies lava from Pu`u`O`o to the ocean entry points (at the time of writing in 2005). Such a wide ranging study needs to be undertaken as the conduit system that supplies Pu`u`O`o is complex and poorly understood, and hence it is difficult to relate system wide processes to the variations present within one small part of the system i.e. the Beehive vent. I proposed that the changing levels in the magma column affect the rate of exsolution of gases and therefore

vesiculation, which due to a lag because of the transit time within the magma column can account for the relationship between the Lunisolar tide and the detected degassing events.

Further work also needs to be carried out to relate the level of magma within a vent such as the Beehive vent to the rate and type of degassing and spattering events recorded in radiometer data such as that discussed in Chapter 2. For instance, without the presence of supporting information it is impossible to infer whether the type of event detected was due to variations in the rate of degassing or the changing level of the free-magmatic surface within the vent. Lower levels of the surface may modulate the detection of molten spatter as more fore is needed to eject the material out of the vent and onto the surrounding surface and in view of the radiometer. Such changing levels of the surface may not noticeable affect the detection of events only involving gas. Furthermore, the growth of spatter ramparts around the vent needs to be known as these will grow with the continuing ejection of molten spatter. Such hornito's will gradually affect the detection of ejected molten material during the study period making it difficult to assume that observation conditions have been consistent throughout the study period. Such techniques using VLF may be able to provide an estimate on the level of molten material within the vent (Kauhikauau et al, 1996), whilst local (the current camera situated on the crater rim was usually clouded in) video imagery could be used to visually confirm the presence of molten spatter with degassing events as well as changing vent morphology. Therefore, in order to definitively relate the rate and type of degassing from vents to the Lunisolar tides a longer study period needs to be used as well as visual confirmation on style of degassing and changing conditions. Chapter 2 has shown that there is a tantalising link, further work using these suggestions may be able to resolve this link definitively.

In Chapter 3 I use those degassing events from the Beehive vent discussed in Chapter 2 that were associated with what appeared to be cooling curves to attempt to gain an estimate on the total mass of molten ejecta where present. I concentrated on using only

those anomalies with protracted cooling durations as it is difficult to quantify the actual volume of gas ejected from such a vent as it will rapidly disperse and cool within the crater. The natural buoyancy as well as the force with which the gas was expelled will also serve to take the gas quickly out of the radiometer FOV. However, those anomalies with cooling curves provide an opportunity to quantify the amount of molten spatter ejected as the material will remain and cool within the radiometer FOV. Due to the simplicity of the radiometer data, only two parameters were available to describe such events: the maximum achieved temperature and the event duration. I calculated the effective FOV of the radiometer, based on the distance to the Beehive vent from the Pu`u`O`o crater wall. The maximum temperature achieved by an anomaly will be a function of the temperature of any hot material (gas or molten spatter) and the total fractional area occupied by this material (as well as the "cool" background temperature). If the initial molten temperature of the material is assumed to be near magmatic (i.e. 1000°C) then it is possible to identify the fractional area radiating at this temperature as the ambient temperature is known. I used spherical thermal diffusion modelling based on the work of Carslaw & Jaeger (1954) and Crank (1975) to provide a method of relating the rate of cooling with the volume of material. Effectively, this modelling quantifies that a larger volume of material will take longer to cool than a smaller volume. However, it is extremely unlikely that the entire volume of molten ejecta will be emplaced as a single spatter bleb! Hence, I used an iterative approach that used the calculated fractional area of the FOV occupied by molten material and an estimate of the size of individual spatter blebs based on the observed cooling duration from the thermal diffusion modelling. The mass of ejecta is simply the number of blebs of the calculated size required to fill the calculated fractional area occupied within the radiometer FOV.

This method allows a basic estimate of the mass of ejecta associated with spattering events at the Beehive vent if certain assumptions are made. For instance, I was only able to test this model rudimentarily in laboratory conditions using a single artifical bleb. This

was done so as to estimate the dimension of the chilled rind (or rim) analogous to the crust that instantly develops on such molten material once it has been ejected and exposed to the cool atmosphere. I then applied this rim value to all events recorded at the Beehive vent, so work needs to be undertaken to ascertain whether this is a valid assumption. Ideally, physical analysis of spatter blebs that were actually recorded cooling by such radiometer data but safety measures may prevent this! Such physical analysis would also be able to confirm whether the estimated mass returned by the "Ejecta-Mass" model is reasonable. There are other areas used in this model that require a visual confirmation that assumptions are valid.

For instance, I suggested for Chapter 2 that video imagery of the vent in question should be obtained in conjunction with the radiometer data to confirm the presence of molten material. This imagery would also confirm the relative volume of ejected material and whether all such material is within the radiometer FOV. Currently I assume that all such ejected material is within the FOV, but in reality the vents spatter ramparts may obscure or "knock-back" any ejected spatter. It is also unlikely that all ejected spatter will be of the same size.

Therefore, in order to validate this model and to ascertain whether it does indeed offer a method of estimating the mass of ejecta from a simple radiometer record this model really needs field validation. I propose this model here as an initial attempt to quantify this as there are many applications that will find the results of this model useful. For instance, the succesful application of this model may help to better quantify the total of effusive products as well as relate the force of degassing based on the assumption that it requires more forceful expulsion of gas to eject a greater mass of material from the free-magmatic surface. This model may be used productively with a longer time series of data required for Chapter 2 to better quantify the relationship between the tides and total effusive activity.

Visual confirmation of spattering accompanied by field observations and collections can further help to refine the assumed parameters within the model and create an effective tool for the ground based remote sensing of volcanoes

7.3. Relating ground-based observations to the orbital viewpoint

Chapters 2 and 3 discussed the application of simple radiometers and the derivation and analysis of events at Pu`u`O`o. Despite being ground-based these simple radiometers have proved to be effective instruments for the remote sensing of volcanoes. In the second section of this thesis I return to more "conventional" forms of remote sensing, using space based instruments. However, in Chapter 4 and 5 I show that the use of ground based observations, in this case high resolution thermal imagery, can play an important role in validating and refining currently used models that apply to the resulting data. Chapters 4 and 5 can be considered the "cross-over" in this thesis's account of remote sensing and volcanology. In Chapter 6 I consider the implications of the previous two chapter's observations in the analysis of a new space based instrument that promises to be a vast improvement for satellite based volcanology.

In chapters 4 and 5 I went on to analyse in depth the performance of that stalwart of remote sensing of volcanoes, the dual-band method. The dual-band method has been used often and its shortcomings are well documented, most recently by Wright & Flynn (2004). Most of these studies rightly point out that it is difficult, and at worst impossible, to simulate the wide continuum of temperatures present on the surface of a lava flow using just 2 components. This situation worsens when we consider that it is more probable that a pixel IFOV will not only contain a lava flow but also the surrounding cooler ground. Such situations will lead to erroneous derivations from the dual-band method. This situation is complicated by the likely saturation of SWIR channels over such volcanic surfaces where

even a small fraction of the pixel IFOV is occupied. The introduction of the new ALI goes some way to addressing the problem of instrument saturation (and I discuss this in Chapter 6) but there are still inherent problems with using the dual-band method.

However, in Chapters 4 and 5 I attempt to quantitatively identify the response of the dual-band method to a range of combinations involving lava flows at various stages of activity and at various occupying fractions of a pixel IFOV. Previously, most studies have based the performance of the dual-band method solely in relation to estimates of likely thermal structure within a pixel by using simple thermal cameras and radiometers that return point temperatures. By repeated use of such a camera a basic model of the thermal structure can be constructed. However, in the time taken to obtain the data the thermal structure can change.

I have used in Chapters 4 and 5 thermal camera imagery which obtains the entire thermal structure within the cameras IFOV instantaneously. This data can therefore be used to provide a much more accurate representation of the thermal structure present at ground level. The thermal imagery I have used was obtained from various lava flows and their immediate environment at various stages of activity from various eruptions at Mt Etna from 1999 to 2001 (Courtesy of H.Pinkerton). However, this imagery was not obtained with the initial intent that it be used to compare with the overhead viewpoint provided by satellite based imagery and was thus obtained from an oblique vantage point.

Therefore I studied the thermal structure present with the imagery and the resulting derived histograms describing this structure I found that it was possible to replicate this thermal structure using artificial histograms based on Gaussian curves, which could be manipulated iteratively until the "best-fit" was found. These artificial histograms could then be converted into an image with a similar range in temperature as found in the original FLIR imagery. Finally, this artificial image as a temperature map could be represented as a single PIT at each of the spectral channel wavelengths used by an instrument such as the

ALI or Landsat7 ETM+ by using the Planck relationship. The original thermal structure could be varied to mimic changing thermal structures, in either a unimodal (where the lava flow fills the entire pixel IFOV) or a bimodal distribution (where the lava flow and surrounding cooler material, such as flow levee's or ambient ground) by manipulating the parameters used in the original Gaussian equation. These variations will result with changing PIT values, and I used this to relate the changing values returned from the dual-band method for the artificial thermal structure to the actual calculated values. However, it is very difficult as I stated earlier, to relate such a complex thermal structure in just two fractional areas. I therefore calculated the heat flux for the entire simulated pixel and those results from the dual-band method and used this as a measure to base the comparison on.

As expected, I found that the dual-band method provides severe underestimates for the actual heat flux calculated using these methods. Importantly however, the variation in heat flux, albeit at much lower values, matched the variation in the original models. As I was able to vary these models in any way I wished, which is difficult to do otherwise, I found that the dual-band method responded to such changes. Therefore the dual-band method can still be of use to identify the likely thermal structure present within a pixel. I found that this can be done most effectively by plotting all returned estimates for fractional area and temperature against the relevant PIT in the same chart for all anomalous pixels. Where these estimates plot in chart-space is indicative of the likely thermal structure.

This finding is useful as the dual-band method is easily applied to most multi-spectral instruments and can therefore still be a useful tool using only two channels. Wright & Flynn (2004) show that a simple lava flow is best modelled with 5 to 7 thermal components, which may then be identified using such Hyperspectral imagery provided by the EO-1 Hyperion instrument. This data is very restricted in availability, whilst instruments such as ETM+ and ASTER with a restricted number of spectral channels still provide ideal platforms for the application of the dual-band method. Therefore, in the

absence of readily available Hyperspectral imagery the dual-band method may still be of use for *indicating* the likely thermal structure present within a pixel.

In chapter 5 I used similar techniques to further show the problems arising from the scenario that a lava flow on the Earth's surface is very likely to be angled away from the ideal viewing geometry of the instrument placed directly over the flow. This is due to a combination of the satellite elevation angle and the likelihood that the flow may be travelling down the angled slopes due to the local topography of the volcano. I have shown here that in such situations the results of the dual-band method are even further removed from reality, but that the method can still distinguish between thermal compositions. This was accomplished using similar methods to those described in Chapter 4 but by taking into account the number and depths of simulated cracks in the simulated flows surface thermal structure and how the likely fractional areas will vary depending on the instrument inclination angle.

Although the original thermal camera data was obtained from active lava flows, these models described in Chapters 4 and 5 require validation from a similar set of imagery obtained at similar angles and perspectives that space based instruments have. Such a study might make use of the thermal camera obtaining imagery from directly over the flows in a quasi-nadir method, although there are safety issues with this method. A comparison could therefore be made between the actual thermal structure and the simulated structure. The model itself may be further refined by the addition of more Gaussian curves and advanced curve fitting techniques. This is limited in my study as using two curves to represent the bimodal thermal structure was adequate. These techniques can be easily applied to hyperspectral imagery, such as the Hyperion instrument. The number of PITs derived from my thermal simulations is effectively unlimited and therefore such a study could just as easily test the veracity of the 7 component model proposed by Wright & Flynn (2004).

This thesis concludes by making a detailed comparison between the Landsat7 ETM+ and the EO-1 ALI with respect to the remote sensing of active volcanoes. The Landsat series of TM/ETM+ instruments has long been used for the detailed study of active volcanism due to a combination of high resolution and a range of channels within the spectrum. The EO-1 ALI is regarded as a "technology try-out" for a future replacement Landsat instrument, and incorporates a number of extra spectral channels. Some of these channels have been placed in a region of the SWIR ideal for the remote sensing of hot surfaces such as lava flows, but where the ETM+ has no channels. Such a study is required to investigate the relative performance of the ALI to the older ETM+ in order to evaluate the advantages offered for volcanic remote sensing by the ALI. I found that the ALI is very much more effective at detecting and evaluating sub-pixel thermal composition than the ETM+. This is due to a combination of better spectral resolution and lower susceptibility to saturation over such hot targets as lava flows.

8. References

Allard.P, Carbonelle.J, Metrich.N, Loyer.H & Zettwoog.P, 1994, Sulphur output and magma degassing budget of Stromboli volcano. Nature, 368: 326-330.

Aries.S.E, Harris.A.J.L & Rothery.D.A, 2001, Remote infrared detection of the cessation of volcanic eruptions. Geophys. Res. Letters, 28(9): 1803-1806.

Baloga.S.M, Glaze.L.S & Peiterson.M.N, 2001, Influence of volatile loss on thickness and density profiles of active basaltic flow lobes. J.Geophys.Res., 106(B7): 13395-13405.

Barker.S.R, Sherrod.D.R, Lisowski.M, Heliker.C & Nakata.J.S, 2003. Correlation between lava-pond drainback, seismicity and ground deformation at Pu`u`O`o, USGS Professional Paper 1676: 53-63.

Barnes.W.L, Pagano.S.T & Salomonson.V, 1998. Prelaunch characteristics of the Moderate Resolution Imaging Spectroradiometer (MODIS) on EOS-AM1. IEEE Trans. Geosci.Rem.Sens, 36(4): 1088-1100.

Baum H R & Mell W E, 2000, Radiation and Velocity Fields Induced by Localised Temperature Fluctuations, 28th Proceedings of the Combustion Institute v1: 473-479.

Behncke.B & Neri.M, 2003, The July-August 2001 eruption of Mt. Etna (Sicily), Bull. Volcanol., 65: 461-476

Bicknell.W.E, Digenis.C.J, Forman.S.E & Lencioni.D.E, 1999. EO-1 Advanced Land Imager. SPIE Conference on Earth Observing Systems IV, 3750: 80-88.

Biggar.S.F, Thome.K.J, Holmes.J.M, Kuester.M.A & Showengerdt.R.A, 1999. In flight radiometric and spatial calibration of EO-1 optical sensors. Proceedings of SPIE 2002.

Blake S, 2000. Comments on "Cooling and crystallisation of lava in open channels, and the transition of pahoehoe lava to 'a'a", Bull. Volcanol. 62(4-5):362 - 364

Blake.S & Bruno.B.C, 2000. Modelling the emplacement of compound lava flows. Earth & Plan. Sci.Letters, 184: 181-197.

Bruno.N, Caltabiano.T & Romano.R, 1999. SO2 emissions at Mt. Etna with particular reference to the period 1993-1995. Bull.Volcanol, 60: 405-411.

Budetta.G & Carbone.D, 1998. Temporal variations in gravity at Mt Etna (Italy) associated with the 1989 and 1991 eruptions, Bull. Volcanol, 59:311-326.

Buongiorno.M.F, Realmuto.V.J & Doumaz.F, 2002. Recovery of spectral emissivity from thermal Infrared multispectral scanner imagery acquired over a mountainous terrain; A case study from Mount Etna, Sicily, Rem. Sens. Environment, 79(1): 123-133.

Burgi P-Y, Caillet M & Haefeli S, 2002. Field temperature measurements at Erta' Ale Lava lake, Ethiopia, Bull. Volcanol 64: 472-485

Caltabiano.T, Romano.R & Budetta.G, 1994. SO2 flux measurements at Mount Etna (Sicily). J.Geophys.Res, 99(D6): 12809-12819.

Calvari.S & Pinkerton.H, 1998. Formation of lava tubes and extensive flow field during the 1991-1993 eruption of Mount Etna, J. Geophys. Res., 103(B11): 27291-27301.

Calvari.S & Pinkerton.H, 1999. Lava tube morphology on Etna and evidence for lava flow emplacement mechanisms. J.Volcanol. Geotherm. Res., 90: 263-280.

Carslaw.H. & Jaeger.C, 1959. Conduction of heat in solids, New York, Oxford University Press

Cashman.K, Pinkerton.H & Stephenson.J, 1998. Introduction to special section: Long Lava flows. J. Geophys. Res., 103(B11): 27281-27289.

Cashman.K.V, Thornber.C & Kauahikaua.J.P, 1999. Cooling and crystallisation of lava in open channels, and the transition of Pahoehoe lava to A'a, Bull. Volcanol, 61: 306-323.

Chapman R. 1994. Physics for Geologists, UCL Press (September 1, 1994).

Cracknell. A. P. 1998. Synergy in remote sensing – whats in a pixel? Int. J. of Remote Sens., 19, 2025-2047

Crank, J. (1975). The Mathematics of Diffusion. 2nd ed. Clarendon Press, Oxford.

Crisp.J. 1995. Volcanic SO2 alert. EOS IDS Volcanology Team Data Product Document, #3288.

Crisp.J & Baloga.S. 1990. A model for lava flows with two thermal components. J.Geophys.Res, 95(B2): 1255-1270.

Crisp.J & Baloga.S. 1994. Influence of crystallisation and entrainment of cooler material on the emplacement of basaltic a'a lava flows, J. Geophys.Res 99: 11819-11831.

Davies.M.A & Rose.W.I. 1998. Evaluating GOES Imagery for Volcanic Cloud Observation at the Soufriere Hills Volcano, Montserrat, EOS Trans AGU, 79:505-507.

De Silva.S.L & Francis.P.W. 1990. Potentially active volcanoes of Peru-Observations using Landsat TM and Space Shuttle Imagery. Bull. Volcanol., 52: 286-301.

Dehn.J, Dean.J, Engle.K & Izbekov.P, 2002. Thermal Precursors in Satellite Imagery of the 1999 Eruption of Shishaldin Volcano, Bull. Volcanol, 64: 525-534.

Denlinger.R.P, 1997. A dynamic balance between magma supply and eruption rate at Kilauea volcano, Hawaii. J.Geophys.Res, 102(B8): 18091-18100.

Dennis.A.M, Harris.A.J.L, Rothery.D.A, Francis.P.W & Carlton.R.W. 1998. Satelite Observations of the April 1993 eruption of Lascar volcano. Int.J.Remote Sensing, 19(5): 801-821.

Donegan.S & Flynn.L, 2004. Comparison of the Landsat 7 ETM+ and EO-1 Advanced Land Imager Over Active Lava Flows, J.Volcanol. Geotherm. Res. V 135, N 1-2

Dozier.J, 1981. A method for satellite identification of surface temperature fields of subpixel resolution. Rem. Sens. Env, 11: 221-229.

Dragoni.M, 1989. A dynamical model of lava flows cooling by radiation, Bull. Volcanol, 51:88-95.

Drury.S, 1987. Image Interpretation in Geology, Allen and Unwin (Publishers) Ltd, London

Durkee.P.A, Jensen.D.R, Hindman.E.E & Vonder Haar.T.H, 1986. The relationship between marine aerosol particles and satellite detected radiance. J.Geophys.Res, 91(D3): 4063-4072.

Dzurisin.D, Anderson.L.A, Eaton.G.P, Koyanagi.R.Y, Lipman.P.W, Lockwood.J.L, Okamura.R.T, Puniwai.G.S, Sako.M.K & Yamashita.K.E, 1980. Geophysical observations of Kilauea volcano, Hawaii, 2, Constraints on the magma supply during November 1975-September 1977, J.Volcanol. Geotherm. Res., 7: 241-269

Edner.H, Ragnarson.R, Svanberg.S, Wallinder.E, Ferrera.R, Cioni.R, Raco.B & Taddeucci.G, 1994. Total fluxes of sulfur dioxide from the Italian volcanoes Etna, Stromboli and Vulcano measured by differential absorption LIDAR and passive differential optical absorption spectroscopy. J.Geophys.Res, 99(D9): 18827-18838.

Endo.E.T & Murray.T, 1991. Real-time Seismic Amplitude Measurement (RSAM): a volcano monitoring and prediction tool. Bull. Volcanol, 53: 533-545.

Ewert.J.W, Murray. T.L, Lockhart.A.B & Miller.C.D, 1993,.Preventing Volcanic Catastrophe: The U. S. International Volcano Disaster Assistance Program: Earthquakes and Volcanoes, vol.24, no.6

Fagents.S.A & Greeley.R, 2001. Factors influencing lava-substrate heat transfer and implications for thermomechanical erosion. Bull. Volcanol, 62: 519-532.

Flynn.L.P, 1996. Thermal anomaly-Low spatial resolution. EOS IDS Volcanology Data Product Document, MOU81-3292.

Flynn.L.P & Mouginis-Mark.P.J, 1994. Temperature of an active lava channel from spectral measurements, Kilauea Volcano, Hawaii. Bull. Volcanol, 56: 297-301.

Flynn.L.P, Harris.A.J.L & Wright.R, 2001. Improved identification of volcanic features using Landsat 7 ETM+. Rem. Sens. Environ, 78: 180-193.

Flynn.L.P, Mouginis-Mark.P.J & Horton.K.A, 1994. Distribution of thermal areas on an active lava flow field: Landsat observations of Kilauea, Hawaii, July 1991. Bull. Volcanol, 56: 284-296.

Francis.P.W & Rothery.D.A, 1987. Using the Landsat TM to detect and monitor active volcanoes: an example from Lascar volcano, N.Chile. Geology, 15: 614-617.

Francis.P.W & Rothery.D.A, 2000. Remote Sensing of Active Volcanoes. Annu. Rev. Earth Planet Sci, 28: 81-106.

Francis.P.W, Chaffin.C, Maciejewski.A & Oppenheimer.C, 1996. Remote determination of SiF4 in volcanic plumes: a new tool for volcano monitoring. Geophy.Res.Letters, 23(3): 249-252.

Francis.P.W, Burton.M.R & Oppenheimer.C, 1998. Remote measurements of volcanic gas compositions by solar occultation spectroscopy. Nature, 396(10 Dec 1998): 567-569.

Galindo.I & Dominguez.T, 2002. Near real time satellite monitoring during the 1997-2000 activity of Volcan de Colima (Mexico) and its relationship with seismic monitoring, J.Volcanol.Geotherm.Res, 117(1-2): 91-104.

Garcia.M.O, Ho.R.A, Rhodes.J.M & Wolfe.E.W, 1989. Petrologic constraints on rift zone processes -results from episode 1 of the Puu Oo eruption of Kilauea volcano, Hawaii. Bull. Volcanol, 52: 81-96.

Garcia.M.O, Rhodes.J.M, Trusdell.F.A & Pietruszka.A.J, 1996. Petrology of lavas from the Puu Oo eruption of Kilauea Volcano: III. The Kupaianaha episode (1986-1992). Bull. Volcanol., 58: 359-379.

Garcia.M.O, Rhodes.J.M, Wolfe.E.W, Ulrich.G.E & Ho.R.A, 1992. Petrology of lavas ffrom episodes 2-47 of the Puu Oo eruption of Kilauea Volcano, Hawaii: evaluation of magmatic processes. Bull. Volcanol., 55: 1-16.

Gasch.J, Arvidson.T & Goward.S.A, 2000. Fire and Ice: An assessment of Landsat7 ETM+ acquisitions over glaciers, volcanoes, Antarctica and sea ice, IEEE Trans on Geosci & Remote Sensing: 457-459.

Giammanco.S, Inguaggiato.S & Valenza.M, 1998. Soil and fumarole gases of Mount Etna: Geochemistry and relations with volcanic activity. J.Volcanol. & Geotherm. Res, 81((1998)): 297-310.

Gillespie.A, Rokugawa.S, Matsunaga.T, Cothern.S, Hook.S & Kahle.A, 1998. A temperature and emissivity separation algorithm for advance spaceborne thermal emission and reflection radiometer (ASTER) images. IEEE Trans. Geosci. Rem. Sens, 36(4): 1113-1126.

Gillespie.A.R, Kahle.A.B & Walker.R.E, 1987. Colour ehancement of highly correlated images. II Channel ratio and 'chromaticity' transformation techniques. Rem. Sens. Env, 22: 343-365.

Glaze.L, Francis.P.W & Rothery.D.A, 1989. Measuring thermal budgets of active volcanoes by satellite remote sensing. Nature, 338: 144-146.

Gottsmann.J & Dingwell.D, 2002. The Thermal history of a spatter fed lava flow: the 8-Ka pantellerite flow of Mayor Island, New Zealand, Bull. Volcanol. 64, 410–422 (2002).

Gupta.R.K & Badarinath.K.V.S, 1993. Volcano monitoring using remote sensing data. Int.J.Remote Sensing, 14(16): 2907-2918.

Hardee H.C, 1987. Heat and Mass Transport in the East Rift Zone Magma Conduit of Kilauea Volcano, USGS Prof.Pap. 1350: 1471-1486.

Harris.A.J.L, Vaughan.R.A & Rothery.D.A, 1995. Volcano detection and monitoring using AVHRR data: the Krafla eruption, 1984. Int. J. Remote Sensing, 16(6): 1001-1020.

Harris.A.J.L & Stevenson.D.S, 1997. Thermal observations of degassing open conduits and fumaroles at Stromboli and Vulcano using remotely sensed data. J.Volcanol. & Geotherm. Res., 76: 175-198.

Harris.A.J.L, Blake.S, Rothery.D.A & Stevens.N.F, 1997a. A chronology of the 1991 to 1993 Mount Etna eruption using Advanced Very High Resolution Radiometer data: Implications for real time thermal monitoring. J.Geophys.Res., 102(B4): 7985-8003.

Harris.A.J.L, Butterworth.A.L, Carlton.R.W, Downey.I, Miller.P, Navarro.P & Rothery.D.A, 1997b. Low cost volcano surveillance from space: case studies from Etna, Krafla, Cerro Negra, Fogo, Lascar and Erebus. Bull. Volcanol, 59: 49-64.

Harris.A.J.L, Flynn.L.P, Keszthelyi.L, Mouginis-Mark.P.J, Rowland.S.K & Resing.J.A, 1998. Calculation of lava effusion rates from Landsat TM data. Bull. Volcanol, 60: 52-71.

Harris.A.J.L & Thornber.C.R, 1999. Complex effusive events at Kilauea as documented by the GOES satellite and remote video cameras. Bull. Volcanol., 61: 382-395.

Harris.A.J.L, Flynn.L.P, Pilger.E & Mathews.S.J, 1999a. Real time monitoring of Lascar using GOES. Volcan Lascar, SNGM Special Monograph, Matthews, S., Gardeweg, M., Sparks, S., (eds.), in review, 1999.

Harris.A.J.L, Flynn.L.P, Rothery.D.A, Oppenheimer.C & Sherman.S, 1999b. Mass flux measurements at active lava lakes: Implications for magma recycling. J.Geophys.Res, 104(B4): 7117-7136.

Harris.A.J.L, Wright.R & Flynn.L.P, 1999c. Remote Monitoring of Mount Erebus Volcano, Antarctica, using Polar Orbiters: Progress and Prospects. Int.J.Remote Sensing, 20(15 & 16): 3051-3071.

Harris.A.J.L, Sherman.S.B & Wright.R, 2000a. Discovery of self-combusting volcanic sulfur flows. Geology, 28(5): 415-418.

Harris.A.J.L, Murray.J.B, Aries.S.E, Davies.M.A, Flynn.L.P, Wooster.M.J, Wright.R & Rothery.D.A, 2000b. Effusion rate trends at Etna and Krafla and their implications for eruptive mechanisms. J.Volcanol. & Geotherm. Res., 102: 237-270.

Harris.A.J.L & Rowland.S.K, 2001. FLOWGO: a kinematic thermo-rheological model for lava flowing in a channel. Bull. Volcanol., 63: 20-44.

Harris.A.J.L, Pilger.E, Flynn.L.P, Garbeil.H, Mouginis-Mark.P.J, Kauahikaua.J & Thornber.C, 2001. Automated, high temporal resolution, thermal analysis of Kilauea volcano, Hawaii using GOES satellite data. Int. J. Remote Sensing, 22(6): 945-967.

Harris.A.J.L, Rose.W.I & Flynn.L.P, 2002. Temporal trends in Lava dome extrusion at Santiaguito. Bull. Volcanol.,65:77-89.

Harris.A.J.L & Neri.M, 2002. Volumetric observations during paroxysmal eruptions at Mount Etna: pressurized drainage of a shallow chamber or pulsed supply? J. Volcanol. & Geotherm. Res., 116: 79-95.

Harris.A, Johnson.J, Horton.K, Garbeil.H, Ramm.H, Pilger.E, Flynn.L, Mouginis-Mark.P, Pirie.D, Donegan.S, Rothery.D, Ripepe,M & Marchetti.E, 2003. Ground-based infrared monitoring provides new tool for remote tracking of volcanic activity, EOS, Vol. 84, No. 40

Harris.D.M & Rose.W.I, 1996. Dynamics of Carbon Dioxide emissions, crystallisation, and magma ascent: hypotheses, theory, and applications to volcano monitoring at Mount St. Helens., Bull. Volcanol. 58:163-174.

Harvey.D, Gaonach.H, Lovejoy.S, Stix.J & Schertzer.D, 2002: Multifractal Sensitivity Related to remotely sensed Volcanic Features: A Case Study from Kilauea Volcano, Hawaii, Fractals 10 (3), 265-274

Heliker.C & Mattox.T, 2003. The first two decades of the Pu`u`O`o-Kupaianaha eruption: Chronology and selected bibliography, USGS Professional Paper 1676: 1-28.

Heliker.C & Wright.T.L, 1991. The Pu'u'O'o-Kupaianaha eruption of Kilauea. EOS, Trans.AGU, 72(47): 521-530.

Heliker.C, Sherrod.D, Thornber.C & Kauahikaua.J, 1997. Kilauea volcano east rift zone eruption update; 1997 brings era of instablility (abs), Eos Trans., AGU, 78, 648, 1997

Hoffmann.J.P, Ulrich.G.E & Garica.M.O, 1990. Horizontal ground deformation patterns and magma storage during the Puu OO erutpion of Kilauea volcano, Hawaii: episodes 22-42. Bull. Volcanol., 52: 522-531.

Holben.B, Vermote.E, Kaufman.Y.J, Tanre.D & Kalb.V, 1992. Aerosol retreival over land from AVHRR data-Application for atmospheric correction. IEE Trans.Geosci & Rem.Sens, 30(2).

Hon.K, Kauahikaua.J, Denlinger.R & Mackay.K, 1994. Emplacement and inflation of Pahoehoe sheet flows: Observations and measurements of active lava flows on Kilauea Volcano, Hawaii, Geol. Soc. America. Bull., 106(3): 351-370.

Horn.R, Papathanassiou.K.P, Reigber.A, Scheiber.R, Hauskneckt.P, Strobl.P, Boehl.R, Scheele. M, Reulke.R, Baerwald.W, Puglisi.G, Coltelli.M & Fornaro.G, 1997. The Mount Etna Case study: A multisensor review, IEEE Trans Geosci & Remote Sensing, 2: 1022-1023.

Johnson.D.J, Sigmundsson.F & Delaney.P.T, 2000. Comment of "Volume of magma accumulation or withdrawal estimated from surface uplift or subsidence with application to the 1960 collapse of Kilauea volcano" by P.T.Delaney and D.F.McTigue, Bull. Volcanol., 61: 491-493.

Kahle.A.B, Gillespie.A.R, Abbot.E.A, Abrams.M.J, Walker.R.E & Hoover.G, 1988. Relative dating of Hawaiian lava flows using multispectral thermal IR images: A new tool for geologic mapping of young volcanic terranes. J.Geophy.Res, 93(B12): 15239-15251.

Kasahara.J, 2002. Tides, Earthquakes and Volcanoes, Science, Vol 297, Issue 5580: 348-349

Kauahikaua.J, Cashman.K, Mattox.T.N, Heliker.C, Hon.K.A, Mangan.M.T & Thornber.C.R, 1998. Observations on basaltic lava streams in tubes from Kilauea volcano, island of Hawai'i. J.Geophys.Res, 103(B11): 27303-27323.

Kauahikaua.J, Mangan.M, Heliker.C & Mattox.T, 1996. A quantitative look at the demise of a basaltic vent: the death of Kupaianaha, Kilauea Volcano, Hawai`i. Bull. Volcanol., 57: 641-648.

Kaufman.Y.J, Justice.O.J & Flynn.L.P, 1998. Potential global fire monitoring from EOS-MODIS. J.Geophys.Res., 103(D24): 32215-32238.

Keszthelyi.L, 1995. Measurements of the cooling at the base of pahoehoe flows, Geophys. Res. Lett., 22: 2195-2198.

Keszthelyi.L & Denlinger.R, 1996. The initial cooling of pahoehoe flow lobes, Bull. Volcanol. 58: 5-18.

Keszthelyi.L & Self.S, 1998. Some physical requirements for the emplacement of long basaltic lava flows. J.Geophys.Res., 103(B11): 27447-27464.

Korb.A.R, 1999. Thermal Infra-red remote sensing and Kirchoffs law,2, feild measurements. J.Geophys.Res, 104(B7): 15339.

Koyanagi R Y, Chouet B & Aki K, 1987. Origin of Volcanic Tremor in Hawaii, USGS Professional Paper 1350: 1221-1257.

Kyle.P.R, Sybeldon.L.M, McIntosh.W.C & Meeker.K, 1994. Sulphur Dioxide emission rates from Mount Erebus, Antarctica. Volcanol & Env. Studies of Mount Erebus, Antarctica; Antarctic research series, 66: 69-82.

Kyle.R.K & Meeker.K, 1990. Emission rates of sulphur dioxide, trace gases and metals from Mount Erebus, Antarctica. Geophys.Res.Lett., 17(12): 2125-2128.

Lencioni.D.E, Digenis.C.J, Bicknell.W.E, Hearn.D.R & Mendenhall. J. A, 1999. Design and performance of the EO-1 Advanced Land Imager. SPIE Conference on Sensors, Systems, and Next Generation Satellites III, Florence, Italy.

Lillesand.T.M & Kiefer.R.W, 1994. Remote Sensing and Image Interpretation. Reference Text, 3rd Ed., John Wiley and Sons Ltd, London.

Lipman.W.P & Banks.N.G, 1987. Aa flow dynamics, Mauna Loa 1984, USGS Professional Paper 1350: 1527-1567.

Love.S.P, Goff.F, Counce.D, Seibe.C & Delgado.H, 1998. Passive infrared spectroscopy of the eruption plume at Popocatepetl volcano, Mexico. Nature, 396(10 Dec 1998): 563-566.

Lovejoy.S, Schertzer.D, Tessier.Y & Gaonac'h.H, 2001. Multifractals and resolution independant remote sensing algorithms: the example of ocean colour. Int.J.Remote Sensing, 22(7): 1191-1234.

Mangan.M.T, Heliker.C, Mattox.T.N, Kauahikaua.J.P & Heltz.R.T, 1995. Episode 49 of the Pu'u 'O'o-Kupaianaha eruption of Kilauea Volcano- breakdown of a steady state eruptive era. Bull. Volcanol., 57: 127-135.

Markham.B.L, 1985. The Landsats Sensors Spatial Responses. IEE Trans. on Geosci. & Rem. Sens, Ge-23(6): 864-874.

Markham.B.L & Barker.J.L, 1985. Spectral characterisation of the Landsat TM sensors. Int.J.Remote Sensing, 6(5): 697-716.

Mastin.L, 1995. Thermodynamics of gas and steam blast eruptions, Bull. Volcanol. 57 (2): 85-98.

Mathews.S.J, Gardeweg.M.C & Sparks.R.S.J, 1997. The 1984 to 1996 cyclic activity at Lascar Volcano, northern Chile: cycles of dome growth, dome subsidence, degassing and explosive eruptions, Bull. Volcanol.,59:72-82.

Matson.M & Dozier.J, 1981. Identification of subresolution high temperature sources using a thermal IR sensor, Photogramm. Eng. Remote Sensing, 87:273-282.

Mattox.T, Heliker.C, Kauahikaua.J & Hon.K, 1993. Development of the 1990 Kalapana flow field, Kilauea Volcano,Hawaii. Bull. Volcanol., 55: 407-413.

Melchior, P, The Tides of the Planet Earth, Pergamon, Paris, 1978, p609.

Melnik.O & Sparks.R.S.J, 1999. Nonlinear dynamics of lava dome extrusion, Nature 402, 37-41.

Mendenhall.J.A Lencioni.D.E & Parker.A.C, 1999. Radiometric calibration of the EO-1 Advanced Land Imager. SPIE Conference on Earth Observing Systems IV, 3750: 117-131.

Mendenhall.J.A, Lencioni.D.A, Hearn.D.R & Digenis.C.J, 2002. Flight test results of the Earth Observing-1 Advanced Land Imager, SPIE 2002, 7-11 July, 2002.

Montalto.A, 1994. Seismic signals in geothermal areas of active volcanism: a case study from 'La Fossa', Vulcano (Italy), Bull. Volcanol., 56(3):220-227.

Mouginis-Mark.P.J, 1995. Preliminary observations of volcanoes with the SIR-C Radar, IEEE Trans. Geosci. Rem. Sens. 33:934-938.

Mouginis-Mark.P.J & Francis.P.W, 1992. Satellite Observations of Active Volcanoes: Prospects for the 1990's. Episodes, 15(1): 46-56.

Mouginis-Mark.P.J et al, 1991. Analysis of Active Volcanoes from the Earth Observing System. Rem. Sens. Environ., 36: 1-12.

Oppenheimer.C, 1991. Lava flow cooling estimated from Landsat Thematic Mapper infrared data: the Lonquimay eruption (Chile,1989). J.Geophys.Res., 96(B13): 21865-21878.

Oppenheimer.C, 1993. Thermal distributions of hot volcanic surfaces constrained using three infrared bands of remote sensing data. Geophys. Res. Lett., 20(6): 431-434.

Oppenheimer.C, 1997. Ramifications of the skin effect for crater lake heat budget analysis. J.Volcanol.Geotherm.Res, 75: 159-165.

Oppenheimer.C, Francis.P.W, Rothery.D.A & Carlton.R.W, 1993. Infrared image analysis of volcanic thermal features: Lascar Volcano, Chile 1984-1992. J.Geophys Res, 98(B3): 4269-4286.

Oppenheimer.C & Francis.P.W, 1997. Remote sensing of heat,lava and fumarole emissions from Erta Ale volcano, Ethiopia. Int.J.Remote Sensing, 18(8): 1661-1692.

Oppenheimer.C, Francis.P.W & Maciejewski.A.J.H, 1998a. Spectroscopic observation of HCl degassing from Soufriere Hills volcano, Montserrat. Geophys.Res.Letters, 25(19): 3689-3692.

Oppenheimer.C, Francis.P.W & Stix.J, 1998b. Depletion of sulfur dioxide in tropospheric volcanic plumes. Geophys. Res. Lett., 25(14): 2671-2674.

Parfitt.E.A & Wilson.L, 1994. The 1983-86 Pu'u'O'o eruption of Kilauea Volcano, Hawaii: a study of dike geometry and eruption mechanisms for a long lived eruption. J.Volcanol. & Geotherm. Res., 59: 179-205.

Patrick.M.R, Smellie.J.L, Harris.A.J.L, Wright.R, Dean.K, Izbekov.P, Garbeil.H, & Pilger.E, 2005. First recorded eruption of Mount Belinda volcano (Montagu Island), South Sandwich Islands. Bull. Volcanol 67:415-422

Pearlman.J, Carman.S, Segal.C, Jarecke.P & Barry.B, 2001. Overview of the Hyperion Imaging Spectrometer for the NASA EO-1 Mission, IGARRS, http://eo1.usgs.gov/documents/hypALI/18.pdf

Pergola.N, Lacava.T, Marchese.F, Scaffidi.I & Tanutoli.V, 2003. A multi-temporal AVHRR satellite records analysis for volcanic activity monitoring: Recent Results achieved during the last of Mt. Etna's eruptive events, Geophys. Res. Abstracts, Vol 5.

Pieri.D.C & Baloga.S.M, 1986. Eruption rate, area and length relationships for some Hawaii lava flows, J.Volcanol. & Geotherm. Res, 30:29-45.

Pieri.D.C, Glaze.L.S & Abrams M.J, 1990. Thermal Radiance observations of an active lava flow during the June 1984 eruption of Mount Etna. Geology, 18(October 1990): 1018-1022.

Pinkerton.H, James.M & Jones.A, 2002. Surface temperature measurements of active lava flows on Kilauea volcano, Hawai`i. J.Volcanol. & Geotherm.Res, 113: 159-176.

Ramsey.M.S & Fink.J.H, 1999. Estimating silicic lava vesicularity with thermal remote sensing: a new technique for volcanic mapping and monitoring, Bull. Volcanol., 61:32-39.

Ramsey.M & Dehn.J, 2004. Spaceborne observations of the 2002 Bezymianny, Kamchatka eruption: the integration of high-resolution ASTER data into near real-time monitoring using

AVHRR, J. Volcanol. Geotherm. Res. 135: 127–146

Realmuto.V.J, 1995. Thermal anomaly-High spatial resolution. EOS IDS Volcanology Team Data Product Document, #3291.

Realmuto.V.J, Abrams.M.J, Buongiorno.M.F & Pieri.D.C, 1994. The use of multispectral thermal infrared image data to estimate the sulfur dioxide flux from volcanoes: a case study from Mt Etna, Sicily, July 29 1986. J.Geophys.Res, 99(B1): 481-488.

Realmuto.V.J, Hon.K, Kahle.A.B, Abbot.E.A & Pieri.D.C, 1992. Multispectral thermal infrared mapping of the 1 October 1988 Kupaianaha flow field, Kilauea volcano, Hawaii, Bull. Volcanol., 55: 33-44.

Rodgers.C.D, 1976. Retreival of atmospheric temperature and composition from remote measurements of thermal radiation. Rev. of Geophy. & Space Physics, 14(4): 609-624.

Romano.R & Sturiale.C, 1982. The Historical Eruptions of Mt. Etna (Volcanological data). Mem.Soc.Geol.It, 23: 75-97.

Rose.W.I & Bluth.G.J.S, 1998. Remote prospects (of Volcanology). Nature, 396(10 Dec 1998): 515-517.

Rose.W.I, Bluth.G.J.S & Ernst.G.G.J, 2000, Integrating retrievals of volcanic cloud characteristics from satellite remote sensors-a summary, Philosophical Transactions of Royal Society, Series A, vol. 358 no 1770, 1585-1606.

Rothery.D.A, Francis.P.W & Wood.C.A, 1988. Volcano Monitering Using Short Wavelength Infrared Data from Satellites. J.Geophys. Res., 93(b7): 7993-8008.

Rothery.D.A, Coltelli.M, Pirie.D, Wooster.M.J & Wright.R, 2001. Documenting surface magmatic activity at Mount Etna using ATSR-2 remote sensing. Bull. Volcanol., 63:387-397.

Rothery.D.A, Thorne.M.T & Flynn.L.P, 2002. MODIS thermal alerts in Britain and the North Sea during the first half of 2001. Int.J.Remote Sensing, 24:817-826.

Rowland.S.K & Walker.G.P.L, 1990. Pahoehoe and aa in Hawaii: volumetric flow rate controls the lava structure, Bull. Volcanol., 52:615-628.

Rymer.H, Cassidy.J, Locke.C.A & Murray.J.B, 1995. Magma movements in Etna Volcano associated with the major 1991-1993 lava eruption: evidence from gravity and deformation. Bull. Volcanol., 57: 451-461.

Rymer.H, Van Wyk de Vries.B & Stix.J, 1998. Pit crater structure and processes governing persistent activity at Masaya Volcano, Nicaragua, Bull. Volcanol., 59:345-355.

Scneider.D.J, Rose.W.I, Coke.L.R, Bluth.G.J.S, Sprod.I.E & Krueger.A.J, 1999. Early evolution of a stratispheric volcanic eruption cloud as observed with TOMS and AVHRR. J.Geophys. Res, 104(D4): 4037-4050.

Segall.P, Cervelli.P, Owen.S, Lisowski.M & Miklius.A, 2001. Constraints on dike propagation from continuous GPS measurements. J.Geophys.Res., 106(N9): 19301-19317.

Self.S & Francis.P.W, 1987. Volcanology. US Nat report to Int. Union. Geodysy & Geophyics, Review of Geophysics, 25(5): 1065-1078.

Shimozuru D, 1987. Tidal effects on Hawaiian Volcanism, USGS Prof. Pap. 1350: 1337-1343.

Stevenson.D.S & Blake.S, 1998. Modelling the dynamics and thermodynamics of volcanic degassing, Bull. Volcanol., 60:307-317.

Sumner.J.M, Blake.S, Matela.R.J & Wolf.J.A, 2005. Spatter, J. Volcanol. Geotherm. Res. 142: 49–65

Sutton.J.A, Elias.T & Kauahikaua.J, 2003. Lava effusion rates for the Pu`u`O`o-Kupaianaha erutpion derived from SO2 emissions and VLF measurements, USGS Professional Paper 1676: 137-148.

Takada.A, 1997, Cyclic flank-vent and central-vent eruption patterns, Bull. Volcanol., 58:539-556.

Tolstoy.M & Vernon.F, 2002. Breathing of the seafloor: Tidal correlations of seismicity at Axial volcano. Geology 30, 5033-506.

Vergniolle.S & Mangan.M, 2000. Hawaiian and Strombolian eruptions. In: Sigurdsson H et al (eds) in Encyclopedia of volcanoes. p 447–461

Vinciguerra.S, Latora.V, Bicciato.S & Kamimura.R.T, 2001. Identifying and discriminating seismic patterns leading flank eruptions at Mt Etna Volcano during 1981-1996, J.Volcanol & Geotherm.Res, 106(3):221-228.

Vosteen.H.D & Schellschmidt.R, 2003. Influence of temperature on thermal conductivity, thermal

capacity and thermal diffusivity for different types of rock, Physics & Chemistry of the Earth 28 (2003) 499–509

Wallace.P.J & Anderson.A.T.Jr, 1998. Effects of eruption and lava drainback on the H20 contents of basaltic magmas at Kilauea Volcano, Bull. Volcanol., 59:327-344.

Waltham.D, 1995, Mathematics: A simple tool for geologists, Blackwell Science,

Watson.K, 1982. Regional thermal inertia mapping from an experimental satellite. Geophysics, 47(12): 1681-1687.

Wayne R, 1996. Chemistry of Atmospheres. Text, Clarendon Press, Oxford.

Wilson.L & Head III.J.W, 1988. Nature of local magma storage zones and geometry of conduit systems below basaltic eruption sites: Pu'u 'O'o, Kilauea East Rift, Hawaii, example. J.Geophys.Res., 93(B12): 14785-14792.

Wolfe.R.E, Roy.D.P & Vermote.E, 1998. MODIS Land data storage, gridding and compositing methodology: Level 2 Grid. IEEE Trans. Geosci. Rem. Sens, 36(4): 1324-1338.

Wooster.M.J & Rothery.D.A, 1997a. Time-series Analysis of Effusive Volcanic Activity Using the ERS Along Track Scanning Radiometer: The 1995 Eruption of Fernandina Volcano, Galapagos Islands. Remote Sens. Env., 62: 109-117.

Wooster.M.J & Rothery.D.A, 1997b. Thermal monitoring of Lascar Volcano, Chile using infrared data from the along-track scanning radiometer: a 1992-1995 time series. Bull. Volcanol., 58: 566-579.

Wooster.M.J, Wright.R, Blake.S & Rothery.D.A, 1997. Coolong mechanisms and an approximate thermal budget for the 1991-1993 Mount Etna lava flow. Geophys. Res. Lett., 24(24): 3277-3280.

Wooster.M.J, Kaneko.T, Nakada.S & Shimizu.H, 2000. Discrimination of lava dome activity styles using satellite derived thermal structures. J.Volcanol. & Geotherm. Res, 102: 97-118.

Wooster.M.J & Kaneko.T, 2001. Testing the accuracy of solar reflected radiation corrections applied during satellite shortwave infrared thermal analysis of active volcanoes. J.Geophys.Res., 106(B7): 13381-13393.

Wright.R, Rothery.D.A, Blake.S, Harris.A.J.H & Pieri.D, 1999. Simulating the response of the EOS Terra ASTER sensor to high-temperature volcanic targets. Geophys. Res. Lett., 26(12): 1773-1776.

Wright.R, Rothery.D.A, Blake.S & Pieri.D.C, 2000. Visualising active volcanism with high spatial resolution satellite data: the 1991-1993 eruption of Mount Etna. Bull. Volcanol., 62: 256-265.

Wright.R, Blake.S, Harris.A.J.L & Rothery.D.A, 2001a. A simple explanation for the space based calculation of lava eruption rates. Earth & Plan. Sci. Letters, 192: 223-233.

Wright.R, Flynn.L.P & Harris.A.J.L, 2001b. Evolution of Lava flow-fields at Mount Etna, 27-28 October 1999, observed by Landsat 7 ETM+. Bull. Volcanol., 63: 1-7.

Wright R & Flynn L, 2004. On the retrieval of lava-flow surface temperatures from infrared satellite data, Geology 31 (10) p893-896.

Wright.R, Flynn.L.P, Garbeil.H, Harris.A.J.L & Pilger.E, 2004, MODVOLC: near-real-time thermal monitoring of global volcanism. J. Volcanol. & Geotherm. Res. 135: 29-49.

Yamaguchi.Y, Kahle.A.B, Tsu.H, Kawakami.T & Pniel.M, 1998. Overview of Advanced Spaceborne Thermal Emission and reflection Radiometer (ASTER). IEEE Trans. Geosci & Rem. Sens, 36(4): 1062-1071.

Zavody.A.M, Gorman.M.R, Lee.D.J, Eccles.D, Mutlow.C.T & Llewellyn-Jones.D.T, 1994. The ATSR data processing scheme developed for the EODC. Int. J. Remote Sensing, 15(4): 827-843.

Zebker.H.A, Rosen.P.A, Goldstein.R.M, Gabriel.A & Werner.C.L, 1994. On the derivation of coseismic displacement fields using differential radar interferometry: the Landers earthquake. J.Geophys.Res, 99(B10): 19617-19634.

9. Appendix I

Example of an IDL program used to identify and extract thermal anomaly data from the "duck" radiometer records discussed in chapter 2.

```
;Program to read a newt duck thermal file and provide a list of times of peaks in thermal output

;****** Steve Donegan USGS Hawaii Volcano Observatory/University Hawaii Manoa October 2001 ******

;****** Volcano Dynamics Group, Open University, UK   (June 2002 -date )          ******

;101001 Finished Program.

;151001     Louie now been repointed to new location--lots of high temperature readings.  Have restricted this
;                  program to sensing peaks in Huey and Dewy as they are still both pointed at the gas jetting source
;081101     Problem detected in output file--the times of the peaks detected for the ducks individually do not match those in the first estimated peak time column
;081101     Looks like this program is far too complicated--it is diffucIt to follow.  amend into a newer simpler program
;                  whose output can then be processed for temperature peaks for each individual duck. --

;091101 DONE!! code below is result of this!

;101002 Adjusted program so that it uses procedures that automatically detect the input file length and midday subscript for greater
;     accuracy.  Also sorted it so that in output file the pm is not a repeat of the am--spotted by Lori Glaze!
;     Have also adjusted the output file name to include the midday and file length subscripts.

;150103 Added capability to identify when the peak ends by studing a moving average--once temperature falls below a defined value
;     for a consistent period looking ahead, then that point is defined as the end of the peak.  This method also helps out the
;     identification of single peaks from original algorithm. NOTE IN PEAK TIMES O/P FILE HAVE TAKEN OUT LOUIE TO PRESERVE FORMATTING for new end
time and duration fields


Pro hueyANDdewey_peak_detect

;**** CHANGE THIS LINE IF YOU NEED TO, TO WHERE YOU KEEP THE DUCK DATA ******
allfilepath='C:\Donegan\IDL_INPUT'
allfilepathOP='C:\Donegan\Duck_dat_OP'
;allfilepath_t='C:\Donegan\Data\ducks\duckRAWdata\2001269.dat'
;*************************************************************************

;**** IF YOU PREFER WHITE BACKGROUND, BLACK AXIS AND COLOR PLOTS SET THIS TO 1, OR 0 FOR REVERSE ***
BG=0; helps when putting into reports!  (Black gives better contrast in general use

;each daily duck file is 9 x 43320 --THIS MIGHT CHANGE SLIGHTLY DEPENDING ON DAY-see just below.

;format:
;YEAR      JD          HOUR      MIN       SEC       HUEY      DEWEY     LOUIE     REDUNDANT

;read raw file in

rawdefaultsize=43325;***** change this if having problems with reading the raw inputfile-see how long using Excel

pm_size=rawdefaultsize-21663;midday falls on this subscript


rawdata=lonarr(9,rawdefaultsize)

print,"
print,'Welcome to Steves magnificent duck peak detector!'
print,"
print,'Program detects all peaks above a user defined threshold temperature in a duck output file--without any messing about with that horrible MS Excel!'
print,"
print,'Recommended that you look at the plot window to see what the distribution and average temperatures are, before entering a threshold temperature'
print,"
print,'Choose a temperature .dat input file '

file=dialog_pickfile(/read,path=allfilepath,filter='*.dat')

print,"
print,'Input file chosen:     ',file
print,"

;work out lenght of input file by polling downwards from maximum likely file length, until sucesful file opening acheived!
Maxrawdefaultsize=43325;
file_width=9 ;input file width (hour;min;second;Huey temp;dewey temp;louie temp)

max_length=Maxrawdefaultsize

fileopener,file,file_width,max_length,file_length,array

rawdefaultsize=file_length

;set OP file length
rawdata=array

;get midday subscript
midday_finder,rawdefaultsize,rawdata,midday

;OK, now rearrange file into AM & PM so can use array arithmetic!
am_size=midday
pm_size=rawdefaultsize-midday;midday falls on this subscript

;stop
;list1=allfilepath_t
;list1=dialog_pickfile(/read,path=allfilepath,filter='*.dat')

;openr,1,list1
```

```
;readf,1,rawdata
;close,1

;must get ingest.in file information so can calculate actual temperatures

;as input file so big and beyond usual subscript allowances, must split raw data into AM & PM files.  Noon falls at 21663


huey_temp_AM=fltarr(am_size)
dewey_temp_AM=fltarr(am_size)
louie_temp_AM=fltarr(am_size)

huey_temp_PM=fltarr(pm_size)
dewey_temp_PM=fltarr(pm_size)
louie_temp_PM=fltarr(pm_size)


;as data set so large, have to separate calculations into 2 loops, as in Excel plottemp_sjd.xls file
;midday should be at subscript am_size
for i=0,am_size-1 do begin

        huey_temp_AM(i)=(1.5731*rawdata(5,i))-1.96

        dewey_temp_AM(i)=(0.9669*rawdata(6,i))-51.842

        louie_temp_AM(i)=(1.5917*rawdata(7,i))-2.24

end

for j=0,pm_size-1 do begin

        i=uint(j+am_size); must convert to unisigned integer as above the usual integer limit for loops

        huey_temp_PM(j)=(1.5731*rawdata(5,i))-1.96

        dewey_temp_PM(j)=(0.9669*rawdata(6,i))-51.842

        louie_temp_PM(j)=(1.5917*rawdata(7,i))-2.24

end


;reform the total input array, but with the newly calculated temperatures

alldata_AM=fltarr(8,am_size)
alldata_PM=fltarr(8,pm_size)

alldata_AM(0:4,*)=rawdata(0:4,0:am_size-1)
alldata_PM(0:4,*)=rawdata(0:4,am_size:rawdefaultsize-1)

alldata_AM(5,0:am_size-1)=huey_temp_AM(*)
alldata_PM(5,0:pm_size-1)=huey_temp_PM(*)

alldata_AM(6,0:am_size-1)=dewey_temp_AM(*)
alldata_PM(6,0:pm_size-1)=dewey_temp_PM(*)

alldata_AM(7,0:am_size-1)=louie_temp_AM(*)
alldata_PM(7,0:pm_size-1)=louie_temp_PM(*)


;work out max and min values so can threshold the graph

;AM
maxval_HUEY_AM=max(huey_temp_AM)
maxval_DEWEY_AM=max(dewey_temp_AM)
maxval_LOUIE_AM=max(louie_temp_AM)

detectAM=fltarr(3)
detectAM(0)=maxval_HUEY_AM
detectAM(1)=maxval_DEWEY_AM
detectAM(2)=maxval_LOUIE_AM

allAMmax=max(detectAM)

;PM
maxval_HUEY_PM=max(huey_temp_PM)
maxval_DEWEY_PM=max(dewey_temp_PM)
maxval_LOUIE_PM=max(louie_temp_PM)

detectPM=fltarr(3)
detectPM(0)=maxval_HUEY_PM
detectPM(1)=maxval_DEWEY_PM
detectPM(2)=maxval_LOUIE_PM

allPMmax=max(detectPM)

;the first series to plot--must be series with highest peak otherwise subsequent datasets with higher values thsan the first will be chopped!

;this algorithm automatically detects which series contains the highest peak
where_AM=(where(detectAM eq allAMmax))          ;this expression results in a lonarr(1), must set to a single value
where_PM=(where(detectPM eq allPMmax))

lineam=fltarr(am_size)
linepm=fltarr(pm_size)

if where_AM(0) eq 0 then lineam(*)=huey_temp_AM(*)
if where_AM(0) eq 1 then lineam(*)=dewey_temp_AM(*)
if where_AM(0) eq 2 then lineam(*)=louie_temp_AM(*)

if where_PM(0) eq 0 then linepm(*)=huey_temp_PM(*)
if where_PM(0) eq 1 then linepm(*)=dewey_temp_PM(*)
if where_PM(0) eq 2 then linepm(*)=louie_temp_PM(*)

;plot the data so the user can see the distribution of peaks and general trends etc
;plot the graphs on the screen on the same window

!P.MULTI = [0, 1, 2]
```

```
if BG eq 0 then backg=0 else backg=16777215
if BG eq 0 then colorg=16777215 else colorg=0

;window, 1, xsize = 600, ysize =650,TITLE='Thermal duck plots'

year=string(fix(rawdata(0,0)))
jd=string(fix(rawdata(1,0)))

amtitle=strcompress('Plot for AM of day: '+jd+'; '+year)
pmtitle=strcompress('Plot for PM of day: '+jd+'; '+year)

red=255
green=255255
blue=16581375+100


am_tickinterval=am_size/12
pm_tickinterval=pm_size/12

;work out the numbers to be used for the array on time axis
;16777215,ymargin=(10.3
;AM
!X.TICKNAME = [ '0:00','1:00', '2:00', '3:00','4:00', '5:00', '6:00', '7:00', '8:00', '9:00', '10:00', '11:00', '12:00']
!x.tickinterval=am_tickinterval ;the data interval at which the above x labels must appear--right bloody pain the arse getting this right!

lineam=huey_temp_AM
linepm=huey_temp_PM

;must plot series with highest value first so full range is displayed

;commented out these for speed of operation --Jan'03 SJD
;plot,lineam,/noclip,color=colorg,ymargin=(5.3),min_value=0,xstyle=8,ystyle=8,background=backg,title=amtitle,subtitle='Huey: BLUE     Dewey: RED Louie:
GREEN',xtitle='Time',ytitle='Temperature ^C';
;oplot,huey_temp_AM, color=blue,max_value=allAMmax
;oplot,dewey_temp_AM,color=red,max_value=allAMmax
;oplot,louie_temp_AM,color=green,max_value=120

;PM
!X.TICKNAME = [ '12:00', '13:00','14:00', '15:00', '16:00','17:00', '18:00', '19:00', '20:00', '21:00', '22:00', '23:00', '24:00']
!x.tickinterval=pm_tickinterval ;the data interval at which the above x labels must appear--right bloody pain the arse getting this right!

;must plot series with highest value first so full range is displayed
;plot,linepm,/noclip,color=colorg,ymargin=(5.3),min_value=0,xstyle=8,ystyle=8,background=backg,title=pmtitle,subtitle='Huey: BLUE     Dewey: RED Louie:
GREEN',xtitle='Time',ytitle='Temperature ^C';,xtickv;color=0
;oplot,huey_temp_PM,color=blue,max_value=allPMmax
;oplot,dewey_temp_PM,color=red,max_value=allPMmax
;oplot,louie_temp_PM,color=green,max_value=allPMmax



print,''
print,'Maximum AM value detected: ',allAMmax,' ^C     ','Maximum PM value detected: ',allPMmax,' ^C'
print,''
print,'Plot completed'
print,''



;threshold temperature?
print,''
print,'What threshold temperature for Huey and Dewey do you require to detect temperatures above? '
read,prompt='What threshold temperature for Huey and Dewey do you require to detect temperatures above? ',threshold
;threshold=35
print,''
print,'Threshold temperature:',threshold,'^C'
print,''

;go through resulting temperature files and find where the temperature exceeds the thresold and where temp does not meet threshold set time to zero in new array
that holds just times
thresh_time_ex_AM=fltarr(5,am_size)
thresh_time_ex_PM=fltarr(5,pm_size)
am_string=strarr(am_size)
pm_string=strarr(pm_size)
am_string_NC=strarr(am_size)
pm_string_NC=strarr(pm_size)
am_stringTXT=strarr(am_size)
pm_stringTXT=strarr(pm_size)
am_stringNUM=fltarr(am_size)
pm_stringNUM=fltarr(pm_size)
am_stringUNIQ=fltarr(am_size)
pm_stringUNIQ=fltarr(pm_size)
count_am=0;for calculating array sizes
count_pm=0
peakcountAM=0;for counting the unique peak times
peakcountPM=0

zero_exceed_AM=fltarr(am_size)
zero_exceed_PM=fltarr(pm_size)

;hour=''
;minute=''
;second=''

;Jan'03: put these arrays in to help calculate when peak finishes
;am_peakFIN_time_A=fltarr

;AM
for i=0,am_size-1 do begin;                this concentrates on Huey and Dewey--Louie never seems to rise much above background

        if(huey_temp_AM(i)  ge threshold) or (dewey_temp_AM(i) ge threshold) then thresh_time_ex_AM(*,i)=alldata_AM(0:4,i) else thresh_time_ex_AM(*,i)=0
        if thresh_time_ex_AM(0,i) gt 0 then count_am=count_am+1 else count_am=count_am+0;count the instances where threshold is exceeded

        zero_exceed_AM(i)=thresh_time_ex_AM(0,i)

        ;work out correct syntax to be inserted into the array holding the time name strings (have to do it as a string first so can manipulate)
        if zero_exceed_AM(i) gt 0 then begin
```

```
                    if thresh_time_ex_AM(2,i) lt 10 then hour=strcompress('0'+string(fix(thresh_time_ex_AM(2,i))),/REMOVE_ALL) else
hour=string(fix(thresh_time_ex_AM(2,i)))

        endif else begin

                    hour='0'

        endelse

        if zero_exceed_AM(i) gt 0 then begin

                    if thresh_time_ex_AM(3,i) lt 10 then minute=strcompress('0'+string(fix(thresh_time_ex_AM(3,i))),/REMOVE_ALL) else
minute=string(fix(thresh_time_ex_AM(3,i)))

        endif else begin

                    minute='0'

        endelse

        if zero_exceed_AM(i) gt 0 then begin

                    if thresh_time_ex_AM(4,i) lt 10 then second=strcompress('0'+string(fix(thresh_time_ex_AM(4,i))),/REMOVE_ALL) else
second=string(fix(thresh_time_ex_AM(4,i)))

        endif else begin

                    second='0'

        endelse

        ;new time syntax was confusing the check for non-zero algorithm--use _NC suffic on old style text time calculator
        hour_NC=string(fix(thresh_time_ex_AM(2,i)));had a string in front
        minute_NC=string(fix(thresh_time_ex_AM(3,i)))
        second_NC=string(fix(thresh_time_ex_AM(4,i)))
        am_string_NC(i)=strcompress(hour_NC+minute_NC+second_NC,/REMOVE_ALL)

        am_string(i)=strcompress(hour+minute+second,/REMOVE_ALL) ;calculate the time string--times we're interested in will not = 0
        ;am_stringTXT(0,i)=strcompress(hour,/REMOVE_ALL)          ;can re-merge later in program
        ;am_stringTXT(1,i)=strcompress(minute,/REMOVE_ALL)
        ;am_stringTXT(2,i)=strcompress(second,/REMOVE_ALL)
        am_stringTXT(i)=strcompress(hour+':'+minute+':'+second,/REMOVE_ALL) ;calculate the time string--times we're interested in will not = 0
        am_stringNUM(i)=fix(float(am_string_NC(i)))

        ;create an array that will hold only the hours and minutes--this will then be put into a uniq function to count the spearate peaks
        am_stringUNIQ(i)=strcompress(hour_NC+minute_NC,/REMOVE_ALL)

end
;maxstringtxt_tst=intarr(3)
;maxstringtxt_tst(0)=n_elements(where(am_stringTXT(0,*) gt 0))
;maxstringtxt_tst(1)=n_elements(where(am_stringTXT(1,*) gt 0))
;maxstringtxt_tst(2)=n_elements(where(am_stringTXT(2,*) gt 0))
;maxstringtxt=max(maxstringtxt_tst)

;print,maxstringtxt
;stop
;openw,1,'C:\Donegan\Data\Ducks\arrayOPtest.txt'
;for i=0,am_size-1 do begin
;printf,1,am_stringTXT(i)
;end
;close,1

;stop
;PM
for j=0,pm_size-1 do begin;          this concentrates on Huey and Dewey--Louie never seems to rise much above background

        ;i=uint(j+am_size); must convert to unsigned integer as above the usual integer limit

        if (huey_temp_PM(j) ge threshold) or (dewey_temp_PM(j) ge threshold) then thresh_time_ex_PM(*,j)=alldata_PM(0:4,j) else thresh_time_ex_PM(*,j)=0
        if thresh_time_ex_PM(0,j) gt 0 then count_pm=count_pm+1 else count_pm=count_pm+0;count the instances where threshold is exceeded

        ;work out correct syntax to be inserted into the array holding the time name strings (have to do it as a string first so can manipulate)
        if thresh_time_ex_PM(2,j) lt 10 then hour=strcompress('0'+string(fix(thresh_time_ex_PM(2,j))),/REMOVE_ALL) else
hour=string(fix(thresh_time_ex_PM(2,j)))
        if thresh_time_ex_PM(3,j) lt 10 then minute=strcompress('0'+string(fix(thresh_time_ex_PM(3,j))),/REMOVE_ALL) else
minute=string(fix(thresh_time_ex_PM(3,j)))
        if thresh_time_ex_PM(4,j) lt 10 then second=strcompress('0'+string(fix(thresh_time_ex_PM(4,j))),/REMOVE_ALL) else
second=string(fix(thresh_time_ex_PM(4,j)))

        ;new time syntax was confusing the check for non-zero algorithm--use _NC suffic on old style text time calculator
        hour_NC=string(fix(thresh_time_ex_PM(2,j)))
        minute_NC=string(fix(thresh_time_ex_PM(3,j)))
        second_NC=string(fix(thresh_time_ex_PM(4,j)))
        pm_string_NC(j)=strcompress(hour_NC+minute_NC+second_NC,/REMOVE_ALL)

        pm_string(j)=strcompress(hour+minute+second,/REMOVE_ALL) ;calculate the time string--times we're interested in will not = 0
        pm_stringTXT(j)=strcompress(hour+':'+minute+':'+second,/REMOVE_ALL) ;calculate the time string--times we're interested in will not = 0
        pm_stringNUM(j)=fix(float(pm_string_NC(j)))

        ;create an array that will hold only the hours and minutes--this will then be put into a uniq function to count the spearate peaks
        pm_stringUNIQ(j)=strcompress(hour_NC+minute_NC,/REMOVE_ALL)


end

;create an array from the calculated number of peaks above the threshold to hold the array positions of these times

;in the event that no peaks are detected above the defined threshold temperature
if count_am eq 0 then print,'No peaks detected for AM above: ',threshold
if count_pm eq 0 then print,'No peaks detected for PM above: ',threshold
print,''

am_peaktimescount=count_am
pm_peaktimescount=count_pm
```

```
if (count_am eq 0) and (count_pm eq 0) then stop
if count_am eq 0 then count_am=1        ;stops the program from faltering if a 0 value is set on either am or pm separeately
if count_pm eq 0 then count_pm=1


am_pos=intarr(count_am)
pm_pos=intarr(count_pm)
am_pos_UNIQ=intarr(count_am);to calculate the unique peaks
pm_pos_UNIQ=intarr(count_pm)
posAM=0
posPM=0

;the business end of the program!--calculates where in the original arrays the times of peaks occur

for i=0,am_size-1 do begin

        if thresh_time_ex_AM(0,i) gt 0 then am_pos(posAM)=i;i is the subscript where

        if thresh_time_ex_AM(0,i) gt 0 then am_pos_UNIQ(posAM)=i

        ;increment the array counter if a value was put into it this time around in readiness for next loop
        if thresh_time_ex_AM(0,i) ne 0 then posAM=posAM+1 else posAM=posAM+0

end

for i=0,pm_size-1 do begin

        if thresh_time_ex_PM(0,i) gt 0 then pm_pos(posPM)=i

        if thresh_time_ex_PM(0,i) gt 0 then pm_pos_UNIQ(posPM)=i

        ;increment the array counter if a value was put into it this time around in readiness for next loop
        if thresh_time_ex_PM(0,i) ne 0 then posPM=posPM+1 else posPM=posPM+0

end

;posAM should equal count_am as the number of instances where the threshold was exceeded
;likewise for posPM

;...which they do!

;unless..
if posAM eq 0 then posAM=1; if count_am eq 0 no arrays can be calculated with 0 subscripts!
if posPM eq 0 then posPM=1

;calculate the unique values now by putting them into an array
am_unique=intarr(posAM)
pm_unique=intarr(posPM)

for i=0,posAM-1 do begin
;here!
        am_unique(i)=am_stringUNIQ(am_pos(i)); put the unique hour and minute values in am unique

end

for i=0,posPM-1 do begin

        pm_unique(i)=pm_stringUNIQ(pm_pos(i)); put the unique hour and minute values in pm unique

end

;number of elements relates directly to the number of peaks above the threshold
;stop
am_no=n_elements(am_unique[UNIQ(am_unique, SORT(am_unique))]); calculates the number of unique elements in am_unique
pm_no=n_elements(pm_unique[UNIQ(pm_unique, SORT(pm_unique))])

;get individual times of peaks;but only the simple minuted version....not used in rest of program anymore
;following 2 lines were casuing the problem--a bloody SORT command!
;am_ind_peak=am_unique[UNIQ(am_unique,sort(am_unique))]; puts into an array all the unique elements
;pm_ind_peak=pm_unique[UNIQ(pm_unique,sort(pm_unique))]

am_ind_peak=am_unique(uniq(am_unique));test line--will this fix the problem? YES YES YES!
pm_ind_peak=pm_unique(uniq(pm_unique))

;must clear out of am& pm_unique all values that are duplictaed etc, so only leaving single entries of times and therefore easy to get position in array of where these
values are
am_unique_clear=intarr(posAM)
pm_unique_clear=intarr(posPM)
;stop

for i=0,posAM-1 do begin

        ;if posAM-1 eq i then q=0 else q=1

        if i eq 0 then q=0 else q=1

        if am_unique(i) eq am_unique(i-q) then am_unique_clear(i)=0 else am_unique_clear(i)=am_unique(i)

end

for i=0,posPM-1 do begin

        ;if posPM-1 eq i then q=0 else q=1

        if i eq 0 then q=0 else q=1

        if pm_unique(i) eq pm_unique(i-q) then pm_unique_clear(i)=0 else pm_unique_clear(i)=pm_unique(i)

end

;must get the position in the arrays of where these unique values that are not 0  occur
am_unique_pos=intarr(am_no)
pm_unique_pos=intarr(pm_no)
am_unique_pos_count=0
pm_unique_pos_count=0

for i=0,posAM-1 do begin
```

```
		if am_unique_clear(i) gt 0 then am_unique_pos(am_unique_pos_count)=i else am_unique_pos(am_unique_pos_count)=0

		if am_unique_clear(i) gt 0 then am_unique_pos_count=am_unique_pos_count+1 else am_unique_pos_count=am_unique_pos_count+0

end

for i=0,posPM-1 do begin

		if pm_unique_clear(i) gt 0 then pm_unique_pos(pm_unique_pos_count)=i else pm_unique_pos(pm_unique_pos_count)=0

		if pm_unique_clear(i) gt 0 then pm_unique_pos_count=pm_unique_pos_count+1 else pm_unique_pos_count=pm_unique_pos_count+0

end

;identify discreet peaks separted my more than just a minute?

;sort the arrays as has earliest entry at the end (found this the hard way!)
am_unique_pos=am_unique_pos(sort(am_unique_pos))
pm_unique_pos=pm_unique_pos(sort(pm_unique_pos))

;we now have the positions in the array where the first instance of a new peak is recorded
;can now apply these positions within the fulltext time array to get distinct full figure times for the peaks

;now goto the original fulltext time array with the above found positions and get the times of each peak
am_fulltext_times=strarr(posAM)
pm_fulltext_times=strarr(posPM)
ftcountam=0
ftcountpm=0

for i=0,am_size-1 do begin ;put the fulltext time array together so can subsequently look at the position of individual peaks

		if thresh_time_ex_AM(0,i) gt 0 then am_fulltext_times(ftcountam)=am_stringTXT(i)

		if thresh_time_ex_AM(0,i) gt 0 then ftcountam=ftcountam+1 else ftcountam=ftcountam+0

end

for i=0,pm_size-1 do begin

		if thresh_time_ex_PM(0,i) gt 0 then pm_fulltext_times(ftcountpm)=pm_stringTXT(i)

		if thresh_time_ex_PM(0,i) gt 0 then ftcountpm=ftcountpm+1 else ftcountpm=ftcountpm+0

end

;put the long text times at the calculated positions from am & pm_unique_pos into a new array
am_ind_peak_times=strarr(am_no)
pm_ind_peak_times=strarr(pm_no)

;stop
;goto to the text file for the individual peak times
for i=0,am_no-1 do begin

		am_ind_peak_times(i)=am_fulltext_times(am_unique_pos(i))

end

for i=0,pm_no-1 do begin

		pm_ind_peak_times(i)=pm_fulltext_times(pm_unique_pos(i))

end

;at the times of the peaks found thus far, what are there temperatures?

;can do this by knowing the alldata(*,i) subscripts at which these times are--then getting the temperatures for the relevant ducks at this time

am_temppeak_a=intarr(posam)
pm_temppeak_a=intarr(pospm)

j=0

;put in the above arrays the subscripts for am and pm of where 0 is exceeded

for i=0,am_size-1 do begin

		if thresh_time_ex_AM(0,i) gt 0 then am_temppeak_a(j)=i
		if thresh_time_ex_AM(0,i) gt 0 then j=j+1 else j=j+0

end

j=0

for i=0,pm_size-1 do begin

		if thresh_time_ex_PM(0,i) gt 0 then pm_temppeak_a(j)=i
		if thresh_time_ex_PM(0,i) gt 0 then j=j+1 else j=j+0

end

;now in the new array work out the unique values by taking subscripts from am_unique etc
am_unique_Noeachsep=intarr(am_no)
pm_unique_Noeachsep=intarr(pm_no)

;count the number of times the threshold is exceeded for each peak,
;09/11 -problem lies in calculation of am_unique_noachsep
for i=0,am_no-1 do begin

		d=where(am_unique eq am_ind_peak(i))

		am_unique_Noeachsep(i)=n_elements(d)

end

for i=0,pm_no-1 do begin
```

```
		d=where(pm_unique eq pm_ind_peak(i))
		pm_unique_Noeachsep(i)=n_elements(d)

end

;idea is to get the maximum temperature associated with each peak, do this by looping through all the subscripts
;(get the i number) and recording the maximum temperature for each


;set up output arrays used in the loops below
am_unique_minmax_huey=fltarr(am_no)
am_unique_minmax_dewey=fltarr(am_no)
am_unique_minmax_louie=fltarr(am_no)
am_unique_minmax_huey_TIME=strarr(am_no)
am_unique_minmax_dewey_TIME=strarr(am_no)
am_unique_minmax_louie_TIME=strarr(am_no)

pm_unique_minmax_huey=fltarr(pm_no)
pm_unique_minmax_dewey=fltarr(pm_no)
pm_unique_minmax_louie=fltarr(pm_no)
pm_unique_minmax_huey_TIME=strarr(pm_no)
pm_unique_minmax_dewey_TIME=strarr(pm_no)
pm_unique_minmax_louie_TIME=strarr(pm_no)


;**AM**			do it for the morning!
if am_no eq 1 then
ONE_PEAK_AM,am_no,am_stringTXT,huey_temp_AM,dewey_temp_AM,louie_temp_AM,am_temppeak_a,one_peak_instance_am_TIME,one_peak_instance_am_
HueyTEMP,one_peak_instance_am_DeweyTEMP,one_peak_instance_am_LouieTEMP else $
MULTIPEAK_AM,am_unique_Noeachsep,am_no,am_temppeak_a,huey_temp_AM,dewey_temp_AM,louie_temp_AM,am_stringTXT,am_unique_minmax_huey,am_
unique_minmax_dewey $
,am_unique_minmax_louie,am_unique_minmax_huey_TIME,am_unique_minmax_dewey_TIME,am_unique_minmax_louie_TIME


;**PM**			do it for the afternoon!
if pm_no eq 1 then
ONE_PEAK_PM,pm_no,pm_stringTXT,huey_temp_PM,dewey_temp_PM,louie_temp_PM,pm_temppeak_a,one_peak_instance_pm_TIME,one_peak_instance_pm_
HueyTEMP,one_peak_instance_pm_DeweyTEMP,one_peak_instance_pm_LouieTEMP else $
MULTIPEAK_PM,pm_unique_Noeachsep,pm_no,pm_temppeak_a,huey_temp_PM,dewey_temp_PM,louie_temp_PM,pm_stringTXT,pm_unique_minmax_huey,pm_
unique_minmax_dewey,pm_unique_minmax_louie $
,pm_unique_minmax_huey_TIME,pm_unique_minmax_dewey_TIME,pm_unique_minmax_louie_TIME

;STOP

;*****************************************************************

;January 15th 2003--needed to know when peaks stopped--following procedure calculates the finish time for each peak handed to it

;define short and long intervals in terms of subscript numbers (remember that 1 subscript=2s --usual duck sampling rate)
short_interval=3		;these seem to be the best ombination at picking consistent times agreeing with the excel algorithm (see procedure notes at bottom!)
long_interval=6

;detection accuracy in ^C
detect_thresh=2

;first the AM peaks..
alldata_arr=alldata_AM
arr_length=am_size

am_finish_peak_times=fltarr(4,am_no)

for i=0,am_no-1 do begin

		if am_peaktimescount ne 0 then begin

			;what is the start time as a text string?
			start_time_string=am_ind_peak_times(i)

			;send to procedure

		Peak_finish_detect,arr_length,alldata_arr,short_interval,long_interval,detect_thresh,start_time_string,threshold,hour_stop,min_stop,sec_stop,dur_secs

			;get the data returned into an array
			am_finish_peak_times(0,i)=hour_stop
			am_finish_peak_times(1,i)=min_stop
			am_finish_peak_times(2,i)=sec_stop
			am_finish_peak_times(3,i)=dur_secs
			;if i eq 2 then stop

		endif else begin

			;no peak data, so just enter 0 into the array
			am_finish_peak_times(0,i)=0
			am_finish_peak_times(1,i)=0
			am_finish_peak_times(2,i)=0
			am_finish_peak_times(3,i)=0

		endelse

end

;Now the PM peaks..
alldata_arr=alldata_PM
arr_length=pm_size

pm_finish_peak_times=fltarr(4,pm_no)

for i=0,pm_no-1 do begin

		if pm_peaktimescount ne 0 then begin

			;what is the start time as a text string?
			start_time_string=pm_ind_peak_times(i)

			;send to procedure

		Peak_finish_detect,arr_length,alldata_arr,short_interval,long_interval,detect_thresh,start_time_string,threshold,hour_stop,min_stop,sec_stop,dur_secs
```

```
                ;get the data returned into an array
                pm_finish_peak_times(0,i)=hour_stop
                pm_finish_peak_times(1,i)=min_stop
                pm_finish_peak_times(2,i)=sec_stop
                pm_finish_peak_times(3,i)=dur_secs
                ;if i eq 2 then stop

        endif else begin

                ;no peak data, so just enter 0 into the array
                pm_finish_peak_times(0,i)=0
                pm_finish_peak_times(1,i)=0
                pm_finish_peak_times(2,i)=0
                pm_finish_peak_times(3,i)=0

        endelse
end

;ok, get the detected peak end times into the same text format as the start times
;work out correct syntax to be inserted into the array holding the time name strings (have to do it as a string first so can manipulate)

;am
am_string_end_time=strarr(am_no)

for i=0,am_no-1 do begin

        if am_finish_peak_times(0,i) lt 10 then hour=strcompress('0'+string(fix(am_finish_peak_times(0,i))),/REMOVE_ALL) else
hour=string(fix(am_finish_peak_times(0,i)))
        if am_finish_peak_times(1,i) lt 10 then minute=strcompress('0'+string(fix(am_finish_peak_times(1,i))),/REMOVE_ALL) else
minute=string(fix(am_finish_peak_times(1,i)))
        if am_finish_peak_times(2,i) lt 10 then second=strcompress('0'+string(fix(am_finish_peak_times(2,i))),/REMOVE_ALL) else
second=string(fix(am_finish_peak_times(2,i)))

        am_string_end_time(i)=strcompress(hour+':'+minute+':'+second,/REMOVE_ALL)

end

;PM
pm_string_end_time=strarr(pm_no)

for i=0,pm_no-1 do begin

        if pm_finish_peak_times(0,i) lt 10 then hour=strcompress('0'+string(fix(pm_finish_peak_times(0,i))),/REMOVE_ALL) else
hour=string(fix(pm_finish_peak_times(0,i)))
        if pm_finish_peak_times(1,i) lt 10 then minute=strcompress('0'+string(fix(pm_finish_peak_times(1,i))),/REMOVE_ALL) else
minute=string(fix(pm_finish_peak_times(1,i)))
        if pm_finish_peak_times(2,i) lt 10 then second=strcompress('0'+string(fix(pm_finish_peak_times(2,i))),/REMOVE_ALL) else
second=string(fix(pm_finish_peak_times(2,i)))

        pm_string_end_time(i)=strcompress(hour+':'+minute+':'+second,/REMOVE_ALL)

end

;if am_no eq 1 then OUTPUT_ONE_PEAK_AM

;OUTPUT THE RESULTS TO FILE & SCREEN

;if pm
OUTPUT_MULTI_PEAK_AM,am_no,am_ind_peak_times,am_unique_minmax_huey,am_unique_minmax_huey_TIME,am_unique_minmax_dewey,am_unique_min
max_dewey_TIME,am_unique_minmax_louie,am_unique_minmax_louie_TIME $
;pm_no,pm_ind_peak_times,pm_unique_minmax_huey,pm_unique_minmax_huey_TIME,pm_unique_minmax_dewey,pm_unique_minmax_dewey_TIME,pm_unique
_minmax_louie,pm_unique_minmax_louie_TIME,opfilename,threshold,am_peaktimescount,pm_peaktimescount

;put it into text file
parta=string(fix(alldata_AM(0,0)))
partb=string(fix(alldata_AM(1,0)))

md_subscript=string(midday)
md_subscript_b=strcompress('_md'+md_subscript,/REMOVE_ALL)
fl_subscript=string(rawdefaultsize)
fl_subscript_b=strcompress('_fl'+fl_subscript,/REMOVE_ALL)

extension1='_peaktimes.txt'
extension2='_tempconv.txt'

;allfilepathOP='C:\Donegan\IDL_INPUT'

opfilenamePK=strcompress(allfilepathOP+'\'+parta+partb+md_subscript_b+fl_subscript_b+extension1,/REMOVE_ALL)
opfilenameTEMPCONV=strcompress(allfilepathOP+'\'+parta+partb+md_subscript_b+fl_subscript_b+extension2,/REMOVE_ALL)

;print out the times of the peaks
print,''
print,'AM:'
print,''
if am_no eq 1 then print,'Peak Time',' ','PEAK END',' ','DURATION',' ','Huey TEMP',' ','Dewey TEMP',' ','Louie TEMP'
else $
print,'est PEAK TIME',' ','PEAK END',' ','DURATION',' ','HUEY',' ','Huey time','','DEWEY',' ','Dewey time',' '
        ,'LOUIE',' ','Louie time','','Time of Temp'

for i=0,am_no-1 do begin

        if am_no eq 1 then print,one_peak_instance_am_TIME(0),' ',am_string_end_time(i),' ',am_finish_peak_times(3,i),' '
        ,one_peak_instance_am_HueyTEMP(0),' ',one_peak_instance_am_DeweyTEMP(0),' ',one_peak_instance_am_LouieTEMP(0)
else $
        print,am_ind_peak_times(i),' ',am_string_end_time(i),' ',am_finish_peak_times(3,i),' ',am_unique_minmax_huey(i),' '
        ,am_unique_minmax_huey_TIME(i),' ',am_unique_minmax_dewey(i),' $
        ,am_unique_minmax_dewey_TIME(i),' ',am_unique_minmax_louie(i),' ',am_unique_minmax_louie_TIME(i)

end

print,''
print,'PM:'
print,''
if pm_no eq 1 then print,'Peak Time',' ','PEAK END',' ','DURATION',' ','Huey TEMP',' ','Dewey TEMP',' ','Louie TEMP'
else $
```

```
print,'est PEAK TIME',' ','PEAK END',' ','DURATION',' ','HUEY',' ','Huey time','','DEWEY',' ','Dewey time',' 
        ','LOUIE',' ','Louie time','','Time of Temp'

for i=0,pm_no-1 do begin

        if pm_no eq 1 then print,one_peak_instance_pm_TIME(0),' ',pm_string_end_time(i),' ',pm_finish_peak_times(3,i),' 
        ',one_peak_instance_pm_HueyTEMP(0),' ',one_peak_instance_pm_DeweyTEMP(0),' ',one_peak_instance_pm_LouieTEMP(0)
else $
        print,pm_ind_peak_times(i),' ',pm_string_end_time(i),' ',pm_finish_peak_times(3,i),' ',pm_unique_minmax_huey(i),' 
        ',pm_unique_minmax_huey_TIME(i),' ',pm_unique_minmax_dewey(i),' '$
        ,pm_unique_minmax_dewey_TIME(i),' ',pm_unique_minmax_louie(i),' ',pm_unique_minmax_louie_TIME(i)

end

if am_peaktimescount eq 0 then am_peaktimescount_final=0 else am_peaktimescount_final=am_no
if pm_peaktimescount eq 0 then pm_peaktimescount_final=0 else pm_peaktimescount_final=pm_no

print,''
print,'Number of peaks in the morning: ',am_peaktimescount_final,' Number of peaks in the afternoon: ',pm_peaktimescount_final
print,''
print,'(Note that the program may count subsequent minutes as separate peaks if peak is of > minute duration!)'
print,''

print,''
print,'Printing output times to: ',opfilenamePK
print,''


openw,1,opfilenamePK

printf,1,''
printf,1,'Threshold temperature is: ',threshold
printf,1,''
printf,1,'Number of peaks in the morning: ',am_peaktimescount_final
printf,1,'Number of peaks in the afternoon: ',pm_peaktimescount_final
printf,1,''
printf,1,'(Note that the program may count subsequent minutes as separate peaks if peak is of > minute duration!)'
printf,1,''

printf,1,''
printf,1,'AM:'
printf,1,''
if am_no eq 1 then printf,1,'Peak Time',' ','PEAK END',' ','DURATION',' ','Huey TEMP',' ','Dewey TEMP' else $
printf,1,'est PEAK TIME',' ','PEAK END',' ','DURATION',' ','HUEY',' ','Huey time','','DEWEY',' ','Dewey time'

for i=0,am_no-1 do begin

        if am_no eq 1 then printf,1,one_peak_instance_am_TIME(0),' ',am_string_end_time(i),' ',am_finish_peak_times(3,i),' 
        ',one_peak_instance_am_HueyTEMP(0),' ',one_peak_instance_am_DeweyTEMP(0),' ',one_peak_instance_am_LouieTEMP(0)
else $
        printf,1,am_ind_peak_times(i),' ',am_string_end_time(i),' ',am_finish_peak_times(3,i),' ',am_unique_minmax_huey(i),' 
        ',am_unique_minmax_huey_TIME(i),' ',am_unique_minmax_dewey(i),' '$
        ,am_unique_minmax_dewey_TIME(i)

end

printf,1,''
printf,1,'PM:'
printf,1,''
if pm_no eq 1 then printf,1,'Peak Time',' ','PEAK END',' ','DURATION',' ','Huey TEMP',' ','Dewey TEMP' else $
printf,1,'est PEAK TIME',' ','PEAK END',' ','DURATION',' ','HUEY',' ','Huey time','','DEWEY',' ','Dewey time',' 
        '

for i=0,pm_no-1 do begin

        if pm_no eq 1 then printf,1,one_peak_instance_pm_TIME(0),' ',pm_string_end_time(i),' ',pm_finish_peak_times(3,i),' 
        ',one_peak_instance_pm_HueyTEMP(0),' ',one_peak_instance_pm_DeweyTEMP(0),' ',one_peak_instance_pm_LouieTEMP(0)
else $
        printf,1,pm_ind_peak_times(i),' ',pm_string_end_time(i),' ',pm_finish_peak_times(3,i),' ',pm_unique_minmax_huey(i),' 
        ',pm_unique_minmax_huey_TIME(i),' ',pm_unique_minmax_dewey(i),' '$
        ,pm_unique_minmax_dewey_TIME(i)

end

close,1
stop
;write converted output file for easy portability once left HVO

openw,1,opfilenameTEMPCONV

for i=0,am_size-1 do begin

        printf,1,alldata_AM(2:7,i)

end

for j=0,pm_size-1 do begin

        printf,1,alldata_PM(2:7,j)

end

close,1


print,''
print,'Thankyou & Godbless ya Guv!'
print,''

stop ; ** activate this line if you need to access arrays in case of problems...

end


;*************************************************************************
;**********          Procedures from here on   **************************
```

```
;*************************************************************************
;

Pro
ONE_PEAK_AM,am_no,am_stringTXT,huey_temp_AM,dewey_temp_AM,louie_temp_AM,am_temppeak_a,one_peak_instance_am_TIME,one_peak_instance_am_
HueyTEMP,one_peak_instance_am_DeweyTEMP,one_peak_instance_am_LouieTEMP

;if just one peak then must use different algorithm to the loops below or it'll booger up!
if am_no eq 1 then one_peak_instance_am_TIME=am_stringTXT(am_temppeak_a(0))
if am_no eq 1 then one_peak_instance_am_HueyTEMP=huey_temp_AM(am_temppeak_a(0))
if am_no eq 1 then one_peak_instance_am_DeweyTEMP=dewey_temp_AM(am_temppeak_a(0))
if am_no eq 1 then one_peak_instance_am_LouieTEMP=louie_temp_AM(am_temppeak_a(0))

end


Pro
ONE_PEAK_PM,pm_no,pm_stringTXT,huey_temp_PM,dewey_temp_PM,louie_temp_PM,pm_temppeak_a,one_peak_instance_pm_TIME,one_peak_instance_pm_
HueyTEMP,one_peak_instance_pm_DeweyTEMP,one_peak_instance_pm_LouieTEMP

;if just one peak then must use different algorithm to the loops below or it'll booger up!
if pm_no eq 1 then one_peak_instance_pm_TIME=pm_stringTXT(pm_temppeak_a(0))
if pm_no eq 1 then one_peak_instance_pm_HueyTEMP=huey_temp_PM(pm_temppeak_a(0))
if pm_no eq 1 then one_peak_instance_pm_DeweyTEMP=dewey_temp_PM(pm_temppeak_a(0))
if pm_no eq 1 then one_peak_instance_pm_LouieTEMP=louie_temp_PM(pm_temppeak_a(0))

end


Pro
MULTIPEAK_AM,am_unique_Noeachsep,am_no,am_temppeak_a,huey_temp_AM,dewey_temp_AM,louie_temp_AM,am_stringTXT,am_unique_minmax_huey,am_
unique_minmax_dewey, $
am_unique_minmax_louie,am_unique_minmax_huey_TIME,am_unique_minmax_dewey_TIME,am_unique_minmax_louie_TIME

;idea is to get the maximum temperature associated with each peak, do this by looping through all the subscripts
;(get the i number) and recording the maximum temperature for each

;if more than one peak..
minarr=intarr(am_no)
maxarr=intarr(am_no)
minarr(0)=0;set the first element to zero

for i=1,am_no-1 do begin;calculate the minimum for the loops

        if i eq 1 then q=0 else q=1
        minarr(i)=total(am_unique_Noeachsep(0:i-q))

end
minarr(1)=am_unique_Noeachsep(0); works best this way--can get very fiddly

for i=0,am_no-1 do begin;calculate the maximum for the loops

        maxarr(i)=total(am_unique_Noeachsep(0:i))

end

;stop

;now go to the original data, using the calulated subscripts and get the maximum temperature
for i=0,am_no-1 do begin

        for j=0,(am_unique_Noeachsep(i))-1 do begin


        temp_max_SUBS=fltarr(am_unique_Noeachsep(i))

        temp_max_TEMP_huey=fltarr(am_unique_Noeachsep(i))                    ;set the array size for temperatures
        temp_max_TEMP_hueySC=strarr(am_unique_Noeachsep(i))                  ;set the array size for time text strings


        temp_max_TEMP_dewey=fltarr(am_unique_Noeachsep(i))
        temp_max_TEMP_deweySC=strarr(am_unique_Noeachsep(i))

        temp_max_TEMP_louie=fltarr(am_unique_Noeachsep(i))
        temp_max_TEMP_louieSC=strarr(am_unique_Noeachsep(i))

        huey_spot=intarr(am_no)
        dewey_spot=intarr(am_no)
        louie_spot=intarr(am_no)

        norm_subscr=0

                for h=minarr(i),maxarr(i)-1 do begin ;create an array that will hold the i subscripts for this run

                        temp_max_SUBS(norm_subscr)=am_temppeak_a(h)

                        if norm_subscr eq ((am_unique_Noeachsep(i))-1) then norm_subscr=norm_subscr+0 else norm_subscr=norm_subscr+1

                end

                for j=0,(am_unique_Noeachsep(i))-1 do begin

                        temp_max_TEMP_huey(j)=huey_temp_AM(temp_max_SUBS(j))    ;get the temperature subscripts
                        temp_max_TEMP_hueySC(j)=am_stringTXT(temp_max_SUBS(j))  ;get the text time subscripts
        am_fulltext_times

                        ;test: temp_max_TEMP_hueySC(j)=am_fulltext_times(temp_max_SUBS(j))
                        ;print,huey_temp_AM(temp_max_SUBS(j)),'          ',am_stringTXT(temp_max_SUBS(j)),'   ',i,'          ',j

                        temp_max_TEMP_dewey(j)=dewey_temp_AM(temp_max_SUBS(j))
                        temp_max_TEMP_deweySC(j)=am_stringTXT(temp_max_SUBS(j))

                        temp_max_TEMP_louie(j)=louie_temp_AM(temp_max_SUBS(j))
                        temp_max_TEMP_louieSC(j)=am_stringTXT(temp_max_SUBS(j))
```

```
                    am_unique_minmax_huey(i)=max(temp_max_TEMP_huey)          ;work out the maximum temperature from
the new array
                    am_unique_minmax_dewey(i)=max(temp_max_TEMP_dewey)
                    am_unique_minmax_louie(i)=max(temp_max_TEMP_louie)

                    ;huey_spot(i)=where((temp_max_TEMP_huey) eq am_unique_minmax_huey(i))  ;where in the array does this maximum
temperature occur?
                    interim_A=where((temp_max_TEMP_huey) eq am_unique_minmax_huey(i))      ;new method takes into
account instances where the maximum value occurs more than once, if so the first instance is recorded
                    if n_elements(interim_A) gt 1 then huey_spot(i)=interim_A(0) else huey_spot(i)=interim_A

                    ;dewey_spot(i)=where((temp_max_TEMP_dewey) eq am_unique_minmax_dewey(i))
                    interim_B=where((temp_max_TEMP_dewey) eq am_unique_minmax_dewey(i))
                    if n_elements(interim_B) gt 1 then dewey_spot(i)=interim_B(0) else dewey_spot(i)=interim_B

                    ;louie_spot(i)=where((temp_max_TEMP_louie) eq am_unique_minmax_louie(i))
                    interim_C=where((temp_max_TEMP_louie) eq am_unique_minmax_louie(i))
                    if n_elements(interim_C) gt 1 then louie_spot(i)=interim_C(0) else louie_spot(i)=interim_C

                    am_unique_minmax_huey_TIME(i)=temp_max_TEMP_hueySC(huey_spot(i))      ;get the text time string at the
location found by the above block
                    am_unique_minmax_dewey_TIME(i)=temp_max_TEMP_deweySC(dewey_spot(i))
                    am_unique_minmax_louie_TIME(i)=temp_max_TEMP_louieSC(louie_spot(i))

            end

                    ;test lines to check calculations at each step of process
                    ;print,"
                    ;read,check
                    ;if check eq 1 then continue else stop

    end
end


end



Pro
MULTIPEAK_PM,pm_unique_Noeachsep,pm_no,pm_temppeak_a,huey_temp_PM,dewey_temp_PM,louie_temp_PM,pm_stringTXT,pm_unique_minmax_huey,pm_
unique_minmax_dewey,pm_unique_minmax_louie, $
pm_unique_minmax_huey_TIME,pm_unique_minmax_dewey_TIME,pm_unique_minmax_louie_TIME

;idea is to get the maximum temperature associated with each peak, do this by looping through all the subscripts
;(get the i number) and recording the maximum temperature for each

;if more than one peak..
minarr=intarr(pm_no)
maxarr=intarr(pm_no)
minarr(0)=0;set the first element to zero

for i=1,pm_no-1 do begin;calculate the minimum for the loops

    if i eq 1 then q=0 else q=1
    minarr(i)=total(pm_unique_Noeachsep(0:i-q))

end
minarr(1)=pm_unique_Noeachsep(0); works best this way--can get very fiddly

for i=0,pm_no-1 do begin;calculate the maximum for the loops

    maxarr(i)=total(pm_unique_Noeachsep(0:i))

end


;now go to the original data, using the calulated subscripts and get the maximum temperature
for i=0,pm_no-1 do begin

    for j=0,(pm_unique_Noeachsep(i))-1 do begin


    temp_max_SUBS=fltarr(pm_unique_Noeachsep(i))

    temp_max_TEMP_huey=fltarr(pm_unique_Noeachsep(i))                    ;set the array size for temperatures
    temp_max_TEMP_hueySC=strarr(pm_unique_Noeachsep(i))                  ;set the array size for time text strings

    temp_max_TEMP_dewey=fltarr(pm_unique_Noeachsep(i))
    temp_max_TEMP_deweySC=strarr(pm_unique_Noeachsep(i))

    temp_max_TEMP_louie=fltarr(pm_unique_Noeachsep(i))
    temp_max_TEMP_louieSC=strarr(pm_unique_Noeachsep(i))

    huey_spot=intarr(pm_no)
    dewey_spot=intarr(pm_no)
    louie_spot=intarr(pm_no)

    norm_subscr=0
        for h=minarr(i),maxarr(i)-1 do begin ;create an array that will hold the i subscripts for this run

            temp_max_SUBS(norm_subscr)=pm_temppeak_a(h)

            if norm_subscr eq ((pm_unique_Noeachsep(i))-1) then norm_subscr=norm_subscr+0 else norm_subscr=norm_subscr+1

        end

        for j=0,(pm_unique_Noeachsep(i))-1 do begin

            temp_max_TEMP_huey(j)=huey_temp_PM(temp_max_SUBS(j))   ;get the temperature subscripts
            temp_max_TEMP_hueySC(j)=pm_stringTXT(temp_max_SUBS(j)) ;get the text time subscripts

            temp_max_TEMP_dewey(j)=dewey_temp_PM(temp_max_SUBS(j))
            temp_max_TEMP_deweySC(j)=pm_stringTXT(temp_max_SUBS(j))

            temp_max_TEMP_louie(j)=louie_temp_PM(temp_max_SUBS(j))
```

```
                                        temp_max_TEMP_louieSC(j)=pm_stringTXT(temp_max_SUBS(j))


                                        pm_unique_minmax_huey(i)=max(temp_max_TEMP_huey)                    ;work out the maximum temperature from
the new array
                                        pm_unique_minmax_dewey(i)=max(temp_max_TEMP_dewey)
                                        pm_unique_minmax_louie(i)=max(temp_max_TEMP_louie)

                                        ;huey_spot(i)=where((temp_max_TEMP_huey) eq pm_unique_minmax_huey(i))  ;where in the array does this maximum
temperature occur?
                                        interim_A=where((temp_max_TEMP_huey) eq pm_unique_minmax_huey(i))            ;new method takes into
account instances where the maximum value occurs more than once, if so the first instance is recorded
                                        if n_elements(interim_A) gt 1 then huey_spot(i)=interim_A(0) else huey_spot(i)=interim_A

                                        ;dewey_spot(i)=where((temp_max_TEMP_dewey) eq pm_unique_minmax_dewey(i))
                                        interim_A=where((temp_max_TEMP_huey) eq pm_unique_minmax_huey(i))            ;new method takes into
account instances where the maximum value occurs more than once, if so the first instance is recorded
                                        if n_elements(interim_A) gt 1 then huey_spot(i)=interim_A(0) else huey_spot(i)=interim_A

                                        ;louie_spot(i)=where((temp_max_TEMP_louie) eq pm_unique_minmax_louie(i))
                                        interim_A=where((temp_max_TEMP_huey) eq pm_unique_minmax_huey(i))            ;new method takes into
account instances where the maximum value occurs more than once, if so the first instance is recorded
                                        if n_elements(interim_A) gt 1 then huey_spot(i)=interim_A(0) else huey_spot(i)=interim_A

                                        pm_unique_minmax_huey_TIME(i)=temp_max_TEMP_hueySC(huey_spot(i))             ;get the text time string at the
location found by the above block
                                        pm_unique_minmax_dewey_TIME(i)=temp_max_TEMP_deweySC(dewey_spot(i))
                                        pm_unique_minmax_louie_TIME(i)=temp_max_TEMP_louieSC(louie_spot(i))

                                end
                        end

end

end

;Pro
OUTPUT_MULTI_PEAK_AM,am_no,am_ind_peak_times,am_unique_minmax_huey,am_unique_minmax_huey_TIME,am_unique_minmax_dewey,am_unique_min
max_dewey_TIME,am_unique_minmax_louie,am_unique_minmax_louie_TIME $
;pm_no,pm_ind_peak_times,pm_unique_minmax_huey,pm_unique_minmax_huey_TIME,pm_unique_minmax_dewey,pm_unique_minmax_dewey_TIME,pm_unique
_minmax_louie,pm_unique_minmax_louie_TIME,opfilename,threshold,am_peaktimescount,pm_peaktimescount


Pro fileopener,file,file_width,max_length,file_length,array


;end
;test program to automatically detect and load duck data files given a maximum length that the files do not exceed (uses error message handling)

failure=999
file_length=max_length

repeat begin

        if (failure ne 0) then file_length=file_length-1

        array=fltarr(file_width,file_length)

        filed,file,array,failure

        ;work out when to stop tracing backwards

        if array(3,file_length-1) ge 58 then goto, got_it

        print,'Trying a file length of: ',file_length

        free_lun,1

endrep until (failure eq 0)

print,failure,'  ',file_length

got_it:

print,'Chosen files actual length; ','        ',file_length

end


Pro filed,file,array,failure

failure=0

openr,1,file

ON_IOERROR, read_prob

readf,1,array
close,1

read_prob: failure=999

end

Pro midday_finder,rawdefaultsize,rawdata,midday

duckdata=rawdata

;must work out at which array subscript Midday falls on --can check against Excel
i=0.0
h=0.0
m=0.0
s=0.0
ss=0.0
stop_lp=0.0

while (stop_lp ne 999) do begin
```

```
		if (i ne rawdefaultsize-1) then incr=1.0 else incr=0.0
		if (i eq rawdefaultsize-1) then stop

		hour=duckdata(2,i)
		minute=duckdata(3,i)
		second=duckdata(4,i)
		next_second=duckdata(2,(i+incr))

		if hour eq 11.0 then h=1 else h=0
		if minute eq 59.0 then m=1 else m=0
		if second gt 55.0 then s=1 else s=0
		if next_second lt second then ss=1 else ss=0

		if ((h+m+s+ss) eq 4) then midday=i+1

		i=uint(i+1)

		;emergency stop if things bugger oop!
		if i eq rawdefaultsize-10 then stop_lp=999

endwhile

print,''
print,'Midday subscript found at: ',midday
print,''

end

Pro Peak_finish_detect,arr_length,alldata_arr,short_interval,long_interval,detect_thresh,start_time_string,threshold,hour_stop,min_stop,sec_stop,dur_secs

;Procedure started 15/01/03 SJD Open University

;Procedure to quickly & efficiently find where a peak finishes.  Use as few inputs as possible..

;Should be called for each peak, and return a duration in seconds back to the main procedure.

;See the MS Excel spreadsheet: "2001251_md21661_fl43322_tempconv_peakSTOP.xls" to see how this works...  look at 09.53 spike for info

detect_PK_time=start_time_string

short_int=short_interval
long_int=long_interval

Threshold_temp_compare=detect_thresh

;extract the numbers out of the text peakstart time
len=strlen(detect_PK_time)

hr_txt=strmid(detect_PK_time,0,2)
min_txt=strmid(detect_PK_time,3,2)
sec_txt=strmid(detect_PK_time,6,2)

hr_n=fix(hr_txt)
min_n=fix(min_txt)
sec_n=fix(sec_txt)

;get temperature of start of peak so can continue from there
for i=0,arr_length-1 do begin

		;hour=alldata_arr(2,*), min=alldata(3,*) & sec= alldata(4,*)

		hr_test=alldata_arr(2,i)
		min_test=alldata_arr(3,i)
		sec_test=alldata_arr(4,i)

		if hr_test eq hr_n then a=1 else a=0
		if min_test eq min_n then b=1 else b=0
		if sec_test eq sec_n then c=1 else c=0

		subscr_a=i

		if (a+b+c) eq 3 then goto,pk_found

end

pk_found:

;what subscript does the peak start
start_subscr=subscr_a

;in order to detect when the peak is finished, will use a system of running averages--when short interval running average
;is consistently close to that of a large interval running average, then the peak can be considered over

;short_int=4                                                    ;subscripts
;long_int=10                                                    ;subscripts
;Threshold_temp_compare=2          ;temperature difference between the 2 intervals--remember how noisy duck data can be!

i=start_subscr

;usually around 2 secs as a sampling rate for the ducks...

halfhour=(3600/2)/2          ;..is the number of increments in half an hour..

;for identifying the tail off of the peak--must know the average of about 1/2 an hour surrounding the peak either way--if all day, get night +day = dodgy  number!

;now--some peaks may be towards the end of the data set, so will therefore need to shftthis half hour period towards the start of the dataset
time_left_check=(arr_length-halfhour)
time_start_check=(i-halfhour)          ;same must be done for start of array --if time_start_check lt 0 then must compensate!

if (i gt time_left_check) and (time_start_check gt 0) then begin

		;compensate if end of array

		post_point=((arr_length-i)-1)
		halfhour_max=post_point
		halfhour_min=(halfhour-post_point)+halfhour          ;this should shift the mean calculation period towards the start of the array
```

```
		;print,'dooby',i

endif else begin

		halfhour_min=halfhour
		halfhour_max=halfhour
		;print,'goober',i

endelse

if (time_start_check le 0) then begin

		;compenate if start of array

		post_point=(abs(halfhour-i))
		halfhour_max=post_point+halfhour
		halfhour_min=(i-1)		;this should shift the mean calculation period towards the start of the array
		;print,'hooby',i

endif

		;no problem--somewhere in the middle!


;now extract that mean, plus a threshold as it will take ages & probably unconnected with peak die off to get below this temperature
threshold_detect=2
huey_data=alldata_arr(5,*)
mean_calc_halfhour=(mean(huey_data(i-halfhour_min:i+halfhour_max)))+threshold_detect

;set up a loop that will calculate the interval windows for half an hour or so after the initial peak onset..
variation_arr=fltarr(4,halfhour_max)	;put the times from the original array in as well as the mean from the shifting window method

variation_arr(0:2,*)=alldata_arr(2:4,i:(i+(halfhour_max-1)))

for j=0,halfhour_max-1 do begin

		i=j+start_subscr

		;need to feed in a correction for peaks near end of array

		;short interval
		need_corr_s=(i+short_int)
		corr_a_s=float(arr_length)-float(need_corr_s)

		;is a correction needed?
		if corr_a_s le 0 then corr_b_s=abs(corr_a_s)
		if corr_a_s le 0 then short_int=short_int-corr_b_s else short_int=short_int

		;long interval
		need_corr_l=(i+long_int)
		corr_a_l=float(arr_length)-float(need_corr_l)

		;is a correction needed?
		if corr_a_l le 0 then corr_b_l=abs(corr_a_l)
		if corr_a_l le 0 then long_int=long_int-corr_b_l else long_int=long_int

		;Look for Huey data
		short_interval_mean_H=mean(alldata_arr(5,(i+short_int)-1))
		long_interval_mean_H=mean(alldata_arr(5,(i+long_int)-1))
		intervals=[short_interval_mean_H,long_interval_mean_H]

		;put the mean from the two windows into the array
		variation_arr(3,j)=abs(mean(intervals))

end

;ok now have the data from the shifting window--need to look into this mean and see when it is consistently similar to the background
check=intarr(halfhour_max)

for k=0,halfhour_max-1 do begin

		if k lt (halfhour_max-(long_int+1)) then begin

			;is the mean over the next 20s less than the half hour average?
			mean_mean_window=mean(variation_arr(3,k:k+long_int))

			if mean_mean_window lt mean_calc_halfhour then check(k)=1 else check(k)=0

		endif else begin

			;put in error flag if at end of array--probably wont be..
			check(k)=999

		endelse

end

;now must look through the 'check' array to see where there are consistent '1's..
check2=intarr(halfhour_max)

for m=0,halfhour_max-1 do begin

		if m lt (halfhour_max-(long_int+1)) then begin

			mean_mean_mean_window=mean(check(m:m+long_int))

			subcr_pk_stop=m		;can use this is the variation_arr array to get the duration

			if mean_mean_mean_window eq 1 then goto, peak_stop_found

		;will do this in the same way as the excel spreadsheet..once the mean=1, this is the point we are looking at!

		endif else begin

			;put in error flag if at end of array--probably wont be..
			check2(m)=999
```

```
		endelse

end

peak_stop_found:

hour_stop=variation_arr(0,subcr_pk_stop+1)
min_stop=variation_arr(1,subcr_pk_stop+1)
sec_stop=variation_arr(2,subcr_pk_stop+1)

;now work out the duration of this peak in seconds
duration_secs=0

for i=1,subcr_pk_stop do begin

		if (variation_arr(2,i)-variation_arr(2,i-1)) gt 0 then begin

			duration_secs=duration_secs+(variation_arr(2,i)-variation_arr(2,i-1))

		endif else begin

			duration_secs=duration_secs+(60-(abs(variation_arr(2,i)-variation_arr(2,i-1))))

		endelse

		;print,duration_secs,(variation_arr(2,i)-variation_arr(2,i-1))

end

;above method leaves us 1 division short, so add on from very first..
correction_s=(variation_arr(2,1)-variation_arr(2,0))
if correction_s gt 0 then correction_s=correction_s else correction_s=(60-(abs(correction_s)))

;final duration value
dur_secs=duration_secs+correction_s

;stop
;if hour_stop eq 9 then stop
end
```

10.Appendix II

Visual Basic Macros and Excel spreadsheets used to apply thermal diffusion algorithm within chapter 3, to the thermal anomalies identified within chapter 2. Procedure uses Microsoft Visual Basic macros that take information from an input "sheet" on the cooling duration and maximum temperature of an anomaly. This information is then placed in an excel spreadsheet (screen-shot below). Further VB macros adjust iteratively parameters of a simulated spike until the estimated cooling time and maximum temperatures match those (within error) of the original anomaly.

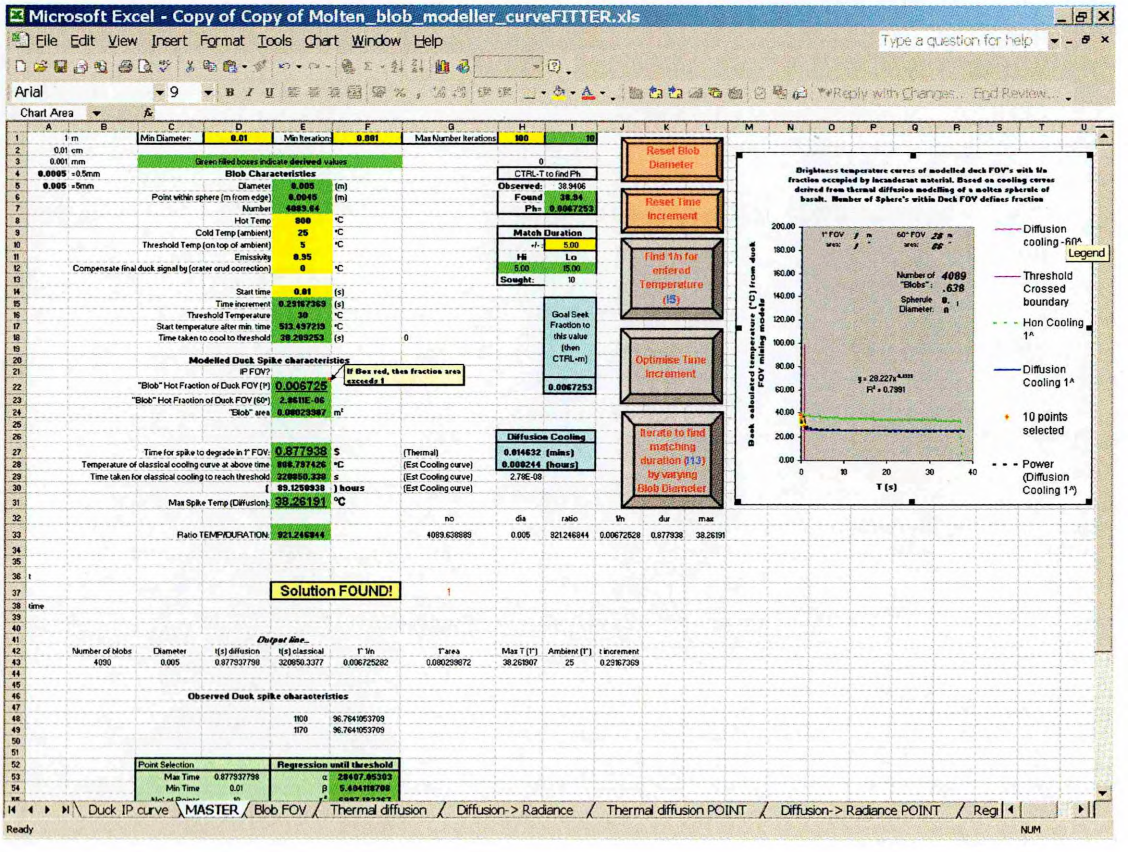

Sample of VB code used to perform part of this operation.

```
Sub NestedTest()
'
' NestedTest Macro
' Macro recorded 20/02/2003 by Steve Donegan
'
' Keyboard Shortcut: Ctrl+o
'
    Range("B36").Select
    Selection.Copy
    Sheets("Thermal diffusion").Select
    Range("B157").Select
    ActiveSheet.Paste
    Application.Run "Molten_blob_modeller_curveFITTER.xls!TimeLength"
    ActiveWindow.ScrollColumn = 7
    ActiveWindow.ScrollColumn = 6
    ActiveWindow.ScrollColumn = 5
    ActiveWindow.ScrollColumn = 4
    ActiveWindow.ScrollColumn = 3
    ActiveWindow.ScrollColumn = 2
    ActiveWindow.ScrollColumn = 1
    Range("B154").Select
    Selection.Copy
    Sheets("MASTER").Select
    Range("B38").Select
    ActiveSheet.Paste
End Sub
Sub TimeLength()
'
' TimeLength Macro
' Macro recorded 20/02/2003 by Steve Donegan
'
' Keyboard Shortcut: Ctrl+y
'
    Sheets("Thermal diffusion").Select
    ActiveWindow.ScrollColumn = 2
    ActiveWindow.ScrollColumn = 3
    ActiveWindow.ScrollColumn = 4
    ActiveWindow.ScrollColumn = 5
    ActiveWindow.ScrollColumn = 6
    ActiveWindow.ScrollColumn = 7
    ActiveWindow.ScrollColumn = 8
    Range("O154").GoalSeek Goal:=Range("B157"), ChangingCell:=Range("B154")
    Sheets("MASTER").Select
    Range("E5").Select
End Sub
Sub Find_FOV_at_Th()
'
' Find_FOV_at_Th Macro
' Macro recorded 20/02/2003 by Steve Donegan
'
' Keyboard Shortcut: Ctrl+t
'
    Range("I6").Select
    Range("I6").GoalSeek Goal:=Range("I5"), ChangingCell:=Range("I7")
End Sub
Sub FindDuration()
'
' FindDuration Macro
' Macro recorded 21/02/2003 by Steve Donegan
'
' Keyboard Shortcut: Ctrl+p
'

' This Macro subsequently adjusted by SJD as MS Goal seek pants at finding a value within a specified range

    Range("E27").Select

    'Set values for input for this "goal seek"
    Set final_val = Range("E27")
    Set sought_val_Hi = Range("I12")
    Set sought_val_Lo = Range("H12")
    Set changing_val = Range("F1")
    Set Max_iteration_val = Range("H1")
    Set min_diameter_val = Range("D1")

    'set up a loop for the maximum number of iterations
    Range("E5") = min_diameter_val
    Count = 0
    Solution_found = 1
    Solution_not_found = 0

  For loop1 = 1 To Max_iteration_val

      Range("E5") = Range("E5") + changing_val

      'Need to optimize the time increment
      Application.Run "Molten_blob_modeller_curveFITTER.xls!TimeLength"

      If (Range("E27") < sought_val_Hi) And (Range("E27") > sought_val_Lo) Then Range("E37") = "Solution FOUND!"
      If (Range("E27") < sought_val_Hi) And (Range("E27") > sought_val_Lo) Then Range("G37") = Solution_found
      If (Range("E27") < sought_val_Hi) And (Range("E27") > sought_val_Lo) Then Exit Sub

      'Need to bomb out the loop if no solution found
      If Range("E27") > sought_val_Hi Then Range("E37") = "NO solution found!!"
      If Range("E27") > sought_val_Hi Then Range("G37") = Solution_not_found
```

```
    If Range("E27") > sought_val_Hi Then Exit Sub

    'If the calculated duration exceeds the current range it will equal 0, in which case stop the loop
    If Range("E27") = 0 Then Range("E37") = "NO solution found!!"
    If Range("E27") = 0 Then Range("G37") = Solution_not_found
    If Range("E27") = 0 Then Exit Sub

    Count = Count + 1

    Range("I1") = Count

  Next loop1

  Range("E37") = "Maximum set iteration number has been EXCEEDED!!"
  If Range("E27") = 0 Then Range("G37") = 999

  'Range("E27").GoalSeek Goal:=Range("H12:I12"), ChangingCell:=Range("E5")
End Sub
Sub Reset_blob_diameter()
'
' Reset_blob_diameter Macro
' Macro recorded 21/02/2003 by Steve Donegan
'
' Keyboard Shortcut: Ctrl+j
'
  Range("E5").Select
  ActiveCell.FormulaR1C1 = "0.005"
End Sub
Sub Reset_Time_Increment()
'
' Reset_Time_Increment Macro
' Macro recorded 21/02/2003 by Steve Donegan
'
' Keyboard Shortcut: Ctrl+s
'
  Sheets("Thermal diffusion").Select
  Range("B154").Select
  ActiveCell.FormulaR1C1 = "0.1"
  Sheets("MASTER").Select

End Sub
```

11.Appendix III

Example of IDL programs used for calculating dual band solutions for either simulated Advanced Land Imager (ALI) or actual ALI pixels. This program is similar to those used for the same purpose for calculating solutions for Landsat 7 ETM+ pixels. This program will calculate solutions for a large number of pixels for the various band combinations discussed in chapters 4, 5 and 6.

```
Pro ALI_model_vs_reality_area_estimator_ALGO_MULTIPIXEL

;Program to check and display solutions to the dual band phenomena.

;********************************************** README!  ***********************************************************************************
;Iterates for all entered BT's (if no BT wanted, enter a zero), will calculate whether an entered BT is within the ETM band in questions sensitivity range
;output is into a tab delimited file that can then be graphed up in Excel.

;algorithm used--this program iterates a variation on the dual band simultaneous equations and assumes Th and Tc, and then iterates on a changing
;ph (fractional area of the hot component), when a match is found, that iteration stops (when 1 radiance is subtracted from another, after a match, a change from -ve
;to +ve{or vice versa} occurs, indicating the paths of the iteration have crossed and therefore a match).
;The program wil then LOOP onto the next value of Tc--and the process carries on.  The result will be a set of data that can be graphed, showing the change in
fractional
;areas (ph) against changing Tc, if Th is kept at 1000^C throughout.

;By emperical analysis, when the results are graphed (Tc vs Ph) where plot lines for the individual channels CROSS there is a solution
;If the lines do not cross then a solution is not possible with that band combination
;If program appears to hang and IDL does not respond at all, then NO solution is possible--choose your bands carefully!
;*************************************************************************************************************************************************
;

;*******************

;260302: Have adjusted program to take into account changes in calculation of ALI BT.
;                        Have also standardised IP file ;Format: {no,x,y,1p,1,2,3,4,4p,5p,5,7}

;020402: Streamlined code and took out the redundant 'large' increment as not needed.  Runs even quicker now

;140303: Added emergency stop procedure to aid production times...

;250303: Changed the dual band solution algorithm to a feedback iterative loop procedure which should increase speed by a few millions!
;                        see "range_quickener.pro" for the basic algorithm.  Hence, blurb at top of this program not particularly accurate anymore
;                        so now use "ALI_dual_band_solution_MODULE2_HiSpeed.pro"  the standard version same name, but no HiSpeed bit!

;260303: Added in more functionality to improve data handling and speed

;*******************

;read in calculated and corrected BT file, as output by other IDL procedure
inputfile='C:\Donegan\IDL_OUTPUT\Results_ALIrad_Ppixel_pixel26.txt'
;inputfile=dialog_pickfile(/read,path='C:\Donegan\IDL_OUTPUT\',filter='*avo*deepcrack*ALI_RADS*.txt')

outputfilename='Results_pixel26'
;read,prompt='Outputfilename',outputfilename

outputfile=strcompress('C:\Donegan\IDL_OUTPUT\'+outputfilename+'_ALI_DB_sols.txt',/REMOVE_ALL)

stop_path='C:\Donegan'

;print output to screen whilst programming running (slows down the HiSpeed version a LOT--makes no difference to the slow older version!
print_to_screen=0          ;1 if print to screen, 0 if not!

size_1=1     ;length of input file (should be equal to the number of pixels to be processed)

corrected_BTs=fltarr(12,size_1)

openr,1,inputfile
readf,1,corrected_BTs
close,1
;stop
;atmospheric transmissivity & emissivity in various bands (lifted from H's LLake.pro)
t7 = 0.95                  ;Transmissivity in band 7
t5 = 0.95                  ;Transmissivity in band 5
t5p = 0.95                 ;Transmissivity in band 5p
t4p = 0.95                 ;Transmissivity in band 4p
t4 = 0.95                  ;Transmissivity in band 4
t3 = 0.95                  ;Transmissivity in band 3
t2 = 0.95                  ;Transmissivity in band 2
t1 = 0.95                  ;Transmissivity in band 1
t1p = 0.95                 ;Transmissivity in band 1p

e7 = 0.95                  ;emissivity in band 7
e5 = 0.95                  ;emissivity in band 5
e5p = 0.95                 ;emissivity in band 5p
```

```
e4p = 0.95                ;emissivity in band 4p
e4 = 0.95                 ;emissivity in band 4
e3 = 0.95                 ;emissivity in band 3
e2 = 0.95                 ;emissivity in band 2
e1 = 0.95                 ;emissivity in band 1
e1p = 0.95                ;emissivity in band 1p

em=0.95
at_t=0.95

;Th=1000 ;tc, will be varied in the loops later.

Th_start=200.0
Th_end=1100.0
temp_increment=1

;adjust Th with every pass..
vary_Th=1   ;if you want to vary Th with every loop of input data Y=1, N=0

if vary_Th eq 1 then begin

        Th_incr=(Th_end-Th_start)/size_1

        it_num=Th_incr/size_1

        ;set up array for multiple samples of the same 1 line input
        array_multiple=fltarr(12,it_num)

        for i=0,it_num-1 do begin

                array_multiple(0:11,i)=corrected_BTs(0:11,0)

        end

endif else begin

        Th_non_var=1000
        it_num=size_1
        array_multiple=corrected_BTs

endelse
;starttemp_loop=450      ;temperature to start solutions test, use if not assuming 1000^C for all loops (use above line)

;set up loop, which will sequentially lop throught the input file, and pass the correct BT's through to the dual band solution
;procedure--it will return the calculated solutions, if any, for each channel.
solution_TC_ITM_large=fltarr(15,it_num)
solution_Ph_ITM_large=fltarr(15,it_num)
solution_TC_ITM_small=fltarr(15,it_num)
solution_Ph_ITM_small=fltarr(15,it_num)

channelname=strarr(15)
channelname(0)='ALI 7 & 5'
channelname(1)='ALI 7 & 5p'
channelname(2)='ALI 7 & 4'
channelname(3)='ALI 7 & 4p'
channelname(4)='ALI 7 & 3'
channelname(5)='ALI 5 & 5p'
channelname(6)='ALI 5 & 4'
channelname(7)='ALI 5 & 4p'
channelname(8)='ALI 5 & 3'
channelname(9)='ALI 5p & 4'
channelname(10)='ALI 5p & 4p'
channelname(11)='ALI 5p & 3'
channelname(12)='ALI 4 & 3'
channelname(13)='ALI 4 & 4p'
channelname(14)='ALI 4p & 3'

for loopm=0.0,it_num-1 do begin

        ;***** emergency stop procedure *******
        emergency_stop,stop_proc,stop_path
        if stop_proc eq 999 then stop
        ;*****************************************
        ;

        ;Th=loopm+starttemp_loop;use this line if you want to vary Th for checking purposes

        if vary_Th eq 1 then Th=(loopm*temp_increment)+Th_start else Th=Th_non_var

        print,''
        print,'STARTING TO ITERATE LINE ',loopm+1,' OF ',size_1,' TOTAL                    Th= ',Th
        print,''

        ;Format: {no,x,y,1p,1,2,3,4,4p,5p,5,7}

        ALI3_rad=array_multiple(6,loopm)

        ALI4_rad=array_multiple(7,loopm)

        ALI4p_rad=array_multiple(8,loopm)

        ALI5p_rad=array_multiple(9,loopm)

        ALI5_rad=array_multiple(10,loopm)

        ALI7_rad=array_multiple(11,loopm)

        ;work out the increment for each Ph value
        it_multiple=0.00001; as 1000 iterations, Ph range is 0.00001 to 1000x0.00001=0.01

        ALI_dual_band_solution_finder2,em,at_t,it_multiple,Th,ALI3_rad,ALI4_rad,ALI4p_rad,ALI5_rad,ALI5p_rad,ALI7_rad,solution7_5_Tc,solution7_5_Ph,sol
ution7_5p_Tc,solution7_5p_Ph,solution7_4_Tc,solution7_4_Ph,solution7_4p_Tc,solution7_4p_Ph, $
        solution7_3_Tc,solution7_3_Ph,solution5_5p_Tc,solution5_5p_Ph,solution5_4_Tc,solution5_4_Ph,solution5_4p_Tc,solution5_4p_Ph,solution5_3_Tc,s
olution5_3_Ph,solution5p_4_Tc,solution5p_4_Ph,solution5p_4p_Tc,solution5p_4p_Ph, $
        solution5p_3_Tc,solution5p_3_Ph,solution4_4p_Tc,solution4_4p_Ph,solution4_3_Tc,solution4_3_Ph,solution4p_3_Tc,solution4p_3_Ph,print_to_screen

        ;output_fractions_l2=output_fractions
```

```
;i=0
;write solutions into arrays for later output

;as no solution error return from the HiSpeed algorithm is 999--need to change this to a zero for ease of data analysis
;(this maintains viability with the older version of the DB solution finder--handy for comparison!)

if solution7_5_Tc gt 0 then solution_TC_ITM_small(0,loopm)=solution7_5_Tc else solution_TC_ITM_small(0,loopm)=0
if solution7_5p_Tc gt 0 then solution_TC_ITM_small(1,loopm)=solution7_5p_Tc else solution_TC_ITM_small(1,loopm)=0
if solution7_4_Tc gt 0 then solution_TC_ITM_small(2,loopm)=solution7_4_Tc else solution_TC_ITM_small(2,loopm)=0
if solution7_4p_Tc gt 0 then solution_TC_ITM_small(3,loopm)=solution7_4p_Tc else solution_TC_ITM_small(3,loopm)=0
if solution7_3_Tc gt 0 then solution_TC_ITM_small(4,loopm)=solution7_3_Tc else solution_TC_ITM_small(4,loopm)=0
if solution5_5p_Tc gt 0 then solution_TC_ITM_small(5,loopm)=solution5_5p_Tc else solution_TC_ITM_small(5,loopm)=0
if solution5_4_Tc gt 0 then solution_TC_ITM_small(6,loopm)=solution5_4_Tc else solution_TC_ITM_small(6,loopm)=0
if solution5_4p_Tc gt 0 then solution_TC_ITM_small(7,loopm)=solution5_4p_Tc else solution_TC_ITM_small(7,loopm)=0
if solution5_3_Tc gt 0 then solution_TC_ITM_small(8,loopm)=solution5_3_Tc else solution_TC_ITM_small(8,loopm)=0
if solution5p_4_Tc gt 0 then solution_TC_ITM_small(9,loopm)=solution5p_4_Tc else solution_TC_ITM_small(9,loopm)=0
if solution5p_4p_Tc gt 0 then solution_TC_ITM_small(10,loopm)=solution5p_4p_Tc else solution_TC_ITM_small(10,loopm)=0
if solution5p_3_Tc gt 0 then solution_TC_ITM_small(11,loopm)=solution5p_3_Tc else solution_TC_ITM_small(11,loopm)=0
if solution4_4p_Tc gt 0 then solution_TC_ITM_small(12,loopm)=solution4_4p_Tc else solution_TC_ITM_small(12,loopm)=0
if solution4_3_Tc gt 0 then solution_TC_ITM_small(13,loopm)=solution4_3_Tc else solution_TC_ITM_small(13,loopm)=0
if solution4p_3_Tc gt 0 then solution_TC_ITM_small(14,loopm)=solution4p_3_Tc else solution_TC_ITM_small(14,loopm)=0

if solution7_5_Ph gt 0 then solution_Ph_ITM_small(0,loopm)=solution7_5_Ph else solution_Ph_ITM_small(0,loopm)=0
if solution7_5p_Ph gt 0 then solution_Ph_ITM_small(1,loopm)=solution7_5p_Ph else solution_Ph_ITM_small(1,loopm)=0
if solution7_4_Ph gt 0 then solution_Ph_ITM_small(2,loopm)=solution7_4_Ph else solution_Ph_ITM_small(2,loopm)=0
if solution7_4p_Ph gt 0 then solution_Ph_ITM_small(3,loopm)=solution7_4p_Ph else solution_Ph_ITM_small(3,loopm)=0
if solution7_3_Ph gt 0 then solution_Ph_ITM_small(4,loopm)=solution7_3_Ph else solution_Ph_ITM_small(4,loopm)=0
if solution5_5p_Ph gt 0 then solution_Ph_ITM_small(5,loopm)=solution5_5p_Ph else solution_Ph_ITM_small(5,loopm)=0
if solution5_4_Ph gt 0 then solution_Ph_ITM_small(6,loopm)=solution5_4_Ph else solution_Ph_ITM_small(6,loopm)=0
if solution5_4p_Ph gt 0 then solution_Ph_ITM_small(7,loopm)=solution5_4p_Ph else solution_Ph_ITM_small(7,loopm)=0
if solution5_3_Ph gt 0 then solution_Ph_ITM_small(8,loopm)=solution5_3_Ph else solution_Ph_ITM_small(8,loopm)=0
if solution5p_4_Ph gt 0 then solution_Ph_ITM_small(9,loopm)=solution5p_4_Ph else solution_Ph_ITM_small(9,loopm)=0
if solution5p_4p_Ph gt 0 then solution_Ph_ITM_small(10,loopm)=solution5p_4p_Ph else solution_Ph_ITM_small(10,loopm)=0
if solution5p_3_Ph gt 0 then solution_Ph_ITM_small(11,loopm)=solution5p_3_Ph else solution_Ph_ITM_small(11,loopm)=0
if solution4_4p_Ph gt 0 then solution_Ph_ITM_small(12,loopm)=solution4_4p_Ph else solution_Ph_ITM_small(12,loopm)=0
if solution4_3_Ph gt 0 then solution_Ph_ITM_small(13,loopm)=solution4_3_Ph else solution_Ph_ITM_small(13,loopm)=0
if solution4p_3_Ph gt 0 then solution_Ph_ITM_small(14,loopm)=solution4p_3_Ph else solution_Ph_ITM_small(14,loopm)=0

;must get rid of 'no-solution' values Ph in array
for j=0,15-1 do begin

        if solution_Ph_ITM_small(j,loopm) eq it_multiple then solution_Ph_ITM_small(j,loopm)=0

end

if print_to_screen eq 1 then begin      ;print output to screen?

        print,channelname(*)
        print,solution_Ph_ITM_small(*,loopm)
        print,solution_Tc_ITM_small(*,loopm)

endif

;if loopm eq 2 then goto, jumpP
;stop
end ;end of main loop

jumpP:

channelname=strarr(15)
channelname(0)='ALI 7 & 5'
channelname(1)='ALI 7 & 5p'
channelname(2)='ALI 7 & 4'
channelname(3)='ALI 7 & 4p'
channelname(4)='ALI 7 & 3'
channelname(5)='ALI 5 & 5p'
channelname(6)='ALI 5 & 4'
channelname(7)='ALI 5 & 4p'
channelname(8)='ALI 5 & 3'
channelname(9)='ALI 5p & 4'
channelname(10)='ALI 5p & 4p'
channelname(11)='ALI 5p & 3'
channelname(12)='ALI 4 & 3'
channelname(13)='ALI 4 & 4p'
channelname(14)='ALI 4p & 3'


;stop
print,"
print,'printing solutions to file:',outputfile
print,"

openw,1,outputfile

printf,1,channelname(0),'  ',channelname(1),'      ',channelname(2),'      ',channelname(3),'      ',channelname(4),'      ',channelname(5),'
        ',channelname(6),'      ',channelname(7),'      ',channelname(8),'      ',channelname(9),'      ',channelname(10) $
,'      ',channelname(11),'     ',channelname(12),'     ',channelname(13),'     ',channelname(14)

for i=0,it_num-1 do begin

        printf,1,format='(1000(F0, :, "      "))',solution_Ph_ITM_small(*,i),solution_Tc_ITM_small(*,i)

end

close,1

print,"
print,'F I N I S H E D ! ! !'
print,"

end


;emergency stop procedure

Pro emergency_stop,stop_proc,stop_path
```

```
continue_loop=fltarr(1)

stopfile=strcompress(stop_path+'\'+'ETM_ALI_production_STOP.txt',/remove_all)

openr,1,stopfile
readf,1,continue_loop
close,1

stop_proc=continue_loop(0)

end

;finished!


Pro
ALI_dual_band_solution_finder2,em,at_t,it_multiple,Th,ALI3_rad,ALI4_rad,ALI4p_rad,ALI5_rad,ALI5p_rad,ALI7_rad,solution7_5_Tc,solution7_5_Ph,solution7_5p_Tc
,solution7_5p_Ph,solution7_4_Tc,solution7_4_Ph,solution7_4p_Tc,solution7_4p_Ph, $
solution7_3_Tc,solution7_3_Ph,solution5_5p_Tc,solution5_5p_Ph,solution5_4_Tc,solution5_4_Ph,solution5_4p_Tc,solution5_4p_Ph,solution5_3_Tc,solution5_3_Ph
,solution5p_4_Tc,solution5p_4_Ph,solution5p_4p_Tc,solution5p_4p_Ph, $
solution5p_3_Tc,solution5p_3_Ph,solution4_4p_Tc,solution4_4p_Ph,solution4_3_Tc,solution4_3_Ph,solution4p_3_Tc,solution4p_3_Ph,print_to_screen
;************************

;250302 adjusted BT ranges and radiance units for complaince with the BT converter programs

;************************

pi=3.14159

maximum_loop=10000;set the threshold for loop runaway to stop and jump to next series

Th_K=Th+273.15

Tc_max_it=1000

;must convert from mW/cm^2 sr um to Wm^2 sr um (see ALI_bt_calculator)

ALI3_rad_measured=((ALI3_rad/1000)*10000)*1e6

ALI4_rad_measured=((ALI4_rad/1000)*10000)*1e6

ALI4p_rad_measured=((ALI4p_rad/1000)*10000)*1e6

ALI5p_rad_measured=((ALI5p_rad/1000)*10000)*1e6

ALI5_rad_measured=((ALI5_rad/1000)*10000)*1e6

ALI7_rad_measured=((ALI7_rad/1000)*10000)*1e6


;set the band paramters for ALI
;ali 3 wav=0.6615e-6
wav_chan3=0.6615e-6
max_chan3_bt=4.2647E+08
min_chan3_bt=1.1533E+07

;ali 4 wav=0.79e-6
wav_chan4=0.79e-6
max_chan4_bt=2.8517E+08
min_chan4_bt=6.6000E+06

;ali 4' wav=0.8675e-6
wav_chan4p=0.8675e-6
max_chan4p_bt=2.3417E+08
min_chan4p_bt=4.7667E+06

;ali 5' wav=1.25e-6
wav_chan5p=1.25e-6
max_chan5p_bt=1.3667E+08
min_chan5p_bt=1.2333E+06

;ali 5 wav=1.65e-6
wav_chan5=1.65e-6
max_chan5_bt=8.2900E+07
min_chan5_bt=5.6667E+05

;ali 7 wav=2.215e-6
wav_chan7=2.215e-6
max_chan7_bt=2.2867E+07
min_chan7_bt=1.3333E+05


;work out if entered values are within their ranges, if not set error codes so wont end up in infinte iteration loop with saturated etc values
;ali3
if ALI3_rad_measured ge max_chan3_bt then print,'Channel 3 SATURATED!'
if ALI3_rad_measured ge max_chan3_bt then ALI3_continue=0 else ALI3_continue=1
if (ALI3_rad_measured lt min_chan3_bt) then print,'No SOLUTION possible--entered BT not high enough! (Chan3)'
if (ALI3_rad_measured lt min_chan3_bt) then ALI3_continue=0 else ALI3_continue=1 ;if solution possible, set continue to 1

;ali4
if ALI4_rad_measured ge max_chan4_bt then print,'Channel 4 SATURATED!'
if ALI4_rad_measured ge max_chan4_bt then ALI4_continue=0 else ALI4_continue=1
if (ALI4_rad_measured lt min_chan4_bt) then print,'No SOLUTION possible--entered BT not high enough! (Chan4)'
if (ALI4_rad_measured lt min_chan4_bt) then ALI4_continue=0 else ALI4_continue=1 ;if solution possible, set continue to 1

;ali4p
if ALI4p_rad_measured ge max_chan4p_bt then print,'Channel 4p SATURATED!'
if ALI4p_rad_measured ge max_chan4p_bt then ALI4p_continue=0 else ALI4p_continue=1
if (ALI4p_rad_measured lt min_chan4p_bt) then print,'No SOLUTION possible--entered BT not high enough! (Chan4p)'
if (ALI4p_rad_measured lt min_chan4p_bt) then ALI4p_continue=0 else ALI4p_continue=1 ;if solution possible, set continue to 1

;ali5
if ALI5_rad_measured ge max_chan5_bt then print,'Channel 5 SATURATED!'
if ALI5_rad_measured ge max_chan5_bt then ALI5_continue=0 else ALI5_continue=1
if (ALI5_rad_measured lt min_chan5_bt) then print,'No SOLUTION possible--entered BT not high enough! (Chan5)'
if (ALI5_rad_measured lt min_chan5_bt) then ALI5_continue=0 else ALI5_continue=1 ;if solution possible, set continue to 1
```

```
;ali5p
if ALI5p_rad_measured ge max_chan5p_bt then print,'Channel 5p SATURATED!'
if ALI5p_rad_measured ge max_chan5p_bt then ALI5p_continue=0 else ALI5p_continue=1
if (ALI5p_rad_measured lt min_chan5p_bt) then print,'No SOLUTION possible--entered BT not high enough! (Chan5p)'
if (ALI5p_rad_measured lt min_chan5p_bt) then ALI5p_continue=0 else ALI5p_continue=1 ;if solution possible, set continue to 1

;ali7
if ALI7_rad_measured ge max_chan7_bt then print,'Channel 7 SATURATED!'
if ALI7_rad_measured ge max_chan7_bt then ALI7_continue=0 else ALI7_continue=1
if (ALI7_rad_measured lt min_chan7_bt) then print,'No SOLUTION possible--entered BT not high enough! (Chan7)'
if (ALI7_rad_measured lt min_chan7_bt) then ALI7_continue=0 else ALI7_continue=1 ;if solution possible, set continue to 1
;stop
;set c1 and c2
c1=0.0000000000000003742;          {c1}
c2=0.0144;                         {c2}

;c1wav^-5
c1wav_3=c1*wav_chan3^(-5)
c1wav_4=c1*wav_chan4^(-5)
c1wav_4p=c1*wav_chan4p^(-5)
c1wav_5=c1*wav_chan5^(-5)
c1wav_5p=c1*wav_chan5p^(-5)
c1wav_7=c1*wav_chan7^(-5)

;preset runaway detection values to 0--once set to 1 WITHIN the loop, should stop any nasty infinite loops...
runaway3=0
runaway4=0
runaway4p=0
runaway5=0
runaway5p=0
runaway7=0

;stop
;set output file array--format: {th,tc,ph_it3,ph_it4,ph_it5,ph_it6,ph_it7,ph_it8}
output_fractions=fltarr(8,Tc_max_it)

for j=0,Tc_max_it-1 do begin

        ;set the cool temperature to be equal to j, for this instance of the loop
        Tc=j
        Tc_K=Tc+273.15

        ;calculated modelled radiances, at specified emissivities and atmospheric transmission
        L_cold_chan3=em*at_t*(((c1wav_3*(1/(((exp(c2/(wav_chan3*Tc_K))))-1)))))/3.14159); {do the main planck calculation}
        L_cold_chan4=em*at_t*(((c1wav_4*(1/(((exp(c2/(wav_chan4*Tc_K))))-1)))))/3.14159); {do the main planck calculation}
        L_cold_chan4p=em*at_t*(((c1wav_4p*(1/(((exp(c2/(wav_chan4p*Tc_K))))-1)))))/3.14159); {do the main planck calculation}
        L_cold_chan5=em*at_t*(((c1wav_5*(1/(((exp(c2/(wav_chan5*Tc_K))))-1)))))/3.14159); {do the main planck calculation}
        L_cold_chan5p=em*at_t*(((c1wav_5p*(1/(((exp(c2/(wav_chan5p*Tc_K))))-1)))))/3.14159); {do the main planck calculation}
        L_cold_chan7=em*at_t*(((c1wav_7*(1/(((exp(c2/(wav_chan7*Tc_K))))-1)))))/3.14159); {do the main planck calculation}

        ;work out L(wav,T) for hot pixel portion
        L_hot_chan3=em*at_t*(((c1wav_3*(1/(((exp(c2/(wav_chan3*Th_K))))-1)))))/3.14159); {do the main planck calculation}
        L_hot_chan4=em*at_t*(((c1wav_4*(1/(((exp(c2/(wav_chan4*Th_K))))-1)))))/3.14159); {do the main planck calculation}
        L_hot_chan4p=em*at_t*(((c1wav_4p*(1/(((exp(c2/(wav_chan4p*Th_K))))-1)))))/3.14159); {do the main planck calculation}
        L_hot_chan5=em*at_t*(((c1wav_5*(1/(((exp(c2/(wav_chan5*Th_K))))-1)))))/3.14159); {do the main planck calculation}
        L_hot_chan5p=em*at_t*(((c1wav_5p*(1/(((exp(c2/(wav_chan5p*Th_K))))-1)))))/3.14159); {do the main planck calculation}
        L_hot_chan7=em*at_t*(((c1wav_7*(1/(((exp(c2/(wav_chan7*Th_K))))-1)))))/3.14159); {do the main planck calculation}

        if ALI3_continue eq 1 then begin          ;so will not unneccesarily process dud values

        ;if value from last round was found to be runaway, this saves doing it all again!
        if runaway3 eq 1 then goto, jump4 ;saves computing time!

        ;need this to succesfully detect when the lines cross, and therefore a solution found
        ;indicator=-1
        i=1

        ph_it3_int=it_multiple;set Ph to start value, same as in loop below

        rad_model3_int=(ph_it3_int*L_hot_chan3)+((1-ph_it3_int)*L_cold_chan3);start value --so can dteect if indicator is -ve or +ve

        if (rad_model3_int-ALI3_rad_measured) lt 0 then sign_3=0 else sign_3=1

        solution3=0  ;prime the detector--see below in loop

        while solution3 ne 999 do begin

                ph_it3=float(i*it_multiple)

                ;work out the model radiance--where this matches the measured radiance, is the true value of Ph!
                rad_model3=(ph_it3*L_hot_chan3)+((1-ph_it3)*L_cold_chan3)

                ;work out when there is a match--once the plotted paths cross, that will be a match--hence a transition in indiactor from -ve to +ve
                indicator3=rad_model3-ALI3_rad_measured

                ;work out when the sign changes so can, detect when they cross over
                if (sign_3 eq 0) and (indicator3 ge 0) then solution3=999;when a solution is found, 999 will be set and the loop will end
                if (sign_3 eq 1) and (indicator3 le 0) then solution3=999

                ;put in line to stop runaway, and where it happens if so
                if i eq maximum_loop then print,'ALI 3 runaway!'
                if i eq maximum_loop then runaway3=1
                if i eq maximum_loop then runaway3_tc=tc
                if i eq maximum_loop then ph_it3=it_multiple ;safety for plotting!
                if i eq maximum_loop then goto, jump4

                ;increment counter
                i=i+1
        endwhile

        endif

        jump4:
        ;channel4
        if ALI4_continue eq 1 then begin          ;so will not unneccesarily process dud values
```

```
if runaway4 eq 1 then goto, jump4p ;saves computing time!

;need this to succesfully detect when the lines cross, and therefore a solution found
;indicator=-1
i=1

ph_it4_int=it_multiple;set Ph to start value, same as in loop below

rad_model4_int=(ph_it4_int*L_hot_chan4)+((1-ph_it4_int)*L_cold_chan4);start value --so can dteect if indicator is -ve or +ve

if (rad_model4_int-ALI4_rad_measured) lt 0 then sign_4=0 else sign_4=1

solution4=0  ;prime the detector--see below in loop

while solution4 ne 999 do begin

        ph_it4=float(i*it_multiple)

        rad_model4=(ph_it4*L_hot_chan4)+((1-ph_it4)*L_cold_chan4)

        ;work out when there is a match--once the plotted paths cross, that will be a match.
        indicator4=rad_model4-ALI4_rad_measured

        ;work out when the sign changes so can, detect when they cross over
        if (sign_4 eq 0) and (indicator4 ge 0) then solution4=999;when a solution is found, 999 will be set and the loop will end
        if (sign_4 eq 1) and (indicator4 le 0) then solution4=999

        ;put in line to stop runaway, and where it happens if so
        if i eq maximum_loop then print,'ALI 4 runaway!'
        if i eq maximum_loop then runaway4=1
        if i eq maximum_loop then runaway4_tc=tc
        if i eq maximum_loop then ph_it4=it_multiple ;safety for plotting!
        if i eq maximum_loop then goto, jump4p

        ;increment counter
        i=i+1
endwhile

endif

jump4p:
;channel4p
if  ALI4p_continue eq 1 then begin      ;so will not unneccesarily process dud values
;need this to succesfully detect when the lines cross, and therefore a solution found

if runaway4p eq 1 then goto, jump5 ;saves computing time!

i=1

ph_it4p_int=it_multiple;set Ph to start value, same as in loop below

rad_model4p_int=(ph_it4p_int*L_hot_chan4p)+((1-ph_it4p_int)*L_cold_chan4p);start value --so can dteect if indicator is -ve or +ve

if (rad_model4p_int-ALI4p_rad_measured) lt 0 then sign_4p=0 else sign_4p=1

solution4p=0 ;prime the detector--see below in loop

while solution4p ne 999 do begin

        ph_it4p=float(i*it_multiple)

        rad_model4p=(ph_it4p*L_hot_chan4p)+((1-ph_it4p)*L_cold_chan4p)

        ;work out when there is a match--once the plotted paths cross, that will be a match.
        indicator4p=rad_model4p-ALI4p_rad_measured

        ;work out when the sign changes so can, detect when they cross over
        if (sign_4p eq 0) and (indicator4p ge 0) then solution4p=999;when a solution is found, 999 will be set and the loop will end
        if (sign_4p eq 1) and (indicator4p le 0) then solution4p=999

        ;put in line to stop runaway, and where it happens if so
        if i eq maximum_loop then print,'ALI 4p runaway!'
        if i eq maximum_loop then runaway4p=1
        if i eq maximum_loop then runaway4p_tc=tc
        if i eq maximum_loop then ph_it4p=it_multiple ;safety for plotting!
        if i eq maximum_loop then goto, jump5

        ;increment counter
        i=i+1
endwhile

endif

jump5:
;channel5
if ALI5_continue eq 1 then begin        ;so will not unneccesarily process dud values

if runaway5 eq 1 then goto, jump5p ;saves computing time!

i=1

ph_it5_int=it_multiple;set Ph to start value, same as in loop below

rad_model5_int=(ph_it5_int*L_hot_chan5)+((1-ph_it5_int)*L_cold_chan5);start value --so can dteect if indicator is -ve or +ve

if (rad_model5_int-ALI5_rad_measured) lt 0 then sign_5=0 else sign_5=1

solution5=0  ;prime the detector--see below in loop

while solution5 ne 999 do begin

        ph_it5=float(i*it_multiple)

        rad_model5=(ph_it5*L_hot_chan5)+((1-ph_it5)*L_cold_chan5)

        ;work out when there is a match--once the plotted paths cross, that will be a match.
        indicator5=rad_model5-ALI5_rad_measured
```

```
		;work out when the sign changes so can, detect when they cross over
		if (sign_5 eq 0) and (indicator5 ge 0) then solution5=999;when a solution is found, 999 will be set and the loop will end
		if (sign_5 eq 1) and (indicator5 le 0) then solution5=999

		;put in line to stop runaway, and where it happens if so
		if i eq maximum_loop then print,'ALI 5 runaway!'
		if i eq maximum_loop then runaway5=1
		if i eq maximum_loop then runaway5_tc=tc
		if i eq maximum_loop then ph_it5=it_multiple ;safety for plotting!
		if i eq maximum_loop then goto, jump5p

		;increment counter
		i=i+1
endwhile

endif

jump5p:
;channel5p
if ALI5p_continue eq 1 then begin	;so will not unneccesarily process dud values

if runaway5p eq 1 then goto, jump7 ;saves computing time!

i=1

ph_it5p_int=it_multiple;set Ph to start value, same as in loop below

rad_model5p_int=(ph_it5p_int*L_hot_chan5p)+((1-ph_it5p_int)*L_cold_chan5p);start value --so can dteect if indicator is -ve or +ve

if (rad_model5p_int-ALI5p_rad_measured) lt 0 then sign_5p=0 else sign_5p=1

solution5p=0 ;prime the detector--see below in loop

while solution5p ne 999 do begin

		ph_it5p=float(i*it_multiple)

		rad_model5p=(ph_it5p*L_hot_chan5p)+((1-ph_it5p)*L_cold_chan5p)

		;work out when there is a match--once the plotted paths cross, that will be a match.
		indicator5p=rad_model5p-ALI5p_rad_measured

		;work out when the sign changes so can, detect when they cross over
		if (sign_5p eq 0) and (indicator5p ge 0) then solution5p=999;when a solution is found, 999 will be set and the loop will end
		if (sign_5p eq 1) and (indicator5p le 0) then solution5p=999

		;put in line to stop runaway, and where it happens if so
		if i eq maximum_loop then print,'ALI 5p runaway!'
		if i eq maximum_loop then runaway5p=1
		if i eq maximum_loop then runaway5p_tc=tc
		if i eq maximum_loop then ph_it5p=it_multiple ;safety for plotting!
		if i eq maximum_loop then goto, jump7

		;increment counter
		i=i+1
endwhile

endif

jump7:
;channel7
if  ALI7_continue eq 1 then begin	;so will not unneccesarily process dud values

if runaway7 eq 1 then goto, jumpEND ;saves computing time!

i=1

ph_it7_int=it_multiple;set Ph to start value, same as in loop below

rad_model7_int=(ph_it7_int*L_hot_chan7)+((1-ph_it7_int)*L_cold_chan7);start value --so can dteect if indicator is -ve or +ve

if (rad_model7_int-ALI7_rad_measured) lt 0 then sign_7=0 else sign_7=1

solution7=0  ;prime the detector--see below in loop

while solution7 ne 999 do begin

		ph_it7=float(i*it_multiple)

		rad_model7=(ph_it7*L_hot_chan7)+((1-ph_it7)*L_cold_chan7)

		;work out when there is a match--once the plotted paths cross, that will be a match.
		indicator7=rad_model7-ALI7_rad_measured

		;work out when the sign changes so can, detect when they cross over
		if (sign_7 eq 0) and (indicator7 ge 0) then solution7=999;when a solution is found, 999 will be set and the loop will end
		if (sign_7 eq 1) and (indicator7 le 0) then solution7=999

		;put in line to stop runaway, and where it happens if so
		if i eq maximum_loop then print,'ALI 7 runaway!'
		if i eq maximum_loop then runaway7=1
		if i eq maximum_loop then runaway7_tc=tc
		if i eq maximum_loop then ph_it7=it_multiple ;safety for plotting!
		if i eq maximum_loop then goto, jumpEND

		;increment counter
		i=i+1
endwhile

endif

jumpEND: ;if last part maxxed out, will jump here to return calculated values

;output to array
```

```
		output_fractions(0,j)=tc
		output_fractions(1,j)=th

		;if solution exists, output to correct part of output array format: {tc;th;ali3;ali4;ali4p;ali5;ali5p;ali7}
		if ALI3_continue eq 1 then output_fractions(2,j)=ph_it3 else output_fractions(2,j)=0
		if ALI4_continue eq 1 then output_fractions(3,j)=ph_it4 else output_fractions(3,j)=0
		if ALI4p_continue eq 1 then output_fractions(4,j)=ph_it4p else output_fractions(4,j)=0
		if ALI5_continue eq 1 then output_fractions(5,j)=ph_it5 else output_fractions(5,j)=0
		if ALI5p_continue eq 1 then output_fractions(6,j)=ph_it5p else output_fractions(6,j)=0
		if ALI7_continue eq 1 then output_fractions(7,j)=ph_it7 else output_fractions(7,j)=0


		;output this particular Tc iterations results
		;print,tc,'	',ph_it3,'	',ph_it4,'	',ph_it7;,'	',indicator


end ;end of main loop

;**************************************
;is there any solutions?
;**************************************

;7 and 5
if (output_fractions(7,0)-output_fractions(5,0)) lt 0 then sign7_5=0 else sign7_5=1;works out what the initial sign is, when this changes a solution has occured
between the 2 channels of interest

solution7_5_Tc_ARR=intarr(Tc_max_it)

for i=0,Tc_max_it-1 do begin

		finder7_5=(output_fractions(7,i)-output_fractions(5,i))

		;work out when the sign changes so can, detect when they cross over
		if (sign7_5 eq 0) and (finder7_5 ge 0) then solution7_5_Tc_ARR(i)=output_fractions(0,i) else solution7_5_Tc_ARR(i)=0
		if (sign7_5 eq 1) and (finder7_5 le 0) then solution7_5_Tc_ARR(i)=output_fractions(0,i) else solution7_5_Tc_ARR(i)=0

end

solution7_5_Tc_ARR_b=(where(solution7_5_Tc_ARR gt 0))
solution7_5_Tc=min(solution7_5_Tc_ARR_b)

if solution7_5_Tc ne -1 then begin

for i=0,Tc_max_it-1 do begin

		if output_fractions(0,i) eq solution7_5_Tc then solution7_5_Ph=output_fractions(7,i)

end

endif else begin

		solution7_5_Ph=it_multiple

endelse

;stop
;7 and 5p
if (output_fractions(7,0)-output_fractions(6,0)) lt 0 then sign7_5p=0 else sign7_5p=1		;works out what the initial sign is, when this changes a solution has
occured between the 2 channels of interest

solution7_5p_Tc_ARR=intarr(Tc_max_it)

for i=0,Tc_max_it-1 do begin

		finder7_5p=(output_fractions(7,i)-output_fractions(6,i))

		;work out when the sign changes so can, detect when they cross over
		if (sign7_5p eq 0) and (finder7_5p ge 0) then solution7_5p_Tc_ARR(i)=output_fractions(0,i) else solution7_5p_Tc_ARR(i)=0
		if (sign7_5p eq 1) and (finder7_5p le 0) then solution7_5p_Tc_ARR(i)=output_fractions(0,i) else solution7_5p_Tc_ARR(i)=0

end

solution7_5p_Tc_ARR_b=(where(solution7_5p_Tc_ARR gt 0))
solution7_5p_Tc=min(solution7_5p_Tc_ARR_b)

if solution7_5p_Tc ne -1 then begin

for i=0,Tc_max_it-1 do begin

		if output_fractions(0,i) eq solution7_5p_Tc then solution7_5p_Ph=output_fractions(7,i)

end

endif else begin

		solution7_5p_Ph=it_multiple

endelse


;7 and 4p
if (output_fractions(7,0)-output_fractions(4,0)) lt 0 then sign7_4p=0 else sign7_4p=1		;works out what the initial sign is, when this changes a solution has
occured between the 2 channels of interest

solution7_4p_Tc_ARR=intarr(Tc_max_it)

for i=0,Tc_max_it-1 do begin

		finder7_4p=(output_fractions(7,i)-output_fractions(4,i))

		;work out when the sign changes so can, detect when they cross over
		if (sign7_4p eq 0) and (finder7_4p ge 0) then solution7_4p_Tc_ARR(i)=output_fractions(0,i) else solution7_4p_Tc_ARR(i)=0
		if (sign7_4p eq 1) and (finder7_4p le 0) then solution7_4p_Tc_ARR(i)=output_fractions(0,i) else solution7_4p_Tc_ARR(i)=0

end

solution7_4p_Tc_ARR_b=(where(solution7_4p_Tc_ARR gt 0))
```

```
solution7_4p_Tc=min(solution7_4p_Tc_ARR_b)

if solution7_4p_Tc ne -1 then begin

for i=0,Tc_max_it-1 do begin

        if output_fractions(0,i) eq solution7_4p_Tc then solution7_4p_Ph=output_fractions(7,i)

end

endif else begin

        solution7_4p_Ph=it_multiple

endelse

;7 and 4
if (output_fractions(7,0)-output_fractions(3,0)) lt 0 then sign7_4=0 else sign7_4=1;works out what the initial sign is, when this changes a solution has occured
between the 2 channels of interest

solution7_4_Tc_ARR=intarr(Tc_max_it)

for i=0,Tc_max_it-1 do begin

        finder7_4=(output_fractions(7,i)-output_fractions(3,i))

        ;work out when the sign changes so can, detect when they cross over
        if (sign7_4 eq 0) and (finder7_4 ge 0) then solution7_4_Tc_ARR(i)=output_fractions(0,i) else solution7_4_Tc_ARR(i)=0
        if (sign7_4 eq 1) and (finder7_4 le 0) then solution7_4_Tc_ARR(i)=output_fractions(0,i) else solution7_4_Tc_ARR(i)=0

end

solution7_4_Tc_ARR_b=(where(solution7_4_Tc_ARR gt 0))
solution7_4_Tc=min(solution7_4_Tc_ARR_b)

if solution7_4_Tc ne -1 then begin

for i=0,Tc_max_it-1 do begin

        if output_fractions(0,i) eq solution7_4_Tc then solution7_4_Ph=output_fractions(7,i)

end

endif else begin

        solution7_4_Ph=it_multiple

endelse

;7 and 3
if (output_fractions(7,0)-output_fractions(2,0)) lt 0 then sign7_3=0 else sign7_3=1;works out what the initial sign is, when this changes a solution has occured
between the 2 channels of interest

solution7_3_Tc_ARR=intarr(Tc_max_it)

for i=0,Tc_max_it-1 do begin

        finder7_3=(output_fractions(7,i)-output_fractions(2,i))

        ;work out when the sign changes so can, detect when they cross over
        if (sign7_3 eq 0) and (finder7_3 ge 0) then solution7_3_Tc_ARR(i)=output_fractions(0,i) else solution7_3_Tc_ARR(i)=0
        if (sign7_3 eq 1) and (finder7_3 le 0) then solution7_3_Tc_ARR(i)=output_fractions(0,i) else solution7_3_Tc_ARR(i)=0

end

solution7_3_Tc_ARR_b=(where(solution7_3_Tc_ARR gt 0))
solution7_3_Tc=min(solution7_3_Tc_ARR_b)

if solution7_3_Tc ne -1 then begin

for i=0,Tc_max_it-1 do begin

        if output_fractions(0,i) eq solution7_3_Tc then solution7_3_Ph=output_fractions(7,i)

end

endif else begin

        solution7_3_Ph=it_multiple

endelse


;5 and 5p
if (output_fractions(5,0)-output_fractions(6,0)) lt 0 then sign5_5p=0 else sign5_5p=1        ;works out what the initial sign is, when this changes a solution has
occured between the 2 channels of interest

solution5_5p_Tc_ARR=intarr(Tc_max_it)

for i=0,Tc_max_it-1 do begin

        finder5_5p=(output_fractions(5,i)-output_fractions(6,i))

        ;work out when the sign changes so can, detect when they cross over
        if (sign5_5p eq 0) and (finder5_5p ge 0) then solution5_5p_Tc_ARR(i)=output_fractions(0,i) else solution5_5p_Tc_ARR(i)=0
        if (sign5_5p eq 1) and (finder5_5p le 0) then solution5_5p_Tc_ARR(i)=output_fractions(0,i) else solution5_5p_Tc_ARR(i)=0

end

solution5_5p_Tc_ARR_b=(where(solution5_5p_Tc_ARR gt 0))
solution5_5p_Tc=min(solution5_5p_Tc_ARR_b)

if solution5_5p_Tc ne -1 then begin

for i=0,Tc_max_it-1 do begin

        if output_fractions(0,i) eq solution5_5p_Tc then solution5_5p_Ph=output_fractions(5,i)
```

```
end

endif else begin

		solution5_5p_Ph=it_multiple

endelse

;5 and 4p
if (output_fractions(5,0)-output_fractions(4,0)) lt 0 then sign5_4p=0 else sign5_4p=1		;works out what the initial sign is, when this changes a solution has occured between the 2 channels of interest

solution5_4p_Tc_ARR=intarr(Tc_max_it)

for i=0,Tc_max_it-1 do begin

		finder5_4p=(output_fractions(5,i)-output_fractions(4,i))

		;work out when the sign changes so can, detect when they cross over
		if (sign5_4p eq 0) and (finder5_4p ge 0) then solution5_4p_Tc_ARR(i)=output_fractions(0,i) else solution5_4p_Tc_ARR(i)=0
		if (sign5_4p eq 1) and (finder5_4p le 0) then solution5_4p_Tc_ARR(i)=output_fractions(0,i) else solution5_4p_Tc_ARR(i)=0

end

solution5_4p_Tc_ARR_b=(where(solution5_4p_Tc_ARR gt 0))
solution5_4p_Tc=min(solution5_4p_Tc_ARR_b)

if solution5_4p_Tc ne -1 then begin

for i=0,Tc_max_it-1 do begin

		if output_fractions(0,i) eq solution5_4p_Tc then solution5_4p_Ph=output_fractions(5,i)

end

endif else begin

		solution5_4p_Ph=it_multiple

endelse

;5 and 4
if (output_fractions(5,0)-output_fractions(3,0)) lt 0 then sign5_4=0 else sign5_4=1;works out what the initial sign is, when this changes a solution has occured between the 2 channels of interest

solution5_4_Tc_ARR=intarr(Tc_max_it)

for i=0,Tc_max_it-1 do begin

		finder5_4=(output_fractions(5,i)-output_fractions(3,i))

		;work out when the sign changes so can, detect when they cross over
		if (sign5_4 eq 0) and (finder5_4 ge 0) then solution5_4_Tc_ARR(i)=output_fractions(0,i) else solution5_4_Tc_ARR(i)=0
		if (sign5_4 eq 1) and (finder5_4 le 0) then solution5_4_Tc_ARR(i)=output_fractions(0,i) else solution5_4_Tc_ARR(i)=0

end

solution5_4_Tc_ARR_b=(where(solution5_4_Tc_ARR gt 0))
solution5_4_Tc=min(solution5_4_Tc_ARR_b)

if solution5_4_Tc ne -1 then begin

for i=0,Tc_max_it-1 do begin

		if output_fractions(0,i) eq solution5_4_Tc then solution5_4_Ph=output_fractions(5,i)

end

endif else begin

		solution5_4_Ph=it_multiple

endelse

;5 and 3
if (output_fractions(5,0)-output_fractions(2,0)) lt 0 then sign5_3=0 else sign5_3=1;works out what the initial sign is, when this changes a solution has occured between the 2 channels of interest

solution5_3_Tc_ARR=intarr(Tc_max_it)

for i=0,Tc_max_it-1 do begin

		finder5_3=(output_fractions(5,i)-output_fractions(2,i))

		;work out when the sign changes so can, detect when they cross over
		if (sign5_3 eq 0) and (finder5_3 ge 0) then solution5_3_Tc_ARR(i)=output_fractions(0,i) else solution5_3_Tc_ARR(i)=0
		if (sign5_3 eq 1) and (finder5_3 le 0) then solution5_3_Tc_ARR(i)=output_fractions(0,i) else solution5_3_Tc_ARR(i)=0

end

solution5_3_Tc_ARR_b=(where(solution5_3_Tc_ARR gt 0))
solution5_3_Tc=min(solution5_3_Tc_ARR_b)

if solution5_3_Tc ne -1 then begin

for i=0,Tc_max_it-1 do begin

		if output_fractions(0,i) eq solution5_3_Tc then solution5_3_Ph=output_fractions(5,i)

end

endif else begin

		solution5_3_Ph=it_multiple

endelse
```

```
;5p and 4p
if (output_fractions(6,0)-output_fractions(4,0)) lt 0 then sign5p_4p=0 else sign5p_4p=1          ;works out what the initial sign is, when this changes a solution has
occured between the 2 channels of interest

solution5p_4p_Tc_ARR=intarr(Tc_max_it)

for i=0,Tc_max_it-1 do begin

        finder5p_4p=(output_fractions(6,i)-output_fractions(4,i))

        ;work out when the sign changes so can, detect when they cross over
        if (sign5p_4p eq 0) and (finder5p_4p ge 0) then solution5p_4p_Tc_ARR(i)=output_fractions(0,i) else solution5p_4p_Tc_ARR(i)=0
        if (sign5p_4p eq 1) and (finder5p_4p le 0) then solution5p_4p_Tc_ARR(i)=output_fractions(0,i) else solution5p_4p_Tc_ARR(i)=0

end

solution5p_4p_Tc_ARR_b=(where(solution5p_4p_Tc_ARR gt 0))
solution5p_4p_Tc=min(solution5p_4p_Tc_ARR_b)

if solution5p_4p_Tc ne -1 then begin

for i=0,Tc_max_it-1 do begin

        if output_fractions(0,i) eq solution5p_4p_Tc then solution5p_4p_Ph=output_fractions(6,i)

end

endif else begin

        solution5p_4p_Ph=it_multiple

endelse

;5p and 4
if (output_fractions(6,0)-output_fractions(3,0)) lt 0 then sign5p_4=0 else sign5p_4=1          ;works out what the initial sign is, when this changes a solution has
occured between the 2 channels of interest

solution5p_4_Tc_ARR=intarr(Tc_max_it)

for i=0,Tc_max_it-1 do begin
        ;if i eq 1 then stop
        finder5p_4=(output_fractions(6,i)-output_fractions(3,i))

        ;work out when the sign changes so can, detect when they cross over
        if (sign5p_4 eq 0) and (finder5p_4 ge 0) then solution5p_4_Tc_ARR(i)=output_fractions(0,i) else solution5p_4_Tc_ARR(i)=0
        if (sign5p_4 eq 1) and (finder5p_4 le 0) then solution5p_4_Tc_ARR(i)=output_fractions(0,i) else solution5p_4_Tc_ARR(i)=0

end

solution5p_4_Tc_ARR_b=(where(solution5p_4_Tc_ARR gt 0))
solution5p_4_Tc=min(solution5p_4_Tc_ARR_b)

if solution5p_4_Tc ne -1 then begin

for i=0,Tc_max_it-1 do begin

        if output_fractions(0,i) eq solution5p_4_Tc then solution5p_4_Ph=output_fractions(6,i)

end

endif else begin

        solution5p_4_Ph=it_multiple

endelse

;5p and 3
if (output_fractions(6,0)-output_fractions(2,0)) lt 0 then sign5p_3=0 else sign5p_3=1          ;works out what the initial sign is, when this changes a solution has
occured between the 2 channels of interest

solution5p_3_Tc_ARR=intarr(Tc_max_it)

for i=0,Tc_max_it-1 do begin

        finder5p_3=(output_fractions(6,i)-output_fractions(2,i))

        ;work out when the sign changes so can, detect when they cross over
        if (sign5p_3 eq 0) and (finder5p_3 ge 0) then solution5p_3_Tc_ARR(i)=output_fractions(0,i) else solution5p_3_Tc_ARR(i)=0
        if (sign5p_3 eq 1) and (finder5p_3 le 0) then solution5p_3_Tc_ARR(i)=output_fractions(0,i) else solution5p_3_Tc_ARR(i)=0

end

solution5p_3_Tc_ARR_b=(where(solution5p_3_Tc_ARR gt 0))
solution5p_3_Tc=min(solution5p_3_Tc_ARR_b)

if solution5p_3_Tc ne -1 then begin

for i=0,Tc_max_it-1 do begin

        if output_fractions(0,i) eq solution5p_3_Tc then solution5p_3_Ph=output_fractions(6,i)

end

endif else begin

        solution5p_3_Ph=it_multiple

endelse

;4 and 4p
if (output_fractions(3,0)-output_fractions(4,0)) lt 0 then sign4_4p=0 else sign4_4p=1          ;works out what the initial sign is, when this changes a solution has
occured between the 2 channels of interest

solution4_4p_Tc_ARR=intarr(Tc_max_it)
```

```
for i=0,Tc_max_it-1 do begin

        finder4_4p=(output_fractions(3,i)-output_fractions(4,i))

        ;work out when the sign changes so can, detect when they cross over
        if (sign4_4p eq 0) and (finder4_4p ge 0) then solution4_4p_Tc_ARR(i)=output_fractions(0,i) else solution4_4p_Tc_ARR(i)=0
        if (sign4_4p eq 1) and (finder4_4p le 0) then solution4_4p_Tc_ARR(i)=output_fractions(0,i) else solution4_4p_Tc_ARR(i)=0

end

solution4_4p_Tc_ARR_b=(where(solution4_4p_Tc_ARR gt 0))
solution4_4p_Tc=min(solution4_4p_Tc_ARR_b)

if solution4_4p_Tc ne -1 then begin

for i=0,Tc_max_it-1 do begin

        if output_fractions(0,i) eq solution4_4p_Tc then solution4_4p_Ph=output_fractions(3,i)

end

endif else begin

        solution4_4p_Ph=it_multiple

endelse

;4 and 3
if (output_fractions(3,0)-output_fractions(2,0)) lt 0 then sign4_3=0 else sign4_3=1;works out what the initial sign is, when this changes a solution has occured
between the 2 channels of interest

solution4_3_Tc_ARR=intarr(Tc_max_it)

for i=0,Tc_max_it-1 do begin

        finder4_3=(output_fractions(3,i)-output_fractions(2,i))

        ;work out when the sign changes so can, detect when they cross over
        if (sign4_3 eq 0) and (finder4_3 ge 0) then solution4_3_Tc_ARR(i)=output_fractions(0,i) else solution4_3_Tc_ARR(i)=0
        if (sign4_3 eq 1) and (finder4_3 le 0) then solution4_3_Tc_ARR(i)=output_fractions(0,i) else solution4_3_Tc_ARR(i)=0

end

solution4_3_Tc_ARR_b=(where(solution4_3_Tc_ARR gt 0))
solution4_3_Tc=min(solution4_3_Tc_ARR_b)

if solution4_3_Tc ne -1 then begin

for i=0,Tc_max_it-1 do begin

        if output_fractions(0,i) eq solution4_3_Tc then solution4_3_Ph=output_fractions(3,i)

end

endif else begin

        solution4_3_Ph=it_multiple

endelse


;4p and 3
if (output_fractions(4,0)-output_fractions(2,0)) lt 0 then sign4p_3=0 else sign4p_3=1          ;works out what the initial sign is, when this changes a solution has
occured between the 2 channels of interest

solution4p_3_Tc_ARR=intarr(Tc_max_it)

for i=0,Tc_max_it-1 do begin

        finder4p_3=(output_fractions(4,i)-output_fractions(2,i))

        ;work out when the sign changes so can, detect when they cross over
        if (sign4p_3 eq 0) and (finder4p_3 ge 0) then solution4p_3_Tc_ARR(i)=output_fractions(0,i) else solution4p_3_Tc_ARR(i)=0
        if (sign4p_3 eq 1) and (finder4p_3 le 0) then solution4p_3_Tc_ARR(i)=output_fractions(0,i) else solution4p_3_Tc_ARR(i)=0

end

solution4p_3_Tc_ARR_b=(where(solution4p_3_Tc_ARR gt 0))
solution4p_3_Tc=min(solution4p_3_Tc_ARR_b)

if solution4p_3_Tc ne -1 then begin

for i=0,Tc_max_it-1 do begin

        if output_fractions(0,i) eq solution4p_3_Tc then solution4p_3_Ph=output_fractions(4,i)

end

endif else begin

        solution4p_3_Ph=it_multiple

endelse

;********** end of solution calculations **********

;ready the solutions for returning to main program control
if solution7_5_Ph eq it_multiple then solution7_5_Tc=0
if solution7_5p_Ph eq it_multiple then solution7_5p_Tc=0
if solution7_4_Ph eq it_multiple then solution7_4_Tc=0
if solution7_4p_Ph eq it_multiple then solution7_4p_Tc=0
if solution7_3_Ph eq it_multiple then solution7_3_Tc=0


if solution5_5p_Ph eq it_multiple then solution5_5p_Tc=0
if solution5_4_Ph eq it_multiple then solution5_4_Tc=0
if solution5_4p_Ph eq it_multiple then solution5_4p_Tc=0
```

```
if solution5_3_Ph eq it_multiple then solution5_3_Tc=0


if solution5p_4_Ph eq it_multiple then solution5p_4_Tc=0
if solution5p_4p_Ph eq it_multiple then solution5p_4p_Tc=0
if solution5p_3_Ph eq it_multiple then solution5p_3_Tc=0


if solution4_4p_Ph eq it_multiple then solution4_4p_Tc=0
if solution4_3_Ph eq it_multiple then solution4_3_Tc=0

if solution4p_3_Ph eq it_multiple then solution4p_3_Tc=0

end

;***************************** Thermametrics modelling solar correction procedures etc **********************

Pro Thermametrics_solarcorr_tempvals,IPfile,no_vals,ambient_temp

;PROCEDURE: Retrieves a file with a number of temperature values selected as background non-volcanic heated (solar heated!)

;********     Steve Donegan, Open University, August 8th 2002     *********

;IMPORT:    Input filepath, number of values in file

;EXPORT:    Mean temperature within file

temps=fltarr(no_vals)

;Open file containing selected values
openr,1,IPfile
readf,1,temps
close,1

ambient_temp=mean(temps)

end

Pro ALI_solar_calc,ambient_temp,rad_corr1p,rad_corr1,rad_corr2,rad_corr3,rad_corr4,rad_corr4p,rad_corr5p,rad_corr5,rad_corr7,rad_corr8

;PROCEDURE:              to calculate the solar correction to be applied to modelled ALI data from thermametrics imagery, from low threshold range imagery

;********     Steve Donegan, Open University, August 8th 2002     *********

;IMPORT:    Mean temperature selected from relevant imagery (same day, sun warmed ground etc)

;EXPORT:    A radiance value for each ALI channel to be subtracted from the calculated PIT in the relevant ALI channels

pi=3.141592

;ali 1p wav=0.443e-6
wav_chan1p=0.443e-6

;ali 1 wav=0.4825e-6
wav_chan1=0.4825e-6

;ali 2 wav=0.565e-6
wav_chan2=0.565e-6

;ali 3 wav=0.6615e-6
wav_chan3=0.6615e-6

;ali 4 wav=0.79e-6
wav_chan4=0.79e-6

;ali 4p wav=0.8675e-6
wav_chan4p=0.8675e-6

;ali 5p wav=1.25e-6
wav_chan5p=1.25e-6

;ali 5 wav=1.65e-6
wav_chan5=1.65e-6

;ali 7 wav=2.215e-6
wav_chan7=2.215e-6

;ali 8 wav=0.585e-6
wav_chan8=0.585e-6

;set c1 and c2
c1=0.0000000000000003742;              {c1}
c2=0.014387;                                    {c2}

;c1wav^-5
c1wav_1p=c1*wav_chan1p^(-5)
c1wav_1=c1*wav_chan1^(-5)
c1wav_2=c1*wav_chan2^(-5)
c1wav_3=c1*wav_chan3^(-5)
c1wav_4=c1*wav_chan4^(-5)
c1wav_4p=c1*wav_chan4p^(-5)
c1wav_5=c1*wav_chan5^(-5)
c1wav_5p=c1*wav_chan5p^(-5)
c1wav_7=c1*wav_chan7^(-5)
c1wav_8=c1*wav_chan8^(-5)

;will produce radiance in Wm^2 um-1 sr-1, as for only a known area, subsequently convert to the actual radiant flux using the areal correction
rad_corr1p=((((c1wav_1p*(1/(((exp(c2/(wav_chan1p*(ambient_temp+273.15)))))-1))))/3.14159)/1e6)          ; {do the main planck calculation}
rad_corr1=((((c1wav_1*(1/(((exp(c2/(wav_chan1*(ambient_temp+273.15)))))-1))))/3.14159)/1e6)                    ; {do the main planck calculation}
rad_corr2=((((c1wav_2*(1/(((exp(c2/(wav_chan2*(ambient_temp+273.15)))))-1))))/3.14159)/1e6)                    ; {do the main planck calculation}
rad_corr3=((((c1wav_3*(1/(((exp(c2/(wav_chan3*(ambient_temp+273.15)))))-1))))/3.14159)/1e6)                    ; {do the main planck calculation}
rad_corr4=((((c1wav_4*(1/(((exp(c2/(wav_chan4*(ambient_temp+273.15)))))-1))))/3.14159)/1e6)                    ; {do the main planck calculation}
rad_corr4p=((((c1wav_4p*(1/(((exp(c2/(wav_chan4p*(ambient_temp+273.15)))))-1))))/3.14159)/1e6)         ; {do the main planck calculation};different pixel area!
rad_corr5p=((((c1wav_5p*(1/(((exp(c2/(wav_chan5p*(ambient_temp+273.15)))))-1))))/3.14159)/1e6)         ; {do the main planck calculation}
rad_corr5=((((c1wav_5*(1/(((exp(c2/(wav_chan5*(ambient_temp+273.15)))))-1))))/3.14159)/1e6)                    ; {do the main planck calculation};different
pixel area!
```

```
rad_corr7=((((c1wav_7*(1/(((exp(c2/(wav_chan7*(ambient_temp+273.15)))))-1))))/3.14159)/1e6)                    ; {do the main planck calculation};different
pixel area!
rad_corr8=((((c1wav_8*(1/(((exp(c2/(wav_chan8*(ambient_temp+273.15)))))-1))))/3.14159)/1e6)                    ; {do the main planck calculation};different
pixel area!


end

Pro ETM_solar_calc,ambient_temp,rad_corr1,rad_corr2,rad_corr3,rad_corr4,rad_corr5,rad_corr61,rad_corr62,rad_corr7,rad_corr8

;PROCEDURE:          to calculate the solar correction to be applied to modelled ETM data from thermametrics imagery, from low threshold range imagery

;********    Steve Donegan, Open University, August 8th 2002    *********

;IMPORT:    Mean temperature selected from relevant imagery (same day, sun warmed ground etc)

;EXPORT:    A radiance value for each ETM channel to be subtracted from the calculated PIT in the relevant ETM channels

pi=3.141592

;etm+ 1 wav=4.75e-7
wav_chan1=4.75e-7

;etm+ 2 wav=5.7e-7
wav_chan2=5.7e-7

;etm+ 3 wav=6.6e-7
wav_chan3=6.6e-7

;etm+ 4 wav=8.4e-7
wav_chan4=8.4e-7

;etm+ 5 wav=1.65e-6
wav_chan5=1.65e-6

;etm+ 6 wav=1.65e-6
wav_chan6=1.15e-5

;etm+ 7 wav=2.22e-6
wav_chan7=2.22e-6

;etm+ 8 wav=7.17e-7
wav_chan8=7.17e-7

;set c1 and c2
c1=0.0000000000000003742;          {c1}
c2=0.014387;                                {c2}

;c1wav^-5
;c1wav^-5
c1wav_1=c1*wav_chan1^(-5)
c1wav_2=c1*wav_chan2^(-5)
c1wav_3=c1*wav_chan3^(-5)
c1wav_4=c1*wav_chan4^(-5)
c1wav_5=c1*wav_chan5^(-5)
c1wav_6=c1*wav_chan6^(-5)
c1wav_7=c1*wav_chan7^(-5)
c1wav_8=c1*wav_chan8^(-5)

;will produce radiance in Wm^2 um-1 sr-1, as for only a known area, subsequently convert to the actual radiant flux using the areal correction
rad_corr1=((((c1wav_1*(1/(((exp(c2/(wav_chan1*(ambient_temp+273.15)))))-1))))/3.14159)/1e6)                    ; {do the main planck calculation}
rad_corr2=((((c1wav_2*(1/(((exp(c2/(wav_chan2*(ambient_temp+273.15)))))-1))))/3.14159)/1e6)                    ; {do the main planck
calculation}
rad_corr3=((((c1wav_3*(1/(((exp(c2/(wav_chan3*(ambient_temp+273.15)))))-1))))/3.14159)/1e6)                    ; {do the main planck
calculation}
rad_corr4=((((c1wav_4*(1/(((exp(c2/(wav_chan4*(ambient_temp+273.15)))))-1))))/3.14159)/1e6)                    ; {do the main planck
calculation}
rad_corr5=((((c1wav_5*(1/(((exp(c2/(wav_chan5*(ambient_temp+273.15)))))-1))))/3.14159)/1e6)                    ; {do the main planck calculation};different
pixel area!
rad_corr61=((((c1wav_6*(1/(((exp(c2/(wav_chan6*(ambient_temp+273.15)))))-1))))/3.14159)/1e6)                   ; {do the main planck calculation}
rad_corr62=((((c1wav_6*(1/(((exp(c2/(wav_chan6*(ambient_temp+273.15)))))-1))))/3.14159)/1e6)                   ; {do the main planck calculation};different
pixel area!
rad_corr7=((((c1wav_7*(1/(((exp(c2/(wav_chan7*(ambient_temp+273.15)))))-1))))/3.14159)/1e6)                    ; {do the main planck
calculation};different pixel area!
rad_corr8=((((c1wav_8*(1/(((exp(c2/(wav_chan8*(ambient_temp+273.15)))))-1))))/3.14159)/1e6)                    ; {do the main planck
calculation};different pixel area!

end
```

12.Appendix IV

This appendix contains the actual results returned from the dual-band method and converted to heat flux in Chapter 4. Due to the complexity and length of this discussion, this information has been shifted to this Appendix. These diagrams relate to sections 4.20 to 4.23.

12.1. Comparison of P_H between dual-band solutions and direct estimates derived from original model runs

Each line within figure 12.2a & b depicts the range of solutions for each of the 10 model runs within figure 12.1a to j at successively assumed values for T_H. These solutions were obtained using the simulated channel radiances for ALI channels 5 & 5p (runs A and B) and channels 5p & 4p (runs C to J).

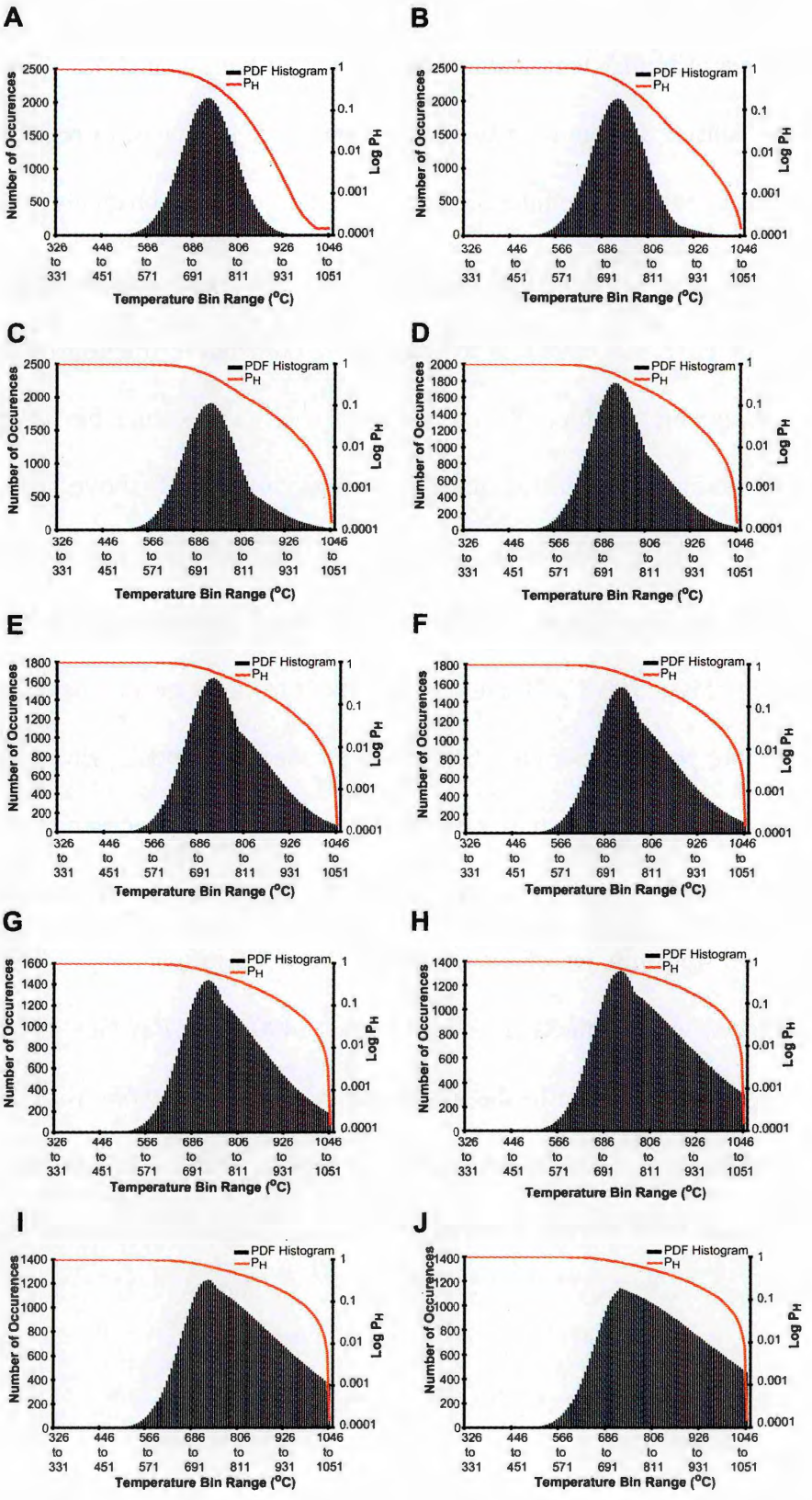

Figure 12.1: Series of Histograms depicting a pixel solely filled by a lava flow. Increasing asymmetry of the bell shaped curve indicates increasing amounts of core material exposed through the crust.

ALI channels 5 & 5p were used for the first two model runs as the in-channel radiances resulting from these two model runs were not sufficient to register within

channels 5p & 4p. This is because the simulated flow surface did not possess sufficient numbers of pixels at higher temperatures to register within channel 4p. The subsequent model surfaces caused to channel 5 to saturate, but were sufficient to register within the channel 4p dynamic range. The final 8 model runs therefore used channels 5p & 4p.

The actual derived value of P_H is shown within each model run in figure 12.1. This 'actual' value for P_H is calculated as the remaining cumulative fraction of all the pixels following each temperature bin. As the value of each temperature bin increases as we move upwards through the histogram, the number of pixels above this value falls (depending on the thermal distribution), and so the fractional area occupied by these pixels will also fall. The peak temperature within the simulated histogram for each model A to J remains between 650 to 700°C. Because of this the true value for P_H does not drop below ~0.5 until after the peak temperature has been exceeded for model. However, with each model run the decline of the actual value of P_H becomes less precipitous after the peak temperature bin. The increasing asymmetry of the histogram curve with each model, reflects the increasing number of pixels within the temperature range of the flow core (800°C +) exposed within cracks in the flow crust (400°C to 700°C). The increasingly shallow P_H curve is responding to the increasing area of hot material associated with the increase in asymmetry of the histogram curve. Therefore, with each model run the number of pixels associated with the hot material or T_H occupying area P_H within the dual-band procedure increases.

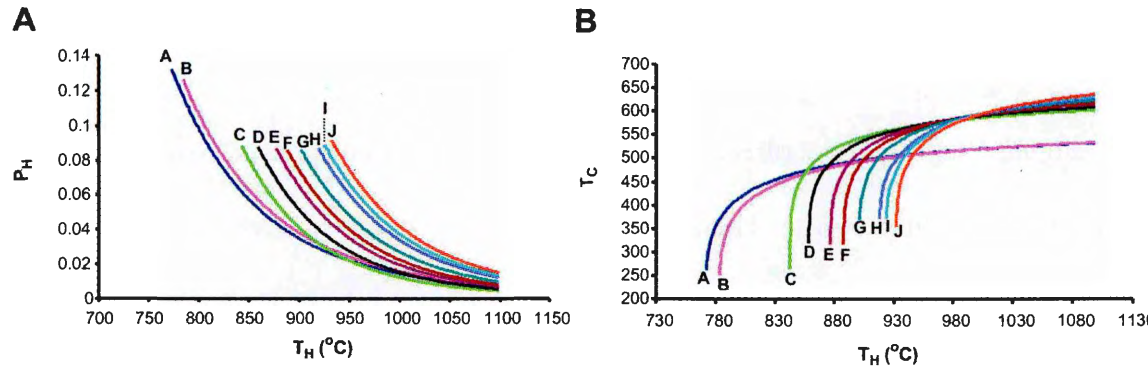

Figure 12.2: Dual-band solutions for varying TH values returned from model runs A to J simulating flows with increasing exposed core area. (A) returned P_H solutions & (B) returned T_C solutions.

The estimates of P_H extracted by the dual-band solution at successive values of T_H within each model run A to J are displayed within figure 12.2a. These dual-band solutions are available from increasingly higher values of T_H supplied to the procedure. Solutions begin for model A at 760°C whereas solutions for model J are available from 930°C. The values at which these solutions begin for models C to J are consistent at ~0.085, whereas values for P_H of 0.13 and 0.125 are recorded for models A and B respectively. There is an inconsistency between the P_H solutions for models A and B and those for model C, because of the differing channel combinations used between the two sets of results. What is apparent from this set of curves representing P_H for each model run, as the area of material associated with exposed flow core increases, the range of T_H values for which solutions are available, decreases. Model J provides solutions over a T_H range of 940°C to 1099°C whilst model C ranges from 845°C to 1099°C. The range of P_H values themselves also becomes increasingly restricted with each progressive model run. This restriction is not as marked as the restriction in solutions with T_H.

Each successive model run however records consistently higher values for P_H than the previous model run. For example at a T_H of 950°C a P_H solution for model J returns a value of 0.09 compared to 0.025 for model C. This is a difference in actual pixel area of 58.5m^2 (assuming a 900m^2 ALI pixel), and so it appears that in this instance the solutions

from the dual-band procedure are able at least to detect increasing values of P_H within each model run.

Figure 12.3 displays a direct comparison between the true value of P_H and all model runs at discrete values of T_H. The actual value of P_H is obtained here by obtaining the number of pixels above a certain temperature threshold within the simulated image for each model run. This number of pixels increases with the increasing asymmetry of the histogram curves within figure 12.1 and can be expressed as a fractional area in the manner of the solved value for P_H. We include here two lines demonstrating actual values for P_H to highlight the difficulty in defining this value. We chose a threshold of 850°C to obtain the number of pixels associated with incandescent cracks within the flow crust (Harris & Rowland, 2001), and 900°C to provide a better comparison with the lowest available set of dual-band solutions within figure 12.3 This enables a direct comparison to be made between the actual and returned solutions for P_H.

For the early model runs in which there were relatively low numbers of pixels associated with exposed flow core, the dual-band solution provides the closest estimate of 0.04 to the actual values of $P_{H(>850°C)}$ at 0.048 when T_H = 900°C. The $P_{H(>900°C)}$ value is lower at ~0.01 due to the shape of the histogram in the early models. This value of $P_{H(>900°C)}$ is similar in value to estimates of P_H at the higher T_H values for the earlier model runs.

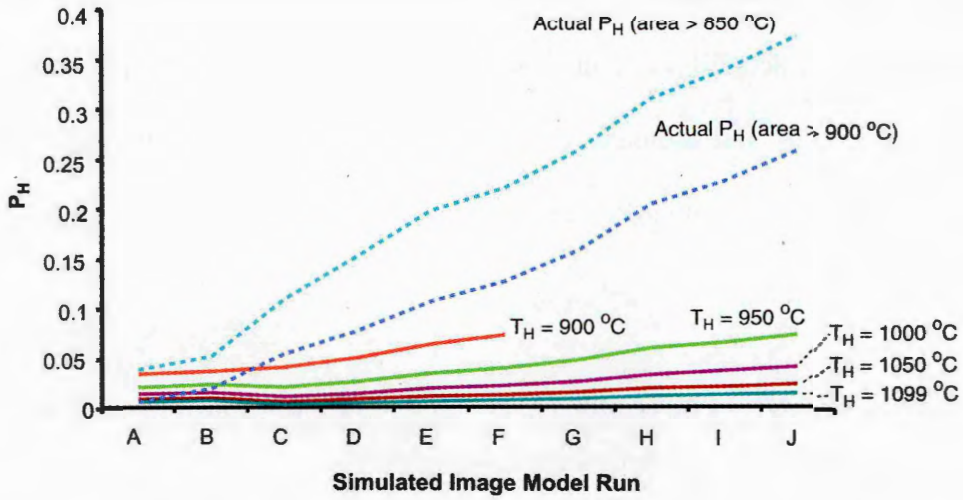

Figure 12.3: Graphical representation of estimated area representing PH from actual synthetic histogram at various model runs A to J. As simulated histogram (figure 12.1) curve asymmetry increases, representing increasing levels of flow core exposed (P_H) the number of pixels above the chosen temperature thresholds (850°C & 900°C) will increase.

Both the actual values for $P_{H(>850°C)}$ and $P_{H(>900°C)}$ increase at a rate over subsequent model runs that is not matched by any of the dual-band solutions for P_H at any T_H value. For all solutions where $T_H > 950°C$ P_H remains below 0.05 whilst both the actual $P_{H(>850°C)}$ and $P_{H(>900°C)}$ attain values of 0.25 to 0.35. This equates to a difference between actual and solved area estimates of $270m^2$ for the final model.

Estimates for P_H remain low at high T_H values due to the effect of the non-linear nature of the Planck function describing the relationship between emitted radiance and temperature used within the dual-band procedure. This effect predicts that even low numbers of pixels at higher temperatures will emit disproportionately larger amounts of radiance than a larger number of pixels at a lower temperature. This effect is especially important within the SWIR, and results in lower returned values for P_H when using higher values of T_H.

Lower values of T_H may therefore prove more accurate at estimating P_H, but if these are input to the dual-band procedure then no solutions are returned for the most active flows depicted within the final models (figure 12.3 solved P_H at $T_H = 900°C$). In the

early model runs the solved P_H values are closest to the actual values, although the discrepancy between actual P_H and dual-band P_H increases with model run. Therefore in this instance the dual-band estimates of P_H are most accurate at lower values of T_H and respond to the increase in actual P_H but fail to match quantitatively the increase in actual P_H.

12.1.1. Comparison of T_C and T_H between dual-band solutions and direct estimates derived from original model runs

Figure 12.2b displays the estimates for T_C returned by the dual-band procedure for each model within figure 12.1. The difference between T_C values provided by the use of channels 5 & 5p for the first two models and channels 5p & 4p for the final 8 models is clear. The first two channel combinations use channel 5 which is at a longer wavelength than channel 4p. This channel is more sensitive to cooler surfaces and this will result in lower values for T_C when output from the dual-band procedure.

There is an initial rapid increase in estimates of T_C once solutions become available that gradually smoothes out with increasing T_H. Estimates for T_C also begin at successively higher temperatures as each model progressively incorporates a greater number of pixels associated with temperatures of exposed core material. The pattern of returned T_C solutions with T_H value supplied to the dual-band procedure also changes in response to changes within the model image. With each successive model run the solutions are available for a shorter span of T_H temperatures and cover a narrower range of temperatures for T_C. Once a T_H value of ~985°C is reached values for T_C are consistently within a range of 30 to 40°C. Within this relatively narrow range (considering the earlier variation in temperatures at the onset of solutions) the highest estimates of T_C are provided for model J with the largest number of high temperatures, and the lowest estimates for model A with the minimum number of pixels with high temperatures.

This pattern of returned T_C solutions appears at least to respond to the changing nature of the synthetic model pixel, but are the actual values estimated for T_C realistic? T_C represents the temperature of the "cool" component within the dual-band procedure, which is defined as the area not occupied by the temperature T_H which we have obtained as P_H from the procedure. As I have shown, due to the nature of such volcanic surfaces no single temperature can be identified in this way and at best the estimates of T_C and T_H represent the mean temperatures of the two components. T_H represents the mean temperature of the area identified as belonging to the hot component of our 2 component flow model and T_C representing the mean temperature of the remaining area, the cool component. Inspection of the original model histograms within figure 12.1 indicate that the peak temperature is consistently in the region 650°C to 750°C, with progressively greater numbers of pixels in the range 700°C to 1050°C.

This increase in numbers of pixels at higher temperatures will inevitably shift the entire mean temperature of the scene upwards. Estimates for T_C do not exceed~630°C for model J at even the highest T_H value input to the dual-band procedure. This is evidently an underestimate of the true value for the mean temperature of even the entire scene. We must discount the values of T_C obtained at lower values of T_H where T_C is displaying a rapid increase after the onset of solutions as these values are within the range of 230°C to 550°C and are below the lowest temperature range within the original models. Once we have done this we are left with consistent estimates for T_C in the range of 550°C to 600°C. As we have already discussed, the final models produce the highest T_C values 30°C to 40°c above the early model runs involving channels 5p & 4p. These T_C values are consistently lower than the peak temperature within each curve, and hence must be underestimating the true value of T_C especially for the later model runs.

The temperature range covered by P_C (depending on model run and T_H value) lies within the range of ~0.75 to ~0.98 (as P_H values range from ~0.25 to ~0.02 at the very

most). This translates to a thermal range spanning from the minimum values of <500°C to ~850°C+. Due to the changing nature of the histogram curve with each model run the numbers of pixels above the peak temperature of ~650°C increases. Therefore the actual T_C temperature representing this thermal range covered by the area P_C must exceed the peak temperature as well as increase with each model run. Because of this we can surmise that the estimates for T_C supplied by the dual-band solution are significantly below the actual mean temperature represented by the area P_C.

Figure 12.4a & b describe the actual calculated values for T_H and T_C obtained from the imagery from the estimates for P_H and P_C extracted from the dual-band solution. These actual calculated values of T_H and T_C are plotted against the assumed value of T_H supplied to the procedure. This is the same format as used within figure 12.2 and can be used to assess any relative changes over the range of assumed T_H values used. The values within figure 12.4 were calculated by taking the fractional area P_H from a dual-band solution using temperature T_H and applying this information to the original simulated FLIR image. By assuming that P_C represents a thermal range from the minimum value upwards and P_H represents a thermal range from the maximum value downwards, we can use the fractional areas to extract the temperature values associated with each pixel within the fractional areas calculated for that image. Once the number of pixels and the temperatures of those pixels have been extracted from the original model image then the mean temperature can be calculated by converting all the temperatures to radiances, calculating the mean radiance and then calculation of the temperature from this integral radiance. This is accomplished by using equation 1.1 and then equation 1.4 to calculate the temperature from the radiance. This process was completed for every solution of P_H and P_C returned for each value of T_H supplied to the dual-band procedure. This method was applied to the solutions form every model run and it is these values that are shown within figure 12.4.

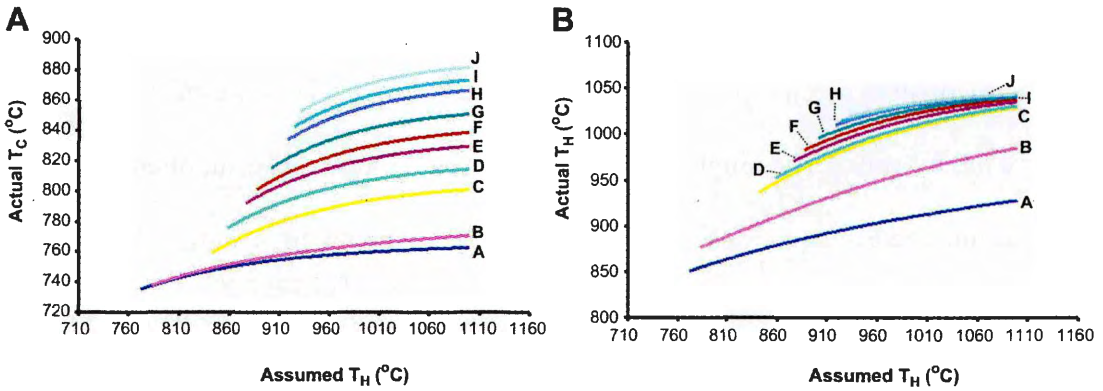

Figure 12.4: Actual temperature values of TC and TH. These values are calculated as the mean radiative temperature represented by the fractional areas returned from the dual-band solutions in figure 12.2 extracted from the original simulated FLIR image for each value of T_H input into the dual-band procedure. Each line A-J represents each model run for pixel with flow showing increasing areas of exposed core (figure 12.1).

Figure 12.4a allows a comparison to be made between the estimated values for T_C within figure 12.3b to be made with the 'actual' value for T_C calculated from the area occupied by the value P_C returned from the solution. It is immediately apparent that the values for T_C returned from the dual-band solution are significantly below the actual value for T_C. Furthermore, the curves describing the variation in actual T_C Vs T_H display a more consistent curve for each model run over the entire range for which solutions are available. With each progressive model run, the values for actual T_C are consistently higher than the previous model run and do not display any of the confusion shown in figure 12.2b. The actual values for T_C are consistent with the temperature values we might expect to extract as variable means from within an image described by the histograms within figure 12.1. It is worth noting that there is far less variation in the actual values of T_C for the varying assumed T_H values for each model run. Variation in T_C is usually less than 20-30°C from the onset of solutions to the final solution. This range appears to be consistent for each model run, despite each successive model run displaying higher overall temperatures. This variation is far less than that obtained for values of T_C from the dual-band solution.

This method also allows us to analyse what specific temperature region relates to the returned value of P_H from the dual-band solution. Figure 12.4b displays the temperatures calculated from the area identified within the original image by P_H. What is

immediately apparent is that the true value for T_H identified with this method is often lower than the assumed value of T_H supplied to the dual-band solution. This is especially the case for the early model runs. The single assumed temperature value of T_H supplied to the two dual-band simultaneous equations is highly unlikely to relate to a single temperature occupying the area P_H. This diagram helps us to ascertain the actual range of temperatures associated with the returned area of P_H. There is no significant difference in values of many hundreds of degrees as we have seen with T_C and there is a variation of between 15°C to 30°C over the entire span of available solutions provided for by the dual-band procedure. Considering model runs in which solutions are obtained using channels 5p & 4p (C thro J) then the entire range of actual T_H values varies less than 80°C at the onset of solutions, reducing to ~10°C at the final available solutions at 1099°C.

In conclusion of this section, I have shown that the dual-band method is capable of detecting an increasing area of hot material within successive model imagery with an increasing number of pixels possessing higher temperatures. Although the dual-band procedure is capable of detecting this change, it is not at all effective when attempting to estimate the true area occupied by this material as it changes. The dual-band estimates of P_H are increasingly inaccurate with increasing T_H and with increasing 'hot' area within the model image. Estimates for the value of T_C representing the temperature of the "cooler" component of the two component surface within the dual-band procedure do make a distinction between each successive model, with estimated higher temperatures of T_C for each model. However these temperatures are far too low to provide realistic estimates of the mean temperature represented by the actual area defined by P_C and display a greater variation between these values for the range of T_H used.

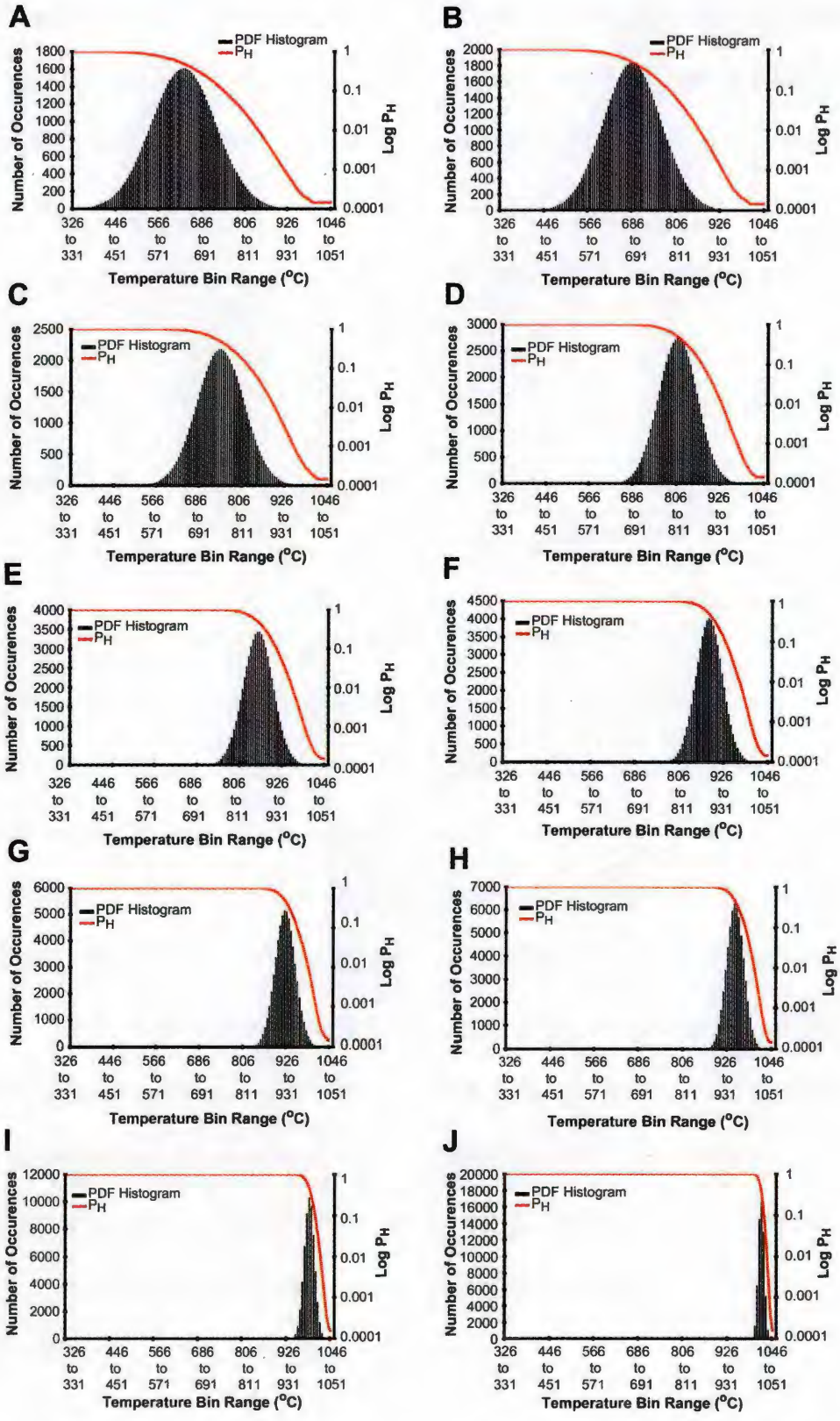

Figure 12.5: Series of histograms depicting a pixel solely filled by a lava flow. The mean temperature of the flow is increasing with each model run (A to J) and the curve is narrowing indicating a restriction if thermal variety. This simulates a series of flows of increasing overall vigour/ youthfulness.

The range of flow surfaces described within figure 12.5 may therefore range from a well defined channelised flow with a well developed crust with very few cracks exposing

near magmatic temperatures within the core to a flow with little or no crust. Such a surface might be found in the immediate vicinity of the active vent. The intermediate imagery within figure 12.5 describes cases that are at intermediate levels of activity between these two extremes. We can now investigate whether the dual-band procedure is able to distinguish this progression in flow activity.

12.1.2. Comparison of P_H between dual-band solutions and direct estimates derived from original model runs

Figure 12.6a displays a set of dual-band solutions obtained from a range of T_H values for the set of integrated radiances calculated from each of the model runs within figure 12.12. In this set of model imagery the mean temperature indicated by the peak within the histogram does not remain fixed unlike that of the models within the previous section. The peak number of pixels within the histogram here ascends from the ~580°C temperature bin to a bin of ~990-1000°C for the final model, J. The actual calculated value for P_H in each temperature bin is shown in each histogram within figure 12.12. The actual value of P_H only drops below 1 at increasingly higher temperatures, reflecting the changes within the histogram. As the model image becomes increasingly restricted in terms of thermal distribution, indicated by the narrowing of the histogram curve, the rate at which P_H drops from 1 towards its minimum value becomes increasingly steep.

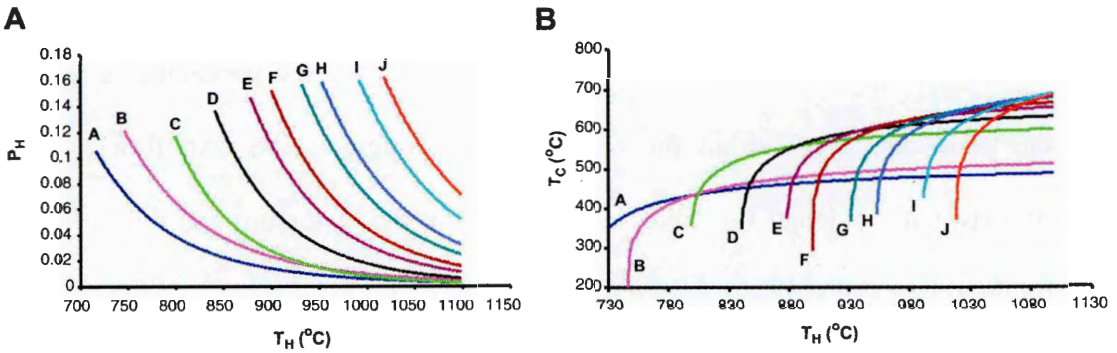

Figure 12.6: Dual-band solutions for varying TH values returned from model runs A to J simulating flows depicted within figure 12.11. (A) returned P_H solutions & (B) returned T_C solutions.

The values for P_H extracted from the dual-band solution displayed within figure 12.6a clearly show a variation in values depending on T_H and model run. Dual-band solutions become available at increasingly higher values of T_H from 710°C for model A through to 1050°C for the final model J. Solutions for P_H begin with values of 0.11 for model A and increase steadily with each successive model with a final onset P_H of 0.16 being the first value for model J. The range of P_H values covered is greater for the early model runs than the later model runs. Model A demonstrates a P_H range of 0.11 to 0.01 that narrows to 0.16 to 0.09 for model J.

The consistently higher P_H values at each T_H value for every successive model run confirm that the dual-band procedure is able to distinguish the increasingly active lava flows within the simulated imagery of figure 12.11. The difference in P_H values for this series of simulated imagery is far clearer than those obtained from the imagery discussed in the previous section. The curves depicting the actual P_H values displayed for each model within figure 12.5 show an increasingly short T_H interval over which the values P_H drop from ~1 to < 0.005. This too is reflected within figure 12.6a. The rate of decrease in P_H values increases with each successive model run over the range of T_H values supplied to the procedure.

The solutions for P_H displayed within figure 12.6a may distinguish between the different model runs in terms of P_H at certain T_H values, but these values are a considerable

underestimate of the true value of P_H. Therefore, estimates for P_H extracted from the dual-band procedure are a poor estimate of the true value of P_H, but the procedure is able to identify the trend displayed within the series of increasingly active lava flows. This comparison between the actual P_H values calculated from the histogram and the estimates returned by the dual-band procedure is confirmed in figure 12.16. Figure 12.16 highlights the values for P_H obtained from the procedure at 7 different values of T_H for each model run. Also shown is the actual value of P_H, which we defined as the area within the simulated flow greater than 850°C. This increases rapidly upwards to ~1 as the entire image histogram constricts and shifts towards higher temperatures. Once the entire thermal range within the image is above the threshold temperature, then P_H will equal 1.

As figure 12.16 shows, the estimates of P_H become increasingly inaccurate with increasing T_H and model run. For the first three model runs a reasonable match between estimated and true values for P_H exist for $T_{H(850°C)}$ and $T_{H(900°C)}$. The rate of change of the estimated value for P_H returned from the procedure shows a higher response than those lines for the previous set of model runs within figure 12.4, but still provides a woefully low estimate of P_H. However, there is still a marked difference between each of the series of solutions for each of the model runs. This shows that the dual-band procedure is at least able to respond to the changes over the series of modelling runs simulating increasingly active flows with markedly different estimates of P_H, albeit considerable estimates of the true value.

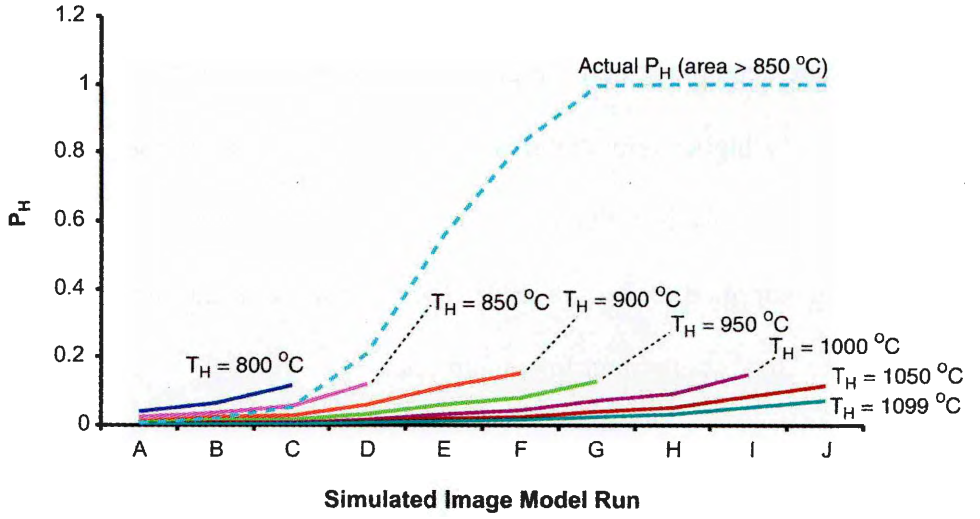

Figure 12.16: Graphical representation of estimated area representing PH from actual synthetic Histogram at various model runs A to J.

Whilst the simulated histogram (figure 12.5) narrows and the mean temperature increases as the curve moves to higher temperatures, the number of pixels above the set 850°C threshold increases until all pixels are above this threshold.

12.1.3. Comparison of T_C and T_H between dual-band solutions and direct estimates derived from original model runs

Values for T_C obtained from the dual-band procedure applied to the models within figure 12.1 are displayed within figure 12.6b. The pattern of these solutions is very similar to that displayed for the previous set of models in figure 12.7b. This is a pattern where the T_H temperatures, at which solutions become available, is greater for each subsequent model run. However the temperature range that this encompasses is greater than that in figure 12.7b. The spread of temperatures obtained for T_C is wider, spanning ~150°C once the initial steep onset has been discounted. Higher values of T_C are obtained for each subsequent model.

The series of models within figure 12.5 depicting increasingly active flows with the temperatures present becoming increasingly restricted within a narrowing thermal span centred at increasingly higher temperatures, will produce an increasingly higher integral radiative temperature. This is reflected within the returned values for T_C. With each successive T_H value supplied to the procedure the resulting estimate for T_C is higher than the previous value. This is consistent for each model.

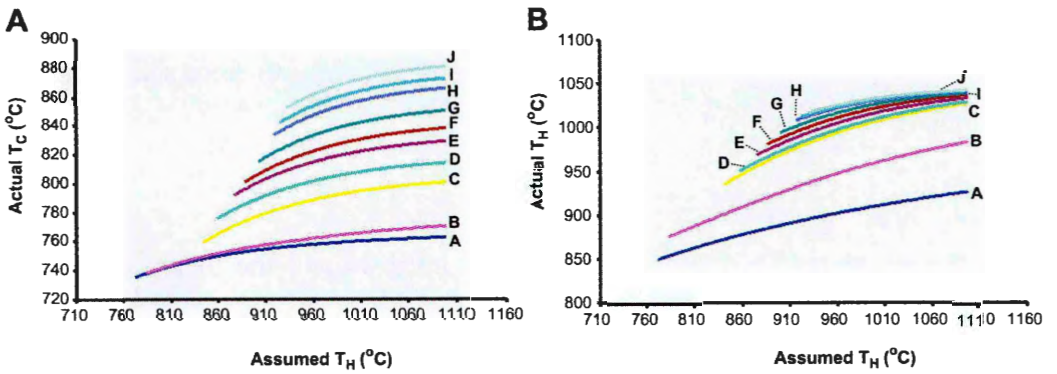

Figure 12.7: Actual temperature values of TC and TH. These values are calculated as the mean radiative temperature represented by the fractional areas returned from the dual-band solutions in figure 12.7 extracted from the original simulated FLIR image for each value of T_H input into the dual-band procedure. Each line A-J represents each model run for pixel with flow showing increasing areas of exposed core (figure 12.16).

The increasing mean temperature of the each of the model histograms within figure 12.5 suggests that by the extreme final model in which the temperature span merely covers ~930°C to ~1040°C, then a value for T_C representing at least a P_C of f 0.9 should be in the region of this temperature span. The highest value for T_C obtained from the dual-band procedure is ~680°C from the final model run J. This is a considerable underestimate of the true value of T_C.

Figure 12.7 displays the actual calculated values for T_C and T_H obtained from the original model imagery (figure 12.7a & b respectively). These were obtained by extracting the mean temperature for the returned areal estimates for P_H and P_C from the original synthetic image, in the same manner as that described within the previous section. Figure 12.7a displays a set of temperatures for P_C that show only a slight increase in actual T_C for

each model run over the range of assumed T_H values supplied to the procedure. This pattern is similar to those obtained for the actual values of T_C and T_H in figure 12.4. The difference in temperatures for both T_C and T_H for each model, are clearly delineated for each value of T_H. These actual values for T_C and T_H are again considerably higher than those values returned from the procedure within figure 12.6, for the same assumed T_H values supplied to the procedure.

It is therefore apparent that the dual-band procedure is again able to detect changes within a pixel containing thermal information from a synthetic image described by a changing unimodal histogram. However, the dual-band procedure is unable to provide quantifiably accurate estimates of the true values of P_H, P_C, T_H and T_C which are in each case considerable underestimates of the true values.

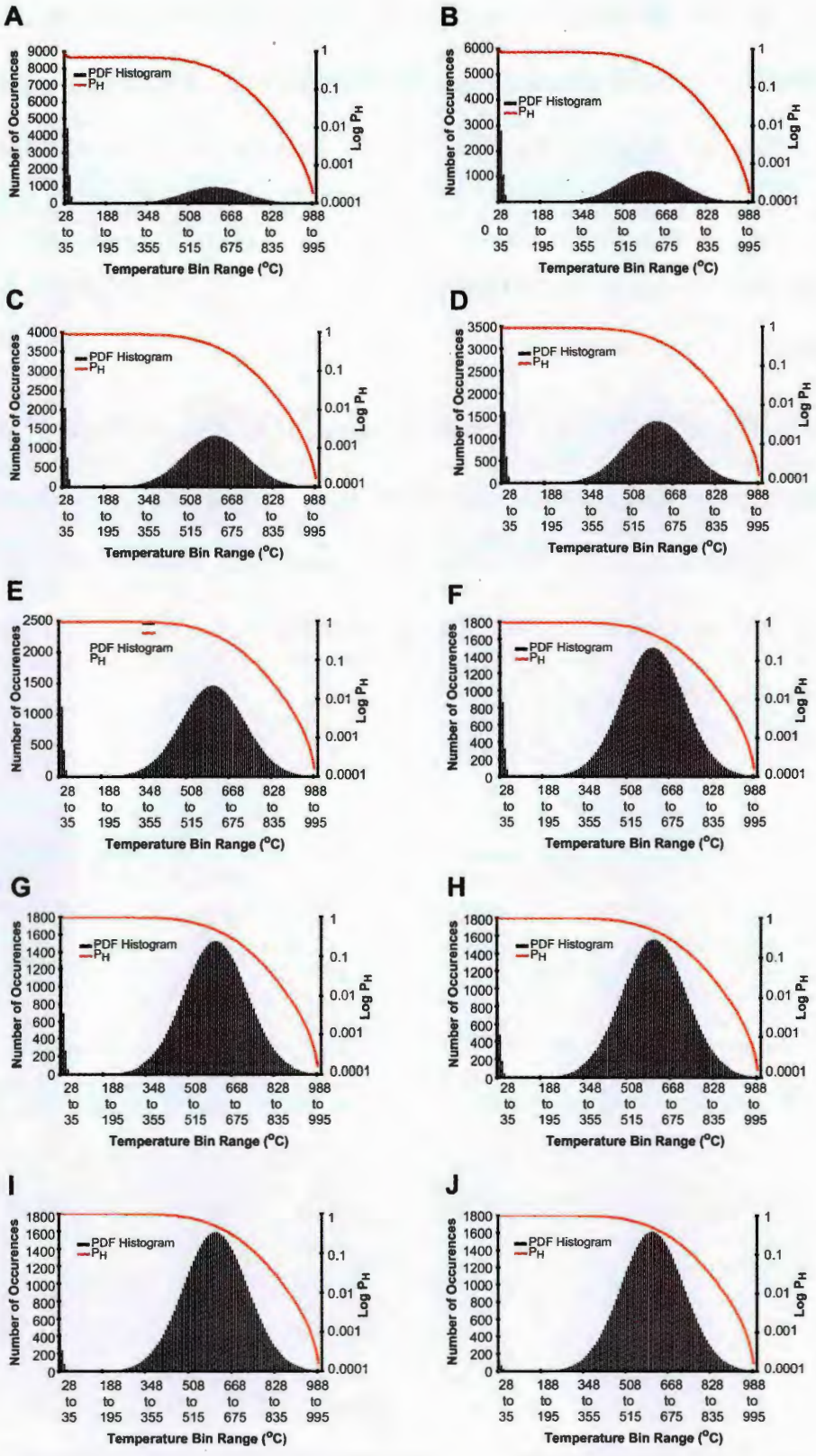

Figure.12.18: Series of histograms depicting a pixel occupied by ground at ambient temperature and a lava flow. The increasing height of the curve describing the thermal distribution of the lava flow with each model run (A to J) indicates that the area within the pixel occupied by the flow increases with each run.

12.1.4. Comparison of P_H between dual-band solutions and direct estimates derived from original model runs

The actual value for P_H displayed within each model in figure 12.9 shows little change in shape with the increase in fractional area occupied by the lava flow. Early model runs possess a slight change in trend of P_H in the temperature bins associated with the cool ground. Due to the method by which the area occupied by the flow increases and the constant ratio between each of the temperature bins, there is very little change in the values of P_H for each temperature bin.

Estimates obtained from the dual-band procedure for P_H and T_C are shown within figure 12.10a and 10.19b respectively. What is immediately apparent is the close spacing between each of the curves for P_H in figure 12.10a. These bears little resemblance to those curves for estimated P_H from models based on the unimodal histograms. Unlike previous models with a unimodal thermal distribution, figure 12.10a shows that the dual-band solutions are available from the same value of T_H supplied to the procedure for each of the 10 model runs.

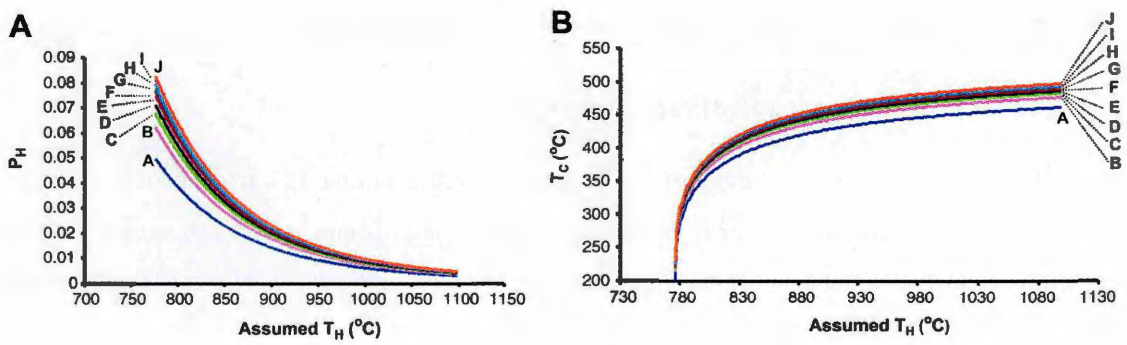

Figure 12.10: Dual-band solutions for varying TH values returned from model runs A to J simulating flows depicted within figure 12.9. (A) returned P_H solutions & (B) returned T_C solutions.

There is also little difference in estimates for P_H at the onset of solutions at T_H =770°C, and the estimates for P_H for each of the model run tends towards a value of 0.006

at the final T_H=1100°C. This is in complete contrast to those solutions obtained for P_H from the previous two unimodal models, in which there was a wider variation between the returned values of P_H and solutions were available from staggered values of T_H with each successive model run. Figure 12.10a does show that despite the low degree of variation between values of returned P_H, the dual-band procedure is able to distinguish between the various input models, with the later model run estimates in the upper region of the solution envelope and the lower models in the lower region of the envelope.

Figure 12.11 displays a comparison between the solutions for P_H derived from each model at 7 differing values of T_H and two estimates of the actual value of P_H. The two lines depicting the estimated actual P_H are defined as the pixel fraction occupied by all areas occupied by temperatures above a set threshold (>100°C and >800°C).

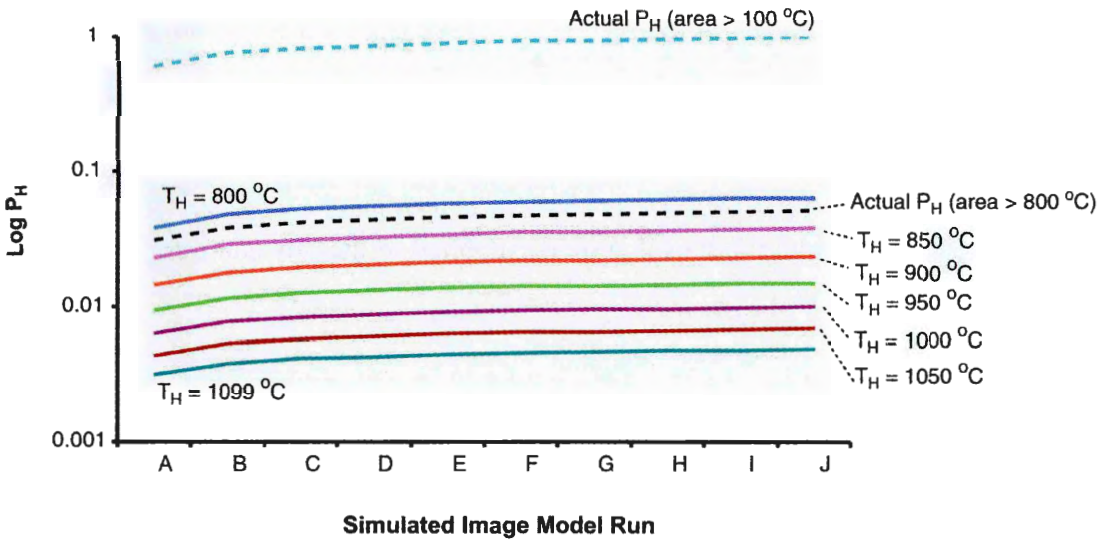

Figure 12.11: Graphical representation of estimated area representing PH from actual synthetic histogram at various model runs A to J. Whilst the simulated histogram (figure 12.9) narrows and the mean temperature increases as the curve moves to higher temperatures, the number of pixels above the two thresholds set at 100°C and 800°C increases.

This enables a comparison to be made considering the bimodal temperature distribution within the model. The >100°C curve allows an estimate of the whole area occupied by the lava flow to be made whilst the area defined as >800°C can be related to the area relating to cracks within the flow crust exposing the flow interior. This latter

estimate allows a direct comparison with the previous unimodal temperature distributions to be made in which P_H is directly linked to the area of exposed flow core.

It is apparent from figure 12.11 that the dual-band solutions obtained from each model run and at all values of T_H seriously underestimate the entire fraction of the pixel occupied by the flow itself ($P_{H>100°C}$). The solutions themselves are obtained over a span of T_H temperatures from 200°C to 1100°C. However solutions are not available until T_H reaches ~770°C. The procedure, at least simulating the ALI channels 5p & 4p, is insensitive to cooler temperatures as no relation to fractional area occupied by the ambient ground surface is present within the returned solutions. As P_H relates to the 'hottest' portion of the sub-pixel thermal structure and has values of f~0.005 to f~0.06 then this will return values of P_C of f 0.995 to f 0.910. The level gradient of the returned solutions for P_H show little response, over the course of the model runs, to the reducing area of cool ground within the pixel area, which at no point is in the region of f ~0.9 in any of the model runs.

The dual-band solution responds better to the fractional area occupied by material at temperatures greater than 800°C. The line $T_{H\ (>800°C)}$ in figure 12.11 is very close in terms of P_H values with solutions obtained over the course of the 10 model runs at values of T_H = 800°C. The shallow rate of increase in actual $P_{H\ (>800°C)}$ over the course of the 10 model runs is mirrored by the solutions for T_H = 800°C, and also the lines depicting solutions at higher values of T_H. Solutions obtained at higher T_H values increasingly underestimate the value of $P_{H(>800°C)}$ for each model run, despite mirroring the trend displayed by actual $P_{H(>800°C)}$. This pattern is reminiscent of the previous models where higher values of T_H used, return increasingly smaller solutions for P_H.

This is a consequence of the Planck relationship in that higher values of assumed T_H will return smaller estimates of P_H as increasingly smaller areas will radiate disproportionately higher radiances with increasing temperature (Rothery et al, 1988). Despite this the estimates for P_H returned by the solution where T_H > 850°C are

underestimates by at least a single order of magnitude, and are comparatively much worse than those solutions provided for model runs based on a unimodal pixel thermal distribution.

12.1.5. Comparison of T_C and T_H between dual-band solutions and direct estimates derived from original model runs

Figure 12.10b displays the set of solutions obtained for T_C for the 10 simulated pixels within figure 12.9. A similar pattern of little variation between these values for T_C from each model run at the same value of T_H exists between these T_C solutions and those obtained for P_H in figure 12.10a. Once the steep initial onset of solutions has passed after solutions become available at ~775°C, the spread of T_C values is at its greatest between ~430°C and ~470°C at the final value of T_H of 1100°C. This range of T_C temperatures is smaller than any of the solutions returned for model pixels possessing a unimodal temperature distribution. The relative lack of variation in the estimates obtained for T_C for each of the model runs actually reflects the changing nature within the thermal distribution of the modelled pixel. If we consider just the lava flow, the mean temperature of the flow will remain the same despite the increase in fractional area. This is because the ratio between the numbers of pixels within each temperature bin of the model histogram representing the thermal distribution of the synthetic lava flow is constant between all the model runs. This produces the same mean temperature for the lava flow for each model run. If, as before, we assume that T_C represents the mean radiative temperature of all surfaces within the area defined by P_C then the slight increase in temperature of the T_C solutions within figure 12.10b is due to the decrease in pixel fraction of the cool ground area at ambient temperature.

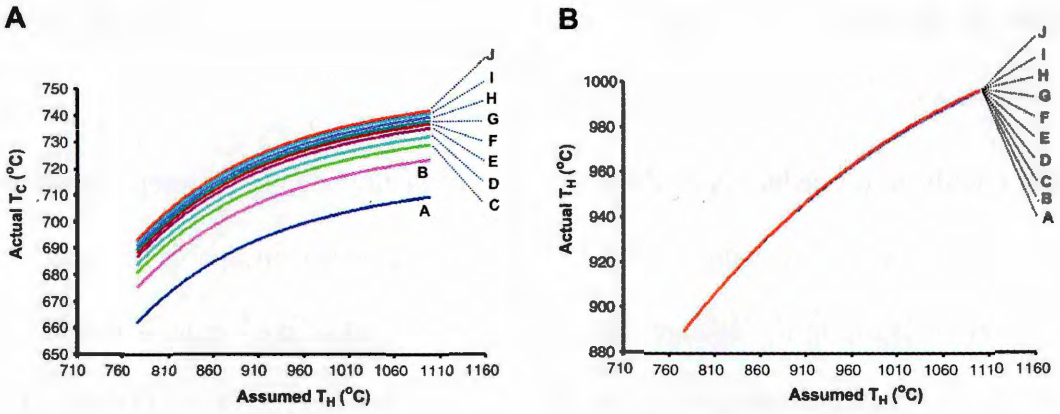

Figure 12.12: Actual temperature values of TC and TH. These values are calculated as the mean radiative temperature represented by the fractional areas returned from the dual-band solutions in figure 12.10 extracted from the original simulated FLIR image for each value of T_H input into the dual-band procedure. Each line A-J represents each model run for pixel with flow showing increasing areas of exposed core (figure 12.9).

Figure 12.12a & b display the respective actual values for T_C and T_H calculated from the values of P_C and P_H applied to the original synthetic imagery. The solutions for actual T_C in figure 12.12a bear a similar relationship between the individual model runs as those estimated solutions obtained from the dual-band procedure in figure 12.10a. There is less variation between increasingly higher model runs at any given T_H value supplied to the procedure. The actual values of T_C are on average 200°C higher than those solutions for T_C obtained within figure 12.10b. There is very little or no variation between the actual values of T_H in figure 12.12b from each model. Due to the nature of the histogram and the method by which it increases its occupying fractional area of the pixel, then the area defined by P_H will lie within the upper temperature bins of the model histogram depicting the lava flow for every simulated pixel.

As I have shown, the mean temperature describing this entire histogram does not change despite increasing fractional area. Therefore any subset area of temperatures chosen consistently from this histogram will not change either. The almost linear relationship between increasing T_H value supplied to the procedure and the actual value of T_H extracted from the synthetic imagery, at area P_H, is also indicative of this effect. Although $T_{H(actual)}$ does not equal exactly $T_{H(assumed)}$ ($T_{H(assumed)}$ lags $T_{H(actual)}$ by ~ 80-110°C)

the gradient of the line indicates that an increase in $T_{H(assumed)}$ is matched by an equal increase in $T_{H(actual)}$.

The dual-band procedure is evidently capable of distinguishing between this set of bimodal model pixels only by using T_H and P_H. The procedure was incapable of obtaining estimates or even detecting the change directly of the amount of cool ground within the pixel. The relative lack of response to cool ground at ambient temperatures is mainly due to the ALI channel combinations used in this simulation. However the use of a combination of longer wavelength channels (i.e. ALI channels 7 & 5) would render the channels likely to saturate over even moderately active flows such as the one simulated here, and hence provide untrustworthy solutions. Therefore the dual-band procedure is sensitive only to the most active areas of the flow, namely those areas >800°C as suggested by the actual $P_{H>800°C}$ curve in figure 12.11. The most accurate estimate of P_H are obtained by solutions using assumed T_H values supplied to the procedure in the region of 800 to 850°C. Higher T_H values here provided considerable underestimates of the $P_{H>800°C}$ curve in figure 12.11.

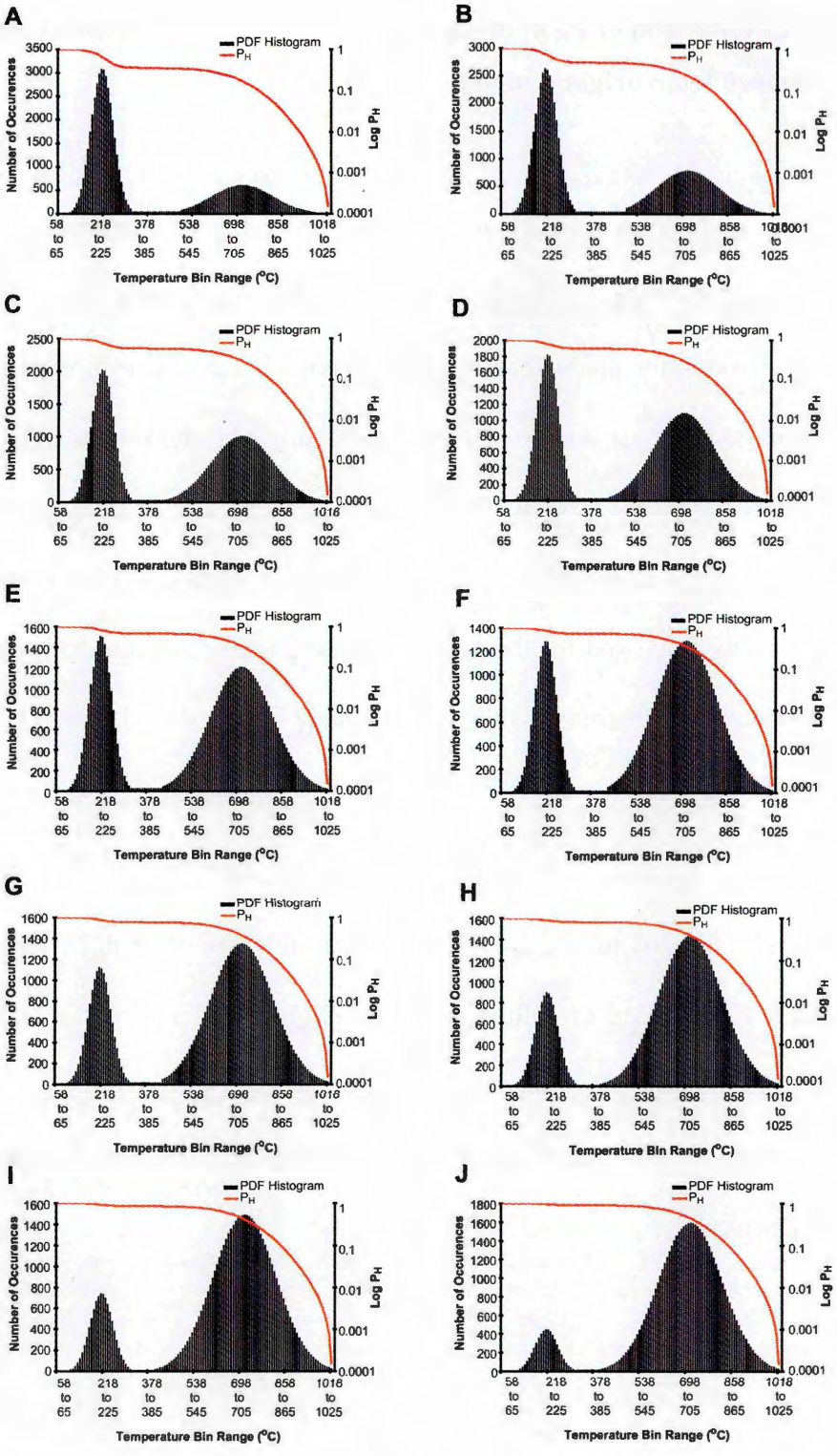

Figure.12.13: Series of histograms depicting a pixel occupied by both a lava flow and cooler material representing varying amounts of levees and stagnating flow material. The increasing height of the curve describing the thermal distribution of the lava flow portion with each model run (A to J) indicates that the area within the pixel occupied by the actual flow increases with each run, whilst the area occupied by the levee material etc, decreases.

12.1.6. Comparison of P_H between dual-band solutions and direct estimates derived from original model runs

Figure 12.19 displays also the actual calculated value for P_H based on the area of the remaining number of pixels exceeding the current temperature bin. This shows a similar set of P_H trends for the successive model runs as the simple bimodal distribution discussed within the previous section. In this model however, the fractional area occupied by the first cooler curve accounts for a f~0.7 which reduces to a f <0.001 within the final models. Little change is observed within these P_H values from the second curve. This is the same situation as discussed for the lava flow in the previous section, as the lava flow simulated here increases in area by the same constant-ratio method. Figure 12.14a & b displays the solutions for P_H and T_C respectively. The pattern of these solutions with assumed T_H value is very similar to that discussed within the previous section.

Dual-band solutions for P_H are available from the same initial T_H value and trend towards f ~0.01. The spread of solutions is very slightly wider over the entire range of assumed T_H values than the previous bimodal model. These estimates range from an initial span of f 0.04 to f 0.095, with higher solutions for P_H obtained consistently from successively later models.

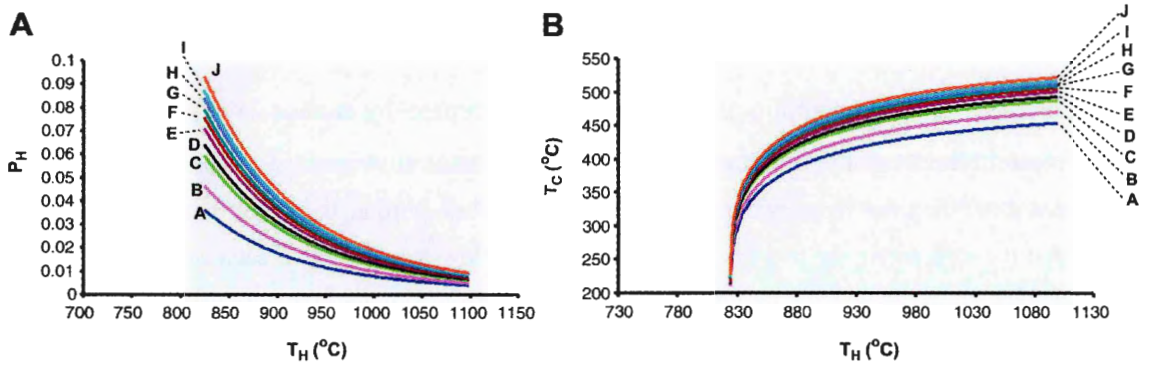

Figure 12.14: Dual-band solutions for varying TH values returned from model runs A to J simulating flows depicted within figure 12.19. (A) returned P_H solutions & (B) returned T_C solutions.

The P_H curves displayed within figure 12.14a trend downwards to a fractional area spanning *f* 0.006 for the early models and *f* 0.012 for later models. This pattern of P_H solutions indicates that the procedure is able to identify the presence of amounts of hot material akin to T_H, occupying increasingly larger fractional areas. Figure 12.15 presents a comparison between the actual amount of material above a set pair of threshold temperatures representing the actual value(s) of P_H and the estimates from the dual-band solutions discussed within figure 12.14a.

The two dashed curves within figure 12.15 indicate two differing threshold temperatures. The $P_{H\ (>497°C)}$ curve enables the fractional area of all temperatures above this threshold to be identified. A threshold temperature of 497°C is a suitable boundary value situated between the two curves of the original histogram, and effectively charts the varying fractional area occupied by the lava flow over the course of the 10 model runs. The threshold of 850°C is a suitable threshold value to identify amounts of exposed flow core material from the actual lava flow.

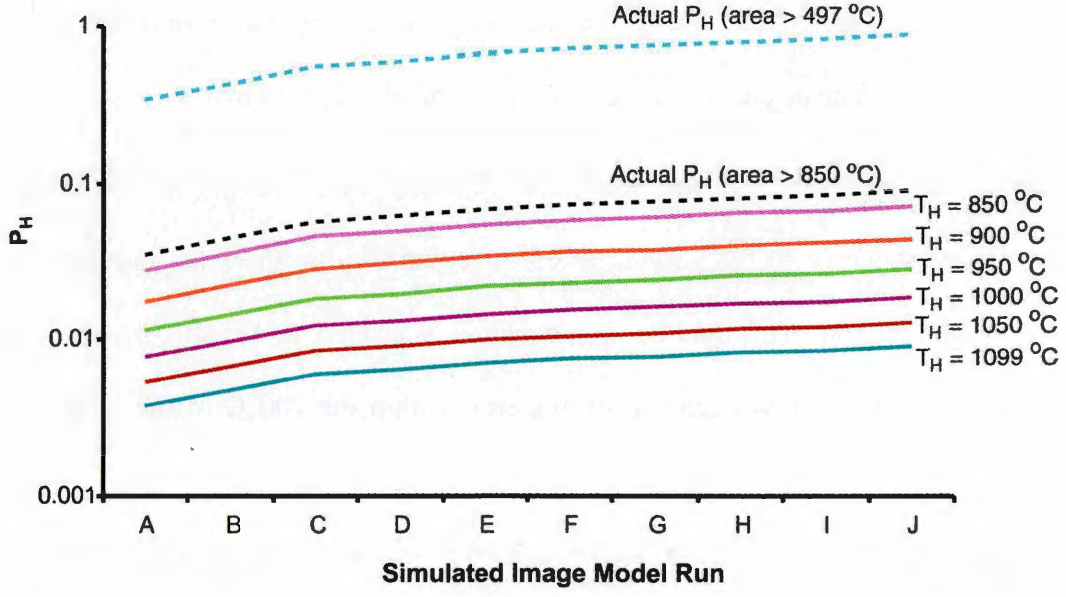

Figure 12.15: Graphical representation of estimated area representing PH from actual synthetic histogram at various model runs A to J. Whilst the simulated histogram (figure 12.19) narrows and the mean temperature increases as the curve moves to higher temperatures, the number of pixels above the two thresholds set at 497°C and 850°C increases. A threshold of 497°C was chosen so as to distinguish the entire curve associated with the flow, and 850°C the relative amount of material associated with exposed core.

This fractional area is akin to the definition of P_H within the unimodal model pixels relating to the "hot" component within Crisp & Baloga's two component model (Crisp & Baloga, 1990). Figure 12.15 shows that all solutions obtained from the dual-band procedure are considerable underestimates of the entire fractional area occupied by the flow itself ($P_{H(>850°C)}$), at all assumed values of T_H used and for each model run. The patterns of returned solutions are very similar for this bimodal temperature distribution as within the simpler bimodal thermal distribution discussed within the previous section. The actual dual-band estimates of P_H are closer to the fractional area defined by $P_{H(>850°C)}$. Over the course of each of the 10 model runs, the lower assumed T_H values provide a closer match to $P_{H(>850°C)}$ than those solutions obtained using higher values for T_H. This pattern is also reminiscent of the pattern of solutions displayed within the previous section and figure 12.11.

Dual-band estimates for P_H obtained from pixels displaying such a bimodal thermal distribution, again identify that the area occupied by the lava flows within each successive model run is increasing. And again, the values provided by the procedure are a considerable underestimate of the actual area within the pixel occupied by the flow.

Due to the placement of the simulated channels used within the SWIR the procedure is more sensitive to the varying areas of regions within the pixel occupied by high temperature material. The dual-band procedure is proved to be still much more sensitive to regions of the flow occupied by material within the 200°C of the magmatic temperature. Even the presence within the pixel of areas occupied extensively by cooled crust or bounding levees, or even surrounding ground heated by radiation and conduction from the flow, is not sufficient for the procedure to obtain estimates for P_H closer to the area occupied by the flow itself. If the procedure was an accurate indicator of the true two-component model structure, which in this case would be the area of cooler material

described by the first curve and the active flow itself described by the second curve, then the procedure would return reasonable estimates of P_C and P_H respectively for these two areas.

12.1.7. Comparison of T_C and T_H between dual-band solutions and direct estimates derived from original model runs

Figure 12.14b displays the dual-band estimates for T_C obtained for the 10 model runs depicted within figure 12.19. There is again a very close parallel between the results obtained for this set of model runs and the previous section. The solutions for T_C are available from a single temperature T_H of ~820°C, and once the steep initial onset of solutions has been by-passed by 880°C, the solutions vary between 420 and 510°C. Solutions from later model runs return consistently higher estimates for T_C than those obtained from the earlier model runs. The envelope of temperatures between model runs covered by the solutions for T_C for each T_H value are wider than that of the previous sections set of model pixels containing purely cool ground and a lava flow. The temperatures for T_C are here consistently higher than those T_C solutions (figure 12.16b) by ~20-30°C. The mean temperature for each of the 10 models that incorporate material in the region of 60 to 400°C as well as the active lava flow itself will be higher for each model than the previous models incorporating cool ground in the region of 0 to 40°C in figure 12.12. We would therefore expect to see the value of T_C obtained from the models within figure 12.14 to record a higher temperature than those values returned for T_C from the models in figure 12.12. The dual-band procedure does extract such higher temperatures for T_C in this instance.

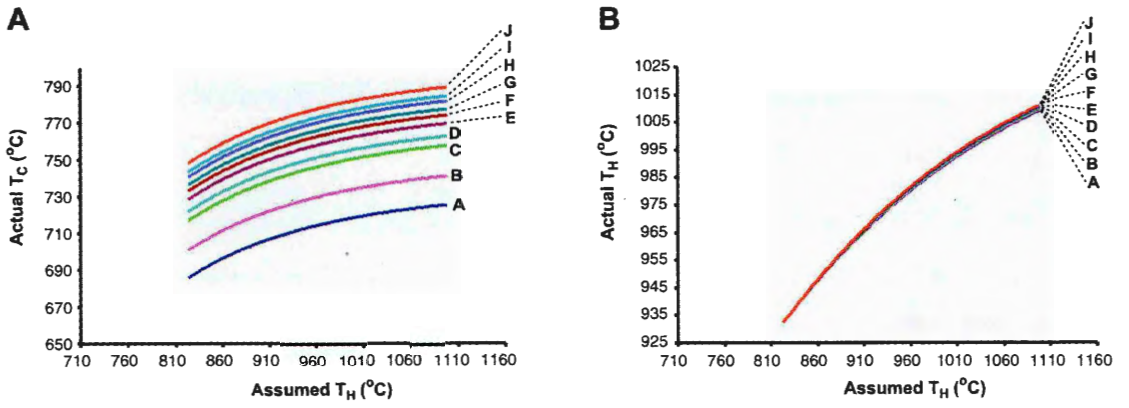

Figure 12.16: Actual temperature values of TC and TH. These values are calculated as the mean radiative temperature represented by the fractional areas returned from the dual-band solutions in figure 12.14 extracted from the original simulated FLIR image for each value of T_H input into the dual-band procedure. Each line A-J represents each model run for pixel with flow showing increasing areas of exposed core (figure 12.19).

Figure 12.16 displays the actual calculated values for T_C and T_H obtained from the original imagery using the fractional areas P_C and P_H returned from the dual-band procedure. We again see here a similar pattern to that for the corresponding figure 12.12 from the previous model run of a relatively narrow envelope of solutions for T_C and T_H. These are markedly different to those obtained from those unimodal thermal distribution models. Those values for T_C displayed within figure 12.16a display an envelope of temperatures for each value of T_H supplied to the procedure that are higher than those values of T_C obtained from the procedure in figure 12.14b. Each value for T_C within figure 12.16a is ~250°C higher than the equivalent value for T_C within figure 12.14b. The values for T_C within figure 12.16a are also higher than those in the corresponding figure 12.12a mirroring the pattern observed between figure 12.14b and fig10.25b. Despite the narrow envelope of T_H temperatures displayed within figure 12.16b the final spread of T_H temperatures are wider than those within figure 12.12b.

The models depicted within figure 12.19 display a slightly greater area of material at higher temperatures > 850°C than those models within figure 12.12. This is in addition to the first curve within the histogram depicting warmer material in the range 60°C to ~400°C. This set of circumstances will result with a higher mean temperature representing

the entire set of models within figure 12.19. This is reflected within the higher temperatures calculated from the models for the returned areas of P_C and P_H from the dual-band procedure within figure 12.16a & b.

The dual-band procedure has in this instance only been able to distinguish the difference between the bimodal thermal distribution scenarios simulated here within figure 12.19 and those previously discussed within figure 12.15, on the basis of the higher temperatures associated with the former model. Estimates for the fractional area P_H occupied by the "hotter" material within the pixel are again serious underestimates of the values indicated from the original imagery, yet mirror the increasing trends of the actual area displayed within figure 12.12.

12.1.8. Comparison of P_H between dual-band solutions and direct estimates derived from original model runs

The actual value of P_H has again been calculated and displayed as a curve on the histogram within figure 12.17. The pattern of values of P_H with increasing temperature is very similar to that shown within figure 12.11, with P_H demonstrating an increasingly steep drop in values with increasing flow activity. The area occupied by the cool ground in the temperature region of 0 to ~45°C occupies a consistent pixel fraction f 0.1 in each of the 10 model runs. As with the unimodal set of simulated pixels discussed within section 10.5, the peak temperature of the second curve increases whilst the bell-shape of this second curve narrows. This indicates a lava flow of increasing activity. With increasing activity more material is exposed at higher temperatures analogous to exposed flow core material. As flow activity increases within each of the 10 model runs, the amount of material associated with a chilled crust within the region 200 to 500°C decreases.

This scenario results with the actual P_H value, relating to those areas within the flow at the highest temperature, displaying a steep descent at ever increasing temperature bin values. This pattern is the same as that displayed within section 10.5. Estimates for P_H and T_C obtained from the dual-band procedure are displayed within figure 12.18a & b respectively.

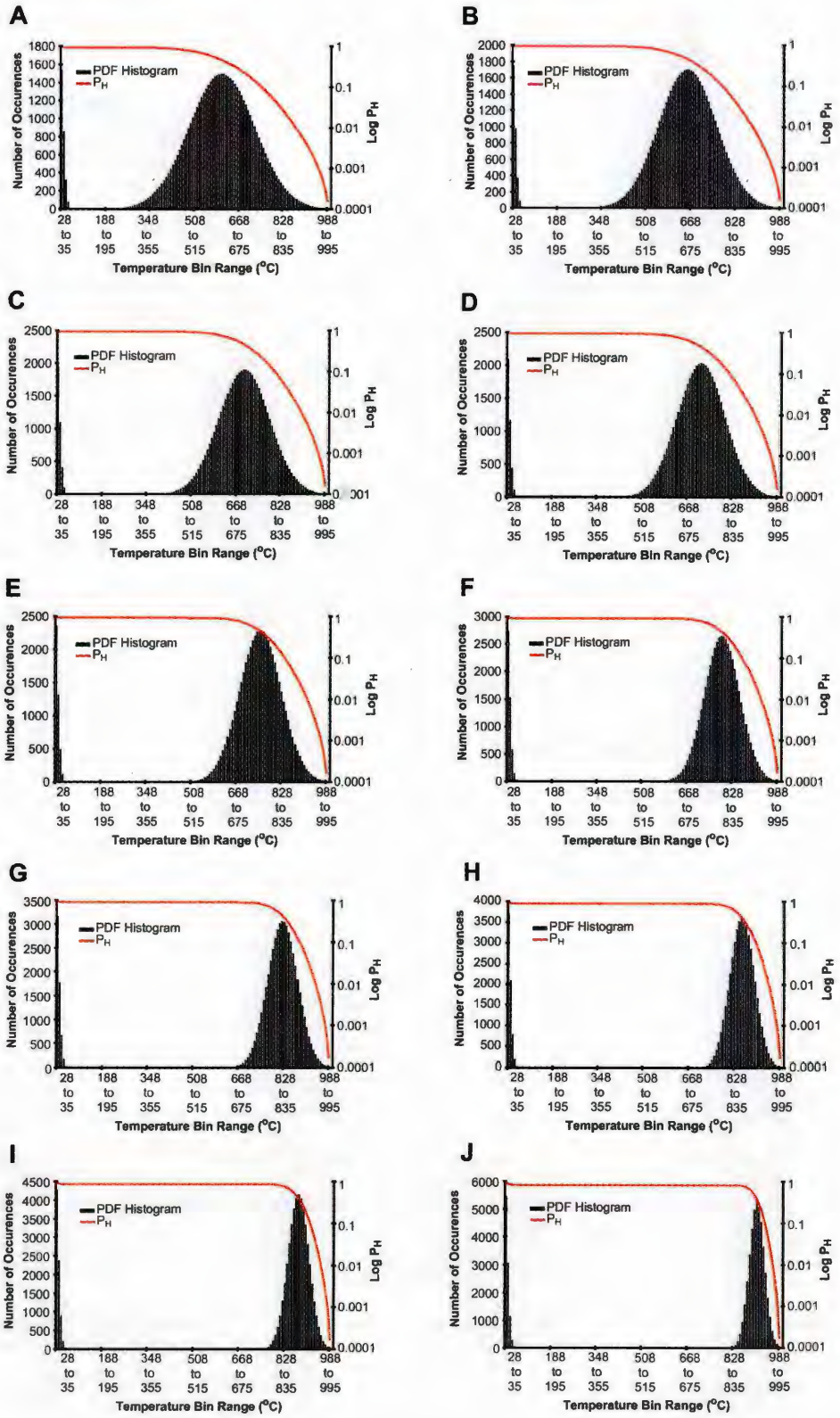

Figure.12.17: Series of histograms depicting a pixel occupied by cool ground and a lava flow. The lava flow in each model run maintains a similar occupying portion of a single pixel area, but increases in mean and in flow vigour indicated by the increasing restriction and profile of the flows curve in each successive model run A to J.

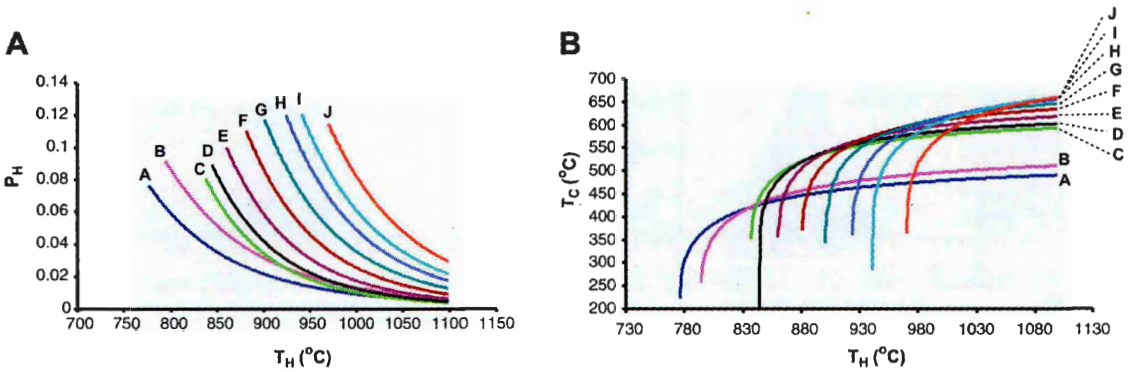

Figure 12.18: Dual-band solutions for varying TH values returned from model runs A to J simulating flows depicted within figure 12.17. (A) returned P_H solutions & (B) returned T_C solutions.

The set of P_H estimates shown within figure 12.18a bear a greater similarity to those solutions displayed within figure 12.12a, obtained from the unimodal models displayed within figure 12.11, than those solutions obtained for the bimodal thermal distributions discussed in the previous two sections.

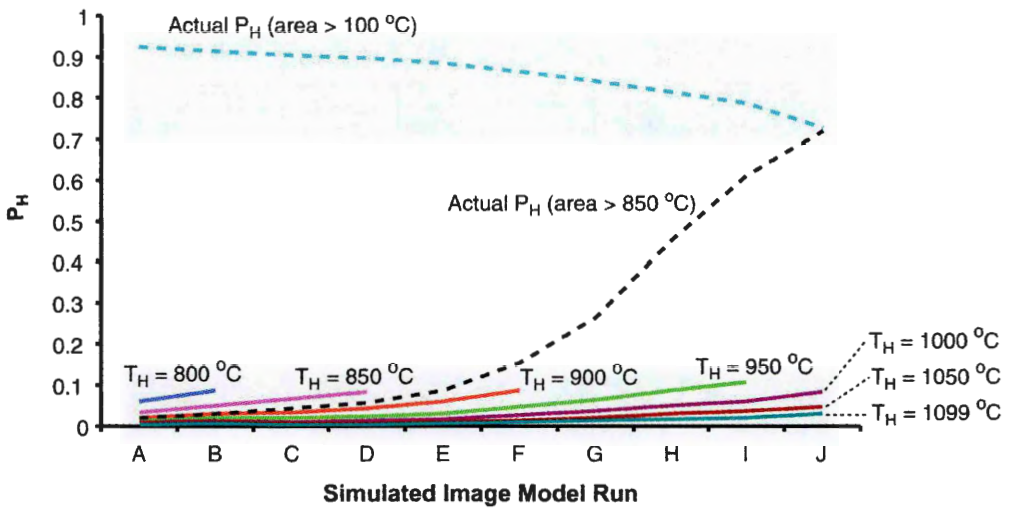

Figure 12.19: Graphical representation of estimated area representing PH from actual synthetic histogram at various model runs A to J.

Whilst the simulated histogram (figure 12.17) narrows and the mean temperature increases as the curve moves to higher temperatures, the number of pixels above the two thresholds set at 100°C and 850°C increases. A threshold of 100°C was chosen so as to distinguish the entire curve associated with the flow, and 850°C the relative amount of material associated with exposed core

Solutions for P_H are available from T_H temperatures that are increasingly staggered with each model run. The range of P_H estimates returned are very similar to those returned within figure 12.12a, with the range of values covered becoming increasingly restricted with each successive model run. Figure 12.19 allows a direct comparison between the solutions returned from the dual-band procedure and an actual value based on the number of pixels present above a threshold temperature.

Two different threshold temperatures are used so as to be able to distinguish between the two curves used to create the synthetic bimodal temperature distribution. A threshold of >100°C identifies all pixels associated with the lava flow simulated by the second bell-shaped curve. This remains mostly constant through the 10 model runs. A threshold of >850°C relates to cracks within a crust of a lava flow exposing the core. The 10 separate models here simulate a set of increasingly active flows, which corresponds to a greater amount of material exposed that is closer to the original eruption temperature. The curve depicting this ($P_{H\ (>800°C)}$) increases sharply within the final 6 runs indicating this increase in simulated flow activity.

This pattern of actual P_H solutions and those obtained from the procedure are again very similar to that from the unimodal simulation of a pixel containing solely a lava flow in figure 12.13. Solutions for P_H increasingly underestimate the value for $P_{H(>850°C)}$ with each successive model run. The final model J returns a P_H of f~0.03 at $T_{H(=1099°C)}$ whilst the actual area present where temperatures >850°C occupies f 0.69. The solutions for P_H obtained from the dual-band procedure for any T_H temperature used identify that each successive model run possesses a greater amount of material exposed at high temperatures. These solutions, as we have encountered previously for each set of simulations, are woeful underestimates of the true area akin to an actual value of P_H.

12.1.9. Comparison of T_C and T_H between dual-band solutions and direct estimates derived from original model runs

Figure 12.18b displays the resulting T_C solutions obtained from the dual-band procedure applied to the simulated pixels highlighted within figure 12.17. A very similar pattern of solutions is returned which are reminiscent of those solutions obtained from the similar unimodal model estimates displayed within figure 12.12b. Solutions are available from staggered values of T_H supplied to the procedure, as in figure 12.18a. The range of temperatures returned for T_C for each of the model runs used within this section do not reflect the rate of increase in temperature of the second histogram curve simulating the flow. If T_H is akin to the areas within the flow that are close or at eruption temperature, then T_C must represent the remaining temperature distribution within the simulated pixel. In this set of model runs the mean temperature, which must be a weighted average due to the constant pixel fraction occupied by the cool ground, increases from ~ 400°C to 820°C+ for the final model pixel. The returned T_C solutions only span a range of 520°C to 620°C, once the steep initial onset in solutions has been discounted.

Figure 12.20a & b displays the mean temperatures of the respective fractional areas P_C and P_H, returned by the dual-band procedure. Figure 12.20a shows a clear distinction between the values of T_C from each model run. These values span a greater range of temperatures than those estimates of T_C returned from the procedure. Each set of calculated T_C temperatures from the area P_C within the original simulated image over the range of T_H temperatures supplied to the procedure, displays only a very slight increase in temperature as T_H increases. This is again a very similar pattern to that displayed within figure 12.14a.

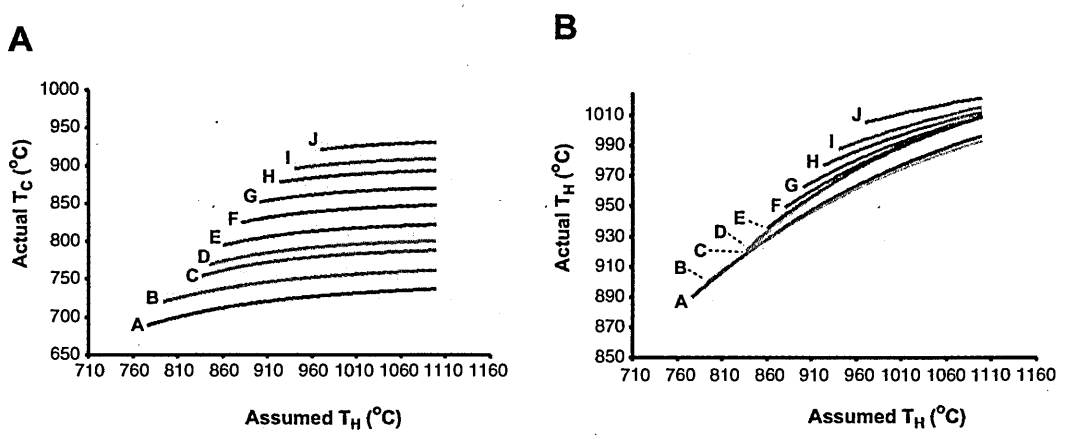

Figure 12.20: Actual temperature values of TC and TH. These values are calculated as the mean radiative temperature represented by the fractional areas returned from the dual-band solutions in figure 12.18 extracted from the original simulated FLIR image for each value of T_H input into the dual-band procedure. Each line A-J represents each model run for pixel with flow showing increasing areas of exposed core (figure 12.17).

The values for T_H calculated from the area occupied by P_H within the original image display a greater range of values than those for T_C. However, with each successive model the gradient of each set of actual T_H values (Y-axis) decreases whilst the actual temperature T_H increases with each successive model. This is a response to the increasing activity dictated by the shape of the histograms within figure 12.32.

The dual-band procedure is here able to identify that flows of increasing activity are present but are not at all sensitive to the areas within the pixel occupied by the cool ground. This is confirmed by the close similarity between the solutions obtained here from these models comprising a bimodal thermal distribution and those solutions discussed within section 10.5 based on a unimodal lava flow thermal distribution model. Estimates for P_H are again underestimates of those obtained by direct extraction from the original synthetic imagery.

13.Appendix V

IDL software used to create image maps of dual-band solutions as discussed in chapter 6.

```
Pro dualband_solution_plotter

;This program produces a graphical format for presentation of dual band solution data in Ph and Tc format.
;Will produce a JPEG or text file with a series of dots, size represented by Ph and colour by Tc.
;Input is a text tab delimited file of format: {ROI number, ROI X, ROI Y, Ph (0:1), Tc}
;Program will work out the dimensions of the ENVI ROI pixels and places a cell based on the 'pix_size_fin' variable (below)
;into a larger image array, exported into the chosen output format.
;As program runs, information on current pixel status, coordinates etc is give in the 'IDL runtime' window'
;so that results can be checked against input data.

;Alongwith the output image format, a scale is also output (size & colour) depending ranges used (automatically calculated)
;this feature can be turned off by setting the 'scale_req' & 'colourSC_req' variables to 0.
;Size of the cell for each pixel represented can be changed by adjusting 'pix_size_fin' to the required value

;WARNING! For single ROI points or very large ROI's, separate ROI into no more than 100x100 chunks to save on processing time
;and likelihood of errors.

;Steve Donegan, UH Manoa April/May 2002

;140502: added in null grid bar onto Ph dot scale for accuracy--forgot to do that before!

;set out all user parameters --change these as required

print,''
print,'                 *******     Welcome to the dual band solution graphical display  *******'
print,''
print,'                 Please check input variables are to your liking -change in code, below this line!'

;*****************************************************************************************************************************************************

;                                                                                                #### CHANGE THESE VARIABLES TO YOUR REQUIREMENTS--SEE NOTES
ABOVE IN HEADER ####

border_req=1                            ;1 if pixel border wanted in output image, 0 if not
border_req_pad=0                ;1 if border required in padded cells, 0 of not
scale_req=1                             ;1 if scale required, 0 if not
colourSC_req=1                          ;1 if colour scale required, 0 if not
background_IMG=1                ;1 if require background to be image pixels (from supplied band in input file), 0 if blank background required
invert_dot=1                    ;1 if require blackdot on blackground, 0 if white dot on background image?
pix_size_fin=25                         ;Size in pixels of each 'box' containing dot representing Tc & Ph (100 large, 25 small)
OP_txt_jpg=0                            ;Output in text file (1) or JPEG (0)
jpeg_quality=100                ;JPEG quality (0-100)
ph_scale_to=0.04                ;Value to which the dots will be scaled to, to avoid tiny dots if a uniform scale is used
;max_temp=1500.0                ;maximum temperature likely to be encountered, used for scaling
temp_bound=25                           ;temperature range either side of maximum and minimum, so that actual min & max are not represented by the
extremes in colour scale (white-black)
scaledev_loop=0                         ;miss out main loop for scale development
ETM_or_ALI=0                            ;1 if ETM or 0 if ALI

;Input file dimensions
xdim_ip=6    ;don't change this!
ydim_ip=1265            ;this is the number of dual band solutions you have --should be the length of your input file

;for the input file the format should be: {no,x,y,Ph,Tc,background info (pixel image data)}        (repeat program for every combination as necesary)
ipfile='C:\Documents and Settings\sjdd2\My
Documents\Donegan\ALI_vs_LANDSAT7_Hawaii_ret\Rawdata_points\290701\ALI\ALI_290701_reg1_1to1265_5pand4p_1265pts.txt'

;General file path
path='C:\Donegan\IDL_OUTPUT'

;OP filename (do not include the 3 letter extension here)
output_filename_A='ALI_290701_reg1_1to1265_5pand4p_1265pts_PICCY_plop'

;*****************************************************************************************************************************************************


print,''
print,'Pixel cell size representation: ',pix_size_fin,' pixels per solution'
if border_req eq 1 then print,'Border Required' else print,'NO border'
if scale_req eq 1 then print,'Scale Required' else print,'No scale'
if colourSC_req eq 1 then print,'Colour scale Required' else print,'NO colour scale'
if ETM_or_ALI eq 1 then print,'SENSOR: ETM+' else print,'SENSOR: ALI'
print,''

if (ETM_or_ALI gt 1) or (ETM_or_ALI lt 0) then begin

        print,'INVALID SENSOR OPTION SPECIFIED!  Duh!'
        stop

endif

if (ETM_or_ALI eq 1) then sensor='ETM+' else sensor='ALI'
if (ETM_or_ALI eq 1) then sensor_units='W/M^2 sr um' else sensor_units='mW/cm^2 sr um'

;Do the do.

;work out the final output filename depending on whether .txt or JPEG requested
if OP_txt_jpg eq 0 then begin
```

```
		ext='.jpg'

		output_filename=strcompress(path+'\'+output_filename_A+ext,/REMOVE_ALL); work out the name

endif

if OP_txt_jpg eq 1 then begin

		ext='.txt'

		output_filename=strcompress(path+'\'+output_filename_A+ext,/REMOVE_ALL); work out the name

endif


;check values
if (pix_size_fin lt 25) or (pix_size_fin gt 100) then print,''
if (pix_size_fin lt 25) or (pix_size_fin gt 100) then print,'Pixel size selected out of bands (25 to 100)'
if (pix_size_fin lt 25) or (pix_size_fin gt 100) then stop

plotpoints=fltarr(xdim_ip,ydim_ip)

;get input file
openr,1,ipfile
readf,1,plotpoints
close,1

;work out the raster points
xmin=min(plotpoints(1,*))
xmax=max(plotpoints(1,*))
ymin=min(plotpoints(2,*))
ymax=max(plotpoints(2,*))

max_temp=max(plotpoints(4,*))
min_arr=where(plotpoints(4,*) ne 0)
min_temp=min(plotpoints(4,min_arr))

;when ROI's collected by ENVI, raster format is used, namely min is top-left

;work out ROI dimensions & whether it is rectangular or not

xdim_plot=xmax-xmin+1	;add one to counter the offset
ydim_plot=ymax-ymin+1

rect_check=(xdim_plot*ydim_plot)

if rect_check eq ydim_ip then print,'Its a rectangle!' else print,'Bugger its not a rectangle!'

;print input ROI attributes
print,''
print,'INPUT ROI ATTRIBUTES:'
print,''
print,'Max X dimension:',xmax,'		Min X dimension:',xmin,'	Min Y dimension:',ymax,'	Min Y dimension:',ymin
print,''
print,'ROI width (X): ',xdim_plot,'		ROI height (Y): ',ydim_plot
print,''
print,'Please wait whilst calculating array final array sizes and rearranging coordinates.....'
print,''

;if not a rectangle must create a null grid into which the points can be plotted--think of it as a square into
;which the chosen points just fit
xdim_rect_create=xdim_plot
ydim_rect_create=ydim_plot

;create an array which holds the coordinates of the no-data 'packing' pixels
rect_create_nodata=fltarr(8,rect_check) ;format: {x,y,actual coordinate true/false? (1/0),Tc,Ph,actual_x,actual_y,image data}
                                                                                                                ;(rect_check is the total
number of coords needed)

count_main=0

for y=0,ydim_rect_create-1 do begin

		for x=0,xdim_rect_create-1 do begin

			rect_create_nodata(0,count_main)=x+xmin
			rect_create_nodata(1,count_main)=y+ymin
			rect_create_nodata(5,count_main)=x
			rect_create_nodata(6,count_main)=y

			count_main=count_main+1.0		;increment the counter, this will be equal to the number of pixels in the padded out ROI

		end
end

;now, which ones are actual pixels found in the original ROI?  use 1 if they are (see format above)
actual_points=fltarr(4,ydim_ip)
actual_points(0,*)=plotpoints(1,*)	;x coords
actual_points(1,*)=plotpoints(2,*)	;y coords
actual_points(2,*)=plotpoints(3,*)	;Ph value
actual_points(3,*)=plotpoints(4,*)	;Tc value

BGimg_points=fltarr(1,ydim_ip)			;create small array for background image data
BGimg_points(*)=plotpoints(5,*)

;if any values less than 0 (i.e. in solar correction -ETM+) then relace with 0's
for h=0,ydim_ip-1 do begin

		if BGimg_points(h) lt 0 then BGimg_points(h)=0

end

BGimg_points(*)=255-(((255/max(plotpoints(5,*)))*BGimg_points(*))/1.9)		;have scaled it to 255 for image output in background colour

;get values to pass onto radiance background scaler
max_rad=(max(plotpoints(5,*)))
min_rad_arr=where(plotpoints(5,*) ne 0)
```

```
min_rad=min(plotpoints(5,min_rad_arr))

;test values
correlation=intarr(rect_check)
match=0
pad=0

dop=fltarr(ydim_ip)

for i=0L,rect_check-1 do begin

        ;if (rect_create_nodata(0:1,i) eq actual_points(0:1,i)) then d=d+1 else d=d+0
        check_x=rect_create_nodata(0:0,i)
        check_y=rect_create_nodata(1:1,i)

        for j=0,ydim_ip-1 do begin

                if check_x(0) eq actual_points(0,j) then det_x=1 else det_x=3      ;dont forget that check_x is classified as an array...
                if check_y(0) eq actual_points(1,j) then det_y=1 else det_y=3

                if (det_x+det_y) eq 2 then dop=i

        end

end



stop
for i=0L,rect_check-1 do begin
print,i
        ;if (rect_create_nodata(0:1,i) eq actual_points(0:1,i)) then d=d+1 else d=d+0
        check_x=rect_create_nodata(0:0,i)
        check_y=rect_create_nodata(1:1,i)

        for j=0,ydim_ip-1 do begin

                if check_x(0) eq actual_points(0,j) then det_x=1 else det_x=3      ;dont forget that check_x is classified as an array...
                if check_y(0) eq actual_points(1,j) then det_y=1 else det_y=3

                ;if coordinates match then coordinates part of original ROI
                if (det_x+det_y) eq 2 then match=match+1
                ;if (det_x+det_y) eq 2 then print,'Yah!'
                if (det_x+det_y) eq 2 then data_Ph=actual_points(2,j)
                if (det_x+det_y) eq 2 then data_Tc=actual_points(3,j)
                if (det_x+det_y) eq 2 then BGimg_data=BGimg_points(j)
                if (det_x+det_y) eq 2 then goto, match_found                                                    ;work out the
solution and record

                ;if coordinates do not match, then padding cell required
                if (det_x+det_y) eq 6 then pad=pad+1
                ;if (det_x+det_y) eq 6 then goto, no_match_found

        end

        match_found:
        print,'match found!'

        ;fill in the Tc & Ph values
        if (det_x+det_y) eq 2 then rect_create_nodata(3,i)=data_Ph
        if (det_x+det_y) eq 2 then rect_create_nodata(4,i)=data_Tc
        if (det_x+det_y) eq 2 then rect_create_nodata(2,i)=1 else rect_create_nodata(2,i)=3
        if (det_x+det_y) eq 2 then rect_create_nodata(7,i)=BGimg_data

end

stop
;ok, we now have the subscripts as to where the true ROI coords are and their data, now must determine whether there is a dual band solution

;draw cell codes are: dual band solution=1, pixel present, but no solution=2, padding pixel required=3

for i=0,count_main-1 do begin

if (rect_create_nodata(2,i) eq 1) and ((rect_create_nodata(3,i) or rect_create_nodata(3,i)) eq 0) then rect_create_nodata(2,i)=2

end

;send out to drawing procedures

;set colours to be used in all procedures for consistency (remember, 8 bit greyscale)

;Background colour
BG_colour=255           ;(WHITE)
DRAW_colour=0           ;(BLACK)    (where Tc not represented by various shades of grey)
if (border_req eq 1) then BORDER_colour=0 else BORDER_colour=255        ;Border black (0) if border required

;set standard array size as defined in definitions at start of program
xmain=pix_size_fin
ymain=xmain;ALWAYS maintain a square array!

null_queary=1
no_data_query=1

image_pos_x=fltarr(2,count_main)
image_pos_y=fltarr(2,count_main)

;now must move through the ROI dual band info in raster format so as to fill up final_array
for j=0,count_main-1 do begin

        ;x start & end
        if rect_create_nodata(5,j) eq 0 then begin
        x_s=float(0)
        x_e=float(x_s+xmain)
        endif

        if rect_create_nodata(5,j) eq 1 then begin
        x_s=float(((rect_create_nodata(5,j)*xmain))+rect_create_nodata(5,j))
```

```
x_e=float(x_s+xmain)
endif

if rect_create_nodata(5,j) gt 1 then begin
x_s=float(((rect_create_nodata(5,j)*xmain))+rect_create_nodata(5,j));+rect_create_nodata(5,j-1))          ;truncate this as extra bit confusing the
final array insertion
x_e=float(x_s+xmain)
endif

;y start & end
if rect_create_nodata(6,j) eq 0 then begin
y_s=float(0)
y_e=float(y_s+ymain)
endif

if rect_create_nodata(6,j) eq 1 then begin
y_s=float(((rect_create_nodata(6,j)*ymain))+rect_create_nodata(6,j))
y_e=float(y_s+ymain)
endif

if rect_create_nodata(6,j) gt 1 then begin
y_s=float(((rect_create_nodata(6,j)*ymain))+rect_create_nodata(6,j));+rect_create_nodata(6,j));truncate this as extra bit confusing the final array
insertion
y_e=float(y_s+ymain)

endif

;feed into coordinate array
image_pos_x(0,j)=x_s
image_pos_x(1,j)=x_e
image_pos_y(0,j)=y_s
image_pos_y(1,j)=y_e

;print,image_pos_x(0,j),image_pos_x(1,j),image_pos_y(0,j),image_pos_y(1,j);,prev_val

end
;stop
;now, must create an array that will hold the final data that can be imaged together
final_width=max(image_pos_x)+1
final_height=max(image_pos_y)+1

final_array=fltarr(final_width,final_height)

if scaledev_loop eq 1 then goto,scaledev

;now main loop for image calculation
for i=0,count_main-1 do begin

print,''
print,'Processing pixel: ',i+1
print,'ROI coordinate      X=',rect_create_nodata(0,i),'          Y=',rect_create_nodata(1,i),'
(',rect_create_nodata(5,i),',',rect_create_nodata(6,i),')'
print,'Tc=',rect_create_nodata(4,i),'      Ph=',rect_create_nodata(3,i)

;draw cell codes are: dual band solution=1, pixel present, but no solution=2, padding pixel required=3
draw_cell=rect_create_nodata(2,i)

;set the data to send to the procedures
ph_val=rect_create_nodata(3,i)
Tc_val=rect_create_nodata(4,i)
ph_scale=ph_scale_to
bord=border_req


if background_IMG eq 1 then BG_colour=rect_create_nodata(7,i)   ;if background image required, set it to the pre calculated 8 bit scaled image output
BG_colour_pad=255      ;set padding background to white where required
scale_d=0                    ;scale not on this round

;go to imaging procedures

;if dual band solution available for representation
if draw_cell eq 1 then begin

        print,'Dual band solution acquired'


DOT_CREATE,scale_d,BG_colour,DRAW_colour,BORDER_colour,max_temp,min_temp,temp_bound,xmain,ymain,ph_val,ph_scale,tc_val,op_arr_size
_x,op_arr_size_y,cell_grid

        returned_array=cell_grid(*,*)
        ;stop
endif

;if dual band solution not available, despite there being a ROI pixel present
if draw_cell eq 2 then begin

        print,'No dual band solution: NULL DATA'


NULL_CREATE,BG_colour,DRAW_colour,BORDER_colour,xmain,ymain,null_queary,x_size,y_size,op_arr_size_x,op_arr_size_y,cell_grid_null

        returned_array=cell_grid_null(*,*)

endif

;rectangular image pixel padding required--will return empty pixel of same area as above with/without border.
if draw_cell eq 3 then begin

        if border_req_pad eq 1 then BORDER_colour_pad=0 else BORDER_colour_pad=255

        print,'Padding cell required'


NO_DATA,BG_colour_pad,DRAW_colour,BORDER_colour_pad,xmain,ymain,no_data_query,x_size,y_sizeop_arr_size_x,op_arr_size_y,cell_grid_nod
ata

        returned_array=cell_grid_nodata(*,*)
```

```
		endif


		;reassemble into main image array

		;print,'x end- xstart= ',x_coord_merge_end-x_coord_merge_start,'   yend-ystart',y_coord_merge_end-y_coord_merge_start

		print,'Inserting into array, AREA: ',image_pos_x(0,i),' : ',image_pos_x(1,i),'          & ',image_pos_y(0,i),' : ',image_pos_y(1,i)
		final_array(image_pos_x(0,i):image_pos_x(1,i),image_pos_y(0,i):image_pos_y(1,i))=returned_array;(*,*)


end

;Due to the way IDL calculates & manipulates arrays, must flip it vertically so that correct orientation is preserved when writing to output file

final_array_trans=fltarr(final_width,final_height)

for i=0,final_width-1 do begin

		for j=0,final_height-1 do begin

			final_array_trans(i,((final_height-1)-j))=final_array(i,j)

		end

end                                                                     ;that SEEMED to work (I hope)!


if OP_txt_jpg eq 1 then begin

		print,''
		print,'Please wait while creating TEXT output file.....'

		;write to an output file, initially text
		openw,1,output_filename

		for j=0,final_height-1 do begin

			printf,1,format='(1000(F0, :, "          "))',final_array_trans(*,j)

		end

		close,1`

endif

If OP_txt_jpg eq 0 then begin

		print,''
		print,'Please wait while writing to JPEG file.....'

		;write to jpeg
		WRITE_JPEG, output_filename, final_array_trans, QUALITY=jpeg_quality

endif

scaledev:

print,'Please wait while writing to creating scale files (if required).....'


;****************** write scale file for colours (greys) ******************

;if required, create colour scale and dot size scales with accompanying text file
max_Tc=max(rect_create_nodata(4,*))
min_Tc=min(rect_create_nodata(4,*))

;create colour scale (as in GREYSCALE 0-255 based on min & max Tc  0=black=coolest 255=white=hottest)

;remember that in the main procedure, maximum temperature is 1000, & so is scaled for this range
scale_width=40
scale_length=100.0
scale_array=fltarr(scale_width,scale_length)
scale_array(*,*)=255
scale_array_border=fltarr(scale_width+2,scale_length+2)

d=fltarr(scale_length)

for j=0,scale_length-1 do begin

		mult=float(max_temp/scale_length)*(j+1)

		bin_colour=(255.0/max_temp)*(mult)

		scale_array(*,j)=bin_colour

end

;add black border of 1 pixel width
scale_array_border(0:*)=0                                               ;left
scale_array_border((scale_width+2)-1:*)=0          ;right
scale_array_border(*,0)=0                                               ;top
scale_array_border(*,(scale_length+2)-1)=0         ;bottom

;fill in the scale data

;scale_array(*,*)=255
scale_array_border(1:(scale_width+2)-2,1:(scale_length+2)-2)=scale_array(*,*)


;write scale to JPEG file
Tc_append='_Tc_scale.jpg'
TC_scale_OPfile=strcompress(path+'\'+output_filename_A+Tc_append,/REMOVE_ALL)

WRITE_JPEG, TC_scale_OPfile, scale_array_border, QUALITY=100
```

```
;****************** write scale file for dots ******************

max_ph=max(rect_create_nodata(3,*))

;must separate out the 0's
no_zero=where(rect_create_nodata(3,*) ne 0)
min_ph=min(rect_create_nodata(3,no_zero))

;will create 5 dots to represent: SMALLEST; quarter; middle; three-quarters; LARGE

;work out the sizes of the dots for these sizes
dot_size_scale=fltarr(5)
dot_size_scale(0)=min_ph                                                    ;smallest
dot_size_scale(1)=((max_ph-min_ph)/4)+min_ph                    ;1/4
dot_size_scale(2)=(((max_ph-min_ph)/4)*2)+min_ph        ;1/2
dot_size_scale(3)=(((max_ph-min_ph)/4)*3)+min_ph        ;3/4
dot_size_scale(4)=max_ph                                                    ;largest

;create a scale that will fit with the main dot drawing program (i.e. use that function/procedure)

;create an image array to hold the returned arrays.  stack 5 vertically
dot_scale_array=fltarr(xmain+1,(ymain+1)*6)
dot_scale_array_final=fltarr((xmain+1)+2,((ymain+1)*6)+2);  final array to include surrounding borders
right_max=((xmain+1)+2)-1
bottom_max=(((ymain+1)*6)+2)-1

dot_scale_image_coords=intarr(2,6)      ;define array start points as top left hand (rastered)

;cell 1
dot_scale_image_coords(0,0)=0
dot_scale_image_coords(1,0)=0

;cell 2
dot_scale_image_coords(0,1)=0
dot_scale_image_coords(1,1)=ymain

;cell 3
dot_scale_image_coords(0,2)=0
dot_scale_image_coords(1,2)=(ymain*2)+1

;cell 4
dot_scale_image_coords(0,3)=0
dot_scale_image_coords(1,3)=(ymain*3)+2

;cell 5
dot_scale_image_coords(0,4)=0
dot_scale_image_coords(1,4)=(ymain*4)+3

;cell 6 (null grid bar)
dot_scale_image_coords(0,5)=0
dot_scale_image_coords(1,5)=(ymain*5)+5

;Do da dots
for i=0,4 do begin

        tc_val=max_temp+temp_bound      ;draw dots as black, represented by highest temperature here
        ph_val=dot_size_scale(i)  ;take the size from the calculated sizes above
        BORDER_colour=255                       ;take out individual cell borders--have one main border
        ph_scale=ph_scale_to            ;scale to max size
        BG_colour=255                                   ;set background colour to white
        scale_d=1

        DOT_CREATE,scale_d,BG_colour,DRAW_colour,BORDER_colour,max_temp,min_temp,temp_bound,xmain,ymain,ph_val,ph_scale,tc_val,op_arr_size
_x,op_arr_size_y,cell_grid

        ;insert returned cell into scale image array
        dot_scale_array(dot_scale_image_coords(0,i):*,dot_scale_image_coords(1,i):dot_scale_image_coords(1,i)+ymain)=cell_grid

end

;Do da null grid bar

NULL_CREATE,BG_colour,DRAW_colour,BORDER_colour,xmain,ymain,null_queary,x_size,y_size,op_arr_size_x,op_arr_size_y,cell_grid_null

returned_array_scale=cell_grid_null(*,*)

dot_scale_array(dot_scale_image_coords(0,5):*,dot_scale_image_coords(1,5):dot_scale_image_coords(1,5)+ymain)=returned_array_scale

;stop
;add main border
dot_scale_array_final(0,*)=0                                    ;topline
dot_scale_array_final(0,bottom_max)=0 ;bottomline
dot_scale_array_final(0,*)=0                                    ;leftline
dot_scale_array_final(0,right_max)=0    ;rightline

;add in centre info from above calculated
dot_scale_array_final(1:right_max-1,1:bottom_max-1)=dot_scale_array

;write scale to JPEG file
Ph_append='_Ph_scale.jpg'
Ph_scale_OPfile=strcompress(path+'\'+output_filename_A+Ph_append,/REMOVE_ALL)

WRITE_JPEG, Ph_scale_OPfile, dot_scale_array_final, QUALITY=100


;Construct scale for background radiance if used.

if background_IMG eq 1 then begin

        ;in the background image, the darker the supplied radiance values, the higher the radiance.

        max_rad_txt=max_rad                                     ;actual value in mW/cm^2 sr um
        min_rad_txt=min_rad
        max_sc_rad=max(BGimg_points)    ;8 bit scaled max
        min_sc_rad=min(BGimg_points)    ;8 bit scaled min
```

```
		rad_scale_width=40
		rad_scale_length=100.0
		rad_scale_array=fltarr(scale_width,scale_length)
		rad_scale_array(*,*)=255
		rad_scale_array_border=fltarr(scale_width+2,scale_length+2)

		d=fltarr(rad_scale_length)

		for j=0,rad_scale_length-1 do begin

			mult=float((max_sc_rad-min_sc_rad)/rad_scale_length)

			bin_colour=(max_sc_rad-(j*mult))

			rad_scale_array(*,j)=bin_colour

		end

		;add black border of 1 pixel width
		rad_scale_array_border(0:*)=0                                   ;left
		rad_scale_array_border((scale_width+2)-1:*)=0     ;right
		rad_scale_array_border(*,0)=0                                   ;top
		rad_scale_array_border(*,(scale_length+2)-1)=0    ;bottom

		;fill in the scale data

		;scale_array(*,*)=255
		rad_scale_array_border(1:(rad_scale_width+2)-2,1:(rad_scale_length+2)-2)=rad_scale_array(*,*)

		;write scale to JPEG file
		BG_RAD_scale_append='_BG_RAD_scale.jpg'
		BG_RAD_scale_OPfile=strcompress(path+'\'+output_filename_A+BG_RAD_scale_append,/REMOVE_ALL)

		WRITE_JPEG, BG_RAD_scale_OPfile, rad_scale_array_border, QUALITY=100

endif

;********************************** Write info on scales to a text file, so can add in in Corel Draw/Adobe Illustrator etc **********************
textINFO='_scales_INFO.txt'
scaleINFO=strcompress(path+'\'+output_filename_A+textINFO,/REMOVE_ALL)

openw,1,scaleINFO

printf,1,'************ INFORMATION ON SCALES **********************
printf,1,''

printf,1,Ph_scale_OPfile
printf,1,TC_scale_OPfile
printf,1,output_filename
printf,1,''
printf,1,'Sensor chosen: ',sensor
printf,1,''
printf,1,'Tc colour grey scale'
printf,1,'Actual Max Temp: ',max_temp
printf,1,'Actual Min Temp: ',min_temp
printf,1,'Scale Max Temp: ',max_temp+temp_bound
printf,1,'Scale Min Temp: ',min_temp-temp_bound
printf,1,''
printf,1,'Ph dot size scale'
printf,1,'Min size (1): ',dot_size_scale(0)
printf,1,'1/4 size (2): ',dot_size_scale(1)
printf,1,'1/2 size (3): ',dot_size_scale(2)
printf,1,'3/4 size (4): ',dot_size_scale(3)
printf,1,'Max size (5): ',dot_size_scale(4)
printf,1,''
printf,1,'Background Radiance scale'
printf,1,'Maximum radiance: ',max_rad,' ',sensor_units
printf,1,'Minimum radiance: ',min_rad,' ',sensor_units
printf,1,''
printf,1,'Program: Steve Donegan UH Manoa Hawaii, April/May 2002, Dual Band solution visualiser'

close,1

;finish 'er off.

print,''
print,'Have printed main image output to a file at: ',output_filename
print,''
print,'Tc greyscale colour scale:                                    ',Tc_scale_OPfile
print,''
print,'Ph dot size scale:                                           ',Ph_scale_OPfile
print,''
print,'Associated text for scales:                                  ',scaleINFO
print,''
print,''
print,'                                                  THANKYOU AND GOODBYE !!'
print,''

;&&&&&&&&&&&&& test code &&&&&&&&&&&&&

;&&&&&&&&&&&&&&&&&&&&&&&&&&&&&&&&&&&&&&&&&

stop            ;so I can access all the lovely numbers!

end             ; END OF MAIN PROGRAM!


;*********************************************************************************************************


;Procedures for drawing dots etc from now on
```

```
Pro
DOT_CREATE,scale_d,BG_colour,DRAW_colour,BORDER_colour,max_temp,min_temp,temp_bound,xmain,ymain,ph_val,ph_scale,tc_val,op_arr_size_x,op_arr_siz
e_y,cell_grid

;IMPORT: single value for Ph & Tc

;EXPORT: size of returned array in x & y dimensions and array itself, ready to be incorporated into main program.

;Procedure to draw a dot of relevant size and colour to represent Ph & Tc data respectively
;refer to "dot_creater.XLS" for info on development of circle drawing algorithmn.

;Steve D, April 30th 2002 UH Manoa

;will represent the size of Ph, by a scaled circle/dot, the color of which is represented by Tc
;use a 8 bit (0-255) greyscale for colour. Each 'cell' which will contain the circle/dot will be 100x100 pixels, for each pixel
;processed by the dual band programs


;Background settings for graphics..

;ok, must work out size of circle/dot.  100/2 pixels
Ph_actual=(1/ph_scale)*ph_val          ;scale to the value entered at the start of the program
dot_multiplier=xmain                   ;multiply to input so dot size relevant to output and input array

;convert to a radius in the 100x100 grid -remember that fractional areas cannot be larger than 1..
;put some logic in to prevent the maximum dot size exceeding the prescribed array size and also to ensure a minimum dot size
if Ph_actual gt 0.9 then dot_rad=(fix((dot_multiplier*Ph_actual)/2)) else  dot_rad=((fix((dot_multiplier*Ph_actual)/2))+1)

;what is the temperature to be represented? (max to be represented=1000)
Tc_colour=tc_val
temp_plus_minus=temp_bound                                                    ;add in for colur highlight
temp_range=(max_temp+temp_plus_minus);+(2*temp_plus_minus);work out the dynamic temp range for this run
bin_colour=255-((255.0/temp_range)*Tc_colour)          ;should give a value on a 0-255 range
BG_colour=BG_colour                                                           ;minimum colour on
greyscale
Border_colour=BORDER_colour                                                   ;pixel border colour
max_arr=xmain                                                                 ;maximum size
of output grid

;if scale set to black
if scale_d eq 1 then bin_colour=0
if bin_colour lt 0 then stop

;safety net
if (Ph_actual*dot_multiplier) ge max_arr then print,''
if (Ph_actual*dot_multiplier) ge max_arr then print,'Ph_actual error in size translation --comprende?'
if (Ph_actual*dot_multiplier) ge max_arr then print,'HINT: check that the ph_scale value accurately represents a likely maximum size for the dot!'
if (Ph_actual*dot_multiplier) ge max_arr then print,''
if (Ph_actual*dot_multiplier) ge max_arr then stop

;create main array of maximum size per pixel
op_arr_size_x=max_arr+1
op_arr_size_y=max_arr+1
cell_grid=fltarr(op_arr_size_x,op_arr_size_y)          ;first to create the dot, create a box of same size as diameter and also a border for the pixel

;development arrays
pi=3.14159

;define the bounding square of the circle into quarters so can compute the circle/dot
;set up array to hold initial quarter/segment of dot
grid_1=intarr(dot_rad,dot_rad)

for y=0,dot_rad-1 do begin
        for x=0,dot_rad-1 do begin

                ;use bloody pythagoras as IDL seems to get arsey about using sin etc.... (and cut number f lines by literally 200!) yeah baby.
                ;method works by calculating a triangle using x & y and working out the length of the hypotoneuse to the maximum array dimensions
                ;where this hyp length exceeds the radius, it is not in circle, where it is equal or less, it is in circle
                ;then transpose and add the arrays to construct a dot

                ;Q1
                hyp1=sqrt((((dot_rad-1)-(x))^2)+(((dot_rad-1)-(y))^2))
                if hyp1 le dot_rad+1 then grid_1(x,y)=bin_colour else grid_1(x,y)=BG_colour

        end
end

;Q2
grid_2=rotate(grid_1,1)

;Q3
grid_3=rotate(grid_1,2)

;Q4
grid_4=rotate(grid_1,3)

;concatenate arrays into one array in order, 2,3,4,1 (to make 1 dot of radius=dot_rad)
topline=[grid_4,grid_3]
bottomline=[grid_1,grid_2]

one_big_nice_dot=intarr(dot_rad*2,dot_rad*2)
one_big_nice_dot(0:(dot_rad*2)-1,dot_rad:(dot_rad*2)-1)=topline
one_big_nice_dot(0:(dot_rad*2)-1,0:dot_rad-1)=bottomline

;merge the dot array into the full array for export back into mainmapping program

;do this by creating new arrays and 'padding' out the one big nice dot
;either side of array
LH_side_same_width=intarr((max_arr-(dot_rad*2))/2,(dot_rad*2))
RH_side_same_width=intarr((max_arr-(dot_rad*2))/2,(dot_rad*2))
LH_side_same_width(*,*)=BG_colour
RH_side_same_width(*,*)=BG_colour

middle_strip=[LH_side_same_width,one_big_nice_dot,RH_side_same_width]

;top of array
top_strip=intarr(max_arr,(max_arr-(dot_rad*2))/2)
```